# $NO_x$ Control Options and Integration for US Coal Fired Boilers

**Final Report**

Reporting Period Start Date: February 14, 2000
Reporting Period End Date: June 30, 2006

Mike Bockelie, REI
Marc Cremer, REI
Kevin Davis, REI
Martin Denison, REI
Adel Sarofim, REI
Connie Senior, REI
Hong-Shig Shim, REI
Dave Swenson, REI
Bob Hurt, Brown University
Eric Suuberg, Brown University
Eric Eddings, University of Utah
Kevin Whitty, University of Utah
Larry Baxter, Brigham Young University
Calvin Bartholomew, Brigham Young University
William Hecker, Brigham Young University

June 30, 2006

DOE Cooperative Agreement No: DE-FC26-00NT40753

Reaction Engineering International
77 West 200 South, Suite 210
Salt Lake City, UT 84101

# Disclaimer

# Abstract

This is the Final Report for DOE Cooperative Agreement No: DE-FC26-00NT40753. The goal of the project was to develop cost-effective analysis tools and techniques for demonstrating and evaluating low-$NO_x$ control strategies and their possible impact on boiler performance for boilers firing US coals. The Electric Power Research Institute (EPRI) provided co-funding for this program.

This project included research on

- in furnace NOx control
- impacts of combustion modifications on boiler operation
- Selective Catalytic Reduction (SCR) catalyst testing
- Ammonia adsorption / removal on fly ash.

Important accomplishments were achieved in all aspects of the project.

Rich Reagent Injection (RRI), an in-furnace NOx reduction strategy based on injecting urea or anhydrous ammonia into fuel rich regions in the lower furnace, was evaluated for cyclone-barrel and PC fired utility boilers. Field tests successfully demonstrated the ability of the RRI process to significantly reduce NOx emissions from a staged cyclone-fired furnace operating with overfire air. The field tests also verified the accuracy of the Computational Fluid Dynamic (CFD) modeling used to develop the RRI design and highlighted the importance of using CFD modeling to properly locate and configure the reagent injectors within the furnace.

Low NOx firing conditions can adversely impact boiler operation due to increased waterwall wastage (corrosion) and increased soot production. A corrosion monitoring system that uses electrochemical noise (ECN) corrosion probes to monitor, on a real-time basis, high temperature corrosion events within the boiler was evaluated. Field tests were successfully conducted at two plants. The Ohio Coal Development Office provided financial assistance to perform the field tests. To investigate soot behavior, an advanced model to predict soot production and destruction was implemented into an existing reacting CFD modeling tool. Comparisons between experimental data collected in a pilot scale furnace and soot behavior predicted by the CFD model showed good agreement.

Field and laboratory tests were performed for SCR catalysts used for coal and biomass co-firing applications. Fundamental laboratory studies were performed to better understand mechanisms involved with catalyst deactivation. Field tests with a slip stream reactor were used to create catalyst exposed to boiler flue gas for firing coal and for co-firing coal and biomass. The field data suggests the mechanisms leading to catalyst deactivation are, in order of importance, channel plugging, surface fouling, pore plugging and poisoning. Investigations were performed to better understand the mechanisms involved with catalyst regeneration through mechanical or chemical methods. A computer model was developed to predict NOx reduction across the catalyst in a SCR.

Experiments were performed to investigate the fundamentals of ammonia / fly ash interactions with relevance to the operation of advanced NOx control technologies such as selective catalytic

reduction. Measurements were performed for ammonia adsorption isotherms on commercial fly ash samples subjected to a variety of treatments and on the chemistry of dry and semi-dry ammonia removal processes. This work resulted in the first fundamental ammonia isotherms on carbon-containing fly ash samples. This work confirms industrial reports that aqueous solution chemistry takes place upon the introduction of even very small amounts of water, while the ash remains in a semi-dry state.

# Table of Contents

# List of Figures

Page

Page

Page

Page

# List of Tables

Page

Page

# Acronyms and Abbreviations

| | |
|---|---|
| AEP | American Electric Power |
| ALTA | Advanced Layered Technology Approach |
| BET | Brunauer, Emmet and Teller |
| Btu/lb | British thermal unit(s)/pound |
| CARM | Computer Assisted Reduced Mechanism |
| CCS | Catalyst characterization system |
| CEM | Continuous emission monitor |
| CFD | Computational Fluid Dynamics |
| CM | Corrosion Management |
| CNCIG | Cyclone NOx Control Interest Group |
| DCS | Distributed control system |
| DOE | US Department of Energy |
| DR | Dubinin-Radushkevich |
| EERC | Energy & Environmental Research Center |
| EPRI | Electric Power Research Institute |
| ESP | Electrostatic precipitator |
| FGR | Flue gas recirculation |
| FTIR | Fourier Transform Infrared |
| GT | Gas tempering |
| IR | Infrared |
| ISSR | *in situ* spectroscopy reactor |
| LNB | Low-$NO_x$ burner |
| LNFS | Low-$NO_x$ firing system |
| LOI | Loss on ignition |
| MS | Mass spectrometry |
| MWe | Megawatt (electric) |
| NETL | National Energy Technology Laboratory |
| NSR | Normalized stoichiometric ratio |
| OCDO | Ohio Coal Development Office |
| PA | Photoacoustic |
| PC | Pulverized coal |

| | |
|---|---|
| PRB | Powder River Basin |
| REI | Reaction Engineering International |
| RMS | Root mean squared |
| RRI | Rich Reagent Injection |
| SCR | Selective Catalytic Reduction |
| SEM | Scanning electron microscopy |
| SNCR | Selective non-Catalytic Reduction |
| SOFA | Separated overfire air |
| SR | Stoichiometric ratio |
| ToFSIMS | Time-of-flight-secondary-ion mass spectroscopy |
| TPD | Temperature programmed desorption |
| UT | Ultrasonic tube |
| XPS | X-ray photoelectron spectroscopy |

# 1. Executive Summary

The work conducted in this project received funding from the Department of Energy under Cooperative Agreement No: DE-FC26-00NT40753. The project had a period of performance that started February 14, 2000 and continued through March 31, 2006.

The goal of the project was to develop cost-effective analysis tools and techniques for demonstrating and evaluating low-$NO_x$ control strategies and their possible impact on boiler performance for boilers firing US coals.

The project involved researchers from REI, University of Utah, Brown University, Brigham Young University and EPRI. The project consisted of four technical tasks:

- In-Furnace NOx Control - evaluation and full scale field tests of Rich Reagent Injection (RRI) for in-furnace $NO_x$ control;
- Impacts of Combustion Modifications - investigate waterwall corrosion and soot generation due to low NOx firing conditions;
- Ammonia Adsorption / Removal From Fly Ash - investigate fundamental issues for ammonia adsorption and removal from fly ash; and
- Selective Catalytic Reduction (SCR) catalyst testing - investigate catalyst deactivation and poisoning fundamentals, field tests of catalysts in a boiler slip stream reactor, catalyst regeneration and SCR model development.

The project was quite successful. There was considerable interest from industry in the project due to the success of the RRI technology and waterwall corrosion monitoring system.

The major accomplishments of the program are highlighted below.

**In Furnace NOx Control**

Rich Reagent Injection (RRI) is a NOx reduction strategy based on injecting urea or anhydrous ammonia into fuel rich regions in the lower furnace. Field tests and Computational Fluid Dynamic (CFD) modeling were used to evaluate the use of RRI to reduce NOx emissions for cyclone barrel and pulverized coal (PC) fired electric utility boilers.

1. The ability of the RRI process to significantly reduce NOx emissions from a staged cyclone-fired furnace operating with overfire air (OFA) was successfully demonstrated in two field tests of this technology.

    a) NOx reductions of 30% with less than 1-ppm ammonia slip were obtained with RRI under full load conditions in a 130 MW, three-barrel cyclone-fired furnace. RRI in combination with SNCR was found to yield up to 55% NOx reduction under full load conditions, to reduce NOx emissions from this unit to as low as 0.23 lb/MMBtu, with less than 5 ppm ammonia slip. Tests indicated that NOx reduction due to RRI and SNCR was nearly additive (i.e., SNCR performance was not negatively impacted by RRI).

b) NOx reductions of approximately 30% with less than 1 ppm ammonia slip were obtained with RRI under full load conditions in a ten-barrel, 500 MW cyclone-fired furnace. RRI was found to reduce NOx emissions from this unit to 0.27 lb/MMBtu from baseline levels (with OFA) of 0.38 lb/. Modeling studies suggest that NOx reductions could be further improved by modifying the FGR operation or reducing the lower furnace stoichiometry. In particular, modeling studies indicate the combination of deeper staged firing conditions, RRI and SNCR would reduce the NOx emissions to less than 0.15 lb/MMBtu – without the use of a SCR.

2. The field tests confirmed the CFD model predictions and demonstrated the importance of accurate CFD modeling for developing a successful RRI design. The CFD predictions of $NO_x$ reduction, ammonia slip, and reagent usage were consistent with the field observations for the two field tests. The CFD modeling results have proven to be very reliable, and are considered essential to proper location and configuration of the injectors.

3. Evaluations of RRI designs for PC fired utility boilers proved more challenging than for cyclone fired units. For a front wall fired system CFD modeling evaluations indicate NOx reductions of up to 18% could be obtained. A critical issue is developing an injection strategy that creates the furnace conditions required for amine enhanced NOx reduction to occur. Results from a single burner modeling study indicated that in-burner reagent injection could provide NOx reductions of up to 20%. Additional NOx reduction can potentially be obtained by layering in-burner injection with other furnace injection strategies. Modeling studies for a corner fired electric utility boiler with an Over Fired Air (OFA) system indicate RRI can provide up to 20% NOx reduction.

4. Licensing arrangements for RRI were completed with the Electric Power Research Institute (EPRI) and two equipment providers, Fuel Tech, Inc. and Combustion Component Associates (CCA). The licensing arrangements provide a pathway for electric utility boiler owners to obtain and install the RRI technology.

5. REI has been awarded two follow-on projects by DOE that provide funding to further study the use of RRI based NOx control technologies for cyclone barrel and PC fired utility boilers.

**Impacts of Combustion Modifications:**

*Corrosion Monitoring*

A novel, multi-pronged approach for managing waterwall corrosion in coal-fired utility boilers operating with low NOx firing conditions was evaluated. The corrosion monitoring system uses electrochemical noise (ECN) corrosion probes to monitor, on a real-time basis, high temperature corrosion events within the boiler. The importance of assessing wastage in real-time is that minor changes in boiler operation have the very real possibility to greatly reduce corrosion attack and thus improve boiler availability and reduce maintenance costs and expensive waterwall replacements or weld overlay. Field tests were conducted in two units.

1. Early in the project the system was field tested at the First Energy Eastlake power station plant, a PC fired station located in Eastlake, Ohio. Co-funding for the field test was

provided by the Ohio Coal Development Office (OCDO). This test provided the first demonstration of real-time high-temperature corrosion assessment in the radiant section of a large coal-fired power generation boiler.

2. Through additional financial assistance from OCDO, a second field test was performed at AEP's Plant Gavin, a 2600 MWnet station with PC fired units. The optimal location of the ECN probes within the boiler was determined through a combination of CFD modeling and corrosion maps for the units. The sensors were observed to respond appropriately to variations in corrosion rate as a function of boiler load, temperature, and combustion chemistry variations. Corrosion rates predicted by the ECN probes were benchmarked against corrosion rates measured with surface profilometry and static corrosion coupons.

3. Bench and pilot scale tests performed in the University of Utah's L1500 furnace were used to calibrate the probes and to conduct "shakedown" tests of the corrosion monitoring system when hardware and/or software upgrades were implemented.

4. The combination of field tests and bench/pilot-scale tests provided valuable experience on establishing operating procedures, identifying needed hardware and software improvements and troubleshooting operational problems.

5. REI is performing three follow-on industrial projects to install and demonstrate corrosion monitoring systems.

*Soot Modeling*

To address the impact on soot behavior for low NOx firing conditions, an advanced model to predict soot production and destruction was implemented into an existing reacting CFD modeling tool.

1. The model was verified through comparisons of soot concentrations predicted by the CFD model and soot concentrations measured in the University of Utah L1500 furnace for low NOx firing conditions. The comparisons highlighted that the model predicts the correct trends for soot production and destruction. The soot measurements were performed with a real-time Photo Acoustic (PA) sampler.

2. The improved CFD model was used to investigate low NOx firing impacts in a full scale boiler.

   a) The impact of burner stoichiometry and OFA location can be significant on soot formation/destruction as well as $NO_x$ emissions. Reducing condition formed by burner staging at the lower furnace will increase the formation of soot while limiting $NO_x$ generation.

   b) The results of full-scale application show limited mixing in the system can cause inefficient destruction of soot in the upper furnace even at high temperatures (>1500 K) can result in potential soot emission in the flue gas.

c) The level of detail provided by the simulations can be a valuable aid in understanding the mechanisms by which combustion modifications affect soot formation/destruction and $NO_x$ emissions.

**SCR Catalyst Testing**

SCR is a commercially proven technology capable of achieving the relatively large $NO_x$ reductions required to comply with the latest (amended) Clean Air Act requirements. SCR systems have been installed in most large-scale utility boilers. However, long-term experience with SCRs for boilers firing low-rank, subbituminous coals (e.g., Powder River Basin coals) is not generally available in the open literature, and there is essentially no information in the open literature on systems co-fired with biomass. This task focused on providing both laboratory and field slipstream data and analyses, including computer models, to fill this information gap.

*Fundamental Analysis of SCR Catalyst Deactivation*

Vanadia supported on titania material is the predominant commercial catalyst used in SCR systems for coal and biomass cofired systems. The relatively rapid deactivation of the vanadia catalyst is a major problem encountered in practice. To investigate the reaction and deactivation mechanism of vanadia catalyst, a series of catalyst activity tests and surface chemistry investigations were performed on fresh commercial catalyst samples, commercial catalyst samples that had been exposed to boiler flue gas and laboratory prepared catalyst samples. The test results suggest the following:

1. fouling, instead of poisoning, is the major deactivation mechanism for vanadia catalyst used in coal fired boiler applications;

2. sulfation of vanadia catalyst occurs on titiania sites, but not on vanadia sites;

3. sulfation enhances vanadia catalyst NO reduction activity by providing more active sites without changing the reaction activation energy;

4. Tungsten increases vanadia catalyst NO reduction activity by about 250%, due to the greatly increased number of active sites;

5. Alkali metals (K and Na) and alkaline earth metals (Ca) are poisons to vanadia catalyst. The deactivation occurs when poisons interact with active sites and decrease both the number and acidity of the active sites; and

6. results of the investigation into the effects of sulfation, tungsten, and poisons suggest that from an acid sites point of view, Brønsted acid sites are the active sites on vanadia catalyst. However, from a structure point of view, the results from NO adsorption comparisons on vanadia and sulfate samples suggests that the active sites are located at the edge, between the titania and vanadia sites;

*Catalyst Deactivation Based on Field Tests in a Slipstream Reactor*

The deactivation of commercial SCR catalysts exposed to a flue gas was measured in two ways:

1) by direct measurement of the $NO_x$ composition of the flue gas before and after it flows through a catalyst in the slipstream reactor in the presence of ammonia; and

2) by laboratory evaluation of the catalysts after periodical removal from the slipstream reactor.

The average catalyst activity from $NO_x$ measurements taken at 750 hours of operation on flue gas was compared with average catalyst activity from $NO_x$ measurements taken at 3,800 hours of operation on flue gas. Activity measured from field data showed a general decline in catalyst activity over the test period.

The data suggest that the mechanisms leading to SCR inactivity are, in order of significance,

1. channel plugging,
2. surface fouling,
3. pore plugging, and
4. poisoning.

In addition to these issues, surface sulfation increases activity. These data illustrate that the fresh catalyst activity initially increases (conversions increase) because of surface sulfation. In this particular sample, this increase is marginally significant, especially at the higher temperatures where conversion tends to be transport rather than kinetically limited.

With increased exposure, surface fouling and pore plugging become increasingly important. If the surface fouling layer is removed, the conversion/activity becomes intermediate between that of the fresh catalyst and that of the fully fouled material, in this case indicating surface fouling alone accounts for a about half of the activity change between 0 and 3800 hours. The other approximately half of the difference is associated with a combination of pore plugging and poisoning.

*Catalyst Regeneration*

Activity can be effectively restored by physical cleaning of the catalyst, especially if physical cleaning includes both removal of the fouling layer and removal of pore plugging, the latter probably requiring a liquid treatment. Most of the current efforts for catalyst regeneration are focused on taking out the exposed catalyst and regenerating it with certain procedures, for example, washing with water or with sulfuric acid solution, followed by sulfation. These regeneration techniques can recover about 80 % of the original activity; however, they require an outage to remove catalyst and to re-install it after regeneration. Modifications of the vanadia catalyst, for instance, in terms of the mechanical aspects (as opposed to the chemical aspects), to extend catalyst lifetime and at the same time to reduce the requirement for post-SCR regeneration could increase SCR catalyst performance.

*Computer Model*

A first-order kinetic model was developed to predict NO reduction across commercial catalysts. The model took into account surface catalysis as well as diffusion along the length of the channels, through the porous catalyst and through a porous deposit of ash on the catalyst surface.

**Ammonia on Fly Ash**

An experimental-based study was performed to investigate the fundamentals of ammonia / fly ash interactions with relevance to the operation of advanced NOx control technologies such as selective catalytic reduction. Measurements were performed for ammonia adsorption isotherms on commercial fly ash samples subjected to a variety of treatments and on the chemistry of dry and semi-dry ammonia removal processes.

1. This work resulted in obtaining the first fundamental ammonia isotherms on carbon-containing fly ash samples. Ammonia adsorption near room temperature was shown to be dominated by adsorption on carbon with only of order 20 ppm on the mineral component.

    a. The adsorption on carbon is a combination of physisorption and chemisorption on acidic surface sites. Introduction of additional oxygen functional groups on carbon increases ammonia adsorption by increasing the number of these acidic sites.

    b. The absolute amounts of ammonia adsorbed on fly ash in this study are much less than those of concern in the utility sector and much less than those found by Muzio in a study using simulated flue gas. Secondary components of the flue gas, either water, $SO_2$, or $SO_3$ are likely responsible for most of the ammonia observed associated with ash in utility practice, with a lesser component attributed to true adsorption on carbon surfaces.

2. This work also demonstrated that ammonia species can be removed from fly ash at or near room temperature by a variety of dry and semi-dry techniques.

    a. The work confirms industrial reports that aqueous solution chemistry takes place upon the introduction of even very small amounts of water, while the ash remains in a semi-dry state for handling.

    b. Rapid ammonia removal occurs from a microscopic water film on surfaces, in fine pores, and in ash particle interstitial regions whenever the film pH is high — achieved either by dissolution of the natural basic components of the ash or by the separate introduction of soluble basic additives

In the remainder of this report are provided further details on the work effort performed for this project. The material is organized by Task into separate chapters as follows:

- Chapter 2 - Program Management
- Chapter 3 – In Furnace NOx Control
- Chapter 4 – Impacts of Combustion Modifications
- Chapter 5 – SCR Catalyst
- Chapter 6 – Ammonia Adsorption onto Fly Ash
- Chapter 7 – Conclusions

Each chapter is self-contained, including all needed literature citations.

# 2. Program Management

The goal of the project was to develop cost-effective analysis tools and techniques for demonstrating and evaluating low-$NO_x$ control strategies and their possible impact on boiler performance for boilers firing US coals.

The project involved researchers from REI, EPRI, University of Utah, BYU and Brown University. The roles and responsibilities for the different organizations is shown by task in Figure 2.1.

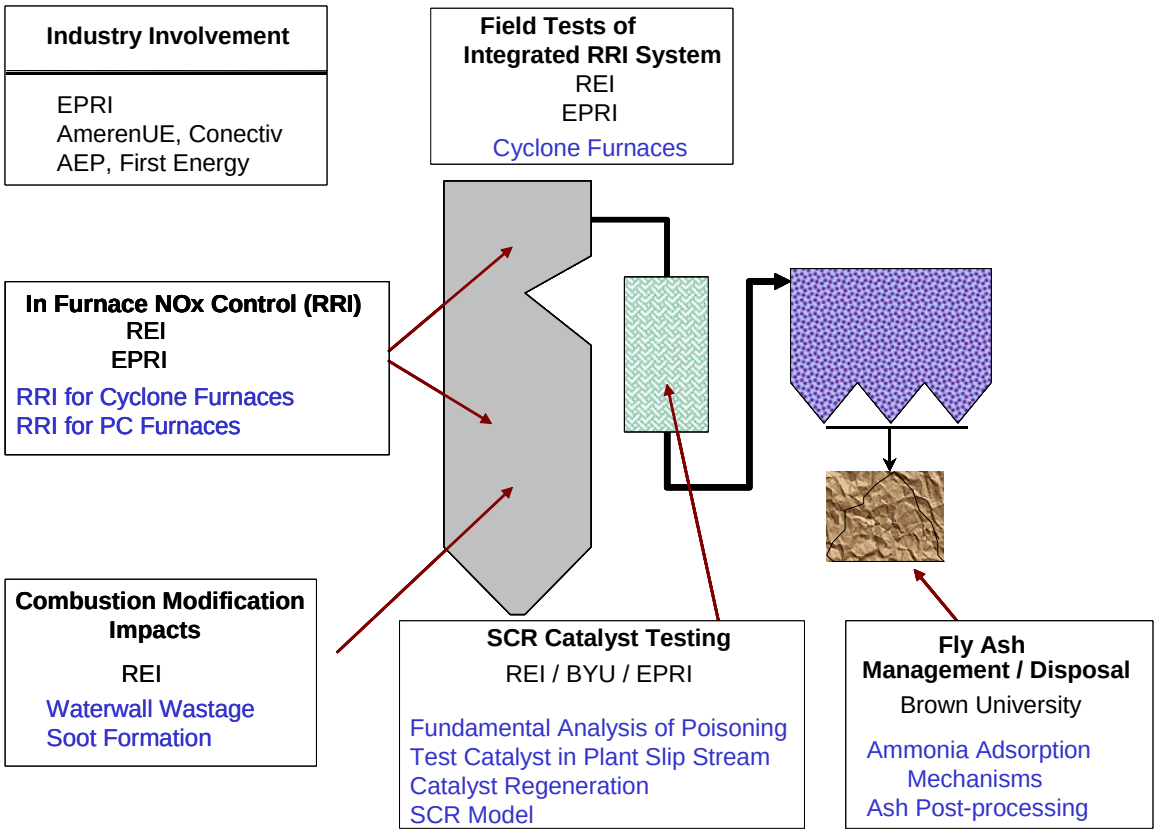


**Figure 2.1 Project Organization.**

Co-funding for the program was provided by EPRI. In addition, EPRI personnel provided technical assistance and guidance on several issues.

Financial assistance to augment the work effort within the corrosion management sub-task was provided by OCDO. Technical and/or financial assistance was also provided by AEP, NS Harding and Associates, Corrosion Management, Ltd and Savvy Engineering for this sub-task.

Technical and/or financial assistance was also provided by AmerenUE and Connectiv (now Atlantic City Electric) for the field testing of RRI and by AEP and Alabama Power (a subsidiary of Southern Company) for the field testing of SCR catalysts.

## *2.1 Industry Involvement*

During the course of this project, REI held project meetings and briefings with electric utility representatives, equipment vendors, EPRI (a co-sponsor of this program), OCDO (provided financial assistance to augment the corrosion management work) and the DOE. Papers and presentations were provided at a wide range of industry conferences, as detailed below in Section 2.4. In addition, articles were published in technical journals and industry trade publications.

## *2.2 Technology Transfer*

RRI was originally co-developed by EPRI and REI. Through this DOE program, field tests of RRI in cyclone fired utility boilers have been performed. The NOx reduction achieved in the field tests using RRI resulted in sufficient interest from industry to warrant establishing licensing agreements. REI holds a license from EPRI that allows REI to utilize the RRI technology. Through this license, REI is allowed to enter into sub-license agreements with $NO_x$ control equipment implementers that will in-turn market, design and install RRI technology in utility boilers. REI has completed sub-license agreements with Fuel Tech, Inc. and Combustion Components Associates (CCA). Multiple implementers are desired to ensure utilities can have RRI installed into their systems on a cost-competitive basis.

## *2.3 Related Efforts*

The results of this program have led to additional research and development programs, funded by DOE and other organizations.

REI has been awarded two follow-on projects to allow further refinement and demonstration of the RRI technology.

- REI was awarded a DOE funded project entitled, "Cyclone Boiler Field Testing of Advanced Layered Technology Approach (ALTA) for $NO_x$ Control" from the DOE NETL (Cooperative Agreement DE-FC26-04NT42297). In the project REI is working with AmerenUE and EPRI to demonstrate the ability of the ALTA approach to reduce NOx emissions in a cyclone-fired boiler to below 0.15 lb/MBtu at less than 75% of the levelized cost of Selective Catalytic Reduction. ALTA combines the use of deep staging with RRI (a NOx control technology evaluated and heavily worked on early in this project) and SNCR in a synergistic fashion to reach very low NOx levels in a cost effective manner. Field testing was performed in 2005. The project is to be completed in 2006. The test site was AmerenUE's Sioux Station near St. Louis, MO.

- REI was awarded a DOE funded project entitled, “Pilot-scale Demonstration of Advanced Layered Technology Approach (ALTA) for NOx Control in Coal-Fired Utility Boilers” from the DOE NETL (Cooperative Agreement DE-FC26-05NT42299). In the project REI is working with EPRI and the University of Utah to demonstrate at pilot-scale the ability of the ALTA approach to reduce NOx emissions in a PC fired boiler to below 0.15 lb/MBtu at less than 75% of the levelized cost of Selective Catalytic Reduction. In this project, the ALTA approach will be combined with combustion modifications to create a well mixed, deeply staged region in the lower furnace, which

when combined with RRI, will provide NOx emissions below that of a low NOx burner. The pilot scale tests will be performed in the University of Utah L1500 1.5MW pilot scale coal fired furnace. REI will perform CFD modeling for the pilot scale tests. The verified CFD model will then be used to evaluate the developed strategies in a full scale PC fired boiler.

The waterwall corrosion task was augmented by additional funding from the Ohio Coal Development Office (OCDO), DOE, REI, American Electric Power (AEP), EPRI, Corrosion Management, Ltd, the University of Utah and NS Harding and Associates. This allowed expansion of the waterwall corrosion task to measurement of corrosion at AEP's Plant Gavin.

The success of field tests for the corrosion management system in the Impacts of Combustion Modification task has led to REI being awarded three industrial projects to install and evaluate corrosion management systems. These projects will be performed in 2005-2006.

A series of measurements for mercury oxidation across the catalyst section within the slipstream reactor were performed with boiler operating at full load. These tests were performed under separate funding from DOE (Cooperative Agreement DE-FC26-03NT41728), with additional funding from EPRI and Argillon GmBH..

## *2.4 Publications and Presentations*

Listed below are the publications and presentations generated as a result of this project. The publications are organized by topic.

<u>In Furnace NOx Control</u>

Adams, B., Cremer, M., and Wang, D., "Use of CFD Modeling to Evaluate NOx Reduction Technologies in Utility Boilers," *Proceedings of POWER-GEN International Conference*, Las Vegas NV, Dec 11-13, 2001.

Boll, D., Cremer, M., O'Connor, D., "Recent Experience with Overfire Air for Cyclone Fired Boilers, " presented at the 2002 Electric Power Conference, St. Louis, MO, March 19-21, 2002.

Cremer, M.A., Wang, D.H., Adams, B.R., Boll, D.E., and Stuckmeyer, K.B. "Evaluation of Cost Effective Non-SCR Options For NOx Control in PRB Fired Cyclone Boilers," presented at the 19th International Conference on Lignite, Brown, and Subbituminous Coals, Billings, MT, October 12-14, 2004.

Cremer, M., Wang, D., Schindler, E., "Improved Rich Reagent Injection (RRI) Performance For $NO_x$ Control In Two Coal Fired Utility Boilers," presented at DOE NETL Conference on SCR and SNCR for Control of $NO_x$, Pittsburgh, PA, October 29-30, 2003.

Cremer, M.A., Adams, B.R., and O'Connor, D., "Improved Rich Reagent Injection Performance for $NO_x$ Control in Coal Fired Utility Boilers," EPRI-DOE-EPA Combined Utility Air Pollution Symposium: The MEGA Symposium, Washington, D.C., May 2003.

Cremer, Marc A., Adams, Bradley R., Boll, David E., O'Connor, David C., "Modeling and Demonstration of Rich Reagent Injection for NOx Control in AmerenUE's Sioux Unit 1," 2002 Conference Proceedings, Power-Gen International, December 10-12, 2002, Orlando, FL.

Cremer, M.A., Adams, B.R., Boll, D., O'Connor, D., and Slaff, R.D., "Demonstration of Rich Reagent Injection for NOx control in Ameren's Sioux Unit 1", presented at the 19th Annual International Pittsburgh Coal Conference, Pittsburgh, PA, September 24-26, 2002.

Cremer, M.A., Adams, B.R., Boll, D., O'Connor, D., and Slaff, R.D., "Demonstration of Rich Reagent Injection in Ameren's Sioux Unit 1", presented as at the DOE 2002 Conference on Selective Catalytic Reduction and Selective Non-Catalytic Reduction for NOx Control, Pittsburgh, PA, May 15-16, 2002.

Cremer, M.A., Adams, B.R., O'Connor, D.C., Bhamidipati, V., Broderick, R.G., "Design and Demonstration of Rich Reagent Injection (RRI) for NOx Reduction at Conectiv's B.L. England Station", *presented at the U.S. EPA/DOE/EPRI MegaSymposium 2001*, Chicago, Illinois, August, 20-23 2001.

Cremer, M.A., Wang, D.H., Montgomery, C.J., and Adams, B.R., "Utilization of Reduced Mechanism Methods in CFD Simulations for Improved $NO_x$ Predictions in Utility Boilers and Furnaces"*, presented at the 2001 Joint International Combustion Symposium organized and sponsored by the American Flame Research Committee, the Japanese Flame Research Committee, and the International Energy Agency*, Hawaii, September 9-12, 2001.

Corrosion Management System

Davis, K.A., Bockelie, M.J., Linjewile, T., Shim, H.-S., Senior, C.L., Adams, B.R., Whitty, K., Hurt, R., Harding, N.S., "Unresolved Technical Challenges to NOx Reduction for Coal-fired Power Generation", presented at the Proceedings of the 27th International Technical Conference on Coal Utilization and Fuel Systems, Clearwater, FL, USA, March 4-7, 2002.

Davis, K.A., Linjewile, T., Valentine, J., Swensen, D.A., Shino, D., Letcavits, J.J., Sheidler, R., Cox, W., Carr, R. and Harding, N.S., "On-line Monitoring of Waterwall Corrosion in a 1300 MW Coal-fired Boiler with Low-$NO_x$ Burners", presented at the Combined Power Plant Air Pollutant Control Mega Symposium in Washington, DC, August 30 – September 2, 2004.

Davis, K.A., Linjewile, T., Valentine, J.R., Swensen, D., Shino, D., Letcavits, J.J., Sheidler, R., Cox, W., Carr, R., Harding, N.S. "A Multi-point Corrosion Monitoring System Applied in a 1,300 MW Coal-fired Boiler," *Anti-Corrosion Methods and Materials*, **2004**, *51*, 321.

Davis, K.A., Linjewile, T.M., Valentine, J., Harding, N.S. and Cox, W.M. "Prediction and Real-time Monitoring Techniques for Corrosion Characterization in Furnaces" Submitted to Materials at High Temperatures, November, 2002.

Davis, K.A., Linjewile, T. and Cox. W., "Prediction and Real-Time Monitoring Techniques for Corrosion Characterization in Furnaces", presented at the 19th Annual International Pittsburgh Coal Conference, Pittsburgh, PA, September 24-26, 2002.

Davis, K.A., Linjewile, T. and Cox. W., "Evaluation of an On-line Technique for Corrosion Characterization in Boilers" presented at the *3rd International Workshop on Life Cycle Issues in Advanced Energy Systems* held June 10-12, 2002 in Woburn, England.

Davis, K.A., Lee, C. Seeley, R., Harding, S., Heap, M. and Cox, W., "Waterwall Corrosion Evaluation in Coal-Fired Boilers Using Electrochemical Measurements," 25th International Technical Conference on Coal Utilization & Fuel Systems, Clearwater, FL, March 2000.

Linjewile, T.M., Davis, K.A., Green, G.C., Cox, W.M., Carr, R.N. and Harding, N.S., "On-Line Technique for Corrosion Characterization in Utility Boilers", accepted for Publication in *Fuel*.

Linjewile, T., Valentine, J., Davis, K.A., Harding, N.S., Cox, W.M. "Prediction and real-time monitoring techniques for corrosion characterization in furnaces," *Materials at High Temperature* **2003**, *20*, 175-183.

Linjewile, T.M., Davis, K.A., Green, G.C., Cox, W.M., Carr, R.N., Harding, N.S. and Overacker. D., "On-Line Technique for Corrosion Characterization in Utility Boilers". Presented at the Engineering Foundation Conference on *Power Production in the 21st Century: Impacts of Fuel Quality and Operations*. Snowbird, Utah, November 28-December 2, 2001.

Soot Modeling and Measurement

Shim, H.-S., Sarofim, A., Davis, K.A., Bockelie, M.J., Eddings, E.G., and Wagner, D., "Modeling The Impacts Of Soot From Low-$NO_x$ Combustion Systems", in the *Proceedings of the 28th International Technical Conference on Coal Utilization & Fuel Systems*, Clearwater, Florida, March 10-13, 2003.

Shim, H.-S., Sarofim, A., Davis, K.A., Bockelie, M.J., Eddings, E.G., and Wagner, D., "Modeling The Impacts Of Soot From Low-$NO_x$ Combustion Systems", presented at the *17th ACERC Conference*, University of Utah, Salt Lake City, Utah, February 20-21, 2003.

SCR Catalyst Study

Davis, K.A., "Selective Catalytic Reduction and Low Rank Fuels" presented at the *EPRI Biomass Interest Group*, held on February 4, 2003, Gainesville, FL, USA.

Gao, Y., Chen, X., Fujisaki, G., Mehta, A., Suuberg, E.M., Hurt, R.H., "Dry and Semi-Dry Methods for Removal of Ammonia from Fly Ash," *Energy and Fuels* **2002**, *16*, 1398-1404.

Guo, X., Nackos, A., Ashton, J., Baxter, L.L., Bartholomew, C.H., Hecker, W.C. "Investigation of deactivation/sulfation on vanadia/titanium dioxide catalyst," presented at the North American Catalysis Society 19th North American Meeting, May, 27, 2005.

Guo, X., Nackos, A., Ashton, J., Bartholomew, C.H., Hecker, W.C., Baxter, L. "Poisoning/Deactivation of $V_2O_5/TiO_2$ SCR Catalyst in Coal and Biomass-Fired Systems" presented at the 30th International Technical Conference on Coal Utilization & Fuel Systems, April 17-21, 2005, Clearwater, Florida.

Senior, C. and Linjewile, T., "Oxidation of Mercury Across SCR Catalysts in Coal-Fired Power Plants," presented at the 29th International Technical Conference on Coal Utilization & Fuel Systems, Clearwater, FL, April 19-22, 2004.

Senior, C. and Linjewile, T., "Oxidation of Mercury Across SCR Catalysts: Field Data from Low Rank Coal Blend," presented at Electric Power 2004, Baltimore, MD, March 31-April 2, 2004.

Senior, C., Linjewile, T., Bockelie, M., Eddings, E., Whitty, L., Baxter, L., "SCR Deactivation Mechanisms Related to Alkali and Alkaline Earth Elements," presented at DOE NETL Conference on SCR and SNCR for Control of $NO_x$, October 29-30, 2003, Pittsburgh, PA.

Senior, C.L., Davis, K.A, Bockelie, M.J., Baxter, L., Bartholemew, C., Whitty, K., Eddings, E., “SCR Deactivation Mechanisms Related To Alkali and Alkaline Earth Elements”, poster presented at the DOE 2002 Conference on Selective Catalytic Reduction and Selective Non-Catalytic Reduction for NOx Control, Pittsburgh, PA, May 15-16, 2002.

Swensen, D.A., Shino, D., et al, "Networked Control System for a Catalyst Deactivation Test Reactor", proceedings for the National Instruments NIWeek 2002, Austin, Texas, August 14-16, 2002.

# 3. In-Furnace $NO_x$ Control

The objective of this task is to improve and apply design and analysis procedures for evaluating different layered $NO_x$ control strategies. This will provide the utility industry with the capability to evaluate these different $NO_x$ control technologies in a reliable, cost effective and timely manner. Of particular interest is the use of Rich Reagent Injection (RRI), a $NO_x$ reduction strategy that is based on injecting urea or anhydrous ammonia into fuel rich regions in the lower furnace. The utility industry has expressed significant interest in the possibility of employing RRI in conjunction with other $NO_x$ control techniques such as low-$NO_x$ firing systems (LNFS), overfire air (OFA), selective non-catalytic reduction (SNCR) and Lean Gas Reburn.

Cyclone-fired boilers have historically been characterized as high $NO_x$ emitting units due to the very high combustion temperatures that are produced in the primary combustion zone. Uncontrolled $NO_x$ emissions ranging from 0.8 to 1.9 lb/MBtu have been typical. Due to the design characteristics of cyclone-fired units, they are not conducive to the application of conventional low $NO_x$ burner technology. In addition, prior to 1997, the conventional wisdom was that cyclone-fired boilers could not be practically operated under two stage combustion conditions due to concerns about the reducing conditions in the cyclone barrel leading to corrosion. Gas reburn technology and SCR were considered to be the technologies of choice in cyclone units for $NO_x$ reduction.

The combination of air staging with OFA in cyclone-fired furnaces has been demonstrated to be an extremely cost effective approach for reducing NOx emissions in the majority of cyclone-fired furnaces currently operating in the United States. With staging/OFA, $NO_x$ that is formed in the cyclone barrels is reduced in the lower furnace. $NO_x$ reduction up to 80% has been achieved in cyclone-fired furnaces when operating the cyclone barrels with 90% of their stoichiometric requirement of air.

In fuel rich flue gases arising from the combustion of fossil fuels, reduction of $NO_x$ can be achieved in a similar manner to the thermal DeNOx process of Lyon (U.S. Patent No. 3,900,544, 1975). It has been previously demonstrated that the injection of $NH_3$ or urea into the high temperature NOx-containing flue gases, in the temperature range from approximately 2400 – 3000°F, using normalized stoichiometric ratios (NSR) of 1 to 4, can lead to noncatalytic $NO_x$ reductions of 80% under idealized conditions (Brogan, U.S. Patent No. 4,335,084, 1982; Arand & Muzio, U.S. Patent No. 4,325,924, 1982). This process, herein referred to as rich reagent injection (RRI), consists of injection of $NH_3$ or urea into the fuel rich zone followed by burnout of the rich flue gases with secondary air. Although $NO_x$ reduction in the thermal DeNOx process has been shown to drop to insignificant levels in the absence of $O_2$, injection of ammonia or urea in the fuel rich environment at significantly higher gas temperatures can lead to very high $NO_x$ reductions.

With cofunding under the current DOE program, REI has shown that the injection of amine reagents, such as ammonia or urea, into the fuel rich lower furnace of a staged cyclone-fired furnace, results in significant $NO_x$ reductions, beyond those that are already being achieved through air staging with OFA. This has been demonstrated through the combination of: 1) Detailed chemical kinetic calculations, 2) Bench and pilot scale tests, 3) Development and application of a CFD model to full-scale cyclone boilers, and 4) Full-scale tests in two cyclone-fired boilers. Additional CFD model simulations were completed in order to evaluate the

potential of RRI for $NO_x$ reduction in boilers that fire pulverized coal (PC). This chapter describes the results of these evaluations, as follows. Section 3.1 discusses the RRI concept including results of chemical kinetics calculations, pilot scale tests, and CFD model development. Sections 3.2 and 3.3 describe the modeling and test results of RRI applied to a 130 MW and a 500 MW cyclone-fired furnace. Section 3.4 describes results of CFD based evaluations of RRI in three PC-fired boilers. Finally, section 3.5 describes the results of additional modeling of the combination of deep staging and RRI applied to the 500 MW cyclone-fired boiler. Section 3.6 contains references cited in this chapter.

## *3.1 Rich Reagent Injection Concept*

Studies carried out by REI and the EPRI Cyclone NOx Control Interest Group (CNCIG) suggest that staging cyclone barrels to operate the lower furnace fuel rich reduces $NO_x$ that is formed in the barrel, within the lower furnace. This is in contrast to normal unstaged operation where $NO_x$ is formed, not destroyed, in the furnace. When the barrel is operated fuel rich, $NO_x$ reduction rates are high near the barrel outlet but in the vast majority of the lower furnace volume they become very slow. Consequently, there is a small benefit in $NO_x$ reduction if the vertical distance between the OFA ports and the top row of barrels is increased. The concept of RRI, applied to a staged furnace is to use a nitrogen-containing additive to increase the $NO_x$ reduction rate in the lower furnace as shown in Figure 3.1.

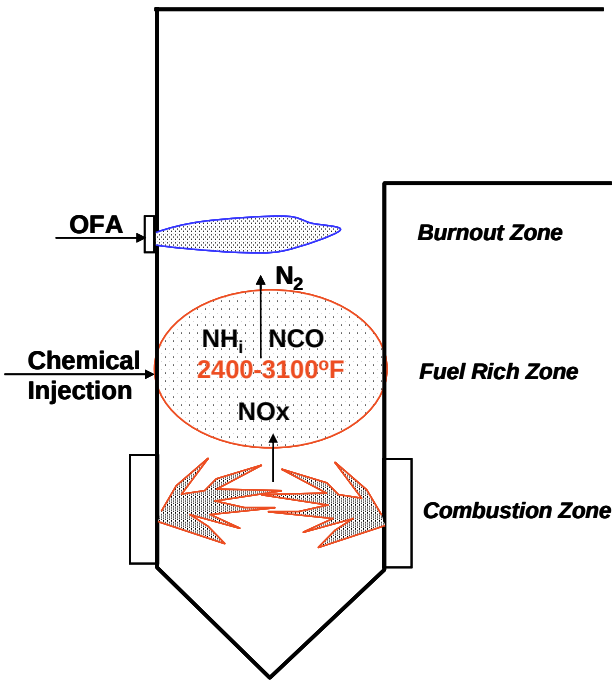


**Figure 3.1. Schematic illustrating the application of RRI in a staged furnace.**

### *3.1.1 Chemical Kinetics Calculations*

To understand the key chemical parameters that impact RRI performance a number of detailed chemical kinetic calculations were carried out during the RRI development. The detailed $NO_x$ mechanism that we have been using to evaluate the kinetics governing reactions between ammonia or urea and coal flue gases containing $NO_x$, is the mechanism of Miller & Bowman (1989) with literature modification (Dean, 1991). This detailed mechanism contains over 60 chemical species and 250 reversible elementary reactions. Figure 3.2 show the typical reactor network that was used in order to perform most of the calculations. This network involved a series of two plug flow reactors, one to represent the fuel rich region at residence time and temperature, $\tau_{pri}$ and $T_{pri}$, and the other to represent the burnout zone at residence time and

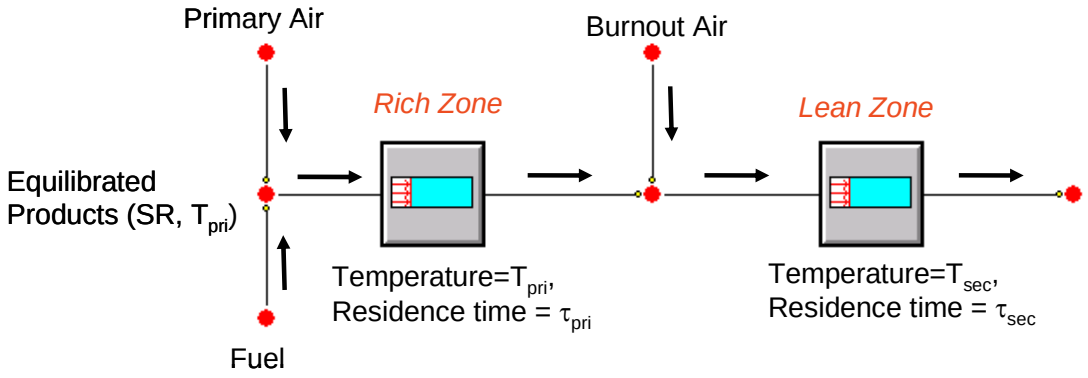


**Figure 3.2. Schematic showing the reactor network consisting of two perfectly stirred reactors in series, used to carry out a sequence of detailed chemical kinetic calculations to evaluate the chemistry dependencies and potential for the RRI process.**

temperature, $\tau_{sec}$ and $T_{sec}$, respectively. Figure 3.3 shows the results of one particular detailed chemical kinetic calculation using the network from Ffigure 3.2 and the conditions specified in Figure 3.3. These results showed: 1) the chemical times are fast (~0.1 sec) and 2) $NO_x$ reductions are very high under well-mixed conditions. Figure 3.4 shows results of a large number of such simulations over a range of primary zone gas temperatures and normalized stoichiometric ratios (NSRs). In each case, the primary and secondary zone residence times, the secondary zone stoichiometric ration (SR), and the initial NO were fixed as shown in the figure. The results showed that optimum performance under these conditions is seen at a primary zone gas temperature of 2780$^o$F (1800 K) and NSR=1.5. Higher gas temperatures lead to lower $NO_x$ reduction in the rich zone and lower gas temperatures lead to higher levels of ammonia slip in the burnout zone leading to oxidation to $NO_x$. A similar tradeoff is seen with NSR. Higher NSRs can produce higher $NO_x$ reduction in the primary zone, but increased reagent oxidation in the burnout zone.

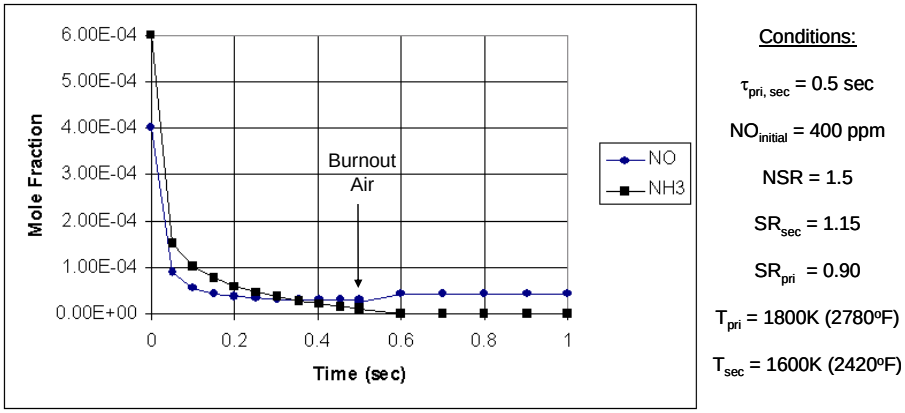


**Figure 3.3. Results of detailed chemical kinetic calculation using the reactor network shown in Figure 3.2 with the conditions detailed above.**

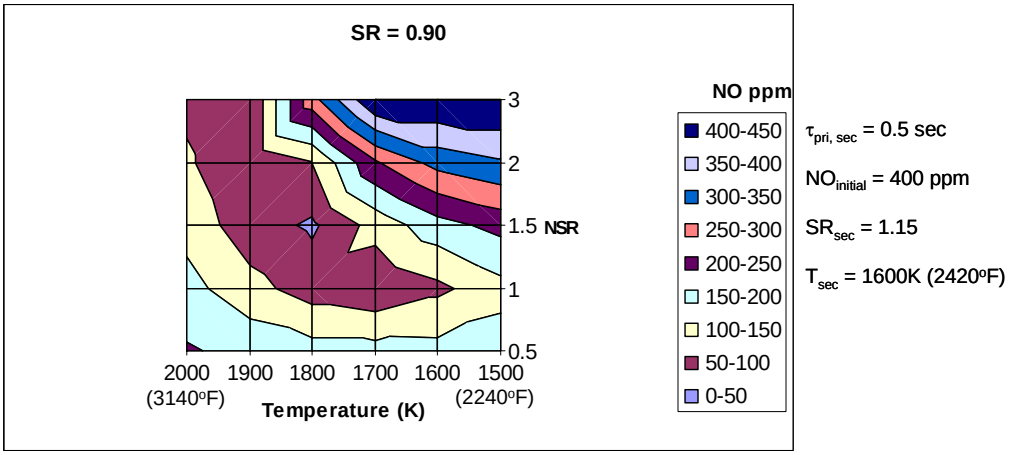


**Figure 3.4. Detailed chemical kinetic calculations of the RRI process assuming a rich zone SR of 0.90 under the primary and secondary zone conditions shown above. Calculations were carried out over a range of rich (primary) zone temperatures from 2240°F to 3140°F and NSRs from 0.5 to 3.0 assuming ammonia reagent.**

Figure 3.5 shows the results of a number of plug flow reactor calculations to evaluate the impact of rich zone gas temperature and flue gas SR on $NO_x$ reduction due to the RRI process only within the rich zone. Subsequent impacts of oxidation of unused reagent in the burnout zone are not taken into account in this figure. Figure 3.6 shows the corresponding predictions of ammonia slip. These results show the transition from RRI conditions to SNCR conditions and the dependencies of both processes on gas temperature and flue gas SR.

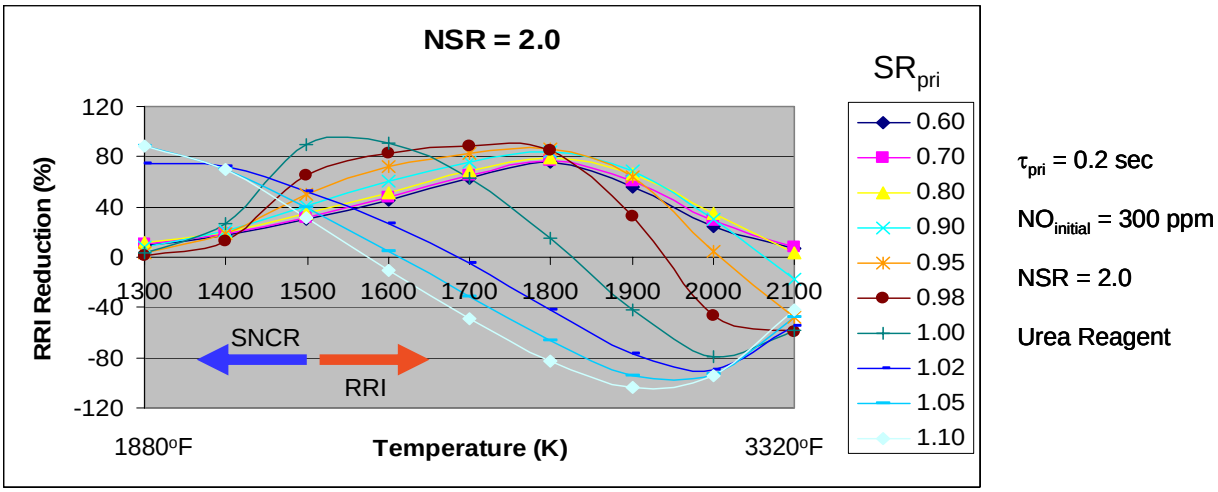


**Figure 3.5. Detailed chemical kinetic calculations in a plug flow reactor geometry to investigate the effect of flue gas temperature and flue gas stoichiometric ratio (SR) on NOx reduction under fuel rich conditions.**

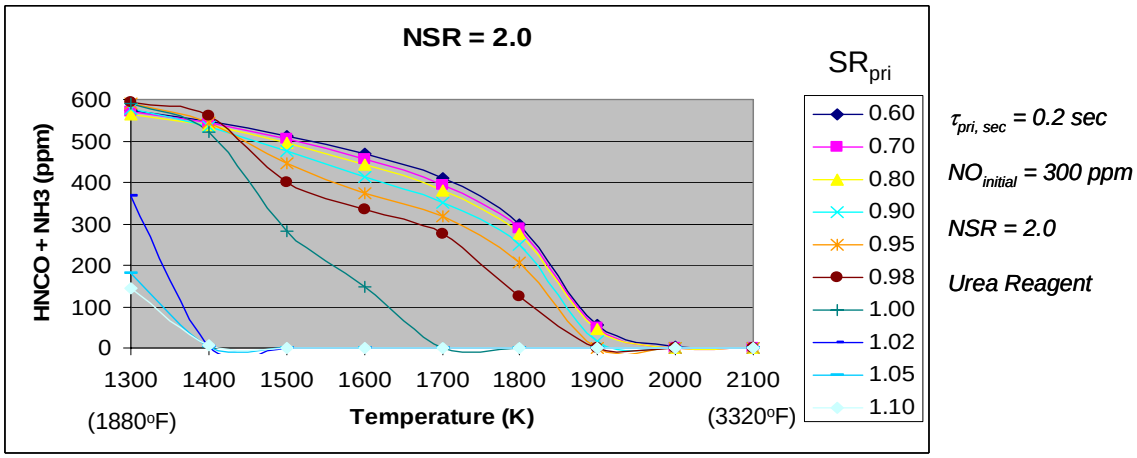


**Figure 3.6. Detailed chemical kinetic calculations in a plug flow reactor geometry to investigate the effect of flue gas temperature and flue gas stoichiometric ratio (SR) on resulting reagent ($NH_3$+HNCO) slip from the primary (fuel rich) zone. The conditions are identical to those in Figure 3.5.**

### *3.1.2 Pilot Scale Tests*

The results of the detailed chemical kinetic calculations were used to identify appropriate test conditions for a series of bench and pilot scale tests. These investigations included:

- bench scale testing in a 0.1 MMBtu/hr facility ("The U Furnace"); and
- pilot-scale testing in a 5 MMBtu/hr facility.

The bench scale testing was conducted in the University of Utah's 0.1 MMBtu/hr "U-furnace" facility using anhydrous ammonia reagent at burner stoichiometric ratios of 0.90, 0.95, and 1.03. In all U-furnace cases, the gas temperatures were most likely too low for maximum effectiveness. Pilot scale testing of the RRI process in a 5 MMBtu/hr facility (L1500) at the University of Utah showed reductions in furnace outlet NOx of up to 90% by injection of either aqueous ammonia or urea. Rich zone stoichiometric ratios from 0.90 to 0.99 were tested in these experiments. Within this facility, higher rich zone gas temperatures were achievable, and efforts were made to provide the most effective reagent mixing scenario possible. The increased NOx removals in these experiments were most likely a result of the ideal mixing conditions and the higher, more optimal injection zone temperatures that were achievable in the L1500 as compared to the smaller U-furnace.

### *3.1.3 Development of CFD Model for RRI Process*

To assess the expected performance of RRI in reducing $NO_x$ emissions in a full-scale boiler, REI developed a CFD model of this process. In order to model this process, chemical kinetic rates describing the rates of reaction of the ammonia and/or urea in the presence of $NO_x$ in the hot, fuel rich region needed to be identified for inclusion in the CFD model. This has been accomplished by using conventional reduced mechanism approaches that have been implemented in a tool named the Computer Assisted Reduced Mechanism (CARM) method (Chen, 1997). A 10-specie reduced mechanism was developed and implemented as a post process to REI's proprietary three-dimensional, multiphase CFD code, *GLACIER*, to model the reduction and oxidation reactions governing $NO_x$ formation/destruction. This chemistry model development has been described elsewhere (Cremer, 2000). Prior to any full-scale demonstrations of RRI, the new model was subsequently applied to predict performance applied to:

- the U Furnace;
- 130 MW, wall-fired cyclone furnace; and
- 500 MW, opposed wall-fired cyclone furnace.

In the U-furnace calculations, both qualitative and quantitative agreement with the measurements was quite good (Cremer, 2000). For both full scale cyclone-fired furnaces that were investigated, the simulations indicated that $NO_x$ reductions of approximately 40%, in addition to the reductions already obtained with OFA, could be achievable using anhydrous ammonia. These results indicated that poor reagent placement in the full scale furnaces could limit $NO_x$ reductions to 10% or even less.

A range of CFD simulations for a single aqueous urea spray injecting into an otherwise homogeneous flue gas flow were conducted to investigate the effects of nozzle flow rate and droplet size over a range of flue gas temperatures. Figure 3.7 shows the computed distribution of

$NO_x$ resulting from the injection of an aqueous urea spray into flue gas typical of products of coal combustion. Typical results of these simulations are shown in Figures 3.8 and 3.9, which indicate the predicted $NO_x$ reduction and $NH_3$ slip over a range of flue gas temperatures (1800, 1900, 2000 K), mean droplet sizes (50 and 300 μm Sauter Mean Diameter), and injector flow rates (2 and 4 gpm). Figures 3.8 and 3.9 suggest that droplet sizes, flue gas temperatures, and nozzle flow rates have a significant effect on $NO_x$ reduction and $NH_3$ slip.

Conclusions from these simple investigations include:

- better performance (i.e., high $NO_x$ reduction, low ammonia slip) is achieved utilizing two 2 gpm injectors rather than one 4 gpm injector, but the difference decreases with increasing temperatures;
- for the temperatures and residence times chosen, performance is best for 150 μm SMD droplets; and
- performance decreases with increasing flue gas temperatures.

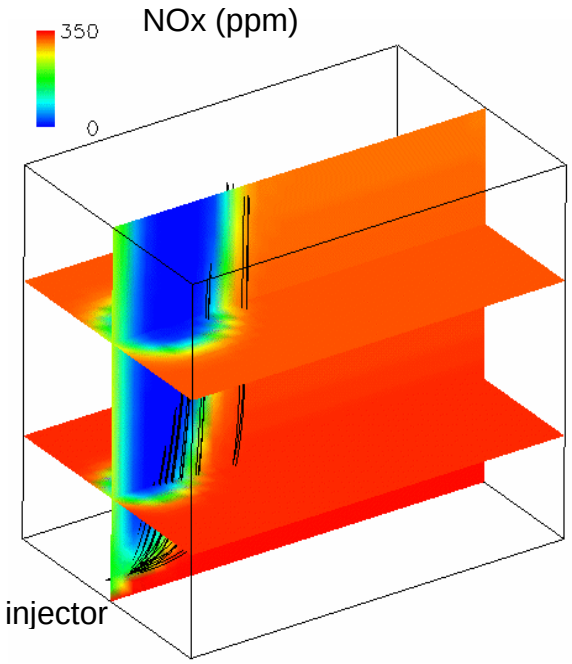


**Figure 3.7. Simple CFD model of a single aqueous urea injector spraying into a cross-flow of flue gas at a uniform velocity and gas temperature.**

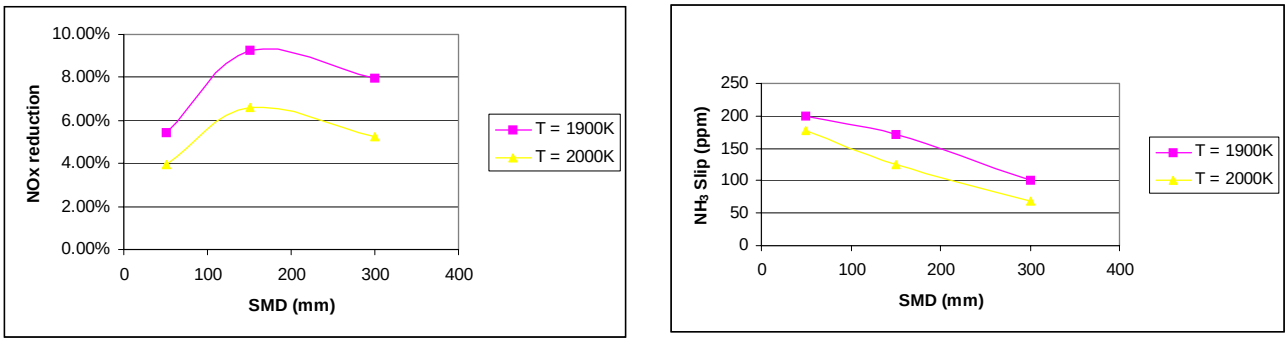


**Figure 3.8. Results of geometrically simple simulations of reagent injection in cross flow (see Figure 3.7) over of range of RRI conditions. Predictions are shown for $NO_x$ reduction and $NH_3$ slip showing the effect of gas temperature and nozzle size on performance at different flow rates.**

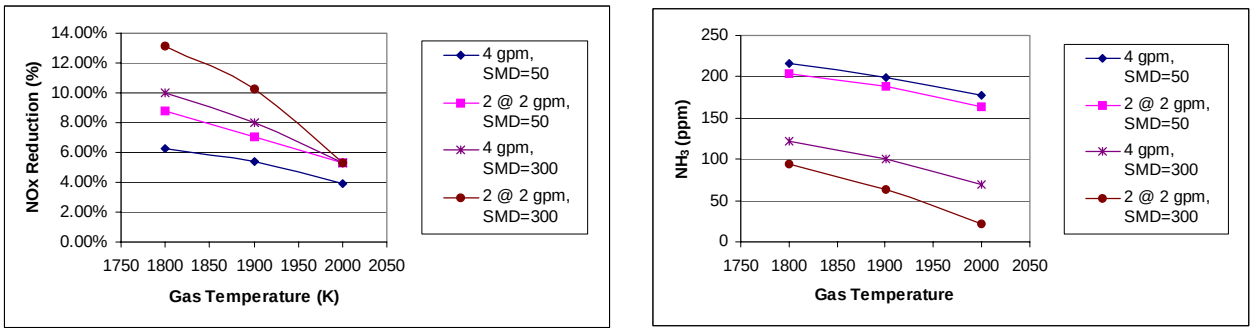


**Figure 3.9. Results of geometrically simple simulations of reagent injection in cross flow (see Figure 3.7) over of range of RRI conditions. Predictions are shown for $NO_x$ reduction and $NH_3$ slip showing the effect of droplet size and gas temperature on performance.**

## *3.2 Field Testing of RRI in a 130 MW Cyclone-fired Furnace*

This section summarizes the design and application of RRI at a nominally 130 MW cyclone-fired boiler. Installation of OFA at this unit, which has three cyclones firing on the front wall in one over two arrangement, has reduced uncontrolled NOx emissions from ~1.2 lb/MMBtu to ~0.5 lb/MMBtu with less than 50 ppm CO stack emissions. An existing aqueous urea SNCR system reduces these emissions an additional 30% with less than 5-ppm ammonia slip.

### *3.2.1 Modeling RRI at 130 MW Cyclone Boiler*

REI's three-dimensional turbulent reacting flow code GLACIER, with additions to represent the RRI chemistry, was used for all of the simulations of RRI in this cyclone-fired furnace. These simulations were carried out in two parts:

- Cyclone Barrel Model
- Furnace RRI Model

#### 3.2.1.1 Cyclone Model

The original cyclone barrel CFD model utilized for the cyclone barrel cases was developed as part of a previously funded program sponsored by CNCIG. Details concerning this model have been published previously (Adams et al., 1997; Stuckmeyer et al., 1996). Barrel simulations were performed for stoichiometric ratios of 1.09 (baseline) and 0.90 (staged). All RRI predictions were based on the staged barrel results.

#### 3.2.1.2 Furnace RRI Model

The results of the cyclone barrel model were interpolated into the inlet of the furnace model as shown in Figure 3.10. Within the GLACIER simulations of the furnace, the dynamics of the injected aqueous urea droplets were modeled as in previously completed studies to evaluate SNCR (Cremer et al., 1998; Cremer et al., 1999. The initial direction and velocity of the droplets was specified according to the assumed spray pattern and initial droplet velocities. The model accounts for the coupling between the particle and gas phases in terms of mass, momentum, and energy. The release of the urea into the gas phase and the subsequent chemical reactions between the urea products and the local flue gas species were accounted for based on the new reduced chemistry (Cremer et al., 2000). This approach allows complete coupling of all the relevant physical processes involved including heat transfer, turbulent mixing, and chemistry so that objective estimates of RRI performance can be obtained.

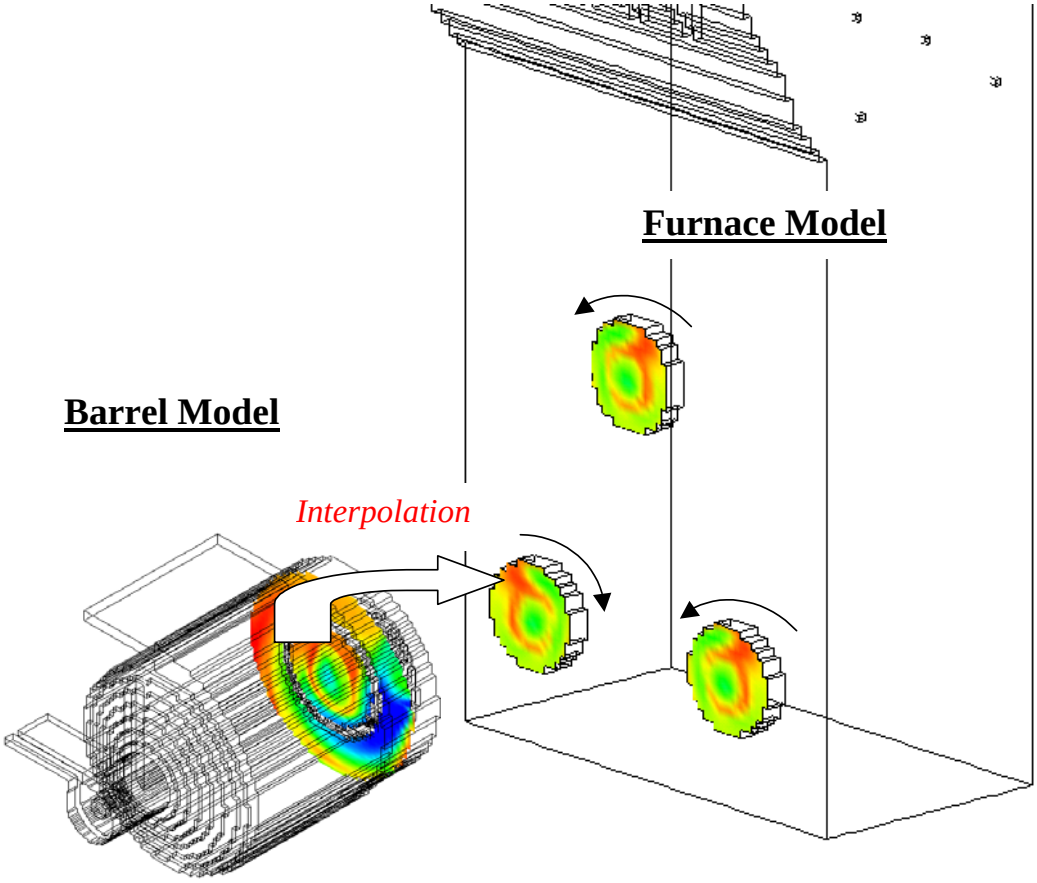


**Figure 3.10. The computed results at the barrel exit are interpolated onto the inlets of the furnace model where the RRI predictions are obtained.**

The enhanced CFD model was utilized to aid in the design of an RRI injection system for the unit as well as to predict RRI performance in the field demonstration. An assessment of the boiler showed that the number of feasible locations for injector nozzle penetrations was limited for a number of reasons including:

- the short elevational distance between the cyclone barrels and the OFA ports;
- lack of access to the front wall (cyclone barrels, risers); and
- location of the windbox.

Feasible locations that were identified and subsequently considered in the CFD modeling are shown in Figure 3.11. The locations included six side-wall injectors at the elevation of the bottom row of cyclone barrels, and two side-wall and two rear-wall injectors at the elevation directly above the top cyclone barrel. The parameters that were considered in the evaluation included:

- reagent distribution between the injectors;
- droplet size and velocity distribution;
- spray pattern; and
- reagent concentration.

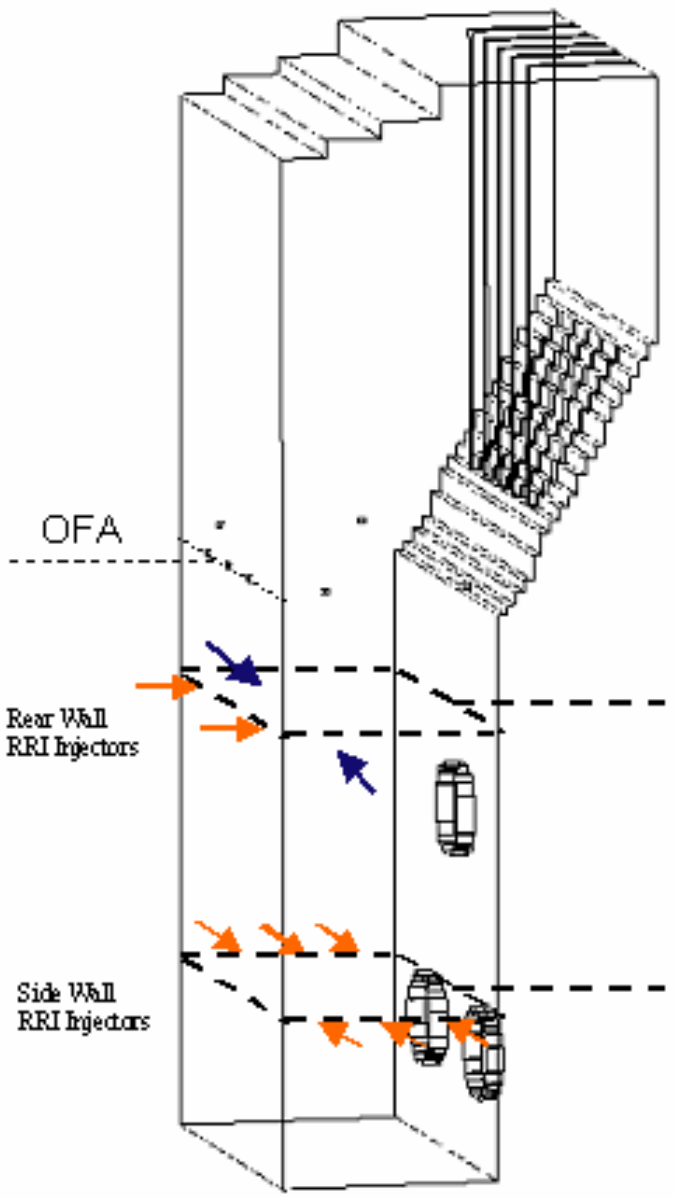


**Figure 3.11. Schematic of furnace showing the extent of the furnace model and the approximate nozzle locations that were evaluated in the CFD model.**

### 3.2.1.3 CFD Model Predictions

Table 3.1 summarizes the cases that were considered and Table 3.2 provides a summary of the CFD model predictions, giving the predicted average $NO_x$ reduction, $NH_3$ slip, and the specified reagent usage. CFD predictions of RRI performance showed $NO_x$ reduction varying between 12 and 35% (beyond reductions obtained with OFA) utilizing equivalent reagent flow rates. Simulations showed that due to the highly stratified flow in the lower furnace, improper reagent injection could result in little to no reduction in NOx emissions, and even a net increase in certain circumstances. Through proper placement of injectors and specification of nozzle characteristics, NOx reductions up to 33% were predicted with less than 1-ppm ammonia slip, utilizing eight injectors and a normalized stoichiometric ratio of approximately 2. $NO_x$ reduction of 35% was predicted if all 10 injectors were utilized. The reagent usage in most cases was 190 gallons per hour (gph) of 50% urea by weight, corresponding to a normalized stoichiometric ratio of approximately 2 (based on the predicted $NO_x$ exiting the cyclone barrels). The analysis also indicated that if the existing SNCR nozzles were utilized for RRI injection, NOx reduction would be significantly limited, due to the achievable liquid flow rates. The modeling suggested that it would be advisable to modify the injectors both in terms of the droplet size distribution and the nozzle capacities

Figure 3.12 illustrates the predicted effect of injection strategy on the NO distribution. The three profiles show the predicted NO distribution in the absence of reagent injection, injection using straight injectors, and injection using angled injectors. Figure 3.13 shows the predicted distribution of $O_2$ concentration. Due to the stratified nature of the gas flows exiting the cyclone barrels, the predictions suggest that significant quantities of $NO_x$ will be formed if the reagent penetrates into the high temperature oxygen containing gases exiting the cyclone barrels. By angling the injectors upward, much less $NO_x$ is formed, and high $NO_x$ destruction rates near the walls result in significant overall $NO_x$ reduction. Other cases indicated that increased penetration of reagent in the region of the cyclone barrels resulted in limited performance.

Overall, the CFD model based analysis showed the importance of injection strategy on RRI performance. The furnace simulations showed that the gas flow exiting the cyclone barrels was very stratified. Even though the barrels are staged to a stoichiometric ratio of 0.90, there are regions in the lower furnace that contain nonzero concentrations of $O_2$. If the reagent is injected into these regions, it will be oxidized to form NOx. The key to optimizing the reagent injection system is understanding how to mix the reagent into the hot, rich, $NO_x$ containing flue gases while minimizing injection into the hot lean zones. The analysis also indicated that if the existing SNCR nozzles were utilized for RRI injection, NO reduction would be significantly limited. The modeling suggested that it would be advisable to modify both the droplet size distribution and the nozzle capacities.

CFD model results suggest that the RRI process can be significantly more robust and effective if the reagent is injected into a relatively homogeneous mixture of fuel rich flue gases (See results for cases ble1_90_6sw_44 and ble1_90_6sw_44_homog in Table 3.2). Both measurements and modeling indicate even though the fluid mechanics within the cyclone barrel are turbulent, the flue gas exiting the cyclone barrel is very stratified with wide variations in local stoichiometric ratio. Reagent injection into regions of hot, lean flue gas near the cyclone barrel exit can produce rather than destroy $NO_x$. It is believed that by injecting #2 fuel oil down the axis of the

cyclone barrel, much of this stratification can be reduced by mixing the oil into regions of high oxygen concentration. Combining oil injection with RRI has the potential for increasing NOx reductions above those that can be achieved by RRI alone.

**Table 3.1. Description of RRI simulations.**

| Case | Description |
|---|---|
| **ble1_90_base** | No urea injection, based on case "ofa15", barrel stoichiometry = 0.9 |
| **ble1_90_6sw_44** | 6 side wall injectors at elevation 44 ft. (3 injectors on each side wall, centered on thirds), NSR=2, 10% aqueous urea (2.9 gpm/injector), 50 μm SMD, $V_{drops}$=300 m/s |
| **ble1_90_6sw_44_up30** | Same as ble1_90_6sw_44. Injectors are angled up 30° from horizontal |
| **ble1_90_6sw_44_up30_nsr1** | Same as ble1_90_6sw_44_up30. NSR=1.0 |
| **ble1_90_6sw_44_homog** | Same as ble1_90_6sw_44. Rich flue gas exiting cyclones is assumed to be homogeneous in terms of temperature and composition. |
| **ble1_90_6sw_1rw_44_up30** | Same as ble1_90_6sw_44_up30 except an additional injector is centered on rear wall at El=44 ft. |
| **ble1_90_6sw_300m_44_up30** | Same as ble1_90_6sw_44_up30 except the droplet size distribution has 300 μm SMD |
| **ble1_90_6sw_44_up30_inj1** | Same as ble1_90_6sw_44_up30 except:<br>- SMD = 142 μm, $V_{drops}$ = 36 m/s, Urea concentration = 22.8% (1.25 gpm/injector) |
| **ble1_90_6sw_44_up30_inj2** | Same as ble1_90_6sw_44_up30_inj1 except:<br>- Urea concentration = 10% (2.9 gpm/injector) |
| **ble1_90_6sw_44_up30_inj3** | Same as ble1_90_6sw_44_up30 except:<br>- $V_{drops}$ = 50 m/s |
| **ble1_90_5sw_44_1rw_62** | Same as ble1_90_6sw_44_up30 except:<br>- Middle injector on left side wall removed<br>- Rear wall injector at 62 ft. elevation is added on rear wall 4.5 ft. from left side wall, angled down 30° from horizontal |

**Table 3.2. Simulation predictions of RRI performance.***

| Case | NOx Red. | NOx (lbs/MMBtu) | Reagent (gph) | $NH_3$ Slip (ppm,wet) |
|---|---|---|---|---|
| ble1_90_base | 0.0% | 0.48 | 0. | 0 |
| ble1_90_6sw_44 (baseline) | 12% | 0.42 | 190. | <1 |
| ble1_90_6sw_44_up30 | 28% | 0.34 | 190. | <1 |
| ble1_90_6sw_44_up30_nsr1 | 19% | 0.39 | 95. | <1 |
| ble1_90_6sw_44_homog | 35% | 0.31 | 190. | <1 |
| ble1_90_6sw_1rw_44_up30 | 26% | 0.35 | 190. | <1 |
| ble1_90_6sw_300m_44_up30 | 16% | 0.40 | 190. | <1 |
| ble1_90_6sw_44_up30_inj1 | 18% | 0.39 | 190. | <1 |
| ble1_90_6sw_44_up30_inj2 | 24% | 0.36 | 190. | <1 |
| ble1_90_6sw_44_up30_inj3 | 29% | 0.34 | 190. | <1 |
| ble1_90_5sw_44_1rw_62 | 32% | 0.32 | 190. | <1 |
| ble1_90_6sw_44_2rw_62 | 33% | 0.32 | 190. | <1 |
| ble1_90_6sw_44_2rw_62_2sw_62 | 35% | 0.31 | 190. | <1 |

*** 0.31 lbs/MMBtu assumes that the furnace outlet $NO_x$ without reagent injection is 0.48 lbs/MMBtu**

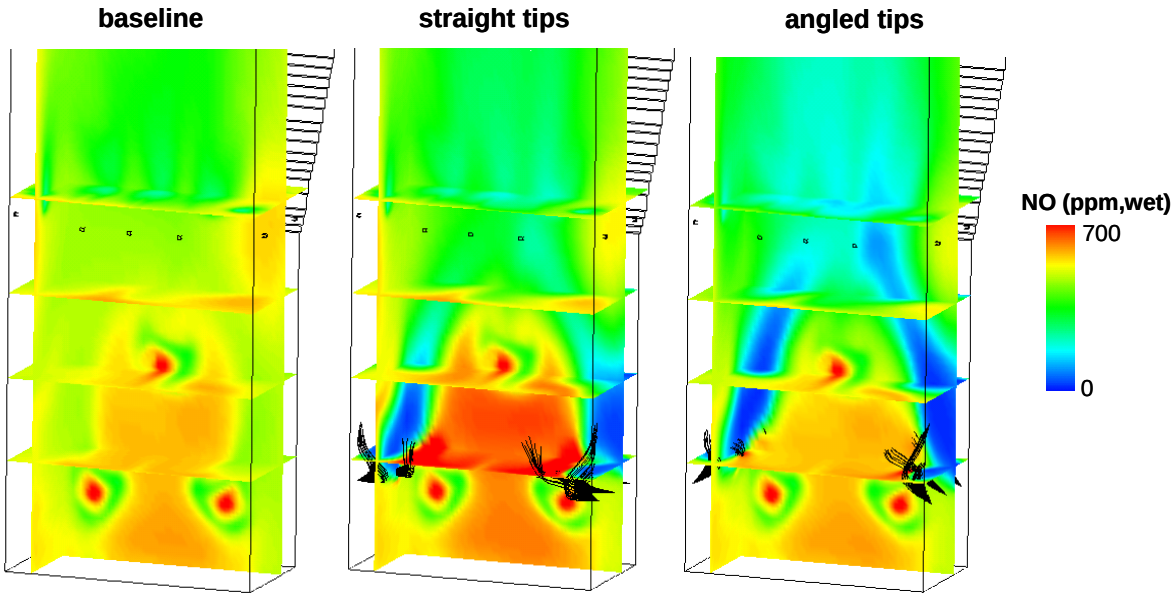


**Figure 3.12. Predicted NO distribution showing the impact of penetration of reagent into the lower furnace. The black lines illustrate typical droplet trajectories.**

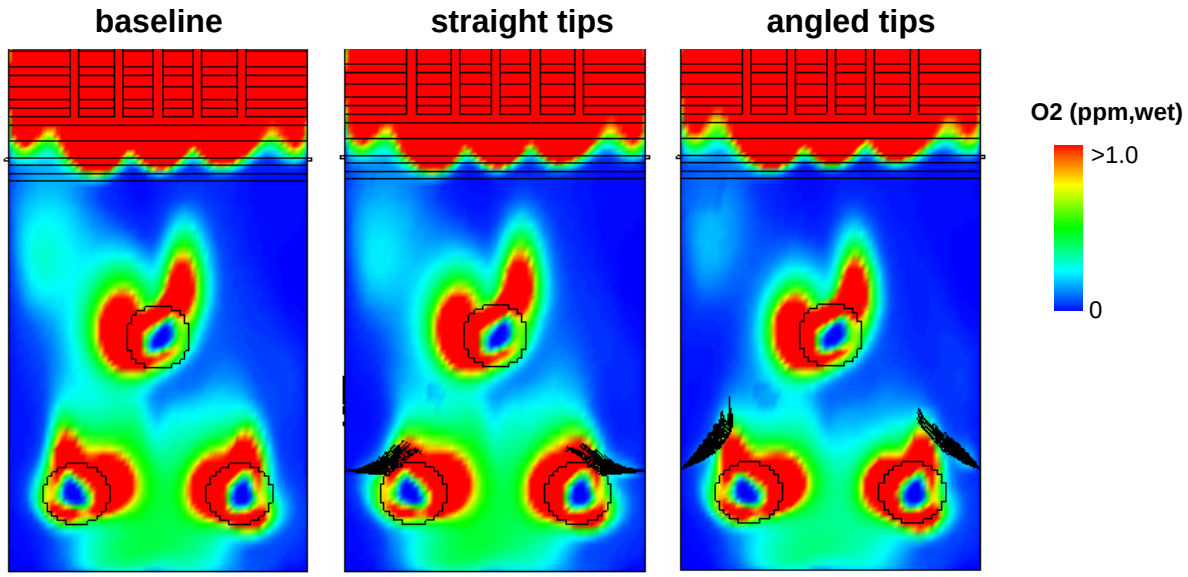


**Figure 3.13. Predicted $O_2$ distribution in a plane through the center sidewall injectors. The black lines illustrate typical droplet trajectories.**

Another possible benefit of oil injection in the barrel is increased $NO_x$ reduction in the furnace even in the absence of RRI. If the oil is injected in a manner such that the oil droplets do not vaporize and react until they are near the cyclone exit, then the furnace can be effectively operated at a lower overall stoichiometric ratio than the barrel, possibly avoiding problems associated with operation of the barrel under very rich conditions. Operation of the furnace at reduced stoichiometric ratios, or in other words staging the furnace more deeply, has been found to lead to increased levels of $NO_x$ reduction.

### *3.2.2 Testing of RRI at 130 MW Cyclone-fired Furnace*

Based on the detailed modeling information, CNCIG, EPRI, and the United States DOE chose to financially support a field test of RRI in a 130 MW cyclone-fired boiler. Bench-scale and pilot-scale testing, and CFD modeling have all produced very favorable results indicating the benefits of this process in reducing $NO_x$ emissions. However, this was the first demonstration of this technology in a full-scale utility boiler. Existing SNCR and OFA systems on the furnace made the unit a cost effective site for a demonstration of the RRI technology since the existing SNCR infrastructure could be used for the test. The majority of the tests were conducted at 120 MWe. The objectives of the RRI testing were to:

- Evaluate the effectiveness of RRI as a $NO_x$ reduction technology in full-scale unit;
- Determine how well RRI performance can be predicted;
- Optimize $NO_x$ reduction by layering OFA, RRI, and SNCR; and
- Apply information from testing to extend modeling and testing to larger cyclone-fired furnaces.

Based on the CFD analysis, eight RRI injection ports were installed. The elevations of the injectors were constrained by the location of the windbox. The side-wall injectors are immediately below the windbox and the rear wall injectors are immediately above the windbox. The locations are shown in Figure 3.11 with gray arrows (red in full color pages). The ports in Figure 3.11 that were not installed are the two upper level side-wall locations (black arrows). RJM Corporation who had installed the original SNCR equipment led the installation of the temporary RRI equipment. The installation was designed to allow testing of the new RRI system in combination with the existing SNCR system. As suggested by the CFD analysis, significant modifications to the existing SNCR injectors were warranted in order to achieve the predicted RRI performance. These modifications were made as specified by REI and EPRI and were restricted to the internals of the nozzle hardware to modify the liquid flow rates and atomization characteristics. Conectiv contracted RJM Corporation to modify the existing SNCR injectors to provide the specified flow rates and droplet size distributions. No significant modifications were made to upgrade the nozzle materials or cooling design to take into account the severe lower furnace conditions. However, the manufactured nozzle tips and outer cooling shields were ceramic coated for increased resistance to the expected high heat fluxes.

Three different nozzle tips were manufactured prior to the RRI testing for evaluation: 1) Straight tips, 30° conically shaped spray (SC); 2) Angled tips, 30° from straight, 30° conically shaped spray (AC); 3) Angled tips, 30° from straight, fan shaped spray (AF). The injectors installed with these three different tips were performance tested prior to the RRI testing to assure that the capacity, droplet size and velocity distributions specified by REI based on the CFD modeling would be achieved.

Since a large number of injector and boiler parameters were varied to assess sensitivity of RRI, the individual tests were relatively short, each lasting less than one hour. The parameters that were evaluated included:

- injector spray pattern (SC, AC, AF);
- normalized stoichiometric ratio (NSR);
- reagent Concentration;
- nozzles out of service (NOOS) and reagent flow biasing;
- cyclone barrel SR; and
- injector atomization air pressure.

#### 3.2.2.1 Baseline Testing

The objectives of the test program were met with relatively short, individual tests. The tests were not intended to evaluate long term operational impacts associated with RRI. A permanent installation would require that RRI performance be verified over the normal range of conditions experienced through day-to-day variations in operation.

The baseline testing was conducted to obtain data under normal baseline unit operation. Baseline conditions are defined to be operation under staged conditions utilizing OFA without RRI or SNCR. These conditions should be considered "typical" operating conditions. The majority of the tests were conducted at a unit net load of 120 MWe. Boiler operation was intended to reproduce conditions that were assumed for the CFD modeling that was previously conducted. Baseline boiler conditions were nominally achieved for the majority of the test program. Baseline operation is defined as:

- Load = 120 MWe (Total thermal input = 1284 MMBtu/hr = 428 MMBtu/hr/cyclone)
- Bst = 0.90, Fst = 1.09 (expected dry O2 = 1.8%)
- Fuel is 100% coal (i.e. no tires)

Bst and Fst are defined to be barrel and furnace stoichiometric ratio, respectively. Approximate cyclone coal and air flow rates to achieve these conditions are given in Table 3.3. Testing was performed with and without the use of the current SNCR system. In all tests for which $\%NO_x$ reduction was to be calculated, "baseline" tests (without reagent) were conducted before, after, or before and after reagent injection.

**Table 3.3. Design barrel and furnace inputs.**

| **Inputs** | |
|---|---|
| Barrel Thermal Input | 428 MMBtu/hr |
| Coal Feed Rate/Barrel | 34,397 lb/hr |
| Total Barrel Air | 285,708 lb/hr |
| Barrel Air Split (P:S:T) | 12%:85%:3% |
| Barrel Stoichiometric Ratio | 0.9 |
| OFA | 180,959 lb/hr |
| Total Furnace Air | 1,038,083 lb/hr |
| Furnace Stoichiometric Ratio | 1.09 |

#### 3.2.2.2 Testing Results

Table 3.4 contains an extensive summary of the tests and the results that were carried out.

Furnace exit $NO_x$ levels were based on the existing calibrated continuous emissions monitors (CEMs). Throughout the testing, NOx levels were nominally based on fifteen-minute averages of the CEMs measurements. For selected test points, single point $NH_3$ samples were obtained within two separate ducts upstream of the air heaters. Analyses of these gas samples were performed by scrubbing the gas sample with a dilute sulfuric acid solution and analyzing with a specific ion electrode (wet method). No effort was made during this test program to correlate these single point measurements with a multipoint average within each duct. Measurements were used only to provide a cursory indication of ammonia slip. Measurements of unburned carbon were also obtained during selected tests using a hot foil loss on ignition (LOI) instrument.

Other relevant operating data during the RRI testing were obtained directly from the Bailey DCS or by extracting archived data using the station's Pi data system. Operational data for air and coal flow rates were obtained in this manner. Reagent flow rates and atomization air pressures for the RRI system were obtained directly from the rotometers on the temporary distribution panels.

**Table 3.4. Test conditions and the results of RRI testing.**

| Test No. | Test Type | Test Day | Test Time | Gross Load MWg | Total OFA (lbh) | Total SNCR Chemical Flow (gph) | Total RRI Chemical Flow (gph) | Baseline # NOX /MMBtu | NH3 Slip (ppm) | Corrected (#NOx /MMBtu) | NOx Reduction (%) |
|---|---|---|---|---|---|---|---|---|---|---|---|
| 1.1 | Baseline | 10-Jul-00 | 9:30 | 128 | 173115 | 0 | 0 | | | | |
| 1.2 | Baseline | 10-Jul-00 | 15:40 | 129 | 183765 | 0 | 0 | | | | |
| | | | | | | | | | | | |
| 2.1 | Baseline | 11-Jul-00 | 8:00 | 128 | 182813 | 0 | 0 | 0.52 | | 0.520 | 0.0 |
| 2.2 | SNCR-Z3 | 11-Jul-00 | 12:15 | 128 | 181638 | 36 | 0 | 0.52 | | 0.420 | 19.2 |
| 2.3 | Baseline | 11-Jul-00 | 17:15 | 128 | 206388 | 0 | 0 | 0.471 | | 0.471 | 0.0 |
| 2.4 | SNCR-Z3 | 11-Jul-00 | 17:30 | 128 | 206899 | 45 | 0 | 0.471 | | 0.360 | 23.6 |
| | | | | | | | | | | | |
| 3.1 | Baseline | 12-Jul-00 | 9:15 | 129 | 209116 | 0 | 0 | 0.539 | | 0.539 | 0.0 |
| 3.2 | RRI | 12-Jul-00 | 11:00 | 129 | 209343 | 0 | 132 | 0.539 | | 0.452 | 16.1 |
| 3.3 | RRI | 12-Jul-00 | 13:30 | 127 | 208939 | 0 | 191 | 0.539 | 0.5 | 0.444 | 17.6 |
| 3.4 | Baseline | 12-Jul-00 | 14:25 | | 210529 | 0 | 0 | 0.541 | | 0.541 | 0.0 |
| 3.5 | RRI - air p | 12-Jul-00 | 16:30 | | 208865 | 0 | 190 | 0.569 | | 0.473 | 16.9 |
| 3.6 | RRI - air p | 12-Jul-00 | 17:30 | 126 | 206337 | 0 | 190 | 0.569 | | 0.466 | 18.1 |
| 3.7 | RRI - air p | 12-Jul-00 | 18:00 | | 207977 | 0 | 189 | 0.569 | | 0.460 | 19.2 |
| 3.8 | RRI - air p | 12-Jul-00 | 18:15 | 127 | 209130 | 0 | 190 | 0.569 | 0.3 | 0.459 | 19.3 |
| 3.9 | Baseline | 12-Jul-00 | 19:30 | | 200658 | 0 | 0 | 0.569 | | 0.569 | 0.0 |
| | | | | | | | | | | | |
| 4.1 | Baseline | 13-Jul-00 | 8:30 | 133 | 209744 | 0 | 0 | 0.514 | | 0.514 | 0.0 |
| 4.2 | RRI | 13-Jul-00 | 9:45 | 132 | 208016 | 0 | 193 | 0.525 | | 0.439 | 16.4 |
| 4.3 | RRI | 13-Jul-00 | 11:00 | 130 | 204958 | 0 | 190 | 0.525 | | 0.457 | 13.0 |
| 4.4 | RRI | 13-Jul-00 | 11:30 | 130 | 208702 | 0 | 190 | 0.525 | | 0.450 | 14.3 |
| 4.5 | RRI | 13-Jul-00 | 12:15 | 129 | 209184 | 0 | 190 | 0.525 | | 0.433 | 17.5 |
| 4.6 | Baseline | 13-Jul-00 | 12:30 | 129 | 210678 | 0 | 0 | 0.536 | | 0.536 | 0.0 |
| 4.7 | RRI - NOOS | 13-Jul-00 | 14:20 | | 212802 | 0 | 188 | 0.525 | 0.2 | 0.403 | 23.2 |
| 4.8 | RRI - NOOS | 13-Jul-00 | 15:45 | 130 | 211741 | 0 | 165 | 0.525 | | 0.432 | 17.7 |
| 4.9 | RRI - NOOS | 13-Jul-00 | 16:00 | 129 | 210811 | 0 | 165 | 0.525 | | 0.432 | 17.7 |
| 4.10 | RRI - NOOS | 13-Jul-00 | 16:30 | | 212686 | 0 | 161 | 0.525 | | 0.431 | 17.9 |
| Test No. | Test Type | Test Day | Test Time | Gross Load MWg | Total OFA (lbh) | Total SNCR Chemical Flow (gph) | Total RRI Chemical Flow (gph) | Baseline # NOX /MMBtu | NH3 Slip (ppm) | Corrected (#NOx /MMBtu) | NOx Reduction (%) |

| | | | | | | | | | | | |
|---|---|---|---|---|---|---|---|---|---|---|---|
| 4.11 | RRI - NOOS | 13-Jul-00 | 17:15 | | 212842 | 0 | 169 | 0.525 | | 0.434 | 17.3 |
| 4.12 | RRI - NOOS | 13-Jul-00 | 17:30 | | 210550 | 0 | 166 | 0.525 | | 0.450 | 14.3 |
| 4.13 | RRI - NOOS | 13-Jul-00 | 17:45 | | 210434 | 0 | 166 | 0.525 | | 0.449 | 14.5 |
| 4.14 | RRI - NOOS | 13-Jul-00 | 18:00 | | 211443 | 0 | 166 | 0.525 | | 0.435 | 17.1 |
| 4.15 | RRI - NOOS | 13-Jul-00 | 18:30 | | 211210 | 0 | 166 | 0.525 | | 0.433 | 17.5 |
| 4.16 | Baseline | 13-Jul-00 | 19:00 | 130 | 210588 | 0 | 0 | 0.525 | | 0.525 | 0.0 |
| | | | | | | | | | | | |
| 5.1 | Baseline | 14-Jul-00 | 8:30 | 132 | 207315 | 0 | 0 | 0.491 | | 0.491 | 0.0 |
| 5.2 | RRI - AC | 14-Jul-00 | 9:45 | 132 | 205458 | 0 | 191 | 0.4755 | | 0.394 | 17.1 |
| 5.3 | RRI - AC | 14-Jul-00 | 11:00 | 132 | 206635 | 0 | 128 | 0.4755 | 3.1 | 0.390 | 18.0 |
| 5.4 | RRI - AC | 14-Jul-00 | 11:45 | 132 | 209153 | 0 | 64 | 0.4755 | 0.2 | 0.403 | 15.2 |
| 5.5 | Baseline | 14-Jul-00 | 12:30 | 130 | 207244 | 0 | 0 | 0.46 | | 0.460 | 0.0 |
| 5.6 | Baseline | 14-Jul-00 | 14:45 | 131 | 170384 | 0 | 0 | 0.535 | | 0.535 | 0.0 |
| 5.7 | RRI | 14-Jul-00 | 15:30 | 130 | 173123 | 0 | 191 | 0.535 | | 0.437 | 18.3 |
| 5.8 | Baseline | 14-Jul-00 | 17:30 | 130 | 172652 | 0 | 0 | 0.58 | | 0.580 | 0.0 |
| 5.9 | RRI - SC | 14-Jul-00 | 18:00 | 129 | 169487 | 0 | 191 | 0.572 | | 0.490 | 14.3 |
| 5.10 | RRI - SC | 14-Jul-00 | 18:15 | 130 | 169118 | 0 | 125 | 0.572 | | 0.485 | 15.2 |
| 5.11 | RRI - SC | 14-Jul-00 | 18:45 | | 172588 | 0 | 64 | 0.572 | 0.1 | 0.511 | 10.7 |
| 5.12 | Baseline | 14-Jul-00 | 19:30 | | 169190 | 0 | 0 | 0.564 | | 0.564 | 0.0 |
| | | | | | | | | | | | |
| 6.1 | Baseline | 17-Jul-00 | 9:00 | 130 | 164904 | 0 | 0 | 0.593 | | 0.593 | 0.0 |
| 6.2 | RRI | 17-Jul-00 | 11:15 | 130 | 161232 | 0 | 129 | 0.604 | | 0.570 | 5.6 |
| 6.3 | RRI | 17-Jul-00 | 12:45 | 130 | 165613 | 0 | 128 | 0.604 | | 0.569 | 5.8 |
| 6.4 | RRI | 17-Jul-00 | 13:30 | | 207181 | 0 | 128 | 0.604 | | 0.479 | 20.7 |
| 6.5 | RRI | 17-Jul-00 | 15:00 | | 192553 | 0 | 127 | 0.604 | | 0.499 | 17.4 |
| 6.6 | RRI | 17-Jul-00 | 16:15 | 129 | 189831 | 0 | 190 | 0.604 | | 0.469 | 22.4 |
| 6.7 | RRI | 17-Jul-00 | 17:00 | 127 | 191476 | 0 | 179 | 0.604 | | 0.448 | 25.8 |
| 6.8 | Baseline | 17-Jul-00 | 17:15 | 124 | 188819 | 0 | 0 | 0.615 | | 0.615 | 0.0 |
| | | | | | | | | | | | |
| 7.1 | Baseline | 18-Jul-00 | 10:00 | 130 | 205601 | 0 | 0 | 0.563 | 0.0 | 0.563 | 0.0 |
| Test No. | Test Type | Test Day | Test Time | Gross Load MWg | Total OFA (lbh) | Total SNCR Chemical Flow (gph) | Total RRI Chemical Flow (gph) | Baseline # NOX /MMBtu | NH3 Slip (ppm) | Corrected (#NOx /MMBtu) | NOx Reduction (%) |
| 7.2 | RRI | 18-Jul-00 | 11:15 | 131 | 199000 | 0 | 185 | 0.5405 | | 0.472 | 12.7 |
| 7.3 | RRI | 18-Jul-00 | 11:30 | 131 | 206319 | 0 | 192 | 0.5405 | | 0.451 | 16.6 |
| 7.4 | RRI | 18-Jul-00 | 11:50 | 131 | 204312 | 0 | 195 | 0.5405 | | 0.435 | 19.5 |

| | | | | | | | | | | |
|---|---|---|---|---|---|---|---|---|---|---|
| 7.5 | RRI | 18-Jul-00 | 12:45 | 131 | 202634 | 0 | 128 | 0.5405 | 0.460 | 14.9 |
| 7.6 | RRI | 18-Jul-00 | 13:15 | 131 | 199458 | 0 | 127 | 0.5405 | 0.463 | 14.3 |
| 7.7 | RRI | 18-Jul-00 | 13:30 | 131 | 138985 | 0 | 129 | 0.5405 | 0.472 | 12.7 |
| 7.8 | RRI | 18-Jul-00 | 14:00 | 131 | 202292 | 0 | 146 | 0.5405 | 0.434 | 19.7 |
| 7.9 | Baseline | 18-Jul-00 | 14:30 | 131 | 199325 | 0 | 0 | 0.518 | 0.518 | 0.0 |
| 7.10 | Baseline | 18-Jul-00 | 15:30 | 121 | 168021 | 0 | 0 | 0.671 | 0.671 | 0.0 |
| 7.11 | Baseline | 18-Jul-00 | 16:00 | 129 | 141039 | 0 | 0 | | | |
| 7.12 | RRI | 18-Jul-00 | | | | 0 | | | | |
| 7.13 | Baseline | 18-Jul-00 | 19:00 | 123 | 167526 | 0 | 0 | 0.539 | 0.539 | 0.0 |
| 7.14 | RRI | 18-Jul-00 | 19:40 | 122 | 167709 | 0 | 126 | 0.534 | 0.482 | 9.7 |
| 7.15 | RRI | 18-Jul-00 | 20:05 | 124 | 170903 | 0 | 62 | 0.534 | 0.482 | 9.7 |
| 7.16 | RRI | 18-Jul-00 | 21:05 | 124 | 169963 | 0 | 127 | 0.534 | 0.477 | 10.7 |
| 7.17 | RRI | 18-Jul-00 | 21:30 | 124 | 167561 | 0 | 127 | 0.534 | 0.461 | 13.7 |
| 7.18 | Baseline | 18-Jul-00 | 22:00 | 125 | 171128 | 0 | 15 | 0.529 | 0.529 | 0.0 |
| | | | | | | | | | | |
| 8.1 | Baseline | 15-Aug-00 | 13:25 | | 202380 | 0 | 0 | 0.533 | 0.533 | 0.0 |
| 8.2 | AF tips 8 inj. | 15-Aug-00 | 14:55 | 128 | 200973 | 0 | 230 | 0.528 | 0.384 | 27.3 |
| 8.3 | AF tips 8 inj. | 15-Aug-00 | 15:26 | 128 | 201290 | 0 | 190 | 0.528 | 0.381 | 27.8 |
| 8.4 | AF tips 8 inj. | 15-Aug-00 | 16:00 | | 203456 | 0 | 143 | 0.528 | 0.395 | 25.2 |
| 8.5 | AF tips 8 inj. | 15-Aug-00 | 16:24 | | 202939 | 0 | 94 | 0.528 | 0.422 | 20.1 |
| 8.6 | AF tips CDEF | 15-Aug-00 | 17:40 | | 202571 | 0 | 230 | 0.528 | 0.406 | 23.1 |
| 8.7 | AF tips CDEF | 15-Aug-00 | 18:13 | | 204745 | 0 | 189 | 0.528 | 0.404 | 23.5 |
| 8.8 | AF tips CDEF | 15-Aug-00 | 19:00 | 129 | 201021 | 0 | 143 | 0.528 | 0.423 | 19.9 |
| 8.9 | AF tips CDEF | 16-Aug-00 | 19:40 | | 202642 | 0 | 94 | 0.528 | 0.447 | 15.3 |
| 8.10 | Baseline | 16-Aug-00 | 20:35 | | 203803 | 0 | 0 | 0.523 | 0.523 | 0.0 |
| 8.11 | AC tIps CDEF | 16-Aug-00 | 21:45 | 130 | 203506 | 0 | 190 | 0.5145 | 0.406 | 21.1 |
| 8.12 | AC tIps CDEF | 16-Aug-00 | 22:13 | | 201371 | 0 | 143 | 0.5145 | 0.418 | 18.8 |
| Test No. | Test Type | Test Day | Test Time | Gross Load MWg | Total OFA (lbh) | Total SNCR Chemical Flow (gph) | Total RRI Chemical Flow (gph) | Baseline # NOX /MMBtu | NH3 Slip (ppm) | Corrected (#NOx /MMBtu) | NOx Reduction (%) |
| 8.13 | AC tIps CDEF | 16-Aug-00 | 22:41 | | 202660 | 0 | 95 | 0.5145 | | 0.422 | 18.0 |
| 8.14 | AC tips 8 inj. | 16-Aug-00 | 23:16 | | 203449 | 0 | 190 | 0.5145 | | 0.376 | 26.9 |
| 8.15 | AC tips 8 inj. | 16-Aug-00 | 23:35 | | 205360 | 0 | 95 | 0.5145 | | 0.409 | 20.5 |
| 8.16 | Baseline | 16-Aug-00 | 0:10 | | 204630 | 0 | 0 | 0.506 | | 0.506 | 0.0 |
| | | | | | | | | | | | |
| 11.1 | Baseline | 18-Aug-00 | 9:25 | | 68501 | 0 | | 0.858 | | 0.858 | 0.0 |

| Test No. | Test Type | Test Day | Test Time | Gross Load MWg | Total OFA (lbh) | Total SNCR Chemical Flow (gph) | Total RRI Chemical Flow (gph) | Baseline # NOX /MMBtu | NH3 Slip (ppm) | Corrected (#NOx /MMBtu) | NOx Reduction (%) |
|---|---|---|---|---|---|---|---|---|---|---|---|
| 11.2 | RRI | 18-Aug-00 | 10:23 | | 68502 | 0 | 190 | 0.858 | | 0.683 | 20.4 |
| 11.3 | RRI | 18-Aug-00 | 11:45 | | 177353 | 0 | 190 | 0.531 | | 0.440 | 17.1 |
| 11.4 | rri | 18-Aug-00 | 13:10 | | 180109 | 0 | 190 | 0.531 | | 0.422 | 20.5 |
| 11.5 | rri + sncr | 18-Aug-00 | 13:45 | | 180022 | 75 | 190 | 0.531 | 7.0 | 0.236 | 55.6 |
| 11.6 | rri | 18-Aug-00 | 15:05 | | 168733 | 0 | 190 | 0.531 | | 0.392 | 26.2 |
| 11.7 | Baseline | 18-Aug-00 | 16:00 | 130 | 184033 | 0 | 0 | 0.531 | | 0.531 | 0.0 |
| | | | | | | | | | | | |
| 12.1 | Baseline | 19-Aug-00 | 8:35 | | 190037 | 0 | 0 | 0.549 | | 0.549 | 0.0 |
| 12.2 | Baseline | 19-Aug-00 | 10:25 | | 198105 | 0 | 0 | 0.562 | | 0.562 | 0.0 |
| 12.3 | rri | 19-Aug-00 | 11:30 | | 198885 | 0 | 190 | 0.533 | | 0.426 | 20.1 |
| 12.4 | rri | 19-Aug-00 | 12:13 | 131 | 201106 | 0 | 190 | 0.533 | | 0.443 | 16.9 |
| 12.5 | rri | 19-Aug-00 | 13:57 | 131 | 200834 | 0 | 190 | 0.533 | | 0.389 | 27.0 |
| 12.6 | Baseline | 19-Aug-00 | 14:40 | | 203255 | 0 | 0 | 0.504 | | 0.504 | 0.0 |
| 12.7 | Baseline | 19-Aug-00 | 15:00 | | 199617 | 0 | 0 | 0.506 | | 0.506 | 0.0 |
| 12.8 | rri | 19-Aug-00 | 15:50 | 131 | 203165 | 0 | 190 | 0.506 | 0.3 | 0.387 | 23.5 |
| 12.9 | rri | 19-Aug-00 | 16:30 | 131 | 200387 | 0 | 190 | 0.506 | | 0.388 | 23.3 |
| 12.10 | rri | 19-Aug-00 | 17:14 | | 201902 | 0 | 190 | 0.506 | | 0.367 | 27.5 |
| | | | | | | | | | | | |
| 13.1 | Baseline | 21-Aug-00 | 8:40 | | 199060 | 0 | 0 | 0.531 | | 0.531 | 0.0 |
| 13.2 | RRI | 21-Aug-00 | 10:10 | | 199580 | 0 | 190 | 0.531 | | 0.469 | 11.7 |
| 13.3 | RRI | 21-Aug-00 | 11:15 | | 198567 | 0 | 190 | 0.531 | | 0.442 | 16.8 |
| 13.4 | Biased RRI | 21-Aug-00 | 11:45 | | 199380 | 0 | 190 | 0.531 | | 0.434 | 18.3 |
| 13.5 | Baseline | 21-Aug-00 | 12:40 | | 202544 | 0 | 0 | 0.585 | | 0.585 | 0.0 |
| 13.6 | Baseline | 21-Aug-00 | 13:45 | | 199218 | 0 | 0 | 0.554 | | 0.554 | 0.0 |
| 13.7 | Baseline | 21-Aug-00 | 15:30 | | 201248 | 0 | 0 | 0.563 | | 0.563 | 0.0 |
| | | | | | | | | | | | |
| 14.1 | Base, low load | 22-Aug-00 | 3:00 | 80 | 238098 | 0 | 0 | 0.397 | | 0.397 | 0.0 |
| 14.2 | RRI | 22-Aug-00 | 3:43 | 80 | 238825 | 0 | 125 | 0.397 | | 0.297 | 25.2 |
| 14.3 | RRI | 22-Aug-00 | 4:08 | 80 | 236095 | 0 | 95 | 0.397 | | 0.311 | 21.7 |
| 14.4 | RRI | 22-Aug-00 | 4:33 | 80 | 237547 | 0 | 55 | 0.397 | | 0.334 | 15.9 |
| 14.5 | RRI + SNCR | 22-Aug-00 | 5:08 | 80 | 240741 | 40 | 125 | 0.397 | | 0.195 | 50.9 |
| 14.6 | RRI + SNCR | 22-Aug-00 | 7:20 | 80 | 136415 | 40 | 125 | 0.506 | | 0.278 | 45.1 |
| 14.7 | Baseline | 22-Aug-00 | 7:50 | 80 | 138608 | 0 | 0 | 0.506 | | 0.506 | 0.0 |

| | | | | | | | | | | | |
|---|---|---|---|---|---|---|---|---|---|---|---|
| 14.8 | Base, full load | 22-Aug-00 | 11:35 | 130 | 172397 | 0 | 0 | 0.611 | | 0.611 | 0.0 |
| 14.9 | RRI | 22-Aug-00 | 12:30 | 130 | 190050 | 0 | 230 | 0.611 | | 0.522 | 14.6 |
| 14.10 | RRI | 22-Aug-00 | 12:55 | 130 | 170000 | 0 | 230 | 0.611 | | 0.460 | 24.7 |
| 14.11 | RRI + SNCR | 22-Aug-00 | 13:20 | 130 | 184345 | 95 | 230 | 0.611 | 11.8 | 0.285 | 53.4 |
| 14.12 | RRI + SNCR + oil | 22-Aug-00 | 14:00 | 130 | 186567 | 95 | 230 | 0.611 | | 0.253 | 58.6 |
| 14.13 | Red. SNCR | 22-Aug-00 | 14:10 | 130 | 185196 | 75 | 230 | 0.611 | 5 | 0.277 | 54.7 |

Figure 3.14 shows a scatter plot of the test results showing furnace exit NO for the tests except the reduced load tests. The plot shows measured values for OFA only, for OFA combined with RRI, and OFA combined with both RRI and SNCR. Baseline testing was at a lower furnace SR of 0.9, but there was some computed variation around that level. The range of lower furnace stoichiometric ratios for the testing was likely 0.8 – 1.0, based on the measured primary and secondary airflows and the coal feeder speed rates. Figure 3.15 shows the same test data computing percent $NO_x$ reduction due to application of RRI or RRI in combination with SNCR. The line passing through the data in Figure 3.15 indicates the NO reductions with RRI in which optimal injection strategies were utilized. As seen in Figure 3.14, $NO_x$ emissions under staged conditions with OFA were approximately 0.55 lb/MMBtu. Addition of RRI to the OFA system reduced the exit NO by approximately 25-30% (Figure 3.15). Combining RRI with SNCR was observed to achieve approximately 55% reduction beyond OFA levels to reduce the $NO_x$ emissions to approximately 0.25 lb/MMBtu. These levels of $NO_x$ reduction were achieved utilizing NSRs of approximately 1 and 2 for SNCR and RRI, respectively. This demonstrates a remarkable reduction in $NO_x$ of approximately 80% through the combination of OFA/RRI/SNCR from baseline $NO_x$ emissions of 1.2 lb/MMBtu.

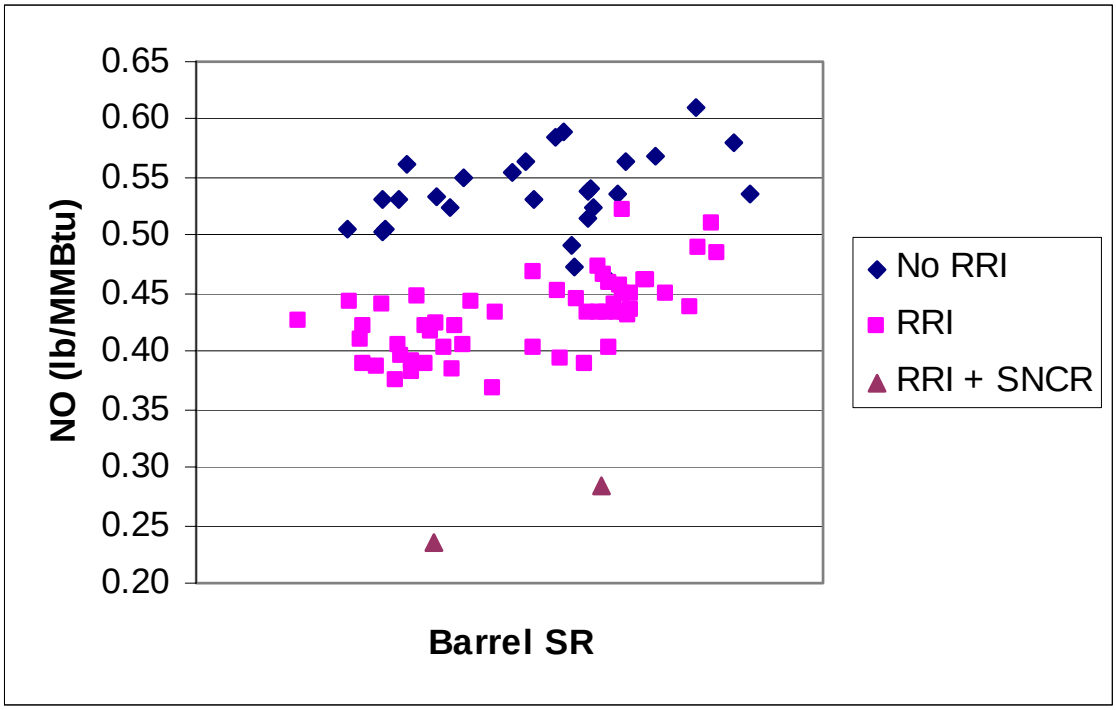


**Figure 3.14. Measured NO emissions during RRI and combined RRI and SNCR testing.**

$NH_3$ measurements during the RRI testing showed < 1 ppm slip for almost all tests. However, the combination of RRI and SNCR yielded higher $NH_3$ slips and was sensitive to the amount of reagent used for SNCR. The testing indicated that the combination of RRI and SNCR was able to 55% reduction in $NO_x$ with approximately 5 ppm $NH_3$ slip. The testing did not show a clear correlation between RRI and increased furnace CO emissions. Figure 3.16 shows the CO emissions from the CEMs for selected tests. Significant variation in CO emissions was observed

during the test program, but the variations were not directly correlated with reagent injection during the RRI process.

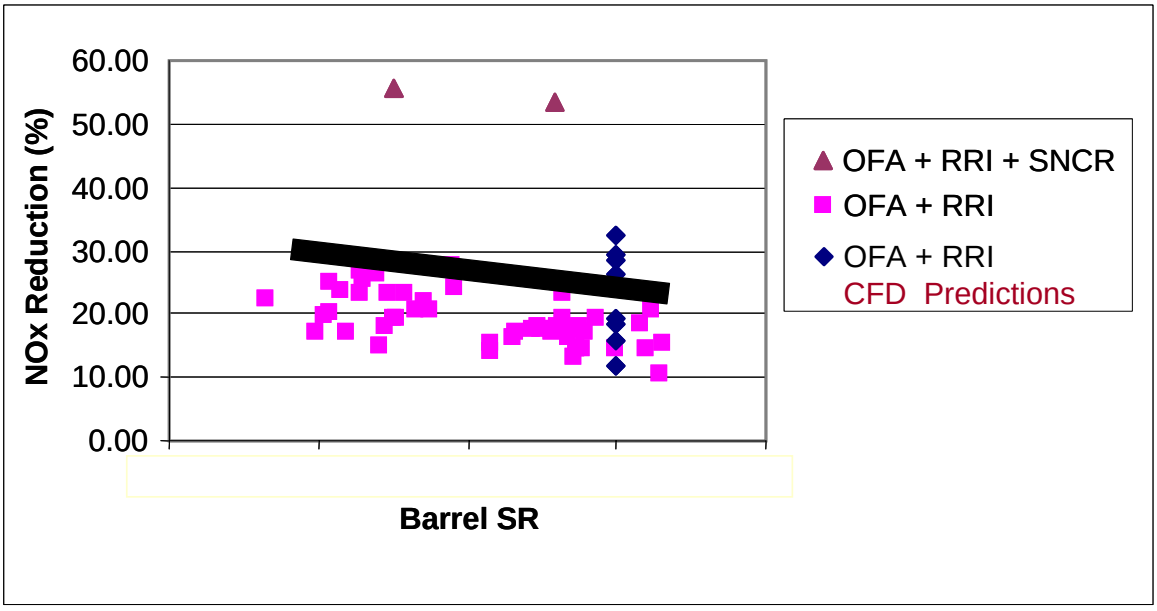


**Figure 3.15. Computed % reduction based on measurements from Figure 3.14.**

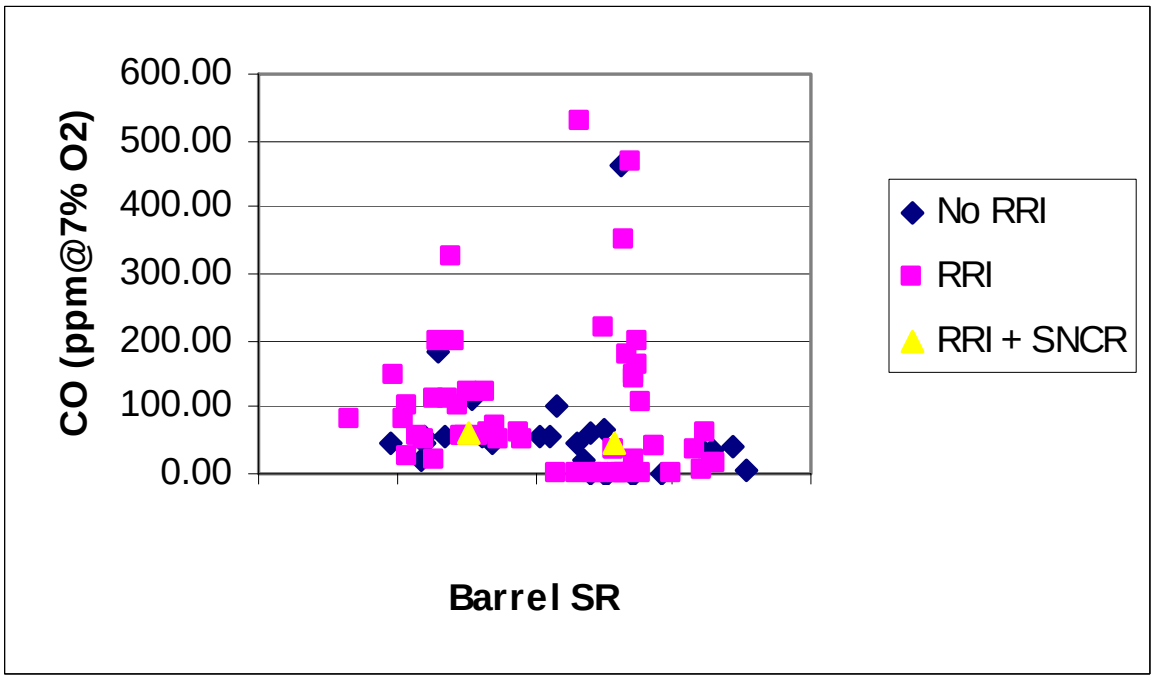


**Figure 3.16. CO emissions during RRI testing. Measurements correspond to test points plotted in Figures 3.14 and 3.15.**

#### 3.2.2.2.1 Impacts of Nozzle Tips, NSR, and Nozzle Pressure

The impacts of tip type, and NSR are shown in Figures 3.17 and 3.18. Figure 3.17 indicates that there may be a slight benefit to the use of the AF tips, which yield a fan shaped spray versus the AC tips, which yield a full cone spray pattern. Figure 3.18 similarly shows that there may be a slight improvement in performance through the use of the angled tips versus the straight tips. In addition, Figure 3.17 shows that $NO_x$ reduction appears to asymptote near an NSR of 2, where increasing the reagent usage appears to achieve no increase in performance. Figure 3.19 shows the observed impact of nozzle air pressure on $NO_x$ reduction and reagent utilization. There appears to be a slight trend of improved performance with reduced atomization air pressure at a fixed reagent flow rate.

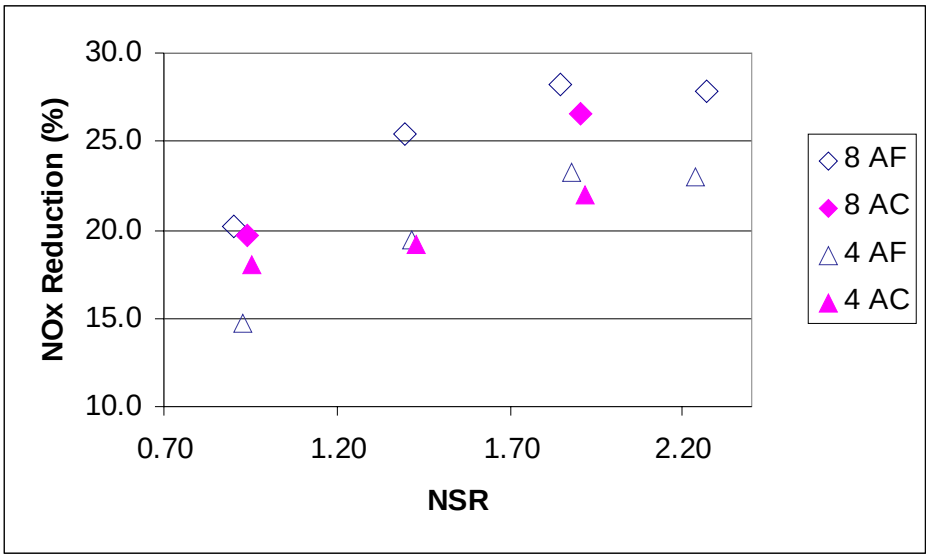


**Figure 3.17. Effects of nozzle type (angled fan (AF) vs. angled cone (AC)), NSR, and nozzle number on measured $NO_x$ reduction with RRI.**

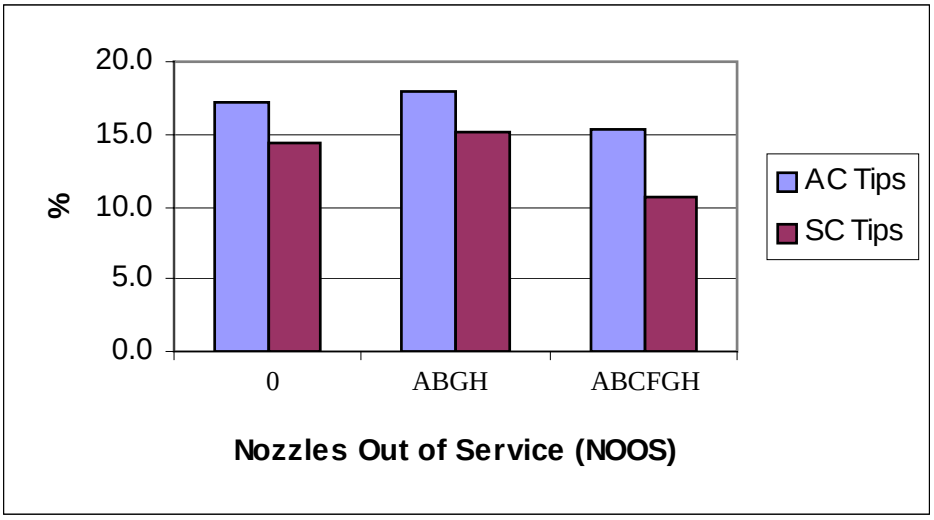


**Figure 3.18. Impact of nozzle type (angled cone (AC) vs. straight cone (SC)) on $NO_x$ reduction with RRI.**

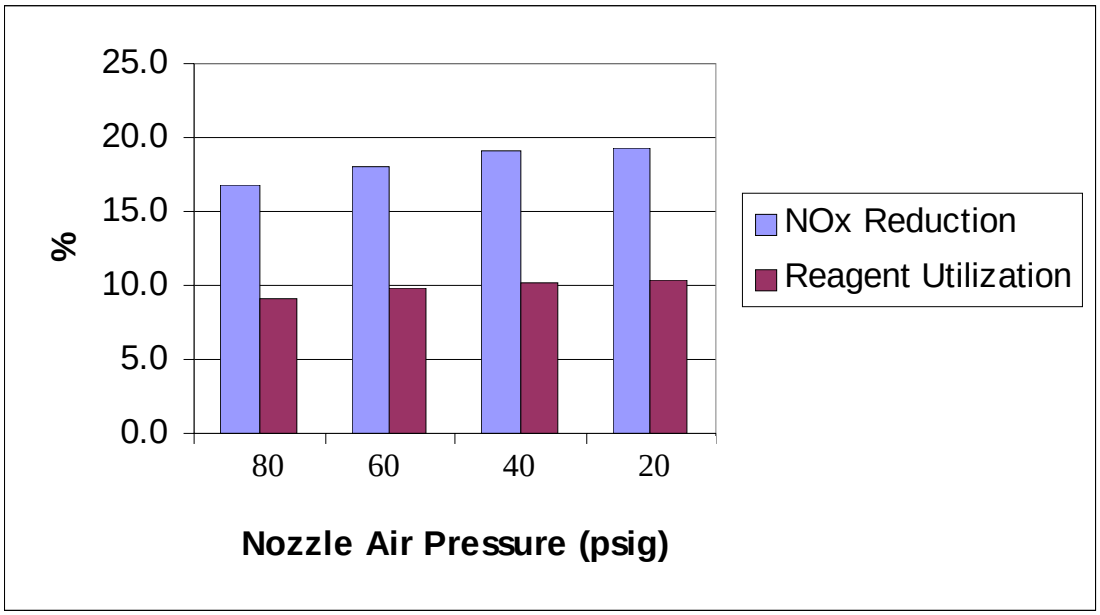


**Figure 3.19. Impact of atomization pressure on $NO_x$ reduction during phase 1 and 2 testing.**

#### 3.2.2.2.2 Impacts of Nozzles Out of Service

Figure 3.20 shows the results of tests to evaluate the impact of single nozzles out of service (NOOS). In this series of tests, all eight RRI nozzles were initially in service. Then, single nozzles were subsequently removed from service, keeping the reagent flows to the remaining injectors unchanged. For example, the impact of removing injector A from service caused a reduction in performance from approximately 23% to 18% $NO_x$ reduction. This drop reflects the reduced reagent flow due to removing injector A from service. Next, injector B was removed from service while A was reinserted. This change resulted in no net change in reagent flow. From these tests, it was observed that removal of injectors D and E from service impacted $NO_x$ reduction most, indicating that these injectors were the most effective of the eight nozzles.

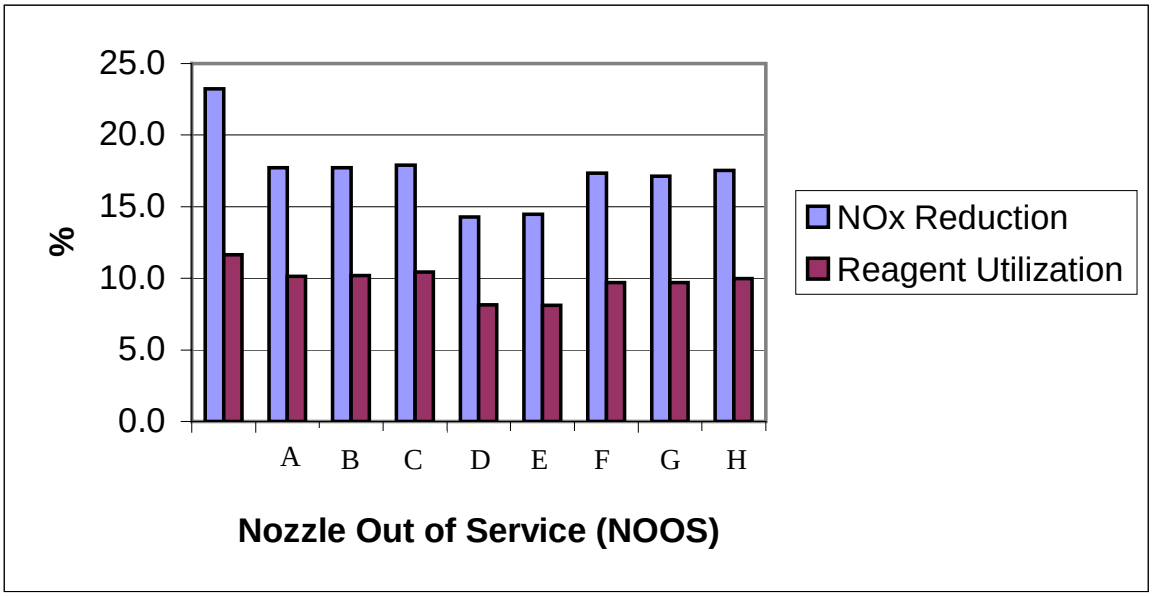


**Figure 3.20. Impact of removing single RRI nozzles from service on NOx reduction and reagent utilization.**

#### 3.2.2.2.3 Impacts of Reduced Load

Performance of RRI and combined RRI/SNCR was briefly tested under reduced load conditions. Testing was carried out at 80 MWe, by removing the third, upper cyclone barrel (barrel C) from service. All eight injectors were utilized and tests were conducted over a range of NSRs. The results are plotted in Figure 3.21 and show that at an NSR of 2, RRI alone achieved approximately 25% reduction in $NO_x$. Combined with SNCR, $NO_x$ reduction up to 51% was achieved with a total NSR of approximately 2.5. No ammonia slip measurements were taken under the reduced load tests.

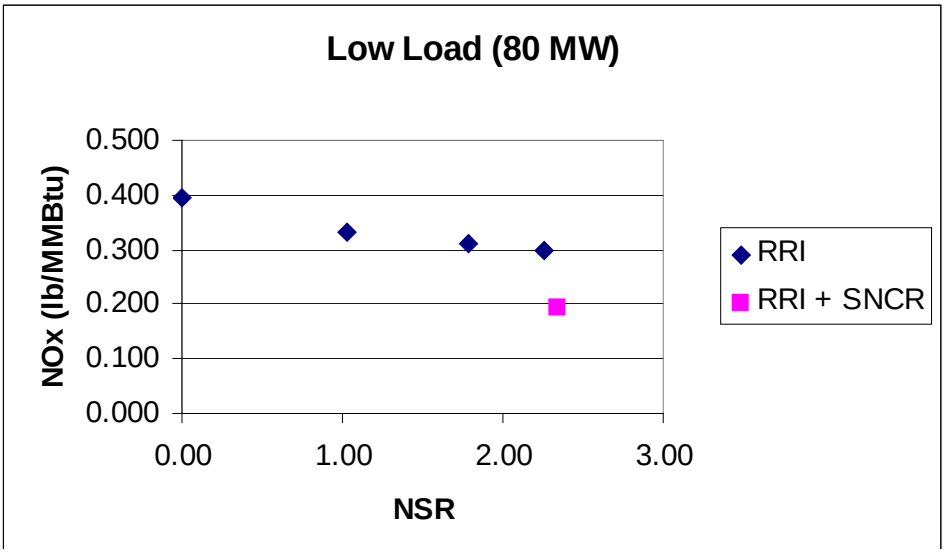


**Figure 3.21. Test results indicating RRI and combined RRI/SNCR performance under reduced load conditions. Data were obtained with cyclone C (upper cyclone) removed from service.**

### *3.2.3 Summary*

Based on previous modeling of the OFA system, REI's combustion simulation software was used to design an amine-based injection system for the staged lower furnace and to evaluate $NO_x$ reduction performance of the RRI system. The ability of the RRI process to significantly reduce $NO_x$ emissions from a staged cyclone-fired furnace operating with overfire air has been demonstrated with a 130 MW cyclone-fired furnace. NOx reductions of 30% with less than 1-ppm ammonia were obtained with RRI under full load conditions (120 MWe) in a three-barrel cyclone-fired furnace. RRI in combination with SNCR was found to yield up to 55% $NO_x$ reduction under full load conditions, to reduce $NO_x$ emissions from this unit to as low as 0.23 lb/MMBtu, with less than 5 ppm ammonia slip. Tests indicated that $NO_x$ reduction due to RRI and SNCR was nearly additive, i.e. SNCR performance did not appear to be negatively impacted by RRI.

The modeling predictions of $NO_x$ reduction, $NH_3$ slip, and reagent usage were extremely consistent with the field observations. In addition to confirming the CFD model predictions the field tests demonstrated the importance of accurate CFD modeling to a successful RRI design. Data suggests that in other units possessing increased residence times in the lower furnace, RRI performance should be higher than those achieved in this unit. The CFD modeling results have proven to be very reliable, and are considered essential to proper location and configuration of the injectors. Although the field results indicate that application of RRI in industrial unit is extremely promising, longer term studies are required to evaluate RRI's performance under substoichiometric conditions over the wide range of normal operating conditions including changes to load, level of air staging, cyclone barrel biasing, soot blowing cycles, etc. The life span of injectors and maintainability of injector materials under extreme lower furnace conditions also need to be evaluated.

## *3.3 RRI at a 500 MW Cyclone-fired Furnace (Sioux)*

Field testing of RRI was conducted in a nominally 500 MW cyclone-fired boiler that had been retrofitted with OFA. This was the second of two demonstrations of RRI, the first being in a 130 MW single wall-fired cyclone furnace, which demonstrated $NO_x$ reductions due to RRI of 30% from baseline emissions of 0.55 lb/MMBtu under full load operation, with less than 1 ppm of ammonia slip.

The objective of the testing described in this section was to determine whether similar performance could be obtained with RRI in a significantly larger unit. This 500 MW has an opposed wall firing geometry with a total of 10 cyclone barrels on the front and rear walls. The OFA system was designed by REI to accommodate subsequent evaluation of RRI in this unit. The evaluation of RRI in this 500 MW consisted of: 1) CFD based modeling to design the RRI injection system and to evaluate expected performance; 2) installation of temporary RRI hardware; and 3) field testing of RRI performance. The field test results were found to be consistent with the CFD model predictions, both showing $NO_x$ reduction of 30% to be achievable with RRI from full load baseline emissions with OFA of approximately 0.40 lb/MMBtu. These reductions were achieved with no predicted or measurable ammonia slip.

### *3.3.1 Modeling of RRI at 500 MW Cyclone-fired Furnace*

The unit studied is a nominally 500 MW opposed wall-fired cyclone boiler equipped with 5 cyclone barrels on each of the front and rear walls. The cyclones are arranged in a two-over-three layout on both walls directly opposite each other. The unit was recently equipped with OFA, based on the conceptual design and evaluation of performance completed by REI. Unit incorporates a flue gas recirculation system for steam temperature control. The unit fires a blend of Power River Basin (PRB) and Illinois bituminous coals along with small amounts of tire derived fuel (TDF) and petroleum coke.

To assess the expected performance of RRI in reducing $NO_x$ emissions in a full-scale boiler, REI developed a CFD model of this unit. REI's three-dimensional, multiphase, turbulent reacting flow CFD code, GLACIER was used to simulate the reacting flow. A 10-specie reduced mechanism post processing tool was used to model the reduction and oxidation reactions governing $NO_x$ formation/destruction. The simulations were carried out in two parts:

- Cyclone Barrel Model
- Furnace OFA/RRI Model

The original cyclone barrel CFD model utilized for this study was developed as part of a previously funded program sponsored by CNCIG. Details concerning this model have been published previously (Adams et al., 1997; Stuckmeyer et al., 1996). Barrel simulations were performed for stoichiometric ratios of 1.19 (baseline), 0.99, 0.95, and 0.90. RRI predictions were based on the staged barrel results for barrel stoichiometric ratios of 0.95 and 0.99.

The results of the cyclone barrel model were interpolated at the barrel exit into the inlet of the furnace model as shown in Figure 3.22. Within the GLACIER simulations of the furnace, the dynamics of the injected aqueous urea droplets were modeled as in previously completed studies to evaluate SNCR (Cremer et al., 1998; Cremer et al., 1999). The model accounts for the

coupling between the particle and gas phases in terms of mass, momentum, and energy. The release of the urea into the gas phase and the subsequent chemical reactions between the urea products and the local flue gas species were accounted for based on the implemented reduced chemical kinetics. This approach allows complete coupling of all the relevant physical processes involved including heat transfer, turbulent mixing, and chemistry so that objective estimates of RRI performance can be obtained.

The OFA design for this unit took into account that an RRI installation and demonstration was likely. As a result, the OFA ports were located above the existing FGR port elevation. The predicted full load NOx emissions for the unit are shown in Figure 3.23. Predictions are shown for baseline (unstaged) operation as well as operation with OFA at lower furnace stoichiometric ratios of 0.99, 0.95, and 0.90. As can be seen in the figure, a significant difference in furnace $NO_x$ emissions is predicted as the lower furnace SR is varied from 0.99 to 0.90. The predicted $NO_x$ emissions for a lower furnace SR of 0.95 with the installed OFA configuration was 0.40 lb/MMBtu, representing a decrease in NOx emissions of 66% from baseline levels. Predicted average furnace exit CO for this condition was less than 50 ppm. Figure 3.3.2 also shows the predicted effect of lowering the OFA ports to FGR elevation on furnace $NO_x$: the longer the residence time from the cyclones to the OFA ports, the greater the NOx reduction achieved. The average annual emissions from this unit are in good agreement with the predicted full load $NO_x$ emissions for a lower furnace SR of 0.95.

The model-based assessment of RRI was performed under full load conditions at a lower furnace SR of 0.95 and 0.99. Numerous reagent injection strategies were evaluated under these conditions. All simulated injector locations were below the elevation of the installed OFA ports, above and below the elevation of the top row of cyclone barrels. Issues that impacted the layout of the RRI injection nozzles included:

- the stratified gas composition in the vicinity of the cyclone barrel exits;
- the locations of the FGR ports, which introduce fuel lean flue gases;
- the relatively short residence time from the elevation of the FGR ports to that of the OFA ports; and
- the structural interferences associated with the FGR ductwork and the windbox.

Parameters that were evaluated in the CFD modeling included:

1) Injector locations
2) Injector spray characteristics
3) Lower furnace SR
4) Reagent flow rate
5) FGR flow rate.

Several furnace configurations with and without RRI were evaluated. Under identical lower furnace conditions (e.g. fixed SR), $NO_x$ reductions ranging from as low as 11% to as high as 42% were achieved through variation in injector location and spray characteristics. In all cases that were evaluated, the predicted furnace exit $NH_3$ slip was less than 1 ppm.

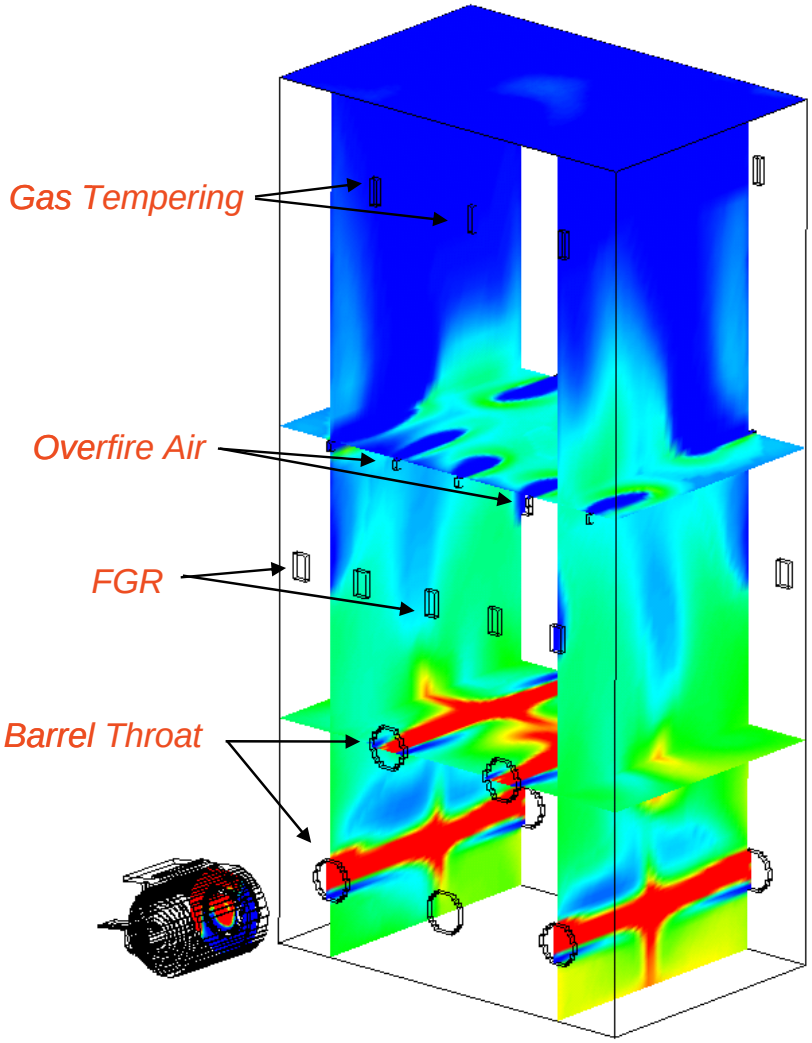


**Figure 3.22. The computed results at the barrel exit are interpolated onto the inlets of the furnace model where the RRI predictions are obtained.**

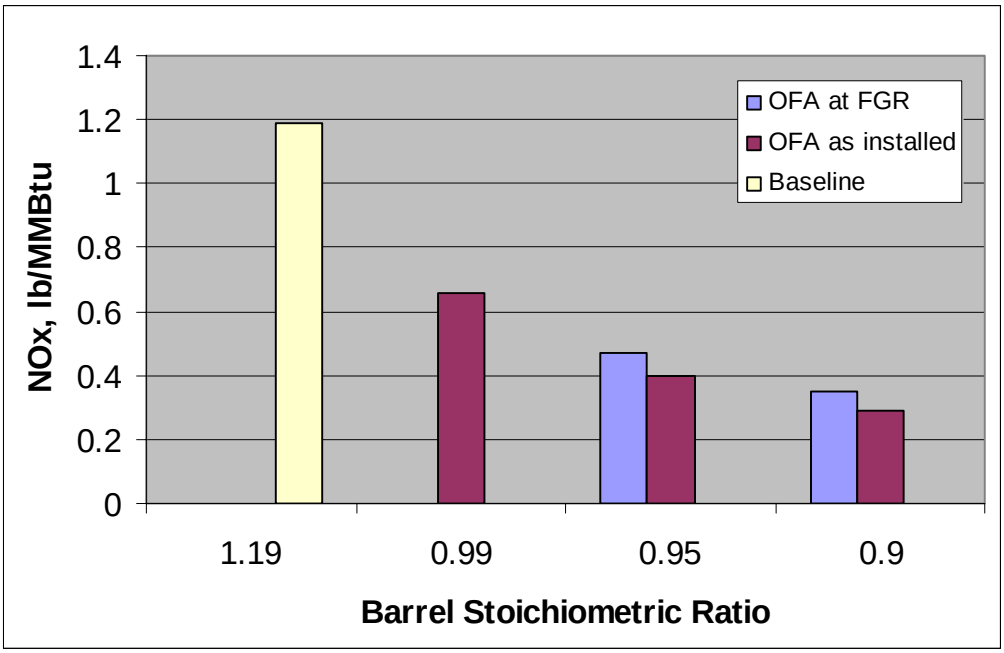


**Figure 3.23. Predicted $NO_x$ emissions under baseline (unstaged) and staged operation.**

Based on the CFD modeling, the final RRI port layout selected for field testing included a total of 20 injectors on the front, rear, and side walls at 4 elevations from the top barrel elevation up to 2 feet below the elevation of the OFA ports. For this port layout, Table 3.3.1 shows the predicted impact of lower furnace SR and the elimination of FGR on the predicted RRI performance. The "as installed" RRI port layout was predicted to achieve a reduction in $NO_x$ from the baseline levels of 0.40 lb/MMBtu to 0.27 lb/MMBtu, a 31% reduction. Figure 3.24 shows the predicted $NO_x$ distribution for the "as installed" injection configuration (Case 1), comparing the distributions with and without RRI. Eliminating the injection of flue gas through the FGR ports was predicted to have a negligible impact on NOx emissions in the absence of RRI injection. However, $NO_x$ reduction due to RRI was predicted to increase to 37% if the FGR was out of service. The reason for this is explained in Figure 3.25, which shows the predicted distribution of NOx formation rate for both cases. When the FGR is in service, there is localized NOx formation in the vicinity of the fuel lean gases due to the excess air in the FGR. Elimination of the FGR eliminates the localized $NO_x$ formation near the front and rear walls due to the reagent injection, resulting in reduced furnace NOx emissions. It can also be seen in Figure 3.25 that there is increased $NO_x$ formation at the elevation of the OFA ports in Case 2. This is due to the existence of a higher concentration of near wall NH3 at the elevation of the OFA ports in Case 2, as compared to Case 1. However, this increased rate of NOx formation is small and does not over compensate for the reduced NOx formation at the location of the FGR ports.

**Table 3.5. Results of simulations evaluating impacts of lower furnace stoichiometric ratio and FGR operation on RRI performance.**

| Case | Lower Furnace SR | FGR | Baseline $NO_x$ – No RRI (lb/MMBtu) | $NO_x$ Emissions – with RRI (lb/MMBtu) | $NO_x$ Reduction (%) |
|---|---|---|---|---|---|
| 1 | 0.95 | yes | 0.40 | 0.27 | 31 |
| 2 | 0.95 | no | 0.40 | 0.25 | 37 |
| 3 | 0.99 | yes | 0.66 | 0.65 | 2 |

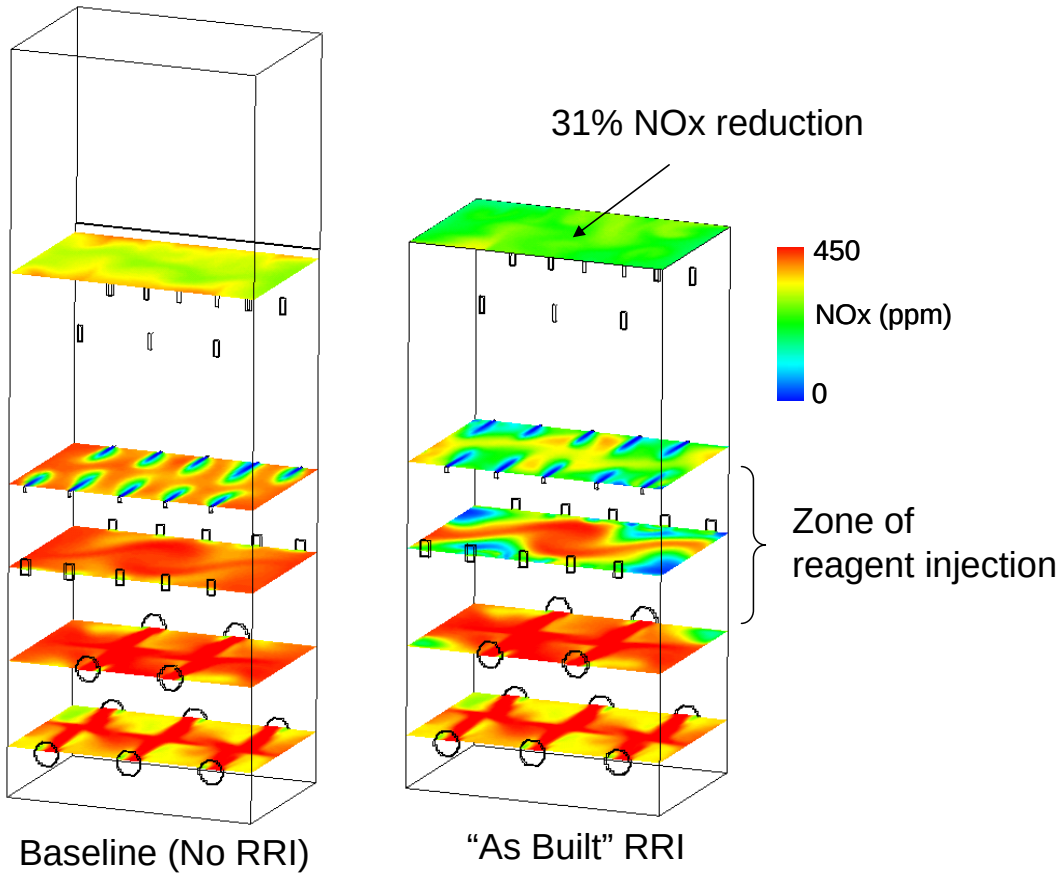


**Figure 3.24. Predicted $NO_x$ distribution in furnace showing impact of RRI.**

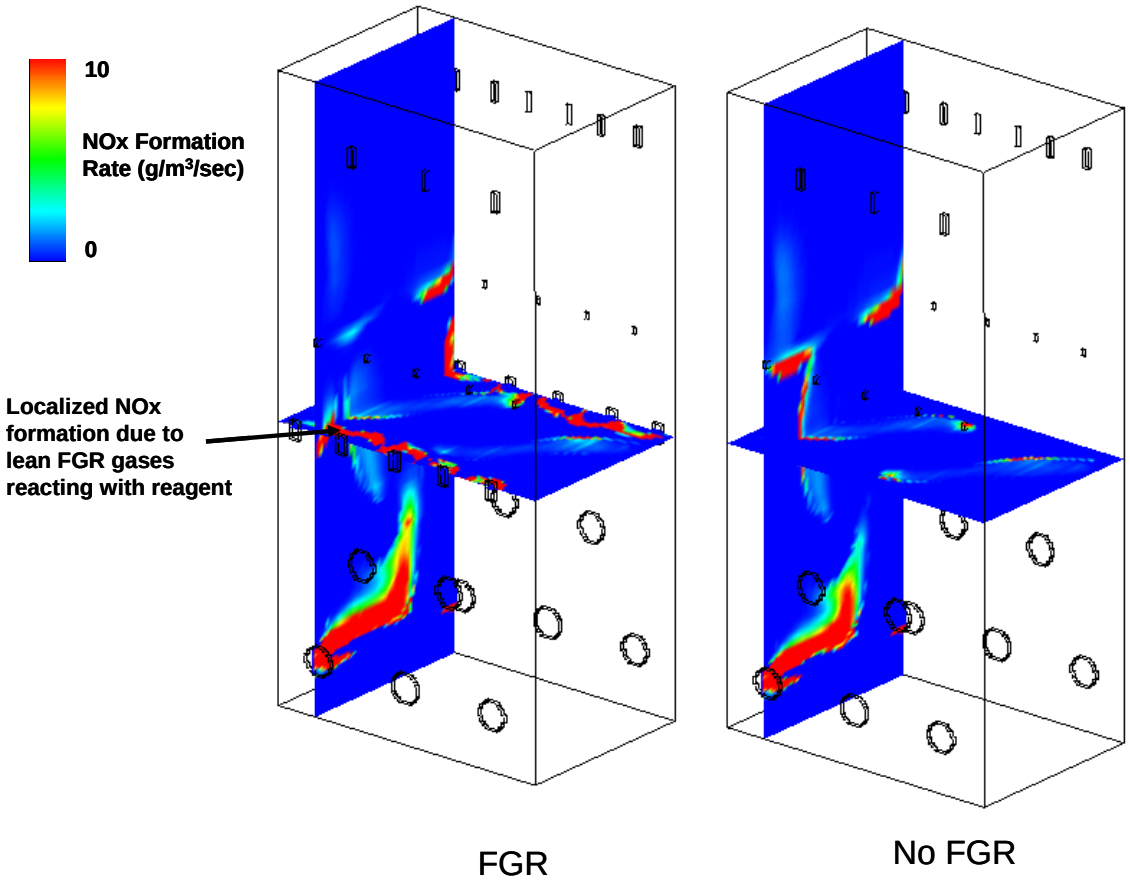


**Figure 3.25. Predicted $NO_x$ formation rate for Case 1 (with FGR) and Case 2 (without FGR). Elimination of the FGR in combination with the modeled RRI injection strategy results in improved $NO_x$ reduction.**

The result of Case 3 shows the predicted impact on RRI performance of increasing the lower furnace SR from 0.95 to 0.99. In this case, RRI led to nearly no predicted reduction in $NO_x$ emissions. This can be explained through examination of the predicted $O_2$ and $NO_x$ distributions for Cases 1 and 3, as shown in Figures 3.26 and 3.27. When the average lower furnace SR is 0.99, there is greater potential for oxidation of the reagent due to the existence of larger regions of fuel lean gases containing excess $O_2$. As seen in Figure 3.27, there are local regions in which $NO_x$ is reduced. However, reagent also enters into fuel lean regions resulting in localized $NO_x$ formation. Overall, the net reduction of $NO_x$ is very small. Although this result shows the importance of sufficient air staging in an RRI system, it is likely that if the injection strategy were modified to reduce the degree of mixing of the reagent into the high temperature fuel lean regions, the $NO_x$ reduction due to RRI could be significantly increased under this condition.

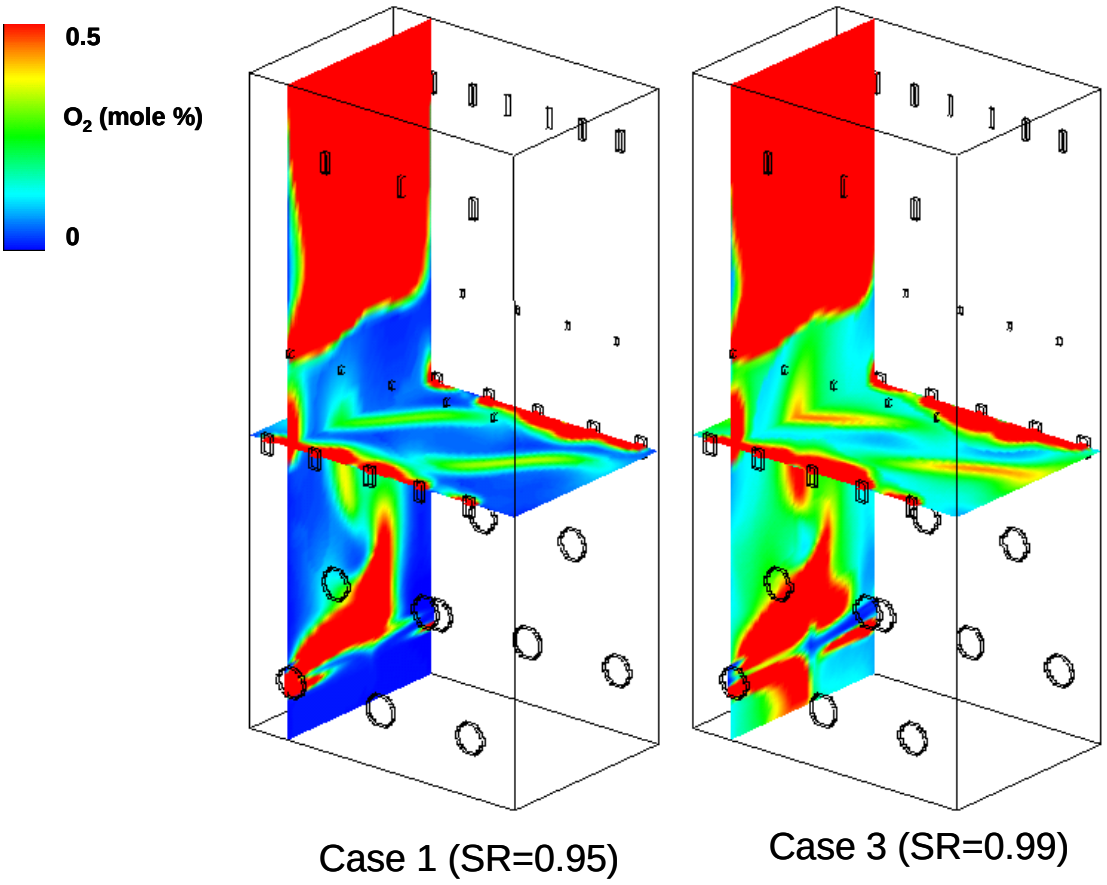


**Figure 3.26. Predicted distribution of $O_2$ for the lower furnace of Cases 1 and 3. In Case 1, where the furnace is staged more deeply than in Case 3, the local $O_2$ concentrations are significantly lower, resulting in significantly improved NOx reduction due to RRI.**

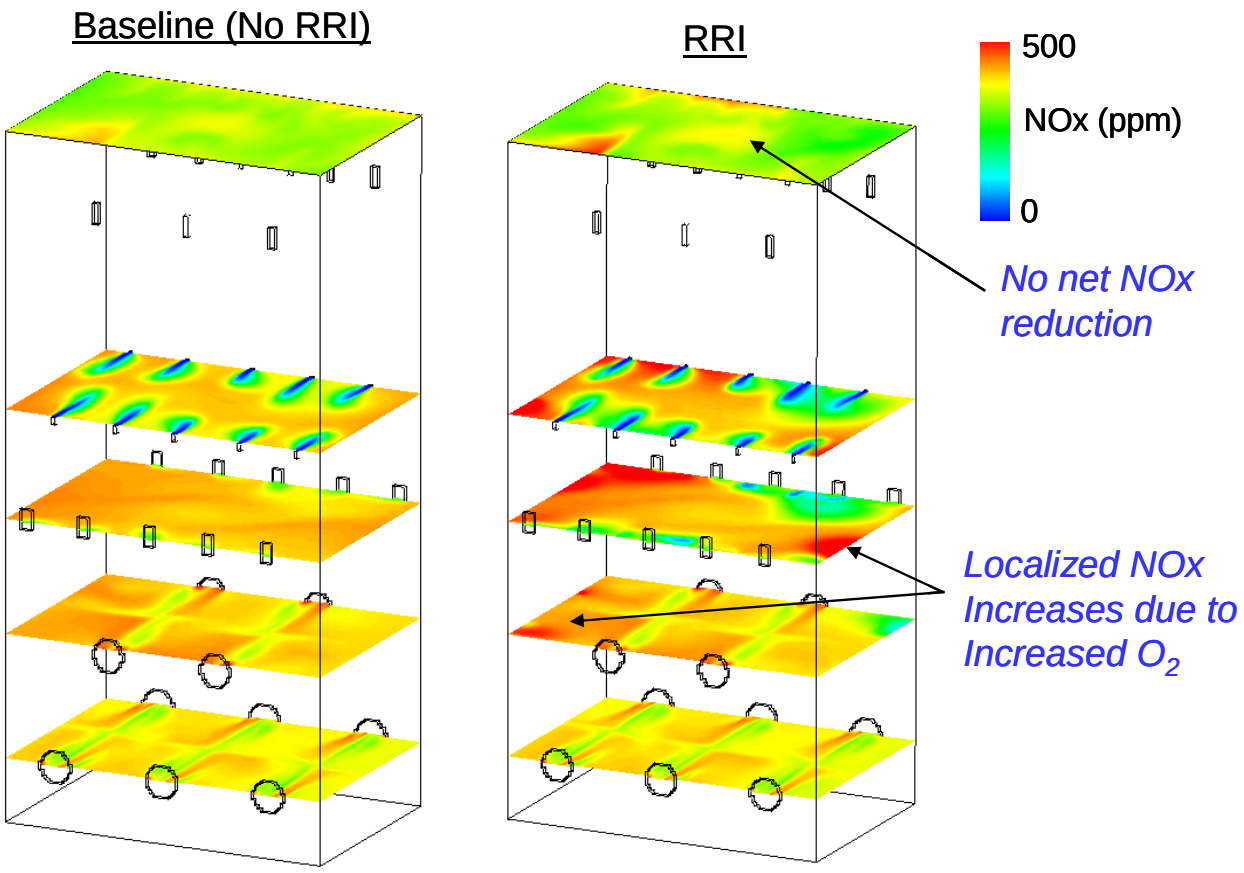


**Figure 3.27. Comparison of $NO_x$ distribution for Case 3 (lower furnace SR=0.99) with and without RRI.**

### *3.3.2 Testing of RRI at a 500 MW Cyclone-fired Furnace*

Air atomized reagent injectors were designed to allow for variation of droplet size, droplet velocity, as well as the air to liquid mass ratio, and spray pattern during the field testing, utilizing the 20 installed port locations. Two portable pump skids, provided by EPRI, supplied both the diluted reagent and air flows to the nozzles. Each skid was configured to supply 10 RRI injectors. A pump transfer skid at ground level was used to pump the concentrated reagent from the reagent supply tank up to the pump skids at the injector elevation.

Since a relatively large number of injector and boiler parameters were varied to assess sensitivity of RRI, the individual tests were relatively short, each lasting approximately one hour. The continuous emissions monitors (CEMs) were used to document the $NO_x$ emissions. $NH_3$ measurements were taken at the economizer exit.

The parameters that were evaluated included:

- injector spray pattern;
- normalized stoichiometric ratio (NSR);
- reagent concentration;
- nozzles out of service;
- cyclone barrel SR;
- injector atomization air pressure; and
- boiler load.

The field testing was conducted in two phases, each spanning approximately one week. The first phase of testing was conducted immediately following the installation of the OFA system in this unit. The second phase of testing was completed half a year later. Throughout the first phase of testing, the baseline $NO_x$ emissions (OFA only) were approximately 0.55 lb/MMBtu, high compared to the expected emissions of 0.40 lb/MMBtu at a lower furnace SR of 0.95. This discrepancy suggested that the average lower furnace SR was higher than the desired level of 0.95. Results of the RRI testing were poor during this round of testing, with sporadic $NO_x$ reductions of approximately 15% from the baseline emissions. These results were not repeatable, with observations of no measurable $NO_x$ reduction under conditions thought to be very similar to those in which previous levels of 15% reduction were measured. In all cases, no measurable levels of $NH_3$ slip were found.

To better understand the low $NO_x$ reduction the first phase of field testing, additional chemical kinetic calculations were completed. The dependence of RRI performance on the local flue gas temperature and stoichiometric ratio were evaluated. Figure 3.28 shows the results of chemical kinetic calculations to evaluate the impact of flue gas temperature and stoichiometric ratio on $NO_x$ reduction due to urea. These results are from isothermal plug flow reactor calculations over a fixed residence time, initial NO level and normalized stoichiometric ratio (NSR). This configuration may be interpreted as idealized conditions within the lower furnace of a staged cyclone-fired boiler, into which urea is injected.

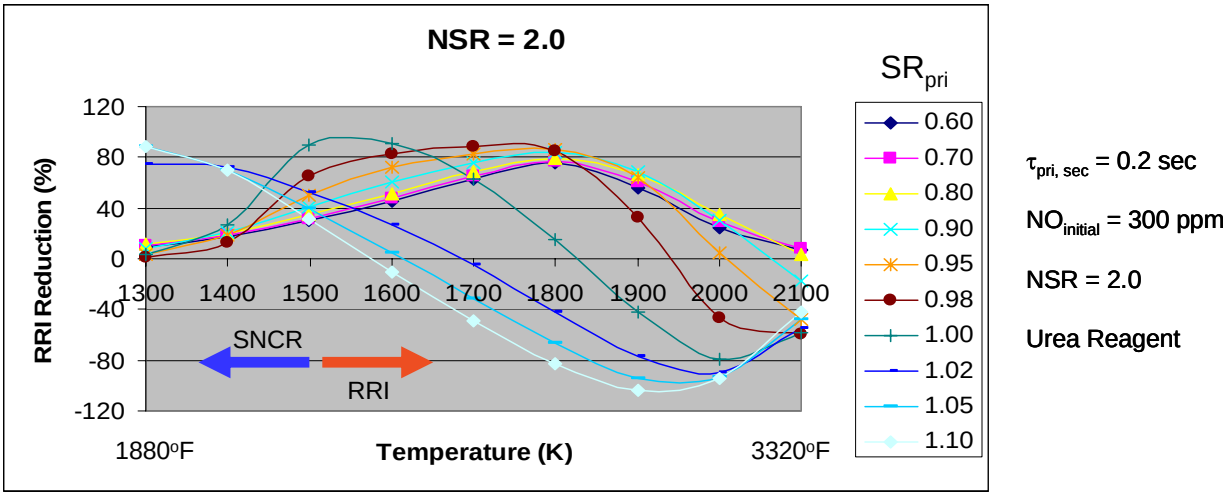


**Figure 3.28. Calculated $NO_x$ reduction due to urea in an isothermal plug flow reactor over a range of flue gas temperatures and stoichiometric ratios.**

The results in Figure 3.28 indicate that the local stoichiometric ratio has a very strong impact on $NO_x$ reduction due to RRI at gas temperatures in the vicinity of 1900-2000 K. For example, at a temperature of 1950 K, these calculations suggest that the difference between an average stoichiometric ratio of 0.95 and 0.98 can result in the difference between 40% and 0% $NO_x$ reduction. Thus, for the range of gas temperatures that exist within the lower furnace of a cyclone-fired furnace, the difference between an average stoichiometric ratio of 0.95 and 0.98 can dramatically impact RRI performance. Chemical kinetic calculations indicate that at a fully mixed SR of 0.99, significant NOx reductions would be expected. In reality, an average SR of 0.99 results in a distribution of SRs in which locally, SRs exceed 0.99. In these regions, $NO_x$ formation occurs, which compensates for the local NOx reduction in the fuel rich regions. If during the phase 1 testing, the average lower furnace SR were actually 0.98 rather than 0.95, then it is understandable why the predicted $NO_x$ reductions were not achieved.

The previously completed CFD modeling of this unit suggested that if the barrels are operated at an average stoichiometric ratio of 0.95, $NO_x$ emissions would be expected to be approximately 0.40 lb/MMBtu. With RRI, $NO_x$ reductions of 25-30% would be expected. However, the first phase of field testing was not able to reproduce the predicted $NO_x$ reductions. Prior to the initiation of the second phase of testing, the lower furnace SR was reduced by approximately 5% by increasing the OFA flow rate and keeping the total excess air fixed. Baseline $NO_x$ emissions (without RRI) were approximately 0.38 lbs/MMBtu throughout the second phase of testing. This is a reduction from the 0.55 lb/MMBtu emissions observed during the first round of tests. The emissions of 0.38 lb/MMBtu are consistent with the predicted baseline emissions of 0.40 lb/MMBtu from the CFD modeling at a lower furnace SR of 0.95 (see Figure 3.23). Figure 3.29 shows the typical results of the testing obtained during this second phase. Reagent flows were initiated at approximately 11:00 AM. At reagent flows corresponding to an NSR of approximately 3 (based on furnace exit $NO_x$ emissions), $NO_x$ emissions dropped to 0.27

lb/MMBtu (29% reduction). The variations in the $NO_x$ data between 11:00 AM and 4:00 PM (16:00 hours) result from reductions in reagent and water flows. As was the case in the first phase of testing, no ammonia slip was observed.

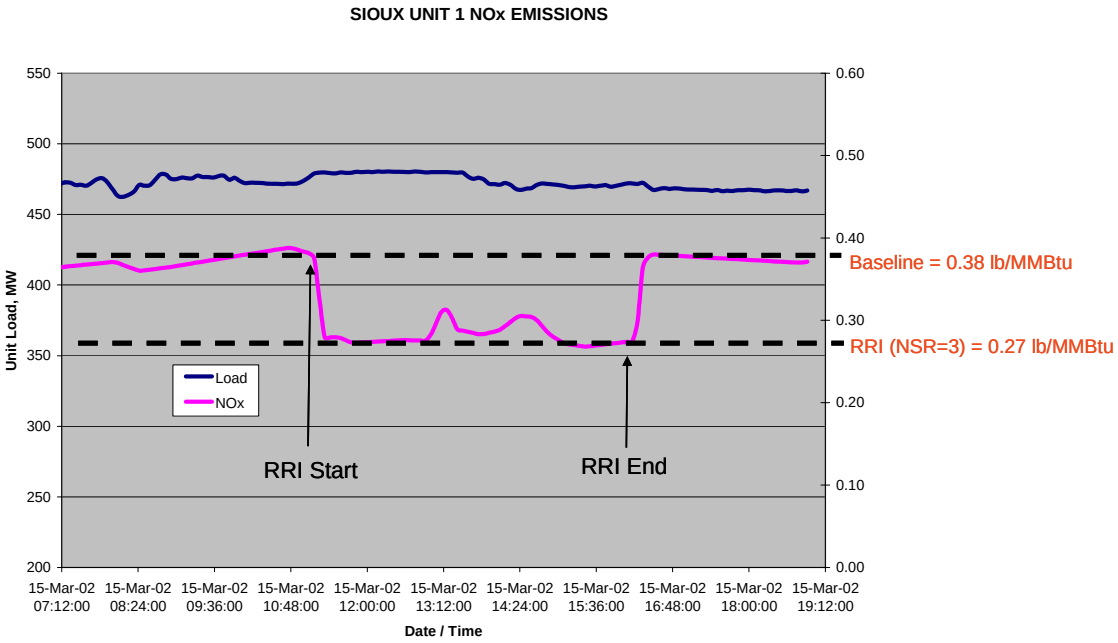


**Figure 3.29. Typical impact of RRI on $NO_x$ emissions during second phase of RRI testing.**

These results are in agreement with the previously completed CFD model predictions of RRI performance for this furnace. In addition, both the test results and the model predictions have shown that sufficient air staging is required for RRI to be effective. Based on the analysis of the coal and air flows during the first and second phases of testing, it is believed that the lower furnace SRs were approximately 0.99 and 0.95, respectively. The CFD model results of RRI performance for SR=0.99 were consistent with the poor field test results obtained during the first phase of testing. The reproducible results obtained during the second phase of testing, along with the baseline $NO_x$ emissions during these tests are consistent with the model predictions for the lower furnace SR=0.95. One short-term test at 400 MW (80% of full load) showed a similar level of NOx reduction under that condition. The impacts of droplet size, spray pattern, and reagent dilution were found to have a second order impact on RRI performance compared to reagent flow rate and the lower furnace SR.

### *3.3.3 Summary*

The ability of the RRI process to significantly reduce $NO_x$ emissions from a staged cyclone-fired furnace operating with overfire air has now been successfully demonstrated in two field tests of this technology. $NO_x$ reductions of approximately 30% with less than 1 ppm ammonia slip were obtained with RRI under full load conditions in a ten cyclone, 500 MW furnace. RRI was found to reduce $NO_x$ emissions from this unit to 0.27 lb/MMBtu from baseline levels (with OFA) of

0.38 lb/MMBtu using reagent flow rates corresponding to an NSR of approximately 3. It is expected that these emissions could be obtained with reduced reagent flow rates through optimization of individual injector flow rates. Modeling of this unit also suggests that NOx reductions could be improved through modification of FGR operation as well as through reduction of lower furnace stoichiometry. The field testing confirmed the CFD model predictions and demonstrated the importance of accurate CFD modeling to a successful RRI design. Based on the results of the testing of both the 130 MW and 500 MW units, the CFD modeling results have proven to be very reliable, and are considered essential to proper location and configuration of the injectors.

## *3.4 Modeling of RRI at PC-Fired Furnaces*

In order to assess performance of RRI in a PC-fired boiler using our CFD model, a number of developments were necessary. The most significant development concerned how to account for the products of devolatilization and char oxidation within the post process, reduced mechanism NOx model. The modeling of RRI in cyclone-fired furnaces did not need to address this issue since it was assumed that all of the coal was combusted in the cyclone barrel and only rich gas phase products were emitted into the furnace. In addition, refinements to the reduced chemistry used in the cyclone furnace simulations were required in order to handle $NO_x$ precursor species, such as HCN, that were not included in the reduced chemistry for the cyclone furnaces. For this implementation, two different reduced mechanisms were developed, one designed for conditions where the flue gas stoichiometry has an equivalence ratio (ER) greater than unity (i.e. fuel rich), and the other for ER less than unity (i.e. fuel lean). These mechanisms were implemented into the NOx model post processor and results were compared with those obtained utilizing the detailed chemistry in CHEMKIN over a wide range of conditions including stoichiometry, gas temperature, and normalized stoichiometric ratio. Figures 3.30 and 3.31 show comparisons between the reduced chemistry implemented into the CFD model with the detailed chemistry in CHEMKIN for a plug-flow reactor geometry. The fuel lean mechanism (Rei97_11) compares with the detailed chemistry very well under fuel lean conditions while the fuel rich mechanism (Rei97_12) compares very well with the detailed chemistry under fuel rich conditions.

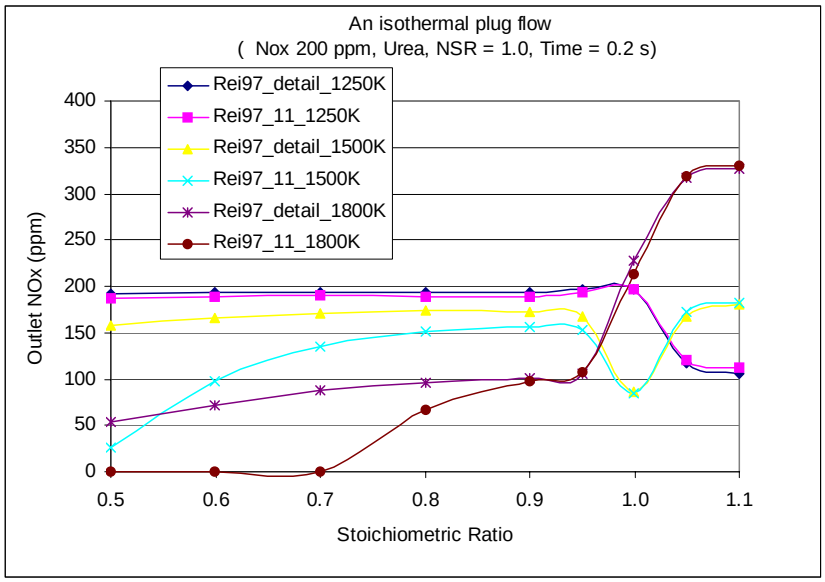


**Figure 3.30. Comparisons between new reduced $NO_x$ model implemented into a CFD model with results of plug flow reactor simulations using detailed chemistry in CHEMKIN. Comparisons show calculated outlet $NO_x$ versus flue gas stoichiometric ratio. The reduced mechanism (Rei97_11) was developed for fuel lean conditions, and the results show that the comparison with the detailed chemistry is very good for SR > 1.**

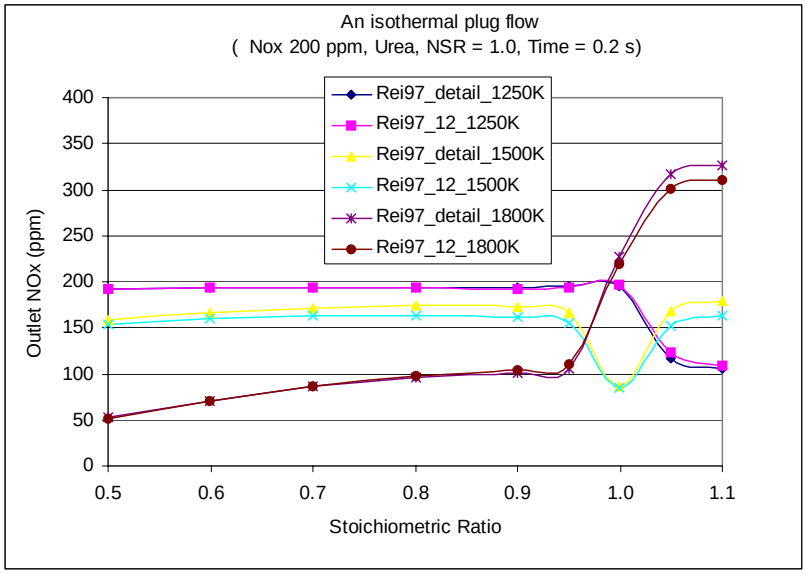


**Figure 3.31. Comparisons between new reduced NOx model implemented into CFD model with results of plug flow reactor simulations using detailed chemistry in CHEMKIN. Comparisons show calculated outlet $NO_x$ versus flue gas stoichiometric ratio. The reduced mechanism (Rei97_12) was developed for fuel rich conditions, and the results show that the comparison with the detailed chemistry is very good for SR < 1.**

After the reduced chemistry was verified by comparison with detailed chemistry over a wide range of conditions relevant to the environment in the lower and upper furnace of a PC-fired furnace, the new model was applied to the problem of predicting the $NO_x$ emissions from a 500 MW twin, tangentially fired PC boiler. This boiler was operated over a range of conditions involving significant variation in staging by adjustment of air flow through the separated overfire air (SOFA) ports. The boiler was previously modeled by REI under this set of conditions and predictions of $NO_x$ emissions were made utilizing the new reduced chemistry as well as REI's commercially used global $NO_x$ model (these conditions do not include reagent injection). The comparisons of the predictions with the data from the continuous emissions monitor are shown in Fig. 3.32. These results indicate that the $NO_x$ predictions utilizing the new reduced chemistry, in the absence of reagent injection, compare quite favorably with the data and even indicate an improvement over the previous estimates utilizing global mechanisms for $NO_x$ formation/destruction. This comparison gives confidence that the newly implemented reduced chemistry is able to accurately describe the mechanisms of $NO_x$ formation/destruction in a PC-fired boiler in the absence of reagent injection.

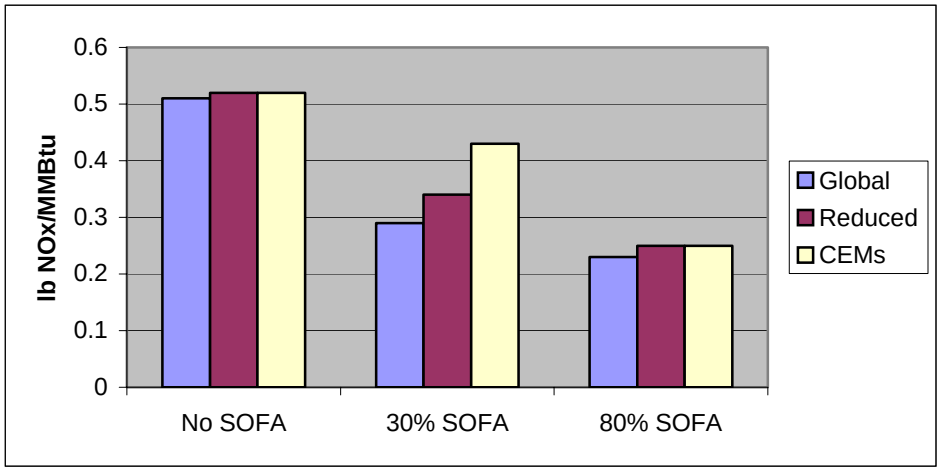


**Figure 3.32. Comparison of measured NOx data from CEMs for 500 MW twin tangentially fired PC boiler with CFD model predictions utilizing a global mechanism for NOx formation and predictions utilizing a new reduced mechanism NOx model developed for application to RRI in PC boilers. The comparisons indicate that the new NOx model results compare favorably with the CEMs data and suggest an improvement over the global chemistry model. For this boiler, the agreement between the model predictions and CEMs data is better than expected.**

### *3.4.1 500 MW Opposed Wall Furnace (Hammond 4)*

The unit studied is a 500 MW opposed wall-fired boiler with 24 Foster Wheeler Controlled-Flow/Split-Flame (CF/SF) burners. Two rich reagent injection strategies utilizing either side-wall injectors or in-burner injectors were simulated. Both strategies utilized 10% urea solution, an NSR of 2.0, and an average droplet size of 100 μm. The results for the side-wall injection strategy showed about 2% $NO_x$ reduction with about 17 ppm $NH_3$ slip. The $NO_x$ reduction for the in-burner injection strategy showed approximately 7% $NO_x$ reduction with less than 1 ppm $NH_3$ slip. The predicted $NO_x$ distribution in the furnace is shown in Figure 3.33.

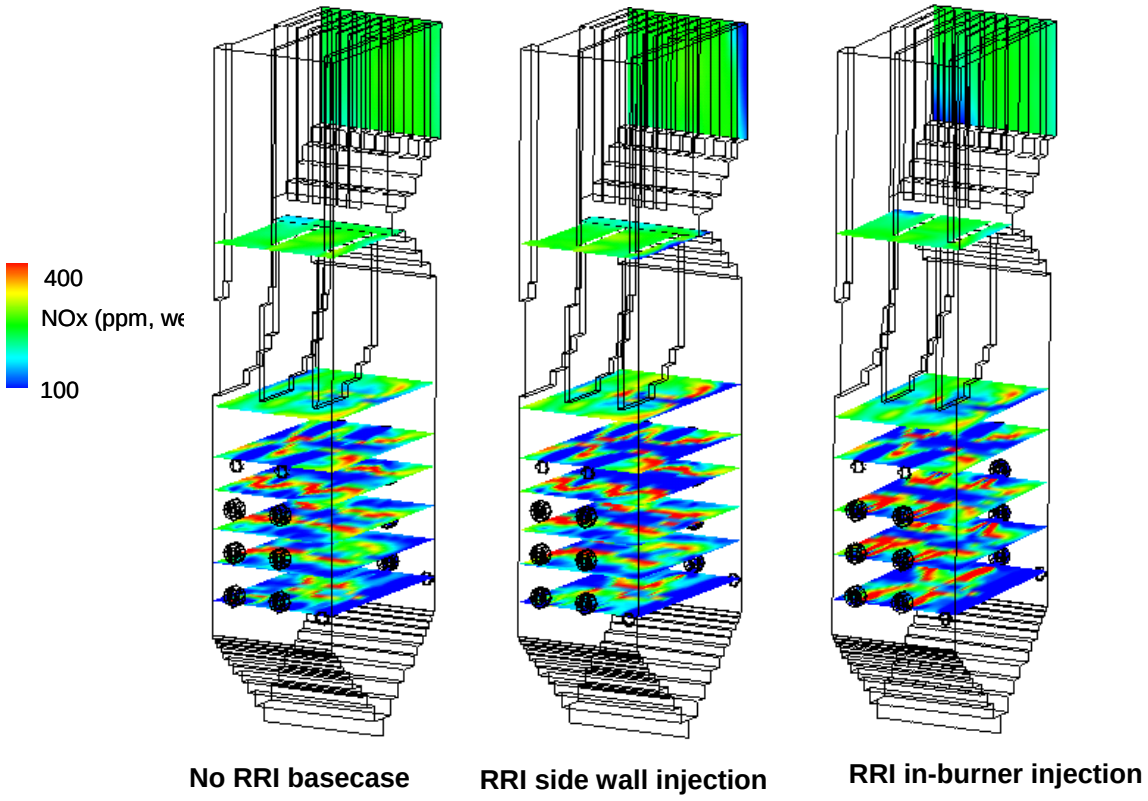


**Figure 3.33. The predicted $NO_x$ distribution in a 500 MW opposed wall-fired furnace.**

### *3.4.2 160 MW Wall-fired Furnace (Indian River)*

A smaller, 160 MW single-wall-fired coal boiler, which was retrofit with Riley low-NOx burners was also studied for RRI. Air was introduced, at normal operating conditions, through 4-level 16 burners, the OFA ports, the boundary air ports on the front wall, and side wall slots at the burner levels and at the OFA level. The overall furnace stoichiometry was run at a value of SR = 1.18, with the burner stoichiometry run at a value of SR = 0.85.Four rich reagent injection strategies, utilizing either rear wall injectors or in-burner injectors or both injectors, have been simulated. All four strategies utilized 10% urea solution at a NSR of 2.0. The results for these simulations are listed in the Table 3.6. The best $NO_x$ reduction achieved through RRI in these four strategies

was approximately 18%. Less than 2 ppm $NH_3$ slip was observed for all rich reagent injection strategies.

**Table 3.6. Rich Reagent Injection simulation results.**

| RRI Strategy | $NO_x$ emission (ppm, wet) | $NH_3$ slip (ppm, wet) | $NO_x$ reduction |
|---|---|---|---|
| **No RRI, Baseline case** | 193.2 | 0 | N/A |
| **1 - Rear wall injection** | 172.7 | 1.5 | 10.6% |
| **2 - In-burner injection** | 164.8 | 0.2 | 14.7% |
| **3 - Biased In-burner injection** | 161.3 | 0.1 | 16.5% |
| **4 - Biased In-burner and rear wall injection** | 158.5 | 0.5 | 18.0% |

Figure 3.34 shows the baseline equivalence ratio distribution in the furnace, which shows that the best region for reagent release is near the rear wall where the flue gases are fuel rich. Figure 3.5 shows $NO_x$ distributions in the furnace for both no rich reagent injection case and four rich reagent injection strategies.

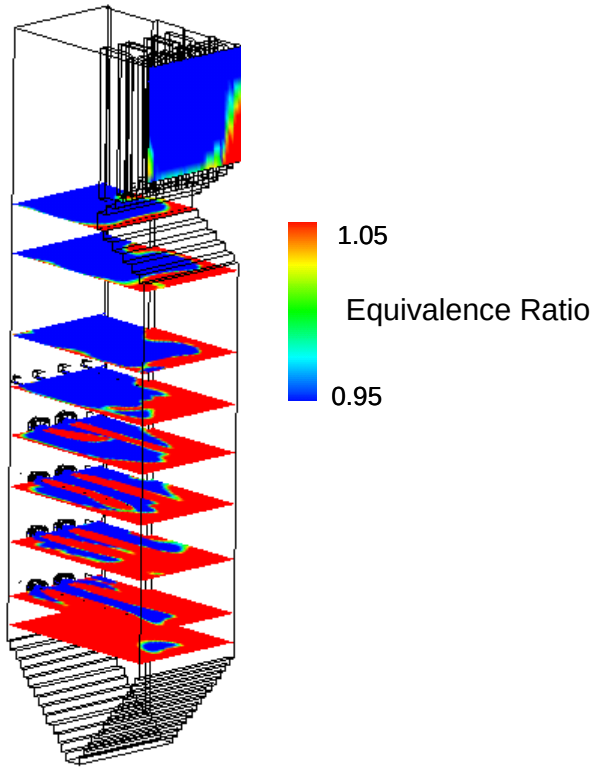


**Figure 3.34. Predicted equivalence ratio distribution for the no RRI baseline case at 160 MW single wall-fired furnace.**

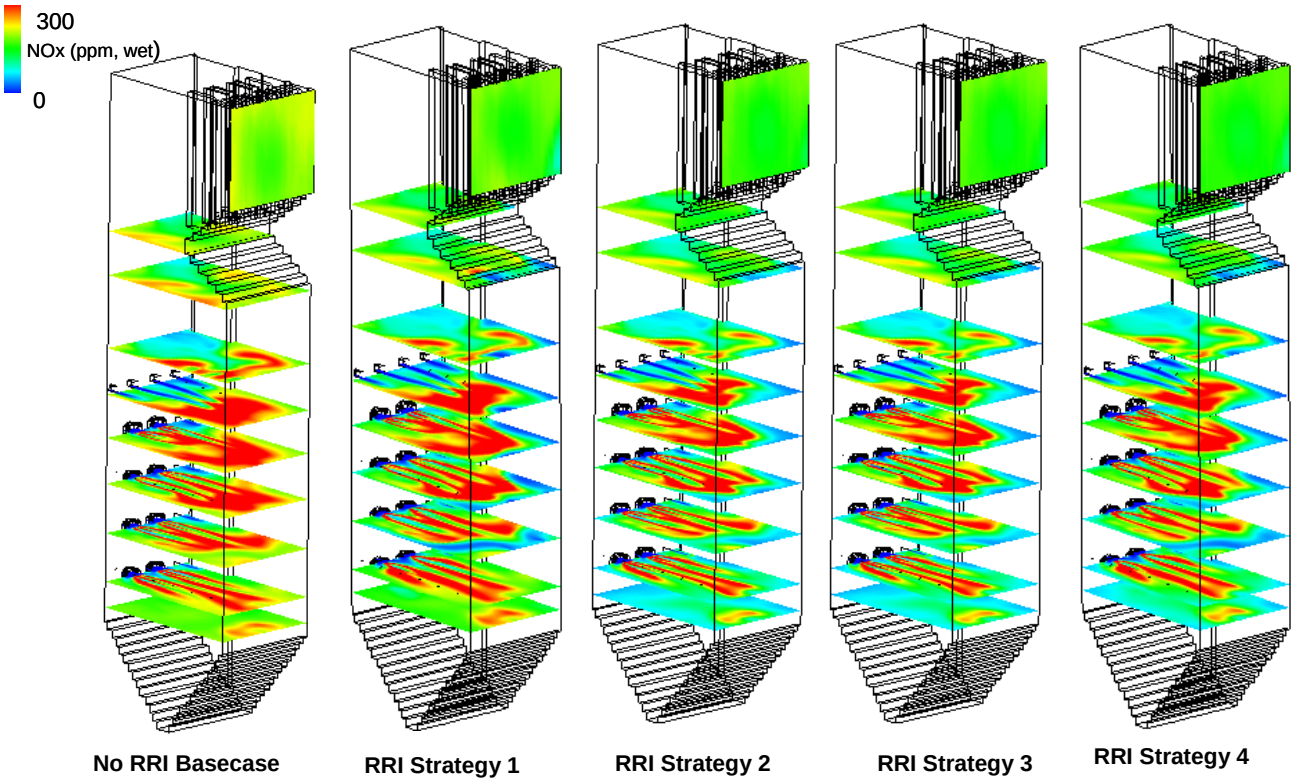


**Figure 3.35. The predicted NOx distribution at 160 MW single wall-fired furnace.**

### *3.4.3 500 MW Tangentially Fired Furnace*

Application of RRI to a 500 MWe corner-fired coal fired utility boiler equipped with a low $NO_x$ firing system with 5 burner levels and advanced overfire air has been investigated. The baseline CFD modeling of this unit has indicated that when the lower furnace is operated under substoichiometric conditions (SR = 0.82), a fuel rich region exists within the central fireball. Based on the baseline CFD model, potential exists to reduce $NO_x$ emissions through RRI if reagent can be released into this fuel rich core.

In burner reagent injection as well as theoretical "reagent seeding" were evaluated. In both cases, an NSR = 2.0 was assumed based on a furnace exit $NO_x$ emission rate of 0.25 lb/MMBtu. In the in-burner injection simulation, equal quantity of reagent was injected through the primary zone of each of the 20 burners. The simulation indicated that this was a very poor design resulting in a 3% net increase in $NO_x$ emissions.

In the "reagent seeding" simulation, urea reagent was assumed to be released into the gas phase in a circular area corresponding to the central "fireball" at each of the five burner levels. In this case, the $NO_x$ emissions were predicted to be reduced 24% from the 0.25 lb/MMBtu baseline

level. This result indicates that if reagent release could be effectively targeted in this unit, RRI could reduce $NO_x$ emissions in excess of 20% with less than 1 ppm NH3 slip.

### *3.4.4 Summary*

PC-fired boilers make up approximately 80% of the generating capacity associated with coal firing in utility boilers. The potential payoff is quite large if RRI can be successfully demonstrated in a PC-fired boiler. In order to assess performance of RRI in a PC-fired boiler a reduced mechanism $NO_x$ model needed to be developed to account for the products of devolatilization and char oxidation and to handle $NO_x$ precursor species, such as HCN. The new reduced chemistry model compares well with the detailed chemistry under both fuel lean and fuel rich conditions.

Several PC units have been modeled to evaluate the potential of RRI to reduce $NO_x$ in PC-fired boilers. Our work on RRI in cyclone furnaces demonstrated that RRI performance is very sensitive to the time, temperature and stoichiometry in the local gas field through which the reagent droplets travel. Hence, we expect that different classes of boilers may require different approaches on how and where to inject the reagent. In general, RRI has the potential to significantly reduce $NO_x$ reduction in PC-fired furnaces. Considerable attention, however, has to be given to evaluating reagent injection and distribution in the furnace model prior to testing. If the reagent is not effectively targeted in the fuel rich region, no $NO_x$ reduction or significant $NO_x$ production can take place. The main conclusion is that RRI performance in PC units under staged conditions is very site specific.

## *3.5 Deep Staging and RRI Predictions for 500 MW Cyclone-Fired Furnace*

In many cases, electric utilities have determined that Selective Catalytic Reduction (SCR) is the NOx control strategy of choice. However, the high capital costs associated with SCRs makes them cost prohibitive in small boilers. In boilers that fire low rank coals, physical blinding of the catalyst due to the high alkali content is a complicating issue. Cyclone boilers that fire Powder River Basin (PRB) and North Dakota Lignite coals fall into this class of boilers. This section presents the results of a study to evaluate non SCR options in a 500 MW cyclone boiler that fires a blend of PRB and Illinois bituminous coals. The non SCR options include a combination of "deep staging" with OFA, RRI, and SNCR. Field testing has demonstrated that consistent full load $NO_x$ emissions of 0.30 lb/MBtu can be achieved in this unit with the existing OFA system with no observable boiler impacts. RRI testing demonstrated 30% additional $NO_x$ reduction, with < 1 ppm ammonia slip, from the as tested $NO_x$ level of 0.38 lb/MBtu. Subsequent CFD modeling predicts that under the current operational conditions RRI will reduce $NO_x$ emissions an additional 35% to achieve < 0.20 lb/MBtu. Field experience as well as CFD model estimates suggest that a combined RRI and SNCR system can reduce full-load $NO_x$ emissions in this unit below 0.15 lb/MBtu.

### 3.5.1 Modeling Conditions

RRI and deep cyclone staging were evaluated in a 500 MW cyclone-fired furnace. The cyclone barrels are 10 feet diameter with five each on the front and rear walls in a two over three arrangement on each wall. The cyclones are equipped with radial burners that utilize primary and tertiary air. Unit incorporates a flue gas recirculation system for steam temperature control. Although the steam generators were designed for Illinois No. 6 high sulfur coal, the unit currently fires a blend of approximately 85% Powder River Basin (PRB) and 15% Illinois No. 6 to achieve net outputs of approximately 440 MW. The unit is equipped with fine grind crushers, allowing high percentages of PRB to be burned. Higher percentages of Illinois coal can be burned in the event full unit capability is needed to meet system demands.

The unit studied for RRI and deep staging has OFA ports at a relatively high elevation above old FGR ports to achieve the higher levels of $NO_x$ reduction with the OFA system, predicted with CFD modeling. This allows the boiler to accommodate the future installation of RRI technology as well.

The simulations presented here were based on firing of a 70% PRB 30% Illinois No. 6 blend. Table 3.7 shows the simulated fuel properties. Four barrel operational conditions were simulated, representing four different cyclone barrel stoichiometric ratios (SR): 1) Baseline (unstaged), SR=1.19; 2) SR=0.99; 3) SR=0.95; and 4) SR=0.90. The results of these simulations were used to provide input conditions for the subsequent furnace simulations that were carried out for the four different staging conditions.

**Table 3.7. Simulated fuel properties for cyclone barrels.**

| | 70/30 Blend |
|---|---|
| C (%) | 52.21 |
| H (%) | 3.54 |
| O (%) | 10.92 |
| N (%) | 1.01 |
| S (%) | 1.15 |
| Ash (%) | 6.58 |
| Moisture (%) | 24.59 |
| HHV (Btu/lb) | 9180 |

To assess the expected performance of staged combustion with and without reagent injection in a nominally 500 MW furnace, a CFD model extending from the furnace floor below the cyclone barrels up to the vertical exit at the entrance to the convective section was used, Figure 3.5.1. For the furnace simulations discussed here, any unburned carbon that was predicted to exit the cyclone barrel model was assumed to be released into the gas phase at the inlet to the furnace model. Furnace simulations were completed assuming four cyclone barrel stoichiometric ratios as shown in Table 3.5.2. For all furnace simulations, the furnace excess $O_2$ was held constant, the operation of the flue gas recirculation (FGR) system was unchanged, and all ten cyclone barrels in each simulation were assumed to operate in an identical manner (other than the direction of rotation). Simulations were conducted with and without reagent injection as part of the RRI process.

**Table 3.8. Operational conditions for furnace simulations.**

| Simulation | Barrel SR | Cyclone Air Flow (%) | OFA Flow (%) | 50% Urea Flow (gph) |
|---|---|---|---|---|
| **Baseline** | 1.19 | 100% | 0% | 0 |
| **SR99** | 0.99 | 83% | 17% | 0 |
| **SR99_RRI** | 0.99 | 83% | 17% | 760 |
| **SR95** | 0.95 | 80% | 20% | 0 |
| **SR95_RRI** | 0.95 | 80% | 20% | 760 |
| **SR90** | 0.90 | 76% | 24% | 0 |
| **SR90_RRI** | 0.90 | 76% | 24% | 520 |

* All simulations assumed a firing rate of 4170 MBtu/hr, coal blend as in Table 3.7, furnace SR=1.19, and fixed FGR+GT flow.

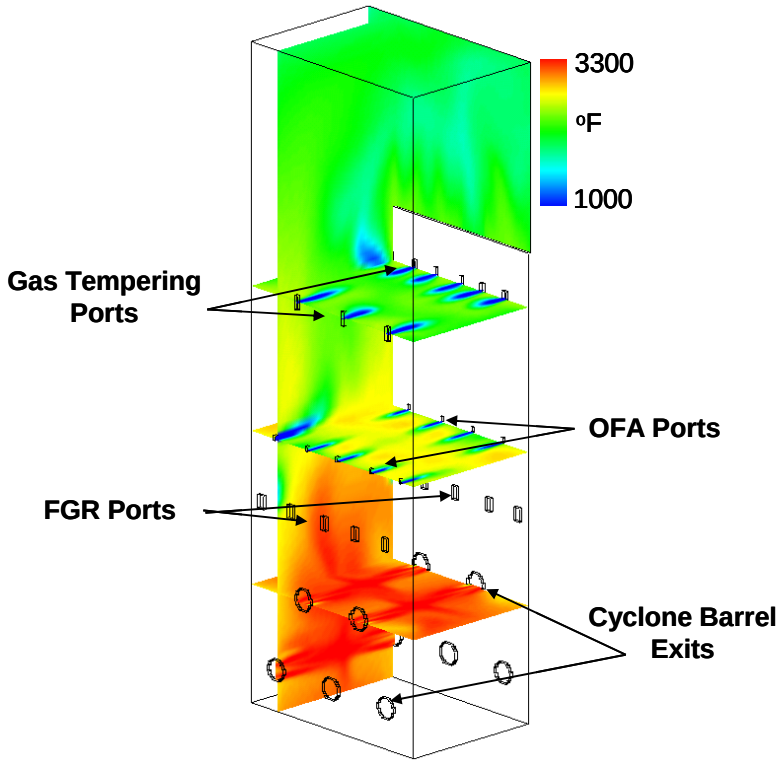


**Figure 3.36. Cyclone-fired Furnace CFD model incorporating the existing OFA and FGR systems.**

Oxygen probes measure economizer exit $O_2$ concentrations. Daily unburned carbon in ash measurements are taken by sampling fly ash from hoppers in the inlet precipitator field and measuring the carbon content using a Leco carbon analyzer. Since these are not isokinetic measurements, a high unburned-carbon measurement could be due to operational conditions that existed several days previous.

### *3.5.2 Modeling Predictions – Deep Staging and RRI*

Figure 3.37 shows the predicted furnace $NO_x$ emissions as a function of average cyclone barrel SR. For the three conditions involving air staging with OFA, results are also shown for application of RRI. The cyclone barrel model predictions showed an increase in average CO concentration and a negligible change to the average gas temperature and $NO_x$ (lb/MBtu) at the barrel exit for the SR=0.90 case compared to the SR=0.95 case. Deeper staging to 0.90 is predicted to lead to a negligible change to the furnace exit temperature, a slight increase in the furnace exit CO, but a significant decrease in $NO_x$ emissions.

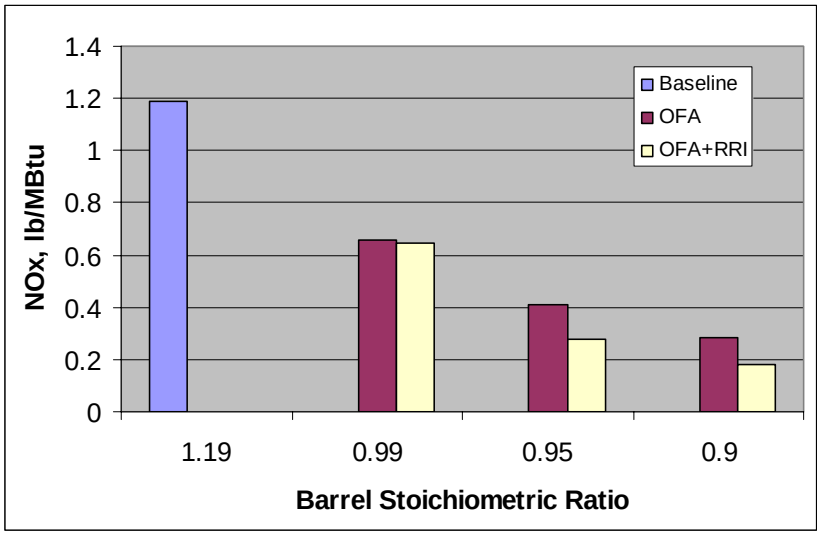


**Figure 3.37. Predicted $NO_x$ emissions as a function of average cyclone barrel SR, with and without RRI.**

### *3.5.3 Deep Staging Testing*

Prompted by the CFD model predictions, personnel at the unit modeled embarked on a testing program to investigate the ability to reduce $NO_x$ emissions with deeper staging in both cyclone units. The approach was to increase the cyclone barrel staging in a manner to ratchet down the NOx emissions in increments of 0.01 lb/MBtu over a weekly time period. Prior to this time period, "baseline" $NO_x$ emissions are 0.4 lb/MMBtu. Figure 3.38 shows data taken during prior testing. During these tests, secondary air flows to the cyclone barrels and OFA ports were adjusted under conditions of fixed total furnace air flow. Minimum OFA flows produced maximum $NO_x$ emissions and vice versa.

Figure 3.39 shows hourly average EPA reported $NO_x$ emissions for the time over which unit began its' deep staging program. Note that these data show a reduction in $NO_x$ emissions from 0.4 to 0.3 lb/MBtu over this time period. Figure 3.40 shows recent detailed control room data for the same unit. Based on these data and the data in Figure 3.38, the associated $NO_x$ emissions from this unit are plotted vs. cyclone barrel average SR in Figure 3.41. Only the data in Figure 3.38, corresponding to times when the OFA flows and $NO_x$ emissions are steady, are used in Figure 3.41. The measured data are compared with the CFD based predictions. The agreement is very good over the stoichiometric ratio range from 1.19 to 0.90.

Daily measurements of unburned carbon in fly ash, taken before and after deeper cyclone barrel staging program, are plotted in Figure 3.42. As Figure 3.42 shows, there is no clear impact of the recent deeper staging conditions on the measured unburned carbon. The fluctuations in unburned carbon are relatively large, but are not clearly related to average cyclone barrel SR.

The trend lines, which are shown for the samples from two ESP hoppers show no clear trend over this time period.

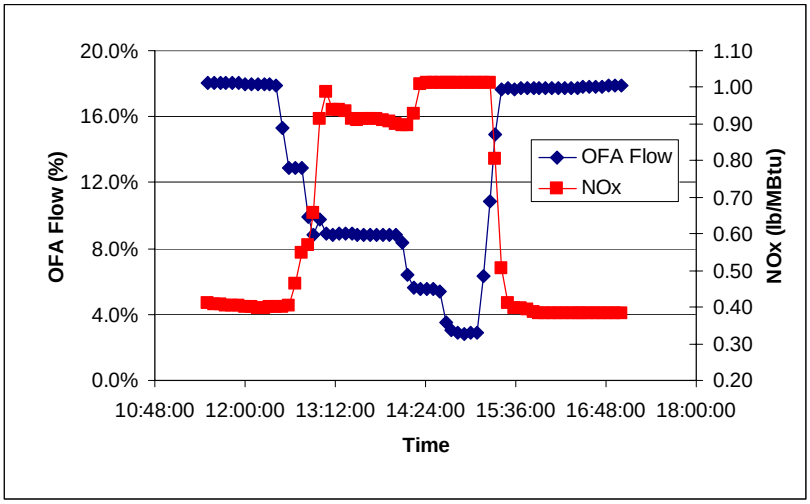


**Figure 3.38. Measured $NO_x$ emissions and OFA flow rate as a percentage of total combustion air flow during testing prior to deep cyclone barrel staging.**

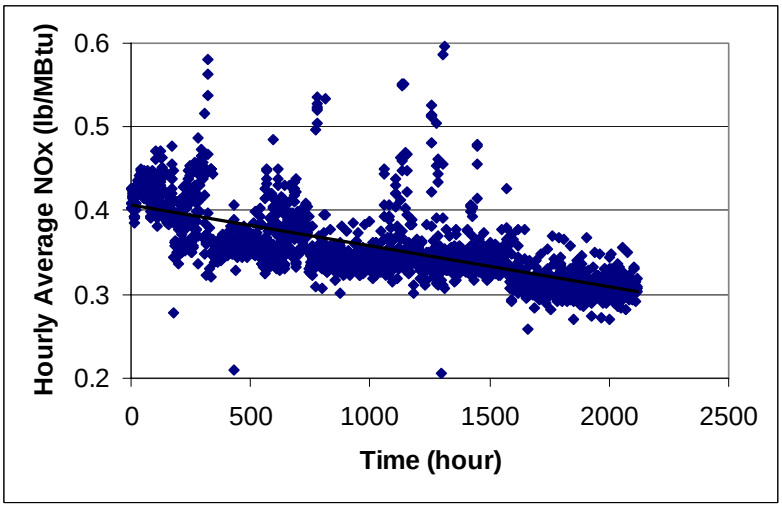


**Figure 3.39. Hourly average $NO_x$ emissions (EPA) after cyclone barrels were incrementally staged deeper. The trendline shows a reduction in $NO_x$ emissions from 0.4 to 0.3 lb/MBtu over this time frame.**

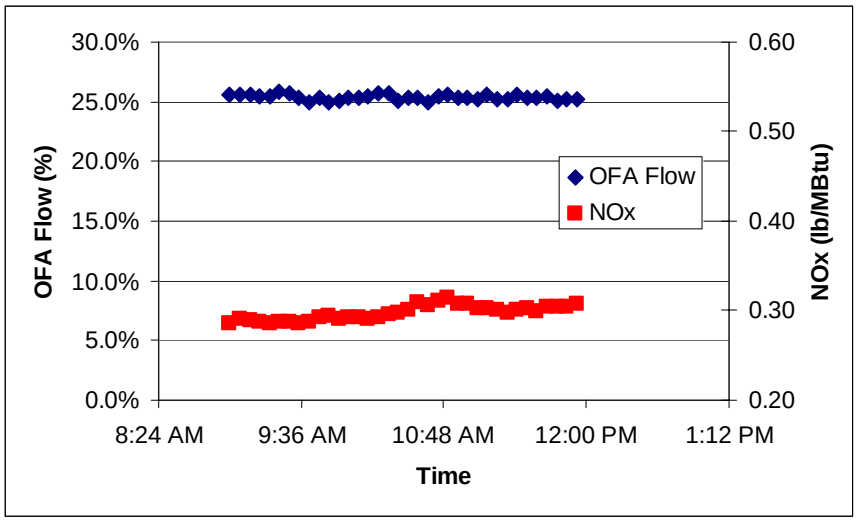


**Figure 3.40. Measured $NO_x$ emissions and OFA flow rate (control room) as a percentage of total combustion air flow during deeper staging testing.**

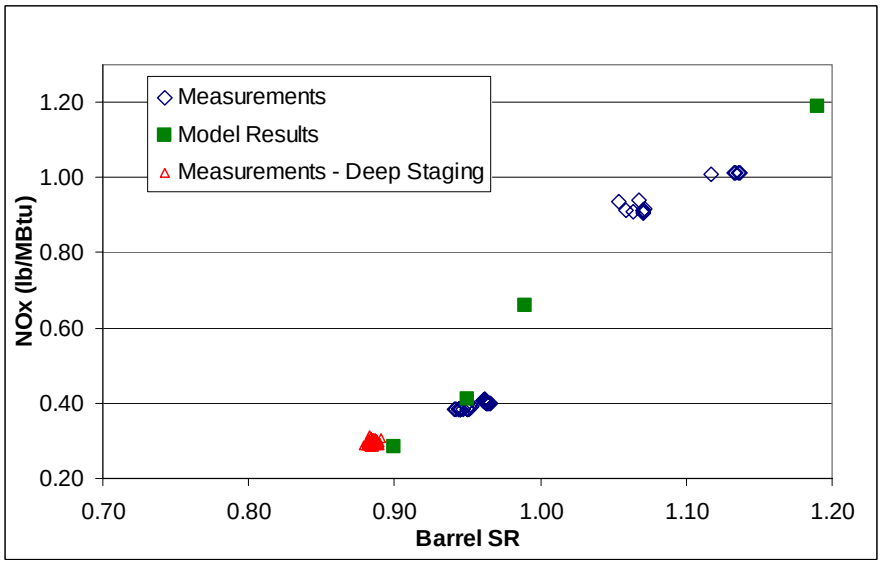


**Figure 3.41. Data shown in Figures 3.38 and 3.40 plotted vs. average cyclone barrel SR computed from the measured coal flow rates, OFA flow rates, and measured economizer $O_2$.**

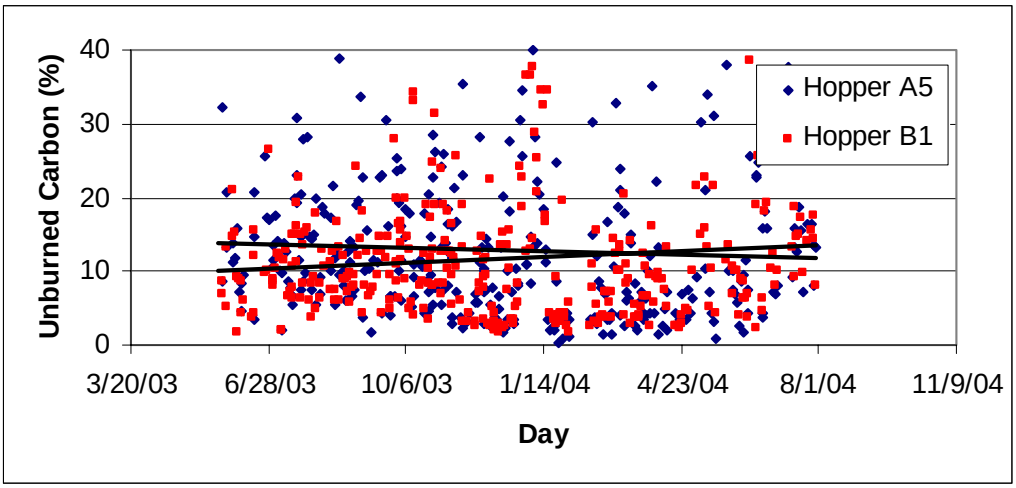


**Figure 3.42. Daily unburned carbon in ash measurements before, during and after the deep staging testing.**

### *3.5.4 Summary*

Recent long term testing has been performed to evaluate deep cyclone barrel staging. It has shown that deeper staging of this unit to average cyclone barrel SRs of approximately 0.85-0.90 has significantly reduced full load $NO_x$ emissions to approximately 0.30 lb/MBtu. There have been no significant detrimental boiler impacts of operation under these staging conditions. No measurable change to unburned carbon in the fly ash has been experienced. No noticeable changes to slag tapping behavior has been experienced. These observations are highly consistent with previously reported CFD model predictions of the impact of cyclone barrel SR on $NO_x$ emissions as well as impacts to furnace exit temperature and CO.

CFD model predictions of the impact of RRI in combination with the existing OFA operational conditions in this unit suggest that $NO_x$ emissions can be reduced to below 0.20 lb/MBtu. RRI has previously been demonstrated in this unit to achieve approximately 30% $NO_x$ reduction from the as tested $NO_x$ emissions of 0.38 lb/MBtu. The combination of deeper staged conditions with RRI and SNCR are expected to be tested at the unit to demonstrate $NO_x$ emissions less than 0.15 lb/MBtu for the first time in a cyclone-fired unit not equipped with an SCR.

## *3.6 References*

Adams, B., Heap, M., Smith, P., Facchiano, A., Melland, C., Stuckmeyer, K., Vierstra, S., "Computer Modeling of Cyclone Barrels," EPRI-DOE-EPA Combined Utility Air Pollutant Control Symposium, Joint Symposium on Stationary Combustion $NO_x$ Control, August, 1997;

Arand & Muzio, U.S. Patent No. 4,325,924, 1982.

Brogan, U.S. Patent No. 4,335,084, 1982.

Chen, J.-Y., Workshop on Numerical Aspects of Reduction in Chemical Kinetics, CERMICS-ENPC, Cite Descartes, Champus sur Marne, France,1997.

Cremer, M.A., Eddings, E., Martz, T., Muzio, L.J., Quartucy, Q., Hardman, R., Cox, J., and Stallings J., 1998 U.S. DOE Conference on SCR and SNCR for NOx Control, Pittsburgh, PA, 1998

Cremer, M.A., Wang, D.H., Phillips, R.A., Smith, R.C., Boll, D.E., Martz, T., and Muzio, L.J., and Stallings J., 1999 U.S. DOE Conference on SCR and SNCR for $NO_x$ Control, Pittsburgh, PA, 1999.

Cremer, M.A., Montgomery, C.J., Wang, D.H., Heap, M. P., Chen, J.-Y., *Proc. Combust. Inst*. **2000**, *28*, 2427-2434.

Dean, A.J., Hanson, R.K., and Bowman, C.T., *J. Phys. Chem*. **1991**, *95*, 3180-3189.

Lyon, U.S. Patent No. 3,900,544, 1975.

Miller, J.A. and Bowman, C.T., *Prog. Energy Combust. Sci*. **1989**, *15*, 287-338.

Stuckmeyer, K. Adams, B., Heap, M. and Smith, P., “Computer Modeling of a Cyclone Barrel,” EPRI $NO_x$ Controls for Utility Boilers Conference, Aug. 6-8, 1996, Cincinnati, OH

# 4. Minimization of Impacts

Implementation of in-furnace $NO_x$ control strategies can produce side effects that may impact boiler operation. Deep staging in the lower furnace, which has been shown to aid in reduction of $NO_x$, can bring about oxygen-deficient conditions that could promote corrosion of waterwalls in the radiant zone. Substoichiometric conditions in the burner zone can result in production of soot particles. If soot does not burn out in the upper furnace, there can be increased opacity in the stack as a result of low-$NO_x$ combustion . The goal of this task is to develop real-time monitoring methods for measuring furnace corrosion and to investigate soot generation for low-$NO_x$ firing conditions.

The material contained in this chapter is organized as follows. Section 4.1 describes our efforts on measurement and quantification of waterwall corrosion. Section 4.2 describes our research on soot measurement and modeling in full-scale boilers. Section 4.3 provides a list of references cited in this chapter.

## *4.1 Waterwall Corrosion*

### 4.1.1 Introduction

This section describes the results of a two-year research and development program carried out by American Electric Power (AEP) and its partners Reaction Engineering International (REI), Corrosion Management, NS Harding & Associates, University of Utah and Electric Power Research Institute (EPRI) to test a novel multi-facetted process for managing waterwall corrosion in coal-fired utility boilers. This project was sponsored by the Ohio Coal Development Office (OCDO) under contract CDO/D-01-15 and the U.S. Department of Energy (DOE) National Energy Technology Laboratory (NETL) under contract DE-FC26-00NT40753.

#### 4.1.1.1 Program Objectives

The goal of this program was to field test a novel multi-pronged approach for managing waterwall corrosion in coal-fired utility boilers. The overall objective of the test program was to evaluate a prototype multi-sensor, real-time, electrochemically-based instrumentation and on-line system for monitoring and managing corrosion in coal-fired utility boilers. The specific objectives included:

- Application of Computational Fluid Dynamic (CFD) software with state-of-the-art corrosion submodels to predict locations and approximate rates of corrosion within a boiler for a meaningful range of operating conditions.
- Development, testing and application of a multi-sensor technology utilizing electrochemical techniques for quantitative, real-time monitoring of waterwall corrosion in a coal-fired boiler.
- Application of an advanced precision metrology technique and inexpensive coupon-based technology to verify predicted and measured corrosion rates.
- Development of a methodology for combining predicted and measured data into corrosion management guidelines for a coal-fired boiler**.**

The importance of assessing wastage in real-time is that minor changes in boiler operation have the very real possibility to greatly reduce corrosion attack and thus improve boiler availability and reduce maintenance costs and expensive waterwall replacements or weld overlay. This has become an increasingly important issue with the installation of low-$NO_x$ burner/OFA systems throughout the power industry. This program has demonstrated that corrosion can be measured accurately in real-time and, hence, waterwall wastage can be assessed immediately following changes in boiler operation. This capability can provide plant personnel the opportunity to optimize operations on a continuous basis in order to minimize tube wastage.

### 4.1.1.2 Background

#### *4.1.1.2.1 Program Motivation*

Until recently, fireside waterwall corrosion in coal-fired boilers was uncommon and was relatively mild in the U.S. electricity generation industry. However, the use of in-furnace combustion modifications such as staged combustion to reduce $NO_x$ emissions has led to a notable increase in the frequency and severity of waterwall wastage. As the extent of air staging increased to satisfy the more stringent restrictions on $NO_x$ emissions, there has been growing concern among utilities about high temperature corrosion and waterwall wastage. The existence of fuel-rich regions near furnace walls is reported to have had the most damaging impact on supercritical pulverized-coal-fired units firing high-sulfur coals. Reaction Engineering International (REI) has worked with the US Department of Energy and Electric Power Research Institute (EPRI) to improve predictive capabilities and provide solutions for furnace wall wastage for a wide range of coal-fired furnaces.

The ability to determine the extent of waterwall wastage on-line provides boiler operators a number of important benefits including:

Reduced cost of unscheduled outages due to tube leaks.

- Reduced maintenance costs. The cost of prevention is much less than the cost of repair. It has been estimated that prevention is about 70% the cost of correction.
- Reduced tube replacement costs. Extending the life of boiler tubes even 1-2 years will greatly reduce the normalized annual operating costs of coal-fired boilers.
- Reduced costs in weld overlay. Measuring and controlling corrosion is much less expensive than the cost of weld overlays, tube cladding, etc. For example, the costs for weld overlay are about \$350/$ft^2$.
- The flexibility to use slight changes in operating procedures to minimize corrosion while at the same time permitting low-$NO_x$ emissions (e.g., operational optimization).
- Ability to alert operators in real time when changes in fuel composition or unintentional excursions in firing conditions can place the boiler tubes at risk from high temperature gaseous corrosion attack.

#### 4.1.1.2.2 Previous Test Programs

REI has studied corrosion impacts in boilers via CFD simulations for the past seven years, but more recently, REI in partnership with Corrosion Management and N.S. Harding & Associates, has begun complementary efforts to improve understanding and management of

the problem by the application of technologies that appear capable of determining in real time, the location and/or rate of waterwall wastage due to high temperature corrosion activity. After consideration of the available technologies, the electrochemical noise (EN) sensing approach was chosen for continued development and demonstration because it offers the best opportunity for real-time corrosion rate evaluation and control.

The concept of using electrochemical technology to measure boiler waterwall corrosion was verified in a previous testing program at the FirstEnergy Eastlake Station sponsored by OCDO ("Corrosion Assessment at FirstEnergy Eastlake Station," Final Report of OCDO Project CDO/D-99-12, SAVvy Engineering and Reaction Engineering International, March 2002). Key conclusions of this project were:

1. The corrosion tests at Eastlake Power Station provided the first demonstration of real-time high-temperature corrosion assessment in the radiant section of a large coal-fired power generation boiler. The successful completion of the tests demonstrated that corrosion could be measured accurately in real-time in normal boiler operations, and an assessment of waterwall wastage could be made without impacting boiler availability.
2. Examination of the plant data revealed that corrosion rate was strongly linked with the boiler load: the higher the boiler load, the higher the rate of corrosion. A strong correlation between corrosion rate and heat flux at the radiant section membrane tube wall also was demonstrated.
3. The performance of the probe settled some previously unresolved technical issues, notably its capability to operate in a particulate-laden combustion environment. Additionally, it was observed that the sensor was not adversely affected by sootblowing or high-pressure water washing of the surrounding boiler tubes, though in general the latter is not considered a desirable operational circumstance.
4. Real-time electrochemical sensors offer the capability to improve operational control, extend tube service life, reduce maintenance and non-availability and avoid the risk of high temperature corrosion damage. If used in conjunction with CFD-based combustion optimization modeling, the approach should also allow combustion conditions to be managed in real time, thereby minimizing the cost and impact of $NO_x$ reduction techniques such as staged combustion and catalytic de-$NO_x$ requirements.
5. Laboratory data, obtained under carefully-controlled test conditions, showed that stoichiometry (CO concentration), flue gas concentration ($H_2S$ and HCl) and probe operating temperature all could affect the measured corrosion rate on carbon steel of similar composition to radiant section membrane tube material. As the stoichiometric ratio was reduced, the concentrations of acid gases increased, the probe sensor temperature increased, and the measured corrosion rate also increased.
6. A comparison of the corrosion results from the Eastlake tests between cumulative rate estimates obtained from the electrochemical instrumentation and high-precision metrology determinations were in good agreement. This combination of methods provided firm evidence that the on-line instrumentation offers a reliable method of high temperature corrosion assessment and on-line combustion management.

Results of the Eastlake tests were encouraging, but left several issues unresolved. Three key recommendations for further development from that program were:

1. Demonstrate that multiple corrosion probes can be utilized in one boiler to obtain a real-time indication of corrosion conditions within the boiler and that real-time assessment of corrosion risk can be summarized for the control room operator at his console.
2. Verify that higher rates of corrosion than were prevalent at Eastlake can be accurately measured with the electrochemical instrumentation. These tests at Eastlake resulted in clear differences in corrosion rate between two boiler levels. However, neither location had very high corrosion rates.
3. Utilize the combination of high precision metrology and electrochemical measurements to verify the reliability of the instrumentation and to provide an on-line indication of corrosion risk and corrosion rate. As more data are accumulated, direct correlation of mechanical and electrochemical results should be made between the profilometry results and the probe results.

The present program attempted to address these recommendations along with other technology development issues as outlined in the program objectives.

#### 4.1.1.3 Test Program Overview

##### 4.1.1.3.1 Project Team

This research and development program was carried out by American Electric Power (AEP) and its partners Reaction Engineering International (REI), NS Harding & Associates, Corrosion Management, Electric Power Research Institute (EPRI) and the University of Utah. Team member responsibilities may be summarized as follows:

AEP – Operator of Gavin Station host site, plant support, program management, technical review

REI – Instrumentation system, profilometry testing, CFD modeling, data correlation, program management, technical review

NS Harding & Associates – Data reduction, data correlation

Corrosion Management – Corrosion monitoring system technical support, technical review

EPRI – Static corrosion measurements using EPRI/KEMA KEMCOP passive probes

University of Utah – Corrosion monitoring system assembly and QA testing

Project funding was provided by OCDO, DOE-NETL and AEP. Cost-sharing was provided by all project participants.

##### 4.1.1.3.2 Test Site

The corrosion testing was carried out at AEP's General James M. Gavin Station on the Ohio River near Cheshire, Ohio. This 2600 $MW_{net}$ station, comprised of two identical opposed-wall-fired units, is the largest coal-fired power plant in the state of Ohio. At program initiation, the plant was burning approximately 7 million tons of high sulfur coal annually with roughly 90% of that originating within the state of Ohio (primarily Pittsburgh seam).

Testing was conducted on Unit 1.

Each unit is base-loaded with some limited low-load operation at night. There is currently 1,000 $ft^2$ of weld overlay on the interior of the boiler waterwall to address the effects of fireside corrosion in the unit. The average cost for weld overlay is approximately \$350/$ft^2$; thus this corrective solution has cost more than \$350,000. Corrosion impacts have been measured previously at the plant using ultrasonic tube (UT) testing to determine side wall tube thicknesses. UT data from testing during the spring of 2002 were used in this program to help site the corrosion sensors and to provide comparison data for CFD model predictions.

#### 4.1.1.3.3 Key Project Tasks

The project was organized into a series of technical work tasks to complete various project objectives. The work tasks are summarized below and task background and results are discussed in more detail in subsequent sections of this report.

- CFD Modeling – Two groups of computer simulations were conducted to predict combustion and waterwall corrosion at Gavin plant. The first group of simulations was conducted to aid in determining appropriate locations for the test probes. The second group of simulations was conducted to evaluate the sensitivity of predicted corrosion results to boiler operating conditions. Model results were also compared with measured data to help verify the corrosion correlations used in the model.
- Probe Siting – Six locations in the boiler were identified for corrosion measurement points based on CFD results, UT measurements previously made at the plant, and plant observations of high corrosion regions. AEP installed ports for the corrosion probes at these locations.
- Corrosion Monitoring System Assembly, Check-out, and Installation – Mechanical and electronic components of the corrosion monitoring system were assembled at REI and the University of Utah. Assembled components were tested at the University of Utah pilot-scale furnace before being shipped to Gavin station and installed.
- Real-time Corrosion Measurements – Real-time corrosion measurements were conducted intermittently at Gavin station over a two-year period. Corrosion system operation and results were monitored remotely at REI offices in Utah.
- Static Corrosion Measurements – Two types of static corrosion measurements, profilometry tests based on short-term corrosion of material at the electrochemical sensor head and KEMCOP passive probe tests based on multi-month corrosion of coupons inserted near the corrosion sensors, were conducted to provide data to which the real-time corrosion data could be compared.
- Correlation of Corrosion Data – Corrosion data gathered from real-time measurements were compared with static measurements and CFD model predictions. Measured data were correlated with boiler conditions to determine the impact of operating conditions on corrosion rates and suggest guidelines for boiler operation to minimize corrosion.

### *4.1.2 Computational Fluid Dynamics (CFD) Model Predictions*

This section of the report describes CFD modeling of waterwall wastage in AEP's Gavin Unit 1 furnace. Modeling was performed in two phases: Phase 1) an initial modeling phase conducted to establish optimal locations for corrosion probes and Phase 2) a second phase for correlation of CFD model predicted corrosion, measured corrosion, and corrosion probe measurements. CFD model setup and results are described for each modeling phase.

#### 4.1.2.1 CFD Model Background

Computer simulation studies of Gavin Unit 1 were conducted using the REI reacting computational fluid dynamics code *GLACIER* for two-phase flow systems (Adams and Smith, 1993; Smith, 1992; Smith and Fletcher, 1988; Smoot and Smith, 1985). *GLACIER* has been developed to model turbulent flow, heat transfer and chemical reaction and has the capability to model reacting and non-reacting flows of gases and particles (or droplets), including gaseous diffusion flames, pulverized coal flames, liquid sprays, coal slurries, isothermal and reacting two-phase flows, injected sorbents, and other oxidation/reduction systems. It has been applied to a wide variety of systems including utility boilers, pyrolysis furnaces, gas turbine combustors, rotary kilns, waste incinerators, smelting cyclones, and others. Applications have been used for basic design, problem solving, and pollution control using many different fuels including coal, natural gas, and waste. Special emphasis has been placed on the simulation of coal combustion systems.

The computational approach involves numerical discretization of the partial differential equation set which describes the physics of the system, including equations for mass, momentum, and energy. Typically, $10^5$ -$10^6$ discrete computational nodes are used to resolve the most relevant features of a three-dimensional combustion process and 40 - 60 variables (including gas velocities, thermodynamic properties, and concentrations of various chemical species) are tracked at each node. Accurate simulation of the combustion processes requires accurate modeling of the dominant or controlling physical mechanisms in the process. Coupled equations of chemical reaction, turbulent fluid flow and mixing, and convective and radiative heat transfer are solved to give a realistic and detailed model of the processes occurring within the furnace.

Turbulence can be modeled using various traditional methods of moment closure including Prandtl's mixing length model, the two-equation k-ε model, (Launder and Spaulding, 1972), and the nonlinear k-ε model (Speziale, 1987). In all simulations discussed in this report, the standard k-ε model was used due to its general applicability in modeling the mean velocity field in reacting flows.

Within the model, the rate at which the primary combustion reactions occur is assumed to be limited by the rate of mixing between the fuel and the oxidizer, which is a reasonable assumption for the chemical reactions governing heat release. The thermodynamic state at each spatial location is a function of the enthalpy and the degree of mixing of two mixture fractions, one of which corresponds to the coal off-gas. The effect of turbulence on mean chemical composition is incorporated by assuming that the mixture fractions are defined by a "clipped Gaussian" probability density function (pdf) having a spatially varying mean and variance. The mean and variance are computed numerically at each grid point and mean chemical species concentrations are obtained by convolution over the pdf.

Particle phase mechanics in *GLACIER* are solved with a particle cloud tracking technique. The mean path and dispersion of an ensemble of particles, referred to as a "particle cloud", are tracked in a Lagrangian reference frame. Dispersion of the cloud is determined with input from the turbulent gas flow field. Particle mass, momentum, and energy sources are coupled to the gas flow field through a particle-source-in-cell technique (Crowe et al., 1977). Particle reaction processes include coal devolatilization, char oxidation, and liquid evaporation. Particle reaction rates are characterized by multiple parallel reaction rates with fixed activation energies. Waterwall deposition is accounted for by evaluating particle/wall interactions.

*GLACIER* particle reaction processes include both coal devolatilization and char oxidation. The dry ash-free portion of the coal undergoes a two-step devolatilization process (Ubhayakar et el. 1976) and the volatiles react further in the gas phase. Rate coefficients for devolatilization have been tabulated by Baxter (1987). Char oxidation is according to a single particle model incorporating the effects of both external oxidizer diffusion and surface kinetics. The oxidation rate is a function of the kinetic rate coefficient and the oxygen concentration. The rate coefficient is of an Arrhenius form, the surface reaction is first order with respect to oxygen concentration, and the product of the reaction is assumed to be CO. Experimentally determined rate parameters (pre-exponential and activation energy) are used when available, otherwise approximations of these kinetic parameters for ranges of coal types are used. Carbon in fly ash is predicted according to these particle reaction models.

Since radiation is typically the most significant mode of heat transfer in a large coal-fired furnace, it is critical that the radiation field be accurately represented. Accurately simulating radiative transfer to specific regions in a system requires a model, which can account for both absorbing-emitting radiation processes and complex system geometries, including arbitrary structures such as convective tube passes. Additionally, it is desirable that any radiative model selected be computationally efficient in terms of execution time and storage to allow coupling with other parts of a comprehensive combustion model. *GLACIER* utilizes the discrete-ordinates method, which has been shown to be a viable choice for modeling radiation in combustion systems, both in terms of computational efficiency and accuracy. This method retains the directional dependency of the radiation intensity a way that other flux models are unable to achieve, yet provides for a finite-difference or finite-volume solution that is more computationally efficient than zone methods and more deterministic than Monte Carlo methods. The development of the discrete-ordinates method and its application to a number of complex geometries have been presented in the literature and serve to validate the use of this method in accurately modeling radiative heat transfer in coal-fired boilers (Adams, 1993; Adams and Smith, 1993; Adams and Smith, 1995).

The potential for waterwall corrosion is evaluated as a function of wall conditions and near wall flue gas composition. The presence of sulfur in wall deposits has been implicated as an important contributor to high corrosion rates (Bakker, 1998), so the emphasis is on the deposition of sulfur containing material on furnace waterwalls.

Sulfur is present in coal in three forms:

1. as excluded pyrite ($FeS_2$) particles separate from the coal particles,
2. as included pyrite bound within the coal particles, and
3. as organic sulfur in the coal particles.

Excluded pyrite particles are tracked separately from the coal particles (due to disparities in size distributions and density) and a model for the decomposition of pyrite (Srinivasachar and Boni, 1989) has been incorporated into *GLACIER*. The model includes the thermal decomposition of pyrite to pyrrhotite ($Fe_xS$, for x ranging from 0.877 to 1) and the oxidation of pyrrhotite to magnetite. Particle boundary layer diffusion and liquid layer diffusion of molten pyrrhotite are accounted for. In evaluation of deposition, particle stickiness is determined as a function of oxidation state and temperature. The kinetics model has been validated through comparison of predictions of pyrite decomposition rates to drop tube measurements.

The fractional release of sulfur bound within the coal particle matrix in pyritic and organic (aliphatic and aromatic) forms is assumed similar to the release of carbon through devolatization and oxidation. This assumption is generally valid during devolatization except for highly aromatic coals (Fletcher and Hardesty, 1992). During oxidation, sulfur release rates can vary widely from those of carbon and appear rank dependent. However, for many types of coals, it appears that fractional sulfur release during oxidation is very similar to that of carbon (Mitchell et al., 1991).

An empirical expression for corrosion rate had been developed by EPRI and incorporated into *GLACIER* to predict corrosion rates. The proprietary correlation is based on the local waterwall tube metal temperature and the local flue gas oxygen and carbon monoxide concentrations. The expression is applied only in the areas where fraction of unburned fuel in the total material deposited is greater than 10% and where the deposition rate of unoxidized material exceeds 0.0001 $lb/ft^2/hr$. This expression was used to predict water wall corrosion rates in Gavin Unit 1.

#### 4.2.2.2 Furnace Model Geometry

The overall geometry of the Gavin furnace model is shown in Figure 4.1. A total of 112 burners are arranged in opposing pairs on the front and rear furnace walls. Gas tempering ports are present on both the front at rear walls and three wing walls extend upward from the rear wall. The model ends at the horizontal nose plane. Figure 4.2 shows burner numbering convention used in the simulations and Figure 4.3 shows secondary air spin directions for the burners (based on 2003 operating data).

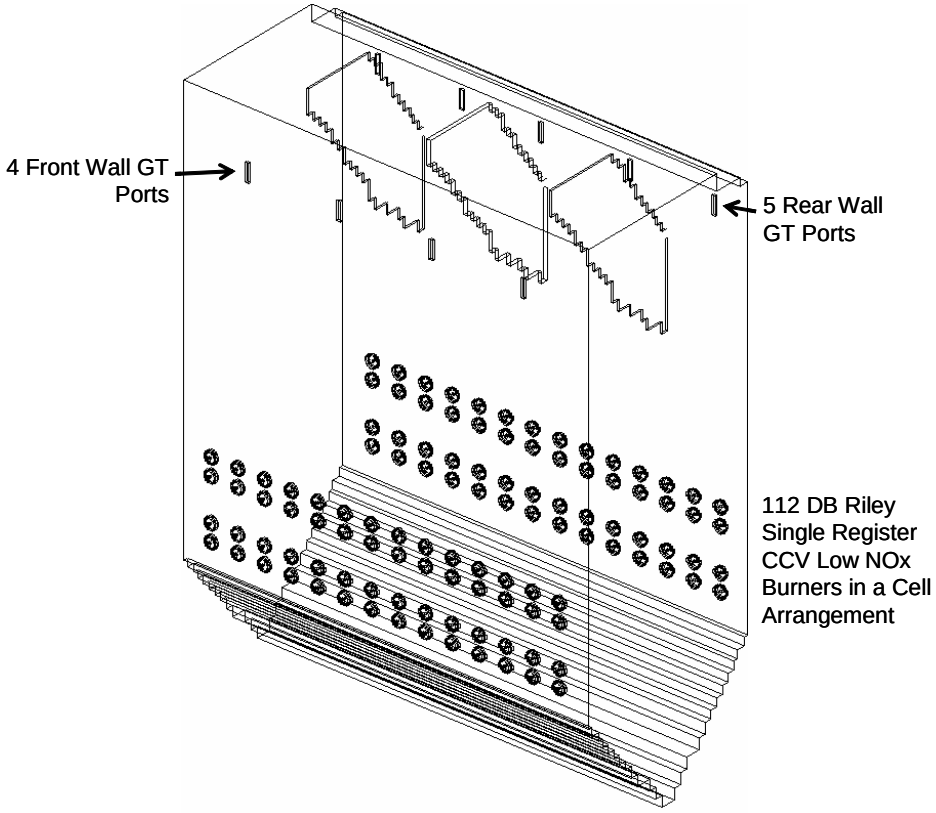


**Figure 4.1. Geometry of the Gavin furnace model showing locations of the burners, gas tempering (GT) ports, and wing walls.**

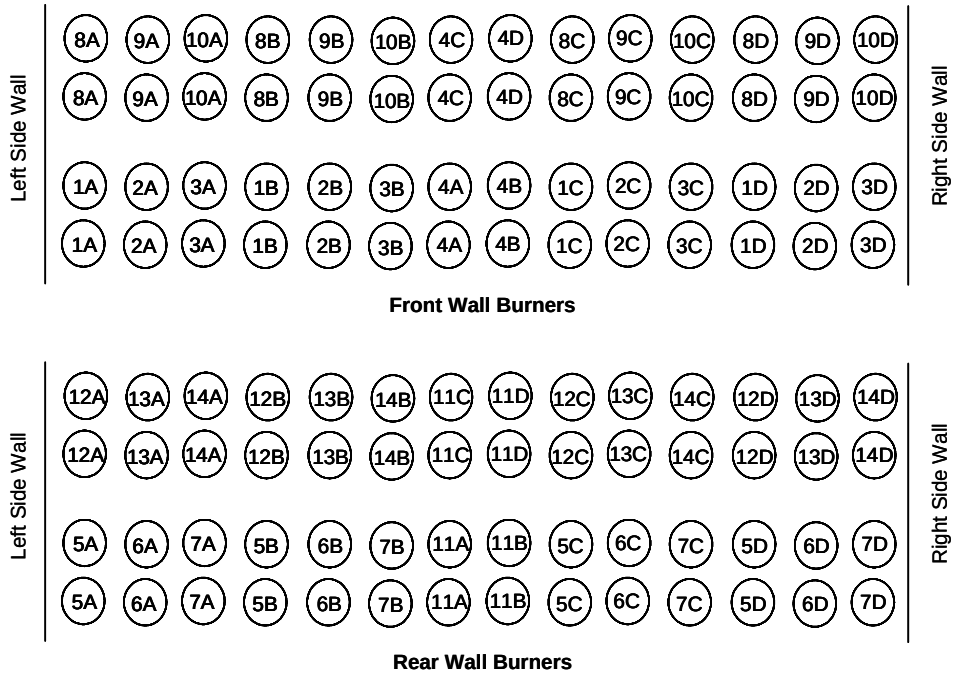


**Figure 4.2. Gavin furnace burner numbering system.**

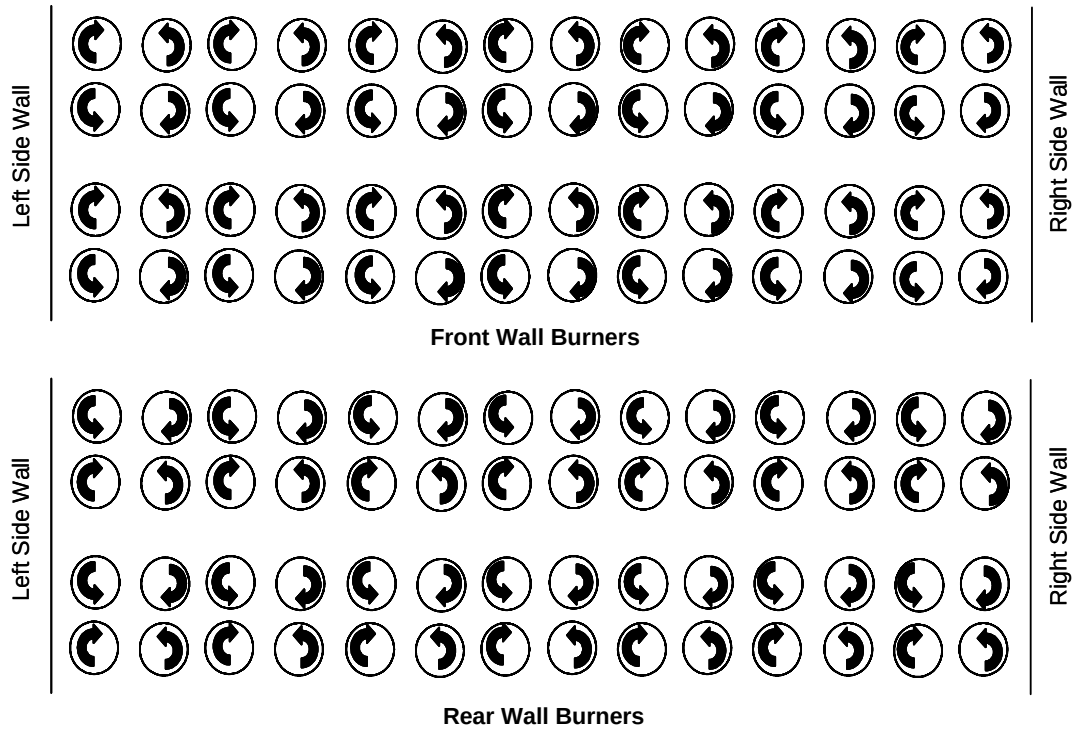


**Figure 4.3. Gavin furnace model burner spin directions.**

### 4.1.2.3 Phase 1 Modeling - Probe Locations

#### 4.1.2.3.1 Phase 1 Model Inputs

The furnace modeling was performed in two phases. The objective of the Phase 1 modeling was to construct a furnace model based on the operating conditions existent at the time the program started (2003). The results from this model were used to predict sidewall corrosion regions for identification of optimal probe locations. The simulation was based on full load operation with all burners in service and with the input conditions listed in Table 4.1. Burner secondary air was biased to the outer, near side-wall burners through the shroud settings tabulated in Table 4.2 and shown in Figure 4.4. Secondary air was assumed to increase linearly with increasing shroud opening. However, it is believed that due to furnace/windbox pressure differential limits, the maximum secondary air flow may be reached at some shroud opening less than the maximum of 15". In this case, the maximum secondary air flow was assumed to be reached at a shroud opening of 10"; at openings greater than this, the air flow did not increase further.

Two additional simulations were performed to assess the sensitivity of the model to variations in inputs. In the first of these simulations, it was assumed that burner secondary air would increase through the entire range of shroud opening and the maximum air flow would not be reached until the shrouds were open to the maximum of 15". This would increase near side-wall burner air flow and presumably would result in higher near wall $O_2$ concentration. The fuel from the near side-wall burners may also tend to oxidize more quickly and

completely, possibly resulting in less side wall deposition of unoxidized material and less corrosion.

In the second simulation, the modeled coal particle size distribution was altered as shown in Table 4.3. Although the altered distribution slightly decreases the size of small particles, the major change is an increase in the size of the large particles, resulting in a somewhat overall coarser size distribution. The larger particles would tend to burn out more slowly, possibly resulting in greater side wall deposition of unoxidized material and corrosion.

**Table 4.1. Gavin furnace model inputs and coal composition.**

**Simulation Inputs**

| | |
|---|---|
| Coal Rate | 1050 klb/hr |
| Total Combustion Air | 11,745 klb/hr |
| Primary Air | 2541 klb/hr (Air/Fuel = 2.42) |
| Sec. Burner Air | 9204 klb/hr |
| Impeller Angle | 15° (30° sidewall burners) |
| Secondary Spin Angle | 45° |
| GT Flow | 2600 klb/hr (645 F, 21% O2) |
| Furnace Stoichiometry | 1.21 |

Primary swirl is 30° for outer column burners

**Coal Compostion**

| | |
|---|---|
| C | 67.10% |
| H | 4.76% |
| O | 6.05% |
| N | 1.23% |
| S | 3.33% |
| Moisture | 7.15% |
| Ash | 10.36% |
| Volatile Matter | 38.09% |
| HHV | 12,292 Btu/lb |

**Coal Fineness**

| |
|---|
| > 99% through 50 mesh |
| 70% through 200 mesh |

**Modeled Distribution**

| Diameter | Mass Fraction |
|---|---|
| 21 μm | 0.05 |
| 30 μm | 0.10 |
| 40 μm | 0.15 |
| 52 μm | 0.20 |
| 68 μm | 0.20 |
| 90 μm | 0.15 |
| 120 μm | 0.10 |
| 183 μm | 0.05 |

Secondary spin angle is estimated.

Coal fineness data of 70% through 200 mesh is assumed, > 99% through 50 mesh was provided.

Wall steam temperature below 240' elevation were assumed to be the average of the 1st pass inlet and 2nd pass exit temperatures (705 F). Above 240' elevation and in the wing walls, steam temperatures were assumed to be the average of the 3rd pass inlet and exit temperatures (673.5 F).

**Table 4.2. Gavin furnace Phase 1 model secondary air burner shroud settings.**

| Burner | Upper/Lower Open (inches) | Burner | Upper/Lower Open (inches) |
|---|---|---|---|
| 1A | 15/15 | 8A | 15/15 |
| 1B | 8/8 | 8B | 8/8 |
| 1C | 9/9 | 8C | 10/10 |
| 1D | 8/8 | 8D | 8/8 |
| 2A | 12/12 | 9A | 10/10 |
| 2B | 8/8 | 9B | 9/9 |
| 2C | 9/9 | 9C | 8/8 |
| 2D | 12/12 | 9D | 12/12 |
| 3A | 10/10 | 10A | 10/12 |
| 3B | 7/7 | 10B | 10/10 |
| 3C | 7/7 | 10C | 7/7 |
| 3D | 15/15 | 10D | 15/15 |
| 4A | 6/6 | 11A | 6/6 |
| 4B | 6/6 | 11B | 6/6 |
| 4C | 6/6 | 11C | 6/6 |
| 4D | 6/6 | 11D | 6/6 |
| 5A | 15/15 | 12A | 14.5/15 |
| 5B | 8/8 | 12B | 8/8 |
| 5C | 8/8 | 12C | 8/6 |
| 5D | 7/7 | 12D | 8/8 |
| 6A | 12/12 | 13A | 12/12 |
| 6B | 8/10 | 13B | 10/10 |
| 6C | 8/6 | 13C | 8/8 |
| 6D | 10/10 | 13D | 10/10 |
| 7A | 10/10 | 14A | 10/10 |
| 7B | 7/8 | 14B | 11/8 |
| 7C | 6.9/7 | 14C | 7/6 |
| 7D | 15/15 | 14D | 15/15 |

**Table 4.3. Comparison of the model coal particle size distribution and a slightly coarser distribution.**

**Model Distribution**

| Diameter | Mass Fraction |
|---|---|
| 21 μm | 0.05 |
| 30 μm | 0.10 |
| 40 μm | 0.15 |
| 52 μm | 0.20 |
| 68 μm | 0.20 |
| 90 μm | 0.15 |
| 120 μm | 0.10 |
| 183 μm | 0.05 |

**Coarser Distribution**

| Diameter | Mass Fraction |
|---|---|
| 19 μm | 0.05 |
| 29 μm | 0.10 |
| 39 μm | 0.15 |
| 52 μm | 0.20 |
| 69 μm | 0.20 |
| 92 μm | 0.15 |
| 126 μm | 0.10 |
| 199 μm | 0.05 |

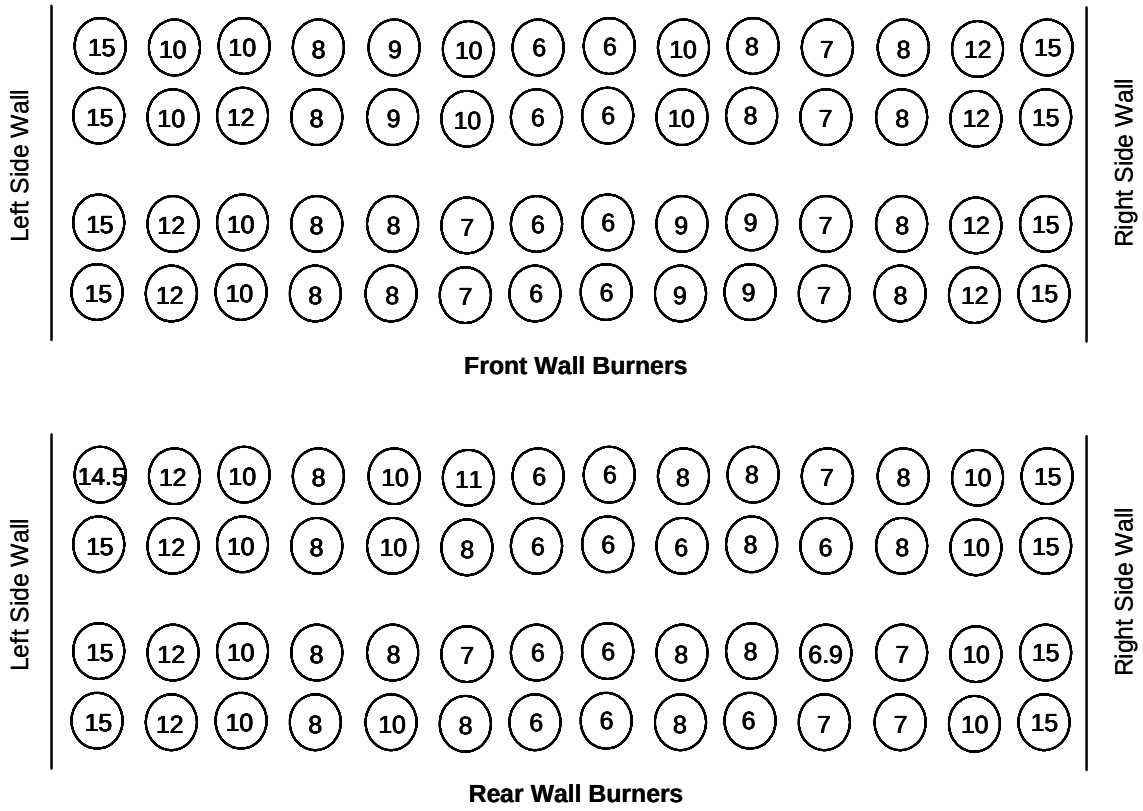


**Figure 4.4. Gavin furnace Phase 1 model secondary air burner shroud settings (inches of shroud opening).**

#### 4.2.3.2 Phase 1 Model Results

The Phase 1 model results were used to identify wastage locations for the placement of corrosion probes in the furnace. As noted earlier, secondary burner air was biased to the outer burners through burner shroud settings. Although the outermost burner shrouds were set at 15" open, for the baseline results shown here, it was assumed that the maximum burner secondary was attained when the shrouds were 10 inches open.

The fraction of unoxidized coal in the total material deposited is shown in Figure 4.5. This parameter has been found to be indicative of waterwall corrosion. In the corrosion model, it provides an on/off switch to predict where corrosion due to deposition of unoxidized FeS may occur. The actual corrosion rate is a function of the local flue gas composition and the tube metal temperature. For the Phase 1 baseline model, the fraction of unoxidized coal in the total material deposited is most extensive in the central region of the furnace side walls at the burner elevations and above. When waterwall wastage occurs in opposed-wall-fired furnaces, it is typically found in this side-wall region. As the hot combustion gases and unburned fuel from opposite wall burners impinge on each other, material is forced to the side walls.

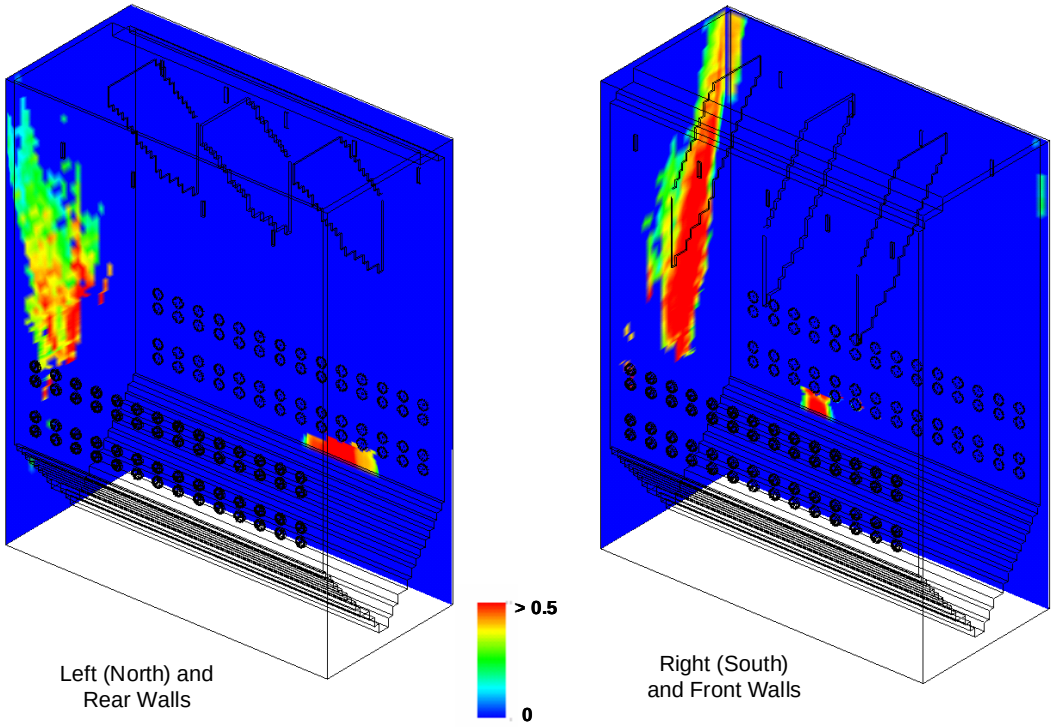


**Figure 4.5. Fraction of unoxidized coal in the total material deposited for the Phase 1 case where secondary burner air is assumed to reach a maximum when burner shrouds are set at 10" or more open.**

The predicted corrosion rate for the baseline Phase 1 model is shown in Figure 4.6. Corrosion is predicted in the same regions where the fraction of unburned coal was deposited. The predicted corrosion region is fairly typical of opposed-wall-fired furnaces, although the region extends higher above the burners than may be actually present in the furnace. Somewhat higher corrosion rates are found near the edges of the region compared to those in the center; this results from the model predicting highest rates when unoxidized material is deposited where local conditions are oxidizing. The predictions shown in Figure 4.6 were one of the factors used to locate corrosion probes in the furnace side walls.

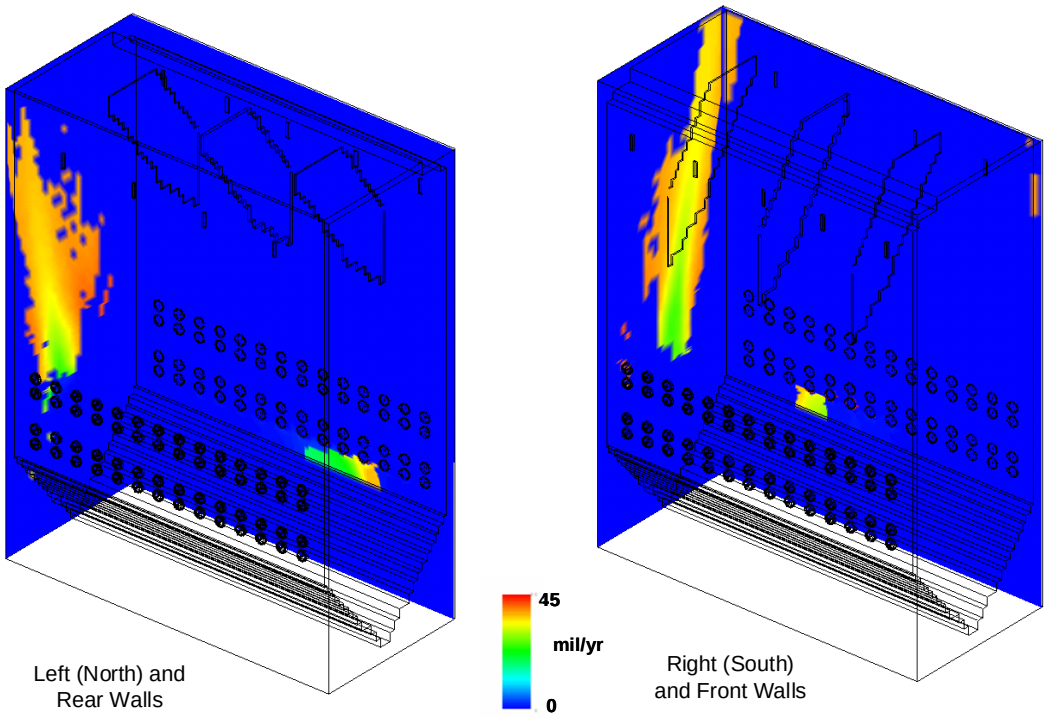


**Figure 4.6. Predicted FeS corrosion rate for the Phase 1 case where secondary burner air is assumed to reach a maximum when burner shrouds are set at 10" or more open.**

Two additional simulations were performed to assess the impact of model variations on the corrosion prediction. In the first of these, it was assumed that the maximum burner secondary air flow was not reached until the burner shrouds were fully open to 15". This assumption permits more biasing of secondary air to the outer burners near the furnace side walls. Predicted corrosion rates for this simulation are shown in Figure 4.7. In this case, the higher near side wall air flow virtually eliminates the side wall corrosion.

A third simulation was performed in which again the maximum burner secondary air was assumed when the shrouds were fully open at 15". In this case, however, the fraction of coal in the larger size bins was increased slightly as described in the inputs section. The larger particles would oxidize more slowly and there would be an increased tendency for unoxidized material to be deposited on the furnace side walls. Predicted corrosion for this simulation is shown in Figure 4.8. With the increase in the fraction of large coal particles, predicted side wall corrosion increases. These two additional simulations demonstrate the sensitivity of the corrosion prediction to model inputs and assumptions.

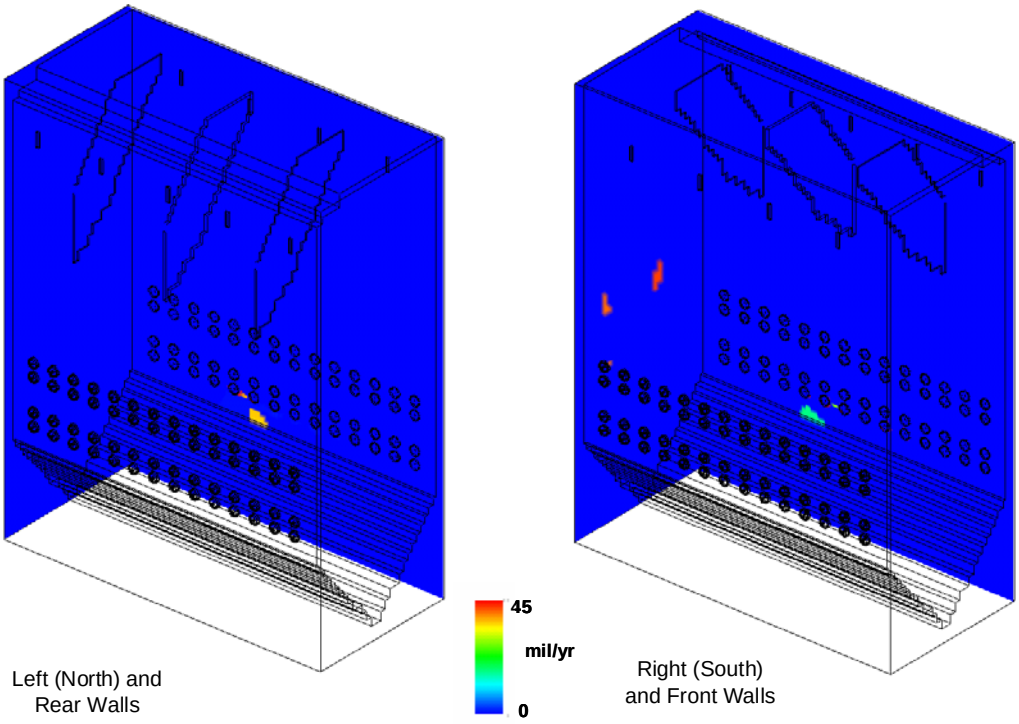


**Figure 4.7. Predicted FeS corrosion rate for the Phase 1 case where secondary burner air is not assumed to reach a maximum until burner shrouds are completely open at 15".**

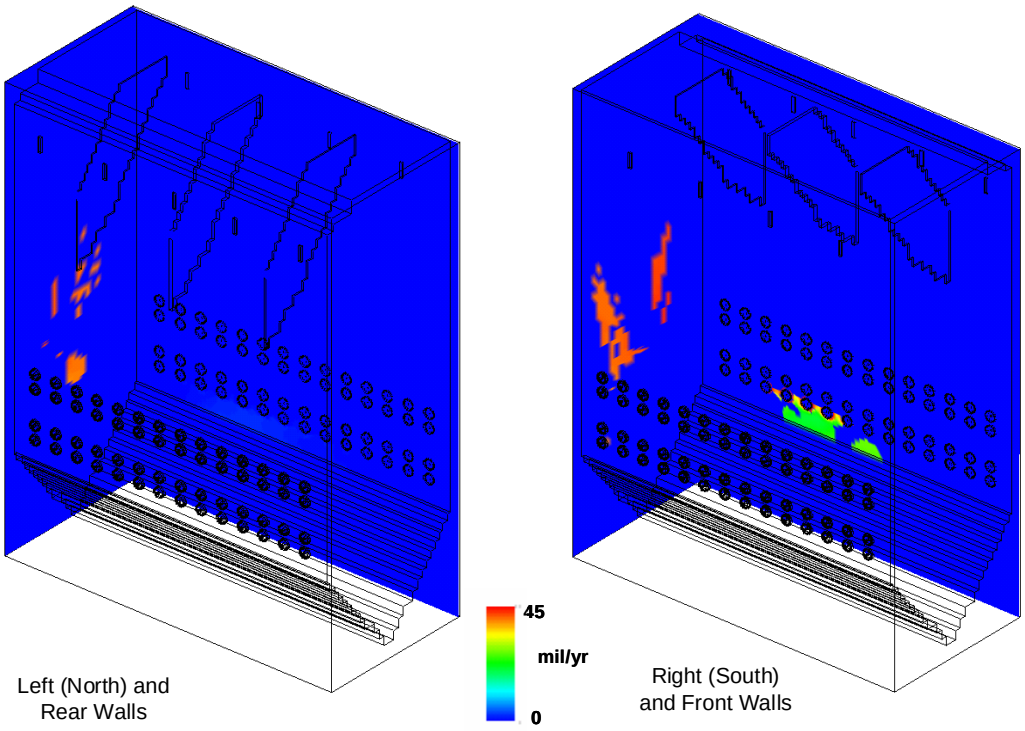


**Figure 4.8. Predicted FeS corrosion rate for the Phase 1 case with coarser grind coal and where secondary burner air is not assumed to reach a maximum until shrouds are completely open.**

### 4.1.2.4 Phase 2 Modeling - Corrosion Sensitivity

#### 4.1.2.4.1 Phase 2 Model Inputs

Phase 2 furnace modeling was performed subsequent to the corrosion probe testing period. The objective of the Phase 2 modeling was to compare model predicted corrosion with measured corrosion and to correlate probe data with CFD predictions.

During the corrosion probe test period, furnace operation was changed from that of the Phase 1 modeling and the model was adjusted accordingly. Burner shrouds were no longer used to bias air flow, and only 92 of the 112 burners were in service. Certain near side wall out-of-service burners were used for cooling.

Four furnace simulations were performed under this part of the project, two at full load and two with furnace load reduced from 1300 $MW_e$ to 1000 $MW_e$. A summary of the cases is found in Table 4.4

During the corrosion probe test period, the furnace was initially operated as in Case 1 (full load) and Case 3 (low load) of Table 4.4, but a burner fire resulted in an operational change to the conditions of Case 2 (full load) and Case 4 (low load) after approximately the beginning of the summer of 2004. Following the burner fire, the right side cooling burners were moved from the rear wall (burners 7D) to the opposite front wall burner pair (burners 3D). Furnace operating conditions for each case are tabulated in Table 4.5, burner operating

conditions are in Table 4.6, and burner configurations are in Figure 4.9 for Case 1 and Case 3 and in Figure 4.10 for Case 2 and Case 4.

**Table 4.4. Summary of Phase 2 modeling case descriptions.**

- **Full load simulations**
  - **Case 1**
    - Full load (1300 $MW_e$), as operated until mid 2004
    - Cooling burners 5A and 7D (lower outside rear wall burner pairs)
    - BOOS 4A, 4B, 4C, 4D, 13A, 13B, 13C, 13D
  - **Case 2**
    - As operated following a burner fire in mid 2004
    - Burner 3D for side cooling rather than 7D (3D is the front wall burner pair opposite rear wall pair 7D)

- **Low load simulations**
  - **Case 3**
    - Similar to Case 1
    - Load reduced from 1300 $MW_e$ to 1000 $MW_e$
  - **Case 4**
    - Similar to Case 2
    - Load reduced from 1300 $MW_e$ to 1000 $MW_e$

**Table 4.5. Gavin furnace Phase 2 model operating conditions and coal composition.**

**Furnace Operating Conditions**

| | Case 1 & Case 2 | Case 3 & Case 4 |
|---|---|---|
| Furnace load | 1300 $MW_e$ | 1000 $MW_e$ |
| Thermal load | 112 | 112 |
| Total # of burners | 112 | 112 |
| Burners out of service | 16 | 16 |
| Side cooling burners | 4 | 4 |
| Burners in service | 92 | 92 |
| Coal flow rate (Lb/hr) | 1,039,263 lb/hr | 799,433 lb/hr |
| PA flow rate | 2,463,054 lb/hr | 2,463,054 lb/hr |
| PA temperature | 150° F. | 150° F. |
| SA flow rate | 9,117,341 lb/hr | 6,624,842 lb/hr |
| SA temperature | 580° F. | 580° F. |
| SA swirl ($V_a/V_t$) | 1.0 | 1.0 |
| Total combustion air | 11,580,395 lb/hr | 9,087,896 lb/hr |
| Furnace SR | 1.21 | 1.23 |
| Excess air | 21.0% | 23.4% |
| GT flow (Lb/hr) | 2,600,000 lb/hr | 2,037353 lb/hr |
| GT fraction of flue gas | 20.76% | 20.76% |
| GT flow temerature (F) | 645° F. | 645° F. |

**Coal Composition**

| | |
|---|---|
| C | 66.95% |
| H | 4.71% |
| O | 6.39% |
| N | 1.25% |
| S | 3.75% |
| Moisture | 7.65% |
| Ash | 9.30% |
| Volatiles | 38.50% |
| HHV | 12,350 Btu/lb |
| Ash sticking temperature | 2080° F. |

**Coal Fineness:**
**99.6% through 50 mesh,**
**91.5% through 100 mesh,**
**61.5% through 200 mesh**

## Table 4.6. Gavin furnace Phase 2 model burner operating conditions.

**Per Operating Burner**

| | Case 1 & Case 2 | Case 3 & Case 4 |
|---|---|---|
| Coal flow rate | 11,296 lb/hr | 8,689 lb/hr |
| PA/Coal ratio | 2.37 | 3.08 |
| PA | 26,772 lb/hr | 26,772 lb/hr |
| PA temperature | 150° F. | 150° F. |
| SA | 89,738 lb/hr | 65,205 lb/hr |
| SA temperature | 580° F. | 580° F. |
| SA swirl ($V_a/V_t$) | 1.0 | 1.0 |
| Total combustion air | 116,510 lb/hr | 91,977 lb/hr |
| Burner SR | 1.120 | 1.149 |
| Excess air | 12.0% | 14.9% |

**Per Side Cooling Burner**

| | Case 1 & Case 2 | Case 3 & Case 4 |
|---|---|---|
| Coal flow rate | 0 lb/hr | 0 lb/hr |
| PA | 0 lb/hr | 0 lb/hr |
| SA | 107,685 lb/hr | 78,246 lb/hr |
| SA temperature | 580° F. | 580° F. |
| SA swirl ($V_a/V_t$) | 1.0 | 1.0 |

**Per Out of Service Burner**

| | Case 1 & Case 2 | Case 3 & Case 4 |
|---|---|---|
| Coal flow rate | 0 lb/hr | 0 lb/hr |
| PA | 0 lb/hr | 0 lb/hr |
| SA | 26,921 lb/hr | 19,562 lb/hr |
| SA temperature | 580° F. | 580° F. |
| SA swirl ($V_a/V_t$) | 1.0 | 1.0 |

**For low load simulations:**

- Coal is reduced by 76.92%
- Primary air is unchanged
- All secondary air is reduced by 72.66% (to get 23.4% excess air)
- GT flow is reduced to maintain flow rate of 20.76% of total combustion flue gas

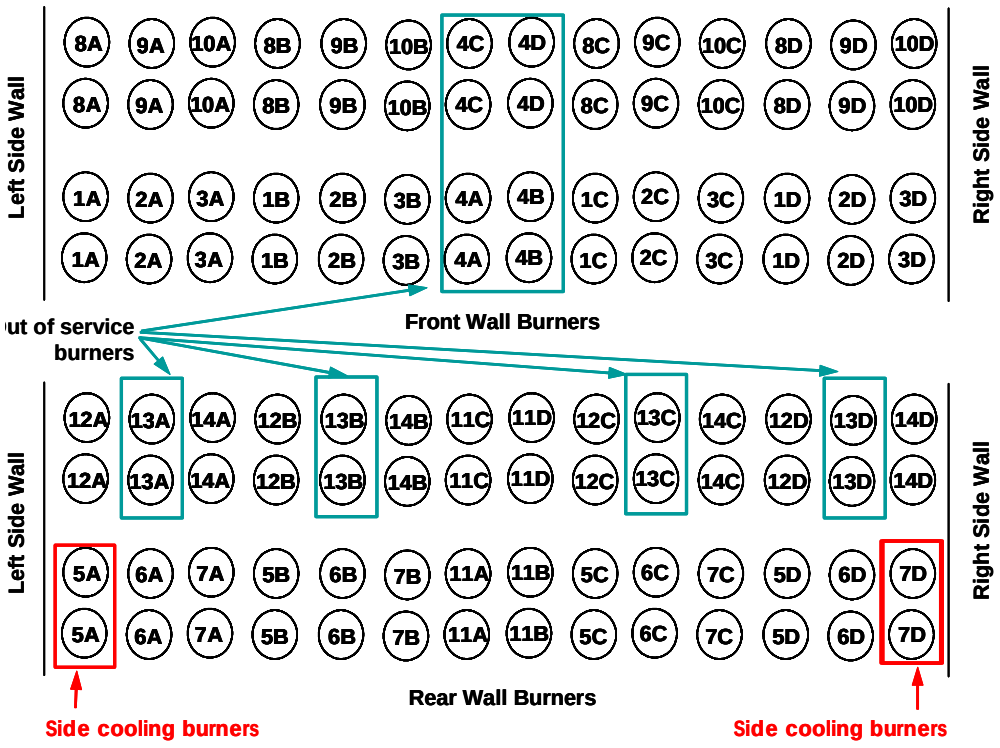


Figure 4.9. Gavin Phase 2 model, Case 1 & 3 burner operational configuration.

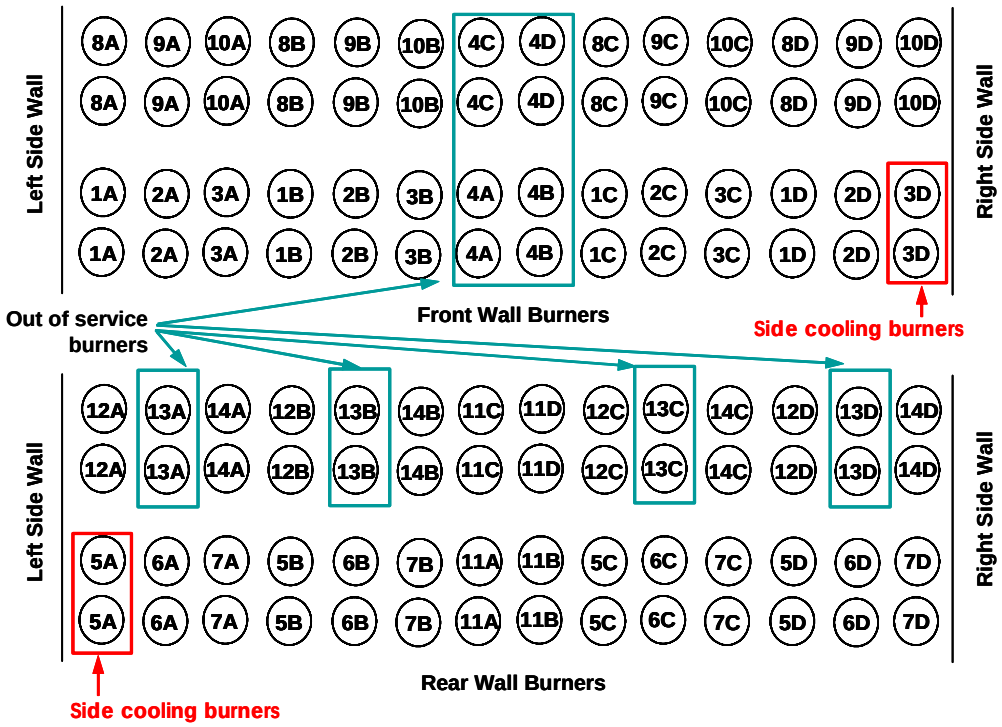


**Figure 4.10. Gavin Phase 2 model, Case 2 & 4 burner operational configuration.**

#### 4.1.2.4.2 Phase 2 Model Results

Ultrasonic (UT) side-wall tube thicknesses measured during the spring of 2002 are shown in Figure 4.11. The highest side wall wastage regions, shown as red, are in central part of the walls beginning near the bottom burner elevation and extending upward, a typical corrosion region for opposed-wall-fired furnaces. Hot combustion gases carrying unburned fuel and ash particles from opposite wall burners impinge on each other in the center of the furnace and spread to the central part of the side walls.

The measurements in Figure 4.11 show a much larger wastage region on the right side wall compared to the left side wall, although if the furnace was operated in a side-to-side symmetry manner as assumed in the model, it is not clear why this would occur. There were changes in the side cooling burners in the early summer of 2004 that could possibly alter right side wall conditions and spread corrosion over a larger region, but the UT measurements were taken prior to that time. Possibly an imbalance was present in the furnace that was not included in the model.

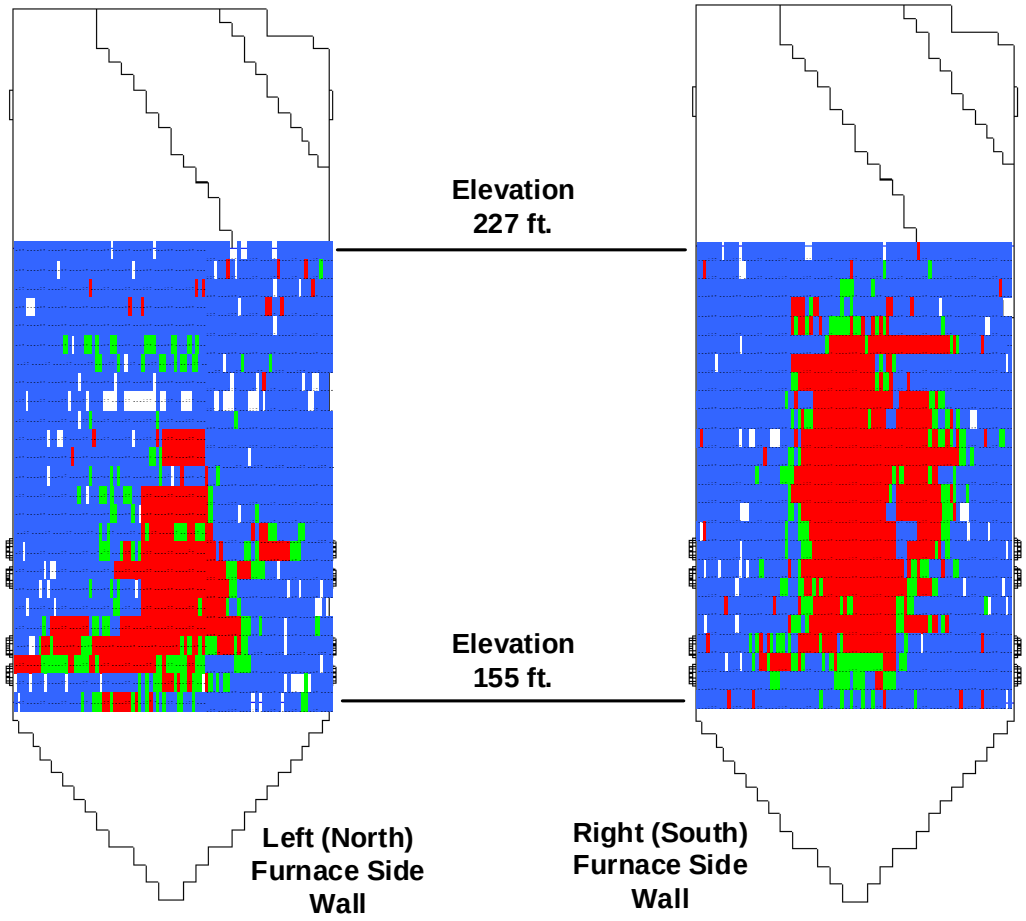


**Figure 4.11. Spring 2002 Gavin Unit 1 ultrasonic tube thickness data. Highest wastage areas are shown in red, more moderate wastage areas as green, and lowest (or no) wastage areas as blue and white.**

Figures 4.12 through 4.16 show predicted near wall $O_2$ and CO concentrations for both side walls. Much of the side-wall region with the highest corrosion appears to be reducing with low $O_2$ and high CO concentrations. The side wall region appears to be somewhat more oxidizing for the low load simulations (Case 3 and Case 4) with the high CO reducing region more limited to the lower part of the side wall. This is consistent with the increase in excess air for the low load cases. Changing the right side cooling burners from the rear wall 7D burner pair (Case 1 and Case 3) to the front wall 3D burner pair (Case 2 and Case 4) has little effect on left side wall conditions as would be expected, but has a noticeable effect on the near right side wall conditions. When the front wall 3D burner pair is used for cooling (Case 2 and Case 4), the near right side wall reducing region is shifted toward the rear of the furnace at the upper burner elevation and above. Changing the near wall conditions could possibly disperse the right side wall corrosion over a larger region. Experience has indicated that changes from reducing to oxidizing may exacerbate waterwall wastage. However, as noted above, this would not be responsible for the larger measured corrosion region on the right side wall compared to the left side wall, since the cooling burner change occurred after the UT measurements were made.

Figure 4.16 and Figure 4.17 show predicted side wall net heat fluxes. Peak heat fluxes occur in the corrosion region and provide a reasonably good map of where corrosion occurs. High heat fluxes can exacerbate corrosion both by increasing tube metal temperatures and by resulting high thermal gradients through the wall. Corrosion rates increase with tube metal temperature and thermal gradients can result in variations in material expansion that cause stress and spalling. In some cases, reaction zones in surface layers may move inward and nearer tube metal in the presence of high thermal gradients. As could be expected, the extent of the high heat flux region decreases when furnace load is decreased in Case 3 and Case 4. Changing the right side cooling burners has some effect on the right side wall heat flux but does not significantly change the peak location.

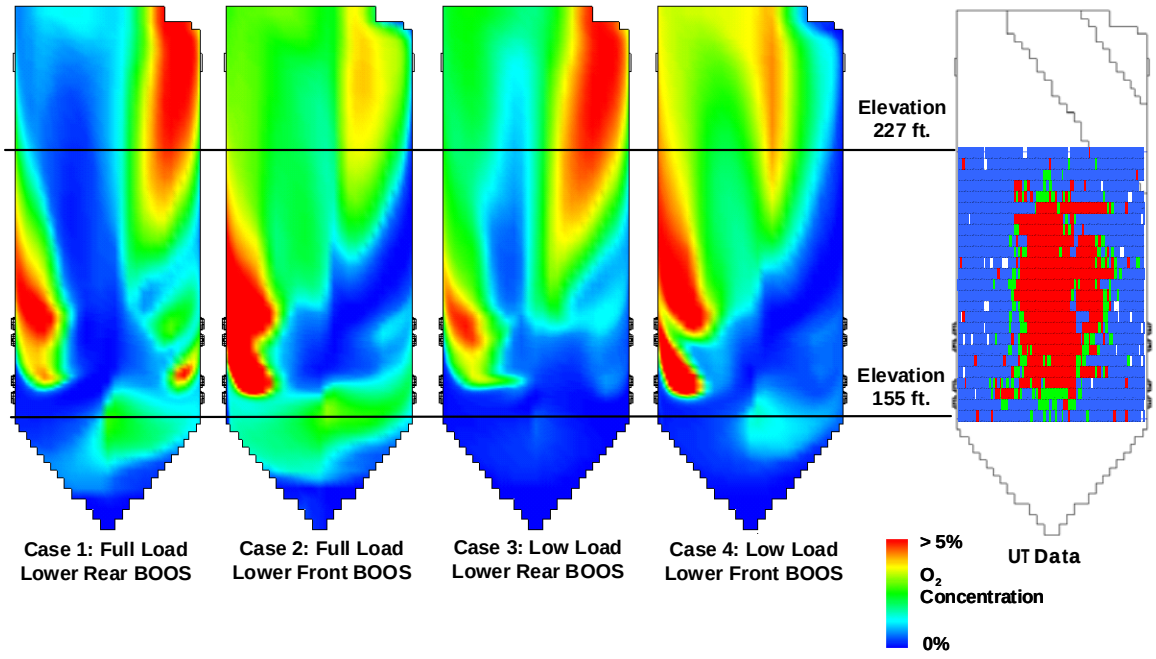


**Figure 4.12. Right side near side near wall (1.2 ft from wall) $O_2$ concentration comparison with UT data.**

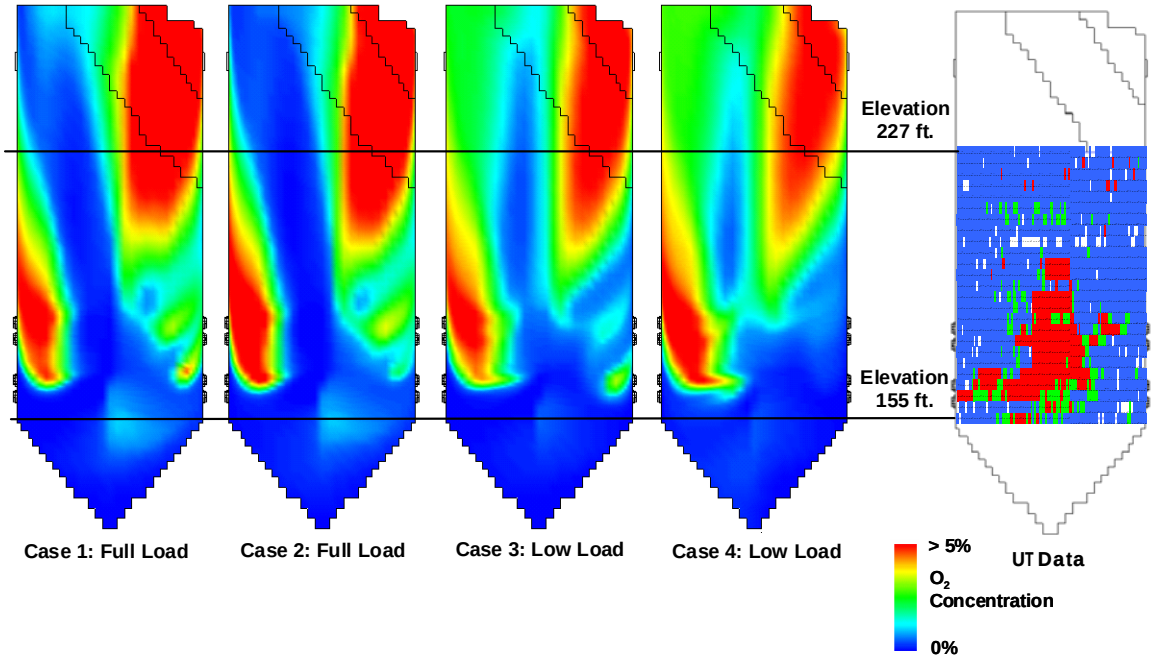


**Figure 4.13. Left side near side near wall (1.2 ft from wall) $O_2$ concentration comparison.**

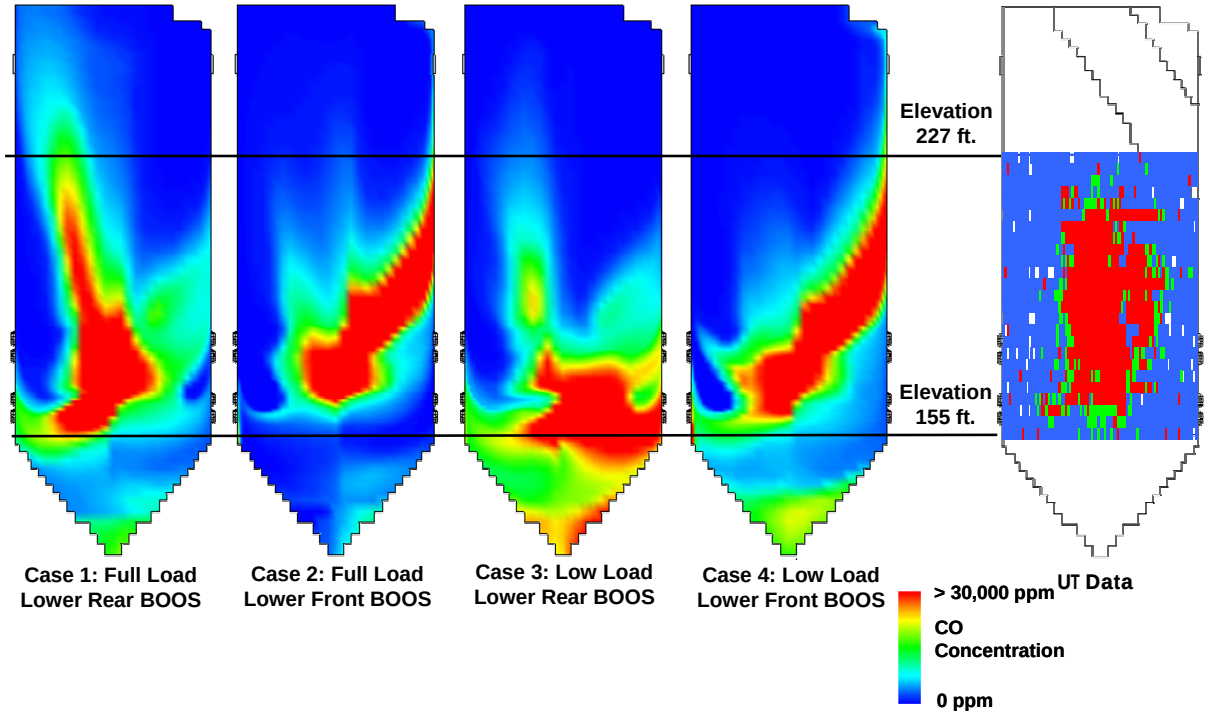


**Figure 4.14. Right side near side near wall (1.2 ft from wall) CO concentration comparison with UT data.**

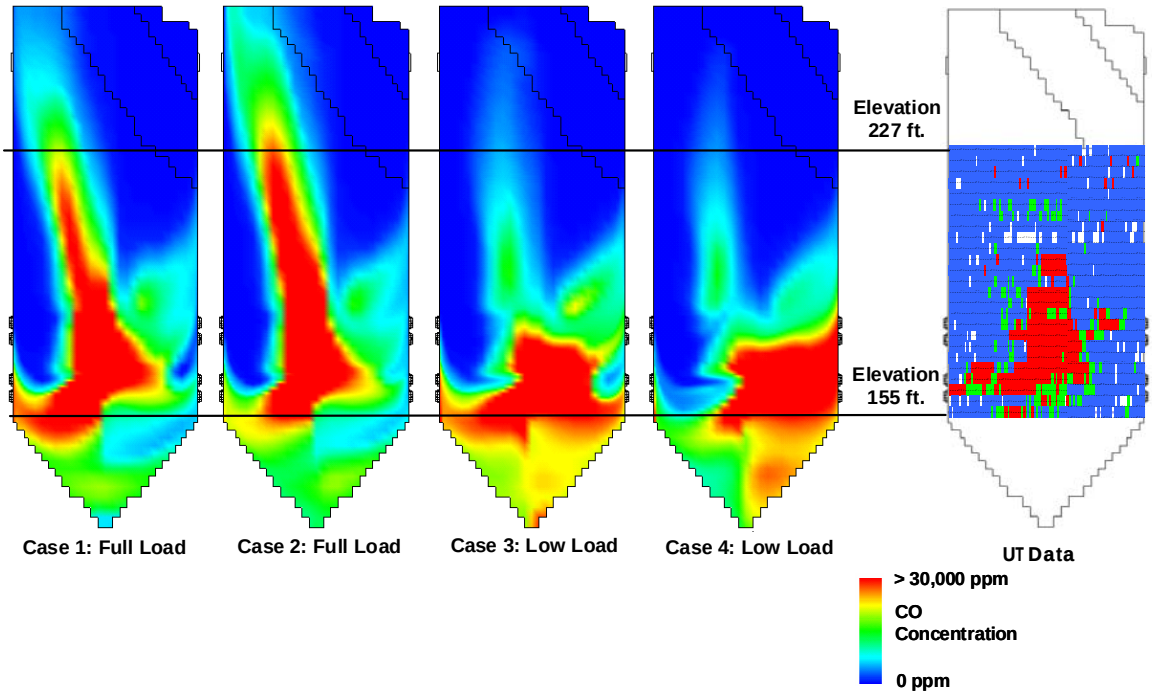


**Figure 4.15. Left side near side near wall (1.2 ft from wall) CO concentration comparison with UT data.**

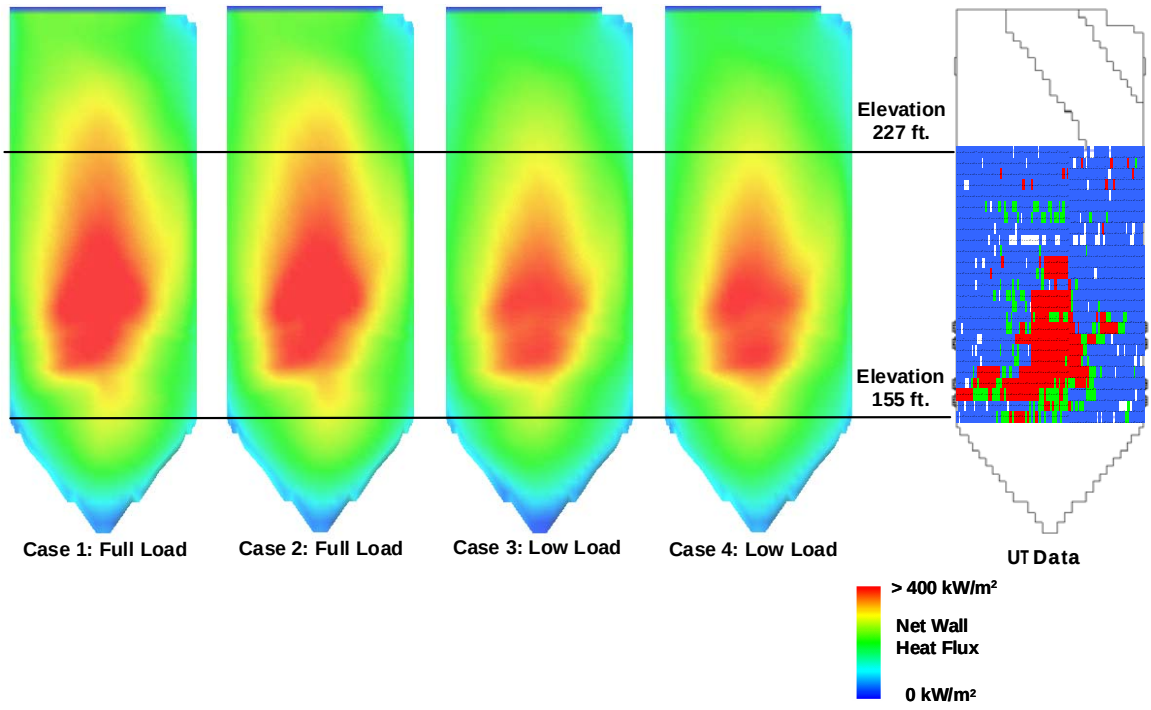


**Figure 4.16. Right side wall net heat flux comparison with UT data.**

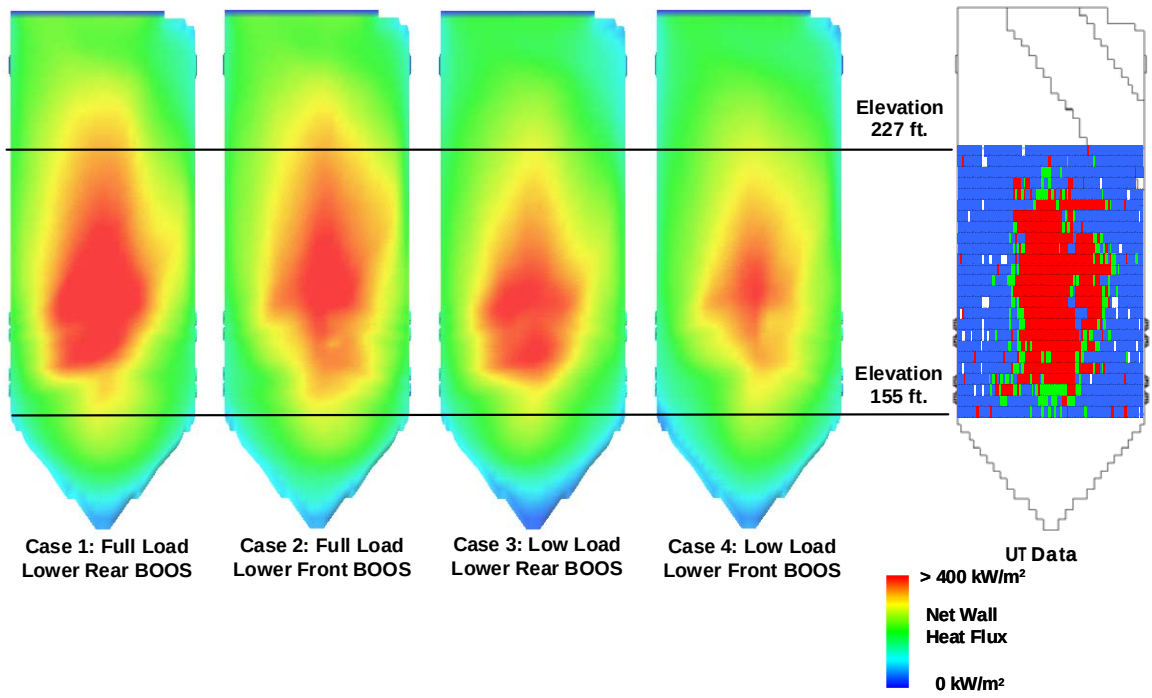


**Figure 4.17. Left side wall net heat flux comparison with UT data.**

Figure 4.18 and Figure 4.19 show the predicted side wall total (unburned coal plus ash) deposition rate Figure 4.20 and Figure 4.21 show the rate for unburned coal alone. Both the total and unburned coal deposition exhibit similar patterns with peak rates in the center of the side walls at the burner elevations where corrosion has been observed. The low load simulations show less total deposition due to lower coal input and less unburned coal deposition due to both lower coal input and faster burnout resulting from the higher excess air. Changing the right side cooling burners alters the locations where material is deposited on the right side wall and for the case of unburned coal deposition; this has the potential to increase the extent of the corrosion region.

Figure 4.22 and Figure 4.23 show the fraction of unburned coal in the total material deposited. This is assumed to be an important indicator of waterwall corrosion and, in the corrosion model described earlier and used in these simulations, this parameter provides an on/off switch for prediction of corrosion. Where the fraction of unburned material in the total material deposited exceeds a critical value (in this case 0.1), the model predicts the potential for corrosion to occur based on tube temperature and near wall gas phase conditions. Figures 4.22 and 4.23 indicate that peak side-wall values ($\geq 0.7$) generally coincide with corrosion regions, but values exceed 0.2 over a large extent of the side walls. Increasing the critical value of this parameter from 0.1 to approximately 0.7 would provide a better map of the corrosion regions for the furnace operating conditions used in the Phase 2 simulations. However, it was observed in the Phase 1 results that increasing secondary air to the outer burners resulted in a less extensive predicted side wall corrosion region, so if burner air was biased to the outer burners, a critical value of 0.1 might provide a better corrosion map than for the operating conditions simulated in Phase 2. We assume the operating conditions simulated in the Phase 2 modeling resulted in the UT measurements shown in Figure 4.11. For the low load simulations, the fraction of unburned material in the total material deposited decreases; this is consistent with the higher excess air in these simulations. When the right side cooling burners are moved from the rear to the front wall, the region of high fraction of unburned material is shifts nearer the furnace rear wall; this is similar to the shift in near wall CO concentration noted earlier.

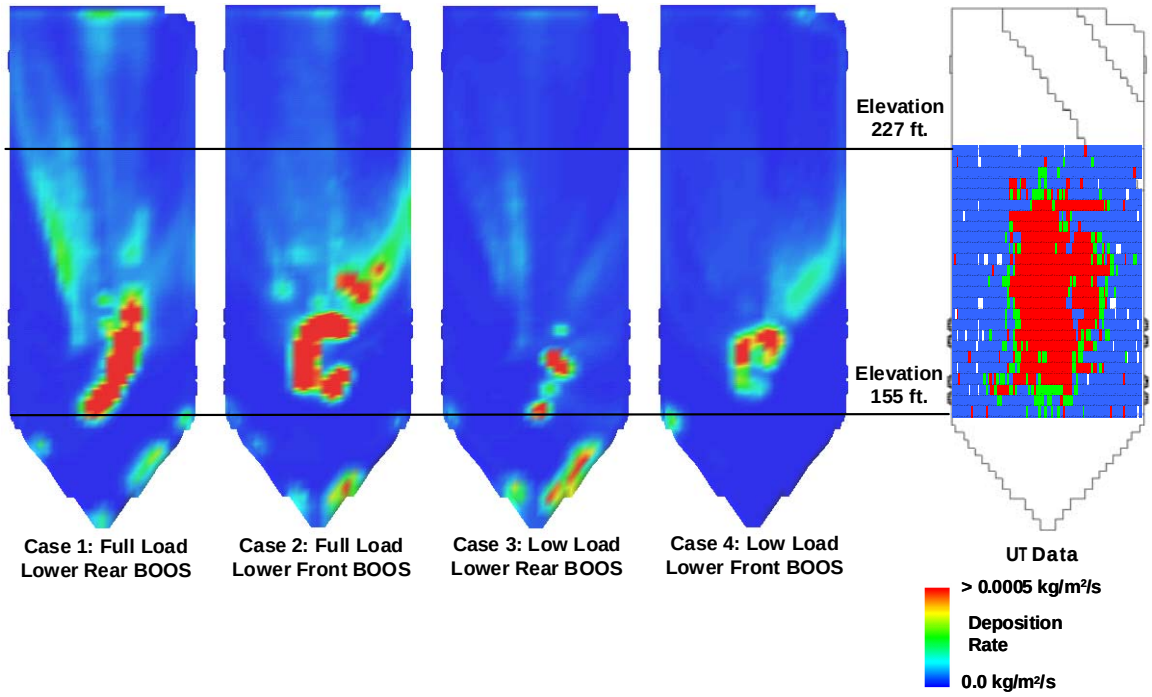


**Figure 4.18. Right side wall total (coal + ash) deposition rate comparison with UT data.**

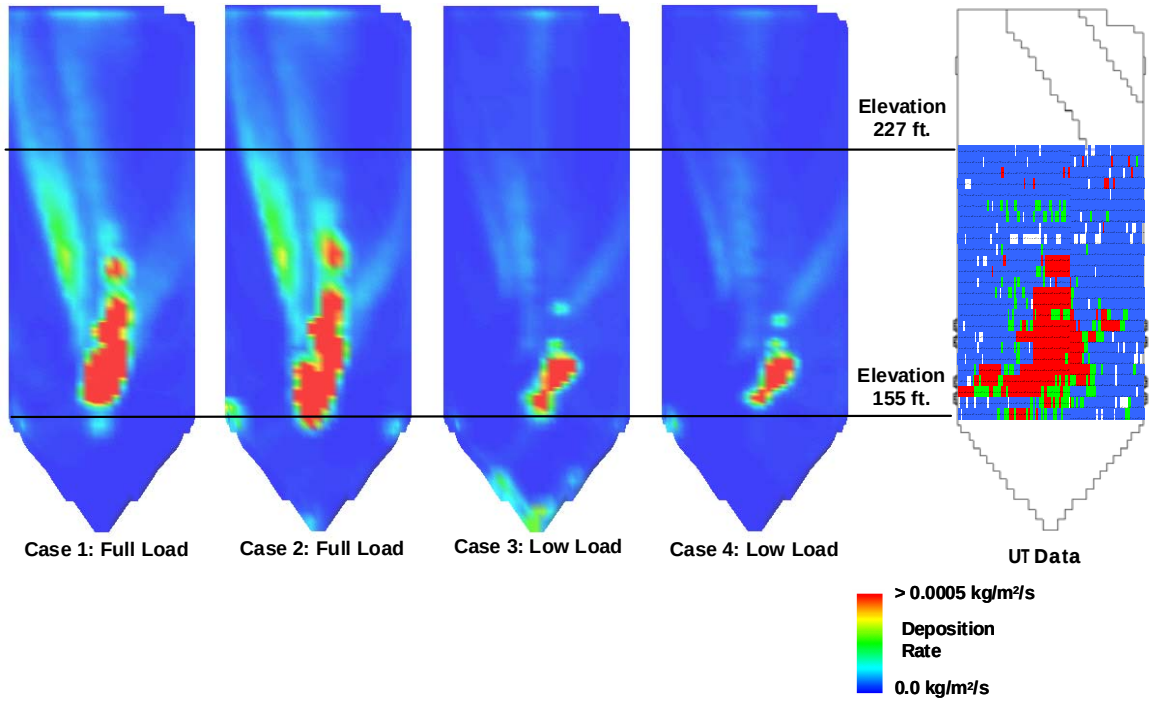


**Figure 4.19. Left side-wall total (coal + ash) deposition rate comparison with UT data.**

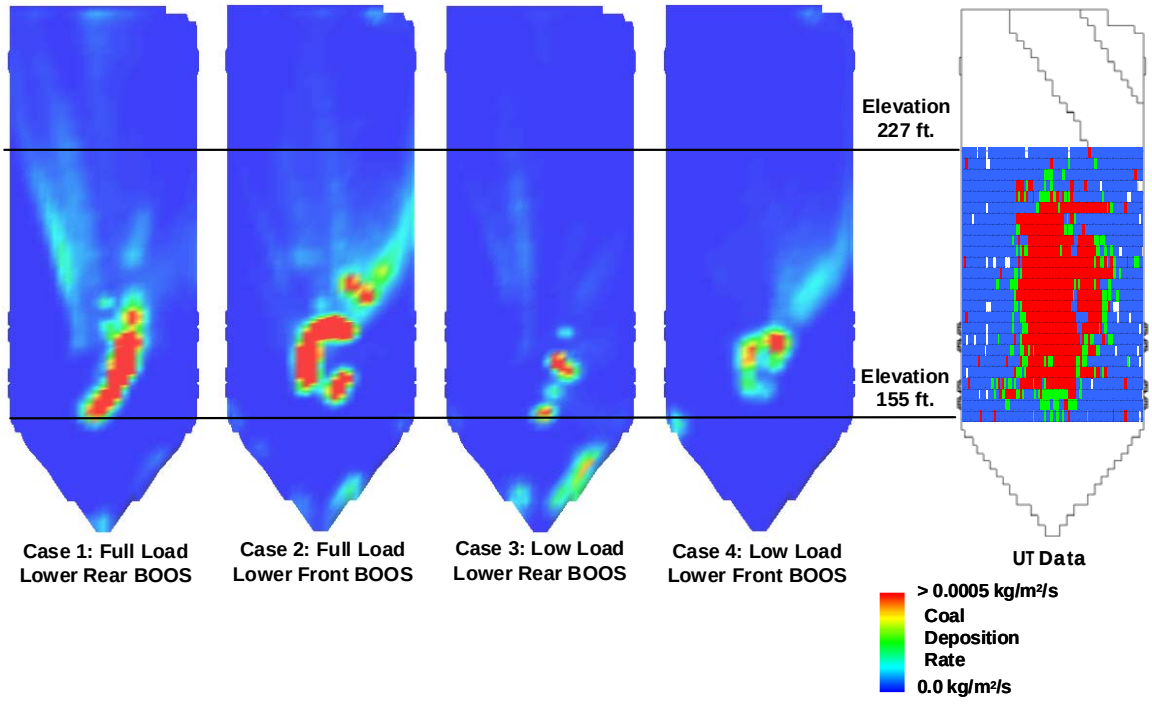


**Figure 4.20. Right side-wall unburned coal deposition rate comparison with UT data.**

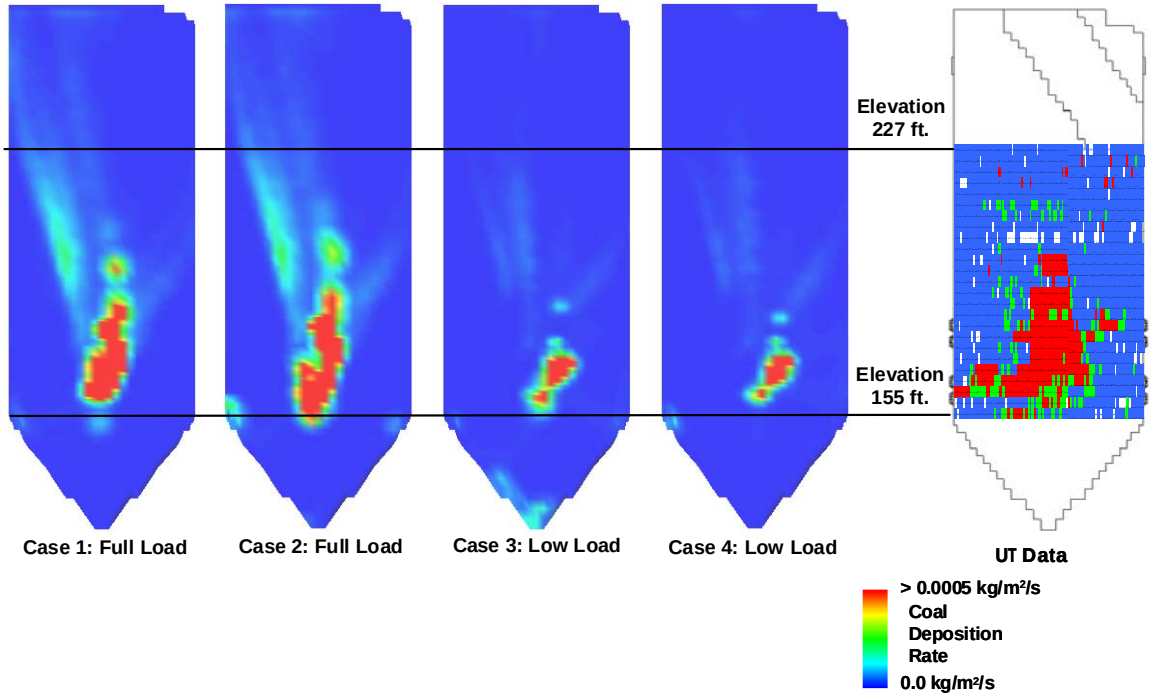


**Figure 4.21. Left side-wall unburned coal deposition rate comparison with UT data.**

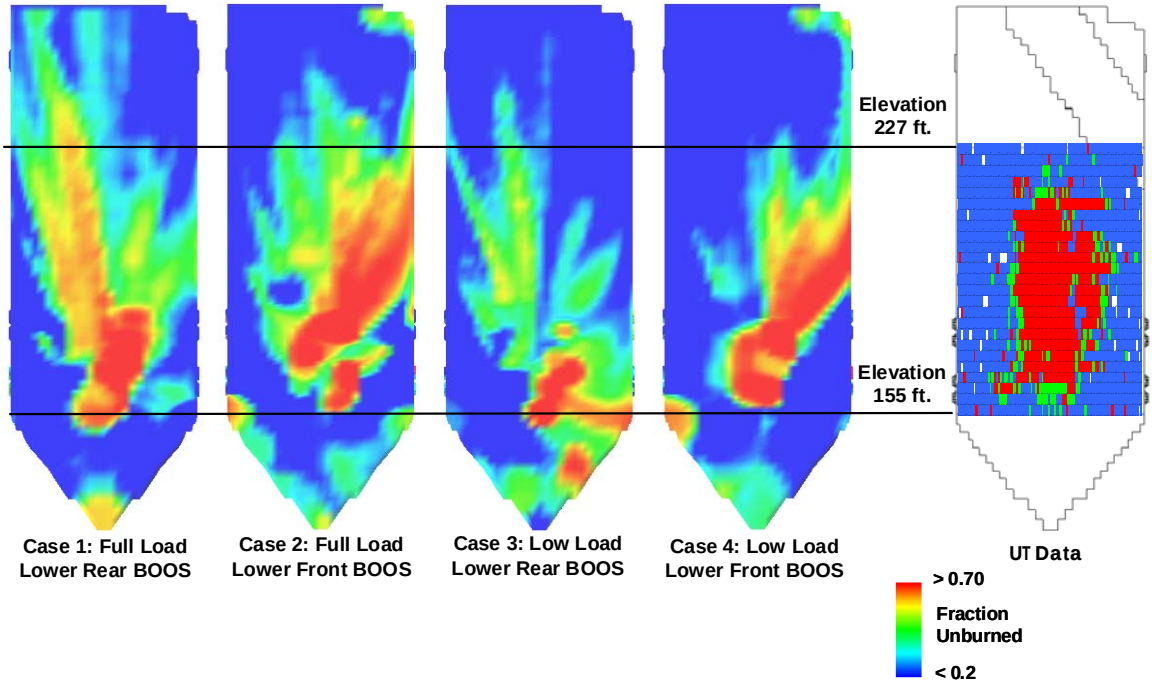


**Figure 4.22. Right side-wall fraction of unburned material in total deposition comparison with UT data.**

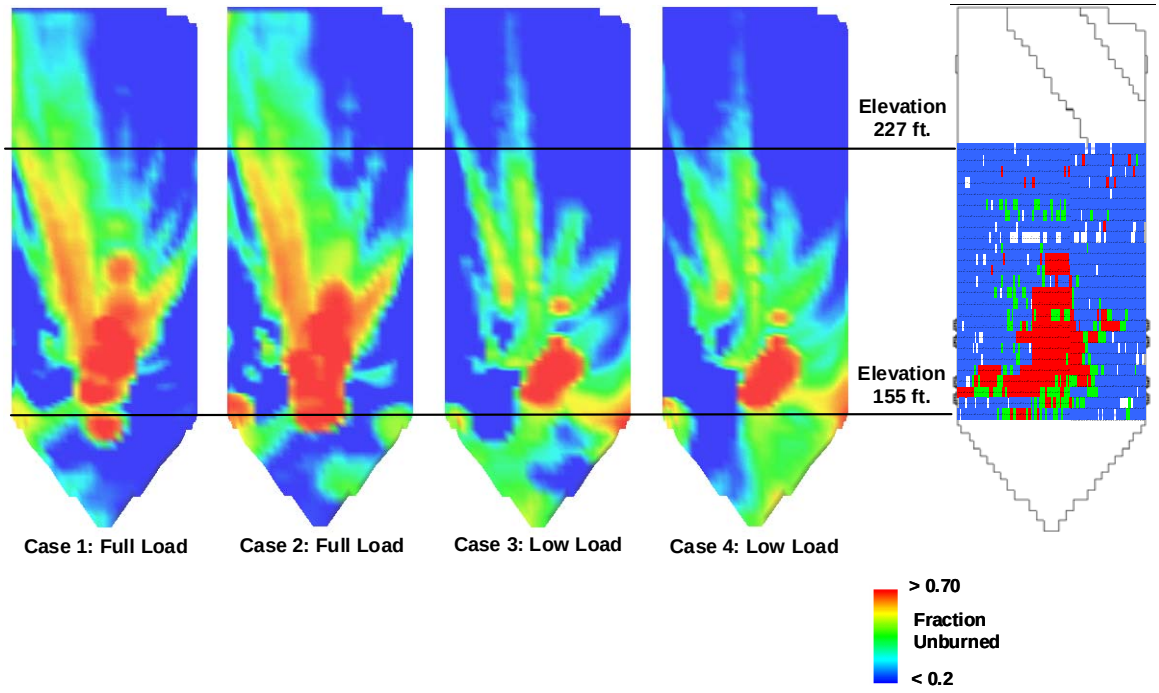


**Figure 4.23. Left side-wall fraction of unburned material in total deposition comparison with UT data.**

Predicted corrosion rates due to FeS deposition are shown in Figures 4.24 and 4.25. Although corrosion is predicted in the regions where it is observed, some of the corrosion indicators, particularly heat flux and the deposition rate of unreacted coal, provide a more accurate prediction of corrosion region than the corrosion model does. Regions of highest predicted corrosion do not coincide well with observed regions of maximum wastage and the extent of predicted corrosion is much larger than that observed. Two factors responsible for the differences between predicted and observed wastage are:

1) The corrosion model predicts highest corrosion rates will occur where unoxidized material is deposited under oxidizing conditions, but the CFD model indicates that most of the area where corrosion has been observed is reducing rather than oxidizing.

2) The region where the model predicts that the fraction of unburned material in the total material deposited is greater than the critical value of 0.1 extends over a greater region of the side walls than the area where corrosion has been observed.

The differences between predictions and measurements could be due to deficiencies in the corrosion model, inaccurate representation of actual furnace operating conditions in the simulations, variation or cycling of actual furnace operating conditions, imbalances in the furnace, or to some combination of these. Measurements of near wall flue gas composition and wall heat fluxes might be useful in determining the accuracy of both the simulated operating conditions and the corrosion model. The results of the Phase 1 and Phase 2 modeling demonstrate the sensitivity of the corrosion model to certain parameters, especially the near wall flue gas composition, and to the simulated furnace operating conditions. A

question arises as to whether the actual wastage is this sensitive to operating conditions or if what seem to be less variable parameters such as heat flux and deposition rate of unoxidized material should be weighted more heavily in the model.

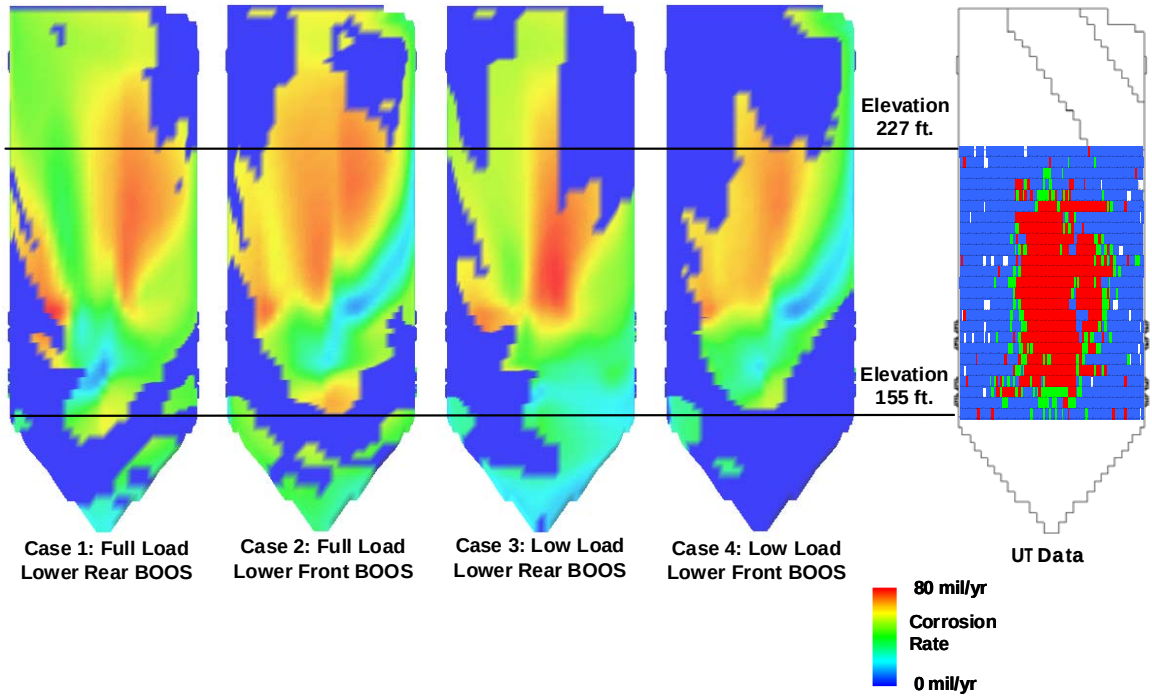


**Figure 4.24. Right side-wall predicted FeS corrosion rate comparison with UT data.**

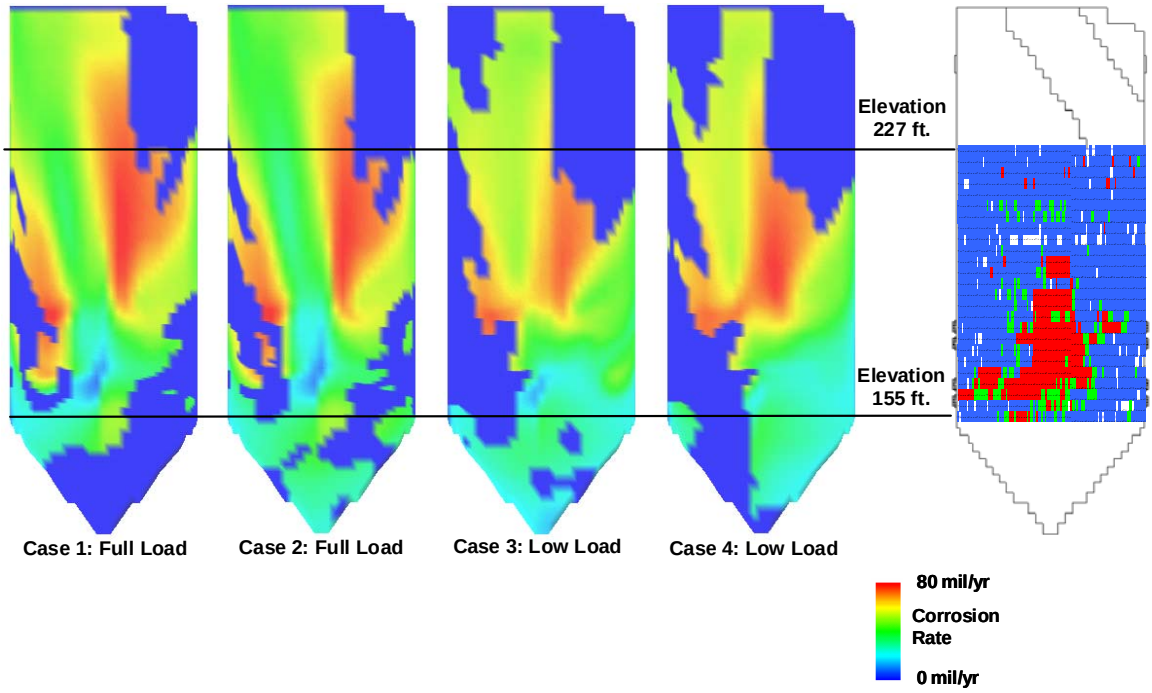


**Figure 4.25. Left side wall predicted FeS corrosion rate comparison with UT data.**

## *4.1.3 Real-Time Corrosion Measurements*

### 4.1.3.1 Electrochemical Approach

Until recently, the use of electrochemical measurements for the determination of corrosion rate was considered unreliable, primarily because the instrumentation used analog signal processing techniques that had long time constants and introduced measurement errors. This meant that although a good qualitative indication of corrosion trend could be monitored, accurate real-time estimates of corrosion rate were difficult or impossible to obtain. However, the introduction of digital signal processing changed the situation dramatically, providing a clean signal response. This development provided the basis for rapid and accurate corrosion rate indications, overcoming the main obstacle to acceptance of the electrochemical technique.

Another issue of contention was the requirement for a conductive medium between the sensor electrodes, as this is needed to fulfill the role of the electrolyte in aqueous corrosion. Some researchers have considered that in order for the probe to work as an electrolytic cell, an ash layer had to be present on the probe face. This is easily achievable in combustion equipment, as has been demonstrated by tests in the lab and in field applications. However, it is possible for the ceramic electrode spacers to achieve the same effect if the material is mildly conductive at the probe operating temperature.

The sensor arrangement of the technology under consideration utilizes non-perturbative measurements to evaluate electrochemical activity associated with corrosion and degradation processes as they occur at the furnace wall. Electrochemical analysis techniques are used to

analyze fluctuations in current and voltage occurring between nominally identical elements as illustrated in Figure 4.26. These fluctuations can be used to characterize the electrochemical condition at a corroding interface. For linear polarization, $\Delta v/\Delta i = R_p$, in a manner similar to Ohm's law, where $\Delta v$ and $\Delta i$ are incremental changes in voltage and current respectively and $R_p$ is a consequent polarization resistance. Similarly, it has been shown that the RMS value of the voltage noise divided by the RMS value of the current noise (defined as the "resistance noise") can be used to determine the rate of a corrosion process, the rate being inversely proportional to the resistance noise magnitude (Eden et al., 1986; Mansfield and Xiao, 1994; Tan et al., 1996).

The fluctuation in the potential signal measured is referred to as electrochemical potential noise (EPN) and the fluctuation in current is defined as electrochemical current noise (ECN). These were used for calculating the noise resistance $(R_n)$. Corrosion current, $I_{Corr}$, is calculated by replacing the polarization resistance $(R_p)$ in the Stern-Geary equation with the noise resistance, $(R_n)$.

$$I_{Corr} = \frac{B}{R_n}$$

where B is the Stern-Geary coefficient. A detailed description of the fundamental principles of electrochemical noise for corrosion measurement can be found in Hladky (patent), Syrett and Cox (1996), and Cottis and Turgoose (1999).

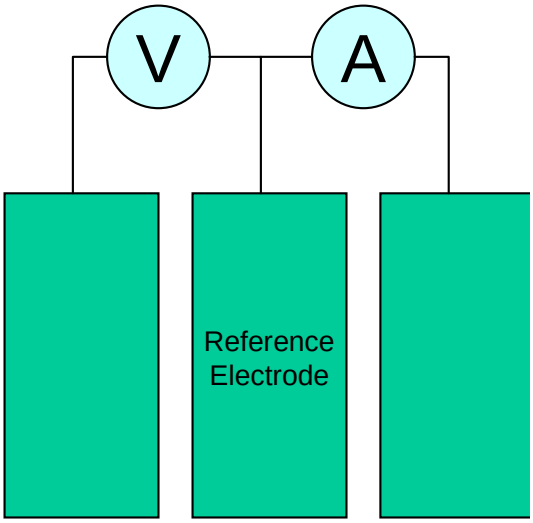


**Figure 4.26. Conceptual diagram illustrating voltage and current noise measurements between "identical" electrodes.**

The corrosion rate is then computed as a product of the corrosion current density and the material constant. The material constant is a term encompassing the atomic mass of the sensor plate material, Faraday's constant, number of electrons produced in the anodic reaction (2 electrons in this case), and the density of the plates.

The following features make electrochemical analysis particularly useful (Syrett and Cox, 1996):

- Current and voltage transients indicative of high corrosion rates are detectable almost instantaneously and, more importantly, well before significant material loss occurs.
- The sensor array is very compact, with the potential to be small enough to insert in the webbing between boiler tubes.
- The nature of these transients provides quantitative and qualitative insight into the rates and mechanisms of the corrosion at the metal surface.

These features make this technology very attractive. As such, further development and testing was carried out to establish its use for application in the demanding environment encountered by the sensors and probe body in, and near, the furnace and the wiring and computer hardware outside the furnace of a coal-fired unit.

#### 4.1.3.2 System Description

The main components needed for the corrosion management system consisted of:

1. Electrochemical-based corrosion probes – probes contained the corrosion sensors, and in certain instances, profilometry plates. The probes were actively air cooled.
2. Temperature controllers – provided control and feedback for probe cooling.
3. Noise modules – processed raw corrosion signals and transferred to data acquisition module.
4. Data acquisition and control module – processed corrosion signals from the noise module, temperature signals from the corrosion probe, and controlled cooling air flow to the probe via the temperature controller.
5. Wireless data transmitter and receivers – provided communication between the remote probe location and the main computer (host PC)
6. Host PC – processed and stored data and provided communication for remote communications.

A schematic of the setup for the on-line measurement of corrosion is shown in Figure 4.27.

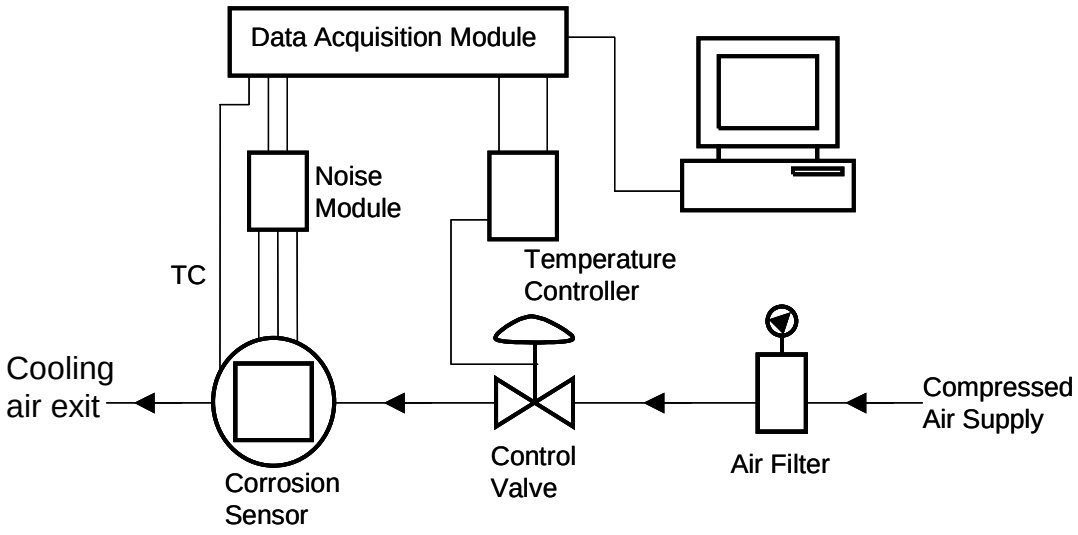


**Figure 4.27. Schematic of the on-line corrosion sensor and auxiliary equipment.**

The sensor electrodes used during the study were made of low-carbon steel having a composition representative of that of boiler tubes. The sensor plates were carefully prepared with an inert border, which served as a reference surface during metrological characterizations. Figure 4.28 shows the inert border in a set of corroded sensor plates. Prior to assembly in the probe, the plates were polished to a mirror finish and the surface roughness was measured using an advanced high-resolution surface profiler. Signal circuitry connected the sensor plates and thermocouple to the noise module and data acquisition module. The probe body housed the circuitry and provided cooling air. Figure 4.29 shows a fully assembled corrosion probe ready for insertion in the boiler. Only selected probes were outfitted with profilometry sensor plates.

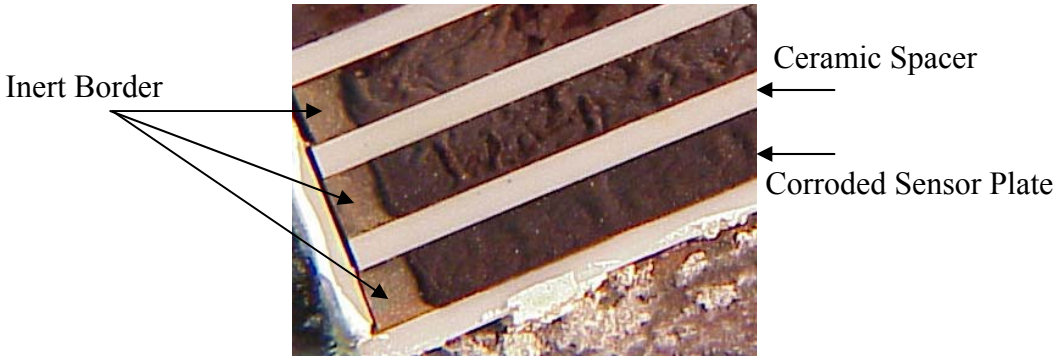


**Figure 4.28. The electrochemical sensor array after a corrosion test showing the inert border.**

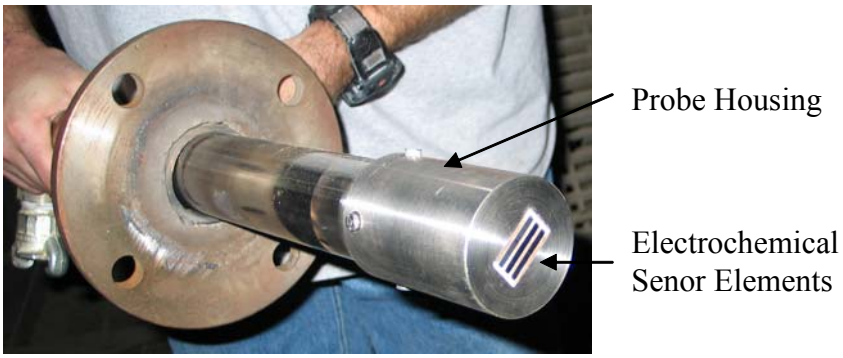


**Figure 4.29. Fully assembled corrosion probe ready for insertion in boiler.**

The data acquisition, noise modules, temperature controllers, and flow controllers were enclosed in rugged dust-free NEMA enclosure cases that were designed for use in the field. A cooling air control valve was used to enable the operating temperature of the sensor elements to be controlled at the same temperature as the adjacent boiler tubes.

The signals from the probe were collected at a specified interval, typically once per second, via the instrumentation. The data analysis software averaged the signals and computed the corrosion rates. Figure 4.30 shows the instrumentation in the Main Probe box. The unit comprised a power supply, signal conditioning modules and a communications interface. Figure 4.31 shows the instrumentation for the remote Probe 5 box.

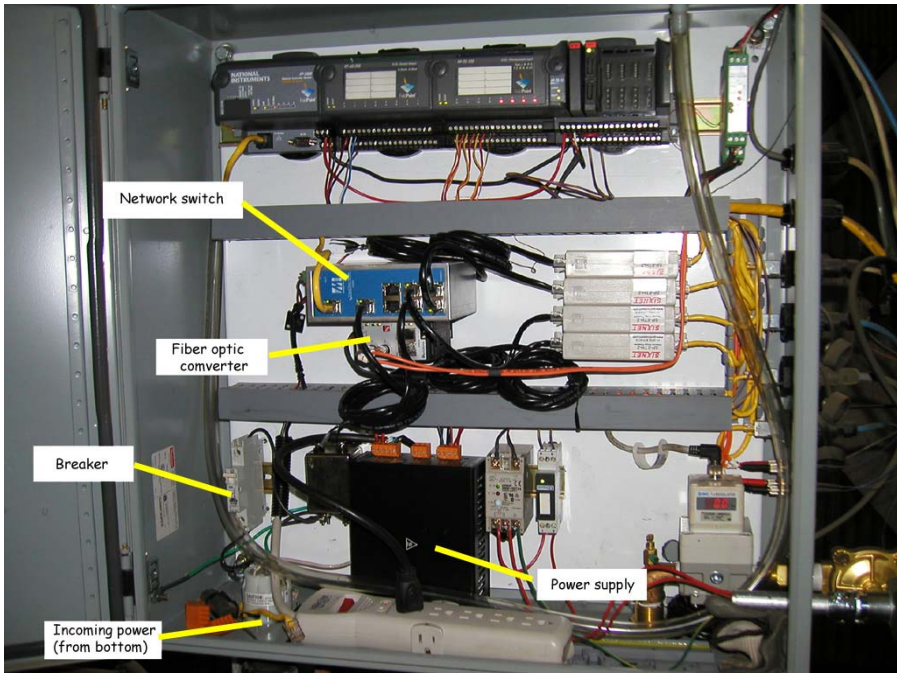


**Figure 4.30. Signal processing and conditioning electronics for Main Probe box.**


**Figure 4.31. Picture of Probe 5 box and instrumentation.**

One of the key technologies implemented and successfully tested during the field test was a robust communications system that combined ethernet, wireless communications, and remote control via a virtual private network (VPN). This allowed remote probes to communicate back to the main computer, which in turn provided data to other plant sites and to REI offices in Salt Lake City, Utah. Figure 4.32 shows a schematic of the communications system.

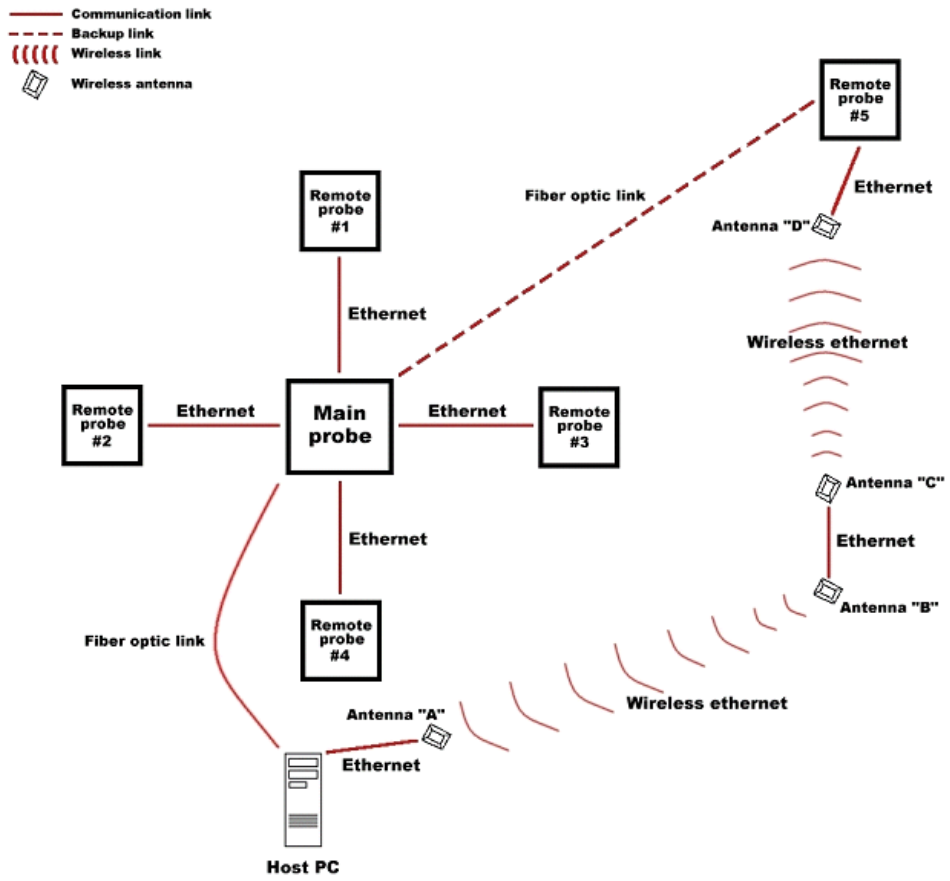


**Figure 4.32. Schematic of the corrosion system communications arrangement.**

Software allowed a display of corrosion rate, probe temperature, and the instantaneous current and potential signals. The data collected could be reviewed on screen, or processed after completion of a corrosion test. In addition, the software had a calendar feature that allowed the user to select previous data by date and time. In this way the user could review past data for any unusual corrosion behavior. Further, once installed, the data also could be viewed from a remote location. During the field test, REI engineers in Salt Lake City were able to access the site computer remotely and transfer data daily. This permitted the engineers to monitor the progress of the field test without having to be physically present at the Gavin Station. Figure 4.33 shows one of the status panels from the software.

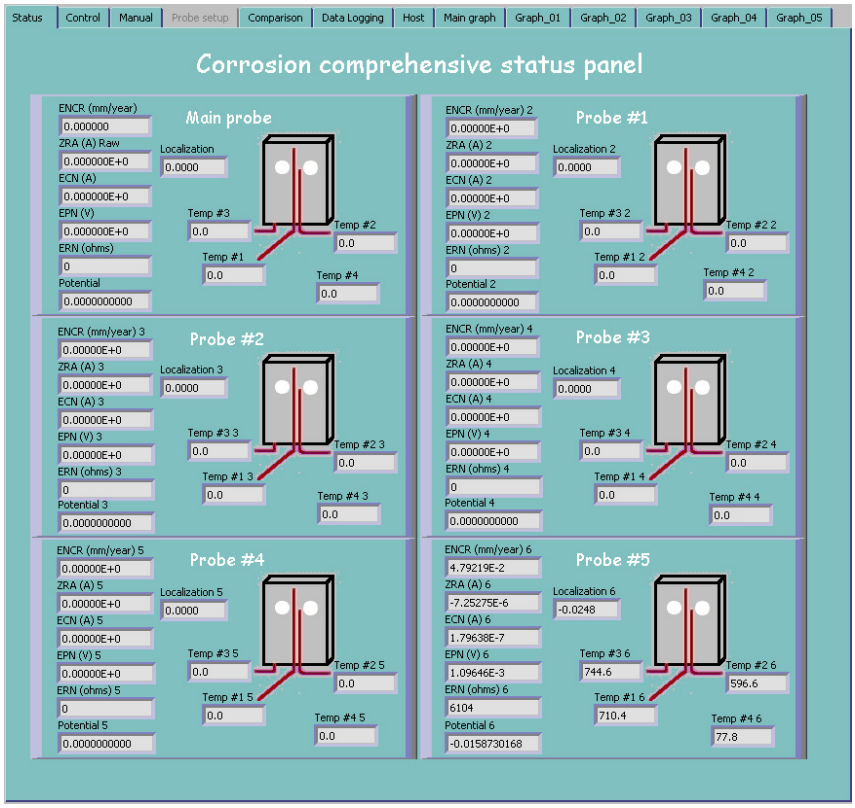


**Figure 4.33. Software display of corrosion system status.**

### 4.1.3.3 System Installation and Operation

The corrosion probes and accompanying instrumentation and computer data collection equipment were first checked out at the University of Utah's 4 MMBtu/hr pilot-scale combustion facility. This facility allowed for a single probe and accompanying electronics to be tested with data measurements being made. It did not permit multiple probes being installed and multiple data being gathered and stored in the computer system. After the system was checked out and each probe tested, all equipment was shipped to Ohio for installation in Gavin Unit 1.

The computer was located in the mechanical drawing room approximately two floors below the main level of probes. The wireless system was used to transmit the data from Probe 5 (center of north side wall) directly to the host pc and to the data control box on the south side of the boiler via a fiber optic cable. There was an additional fiber optic link between the central data collection system and the laptop computer in the mechanical room. The laptop monitored the corrosion rate and associated measurements for all probes. The wireless system worked very well even in the plant environment.

The six probes were located as was shown in Figure 4.34. As was mentioned previously, the intent of locating the probes was to be able to verify that different corrosion rates could be measured at the same time from different probes located in various positions within the

boiler. Waterwall tubes were cut out of the boiler wall and standard 3” openings containing the bent tubes were welded back in their place.

**Error!**

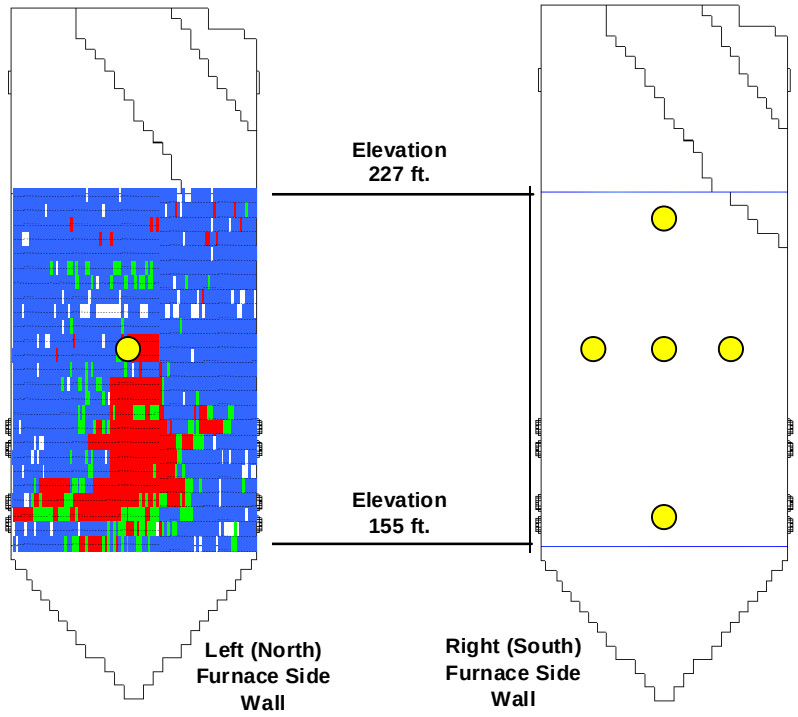


**Figure 4.34. Illustration of six electrochemical corrosion probe locations in Gavin Unit 1.**

Figure 4.35 shows the main probe installed in the boiler. The cutout area next to the electrochemical sensor is the location of some passive probes. Figure 4.36 shows the access port for the electrochemical probe into the boiler and the condition of the sensor after a period of successful operation in the boiler.

**Figure 4.35. Main corrosion probe installed at Gavin Unit 1. Cutout at right was for access to passive probes installed adjacent to electrochemical probe.**

**Figure 4.36. Corrosion probe boiler access port and probe after operation in boiler.**

All corrosion monitoring equipment was sent to Gavin the week of October 20th, 2003 and installation began on the week of October 26th. All probes were installed and initially checked out during that week. While the probes were designed to withstand the harsh environment of the boiler, care was taken to insert them slowly into the boiler. This allowed for the sensor temperature control to maintain safe operating conditions. The procedure took about 30 minutes for each probe.

The current and voltage ranges need to be adjusted after a probe has been in operation about 2-3 hours. This is a manual adjustment and is done so that the software that uses the voltage and amperage readings to calculate the corrosion rates are synchronized. The usual procedure was to make adjustments on each of the probe electronics after a few hours and then re-verify after about one day of operation. Following this verification, no further adjustments are needed with the electronics.

Figure 4.37 shows a timeline when the different corrosion probes were installed in the boiler and data were being collected. Also shown in Figure 4.37 is the corresponding times when the EPRI passive probes were installed.

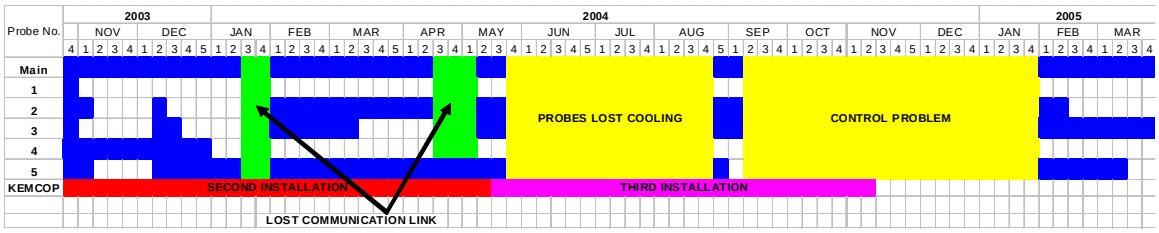


**Figure 4.37. Timeline showing weeks various corrosion probes were in service.**

There are several items of note in Figure 4.37. First, there were two episodes when the probes were severely damaged. This damage essentially ruptured the probe heads and destroyed the sensor elements. Both of these occurred just following an unscheduled outage; the first occurred the third week of May 2004 and the second occurred the last week of August 2004. Following these probe failures, all probe sensors and heads needed to be

rebuilt. After the second occurrence, the probe heads were reinforced and considerable time was spent fine-tuning the temperature control for the probes. The reinstallation of the four probes in February 2005 demonstrated the success of these modifications. No damage was noted to any of the probes and temperature control was maintained on all probes.

In addition to the probe failures, there were two times when communication between the data collection electronics and the data recording computer was lost. These are noted in January 2004 and April/May 2004. Note that the wireless system, used on Probe 5, did not lose communication during the April/May failure. These problems were easily fixed once we were able to go on-site and discover the problem. After the second communication problem, plant operators were trained on how to recognize a problem and make the necessary adjustments. The adjustments were quickly and easily accomplished.

Unfortunately, Probe 1 was only in service the initial week for a couple of days. There were problems from the outset with this probe and it was decided to abandon future attempts to replace it. The electronics for Probe 1 were then used as spares for the other Probes. Electronic failures occurred during various times on the different probes that resulted in no data being collected. In addition, it was difficult to get at Probes 1 and 4; therefore they were not always replaced.

Clearly Figure 4.37 shows that the program objective was met in having multiple probes installed in the unit collecting data for 6 months. In fact, the main probe collected data for about 8½ months, Probe 5 about 7 months, Probes 2 and 3 about 5 months and Probe 4 about 2 months. The final installation (February and March 2005) had very few problems with three of the four installed probes.

#### 4.1.3.4 Operational Challenges

This program provided several opportunities for improvement to the corrosion management system over the system used in the previous two boiler installations. By the completion of the program, it was felt that the operational challenges had been sufficiently addressed and significant progress made. Many of these challenges and the methods used to overcome the issue will be discussed.

##### 4.1.3.4.1 Thermal Fatigue/Probe Failure

At both previous plant installations, no probe had ever failed due to thermal fatigue. This occurred twice at Gavin (see Figure 4.38). To remedy this situation, instrument air must be used to cool the probe head and sensor. Plant air, even passing through filters, contained too much liquid and oils that could possibly flash to steam if temperature control was interrupted or marginal and rupture the probe head. In addition, the probe heads were redesigned to be more robust to reduce warpage and eventual failure.

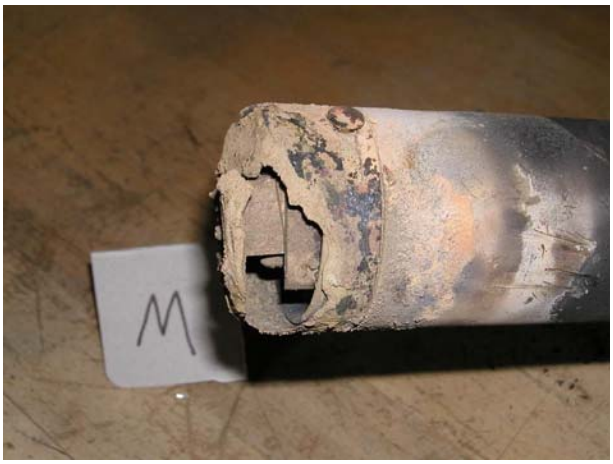


**Figure 4.38. Damaged Main Probe illustrating failure due to thermal fatigue.**

Other changes incorporated to prevent probe failures included the use of a bypass on the cooling air line to permit better control of the probe sensor temperature. This upgrade resulted in very good temperature control on all probes.

#### 4.1.3.4.2 Probe Hardware and Electronics

Several improvements were made to the probe temperature control system and electronics. The air bypass has already been mentioned, but solenoids were also installed to shut off the air completely when the probe face was relatively cool. This occurred when slag had built up on the probe face, insulating the probe from the radiant heat flux of the flame. It was found that certain electronic pieces were more critical than others; as a result a better idea of spare parts was determined.

While most of these challenges were not encountered in the previous two boiler installations, they did occur at the Gavin site. This provided the team the opportunity to improve on the original corrosion probe assembly as well as the control methodology. As a result, the instrumentation was considerably more robust and reliable at program end than when originally installed.

#### 4.1.3.4.3 Plant Personnel Training

After the initial installation of the corrosion probes, there were only a few items that needed an on-site engineer to monitor. It was important that the plant buy into the support of the corrosion management system so that the probes and measurement system could be checked on a regular basis. The responsibilities of this on-site engineer included:

1. Be available for telephone calls or emails as necessary
2. Daily walk-down past each corrosion probe
    a. Verify air flow
    b. Verify probe depth
    c. Verify filter not full
3. Push/pull probes in/out according to temperature data (as needed)
4. Control box electronics check (as needed)
    a. Shutdown procedure
    b. Startup procedure
    c. Fieldpoint status checks

   d. Network status checks (*Main probe box only*)
   e. General checks
5. Emergency Shutdown
   a. Pull probes out of furnace, leave air on
   b. Pull electrical plug to each control box

Under normal operation, these responsibilities require about 1-2 hours per week. However, they are critical in that many of the multi-day outages could have been prevented had plant personnel been properly trained.

Plant personnel were also very critical in obtaining boiler operating data for comparison with the measured corrosion rates. The requested operating data from the DCS system was regularly received; however, other data such as burners-out-of-service, air/fuel biasing, sootblowing, coal feed changes, etc. were more difficult to come by.

#### 4.1.3.5 Plant and Corrosion Data

Considerable amounts of data were collected over the period of this program. Therefore, a general overview of all plant and corrosion data will be given and then specific examples showing the utility and the effectiveness of the corrosion management system will be shown.

##### 4.1.3.5.1 Gavin Plant Data

Selected information from the plant DCS system were requested and received. These included, among other items, date, time, net load, gross load, steam flow, steam temperature, excess air, and emissions. Figures 4.39 through 4.41 show the hourly average net load (MW) and the excess air (%) for the years 2003, 2004 and first quarter of 2005 for Gavin Unit 1. These data show that the boiler operates a significant portion of the time at full load (1300 MW) with between 25% and 30% excess air (3.5-4.5% $O_2$). The next most prevalent operating condition was perhaps 1000 MW (net) load.

In addition to the DCS data received, some information regarding burner settings and conditions were provided. For example, Figure 4.42 denotes the burners-out-of-service in mid-2004 (which differed from 2003) whereas Figure 4.43 shows those burners out-of-service at the end of the project. Some changes were also noted between the mid-2004 burner shroud settings and the settings provided at the end of the project (April 1, 2005). These changes can have a significant effect on corrosion rates at various locations in the boiler and illustrate the variability in boiler operation over time. On-line monitoring of corrosion rates can provide a better correlation with operating conditions than can a coupon-type averaged measurement.

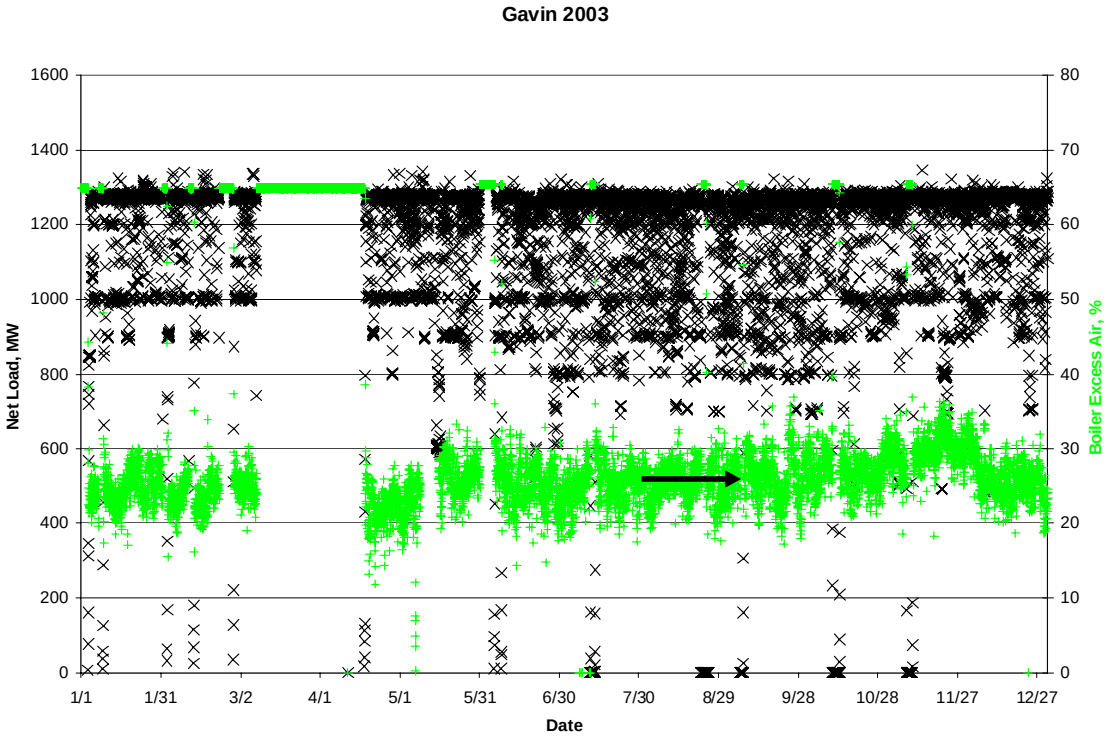


**Figure 4.39. Gavin operating data – 2003.**

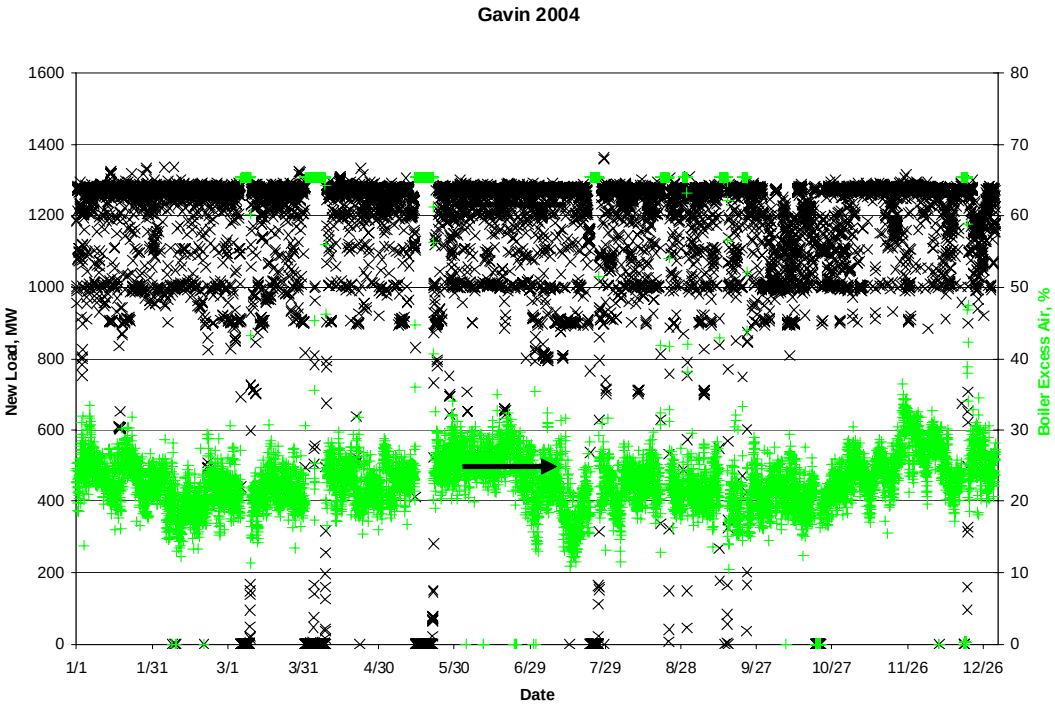


**Figure 4.40. Gavin operating data – 2004.**

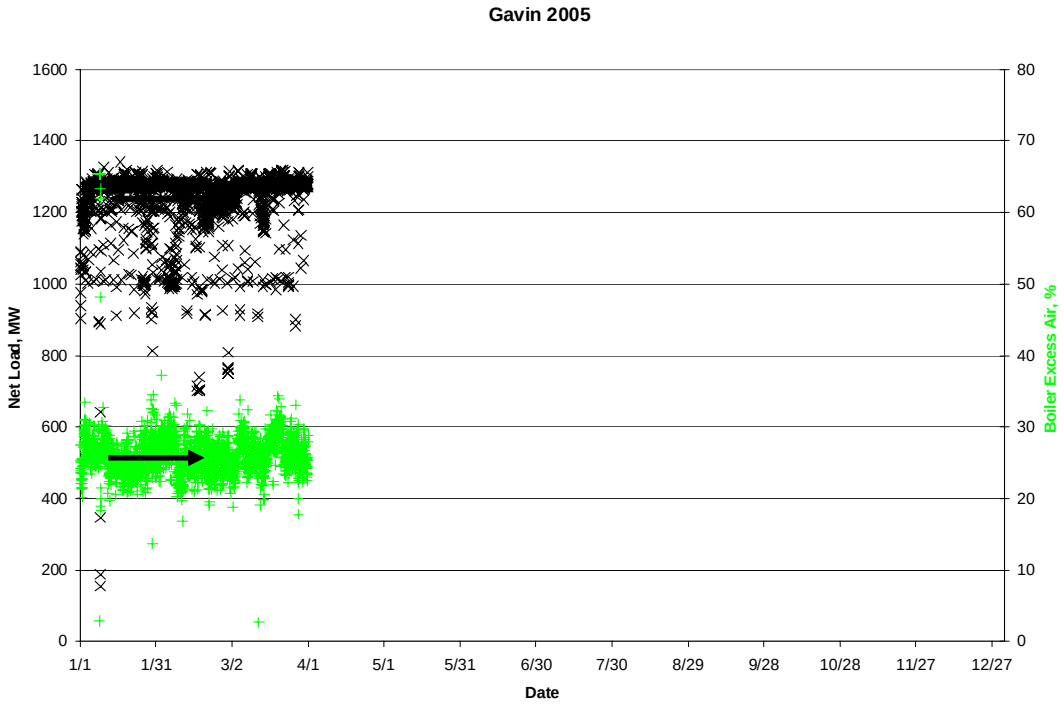


**Figure 4.41. Gavin operating data – 2005.**

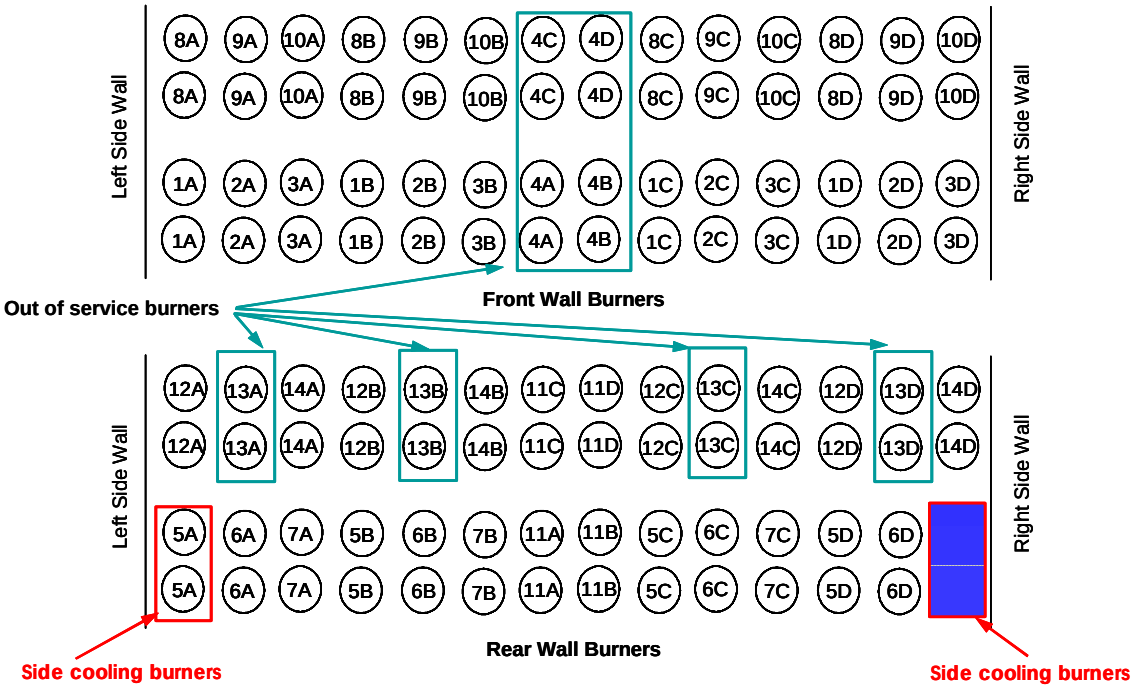


**Figure 4.42. Burner conditions in 2004.**

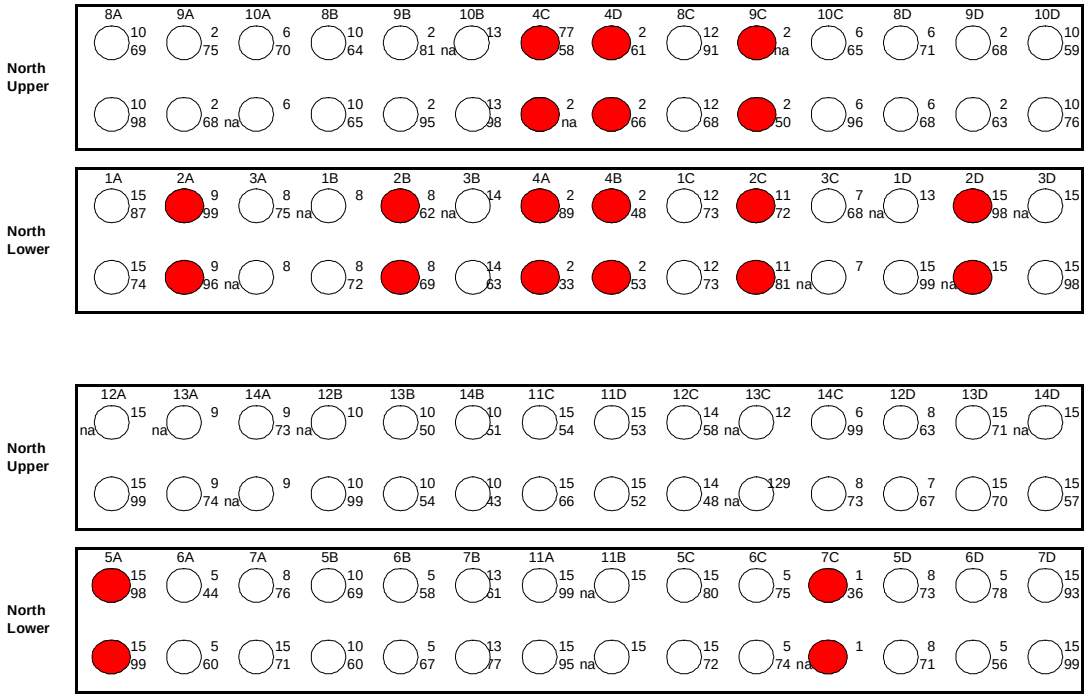


**Figure 4.43. Burner conditions in 2005.**

#### 4.1.3.5.2 Corrosion Data

The focus of the program was to demonstrate the utility of real-time corrosion measurements. Throughout the project, real-time has been defined as about 8 hours. This refers to the amount of time a pseudo-steady state boiler condition can be reached after a change in operating conditions. This time period allows the surfaces (waterwall tubes and deposits) to reach some reasonably steady condition. The actual corrosion sensor can track nearly instantaneous changes in local corrosion rates, but correlation of rates with operating conditions requires the system to reach a steady-state condition.

Currently there are not methods to reliably measure corrosion rates in short periods of time. Therefore, the data from this program have been reduced and analyzed to show that corrosion trends can be developed and that changes in boiler operation can affect corrosion rates. The overall corrosion data will be first discussed; these data will be followed by selected examples of how the corrosion data can be correlated with various parameters.

Figures 4.44 through 4.48 are hourly rolling average corrosion rates (mils/yr) for the five probes throughout the entire program (October 2003 to April 2005). Because of the frequency of the individual data collection (approximately every second), when the overall data are plotted with a rolling hourly average, it appears to just show spikes. However, as will be shown in subsequent sections, if plotted over shorter time periods, the data show distinct corrosion trends.

These data plots were drawn using a logarithmic scale just to show the range of corrosion values measured. As an example, the main probe corrosion rate (located in the center of the south side wall) after about February 2004 was less than 1 mil/yr. However, in the end of 2003, some high corrosion rates were measured, approaching 100 mils/yr and averaging about 40 mils/yr for the two month period.

Obviously if rates that high continued for a long period of time, tube life would be greatly reduced. Comparing these corrosion data sets (November-December 2003 and February-May 2004) with the boiler load and excess air data during the same periods, no clear correlation is evident. Therefore, it is thought that other operational changes such as burners, biasing, fuel quality, etc. may account for the differences.

Comparing the measured corrosion rates from Probes 2-5 with the main probe shows that most of the time, the main probe has the highest corrosion rate and that the other probes are about one order of magnitude less. This observation agrees with the original corrosion maps received from AEP based on ultrasonic thickness measurements.

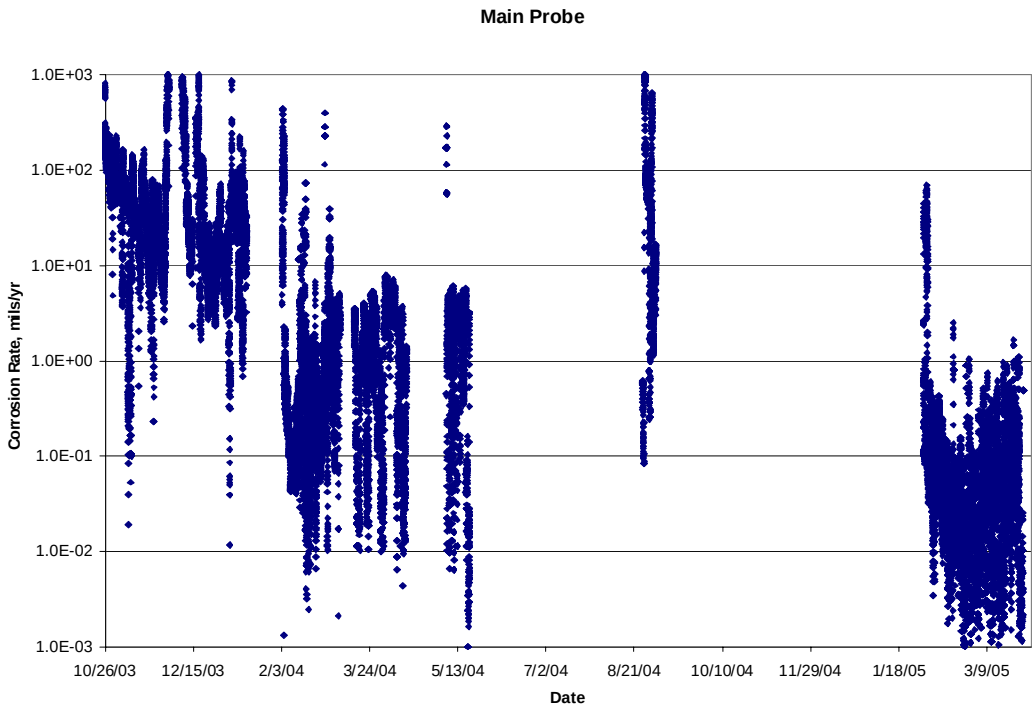


**Figure 4.44. Main probe corrosion data – entire test program.**

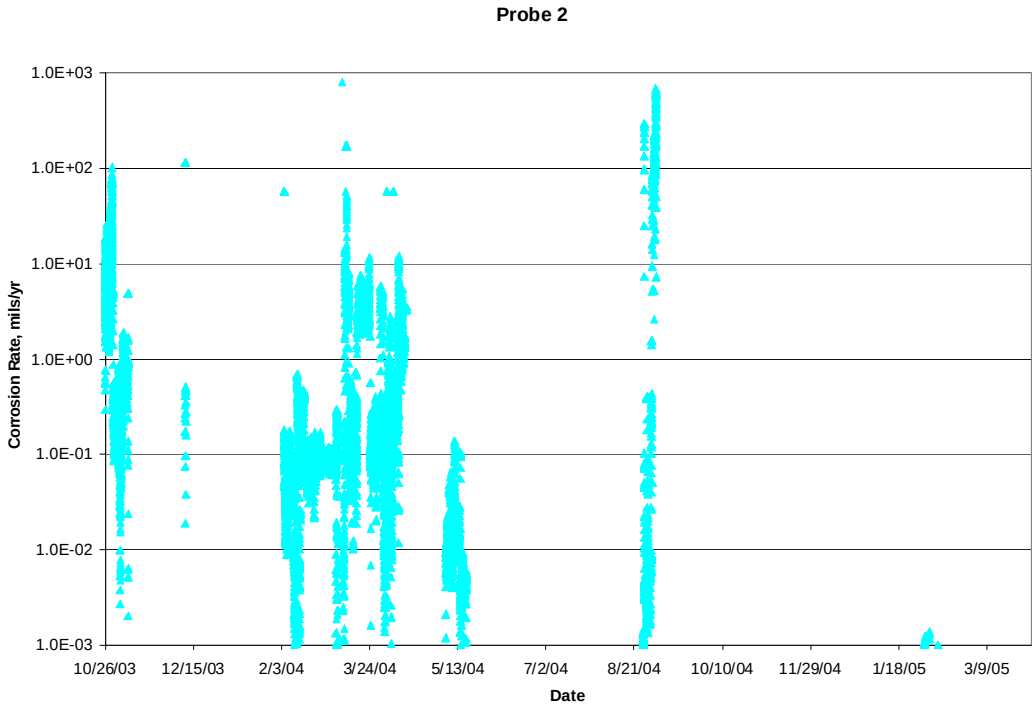


**Figure 4.45. Probe 2 corrosion data – entire test program.**

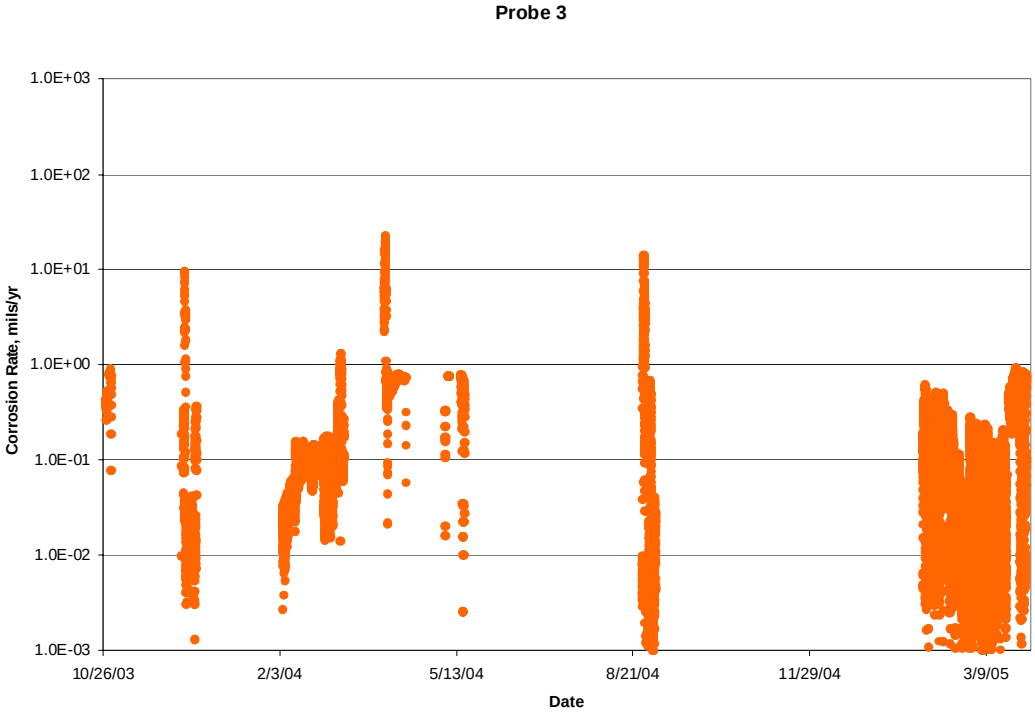


**Figure 4.46. Probe 3 corrosion data – entire test program.**

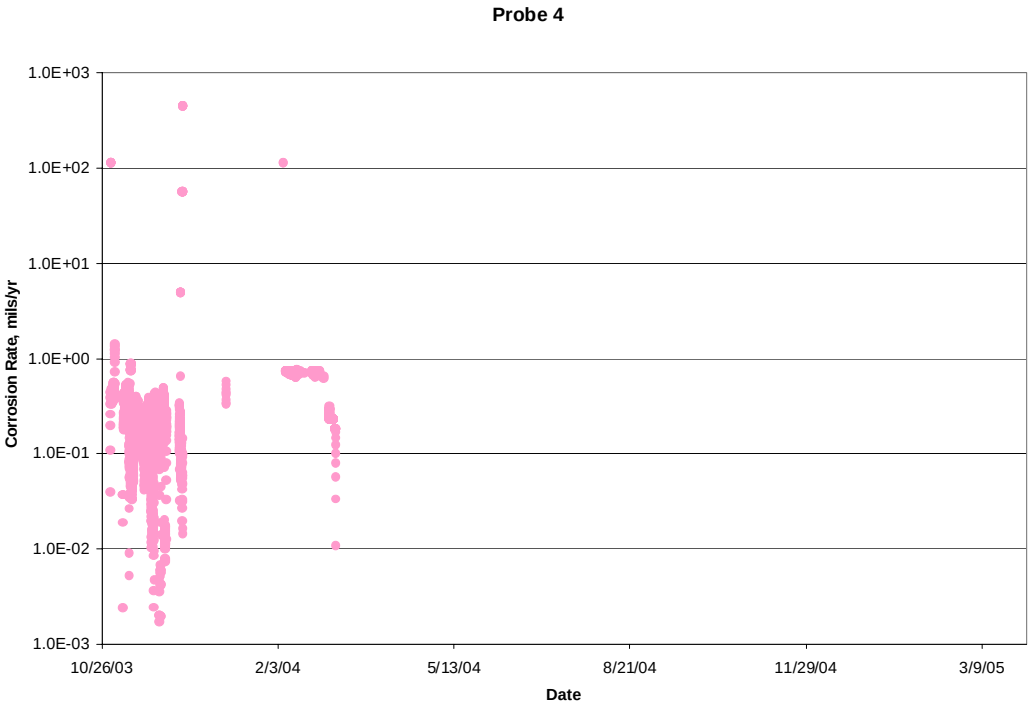


**Figure 4.47. Probe 4 corrosion data – entire test program.**

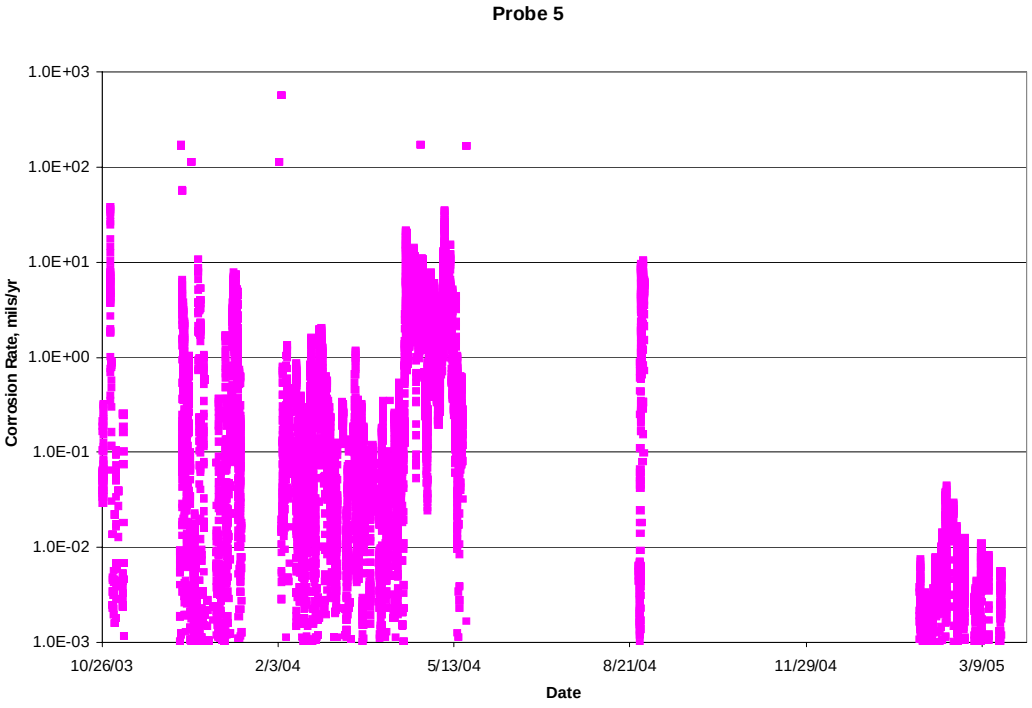


**Figure 4.48. Probe 5 corrosion data – entire program.**

### *4.1.4 Static Corrosion Measurements*

#### 4.1.4.1 Profilometry Background and Approach

The amount of material removed by corrosion during a brief test was extremely small. Conventional efforts using corrosion coupons require periods of months or longer for accurate determinations of a corrosion rate. To allow comparisons to be made over a brief period of time in order to avoid large fluctuations in operating conditions and fuel properties, a novel technique was developed that relies on a small section of corrosion resistant alloy to define an uncorroded surface, a modified high resolution profilometer for surface characterization, and software tailored to determine the volume of material removed relative to the original surface of the sensor face. The details of this procedure are as follows:

- Corner sections of the short edges of the sensor elements were machined away and a corrosion-resistant alloy tailored to the conditions to be experienced under fuel-rich deposits at Gavin were welded in their place.
- The sensor element face was polished and inserted into a corrosion probe for a test of less than 48 hours. The probe was placed in service during relatively stable operation. After removal the sensor elements were removed and returned to REI.
- The electrodes were cleaned with a soft brush to remove loose solids from the surface, and then immersed in Clarke's solution, according to ASTM G1-81 7.7.2 to remove residual corrosion products.
- The surface was then mounted in a modified stage that was prepared specifically for this application allowing for the tall, thin specimen. A KLA Tencor P-10 surface profiler with a range of 327 μm and a resolution of 0.1953 Å was then used to trace the surface of the element in 20-micron steps such that the height at each step could be recorded. Figures 4.49 and 4.50 show typical results from a profilometer scan of the sensor element surface exposed to a corrosive environment.
- Software was written to use the data in the form provided by the KLA-Tencor equipment and to (1) identify the portion of the surface composed of the corrosion resistant alloy, (2) correct the data for any remaining ash or contaminants, (3) determine a "best-fit" plane through these data, (4) determine the average depth of material removed from the sensor element relative to the "best-fit" plane defined by the corrosion resistant section, and (5) illustrate the location of the corrosion resistant border and relative dimensions of the sensor element face.

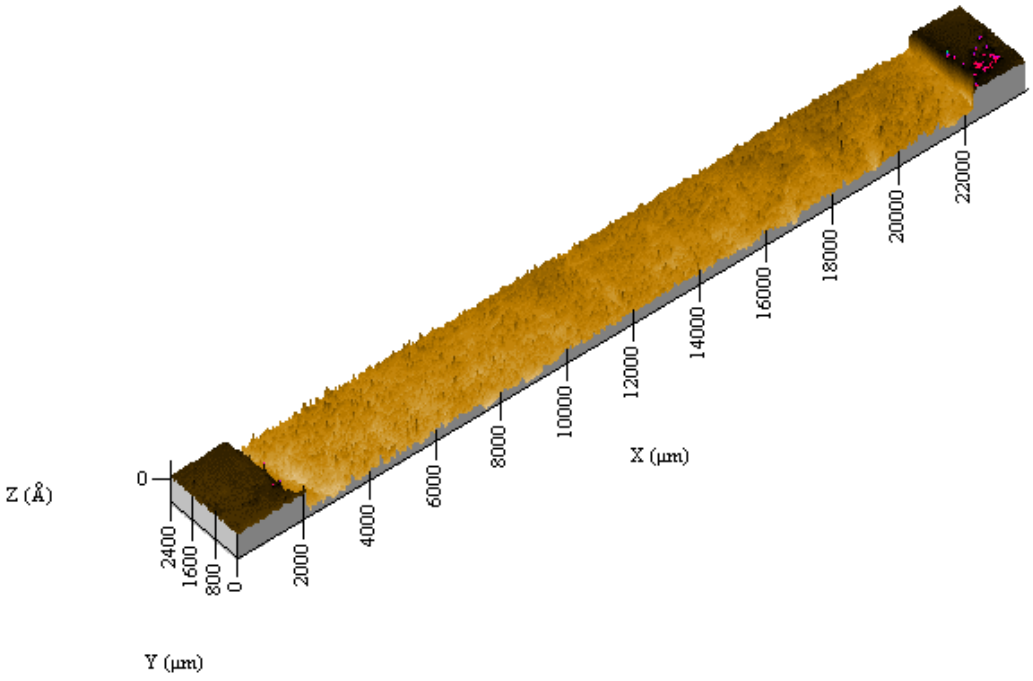


**Figure 4.49. Surface profile of a corroded electrode face showing the inert border at the left and right hand side edges.**

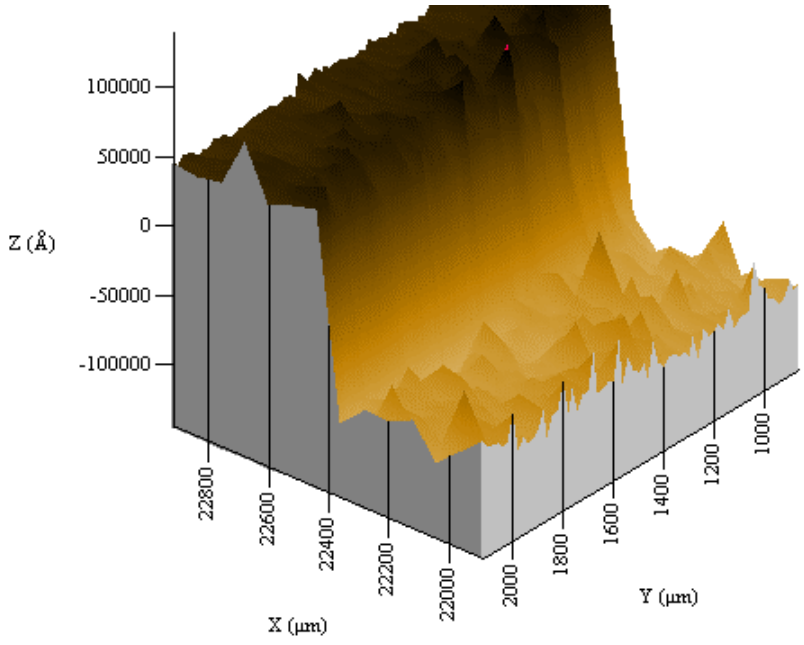


**Figure 4.50. A close-up of the inert border/carbon steel interface. The inert border is the raised part on the left hand side of the image.**

### 4.1.4.2 Profilometry Data

The approach described above was used prior to final removal of the probes from the boiler during a three day period in late March 2005. The two probes selected for profilometry were the "main" (the center of the most corrosive region on the south wall) and "#1" (directly above main in an area at the edge of the high corrosion region). The two original probes at these locations were removed on March 29, 2005 and the sensor elements were replaced with the modified elements. The two modified probes were left in place for a period of 44 hours, the sensors were removed and the elements were returned to Utah for precision metrology using the approach described above.

Each of the two probes contains three sensor elements that were exposed to nominally identical conditions. All six elements were analyzed and the data reduced. Figures 4.51 and 4.52 illustrate the profiles resulting from these tests at the two locations:

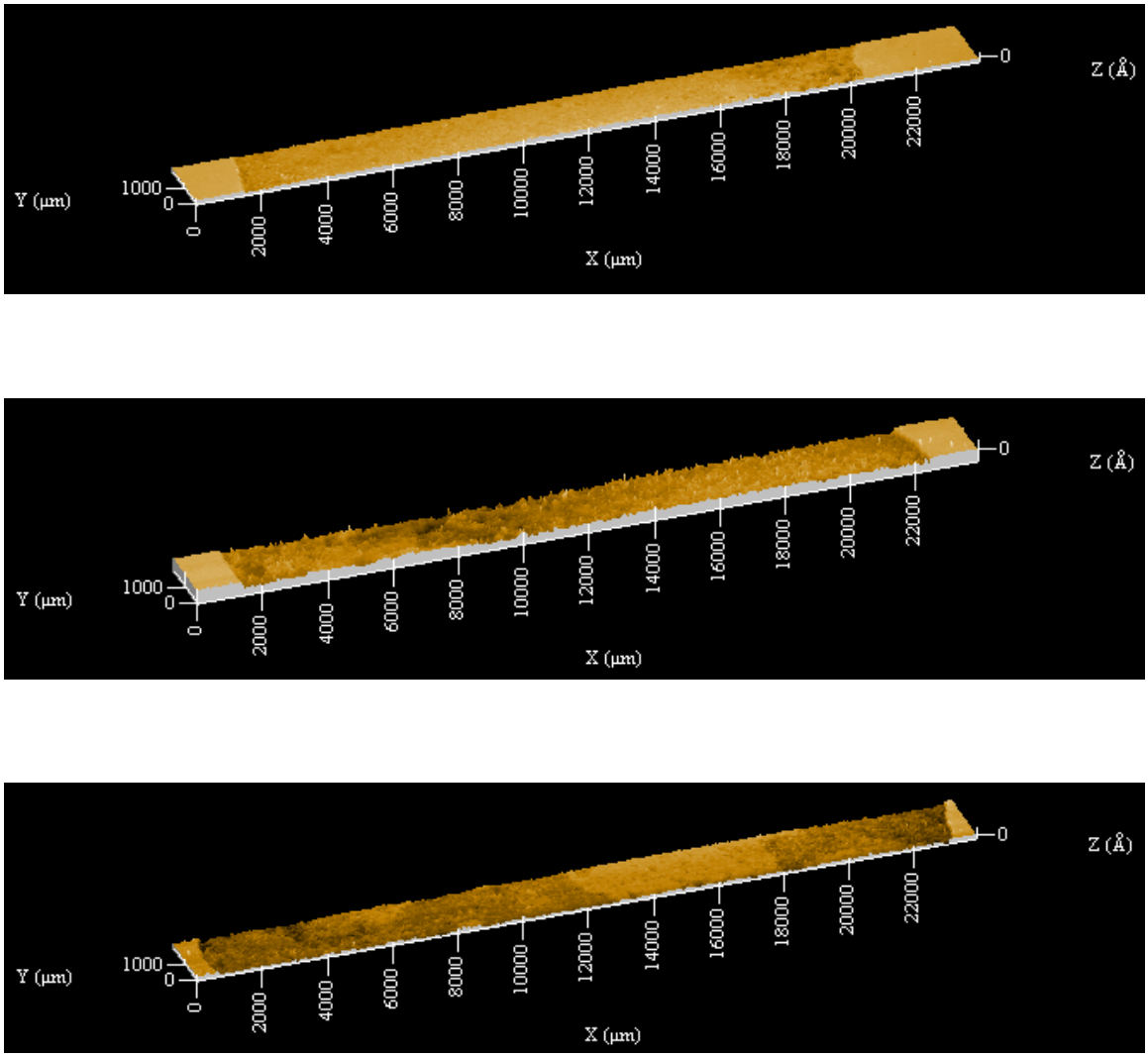


**Figure 4.51. The profilometry results from the three sensor elements in the probe at the "main" location.**

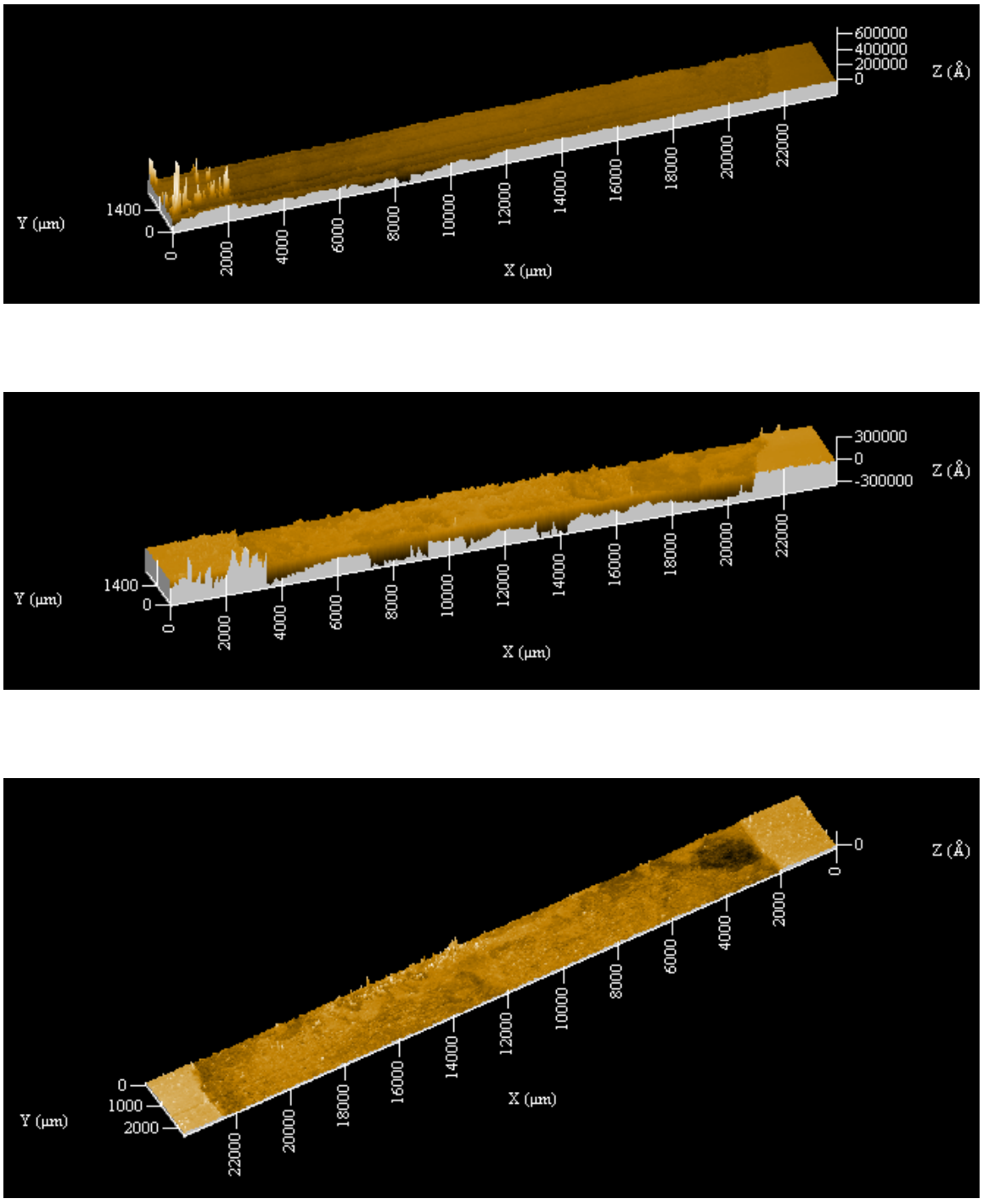


**Figure 4.52. The profilometry results from the three sensor elements in the probe at the "one" location.**

The mounting of the samples in the profilometer is challenging and can introduce rotation about three axes. It is important to correct for this by processing the data to determine a corrected depth of corrosion. In addition, correction for sample contamination primarily related to ash deposition can significantly improve the quality of the result. For example, the first two images in Figure 52 show substantial deposit formation on the corrosion resistant border. This can be recognized as spurious in comparison to the relatively flat sections.

The average depths determined using this analysis are indicated in Table 4.7.

**Table 4.7. Results of profilometry.**

| Location | Element | Average Depth (microns) |
|---|---|---|
| **Main** | **#1** | **1.10** |
| | **#2** | **2.71** |
| | **#3** | **2.17** |
| **One** | **#1** | **1.78** |
| | **#2** | **4.07** |
| | **#3** | **2.22** |

Upon further evaluation it is clear that the data from two of these samples are not representative of the corrosion occurring at these locations. The bulk of the surface height data in the center region of Main #1 is actually above the uncorroded regions at the edges. It appears that a deposit buildup occurred in this region that was not dissolved by the Clarke's solution. Similarly, sample One #2 has an edge region with so much ash that the analysis can not effectively remove this region from the base plane determination. Eliminating these two points, the following corrosion rates were indicated from the four reliable samples.

**Location Main Corrosion Rate = 19±2 mils/yr**

**Location One Corrosion Rate = 16±2 mils/yr**

#### 4.1.4.3 Passive Probe Background and Installation

The passive corrosion probe and fouling monitoring system consists of small probes, which are mounted in the web between the tubes of the membrane walls. The probe is able to monitor the actual local corrosive conditions in a boiler of a coal-fired plant or a waste incineration plant. It is constructed in such a way that it can be exchanged during operation of the boiler. The probe is small enough (.32" [8 mm]) to be installed in the web between tubes (see Figure 4.53). The probes are removable during boiler operation and are claimed to measure losses greater than 0.5 mil (12 micron). Analysis of scales and deposits left on the surface of the probe upon removal can be made to determine corrosion mechanisms. Over 300 probes installed in boilers in Netherlands and over 50 probes have been installed in the US in recent years.

In order to measure corrosion rates of T-11 tube steel, 625 alloy and 622 alloy overlay, one column with four passive corrosion probes was installed in adjacent tubes next to the REI electrochemical probe locations as illustrated in Figure 4.54.

**Figure 4.53. Passive Corrosion Probe prior to installation.**

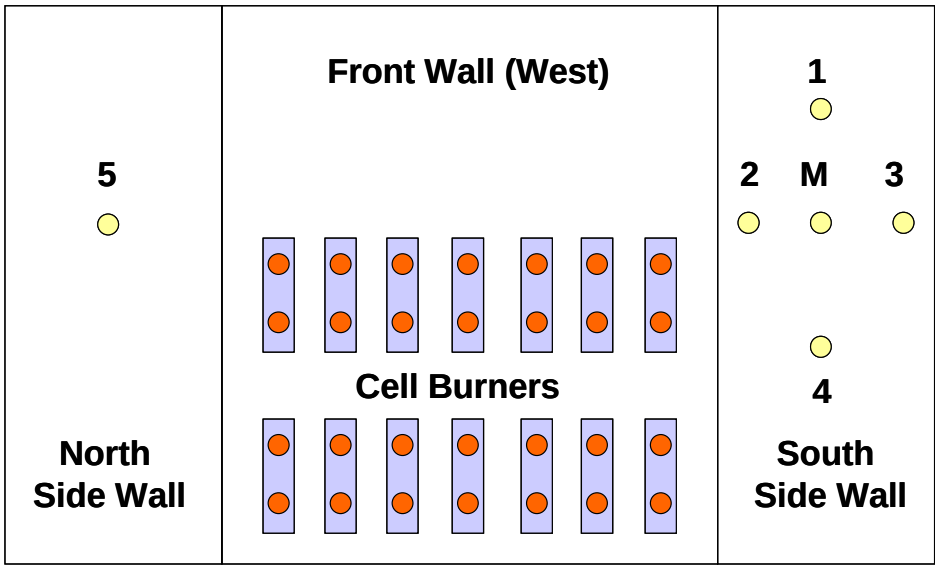


**Figure 4.54. REI electrochemical probe and EPRI passive probe installation locations.**

Installation of the probes required the following steps:

- AEP provided suitable access to the waterwall locations selected.
- Removal of the insulation on three locations by AEP personnel.
- Drilling holes in the web strips using a 6.8 mm drill. The holes were drilled by maintenance contractors of AEP.
- Tapping screw thread in the holes by using a size M8-machine tap. The holes were tapped by contractors of AEP.
- After tapping the holes, the probes were inserted by KEMA and EPRI engineers.
- After the insertion of the probes removable wire meshed insulation mats were installed to close the probe location and retain radiant heat.

A total of 24 holes were made to place the probes in the webbing of tubes near the REI's electrochemical probes installation. The probes were installed in three to four tubes over to the right or left from the center line of the 2" wall box opening installed for the REI electrochemical probe. At each location, four probes were vertically installed in the webbing about a foot apart, with protrusion lengths ranging from 0.5 to 3 mm. Alloy 622/625 coupons were installed with 1.0 mm protrusion length followed by T-11s installed at 3.0 mm, 1.5 mm and 0.5 mm accordingly as seen in Figure 4.55.

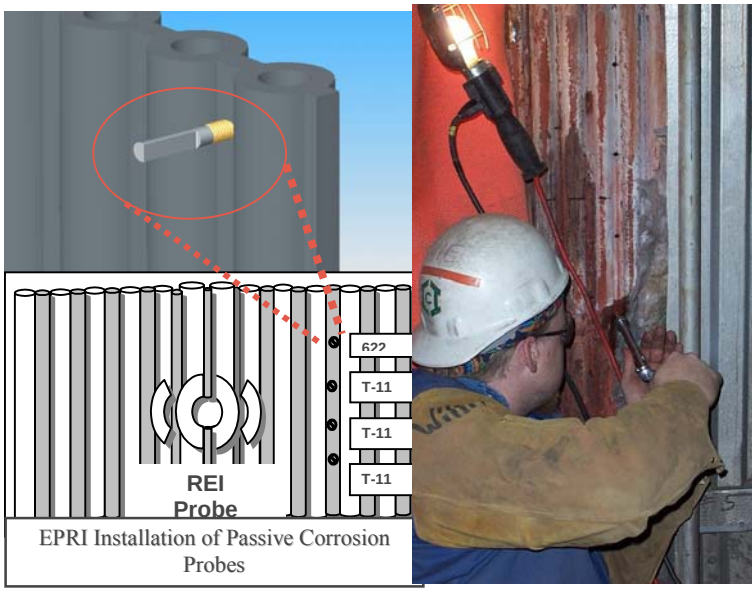


**Figure 4.55. Installation of the four passive corrosion probes.**

A total of 18 T-11 and 6 alloy 625 probes were inserted at the locations described above during the first exposure period extending from April 11th 2003 to October 23rd 2003. The first set of probes was then removed and packaged for analysis, followed by spot temperature measurements and web thickness measurements taken to calibrate the second set of probe insertion lengths.

The second set of probes were prepared on site and installed while the boiler was in operation. A total of 17 T-11 and 6 alloy 622 probes were installed at the six locations during the second exposure period from October 23rd 2003 through May 19th 2004. Due to a broken tap on elevation 155' probe location Y prior to the second installation, no probe was placed in the location in the subsequent installations.

The third set of probes were installed on May 20th and were removed on November 11th 2004; dummy alloy 625 probes were then installed flush with the wall to close up the holes and conclude the tests.

#### 4.1.4.4 Passive Probe Corrosion Data

After removal of the probes from the furnace, the following information was obtained:

- Change in probe length by thickness measurement
- Corrosion rates
- Deposit analysis
- Hardness test for alloys 622/625

From the change in probe length the corrosion rate can be calculated, through dividing the loss observed by the exposure time. However, since the wastage is small in comparison with the total probe length, the residual length measurement has to be very precise. For instance, if the corrosion rate is 84 mils/year (2.1 mm/year), the loss after a 3-month exposure is 0.7 mm (28 mils). Since the probe length is about 48 mm (1.92 inch) the loss expected for a relatively high corrosion rate is only 1.45% of the probe's length. For low corrosion rates <20 mils/year (0.5 mm/year), the expected loss will be much less than 1% of the original length. Therefore, this method has been used for all thickness measurements.

During the first installation different insertion lengths were tested, and probes with the insertion length of 3 mm showed significant corrosion rates but lower than those measured by NDE methods prior to the installation of the alloy 622 weld overlay. A typical probe after service is illustrated in Figure 4.56.

**Figure 4.56. Passive probe after service.**

#### 4.1.4.4.1 Passive Probe Corrosion Results

The second installation was during the operating period from October 2003 to May 2004. Corrosion rates of the 2nd set were in good agreement with the UT data as seen in Table 4.8.

**Table 4.8. Passive Probe Corrosion Data.**

| REI Ref | Location | ID | Material | Insertion Length (mm) | 1st Set (Apr 03-Oct 03) (mils/yr) | (oper hrs ) | 2nd set (Oct 03-May 04) (mils/yr) | (oper hrs ) | 3rd set (May04-Nov04) (mils/yr) | (oper hrs ) | Avg. Wastage (mils/yr) | Tube Remaining Thickness (inch) |
|---|---|---|---|---|---|---|---|---|---|---|---|---|
| 5 | E 189 NW | A | Inc 622/625 | 1 | 3.19 | 4181 | 0.48 | 4693 | 2.24 | 3813 | 1.97 | 0.245 |
| | | B | T-11 | 3 | 11.53 | | 32.27 | | 24.42 | | 22.74 | |
| | | C | T-11 | 1.5 | - | | 16.77 | | 11.56 | | 14.16 | |
| | | D | T-11 | 0.5 | 13.08 | | 12.78 | | 27.77 | | 17.88 | 0.117 |
| 2 | E189 SW Tubes 85-86 | E | Inc 622/625 | 1 | 3.44 | | - | | 1.75 | | 2.60 | 0.215 |
| | | F | T-11 | 3 | 0.10 | | - | | 42.60 | | 21.35 | |
| | | G | T-11 | 1.5 | 5.35 | | 8.94 | | 15.49 | | 9.93 | |
| | | H | T-11 | 0.5 | 4.11 | | 2.27 | | 12.16 | | 6.18 | 0.214 |
| M | E189 SW Tubes 152-152 | I | Inc 622/625 | 1 | 4.70 | | 0.55 | | 11.59 | | 5.61 | 0.137 |
| | | J | T-11 | 3 | 28.21 | | 56.56 | | - | | 42.39 | |
| | | K | T-11 | 1.5 | 8.56 | | 28.40 | | 19.61 | | 18.86 | |
| | | L | T-11 | 0.5 | 4.70 | | 17.03 | | - | | 10.86 | 0.148 |
| 3 | E189 SW Tubes 220-221 | M | Inc 622/625 | 1 | 6.92 | | 37.05 | | 6.36 | | 16.78 | 0.156 |
| | | N | T-11 | 3 | 27.37 | | 109.64 | | 53.74 | | 63.58 | |
| | | O | T-11 | 1.5 | 1.22 | | 12.23 | | 5.03 | | 6.16 | |
| | | P | T-11 | 0.5 | 6.34 | | 87.77 | | 57.11 | | 50.40 | 0.161 |
| 1 | E214 SW | Q | Inc 622/625 | 1 | 4.16 | | 1.98 | | 5.27 | | 3.80 | 0.181 |
| | | R | T-11 | 3 | 1.89 | | 7.50 | | 28.50 | | 12.63 | |
| | | S | T-11 | 1.5 | 0.17 | | 7.17 | | 41.86 | | 16.40 | |
| | | T | T-11 | 0.5 | 2.94 | | 1.04 | | 1.82 | | 1.93 | 0.131 |
| 4 | E155 SW | U | Inc 622/625 | 1 | 4.20 | | 2.84 | | 5.68 | | 4.24 | 0.211 |
| | | V | T-11 | 3 | 10.78 | | 47.18 | | 21.23 | | 26.40 | |
| | | W | T-11 | | 1.01 | | 42.94 | | 12.38 | | 18.78 | |
| | | Y | T-11 | | 7.55 | | -- | | -- | | 7.55 | |

* Warped probes
** Broken Tap

The data presented in Table 4.8 also point to a shift in corrosion rates, indicating some operational changes occurred during that period. Much higher rates were measured at location 3 than previously. It was confirmed with plant personnel that a nearby burner which was originally providing air to the side wall during the first probe installation period was put in service during the second installation of the probes, this may have increased reducing conditions and deposition on the wall around location 3.

The Final probe set yielded corrosion rates intermediate between the first period and second set thus reaffirming the corrosion rates found previously. Results again show that the highest wastage rates are seen in REI's probe locations Main and 3 and lowest at location 2.

Corrosion of weld overlay alloys 625/622 was low in all locations except location 3 where rates as high as 37 mils/yr were measured during the second period only. However, the average rate for the location was less than 20 mils/yr. The high corrosion rates at location 3 may be due to the presence of corrosive chlorides.

#### 4.1.4.4.2 Deposit Analysis

SEM analysis was performed in a few of the removed samples, in particular the ones where the highest corrosion rates were measured to identify the root corrosion mechanism. During the second installation probes M, N, and P (REI location 3) were analyzed using SEM (Figures 4.57 and 4.58) and provided the following results:

- The dark colored scale layer was mainly comprised of iron, oxygen, sulfur, chromium, and silicon.
- The light colored veins within the scale of sample consisted of iron and sulfur.
- Remnant chlorides were noted in a thin layer along the side of the sample N (highlighted by red arrow).
- A chlorine-rich layer between the scale and the probe metal was found before the scale and the probe metal in the probe sample with the worst wastage (see Figure 4.58).

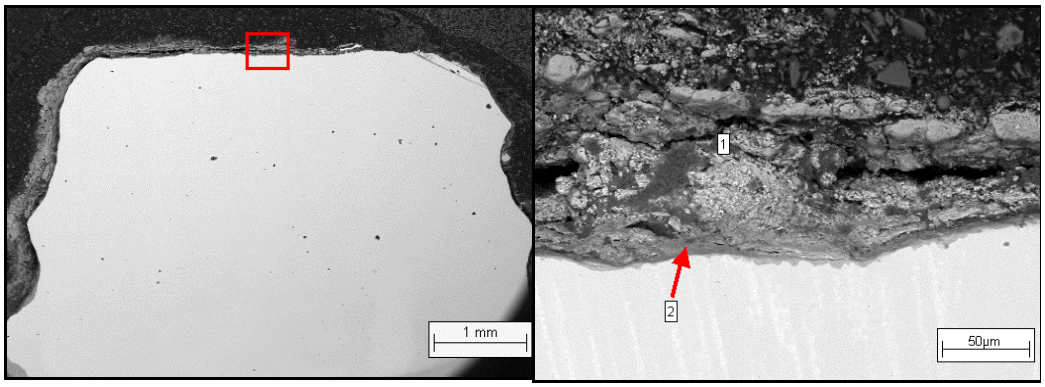


**Figure 4.57. SEM Analyzed sample outer scale.**

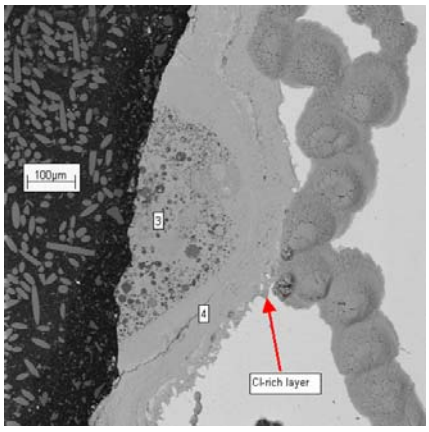


**Figure 4.58. SEM Analyzed sample inner scale.**

#### 4.1.4.4.3 Hardness Measurements of Alloy 622/625

The alloy 625/622 passive probes were tested for hardness increase to attain information about weld overlay alloy materials in service. The results are listed in Table 4.9.

**Table 4.9. Measured Hardness Data.**

| | | | First Set | | |
|---|---|---|---|---|---|
| ECN probe ID | Probe ID | Sample Type | *Tip* | *1st Thread* | *2nd Thread* |
| 5 | A | IN 625 | 27 - 33 HRC | 23 - 27 HRC | 26 - 27 HRC |
| 2 | E | IN 625 | 29 - 34 HRC | 32 HRC | 31 HRC |
| M | I | IN 625 | 33 - 36 HRC | 32 HRC | 30 HRC |
| 3 | M | IN 625 | 39 - 42 HRC | 33 HRC | 34 HRC |
| 1 | Q | IN 625 | 29 - 37 HRC | 31 HRC | 29 HRC |
| 4 | U | IN 625 | 29 - 36 HRC | 36 HRC | 35 HRC |
| | | | Second Set | | |
| | | | *Tip* | *1st Thread* | *2nd Thread* |
| 5 | A | IN 622 | 24-26 HRC | 20-21 HRC | 98 HRB |
| 2 | E | IN 622 | 97 HRB- 23 HRC | 24-26 HRC | 21 HRC |
| M | I | IN 622 | 94-97 HRB | 96 HRB | 95 HRB |
| 3 | M | IN 622 | 25-30 HRC | 25-27 HRC | 25-31 HRC |
| 1 | Q | IN 622 | 36- 43 HRC | 34-39 HRC | 21 HRC |
| 4 | U | IN 622 | 98 HRB - 22 HRC | 22-28 HRC | 25 HRC |
| | | | Final Set | | |
| | | | *Tip* | *1st Thread* | *2nd Thread* |
| 5 | A | IN 625 | 23.5 to 33.5 | 27 HRC | 30 HRC |
| 2 | E | IN 625 | 33 TO 34 HRC | 30 HRC | 30 HRC |
| M | I | IN 625 | 35 TO 37.5 HRC | 31 HRC | 30 HRC |
| 3 | M | IN 625 | 32 TO 38 HRC | 28 HRC | 26 HRC |
| 1 | Q | IN 625 | 33 TO 39 HRC | 32 HRC | 28 HRC |
| 4 | U | IN 625 | 39 HRC | 35 HRC | 31 HRC |

#### 4.1.4.5 Passive Probe Measurement Summary

Key findings from the passive probe testing may be summarized as follows:

1. The passive corrosion probe system is relatively easy to install and remove, provided exposure times for low alloy steels are limited to six month and those of corrosion resistant alloys to one year. Optimum installation period appears to be in the 6-12 weeks (1-3 months) range.
2. Probes with protrusion lengths of 3mm provided the best correlation to measured tube metal loss survey (UT) data.
3. Results from the Corrosion probe installation at Gavin yielded wastages close to those measured by material loss ultrasonic measurements (UT). Although the original set showed low corrosion rates, probably due to slag deposition in the grooves in between the tubes during initial operation, the second set and final set provided better correlations and information on the corrosion loss and mechanism. It is then likely that the wastage varies with time and location.
4. Retention of scales and deposits on the probes was satisfactory. This allowed determination of prevailing corrosion mechanisms, such as FeS found in most of the probes. In some high wastage areas chlorides were detected as well, as seen in Figure 58.
5. Some probes had much higher than average wastage rates, possibly due to chloride deposition and corrosion, particularly the ones at REI Location 3, during the second exposure period.
6. Probes installed at REI location 1 had significant corrosion rates up to 40 mils/year (~1 mm/year) during period 3, indicating a potential need for additional weld overlay.
7. The excellent corrosion resistance of Cr-Ni alloys 625 and 622 was confirmed at all locations, except for one reading at Location 3.
8. Alloy 625 probes experienced considerable increases in hardness to > 30 HRC at all locations. Hardness increases of alloy 622 were variable. The highest hardness increase was found in the location (3) experiencing high corrosion rates on both T-11 and 622.

Overall the corrosion rates found by the passive probe system correlated well with the prior metal loss measurements data. They are therefore a good inexpensive tool to monitor long-term average wastage rates during boiler operation.

## *4.1.5 Discussion of Results*

Discussion of program results is divided into two sections, correlation of electrochemical data with boiler conditions and comparison of electrochemical results with other measured corrosion data.

### 4.1.5.1 Correlation of Results

#### 4.1.5.1.1 Correlation with Probe Temperature

One of the first evaluations conducted with the probes was to demonstrate the effect of waterwall temperature on corrosion rate. This could be done with the corrosion probes by varying the sensor temperature. Figures 4.59 and 4.60 are examples of this evaluation. Figure 4.59 shows the drop in corrosion rate when the main probe temperature was reduced (due to an unscheduled outage) and then its increase when the temperature began controlling to the set point of 800ºF. Figure 4.60 shows a similar trend from Probe 5 (opposite the main probe) during April 2004. These two plots are representative of many occurrences of this type.

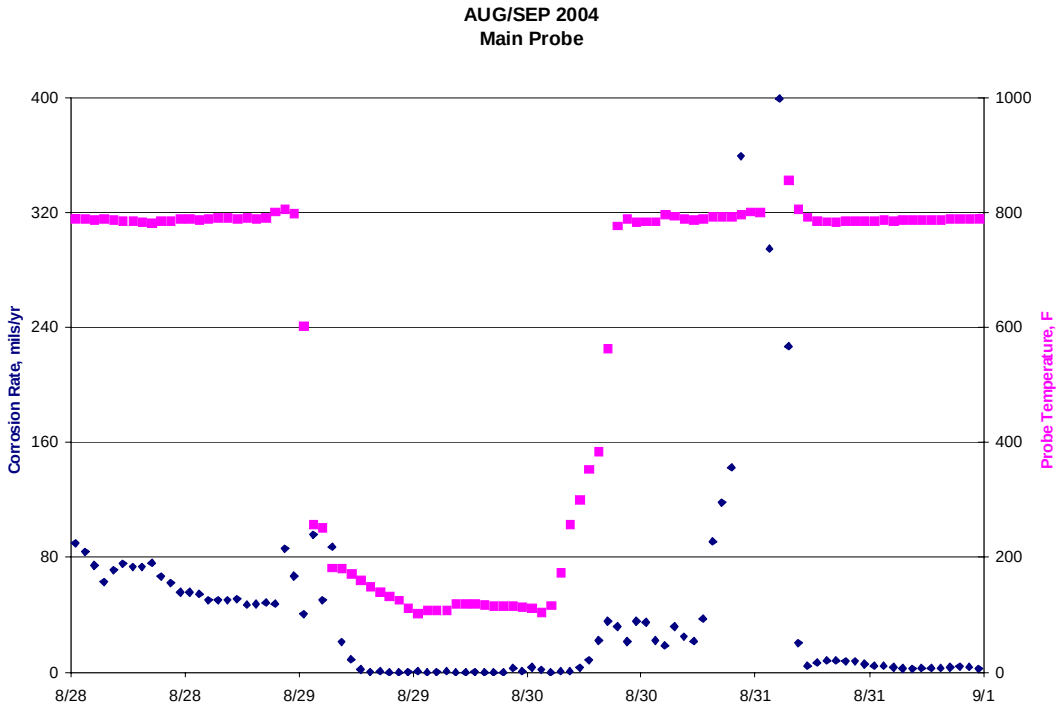


**Figure 4.59. Corrosion rate as affected by probe temperature.**

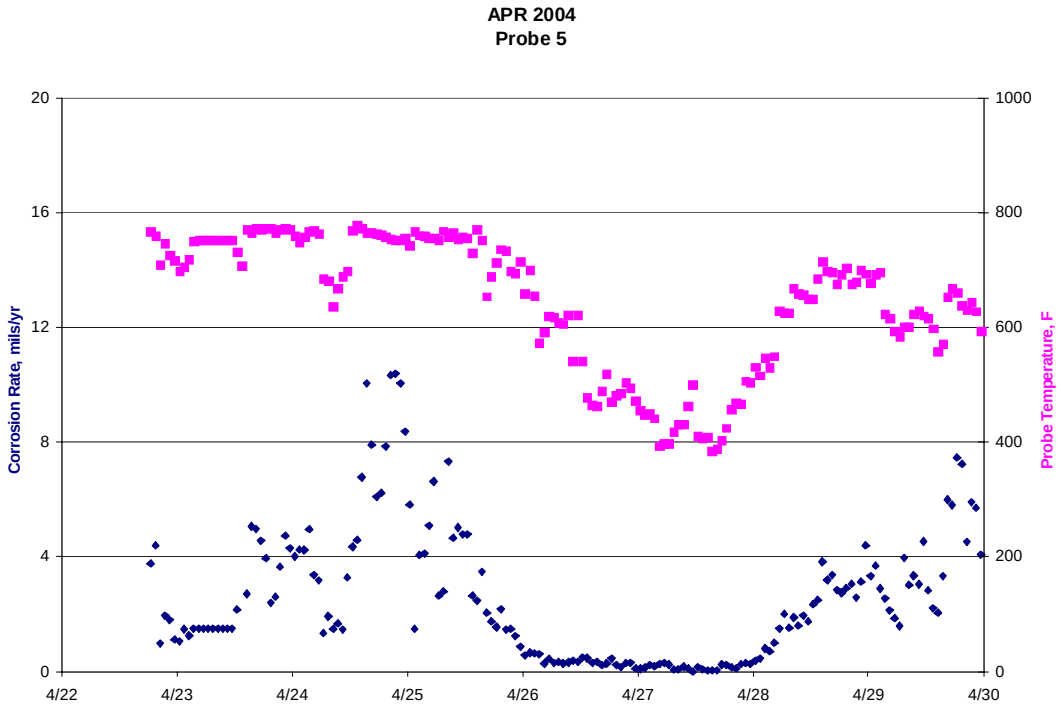


**Figure 4.60. Probe 5 corrosion as a function of probe temperature.**

One interesting phenomenon noticed during these tests was the effect of slag build-up on the probe. Figure 4.61 shows the temperature decrease when slag was building up on the probe face and then the quick rise back to the control temperature (800ºF) when the slag was shed or sloughed off the face. This presented problems during several days of testing. If the slag covered the face of the probe, the temperature dropped and, as shown in the previous two figures as well as in Figure 4.61, the corrosion rate then decreased. Since the waterwalls remain at their set temperature due to the steam flow within, their corrosion rates may not decrease when a slag layer is present on the tubes. This phenomenon was one of the reasons solenoid valves were installed to completely shut off the air to prevent excessive decrease in sensor metal temperatures.

When the temperature decreased, as is shown in Figure 4.61, the probe was inserted a little deeper into the furnace in order to ensure that the sensor elements were not recessed in the access port, as this exacerbated the formation of the slag layer. This approach was not continuously effective, though the intent was to achieve as close a simulation as possible to the normal operating condition of the wall tubes.

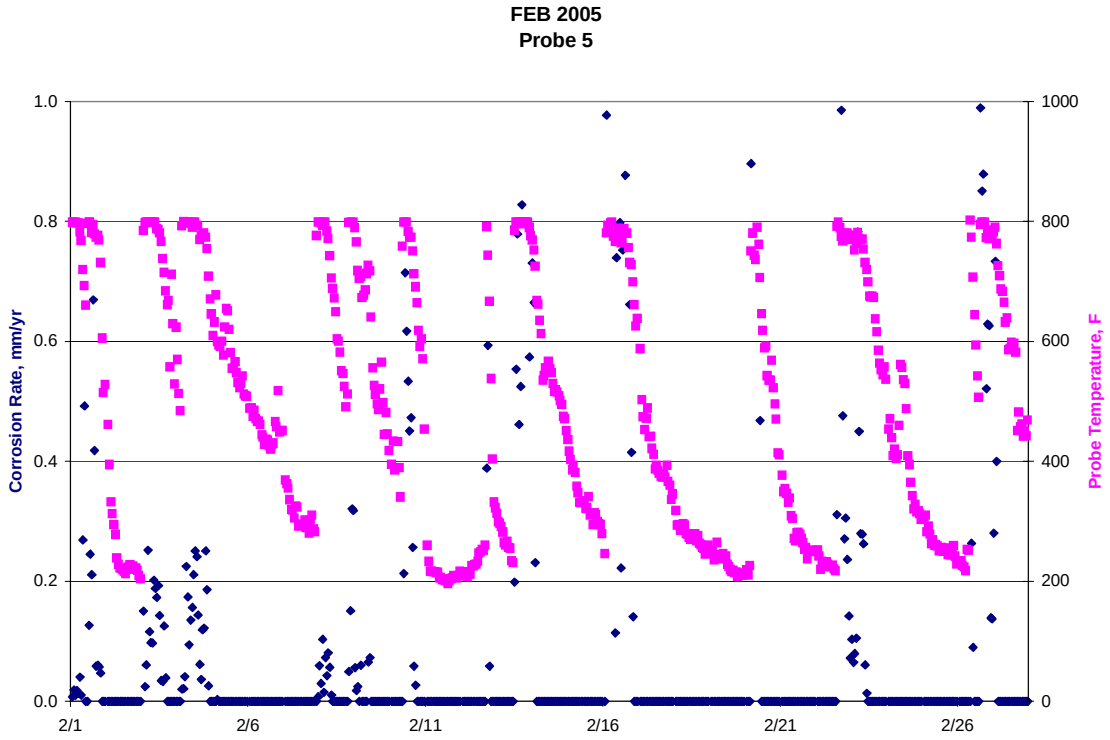


**Figure 4.61. Probe 5 showing slag build-up and sloughing on temperature.**

#### 4.1.5.1.2 Correlation with Boiler Load and Excess Air

The corrosion rate definitely was affected by boiler load. As the load was dropped, the corrosion rate would decrease. Two examples are shown; the first is from the main probe and is taken from the early period of testing. Figure 4.62 clearly shows a moderate corrosion rate followed by a distinct decrease in corrosion rate as the boiler load was reduced. Then as the boiler was brought back on-line, the corrosion rate again increased followed by a further decrease as the load was reduced once again. This figure also illustrates probe temperature control during such episodes.

The second example (Figure 4.63) is from Probe 2 during the month of April 2004. Midway through April 4$^{th}$ the plant was trying to bring the unit back into service. The corrosion data clearly showed an increase, followed by a decrease in rate, as the load was not maintained. Then on April 9$^{th}$ when the unit was brought back on-line, the corrosion rate increased and then returned to a low rate.

With the continual variability of the excess air during operation, it was not possible to correlate directly the corrosion rate measurements with excess air levels. However, it is safe to conclude that as the excess air level was decreased, the corrosion rate typically would increase.

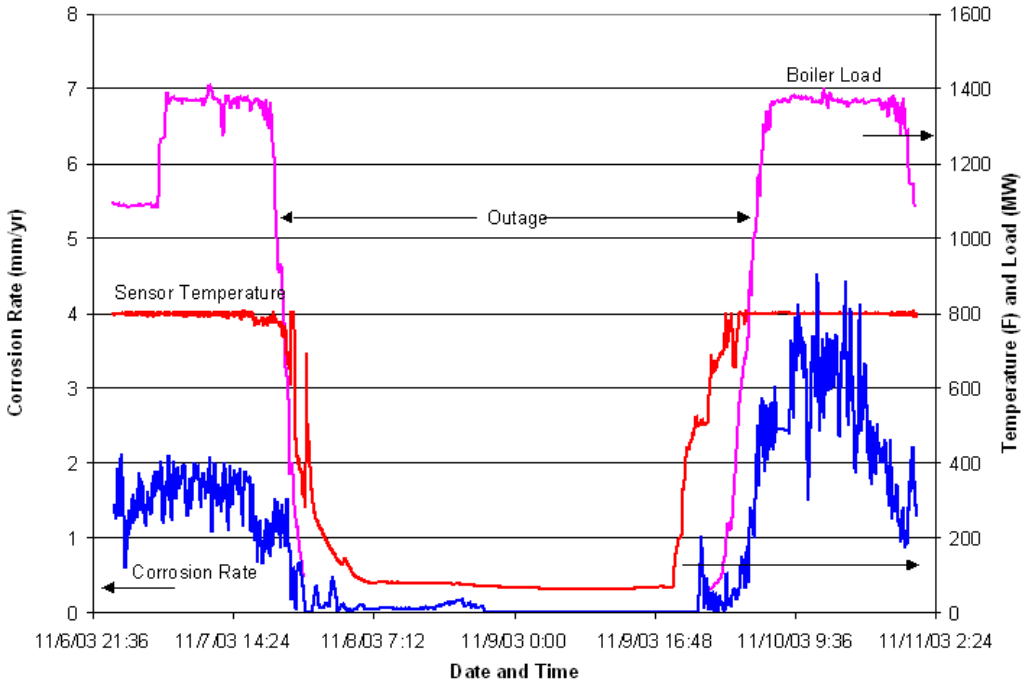


**Figure 4.62. Effect of load on corrosion rate – main probe.**

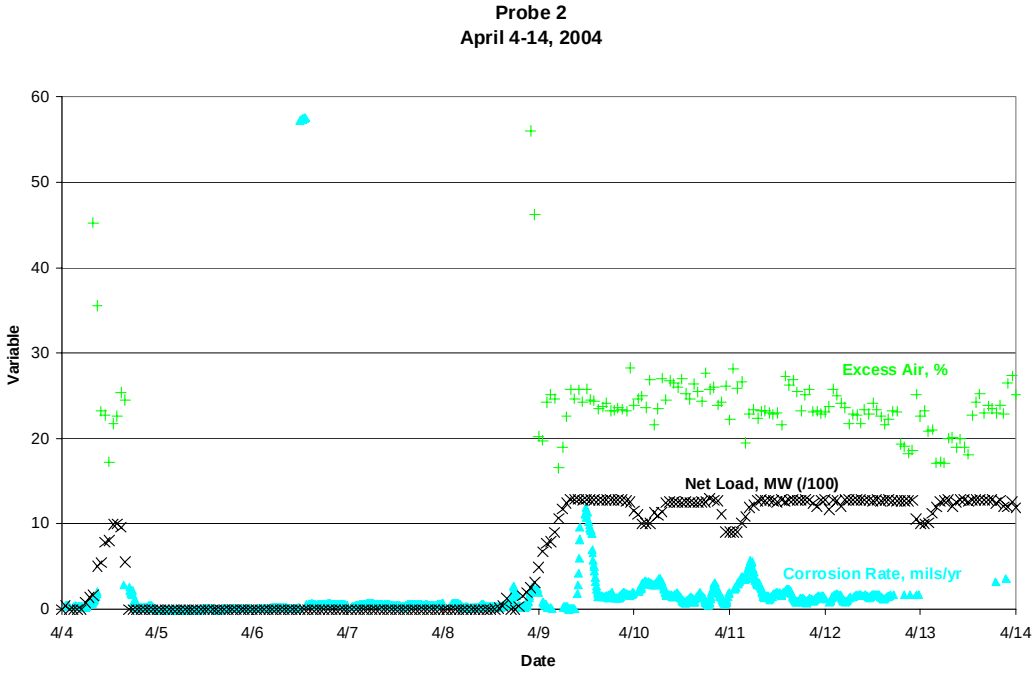


**Figure 4.63. Effect of load on corrosion rate – Probe 2.**

#### 4.1.5.1.3 Correlation with Probe Location

The locations for the installation of the corrosion probes were selected to represent different corrosion conditions (and therefore corrosion rates) within the boiler during normal operations. This approach was very successful as is shown in the figures plotting the overall corrosion rates for the various probes. However, the figures contain all the data and are difficult to compare directly. Figure 4.64 shows the corrosion rates for the four probes installed in August/September 2004. Also shown in this figure are the boiler load and excess air levels. The probes were installed on August 26th and began measuring corrosion rates from the end of the 26th onward.

Note that initially, the Main probe and Probe 2 had significantly higher corrosion rates than did Probes 3 and 5. However, by the 28th of August, Probe 5 measured the highest corrosion rate until the unit went off-line. On the 31st of August, again Probe 2 measured high corrosion rates that dropped off quickly.

Probe 3 showed comparable corrosion rates to Probe 5 on the 27th of August, but the rate then dropped off to very low values throughout the remainder of the period. Note on the 30th and 31st there are two "bumps" in the Probe 3 corrosion rate that corresponded to short-term increases in boiler load.

In general, it appeared from the data that the main probe measured a corrosion rate approximately ten times higher than the other probe locations. This was consistent with the UT data received before the program began.

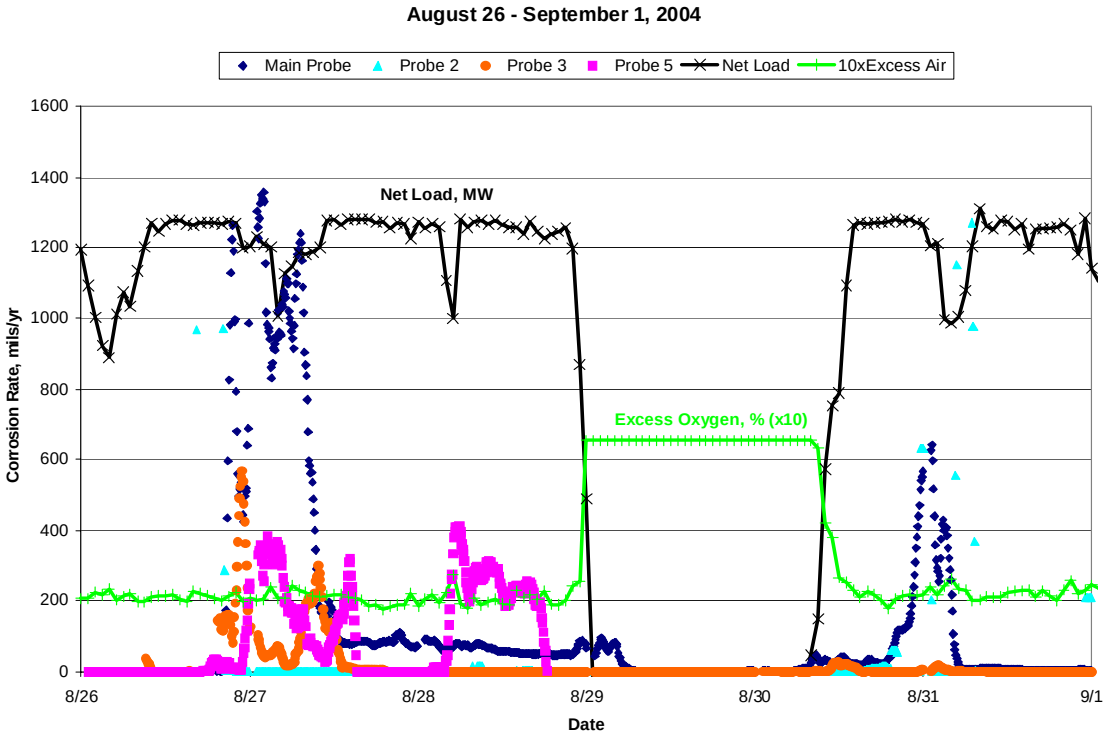


**Figure 4.64. Effect of probe location on corrosion rates.**

#### 4.1.5.1.4 Correlation with Other Boiler Conditions

Boiler operating changes could have a major effect on corrosion rates at the various locations throughout the boiler. This is clearly shown in Figure 4.65 taken from the December 2003 data. While the boiler load and excess air were "normal" there were two occurrences of high corrosion activity. One occurred on the 9th of December and the other on the 16th. Interestingly, all of the probes showed an increase in corrosion during these two time periods even though there was very little change in boiler load. Other plant data are required in order to correlate these two occurrences with boiler operations.

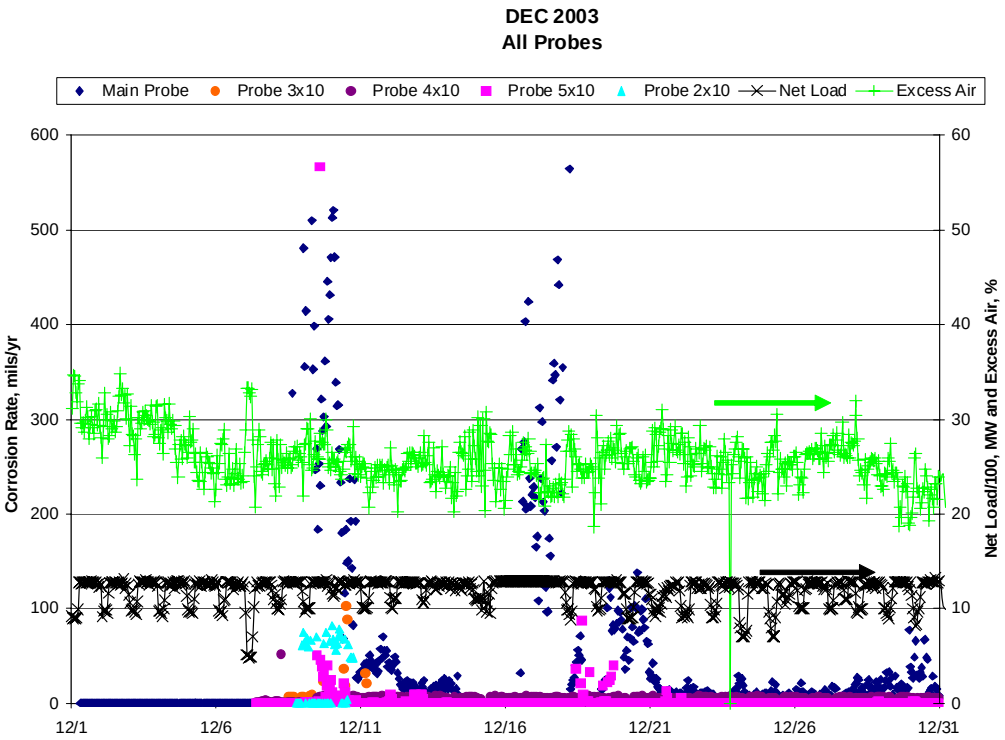


**Figure 4.65. Effect of boiler conditions on corrosion rate.**

### 4.1.5.2 Comparison of Approaches

This program provided a unique opportunity to compare the results of a range of tools for predicting, understanding and monitoring corrosion:

- CFD-based predictions based on empirical correlations
- Electrochemical-based monitoring
- Fixed depth coupon measurements
- Temperature-controlled coupon measurements
- Ultrasonic tube thickness measurements

Each of the techniques has strengths and weaknesses and each can deliver an independent view of the corrosion behavior of a boiler. A comparison of the results serves not only to

provide confidence in the measurements delivered, but also to provide insight into the nature of the corrosion mechanism.

The distinctions between the techniques include:

- Response time
- Temperature
- Deposit condition
- Sensitivity
- Complexity

One element to be considered when comparing the results obtained during the course of this project is the varying combustion condition within the boiler. The test period for each of the techniques was not identical and in some instances simultaneous testing was limited by (1) the activity of the plant in adjusting the unit performance during the period of study and (2) the challenges faced in obtaining reliable power and cooling air supplies for the on-line monitoring system. The availability of CFD modeling results was constrained only by knowledge of the precise inputs for specific periods of operation. The initial modeling was performed per the inputs from a pre-June 2003 condition and was not relevant for comparison with the monitoring data beyond the qualitative evaluations described in section 2. The remainder of the modeling was performed based on conditions that were common during early 2005. The active monitoring periods for the electrochemical sensors and passive probes were described earlier. The confirmatory profilometry results were obtained during a 2-day "snapshot" at the end of March 2005.

During the period from late 2003 to early 2004, data were available for both the electrochemical sensors and the passive probes. The CFD results and UT data were reasonably consistent, given the inherent fluctuations associated with the boiler operating conditions. In addition, it was known that substantial changes in the operation of the boiler were made during this period of tests. Nevertheless, the results showed a ranking order of corrosion activity between the various sensors as follows:

MAIN > 5 > 1, 2, 3

The location 4 data was inconsistent. This may have been the result of anomalous circumstances following a February 2004 outage. The CFD results from four simulations relevant to this period predict corrosion rates over the following ranges:

| CFD Predictions | Probe Location | | | | | |
|---|---|---|---|---|---|---|
| | Main | 1 | 2 | 3 | 4 | 5 |
| Corrosion Rate (mils/yr) | 38-75 | 38-69 | 49-62 | 37-61 | 17-57 | 34-75 |

The passive probe results represented a fairly broad range because the exposure temperature could vary substantially as the coupon insertion depth was varied from 0.5 to 3 inches. The location 3 data variation, as a function of insertion depth was difficult to explain and must be

considered as being unrepresentative of other trends, though precisely why that might have been the case is not certain:

| Passive Probe Measurements | Probe Location | | | | | |
|---|---|---|---|---|---|---|
| | Main | 1 | 2 | 3 | 4 | 5 |
| Corrosion Rate (mils/yr) | 5-57 | 0.2-8 | 0.001-11 | 1-110 | 1-47 | 12-32 |

The electrochemical sensors provided a substantial amount of data and, by capturing second-by-second fluctuations, were also capable of illustrating the substantial short-term variation in corrosion rate. It should be noted that (1) the early autumn 2003 rates observed at the main probe location were substantially higher than the later rates and (2) the high end of the range for probe 4 was due to an unusual spike following an outage during the first week of February 2004. In approximate terms, the 48-hour rolling average corrosion rates varied as follows:

| Electrochemical Measurements | Probe Location | | | | | |
|---|---|---|---|---|---|---|
| | Main | 1 | 2 | 3 | 4 | 5 |
| Corrosion Rate (mils/yr) | 0-495 | 0-25 | 0-40 | 0-40 | 0-290 | 0-70 |

During later periods the overlap was limited. Although simultaneous data were not available, it was noted that the profilometry data, ~16 mils/yr at location 1 and ~20 mils/yr at the main location, were consistent with much of the data described above.

### *4.1.6 Market Application*

Until recently, fireside waterwall corrosion in coal-fired boilers was uncommon and was relatively mild in the U.S. electricity generation industry. However, the use of in-furnace combustion modifications such as staged combustion to reduce $NO_x$ emissions has led to a notable increase in the frequency and severity of waterwall wastage. As the extent of air staging increased to satisfy the more stringent restrictions on $NO_x$ emissions, there has been growing concern among utilities about high temperature corrosion and waterwall wastage. The existence of fuel-rich regions near furnace walls is reported to have had the most damaging impact on supercritical pulverized-coal-fired units firing high-sulfur coals. REI has worked with the US Department of Energy and EPRI for several years to improve predictive capabilities and provide solutions for furnace water wall wastage for a wide range of coal-fired furnaces firing high-sulfur coals.

The ability to determine the extent of waterwall wastage on-line provides boiler operators a number of important benefits including:

- Reduced cost of unscheduled outages due to tube leaks.
- Reduced maintenance costs. The cost of prevention is much less than the cost of repair. It has been estimated that prevention is about 70% the cost of correction.
- Reduced tube replacement costs. Extending the life of boiler tubes even 1-2 years will greatly reduce the normalized annual operating costs of coal-fired boilers.
- Reduced costs in weld overlay. Measuring and controlling corrosion is much less expensive than the cost of weld overlays, tube cladding, etc. For example, the costs for weld overlay are about $\$350/ft^2$.
- The flexibility to use slight changes in operating procedures to minimize corrosion while at the same time permitting low NOx emissions (e.g., operational optimization).
- Ability to alert operators in real time when changes in fuel composition or unintentional excursions in firing conditions can place the boiler tubes at risk from high temperature gaseous corrosion attack.

There are several methods of measuring or assessing water tube corrosion in steam boilers; these include tube thickness measurements, corrosion coupons, metal loss, etc. Essentially all of these methods require very long time periods, on the order of hundreds of hours, or necessitate the boiler being out of service for the assessment to be made. These methods give an accurate but retrospective averaged estimate of the rate of corrosion attack over the time period over which the measurements are taken. The disadvantages of these measuring methods are that the majority of corrosion may occur during a relatively short time period under particular operating conditions, perhaps one day or even one hour, and the averaged data do not enable the boiler operator to determine when this might have taken place or forecast when it might recur. Episodes of high corrosion occurrence cannot be reliably determined with conventional measurement techniques. As a result, the conditions that led to the high corrosion occurrence cannot be characterized or avoided.

This demonstration into on-line high temperature electrochemical monitoring, sponsored by OCDO and DOE NETL, has confirmed its ability to provide a real-time on-line indication of corrosion risk. With that capability, there is now a clear opportunity to combine the strengths

of advanced combustion modeling with practical on-line instrumentation to achieve optimal firing conditions with minimal risk of damage to the boiler, even when using high sulfur coal under staged, low-$NO_x$ combustion.

This approach is essentially suitable for use on any boiler using high sulfur, high iron coals, as well as those units needing to operate the boiler in an intermittent or staged combustion mode (e.g., for $NO_x$ reduction). For example, in Ohio there are approximately 24,000 MW of electrical generating capacity. More than 95% of this power is produced from coal, and much of it from high sulfur Ohio coal. Thus, the opportunity for an improved management of advanced combustion and high temperature corrosion avoidance in the state of Ohio alone is significant. Beyond that, however, the approach should be applicable to any heater, furnace, gasifier or smelter where thermal efficiency and combustion optimization would provide significant operational and/or environmental benefits.

Since the technology fulfilled its objective, the use of high-sulfur Ohio coal should not be penalized as a result of a perceived risk of high water tube corrosion rates. In fact, if a boiler can ascertain any areas of potentially high corrosion rate while the boiler continues in service, minor adjustments to operational parameters can be made immediately, thereby minimizing corrosion attack and increasing the time between outages due to waterwall leaks. This should provide significant economic benefit in terms of reduced maintenance, increased availability, and lower $NO_x$ reduction costs for the user.

With the successful completion of this program, the technology is now ready for commercialization, including the fabrication and installation of the corrosion assessment system for long-term installations. This will take approximately 12 months. During this time, REI also plans to further evaluate and improve the corrosion measurement and recording equipment by using the system in short-term consulting projects. REI is currently scheduled to participate in three commercial projects during 2005 where the corrosion instrumentation will be used to support short-term boiler tests. These projects should provide further knowledge of the system performance, the development of improved installation procedures, additional experience with multiple-sensor systems, and supplementary data for the correlation of CFD predictions with measured corrosion rates, boiler operating conditions, and combustion chemistry.

### *4.1.7 Summary*

The goal of this program was to field-test a novel multi-pronged approach for managing waterwall corrosion in coal-fired utility boilers. The overall objective of the test program was to evaluate a prototype multi-sensor, real-time, electrochemically-based instrumentation and on-line system for monitoring and managing corrosion in coal-fired utility boilers. This objective was successfully completed during the two-year development and testing program. The results presented in this report illustrate the successes and challenges experienced during this research and development effort.

Specific objectives accomplished were:

- Application of Computational Fluid Dynamic (CFD) software with state-of-the-art corrosion submodels to predict locations and approximate rates of corrosion within the Gavin Unit 1 boiler. These predictions were used to help identify the corrosion probe locations for on-line testing, to understand the sensitivity of corrosion to certain operating conditions, and to correlate and verify predicted with actual corrosion rate measurements.
- Development, testing and application of a multi-sensor technology utilizing electrochemical techniques for quantitative, real-time monitoring of waterwall corrosion in a coal-fired boiler. The six-probe system was developed, installed, and used to monitor corrosion rates at Gavin Unit 1. The system featured corrosion sensors, sensor temperature controllers, signal processing electronics, data acquisition and processing hardware and software, and a novel communications system that included wireless data transfer within the power plant and remote system monitoring at the REI offices in Utah. Several operational challenges were identified during testing and were dealt with by a combination of modified system hardware and modified installation and maintenance procedures.
- Application of an advanced precision metrology technique (profilometry) and the passive probe technology to verify predicted and measured corrosion rates. Profilometry data were more difficult to acquire on site than had been expected on the basis of earlier laboratory experiences, as a result of mechanical damage to the sensors sustained at various times during the testing, primarily from unforeseen extraneous causes. Nevertheless, the metrology provided excellent short-term correlation data, which corroborated electrochemical results recorded during the same exposure period. The passive probes provided six-month averaged variable-temperature corrosion results and gave an interesting comparison with the predicted and measured corrosion rates. CFD predictions, profilometry data, and passive probe data showed reasonably good agreement considering the different time-scales, exposure temperatures, coupon and sensor locations, and compromises inherent in each technology.
- Limited development of a methodology for combining predicted and measured data into corrosion management guidelines for a coal-fired boiler. This ambitious task was the most difficult to achieve and, ultimately, was the least complete at the end of the present project, due to discrepancies in data obtained from the various techniques and the limited availability of the necessary plant operating data.

In spite of some operational challenges, which limited the on-line corrosion measurements, the data obtained during this program clearly demonstrated the value of a real-time corrosion measurement capability. Measured short-term corrosion rates often were significantly higher than the averaged rates typically reported from previous boiler tests, indicating that a considerable opportunity exists for refining the operational control of the combustion process. The corrosion probes, located at the various points in the boiler, were able to detect substantial differences in corrosion rates under different boiler operating conditions. This is important both in developing a more complete understanding of how various boiler operating changes affect corrosion and to facilitate improved combustion efficiency and unit availability in the future. Furthermore, it should be possible to control, or even to adjust, the location of highest corrosion within the boiler.

The sensors were observed to respond appropriately to variations in corrosion rate as a function of boiler load, temperature, and combustion chemistry variations. Plotting the data in real-time can allow unit operators to witness the effects of subtle changes in coal feed, combustion air and other parameters on the corrosion distribution within a boiler. The initial goal for these measurements is likely to be to reduce corrosion risk, and thereby to increase the service life of the boiler tubes. The capability to access measured corrosion data remotely provides a means for multiple groups within (and without) a utility to access real-time and historical operations and corrosion data for a variety of purposes (i.e., operations, maintenance, inspection, planning) whenever needed and without having to interrupt local plant personnel to obtain the data.

The complementary strengths of CFD predictions, real-time electrochemical measurements and retrospective averaged static corrosion results indicate that the combination of such approaches can provide the most comprehensive overview of a combustion unit while establishing the most effective operational and corrosion prevention strategy for coal-fired electric power generation boilers.

### *4.1.8 Recommendations*

Recommendations for improving the corrosion instrumentation system described above include:

- Provide more rigorous and site-tailored installation specifications, including requirements for clean instrument air and reliable instrumentation power supplies for such equipment.
- Further refine the sensor design to improve temperature response and, where appropriate, avoid slag deposits, especially in boilers that are known to be susceptible to slagging in regions where sensors may be installed (though it should be noted that the service condition of the sensor should reflect accurately that of adjacent tubes and hence if a slag layer is generally present, the sensor should be similarly located beneath a slag layer in order that tube corrosion conditions are modeled appropriately).
- Develop an improved training scheme for on-site personnel with the objective of improving system supervision and collection of boiler operating data (i.e., data not supplied by the plant PI system such as fuel type, burners out of service, changes in air port settings, etc.).
- Obtain additional corrosion data and plant operating data to confirm correlation trends observed in this program.

As a means of further developing and testing the technology, REI is currently scheduled to participate in three commercial projects during 2005-2006 where the corrosion instrumentation will be used to support short-term boiler tests. These projects should provide further knowledge of the system performance, the development of improved design and installation procedures, additional experience with multiple-sensor systems, and supplementary data for the correlation if CFD predictions with measured corrosion rates, boiler operating conditions, and combustion chemistry.

## 4.2 Soot Formation

Low-$NO_x$ firing systems and combustion modifications, such as OFA have been implemented by many US utilities to meet existing and impending restrictions on NOx emissions. In boilers with OFA system, part of the combustion air is introduced into the furnace above the firing zone, which is taken from the burner secondary air. By delaying mixing between fuel and air, lower furnace becomes sub-stoichiometric conditions that inhibit NOx production. However, a reducing environment within the boiler can result in significant concentrations of sub-micron soot particles. The potential impacts of soot include increases in fine particulate emissions (Veranth et al., 2000) and opacity, boiler heat imbalances due to enhanced lower furnace radiation, potential decrease in the effectiveness of air staging for NOx control, and ash salability. In addition, soot particles can deposit on the surface of heat transfer device within a convective pass resulting in performance degradation. In this study we have implemented into REI's two phase combustion CFD code, *GLACIER*, an advanced soot model that utilizes Fletcher's chemical percolation devolatilization (CPD) model for tar and soot formation during pyrolysis and a semi-empirical model for soot oxidation and gasification (Brown and Fletcher, 1998). Computer simulations have been performed for the University of Utah 1.5Mwatt pilot-scale test facility and a full-scale coal fired utility boiler to evaluate the impact of burner and OFA operation on soot formation and destruction. Verification of the soot model was performed by comparing simulation results with soot measurements taken within the pilot-scale test furnace using a real-time monitoring Photoacoustic (PA) system.

### *4.2.1 L1500 Experiments*

A series of experiments for low NOx firing conditions was performed in the L1500 (4.5 MMBTU) pilot scale test furnace at the University of Utah Combustion Research Laboratory (CRL). The purpose of the tests was to (1) verify the presence of soot for certain firing conditions and (2) provide experimental data to use in verification of the soot model implemented into our CFD code.

#### 4.2.1.1 Pilot-scale Test Furnace

A schematic of the L-1500, a pilot-scale test furnace at the University of Utah, is shown in Figure 4.66. The L-1500 combustor is capable of firing natural gas and/or pulverized coal at a rate of 5 million Btu/hr. The facility is designed to simulate low emission, pulverized coal-fired boilers with wet walls and is used to investigate full-scale commercial electric power generating unit design and operation. The horizontal-fired furnace is 1.1 m x 1.1 m square and 12.5 meters long and equipped with a low NOx burner. The furnace is made of 10 sections and each section has multiple sampling ports for experimental measurements.

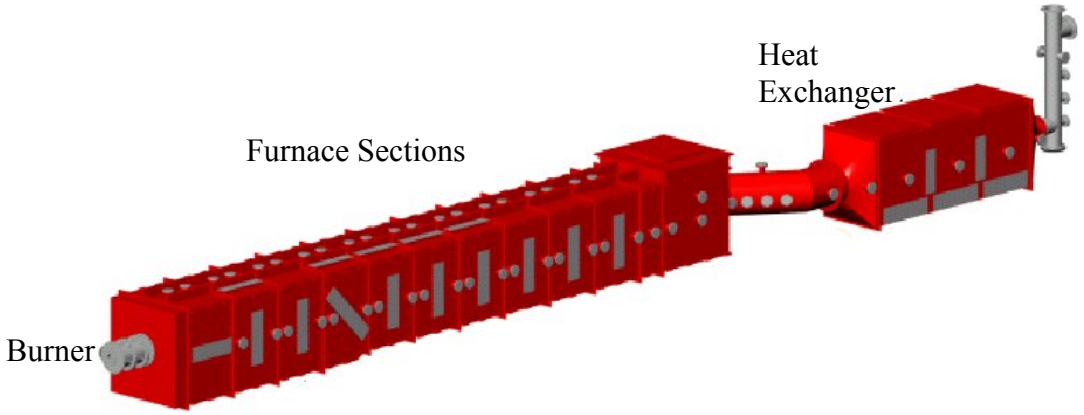


**Figure 4.66. Schematic of the L-1500, a pilot-scale test furnace at the University of Utah.**

### 4.2.2.2 Photoacoustic Instrument

Soot concentration was measured in situ by a photoacoustic (PA) instrument that was developed by the Desert Research Institute (Moosmuller, 1998). A schematic view of the PA is shown in Figure 4.67. The PA uses resonant photoacoustic detection where light from an intensity modulated source is absorbed by soot or black carbon resulting in periodic heating and subsequent expansion of the surrounding air. This expansion results in an acoustic pressure wave at the modulation frequency that can be detected with a sensitive microphone. The instrument measures light absorption at a laser wavelength of 1,047 nm where black carbon or soot absorbs very strongly in contrast to other aerosols and gases. The sampled air is continuously pulled in for the measurements. The entire measurement procedure was automated by a computer.

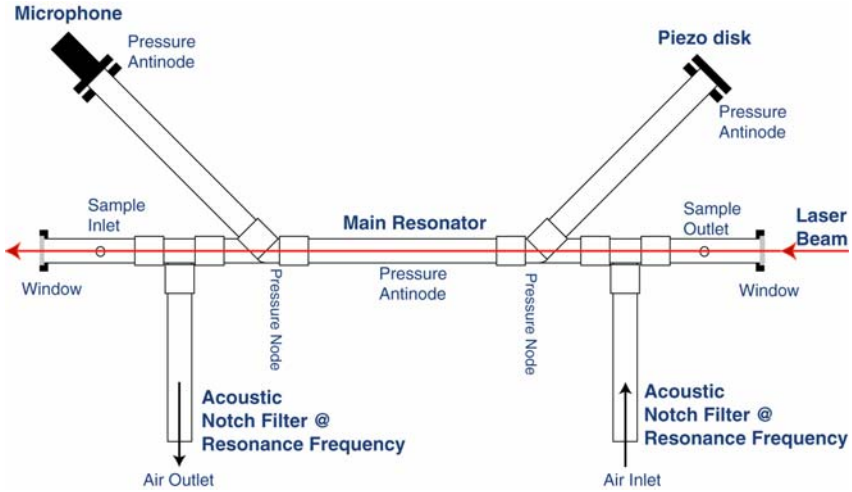


**Figure 4.67. Schematic of the photoacoustic instrument.**

#### 4.2.1.3 Sampling System

A water-cooled, air-quenched transpiration sampling probe was used to sample soot particles from the furnace. A schematic of the sampling setup is shown in Figure 4.68. The sampled soot particles flow through four stages of diluters before entering PA instrument. Various dilution ratios ranged from 400 to 3800 at ambient temperature were employed to measure the soot volume fraction at various sampling locations. The dilution ratios were calculated by measuring in and out flow rates at each stage.

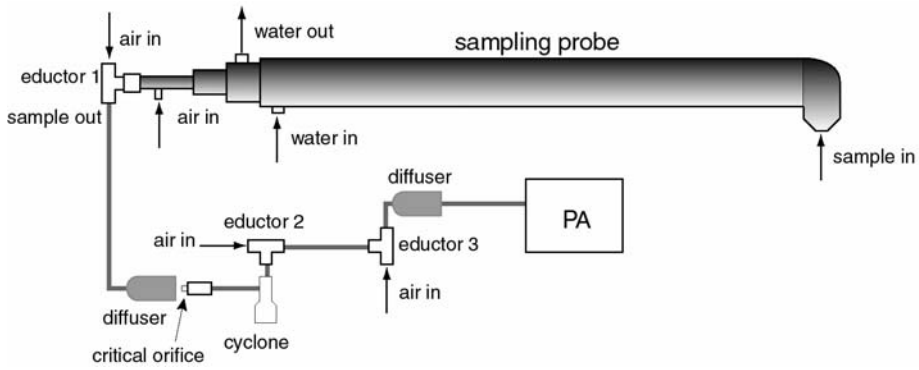


**Figure 4.68. Schematic of a soot sampling system with a photoacoustic (PA) instrument.**

Figure 4.69 shows the tip of the sampling probe after the experiment. The probe tip was covered with soot-like material as were the inside walls of the probe. This will result in a measurement somewhat lower than the actual concentration. On the other hand, the low sampling flow rate (lower than isokinetic sampling flow rate) will result in an increase in the measured concentration. However, this may not be a significant factor since soot particles are normally small. Particle size from the simulation was less than 1 μm. Wall deposition in the water-cooled probe may be a dominant factor in explaining the lower experimental concentrations in comparison to computational results. The calibration of the PA system is being verified, because it tends to give significantly lower concentrations than observed in the previous pool-fire measurements.

**Figure 4.69. Tip of the sampling probe after testing in the pilot-scale facility.**

#### 4.2.1.4 Experimental Results

Figure 4.70 shows the measured soot volume fraction for case 1 (burner stoichiometry of 0.75) as a function of the axial distance from the burner exit along the centerline and the radial distance from the side wall. After a peak at about 2 meters from the burner exit, the soot volume fraction decreases with increasing distance as shown in Figure 4.70a.

- The competing nature of two processes, soot formation and destruction can be clearly seen in Figure 4.70a. Near the burner, there is significant soot formation from the coal off-gas. After reaching a peak, the soot volume decreases due to oxidation (destruction) of the soot. Soot exists even after additional air introduction from the staging port located at 4.48 meters.
- The radial distribution of soot volume fraction is illustrated by Figure 4.70b. At 0.81 and 2.03 meters, the distributions are similar with a high soot volume fraction at the centerline. However, further downstream the highest soot volume fraction exists at a region close to the side walls. This may be a result of the burner swirl or re-circulation patterns within the furnace.

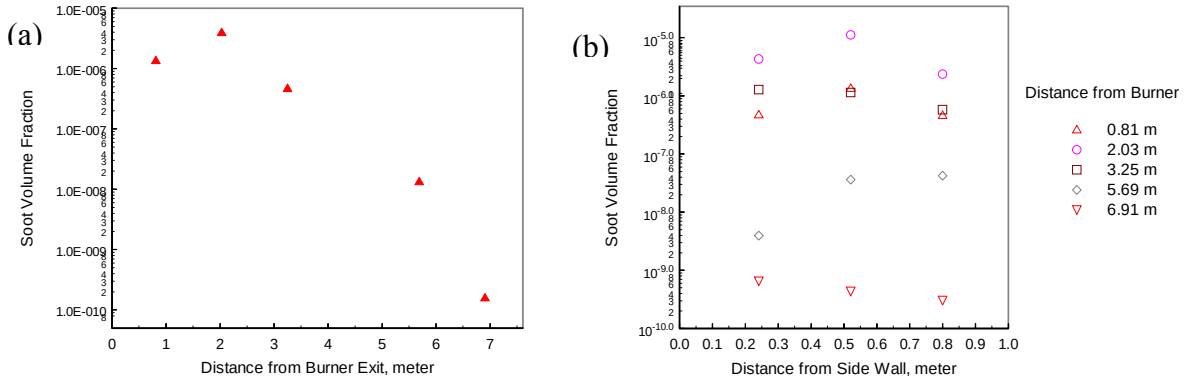


**Figure 4.70 Soot volume fraction along furnace centerline and at radial positions.**

Figure 4.71a shows the impact of burner stoichiometry on soot volume fraction measured 3.25 m downstream of the burner. As shown in the figure, the soot volume fraction decreases with increasing burner stoichiometry due to increasing oxygen availability for soot destruction (oxidation). Generally, NOx is expected to decrease as air staging is increased (decreasing burner stoichiometry). This is confirmed in Figure 4.71b, which plots the soot volume fraction as a function of exit NOx. With increasing NOx, the soot volume fraction decreases.

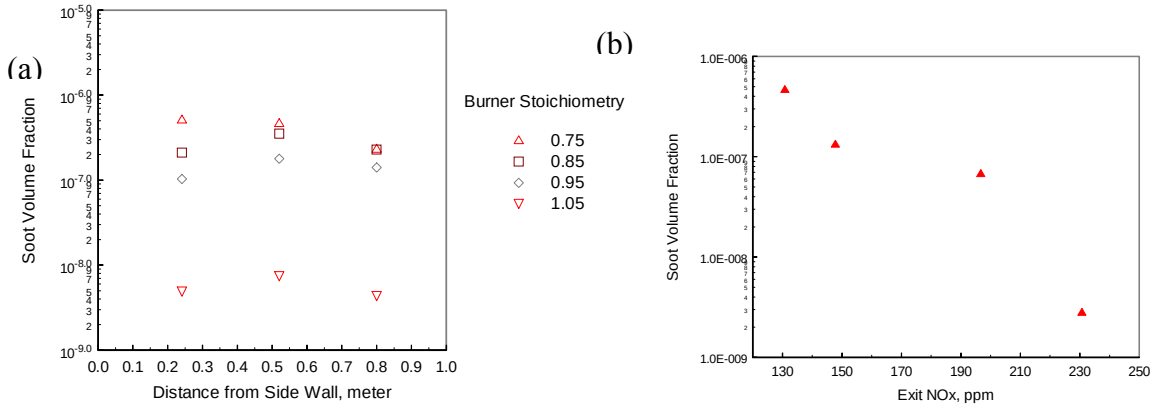


**Figure 4.71. Soot volume fraction measured at 3.25 meters from the burner exit as a function of the radial distance from the side wall for various burner stoichiometries (a) and exit NOx (b).**

Generally, PA measurements show a similar trend to simulation results along the centerline of the furnace but with much lower concentrations by two orders of magnitude. One of the factors that may explain this is wall deposition. A water cooled sampling probe was used instead of a transpiration probe because the small cyclone in the sampling system limits the possible sampling flow rate. In addition, a low sampling flow rate will make wall deposition worse.

## *4.2.2 Modeling of Soot Formation*

Brown et al's soot model (Brown and Fletcher, 1998) was implemented into REI's two-phase combustion CFD code, *GLACIER.* A detailed description of the model can be found elsewhere (Brown and Fletcher, 1998). Briefly, the model is comprised of three transport equations for tar mass fraction, soot mass fraction, and soot number density. Coal-derived soot is assumed to form only from tar. Tar evolution is calculated from Lagrangian particle phase equations, which use the Chemical Percolation Devolatilization (CPD) model to determine devolatilization rates and tar yields. The CPD model describes the devolatilization behavior of a rapidly heated coal based on the chemical structure measured by $^{13}C$ NMR (Fletcher et al., 1992). In this study, the NMR-based coal structure parameters were calculated from the correlation developed by Genetti et al. (1999) using the proximate and ultimate analysis data on coal.

### 4.2.1.1 Drop Tube Simulations

A simple drop tube test case has been run with Fletcher's soot model implemented into ***GLACIER***. As shown in Figures 4.72a-d, the simulation predicts reasonable soot volume fractions, on the order of $10^{-6}$ , with the highest concentration occurring in the fuel rich region (i.e., along the center of the drop tube). However, as shown in Figure 4.66e, the model predictions also highlight some deficiencies in the model because it predicts a non-zero soot number density in regions where there the soot mass fraction is zero. This behavior has been previously reported by Brown (1997). In private communications, Fletcher has suggested model modifications that should eliminate this non-physical behavior and lead to a more robust model.


**Figure 4.72a. Gas temperature (K).**

**Arrow shows the direction of gravitational force (g).**


**Figure 4.72b Soot volume fraction (%)**


**Figure 4.72c Tar mass fraction (%)**


**Figure 4.72d Soot number density**

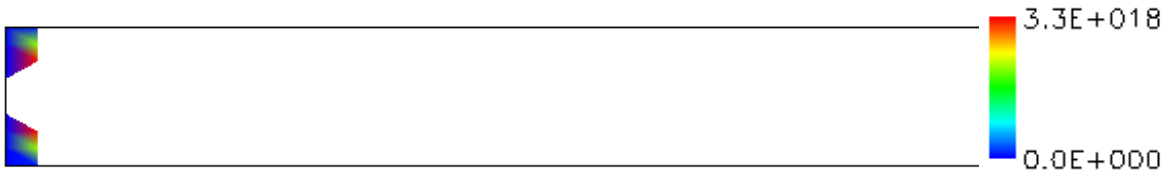


**Figure 4.72e Soot number density shown only in the region in which soot volume fraction equals zero**

#### 4.2.2.2 L1500 Simulations

The L-1500 pilot scale test furnace was operated with various burner stoichiometries while firing Utah coal. The operating conditions and coal properties are shown in Table 4.10. A staging air port was located at 4.5 meter from the burner exit for all cases. Soot volume fractions were measured along the long axis of the furnace as a function of axial distance from the burner exit as well as radial distance from the centerline using the PA instrument. Computational simulations were also performed using the same operating conditions.

**Table 4.10. Pilot-scale test furnace operating conditions and coal properties.**

| | case 1 | case 2 | case 3 | case 4 | Utah Coal Properties | |
|---|---|---|---|---|---|---|
| Burner Stoichiometry | 0.75 | 0.85 | 0.95 | 1.05 | | |
| Overall Stoichiometry | 1.15 | 1.15 | 1.15 | 1.15 | | As Received, % |
| | | | | | C | 69.65 |
| Coal Feeding Rate [lb/hr] | 320 | 323 | 323 | 325 | H | 4.42 |
| Air Flow Rate [lb/hr] | | | | | O | 9.16 |
| primary | 448 | 449 | 450 | 449 | N | 1.25 |
| secondary | 607 | 693 | 796 | 900 | S | 0.4 |
| tertiary | 1,211 | 1,382 | 1,592 | 1,805 | Ash | 10.44 |
| staging | 1,197 | 896 | 597 | 383 | Moisture | 4.68 |
| | | | | | HHV (BTU/LB) | 12,303 |
| Exit $O_2$, dry | 3.0 | 3.0 | 3.0 | 3.0 | | |

Figure 4.73 shows the measured and the predicted soot volume fraction for case 1 (burner stoichiometry of 0.75) as a function of the axial distance from the burner exit along the centerline. The predicted soot volume fraction from *GLACIER* showed a peak at about 1.5 meters from the burner exit and decreased with increasing distance.

- *GLACIER* under-predicted the soot concentration by a factor of 5 at the region close to burner. The predicted maximum soot volume fraction along the centerline of the furnace was about $1\times10^{-6}$ at 1.5 meter from the burner exit while the measurement had about $5\times10^{-6}$ at 2 meter from the burner exit.
- The predicted soot volume fraction along the centerline showed a dip in the middle of furnace, where staging air ports were located. The swirl of the combustion air, re-circulation patterns within the furnace, or the additional air introduction shifted the soot particle off the centerline. This feature was not captured in the axial measurements, but was shown in the radial measurements (see Figure 4.74).
- At further downstream of the staging air ports, *GLACIER* showed higher soot volume fraction by a factor of 40 than the measurements.

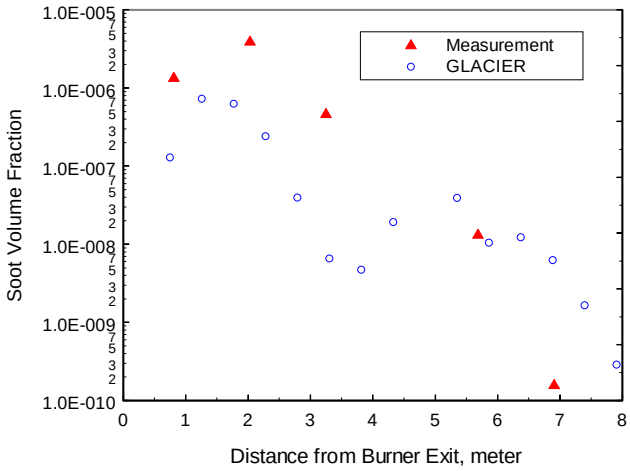


**Figure 4.73. Comparison of the predicted soot volume fraction with the measurements along the centerline of the furnace for Case1 (burner stoichiometry of 0.75).**

Figure 4.74 illustrates the radial distribution of soot volume fraction at 3.25 meters from the burner exit and at various distances from the furnace floor for both simulations and measurements for Case 1 (burner stoichiometry of 0.75).

- Both prediction and measurement show a non-uniform distribution of soot. This may have resulted from a flow recirculation in the furnace. *GLACIER* over-predicted soot concentration at a region close to the side wall by a factor of 3, but under-predicted the soot concentration at a region close to the opposite side wall.
- The highest predicted soot volume fraction existed at a region close to the side walls, which had been found in the measurements. This may be a result of the burner swirl or re-circulation patterns within the furnace.
- The vertical soot distribution showed peak soot concentrations at the center in both calculation and measurement. In measurements, the top section (0.8 meter from the furnace floor) had lower soot volume fraction than the bottom section (0.24 meter from the furnace floor). However, the model showed the opposite trend with higher soot concentration at the top section.

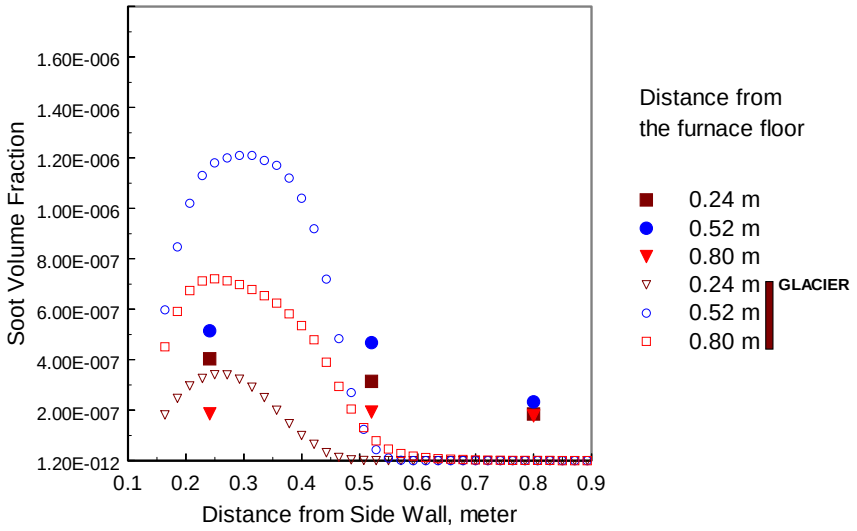


**Figure 4.74. Comparison of the predicted soot volume fraction with the measurements as a function of the radial distance from the side wall of the furnace for Case 1 (burner stoichiometry of 0.75).**

Figure 4.75a shows the impact of burner stoichiometry on soot volume fraction at 3.25 m downstream of the burner and NOx at the exit of the furnace. The measured soot volume fraction decreased with increasing burner stoichiometry due to increasing oxygen availability for soot destruction (oxidation). Generally, NOx is expected to decrease as air staging percentage is increased (decreasing burner stoichiometry). This was confirmed by the measurements as shown in Figure 4.75a. The calculation also captured this trend as shown in Figure 4.75b, which plots the calculated soot volume fraction as a function of exit NOx. Corresponding measurements are also shown in the figure. The predictions showed good agreement with the measurements.

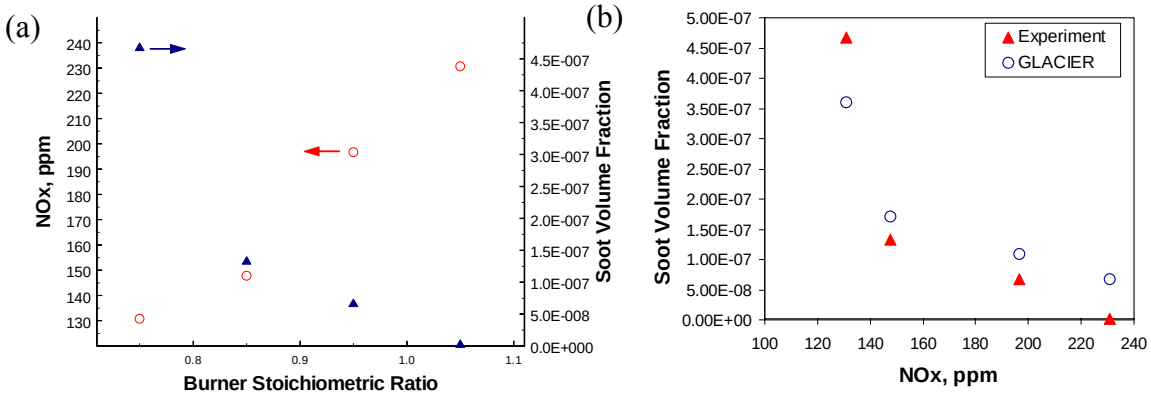


**Figure 4.75. (a) Measured NOx at the exit of the furnace and soot volume fraction at 3.25 meters from the burner exit as a function of burner stoichiometric ratio; (b) Soot volume fraction at 3.25 meters from the burner exit as a function of exit NOx (ppm).**

Overall, agreement between the predictions and measurements is considered to be very good. The soot model was able to predict the right trend as a function of axial distance from the burner exit. The radial distribution showed an asymmetric nature that was slightly exaggerated in the model. The predicted impact of burner operating conditions on soot concentration was also in good agreement with the experimental measurements.

More computational simulations of the L-1500 were performed for the purpose of better understanding the impact of the location of staged air injection on soot formation/destruction. The residence time from fuel injection to OFA injection in a utility boiler can vary depending upon a number of factors including the relative importance of NOx reduction vs. fuel conversion efficiency (as determined by CO emissions or carbon-in-fly ash) and structural constraints (such as boiler size, the location of backstays, and the location of division- or wing- walls). Two cases with different OFA locations, 3.25 (OFA 3) and 10.5 (OFA 9) meters from the burner exit (residence times from 2 to 12 seconds) were simulated. Operating conditions and coal properties (Illinois #5) are shown in the Table 4.11. The backside furnace wall temperature and inlet temperature for coal/air were set to 350 K and 300 K, respectively.

**Table 4.11. Pilot-scale test furnace operating conditions and coal properties.**

| | OFA3 & 9 | | Illinois #5 |
|---|---|---|---|
| Burner Stoichiometric Ratio | 0.85 | | As Received [%] |
| Overall Stoichiometric Ratio | 1.15 | C | 65.99 |
| Primary air flow rate [lb/hr] | 473 | H | 3.97 |
| Secondary air flow rate [lb/hr] | 700 | O | 8.47 |
| Tertiary air flow rate [lb/hr] | 1,392 | N | 1.29 |
| Staging air flow rate [lb/hr] | 929 | S | 3.49 |
| Coal feeding rate [lb/hr] | 345 | Ash | 9.87 |
| Coal firing rate [MMBTU/hr] | 4.01 | Moisture | 6.92 |

Selected OFA 3 simulation results are shown in Figure 4.76. As coal-off gases including tar evolve near the burner, soot also starts to form from tar resulting in increase in soot volume fraction and soot number density, as shown in the figure. At the same time, oxidation process reduces tar and soot concentrations. At around the staging port, there is nearly complete combustion of soot due to increased oxygen availability.

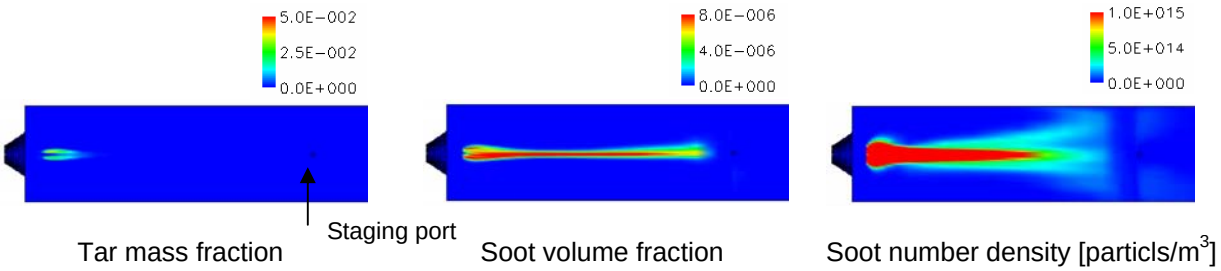


**Figure 4.76. Calculated tar mass fraction, soot volume fraction, and soot number density at center Cross-section of the furnace for OFA 3 case.**

Figure 4.77 shows soot volume fraction and oxygen concentration as a function of distance from burner exit. The maximum soot volume fraction occurs at about 1 m from the burner exit for all cases. After the peak, there is a rapid reduction of soot volume fraction. The rate of soot reduction slows down as the oxygen level goes to zero at about 2 meter from the burner exit. OFA 3 case shows nearly complete soot burnout close to the staging port. OFA 9 case shows relatively high soot volume fraction at the upstream of the staging port, as there is no available oxygen to oxidize soot. In addition, soot volume fraction slowly increases and number density decreases (not shown in the figure) as agglomeration of soot particles occurs at the upstream of the staging port. Complete soot burnout does not occur in the OFA 9 case, possibly due to lower gas temperature and high soot concentration to be removed.

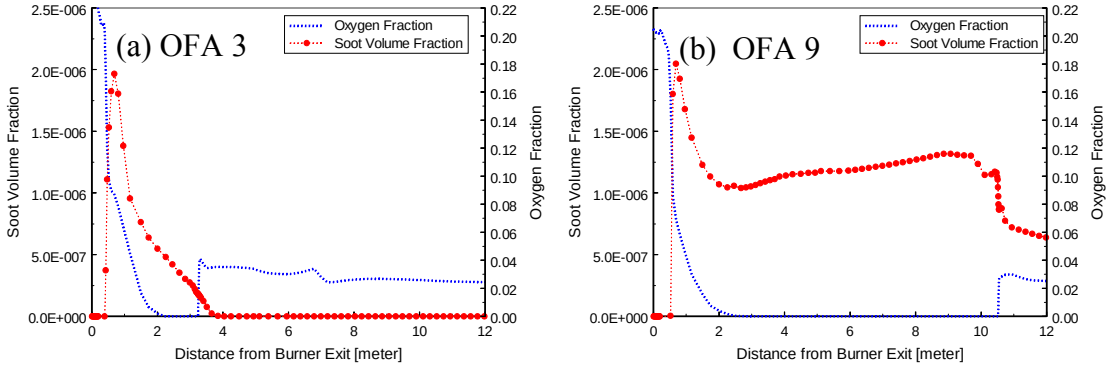


**Figure 4.77. Average soot volume fraction and oxygen Fraction as a function of distance from burner exit for three different OFA locations: (a) 3.25 meter and (b) 10.5 meter from the burner exit.**

Competing nature of two processes, soot formation and destruction can be clearly seen in the above results. Near the burner, there is significant soot formation from the coal off-gas. After reaching a peak, the soot volume decreases due to oxidation (destruction) of the soot. However, as the available oxygen is consumed, the net destruction of soot slows. Eventually, there is no available oxygen and the net production of soot again increases. Downstream of the air staging port, the model predicts a rapid oxidation of soot. The impact of different staging port location seems to be significant in determining soot concentration in flue gas. The two cases studied employed a wide range of residence times, 2 ~ 12 seconds from fuel injection to over-fire air injection. As shown in Figure 4.77, increased residence time may cause inefficient soot burnout at the staging port and result in a relatively high soot concentration in the flue gas. Even though the residence time in the OFA 9 case is long (12 seconds), this result has important practical implications in a boiler. Streamlines beginning in lower burner elevations can involve multiple recirculations in the rich lower regions of a furnace that has undergone combustion modifications for $NO_x$ control.

### 4.2.2.3 Full-Scale Simulations

The boiler simulated is an 800 MW front- and rear-wall-fired unit with 16 single register B&W low $NO_x$ burners in four elevations and four columns at each wall and an overfire air system. Computational mesh generated for the unit is shown in Figure 4.78. Top row burners

at each wall are out of service. 6 $NO_x$ ports at the front wall and 5 at the rear wall are used to introduce staged air at the same elevation. The exit of the model was at the horizontal nose plane of the furnace. Three levels of air staging were simulated with a fixed overall stoichiometry of 1.165 and a fixed firing rate of 7,800 MMBtu/hr to evaluate the impacts of staging level on soot formation. The burner stoichiometric ratios and air splits of each parametric case are shown in Table 4.12. In Param1, the burner was staged deeply using a burner stoichiometric ratio of 0.7. In Param2, burner stoichiometry was increased from 1.067 of Base to 1.118 and $NO_x$ ports were not used for air injection. Though soot measurements are not available for the unit, the boiler operators have reported soot problems in the stack with Base operating condition.

**Table 4.12. Operating conditions for the full-scale CFD simulations.**

| | Base | Param1 | Param2 |
|---|---|---|---|
| Overal SR* | 1.165 | 1.165 | 1.165 |
| Burner SR | 1.067 | 0.7 | 1.118 |
| ***Air distribution:*** BOOS# | 4.0% | 4.0% | 4.0% |
| NOx ports | 4.4% | 35.9% | 0.0% |
| Burner | 91.6% | 60.1% | 96.0% |

* SR = stoichiometric ratio

# BOOS = Burner Out Of Service, top row burner

The standard fuel fired in this unit is a blend of McElory and Cumberland bituminous coals with a grind of 99% through 50 mesh and 75% through 200 mesh. Table 4.13 summarizes the properties of these fuels.

**Table 4.13. Fuel properties for coal as used in the full-scale CFD simulations.**

| Ultimate Analysis | | Proximate Analysis | |
|---|---|---|---|
| C | 67.3% | Volatiles | 30.8% |
| H | 4.2% | Fixed Carbon | 50.6% |
| O | 5.6% | Moisture | 7.0% |
| N | 0.8% | Ash | 11.6% |
| S | 3.6% | HHV (Btu/lb) | 12158.8 |
| Ash | 11.6% | | |
| $H_2O$ | 7.0% | | |

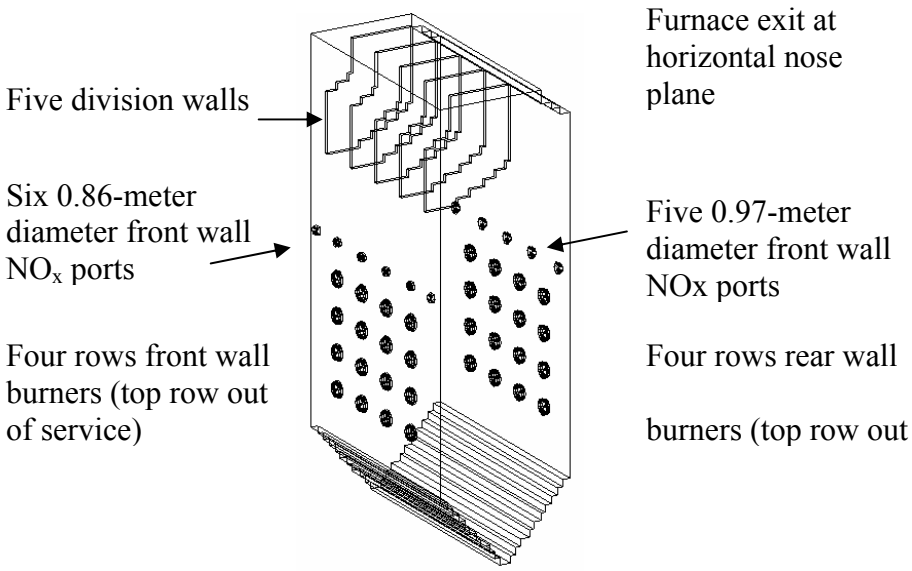


**Figure 4.78. Computational mesh generated for an 800 MW pulverized coal-fired unit.**

Table 4.14 summarizes the full-scale CFD simulation results. The effects of air staging were generally positive. As the burner was staged more deeply in Param1, the $NO_x$ emission was reduced 34 % reduction from Base. In Param2, with no air staging, the $NO_x$ increased by 9 % from Base. In Param1, CO and LOI were also reduced by 68 % and 17 %, respectively. In Param2, CO and LOI decreased by 35 % and 35 %, respectively. Figure 4.79 illustrates $NO_x$ generation rate as a function of the distance from the bottom of hopper for three cases. Deeply staged Param1 showed lowest the $NO_x$ generation rate. The case with no air staging (Param2) showed the highest $NO_x$ generation rate, resulting in high $NO_x$ concentration at the exit.

**Table 4.14. Full-scale CFD simulation results.**

| | Base | Param1 | Param2 |
|---|---|---|---|
| NOx (ppm at 3% $O_2$ dry) | 336 | 221 | 367 |
| LOI (%) | 7.9 | 6.6 | 5.1 |
| CO (ppm, dry) | 3,695 | 1,170 | 2,400 |
| Exit Temperature (K) | 1,516 | 1,561 | 1,513 |

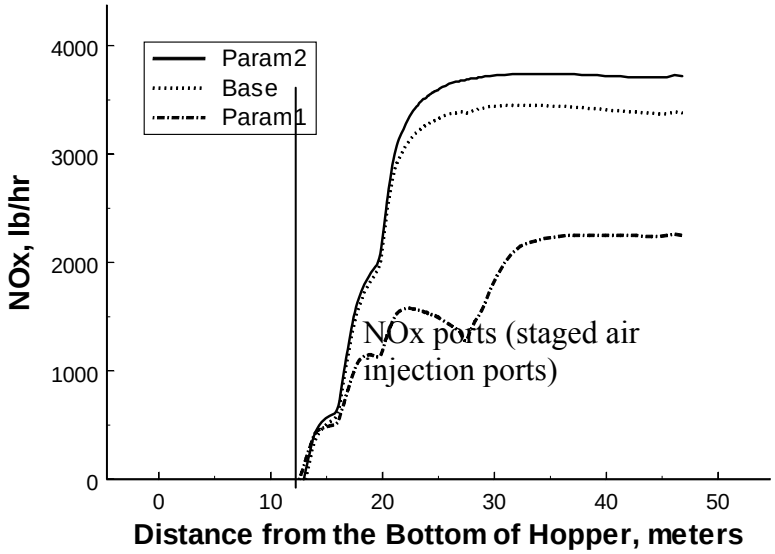


**Figure 4.79. $NO_x$, lb/hr as a function of distance from the bottom of hopper for three cases.**

Figure 4.80 shows the average soot volume fraction and equivalence ratio as a function of the distance from the bottom of hopper. High soot concentration occurs at fuel rich conditions (equivalence ratio > 1.0) near the burners. The model shows that even at the stoichiometric or fuel-lean condition (overall), soot particles are not fully oxidized or destroyed and those soot particles will end up in flue gas. This can be explained by a limited mixing between fuel and air and resulting oxygen deficient condition in the system, which prevents soot destruction and facilitates soot growth/agglomeration. Figure 4.81 shows the predicted average soot volume fraction for three cases as a function of distance from the bottom of hopper. The figure shows the general trend that the deeper the staging, the more soot is formed. Additional air introduction in Base and Param1 beyond the firing zone and overall fuel-lean condition in Param2 were not enough to burn out soot particles due to limited mixing. Predicted average soot particle sizes at the exit were also increased as shown in Figure 4.81. The average soot particle size in Param1 is over 1 μm in diameter possibly due to long residence time under fuel-rich condition resulting in extensive soot growth and agglomeration (the model does not distinguish between single soot particles and agglomerated particles). Figure 4.82 illustrates the profiles of soot volume fraction and oxygen concentration at the exit plane of the furnace. It can be clearly seen that the local oxygen deficiency prohibits complete burn out of soot particles even at high temperature (exit temperature for all three cases > 1500 K). In addition, the decreasing gas temperature beyond the nose of the furnace and at the heat transfer sections will make it difficult to achieve further oxidation of soot particles. Therefore, those soot particles at the nose plane shown in Figure 4.81 and 4.82 have a high potential to remain in flue gas.

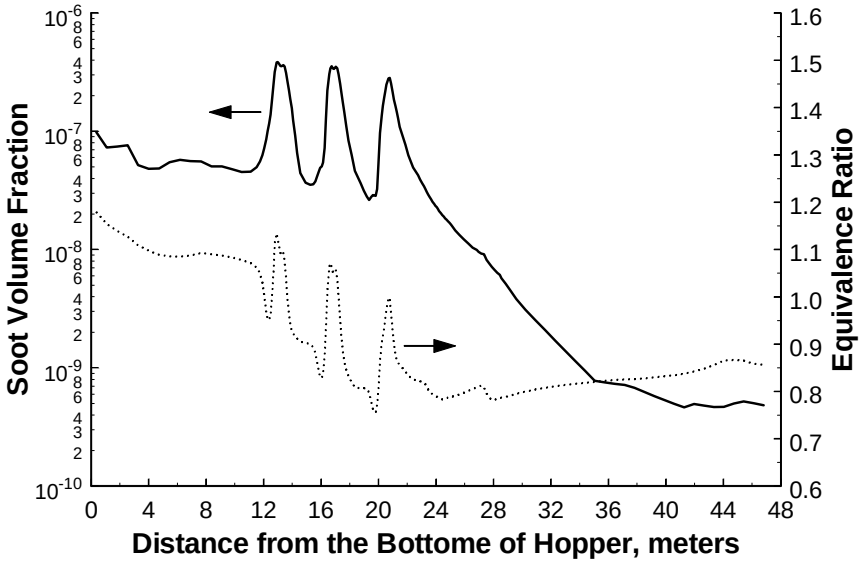


**Figure 4.80. Soot volume fraction and equivalence ratio as a function of distance from the bottom of the hopper for Base.**

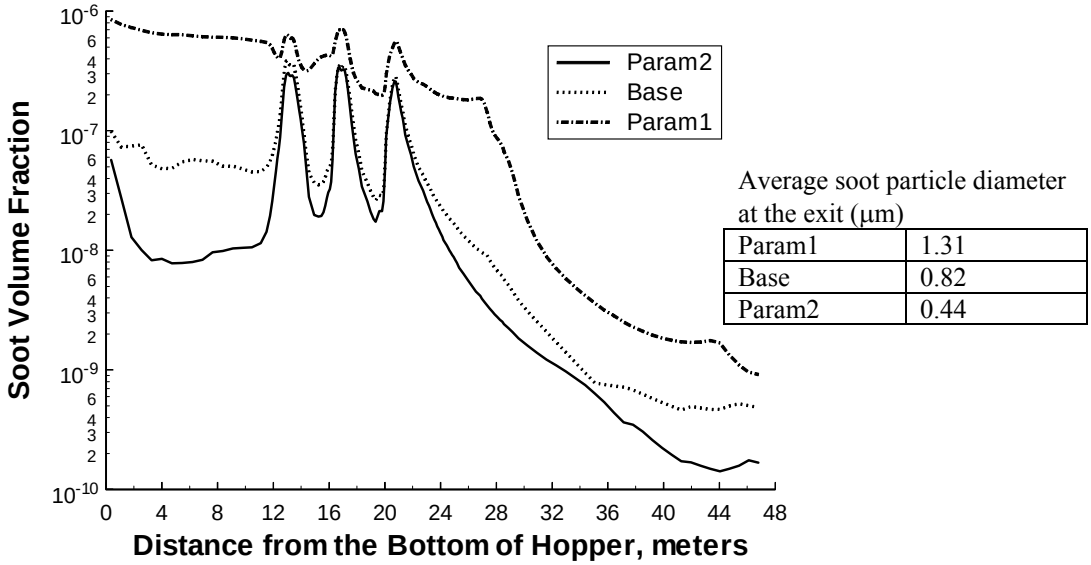


Average soot particle diameter at the exit (μm)

| | |
|---|---|
| Param1 | 1.31 |
| Base | 0.82 |
| Param2 | 0.44 |

**Figure 4.81. Soot volume fraction as a function of distance from the bottom of hopper for three cases. Predicted soot particle diameters at the exit are also shown.**

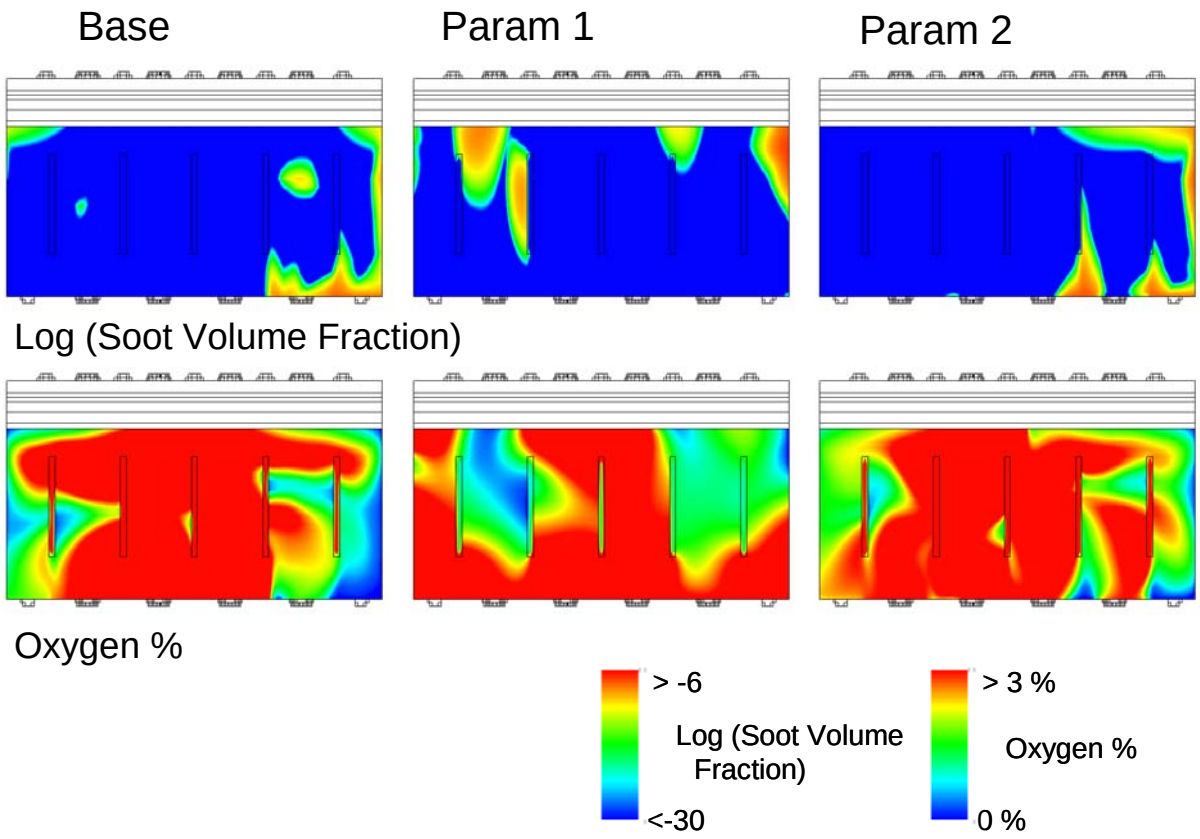


**Figure 4.82. Soot volume fraction and oxygen concentration at the exit plane for Base, Param 1, and Param 2.**

### *4.2.3 Summary*

Comparisons of the predicted and measured soot values for the pilot- scale test furnace and the results of our full scale boiler simulations highlight the potential impacts of burner operating conditions on soot and $NO_x$ generation within a coal fired utility boiler:

- An advanced soot model (tailored for coal combustion) implemented in *GLACIER* showed good agreement with the measurements in a pilot-scale application.
- The impact of burner stoichiometry and OFA location can be significant on soot formation/destruction as well as $NO_x$ emissions. Reducing condition formed by burner staging at the lower furnace will increase the formation of soot while limiting NOx generation.
- The results of full-scale application show limited mixing in the system can cause inefficient destruction of soot in the upper furnace even at high temperatures (> 1500 K) resulting in potential soot emission in flue gas.
- The level of detail provided by the simulations can be a valuable aid in understanding the mechanisms by which combustion modifications affect soot formation/destruction and $NO_x$ emissions.

## 4.3 References


Adams, B. R., "Computational evaluation of mechanisms affecting radiation in gas and coal fired industrial furnaces," Ph.D. Dissertation, Department of Mechanical Engineering, University of Utah, 1993.

Adams, B. R., and Smith, P. J., "Three-Dimensional discrete-ordinates modeling of radiative transfer in a geometrically complex furnace," Combust. Sci. and Tech., 88, 293, 1993.

Adams, B. R., and Smith, P. J., "Modeling effects of soot and turbulence-radiation coupling on radiative transfer in turbulent gaseous combustion," Combust. Sci. and Tech., 109, 121 1995.

Bakker, W.T., Mok, W.Y. and Cox, W.M., "High-Temperature Fireside Corrosion Monitoring in the Superheater Section of a Pulverized-Coal-Fired Boiler." EPRI, Palo Alto CA: 1992. TR-101799.

Bakker, W., *Waterwall Wastage in Low NOx Boilers, Root Causes and Remedies*, EPRI Report TR111155, 1998.

Baxter, L.L., Department of Chemical Engineering, Brigham Young University, Provo, UT, unpublished, 1987.

Brown, A.L. "Modeling Soot in Pulverized Coal Flames", M.S. Thesis (Mechanical Engineering), Brigham Young University, Provo, UT, 1997.

Brown, A.L.;Fletcher, T.H. *Energy Fuels* **1998**, 12, 745-757.

Cottis, R., and Turgoose, S., "Electrochemical Impedance and Noise," in Corrosion Testing Made Easy, Barry C. Syrett, Series Editor, NACE International, 1999.

Crowe, C. T., Sharma, M.D., and Stock, D.E., "The Particle-Source-in-Cell (PSI-Cell) Model for Gas-Droplet Flows," *Journal of Fluids Engineering*, **99**, pp. 325-332, 1977.

Eden, D. A., Hladky, K, John, D. G., and Dawson, J. L., Corrosion 86, Paper 274, NACE 1986.

Fletcher, T. H. and Hardesty, D. R., Compilation of Sandia Coal Devolatization Data: Milestone Report Sandia Technical Report, 1992.

Fletcher, T.H.;Kerstein, A.R.;Pugmire, R.J.;Solum, M.S.;Grant, D.M. *Energy Fuels* **1992**, *6*, 414-431

Genetti, D.B., Fletcher, T.H., Pugmire, R.J. *Energy Fuels* **1999**, *13(1)*, 60-68.

Hladky, K., US Patent 4575678.

Launder, B.E., and Spalding, D.B., Mathematical Models of Turbulence, Academic Press, London, England, 1972.

Mansfeld, F., and Xiao, H., *J. Electrochem. Soc.,* Vol. 141, p. 1403, 1994.

Mitchell, R. E., Hurt, R. H., Baxter, L. L., and Hardesty, D. R., Compilation of Sandia Coal Char Combustion Data and Kinetic Analyses: Milestone Report Sandia Technical Report, 1991.

Moosmuller, H, Arnott, W.P., Rogers, C.F., Chow, J.C., Frazier, C.A., Sherman, L.E., Dietrich, D.L. *Journal of Geophysical Research* **1998,** *103*, 28149-28157.

Smith, P.J., 3-D *Turbulent Particle Dispersion Submodel Development* (*Quarterly Progress Report #4*), Department of Energy, Pittsburgh Energy Technology Center, Pittsburgh, PA, 1992.

Smith, P.J. and Fletcher, T.H., "A Study of Two Chemical Reaction Models in Turbulent Coal Combustion," Combust. Sci. Tech., 58, p. 59, 1988.

Smoot, L.D. and Smith, P.J., *Coal Combustion and Gasification*, Plenum Press, New York, 1985.

Srinivasachar, S. and Boni, A.A., "A kinetic model for pyrite transformations in a combustion environment," Fuel 68:829-836, 1989.

Speziale, C.G., "On Nonlinear k-l and k- Models of Turbulence," Journal of Fluid Mechanics, 178, pp. 459-475, 1987.

Syrett, B. C., and Cox, W. M., "A Review of EPRI Projects Since 1984 that Used Electrochemical Noise Instrumentation," in Electrochemical Noise Measurement for Corrosion Applications STP 1277, Jeffrey R. Kearns, John R. Scully, Pierre R. Roberge, David L. Reichert, and John Dawson, Eds., ASTM, 173-185, 1996.

Tan, Y. J., Bailey, S., and Kinsella, B., *Corros. Sci.* vol. 38, p. 1681, 1996.

Ubhayakar, S.K., Stickler, D.B, Von Rosenberg, C.W., and Gannon, R.E., "Rapid Devolatilization of Pulverized Coal in Hot Combustion Gases," 16th Symposium (International) on Combustion, The Combustion Institute, Pittsburg, PA, p. 427, 1976.

Veranth, J.M., Fletcher, T.H., Pershing, D.W., Sarofim, A.F. *Fuel* **2000**, *79*, 1067-1075.

# 5. SCR Catalyst Testing

Selective catalytic reduction (SCR) represents the only commercially proven technology capable of achieving the relatively large $NO_x$ reductions required to comply with the latest (amended) Clean Air Act requirements. SCR systems are being installed in most large-scale utility boilers. However, most long-term experience with SCR comes from Germany and Japan and most of this is based on high-rank coal combustion. Less experience with low-rank, subbituminous coals specifically Powder River Basin coals, appears in the literature. The literature also provides essentially no US and little foreign experience with systems co-fired with biomass. The purpose of this task is to provide both laboratory and field slipstream data and analyses, including computer models that fill this information gap.

Within this task there are for principal sub-tasks:

1. technology assessment and fundamental analysis of chemical poisoning of SCR catalysts by alkali and alkaline earth materials;
2. evaluation of commercial catalysts in a continuous flow system that simulates commercial operation;
3. evaluating the effectiveness of catalyst regeneration; and
4. develop a model of deactivation of SCR catalysts suitable for use in a CFD code.

Items 1 and 3 were principally performed at Brigham Young University (BYU) under the direction of Profs. Larry Baxter, Calvin Bartholomew, and William Hecker. The work effort for items 2 and 4 was performed by REI, with assistance from the University of Utah and BYU.

## *5.1 Technology Assessment/Fundamental Analysis*

### *5.1.1 Introduction*

Many techniques have been developed to reduce $NO_x$ emission from fuel combustion processes in response to increasingly stringent regulations. Current major $NO_x$ control technologies for boilers includes:

- Low-$NO_x$ burners (LNB)
- Overfire air (OFA)
- Reburning
- Selective non-catalytic reduction (SNCR)
- Selective catalytic reduction (SCR)

The first three technologies involve modifying combustion in the boiler, whereas the latter two are post-combustion processes that are applied to the flue gas. Combustion modification technologies are relatively inexpensive, but alone they cannot achieve the $NO_x$ reduction required by current emission standards. For that purpose, post-combustion technologies must be applied. Between the two technologies, SCR is the predominant post-combustion technology because of its high efficiency.

Selective catalytic reduction (SCR) represents the leading technology capable of highly efficient $NO_x$ reduction from stationary sources such as power plants. SCR uses $NH_3$ to reduce $NO_x$ over a vanadia-based catalyst. A major advantage of SCR is that the reaction products, nitrogen and water, are innocuous compounds already present in the air (DOE, 2005). The process is termed selective reduction because it reduces only $NO_x$ compounds and not carbon-, sulfur-, or other oxygen-containing compounds.

The results of Clean Coal Demonstration Technology Program (CCDTP) project from Department of Energy (DOE) confirmed the applicability of SCR for U.S. coal-fired power plants. A significant number of commercial SCR units have been installed and are operating successfully in the United States. By 2007, the total installed SCR capacity on U.S. coal-fired units will number about 200, representing about 100,000 MWe of electric generating capacity or x% and y% of total units and capacity, respectively.

The most common SCR process for coal-fired power plants in the US is the high-dust (HD) configuration, in which the SCR catalyst is upstream of the precipitator or other particle collection devices and processes the full dust loading leaving the boiler. HD configuration may cause serious catalyst deactivation problems, especially for low-rank coals and biomass that contain both high alkali (mainly sodium and potassium) and alkaline earth (mainly calcium) concentrations. Alkali and alkaline earth materials contribute to both fouling and possibly chemical poisoning of catalysts.

In spite of many investigations, mechanisms of vanadia/titania catalysis and deactivation during SCR applications remain uncertain. The consensus opinion indicates that vanadium catalytic activity correlates with acid site concentration on the catalyst surface. However, it is not clear which of the two principal types of acid sites on the catalyst surface, Lewis or Brønsted sites, provides the catalytic properties. Furthermore, much of the laboratory analysis on such catalysts uses $SO_2$-free gases, representing most situations of natural gas firing, even though SCR catalysts are known to at least partially sulfate and to actively promote $SO_2$ to $SO_3$ reactions. As for catalyst deactivation, Siemens (2000) and Pritchard et al. (1995) among others, investigated different deactivation mechanisms. This previous work indicates that inorganic material from fly ash may cause fouling, masking, and poisoning to the catalysts. The relative importance of these different mechanisms for different coal and biomass fly ash streams is unclear. The present work focuses on poisoning of SCR catalysts by fly ash inorganic material and the effects of $SO_2$ interactions with the catalysts. The results of this work will present an improved understanding of poisoning, deactivation, and sulfation that provides new information needed to understand and manage commercial SCR systems.

### *5.1.2 Literature Review*

The literature review below first briefly summarizes the background of SCR, and then discusses current investigations of the effects of $SO_2$ interaction with catalysts and catalyst deactivation.

#### 5.1.2.1 Background of SCR and SCR catalysts

##### 5.1.2.1.1 SCR Chemistry

The SCR process consists of injecting ammonia ($NH_3$) into boiler flue gas and passing the flue gas through a catalyst bed where the $NO_x$ and $NH_3$ react to form nitrogen and water vapor (DOE, 2005).

In the SCR process, ammonia, the reductant, is injected into the flue gas to reduce $NO_x$ and form $N_2$ and water at 300-400 ˚C, near atmospheric pressure, with high selectivity. Two overall stoichiometric reactions of $NO_x$ reduced by $NH_3$ are (Busca et al., 1998):

$$4NH_3 + 4NO + O_2 \rightarrow 4N_2 + 6H_2O \quad (5\text{-}1)$$

$$4NH_3 + 2NO_2 + O2 \rightarrow 3N_2 + 6H_2O \quad (5\text{-}2)$$

More water is produced than molecular nitrogen in each of these reactions. Janssen et al. (Farrauto and Bartholomew, 1997) conducted isotopic labeling experiments with $^{15}NH_3$, NO and $^{18}O_2$ confirming that the two atoms in the product $N_2$ are from $NH_3$ and NO separately.

In high-temperature systems such as pc and pc-biomass cofiring, only enough ammonia is supplied for the first reaction to do the conversion and the dominant form of $NO_x$ is NO.

Side reactions also occur and produce the highly undesirable products $N_2O$ and $SO_3$, as follows.

$$4NH_3 + 4NO + 3O_2 \rightarrow 4N_2O + 6H_2O \quad (5\text{-}3)$$

$$SO_2 + \tfrac{1}{2}O_2 \rightarrow SO_3 \quad (5\text{-}4)$$

Moreover, when the temperature increases above about 350 °C, $NH_3$ reacts with oxygen rather than NO to form nitrogen and nitrogen oxides (Busca et al., 1998).

$$2NH_3 + \tfrac{3}{2}O_2 \rightarrow N_2 + 3H_2O \quad (5\text{-}5)$$

$$2NH_3 + 2O_2 \rightarrow N_2O + 3H_2O \quad (5\text{-}6)$$

$$2NH_3 + \tfrac{5}{2}O_2 \rightarrow 2NO + 3H_2O \quad (5\text{-}7)$$

#### 5.1.2.1.2 Reaction Kinetics

Reaction kinetics is important in modeling catalyst deactivation. A general global rate expression for the SCR reaction is $r = K_c C_{NO}^{\alpha} C_{NH3}^{\beta} C_{O2}^{\gamma} C_{H2O}^{\delta}$ (Busca et al., 1998). The reaction order, $\alpha$ with respect to NO is usually found to be 0.5~1.0, depending on reaction temperature and $NH_3$/NO molar ratio. Most authors report that ammonia concentration has no effect on reaction rate, meaning that $\beta \approx 0$, near stoichiometric conditions, that $\beta \approx 0.2$ when molar $NH_3$/NO ratio exceeds unity, and that $\beta \approx 1$ when the ammonia concentration is low (Wachs et al., 1996). During industrial vanadia catalysis, where $H_2O$ concentration is generally greater than 10 mole %, water negligibly impacts the kinetics, although there are reports of inhibiting effects of water (Wachs et al., 1996). Under practical conditions, oxygen is in excess; therefore $\gamma$ is usually taken as 0. In general, the kinetics of SCR reactions can be modeled with a simple rate expression $-r = K_C C_{NO}$, where the reaction rate is first order in NO and zero order in ammonia, water, and oxygen.

#### 5.1.2.1.3 $V_2O_5$—$WO_3$ ($MoO_3$) /$TiO_2$ catalyst

Vanadia catalytic activity in reducing NO was discovered in the 1960s, and its high activity when supported on $TiO_2$ was recognized in the 1970s (Forzatti, 2001). The original shapes for vanadia catalysts were pellets or spheres. Current technologies use honeycomb monoliths, plates and coated metal monoliths because of lower pressure drop, higher geometric surface area, attrition resistance, and low plugging tendency from fly ash relative to the other options (Forzatti and Lietti, 1996). Unfortunately, vanadia also catalyzes $SO_2$ oxidation to $SO_3$, the latter of which is a pollutant, highly corrosive, and can cause catalyst deactivation. $TiO_2$, however, only weakly and reversibly sulfates under SCR conditions. Also, $TiO_2$ promotion of vanadia catalytic activity makes titania a preferred support in comparison to other materials such as $Al_2O_3$ and $ZrO_2$. Tungsten or molybdenum is commonly added to SCR catalysts in quantities significantly higher than vanadium (9 to 1 molar ratios are common) to increase acidity, which is directly related to the activity, to increase the thermal stability of the catalyst, and to suppress $SO_2$ oxidation (Forzatti, 2001). In addition, Molybdenum is used to decrease arsenic poisoning from the exhaust gas (Forzatti, 2001).

Typically, commercial $V_2O_5$-$WO_3$/$TiO_2$ catalysts guarantee $NO_x$ reduction efficiencies close to or over 80%, with an ammonia slip (excess ammonia in the flue gas) of 1-5 ppm and $SO_2$ conversion to $SO_3$ lower than 1-2%. Therefore, commercial vanadia catalysts usually contain ~1% vanadia and ~9% tungsten/molybdenum (molar basis) on a titanium (anatase) substrate.

The operating temperature for $V_2O_5$-$WO_3$/$TiO_2$ catalysis varies from 550 K to 700 K. In some coal- and biomass-fired power plant applications, deactivation is a major problem for vanadia catalysts.

#### 5.1.2.1.4 Surface analysis of vanadia catalysts

Vanadia catalyst surface chemistry provides some critical information to understand SCR reaction and deactivation mechanisms. The current project focuses on further developing this understanding through surface analysis and identification of surface components and structures.

*Surface structure of vanadia/titania*

Vanadia species exist on catalyst surfaces in three phases: isolated monomeric vanadyl (V=O) species, polymeric vanadate species (polymeric chain of isolated vanadyl species), and crystalline vanadia $V_2O_5$. Went proposed structures of monomeric and polymeric vanadia species based on Raman and NMR investigations as appear in Figure 5.1 (Went et al., 1992a).

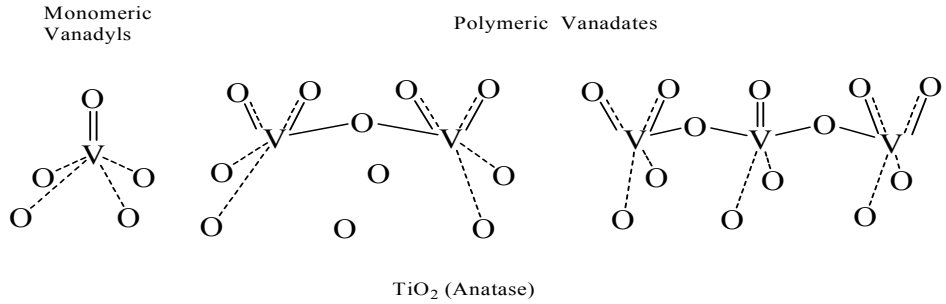


**Figure 5.1. Schematic depicting structure of the monomeric vanadyl and polymeric vanadate species on anatase $TiO_2$ (Went et al., 1992a).**

Under monolayer coverage (the maximum amount of amorphous or two-dimensional vanadia in contact with the oxide support (Reddy et al., 1999)), both monomeric vanadyl and polymeric vanadate species appear on the catalyst surface, with monomeric vanadyl species dominant on lightly loaded (e.g. 1.3%) catalyst surfaces (Topsøe et al., 1995; Went et al., 1992b). Monomeric vanadyl species could transform to polymeric vanadate species with increasing vanadia content (up to 6%) by breaking M-O-V bonds to form V-O-V bonds (Dunn et al., 1998a). Crystalline vanadia species form from polymeric vanadate species only when the loading exceeds the monolayer capacity (about 6%) (Went et al., 1992a, Dunn et al., 1998a). It is important to note that commercial catalysts are made from $TiO_2$/$V_2O_5$/inhibitor mixtures, not by surface coating $V_2O_5$ on the surface of a $TiO_2$ substrate.

*Active sites identification*

*Active sites investigation based on structures*

Polyvanadate reportedly has higher SCR activity than monomeric vanadyl (Went et al., 1992b; Lietti et al., 1998; Lietti and Forzatti, 1994). The group of V-O-support may also provide the active center (Wachs and Weckhuysen, 1997). Crystalline $V_2O_5$ oxidizes $NH_3$ at high temperatures (Ozkan et al., 1994; Choo et al., 2000). A dual-site mechanism involving a surface vanadia redox site and an adjacent surface non-reducible metal oxide site has been suggested as well (Wachs et al., 1996; Topsøe et al., 1995).

*Active sites investigation based acid sites*

Both Lewis and Brønsted acid sites exist on vanadia/titania catalyst surfaces. The V-OH bond appears to be directly related to Brønsted acid sites (Topsøe et al., 1995), while the V=O bond forms a Lewis acid site that can convert to V-OH by water adsorption (Busca et al., 1998). Therefore monomeric vanadyl and polymeric vanadate species (Figure 5.1) could provide both Lewis and Brønsted acid sites. No acidity assignment for the V-O-site appears in the literature thus far. Both Brønsted acid sites (Topsøe et al., 1995; Chen and Yang, 1990) and Lewis acid sites (Went et al., 1992b; Lietti et al., 1998; Centeno et al., 2001) reportedly form active centers for SCR catalysis. Convincing evidence supports each argument, as will be discussed later in the reaction mechanism section.

There is no general consensus regarding the identity of the active sites on vanadium-based SCR catalysts from the view of either vanadia surface structures or the acid sites. The $NH_3$, NO, and $NH_3$/NO surface adsorption and spectroscopy investigations planned as part of this investigation may resolve some of the confusion on this issue. Related investigations recorded in the literature are reviewed here.

*$NH_3$ adsorption*

$NH_3$, the reductant of $NO_x$ in the SCR reaction, demonstrates strong adsorption-desorption behavior on both titania and vanadia catalysts observed by Fourier-transform infrared (FTIR) spectroscopy, laser Raman spectroscopy (LRS), temperature programmed desorption (TPD), and transient response investigations, as discussed below.

*FTIR and Raman study summaries*

The following list summarizes generally accepted results from FTIR spectroscopy and LRS from the literature:

1. Ammonia adsorbs on both support titania and vanadia/titania catalysts at room temperature, with major associated adsorption bands on Brønsted acid sites at 1430 and 1670 $cm^{-1}$ and on Lewis acid sites at 1220 and 1605 $cm^{-1}$ (Went et al., 1992a; Topsøe et al., 1995; Chen and Yang, 1990; Ozkan et al., 1995).
2. Pure titania possesses only Lewis acid sites (Yang et al., 1998; Amiridis et al., 1996).
3. Vanadia/titania catalysts provide both Lewis and Brønsted acid sites, vanadia species introduce Brønsted acid sites on the catalyst surface (Topsøe et al., 1995).
4. Sulfate species enhance Lewis acid sites on pure titania, introduce Brønsted acid sites onto the sulfated titania surface (Yang et al., 1998), and may enhance the number and strength of acid sites on vanadia catalyst surfaces (Khodayari and Odenbrand, 2001).
5. Ammonia adsorbs on Lewis acid sites as coordinated ammonia and on Brønsted acid sites as protonated ammonia. $NH_3$ absorption is stronger on Lewis acid sites than on Brønsted acid sites (Topsøe et al., 1995).
6. $NH_3$ desorbs from SCR surfaces with increasing temperature and is practically removed above 300 ˚C (Topsøe, 1991).
7. Poisons ($Li_2O$, $Na_2O$, $K_2O$) interact primarily with Brønsted acid sties (Chen and Yang, 1990).

The following issues remain controversial or have not been thoroughly investigated:

1. The extent to which ammonia adsorbs on the SCR surface at reaction temperature, and
2. Whether sulfation of the surface increases the number of acid sites or strengthens the acidity of existing sites on SCR catalysts.

*TPD study summaries*

The following lists generally accepted results from TPD literature reviews:

1. Ammonia adsorbs on both titania and vanadia/titania catalyst surfaces (Went et al., 1992a ;Lietti and Forzatti, 1994; Srnak et al., 1992; Topsøe et al., 1992), consistent with the spectroscopic results.
2. Ammonia adsorbs stronger on Lewis acid sites than on Brønsted acid sites (Went et al., 1992a ;Srnak et al., 1992; Topsøe et al., 1992), again consistent with the spectroscopic results.
3. Ammonia adsorption energy is about 18~26 kcal/mol (Srnak et al., 1992).
4. Multiple ammonia adsorption species exist on vanadia/titania catalyst surfaces but are not distinguishable from TPD profiles.
5. Poisons occupy strong acid sites on vanadia catalysts (Khodayari and Odenbrand, 2001; Lisi et al., 2004). This disagrees with spectroscopy investigations since FITR spectroscopy analyses indicates poisons occupy Brønsted acid sites, which are weak acid sites relative to Lewis acid sites.

The following issues remain controversial or have not been thoroughly investigated:

1. Whether different peak temperatures observed in ammonia TPD profiles arise from different vanadia catalyst sites or are artifacts of preparation methods,
2. The effects of sulfate species on ammonia TPD profiles on titania and vanadia catalysts, and
3. The correlation between total acidity and SCR activity.

*NO adsorption*

The following are generally accepted results from FTIR spectroscopy analyses of NO adsorption:

1. NO adsorption occurs on both non-sulfated (Ozkan et al., 1994; Yang et al., 1998; Ramis et al., 1990) and sulfated titania (Yang et al., 1998), and on reduced vanadia catalyst at room temperature (Topsøe, 1991; Hadjiivanov, 2000).
2. NO adsorption does not occur on fully oxidized or $NH_3$ pre-adsorbed vanadia catalyst (Topsøe, 1991; Hadjiivanov, 2000).
3. Vanadium atoms with a lower oxidation state and Ti-OH sites represent possible adsorption centers for NO (Topsøe, 1991; Hadjiivanov, 2000).
4. NO adsorption reversibility increases on sulfated $TiO_2$ compared to bare $TiO_2$ (Yang et al., 1998).

The following issues have not been investigated:

1. The effect of alkali and alkaline earth metals on NO adsorption on either titania or vanadia catalyst.
2. The effect of sulfate on NO adsorption on vanadia catalysts.
3. NO TPD study on titania and vanadia catalysts.

In summary, ammonia adsorption and NO adsorption are well studied on sulfur- and poison-free titania and vanadia catalysts, whereas investigations regarding the effects of sulfate and poisons on ammonia and NO adsorption are inconclusive.

*$NH_3$ and NO coadsorption*

Several investigators document the behavior of $NH_3$ and NO coadsorption, which can elucidate the active center, structures of the active site, and the intermediate species.

The following generally accepted conclusions arise primarily from different responses of NO and $NH_3$ during coadsorption investigations.

a. An Eley-Rideal mechanism reasonably represents the SCR reaction involving a strongly adsorbed $NH_3$ and a gas-phase or weakly adsorbed NO molecule (Lietti et al., 1998).

b. Lietti et al. observed that more coordinated adsorbed ammonia is consumed than protonated $NH^{4+}$ during NO and $NH_3$ coadsorption (Lietti et al., 1998).

c. Centeno et al. found V=O has a redox property, and suggested a redox mechanism with V=O, a Lewis acid sites, as the active center for the SCR reaction (Centeno et al., 2001).

d. Topsøe et al observed both V-OH and V=O play an important role in the SCR catalytic cycle, and Brønsted acid site concentration directly correlates to NO conversion for a range of vanadia concentrations (0-6 wt %) (Topsøe et al., 1995). However, Topsøe's approach only measured protonated ammonia bands, not the coordinately-adsorbed ammonia bands which occur at 1300 $cm^{-1}$ as reported by Lietti et al (Lietti et al., 1998).

Thus, both Lewis and Brønsted acid sites have been reported to be the active center based on convincing evidence from various IR investigations. The disagreement upon the properties of active sites may arise from different sample preparation methods and materials applied, as well as different IR regions investigated. The effects of surface sulfate and alkali and alkaline earth metals on $NH_3$ and NO coadsorption behavior on titania and vanadia/titania acid site concentrations have not been reported.

#### 5.1.2.1.5 Proposed reaction mechanism

Based on the above investigations, different mechanisms appear in the literature with some points of agreement: (1) the active sites are acidic; (2) a redox reaction is involved in the mechanism; (3) an Eley-Rideal type reaction mechanisms appear important with $NH_3$ as the adsorbed species and NO as the gas-phase or weakly adsorbed species; and (4) V sites provide the active centers.

The disagreements include: (1) the nature of the acid sites – Lewis or Brønsted acids; and (2) the number of vanadia atoms involved – single or multiple atoms with reaction either on the vanadia or at the interface/terminal vanadia atom. Busca et al. provides a review of these suggested active sites and intermediates, as shown in Table 5.1 (Busca et al., 1998).

**Table 5.1. Proposed reactant species, intermediates and active sites in different mechanism from Busca et al. (1998).**

| Reactant species | | Intermediate | Catalyst | Supposed active site | Reference |
|---|---|---|---|---|---|
| From $NH_3$ | From NO | | | | |
| $NH_4^+$ | O-N-O<br>\| | | $V_2O_5$ | | Takagi et al. |
| $NH_4^+$ | NO gas | H-bonded complex | $V_2O_5$ | O OH<br>‖ \|<br>-O-V-O-V-O | Inomata et al. |
| $O\text{-}NH_2$<br>\|<br>V | NO gas | | $V_2O_5$/supp | O O<br>‖ ‖<br>-O-V-O-V-O | Janssen et al. |
| $NH_4^+$ | NO gas | | $V_2O_5$ | OH<br>\|<br>V + V-O-V | Gasior et al. |
| $NH_2$<br>\|<br>V | NO gas | $NH_2NO$<br>\|<br>V | $V_2O_5/TiO_2$ | O<br>‖<br>V | Ramis et al. |
| $NH_3$ads<br>$NH_2$ | $N_2O$ads<br>adsorbed NO | | $V_2O_5$/supp<br>$V_2O_5/TiO_2$ | Lewis sites | Maragonzis et al.<br>Went et al. |
| $O^-$ $H_3N^+$ HO<br>\| \|<br>V V | NO gas | $O^-{}^+H_3N\text{-}N{=}O$ HO<br>\| \|<br>V V | $V_2O_5/TiO_2$ | O HO<br>‖ \|<br>-V- -V- | Topsøe et al. 1993 |
| $NH_4^+$ | $O\text{-}NO_2$<br>\|<br>$V^{4+}$ | $NH_4NO_2$ | $V_2O_5/TiO_2$ | O<br>‖<br>$V^{5+}$ | Kantcheva et al. |
| $NH_4^+$ | $NO_3^-$ | | $V_2O_5/ZrO_2$ | | Indovina et al. |

The $DeNO_x$ catalytic cycle suggested by Topsøe based on *in situ* FTIR combined with on-line mass spectrometry investigations, as shown in Figure 5.2, is among the most accepted pathways for SCR catalysis (Topsøe et al., 1995). In this mechanism, $NH_3$ first adsorbs on V-OH, the Brønsted acid site, and acts in conjunction with an oxidation-state shift of the V=O site to reduce gas-phase NO.

In another mechanism scheme proposed by Ramis et al., shown in Figure 5.3, Lewis acid sites act as the active centers (Busca et al., 1998). Ammonia first adsorbs on V=O sites by interacting with V instead of O in the V=O bond. The adsorbed ammonia species reacts with gas-phase NO on V=O sites and produces $N_2$ and $H_2O$. Gas-phase oxygen then oxidizes the V=O site, preparing the site for another cycle of SCR reaction.

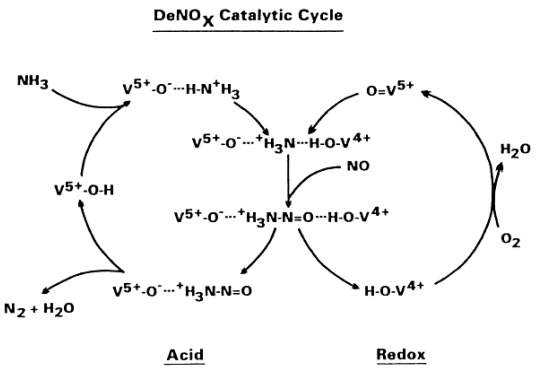


**Figure 5.2. Scheme illustrating the cycle of the SCR reaction over vanadia/titania catalyst by Topsøe et al. (1995).**

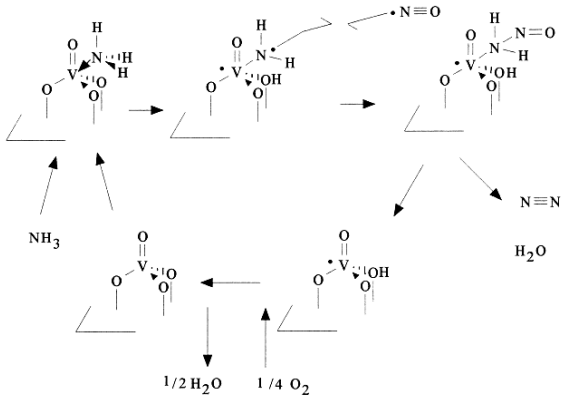


**Figure 5.3. Mechanism of the NO-$NH_3$ reaction on supported vanadium oxide catalyst proposed by Ramis and Busca (1990).**

Both mechanisms involve similar steps during the catalytic cycle. The difference is that Topsøe's mechanism involves two active sites, with Brønsted acid sites as the active center, while Ramis's mechanism only involves a single active site (V=O), which is a Lewis acid. Neither mechanism clarifies the role of the V-O-support during the SCR reaction, which has been suggested as the active center by Wachs et al. (1996). Therefore, there is no general agreement about the identity of the active center either from a structural perspective – whether V=O, V-OH, or V-O-support or some combination represents the active center – or from the acidity perspective – whether Lewis or Brønsted acid sites provide the active center.

Furthermore, most surface investigations involve non-sulfated surfaces. At least some of the surface sites sulfate under commercial SCR catalysis conditions with $SO_2$-laden gases, which would include essentially all coal-related applications. Such sulfation has a high likelihood of impacting surface reactions, activity, and poisoning.

### 5.1.2.2 Interactions with sulfur dioxide

$SO_2$ represents a major gas species in all coal-fired power stations. Prior to desulfurization units, $SO_2$ concentrations in coal-based power plant flue gas ranges from 0.03 to 0.4%. Sulfur dioxide appears in the effluent from the power plant and plays a dramatic role in the SCR process. It can increase SCR catalyst activity by increasing the number and strength of Brønsted acid sites (Khodayari and Odenbrand, 2001). On the other hand, sulfur trioxide, formed during oxidation of $SO_2$ catalyzed by the same vanadia catalysts, reacts with ammonia to form ammonia sulfate (white) and ammonia bisulfate (black and tar like, most corrosive) at temperatures lower than typical SCR reactions. Moreover, $SO_2$ and $SO_3$ react with free CaO or other alkaline earth compounds in the flue gas to produce $CaSO_4$ or other alkaline earth metal sulfates. These products introduce potentially serious deactivation- and corrosion-related problems for both the catalyst and other equipment.

Yang et al. indicate that the sulfate species on titania is probably $SO_4^{-2}$, since the observed peak in XPS spectra occurs at 168.5 eV, which is typical of $S^{+6}$ (Chen and Yang, 1993). This agrees with the analysis of Soo Tae Choo et al.(2000). TPD analyses show that sulfate species start to decompose thermally at about 800 K and are completely removed around 1073 K on both titania and vanadia catalysts (Lietti et al., 1998; Choo et al., 2000). In addition, R.T. Yang et al. propose two types of sulfate on the titania surface: bridge bidentate and chelating bidentate $SO_4^{-2}$, with bridged bidentate as the most prevalent form (Yang et al., 1998).

However, there is no general agreement about the site where sulfates form on vanadia catalysts. Orsenigo compared catalyst conditioning between $NO_x$ reduction and $SO_2$ oxidation and suggested that sulfation occurs first at vanadia sites, then on titania and tungsten sites (Orsenigo et al., 1998). But no further verification data were provided. Choo et al. pointed out from FTIR spectroscopy analysis that both vanadia and sulfate species compete for hydroxyl group sites on the catalyst surface (Choo et al., 2000). FTIR spectra from Dunn et al. (1998a) and Amiridis et al. (1996) show that the concentration of surface sulfate species (centered at 1373 $cm^{-1}$) decreases with increasing vanadia coverage on the catalyst supported on $TiO_2$, $ZrO_2$, or $Al_2O_3$.

To date, only a few investigations of sulfation have been conducted, and no *in situ* investigations appearing in the literature. The sulfation mechanism on the vanadia/titania surface is still uncertain. More importantly for practical systems and for this document, the effects of surface sulfates on catalyst BET surface area, NO adsorption-desorption, $NH_3$ TPD behavior, and catalytic activity do not appear in the literature. The effect of sulfate on catalyst deactivation by alkali and alkaline earth metals is still under debate. Conditions involving sulfur dioxide are common in industrial practice, including essentially all systems that involve coal combustion. Investigations of the sulfate effect on vanadia catalyst performance will provide additional critical information on the SCR reaction and deactivation mechanisms.

#### 5.1.2.3 Deactivation of Vanadia Catalysts

Catalyst deactivation is a normal function of aging. The mechanisms for deactivation are complex, and include fouling (surface deposition), pore condensation and/or blocking, poisoning, and thermal sintering, among others. Changes in system performance also occur as a result of monolith plugging by large ash particles often called popcorn ash. For a given situation, one or more of these mechanisms may be involved. All of them are functions of the nature and quantity of inorganic material in the coal, including compounds containing sodium, potassium, calcium, arsenic, and others. The degree of deactivation is more pronounced with lower rank fuels such as lignite or subbituminous coals, which generally contain larger amounts of alkali and alkaline earth material. Popcorn ash plugging of catalyst passages differs from the remaining mechanisms in that it generally involves no local changes in catalyst properties but rather system changes in flow patterns, although it creates the same observable changes in system behavior ($NO_x$ conversion reduction, etc.).

Deactivation is a major problem for vanadia catalysts in SCR applications. For example, the typical design lifetime of vanadia catalyst for coal-fired power plants is 3-5 years (Zheng et al., 2004). Some existing anecdotal evidence indicates that catalysts may deactivate 3-4 times faster in low-rank-coal-fired and biomass-coal-cofired boilers (Khodayari and Odenbrand, 2001). Poisoning, fouling, and thermal sintering are common categories of catalyst deactivation, and different mechanisms dominate in different SCR applications. For instance, sintering and rutilization (rutile formation) of titania after long-term operation is one of the major deactivation mechanisms during natural gas firing, while poisoning of the catalyst active sites by alkali metals is significant in oil firing (Pritchard et al., 1995). In the case of coal firing and bio-fuel applications, plugging, fouling and poisoning are probable deactivation mechanisms. Table 5.2 summarizes different major deactivation mechanisms for different fuels. Table 5.3 identifies some of the major differences between commercially important coals and biomass in the US. The great majority of SCR experience is with bituminous coals. These fuels pose the fewest deactivation risks to vanadium-based catalysts. Figure 5.4 illustrates several general mechanisms of poisoning, fouling, and plugging.

**Table 5.2. Deactivation mechanism related to fuel types.**

| Fuel type | Main deactivation | Deactivation substance |
|---|---|---|
| Coal | Fouling | Sub-micron ash particle |
| Biomass | Poisoning | Soluble Alkali(K) compounds |
| Oil | Poisoning | Soluble Alkali (K, Na) compounds |
| Gas | Sintering | |
| Waste incineration | Poisoning | Lead compounds |

**Table 5.3. Difference between different coals in US.**

| Constituent | Bituminous coal | Subbituminous (including PRB) coal | Biomass |
|---|---|---|---|
| Sulfur | High | Intermediate | Low |
| Arsenic | Intermediate | Intermediate | Varies |
| Active Alkali Compounds | Low | High, especially Na | High, especially K. |
| Active Alkaline Earth Compounds | Low | High, especially Ca | Intermediate, generally Ca |

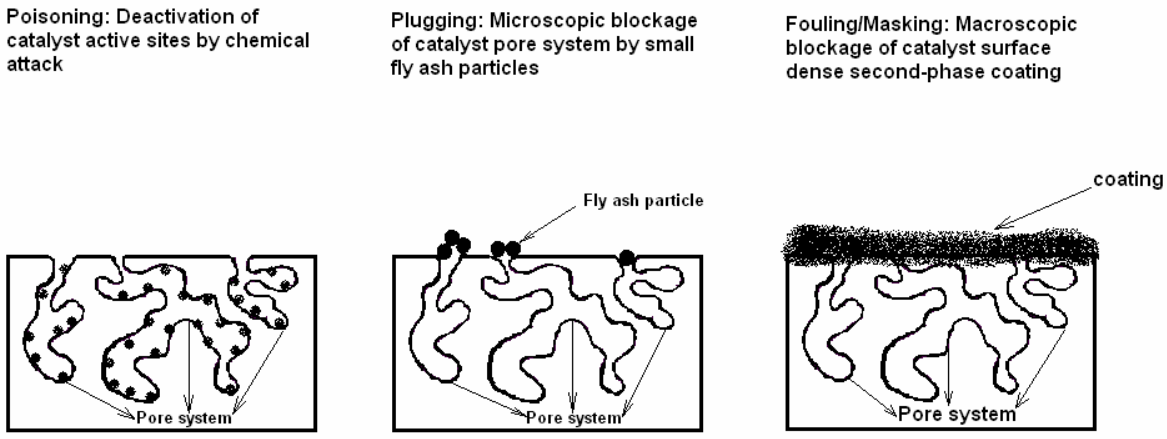


**Figure 5.4. Overview of general mechanism that can contribute to SCR catalyst deactivation.**

A. Poisoning can be caused by arsenic, alkali-metal-containing compounds, alkaline-earth-containing compounds, lead, and hydrochloric acid (HCl).

1. Arsenic in coal may vaporize into arsenic oxides, generally As (III), which nucleates to submicron particles that penetrate the catalyst fine structure and react with vanadia to form stable vanadia-arsenate compounds. Thus, poisoning by arsenic is irreversible. Arsenic concentration in the flue gas is usually low. It is most significant in wet-bottom (high-temperature slagging) boilers where arsenic is built up through flue-gas recirculation (Chen et al., 1990).

2. Water soluble or ion exchangeable alkali- and alkaline-earth-containing compounds, especially K and Na, react directly with active sites which are acid sites, resulting in acidity neutralization and subsequent deactivation. This is a major deactivation problem in oil-fired applications (Pritchard et al., 1995).

3. Lead poisoning is significant in waste incineration application (Tokarz et al., 1991; Stuart and Kossan, 1994; Khodayari and Odenbrand, 1998). Lead is preferentially deposited on the fly ash by either volatilization or entrainment in three forms: elemental lead, lead oxide, and lead chloride (Stuart and Kossan, 1994; Lin and Biswas, 1994). Catalyst poisoning is more likely due to chemisorption of lead onto the active sites instead of pore blocking because of little change of catalyst BET surface area and pore volume before and after lead addition (Stuart and Kossan, 1994).

4. HCl deactivates vanadia catalyst by either forming $NH_4Cl$, which consumes ammonia and blocks the active surface area, or reacting with vanadate to form $VCl_4$ and $VCl_2$ (Chen et al., 1990).

   Several issues complicate deactivation caused by alkali- and alkaline-earth-containing compounds: (1) physical form: alkali-containing compounds exit as alkali salts in fly ash and in the aerosol (particle, liquid or gas); (2) location: IR spectroscopy results show alkali metals occupy Brønsted acid sites (weaker acid sites), while TPD results show alkali metals first occupy strong acid sites (Lewis acid sites). Reports indicate that Lewis acid sites are stronger than Brønsted acid sites on vanadia catalyst surface (Went et al., 1992a; Topsøe et al., 1995; Srnak et al., 1992; Topsøe et al., 1992); (3) Mechanism: Alkali metal compounds deactivate vanadia catalysts by poisoning or by pore blockage; (4) Transformations: Alkali metal oxides may reduce catalyst BET surface area, pore volume, and average pore diameter. Investigators generally agree that poisoning by alkali metals does not change the underlying reaction mechanism so much as its rate. *In situ* and post fly ash property characterizations are critical to resolve these issues.

   Yang performed a thorough investigation on the poisoning mechanism of alkali- and alkaline-earth-containing oxides, and found that the deactivation directly relates to the basicity of metals, as shown in Figure 5.5. The strength of the poison oxide is as follows: $Cs_2O > Rb_2O > K_2O > PbO > Na_2O > LiO > CaO > P_2O_5$.

   A great deal of the evidence for chemical poisoning of SCR catalysts is either anecdotal or contained within proprietary company reports. The quality of this information varies, resulting in a weak case for chemical deactivation despite relatively widespread suspicion that poisoning is a significant deactivation mechanism. The proposed investigation intends to provide scientifically credible information on poisoning from systems of commercial interest and will make a significant contribution in this regard.

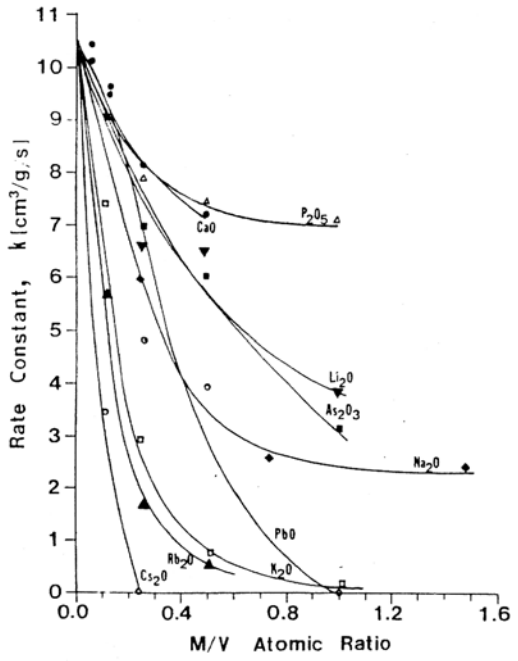


**Figure 5.5. Activities of 5% V2O5/TiO2 doped with different amount of metal oxide poisons, M=metal, 300 C, $O_2$= 2%, NO=$NH_3$=1000 ppm, $N_2$= balance, GHSV=15000$hr^{-1}$ (Chen and Yang, 1990).**

B. Fouling and masking may prevent $NO_x$ and ammonia from reaching active catalyst sites and may deactivate catalysts. Free CaO particles on the surface may react with $SO_3/SO_2$ in the gas to form less porous $CaSO_4$ layers, potentially masking the catalyst surface. This mechanism is potentially related to the chemical deactivation mechanism in that $CaSO_4$ is basic and could neutralize the acidic catalyst sites in addition to fouling the surface. This problem is especially significant in boilers burning Powder River Basin (PRB) coals, since PRB coals have almost three times more free CaO than US bituminous coals (Siemens, 2000). In addition, fly ash accumulation on surfaces (fouling), even in the absence of chemical reactions, may present physical barriers to gas reactions with the catalyst.

C. Pore plugging caused by ammonia salt and fine fly ash particles represents a third potential mechanism. Ammonia salt refers to ammonium sulfate and bisulfate, which are small (< 10μm (Franklin, 1996)) sticky particles that cause major plugging problems in the air heater and on the catalyst surface. Small fly ash particles lodge in the large pores on the catalyst surface, blocking the entrance to the pores.

D. Possibly the single most significant cause of poor SCR catalyst performance is channel plugging, that is, plugging of monolith channels by rogue large particles called popcorn ash. This completely mechanical mechanism is difficult to distinguish from surface fouling or chemical deactivation based on commonly available field measurements. However, channel plugging leads to larger increases in pressure drop than to any of the other mechanisms. While this mechanism substantially affects SCR performance, its prevention is largely a matter of more effectively separating large fly ash particles from the gases prior to their entrance into the SCR reactor and there is little chemistry- or reaction-related research needed for this activity.

E. There are also deactivation mechanisms involving catalyst erosion by abrasive fly ash. The catalyst is sensitive to the flue gas constituents, which are determined by the fuel

properties (main and trace elements) and method of firing. When system design, catalyst durability, and catalyst edge hardening are proper, erosion is not a significant deactivation factor (Pritchard et al., 1995).

Pore plugging by ammonia sulfate and poisoning by arsenic may be the main deactivation mechanisms for bituminous coals. Since strict $SO_2$ emission limits have led to an increase in the number of US utilities burning subbituminous coals, where poisoning by alkali and alkaline earth metals and masking by calcium sulfate may be more important for subbituminous (PRB) coals and biomass. Thus, understanding poisoning mechanisms by alkali- and alkaline-earth-containing compounds could become a critical issue in vanadia/titania catalysts for SCR applications in coal and biomass combustion.

#### 5.1.2.4 Summary of Literature Review

Surface vanadia species are the active sites with several suggested structures, while no general agreement appears on the active structures and the role of acidity. The SCR reaction is a redox reaction following an Eley-Rideal mechanism that involves reaction of adsorbed ammonia and gas phase NO. Since most catalyst compounds form stable sulfates, $SO_2$ in the gas potentially changes the chemical composition of both the active and inactive surface sites and measurably increases specific activity. However, no convincing evidence indicates the site with which sulfur interacts or the mechanism of activity enhancement by the sulfur species. Alkali- and alkaline-earth-containing compounds can potentially deactivate SCR catalysts by fouling and chemical poisoning.

Current available investigations outlining the variations of vanadia catalyst surface chemistry and reaction kinetics caused by addition of alkali and alkaline earth metals do not provide definitive data , especially in the areas of $NH_3$ and NO adsorption/desorption, $SO_2$ impact on catalyst activity and mechanisms, poisoning for commercially significant catalyst formulations (containing molybdenum or tungsten), and poisoning impact in $SO_2$-laden environments. There is a need to develop a better understanding of SCR reaction mechanisms and rates relevant to coal and biomass combustion conditions, with a particular emphasis on the role of sulfur, alkali metals, and alkaline earth metals on catalyst activity and deactivation, and provide contributions to deactivation modeling.

The current boundaries of established knowledge with respect to SCR application in coal-based systems are illustrated in Figure 5.6 in several areas of relevance to this proposed body of work. The ordinate represents increasing knowledge while the abscissa represents various aspects of SCR reactions, with those most closely related arranged next to each other. The bottom row represents the status of current investigations, and the envelope illustrates how this proposed work contributes to the ultimate goal of developing enough information about SCR processes to make fundamentally based performance predictions in complex practical applications such as coal combustion systems.

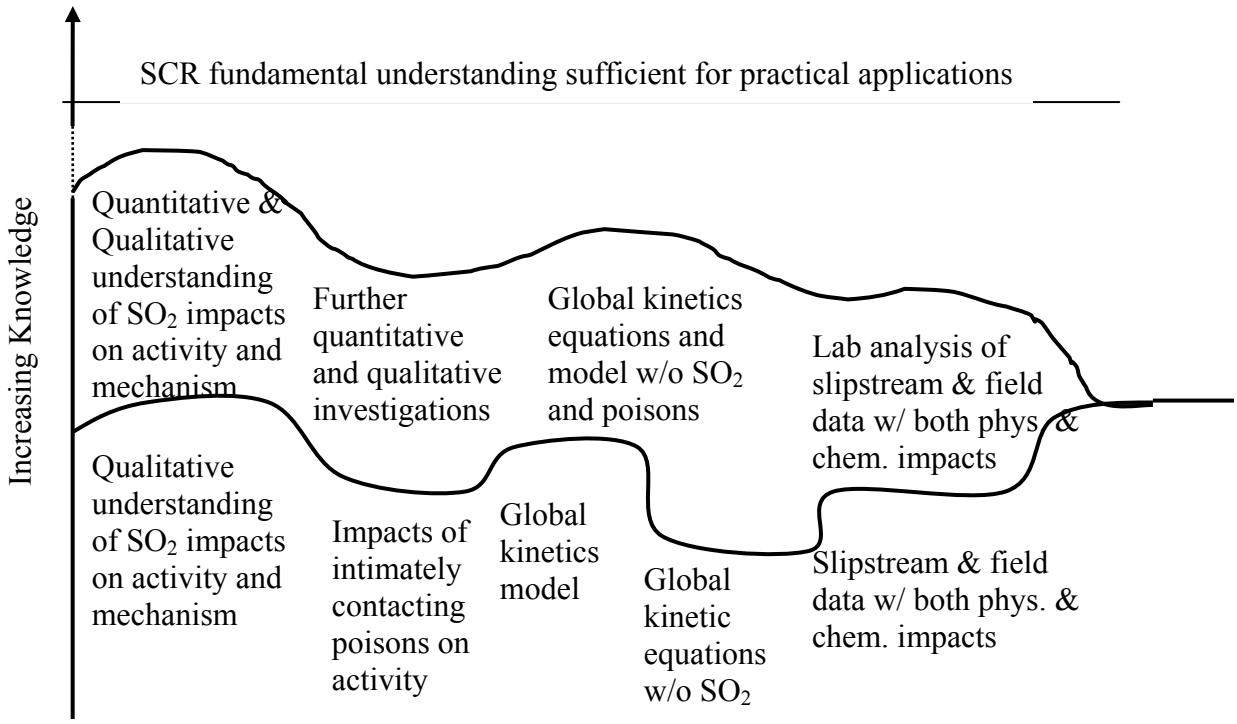


**Figure 5.6. Overview of SCR research field and contribution of the present work (within the envelope).**

### *5.1.3 Objectives*

The objectives of this project are:

1. To investigate the impacts of low-rank coal and coal-biomass co-firing on SCR activity under conditions representative of commercial-scale systems,
2. To determine the impact of sulfation on SCR performance,
3. To determine the impact of poisoning by alkali and alkaline earth metals on SCR performance,
4. To adapt impacts of sulfation and poisoning to existing simple models describing such performance for use in comprehensive combustion and fluid dynamics simulation.

Specifically, this project will investigate both laboratory-prepared and commercially exposed SCR catalyst samples and determine the impact of fuel-ash-derived components on catalyst activity. With respect to sulfation, this investigation will determine which catalyst sites sulfate in $SO_2$-laden flows and how this sulfation and in the presence of alkali metals affect catalyst surface acidity, species absorption and activity. Catalysts exposed to typical flu gases combined with laboratory-prepared samples will determine the extent to which laboratory experiments simulate field behavior. Conceptual mechanistic details regarding the active sites, mechanistic role of substrates and catalyst, and impacts of catalyst contaminants (sulfur and alkali metals) on reaction pathways will be postulated and supported by spectroscopic and activity data. *In situ* infrared spectroscopic techniques will be used to distinguish between Brønsted and Lewis acid sites and among adsorbed species. XPS (x-ray photoelectron spectroscopy) will determine compositions and oxidation states of surface materials. Modifications to existing computationally efficient (and therefore relatively simple) models in the literature will be made to capture the major impacts of SCR catalyst activity in ways appropriate for inclusion in a comprehensive combustion model for coal-based boilers.

These objective have several major limitations in scope:

1. This work focuses on chemical poisoning deactivation. Deactivation by fouling, pore plugging, or other non-kinetic mechanisms may be important, and this investigation will outline their roles where possible, but this work focuses on kinetic deactivation (poisoning).
2. All experiments will be performed in laboratory-scale reactors, although several will be done on samples collected from field exposure of catalysts in commercial combustion environments.
3. The primary instrument used for this investigation is an *in situ* FTIR (Fourier transform infrared) spectroscopy reactor system coupled with a mass spectrometer and supplemented by BET surface area analyses. *Ex situ* analyses, including XPS surface analyses, TOFSiM (time-of-flight secondary ion mass spectroscopy) analyses, and SEM-based investigations supplement the *in situ* techniques. The investigation will be limited to conclusions that can be drawn from this instrumentation and will not include, for example, UV-vis spectroscopy, Raman spectroscopy, or other techniques that have been used to advantage in other investigations. Additional monolith characterization from a slipstream reactor in a purpose-built laboratory system will also be included, though the construction of both the slip stream reactor and the laboratory system and some of the analysis was done by others.
4. The *in situ* investigations involve only wafers made from catalyst powder and is not performed on surfaces of commercial catalysts in their original form (that is, not on monoliths or plates themselves but on material obtained from the surfaces of monoliths and plates).

A series of tasks and the associated equipment designed to accomplish these objectives are discussed in the following chapter.

### *5.1.4 Experimental Design*

This investigation requires substantial mechanistic and kinetic experimentation. The intention is to supplement the existing literature by investigation of sulfur-laden gases using the equipment and techniques described below. The effort to understand vanadia catalyst reaction and deactivation mechanisms in typical coal and coal-biomass co-combustion involves several different types of analytical systems:

1. The catalyst-activity characterization system measures the NO reduction activity of monliths prepared at BYU as well as five commercial vanadia-based catalysts.
2. *In situ* FTIR surface spectroscopic investigations of vanadia catalysts provide mechanistic information, such as definite indications of surface-adsorbed species, and kinetic information, such as surface-active site coverage (ratio of the number of active sites to the total number of sites on the catalyst surface),
3. MS reactivity investigations provide global kinetic parameters, such as activity and activation energy for $NO_x$ reduction of fresh, sulfated, and poisoned catalysts,
4. Other surface characterization tests to provide information such as the effects of sulfate and poisons on BET surface area, pore-size distribution, geometry changes observed from SEM (scanning electron microscopy), and surface elemental compositions by XPS (x-ray photon spectroscopy), and standard (bulk) analyses that

supplement the reactor data. All of the above experiments should provide sufficient data to develop a deactivation sub-model for incorporation into a CFD model.

Two types of catalyst samples will be investigated and are summarized below:

- Commercial catalysts installed in a slipstream reactor with various exposure times. Detailed sample information appears in the results section (CCS).
- Laboratory-prepared catalysts
  1. One fresh sample of each of four vanadia-based catalysts (4 samples total) with total vanadia concentrations of 0, 1, 2, and 5 % (by mass).
  2. One deliberately contaminated sample of each of three vanadia-based catalysts (3 samples total) using each of three contaminants (K, Na, and Ca, – the details in Section B). All deliberately contaminated samples will be based on 1% vanadia catalyst preparations.
  3. One sample of each of the fresh and deliberately contaminated samples (7 additional samples in total) after complete sulfation of surface.

Laboratory-prepared catalysts use an incipient impregnation method for preparation. The procedure results in intimate association of catalyst and contaminant. All contaminants dissolve in solution in nitrate form but eventually form oxides. Two categories of catalysts (field-exposed and laboratory-prepared) are chosen for comparison, especially in cases of contaminated catalysts, to indicate differences between field-exposed and laboratory-prepared catalysts with similar contaminants since there are no reports dealing with these differences. Details of the experimental equipment and procedure appear in the task statements below.

#### 5.1.4.1 Vanadia catalyst *in situ* surface chemistry investigation

The purpose of this task is to gain knowledge of surface chemistry of vanadia-based SCR catalysts. Intentions include identification of acid sites, interaction pattern between reactant gases ($NH_3$, NO, and $SO_2$) and surface sites before and after contamination, and the extent of sulfation on poisoned and fresh SCR catalyst surfaces. These investigations will provide indicators of how poisons impact vanadia catalyst surface chemistry.

The experimental apparatus includes the ISSR (*in situ* surface spectroscopy reactor) and the TPD (temperature-programmed desorption) systems. The ISSR provides *in situ* transmission FTIR spectra of adsorbed $SO_2$, $NH_3$, and $NO_x$, among other species, and the TPD provides quantitative measures of behavior with lower detection limits, but with no direct surface-adsorption information.

This task includes the following specific activities.

A. $NH_3$ transient adsorption and NO transient adsorption (each 1000 ppm in helium) at temperatures from 25-380˚C are conducted by monitoring *in situ* FTIR spectra of adsorbed species on laboratory-prepared catalyst surfaces exposed to a variety of laboratory and field conditions. This study should provide qualitative and quantitative critical parameters, including Brønsted and Lewis acid site densities, their relative acidities, and changes of acidities induced by surface sulfation and poisoning. Another intent is to acquire $NH_3$ adsorption site coverage on the catalyst surface by correlating the change of $NH_3$ adsorption IR peak areas with the MS signal of desorbed $NH_3$.

B. Similar techniques will be used to identify the surface active sites (surface titania or vanadia or sulfated species) for each reactant gas ($NH_3$, NO, $SO_2$) and interacting surface

species (vanadia and sulfate species) to help elucidate SCR reaction mechanisms and specifically the impact of sulfur on such mechanisms. Tests will be based on laboratory-prepared catalysts. Hypotheses are already established (Table 5.4, Table 5.5 and Table 5.6) and will be tested with different experiments as shown in follow schemes:

1. NO adsorption site identification:

Possibilities:

A: NO adsorbs on titania sites (A)

B: NO adsorbs on vanadia sites (Figure 5.7). Absorption frequencies observable in the infrared do not distinguish between the various sites (1, 2, 3, and 4) on which $NH_3$ absorbs.

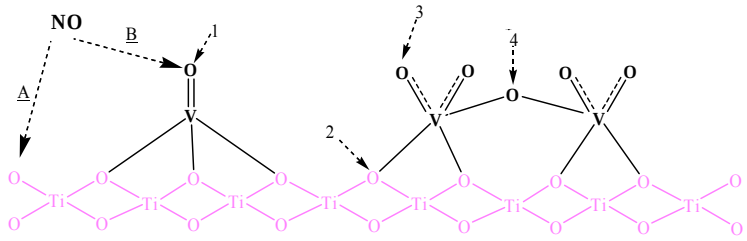


**Figure 5.7. Schematic of NO adsorption mechanism on vanadia sites.**

**Table 5.4. Expected experimental outcomes for NO adsorption study.**

| Hypothesis | Observations |
|---|---|
| A | NO adsorption intensity↓ vs. V% ↑ |
| B | NO adsorption intensity ↑ vs. V% ↑ |

2. Sulfate adsorption site identification:

Possibilities: A: Sulfate interacts with titania surface

B: Sulfate interacts with vanadia surface

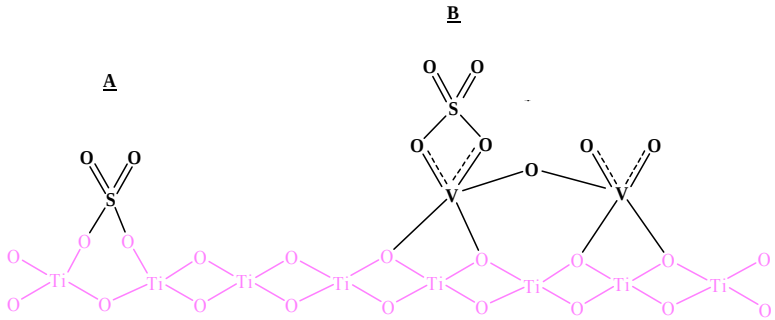


**Figure 5.8. Schematic of $SO_2$ adsorption mechanism on vanadia sites.**

**Table 5.5. Expected experimental outcomes for $SO_2$ adsorption study.**

| Hypothesis | Observation |
|---|---|
| A | Sulfate IR adsorption intensity or Sulfur % ↓ vs. V% ↑ |
| B | Sulfate IR adsorption intensity or Sulfur % ↑ vs. V% ↑ |

3. $NH_3$ adsorption sites identification:

Possibilities A: $NH_3$ adsorbs on titania site

B: $NH_3$ adsorbs on vanadia site

C: $NH_3$ adsorbs on sulfate site (which could be attached to a vanadia or a titania atom)

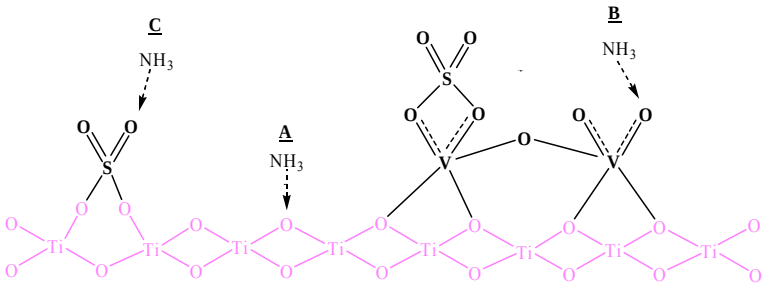


**Figure 5.9. Schematic of $NH_3$ adsorption mechanism on vanadia sites.**

**Table 5.6. Expected experimental outcomes for $NH_3$ adsorption study.**

| Hypothesis | Peak ($cm^{-1}$) | Observation |
|---|---|---|
| A | | $NH_3$ IR adsorption most intense on pure $TiO_2$ |
| B | | $NH_3$ IR adsorption intensity increases as V% increases |
| C | | $NH_3$ IR adsorption intensity increases as S% increases |

Identification of active adsorption sites for NO, $NH_3$, and $SO_2$ provides additional information to SCR reaction and poisoning mechanism.

C. Co-adsorption tests involving $NH_3$ and $NO_x$ help elucidate mechanisms and rates of both reaction and deactivation by monitoring variation of $NH_3$ and NO adsorption IR peaks during co-adsorption on laboratory-prepared catalysts, where temperature is increased from 25-380 ˚C. From these co-adsorption tests we determine which are the active sites for adsorption and the effect of surface sulfates and poisons on active site coverage and reactivity.

D. Surface sulfation represents a critical issue in this investigation since the practical applications of low-rank coal combustion and coal-biomass co-firing involve $SO_2$-laden gases. As discussed earlier, literature opinion regarding the impacts of $SO_2$ on SCR surface sulfation differ and the majority of the literature comes to conclusions different from those indicated by our results. This test uses *in situ* FTIR spectra obtained during 24-hour sulfation of each fresh laboratory-prepared catalyst. IR spectra of fresh, sulfated vanadia catalyst, and vanadyl sulfate indicate with which site sulfate interacts and where it forms. Subsequent XPS surface chemistry analyses of both fresh and sulfated vanadia

catalysts provide evidence for identifying sulfate species oxidation state and concentration. Also, the extent to which each field-exposed catalyst is sulfated is determined.

#### 5.1.4.2 $NO_x$ reduction kinetic investigation

An NO reduction kinetics investigation was conducted in two characterization systems, the catalyst characterization system (CCS) and the in situ spectroscopy reactor (ISSR).

##### 5.1.4.2.1 CCS Overview

The catalyst characterization system (CCS) provides capabilities for long-term catalyst exposure tests required for ascertaining deactivation rates and mechanisms and a characterization facility for samples from the slipstream reactor to determine changes in reactivity and responses to well-controlled environments. This system simulates industrial flows by providing a test gas with the following nominal composition: NO, 0.1%; $NH_3$, 0.1%; $SO_2$, 0.1%; $O_2$, 2%; $H_2O$, 10%; and He, 87.7%. Both custom and commercial catalysts are tested as fresh samples and after a variety of laboratory and field exposures under steady conditions.

##### 5.1.4.2.2 ISSR Overview

The purpose of the FTIR *in situ* spectroscopy reactor (ISSR) is to provide definitive indication of surface-active species through *in situ* monitoring of infrared spectra from catalytic surfaces exposed to a variety of laboratory and field conditions. The ISSR provides *in situ* transmission FTIR spectra of adsorbed $SO_2$, $NH_3$, and $NO_x$, among other species. Adsorption and desorption behaviors of these and other species change with temperature, catalyst formulation, extent of sulfation, and gas composition, as quantitatively indicated by changes in the spectral features of the sample. Quantitative indications of critical parameters, including Brønsted and Lewis acidities on fresh and exposed catalysts, based on these data provide among the most direct indications of surface conditions of all available analytical systems. Indications of coadsorption of $NH_3$ and $NO_x$ help elucidate mechanisms and rates of both reactions and deactivation.

Mass-spectrometry-based kinetics (activity in steady state) investigations compared reactivity of the various SCR catalysts under overall nominal gas-phase conditions of: 0.1% $NH_3$, 0.1% NO, 5% $O_2$, and helium. Helium rather than nitrogen was used in all experiments for several reasons, mostly pertaining to attempts to measure $N_2$ as a product of the reactions. All reactivity in this investigation were based on relatively simple reaction mechanisms, such as mechanisms assumed to be first order in NO and zero order in ammonia, water, oxygen, and all other reactants. The details of the assumed mechanism vary, but in any case the detailed mechanisms did not include elementary or completely fundamental descriptions as these unrealistically expand the scope of this work. These tests involved temperatures relevant to commercial operation but in differential mode. Temperatures up to 300 °C providedmeaningful data.

A statistically designed experiment (Table 5.7) determines effects of poisons and sulfates on catalyst activity as well as interactions among sulfates and poisons, since no previously published investigation clarifies whether interactions among poisons and sulfates exist, and how important interactions are if they do exist. Table 5.7 summarizes factors and factor levels to be investigated. Four factors will be studied including 3 poisons (K, Na, and Ca) and 1 sulfate on a 1% vanadia catalyst surface, each with two levels. $NO_x$ reduction activity will be chosen as the response.

**Table 5.7. Statistical experimental design of interactions between poisons.**

| Runs | Poison types with 2 concentration | | | | Response-$X_{NO}$ | Runs | Poison types with 2 concentration | | | |
|---|---|---|---|---|---|---|---|---|---|---|
| | K | Na | Ca | $SO_4$ | | | K | Na | Ca | $SO_4$ |
| 1 | 0.5 | 0 | 0 | 0 | | 8 | 0.5 | 0 | 0 | 1 |
| 2 | 0 | 0.5 | 0 | 0 | | 9 | 0 | 0.5 | 0 | 1 |
| 3 | 0 | 0 | 0.5 | 0 | | 10 | 0 | 0 | 0.5 | 1 |
| 4 | 0.5 | 0.5 | 0 | 0 | | 11 | 0.5 | 0.5 | 0 | 1 |
| 5 | 0.5 | 0 | 0.5 | 0 | | 12 | 0.5 | 0 | 0.5 | 1 |
| 6 | 0 | 0.5 | 0.5 | 0 | | 13 | 0 | 0.5 | 0.5 | 1 |
| 7 | 0.5 | 0.5 | 0.5 | 0 | | 14 | 0.5 | 0.5 | 0.5 | 1 |

#### 5.1.2.4.3 Other surface characterization investigations

BET surface area and pore size distribution analyses for all samples provide physical and structural information about the catalysts. A Micromeritics Tri-star Instrument (Model 3000) using the $N_2$ surface area method provides all data for these measurements. The test matrix includes all samples, that is, fresh and exposed commercial samples, sulfated and non-sulfated laboratory samples, and contaminated and uncontaminated laboratory samples. Several other surface-sensitive laboratory diagnostics such as XPS and ToFSIMS (time-of-flight-secondary-ion mass spectroscopy) as well as standard (bulk) analyses supplement the reactor data collected in our laboratory.

The above experiments involve comparisons of sulfated and non-sulfated samples of uncontaminated and contaminated laboratory-prepared catalysts with known amounts and forms of contaminants and catalyst. Uncontaminated SCR material and at least one sample of the same material contaminated with each poison provide a database with which to compare commercially exposed materials (discussed next). The completion of this activity occurs when a database of FTIR-MS and TPD results describing surface spectra, reactor effluent compositions, and transient concentration profiles for contaminated and uncontaminated catalysts is completed for both sulfated and non-sulfated catalyst surfaces. The experimental design is shown in Table 5.8.

**Table 5.8. Experimental design for sulfation and poison tests of catalyst samples.**

| Samples | | | | Adsorption (FTIR) | Reactivity (MS) | Surface Characterization (BET, XPS, SEM, ToFSIMS) |
|---|---|---|---|---|---|---|
| | $V\%/TiO_2$ | Poisons | sulfation | | | |
| B | 0 | 0 | × | 2 | 2 | 2 |
| Y | 0 | 0 | | 2 | 2 | 2 |
| U | 1 | 0 | × | 2 | 2 | 2 |
| \| | 1 | 0 | | 2 | 2 | 2 |
| P | 5 | 0 | × | 2 | 2 | 2 |
| R | 5 | 0 | | 2 | 2 | 2 |
| E | 1 | K | × | 2 | 2 | 2 |
| P | 1 | K | | 2 | 2 | 2 |
| A | 1 | Na | × | 2 | 2 | 2 |
| R | 1 | Na | | 2 | 2 | 2 |
| E | 1 | Ca | × | 2 | 2 | 2 |
| D | 1 | Ca | | 2 | 2 | 2 |

Based on the above designed experiments, the effect of sulfur and poison addition on vanadia catalyst surface chemistry and kinetics should be acquired to supplement the existing

literature, to help elucidate the mechanism of SCR catalysts deactivation, and to support developing deactivation modeling in Task 4.2.

### *5.1.5 Experimental*

#### 5.1.5.1 Catalyst Preparation

##### 5.1.5.1.1 Lab-prepared non-contaminated powder catalyst

Titanium dioxide (P25, Degussa), the catalyst support, was first densified by mixing with distilled water at 1:1.75 ratio by weight, and then dried at 120 ˚C for 24 hours followed by calcination at 600 ˚C for four hours. The densified titanium dioxide was then grinded with an agate mortar and pestle into fine powders.

Vanadia/titania catalysts with various vanadia weight loadings (1, 2, and 5%) were prepared using incipient impregnation method. Ammonia metavanadate, the precursor of vanadia, was added into a warm oxalic acid solution in a stoichiomatirc ratio, resulting in a deep blue solution. After the precursor solution cooled down, titainia powder was added and slurry formed, which was then dried at 120 ˚C over night, followed by calcinations at 550 ˚C for six hours. After calcinations, the catalysts were grinded with an agate mortar and pestle into fine powders.

##### 5.1.5.1.2 Lab-prepared contaminated powder catalyst

Poisoned powder catalysts were prepared by impregnating the non-contaminated powder catalyst with poison precursor solution, followed by drying at 120 ˚C over night and then calcining at 550 ˚C for five hours.

##### 5.1.5.1.3 Lab-prepared non-contaminated monolith catalyst

The monolith pieces were immersed in an aqueous 1 M nitric acid solution for 30 minutes at 80 °C, where the acid bath roughens the surface of the cordierite and improves washcoat adhesion. Following the acid treatment, the monolith pieces were rinsed with distilled water and dried at 120 °C overnight.

The P25 Titania from Degussa was mixed with distilled water at a ratio of 1:1.75 by weight. The paste that was produced was dried at 120 °C for 24 hours. After drying, the titanium dioxide was crushed with a mortar and pestle. The crushed titanium dioxide was then calcined at 600 °C for 4h. After calcinations, titanium dioxide was then mixed with distilled water at a 1:1 ratio by weight and poured into a ball mill. The resulting slurry was ball milled at 45 rpm for 90 min. The ball-milled slurry product had a bimodal particle size distribution with major peaks at 2 microns and 20 microns. This particle sizing produces a tough, non-cracking coating.

Ludox® AS-40 was added to the ball milled slurry. Ludox® AS-40 contains 40 weight % silica. Enough of this colloidal silica was added to create a 9:1 ratio of titanium dioxide to silica by weight.

Barium sulfate can be added to the SCR catalyst support as a binder according to U.S. Patent 4,975,256. Enough barium nitrate was dissolved into the balled-milled titania slurry that the resulting ratio of barium sulfate to titanium dioxide will be 1:9 by weight. Reagent-grade sulfuric acid was then added at 5% excess to precipitate virtually all of the barium, to barium sulfate.

The resulting slurry was thinned with a small amount of distilled water so that the dry coating would account for 20% of the total mass of the coated monolith. The monolith pieces were dipped in the titania slurry, and then compressed air was used to blow out the passages of the

monolith. The coated monoliths were then dried for 15 hours at 120 °C followed by calcining at 600°C for 4 hours.

The desired amount of active metal for one monolith piece needs to be dissolved in 45 mL of precursor solution, which was prepared by dissolving the ammonium metavanadate and oxalic acid in warm water, and then dissolving the ammonium metatungstate. After the impregnation solution was prepared, each titania coated piece of monolith was immersed in the solution, the excess was blown off with compressed air. The impregnated monoliths were then dried at 120° for 15 hours followed by calcination at 550° for five hours.

This procedure yields a suitable $V_2O_5/WO_3/TiO_2$ catalyst washcoated on a cordierite monolith.

#### 5.1.5.1.4 Lab-prepared contaminated monolith catalyst

Poisoned monolith catalysts were prepared by impregnating the non-contaminated monolith catalysts with poison precursor solution, followed by drying at 120 ˚C over night and then calcining at 550 ˚C for five hours.

#### 5.1.5.1.5 Commercial monolith catalyst

Five vendor-supplied commercial catalysts, three of which are monoliths and two of which are plates, and a BYU prepared monolith (M4) have been exposed to the flue gas in a slipstream reactor. Those catalysts were analyzed to help characterize the deactivation that occurs in coal-boiler flue gas over time. Of each catalyst type a fresh, unused sample is available, a sample that has been exposed for about 2,063 hours, and a sample that has been exposed for 3,800 hours are available for examination.

The flow rate capacity of mass flow controllers at BYU laboratory requires small size of samples, therefore, each monolith and plate catalyst were cut into small pieces for testing.

A common scroll saw was used to cut sections out of the monolith catalysts. These sections were then sanded down around the sides and on the ends to yield samples of four channels, in a two by two arrangement. M3, which doesn't have square channels, was cut in a shape shown in Figure 5.10 with a metal snip. When preparing the exposed catalyst samples, some ash was dislodged due to movement and vibrations caused by the scroll saw and sanding. Care was taken to dislodge as minimal amount of ash as possible.

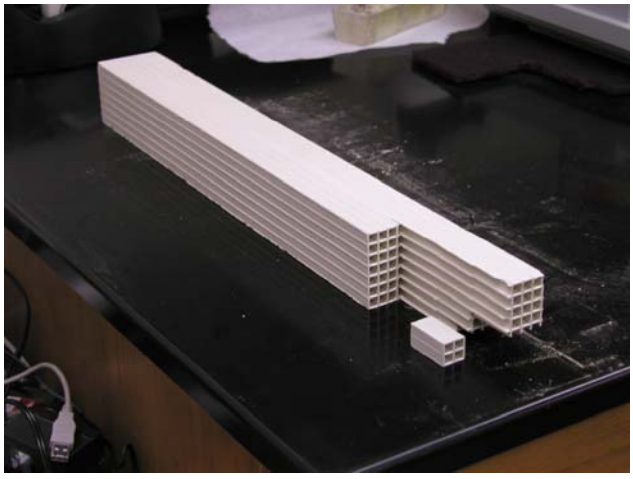

**Figure 5.10. Commercial catalyst sample C2.**

All samples taken from catalysts that had been exposed in the slipstream reactor were taken from the upstream end of the catalyst.

### 5.1.5.2 Analytical Methods

#### 5.1.5.2.1 BET analysis

Samples specific surface area and pore size distribution were measured by nitrogen adsorption at 77 K by the BET method using a Micromeritics 3000. About 0.5 gram of sample was weighted in the sample tube and then degassed at 120 ˚C in helium for four hours. After degassing, the sample weight was measured again and recorded as the accurate sample weight for BET analysis.

#### 5.1.5.2.2 In Situ FTIR analysis

A Nicolet, Model 730 FTIR spectrometer provides the *in situ* information. This system is illustrated in Figure 5.11. The spectrometer was used in transmission mode with a reactor cell designed to provide surface-sensitive, *in situ* data on adsorbed species.


**Figure 5.11. FTIR spectrometer with gas cell in sample analysis compartment.**

Figure 5.12 presents a schematic diagram of the reactor cell. This cell, which is specifically designed and fabricated for this study, is machined from a 316 SS rod to allow the infrared beam to pass through a catalysts wafer. The wafer is sandwiched between transparent crystal IR windows. The overall length and inside diameter of the cell are 10.9 cm and 2.6 cm, respectively. The catalyst wafer is supported by two aluminum wafer holders to prevent it from being crushed by the tight-fitting crystal windows and to allow the gas stream to enter and pass over the wafer. The gas ports are on opposite sides of the middle section of the reactor to allow continuous flow of reactants or adsorbing gases over the wafer. A thermocouple can be inserted into the reactor so that it just touches the catalyst wafer, providing accurate temperature monitoring. Cooling jackets on the far ends of the tube allow the center of the reactor to be operated at up to 773 K while the ends are kept below the melting temperature of the nitrile or Buna-N and Kalrez O-rings that provide air-tight seals. Reactor preparation involves sliding the KCl circular windows and sample wafer into the tube, positioning the thermocouple into the grooved wafer holder, inserting the O-rings and teflon window holders, and tightening the end caps. The whole apparatus is insulated with high-temperature insulation and aligned in the path of the IR beam so that the beam passes through the reactor and sample wafer (Figure 5.13).

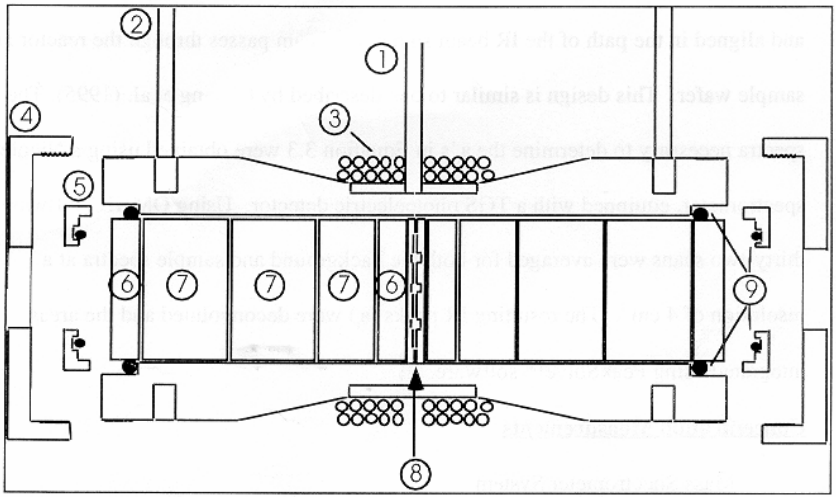


**Figure 5.12. Schematic diagram of the *in situ* reactor cell used in the FTIR system.**

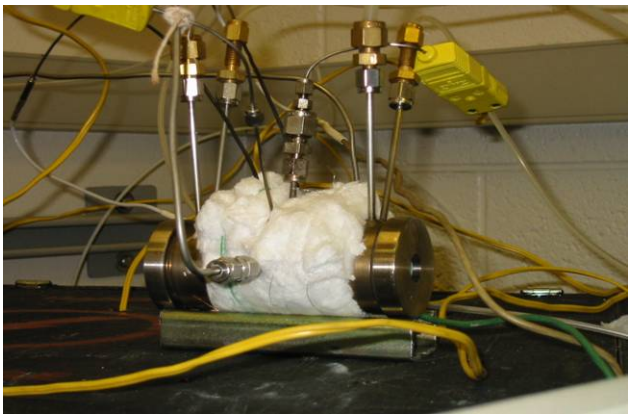

**Figure 5.13. Photograph of the reactor cell.**

Samples are prepared from powdered catalyst. Approximately 900 mg catalyst powder pressed into a 1.9 cm diameter wafer with 0.2 mm thickness provides a suitable diagnostic reactor volume for this technique. Fresh catalyst is oxidized prior to testing in the chamber using 5 % by weight $O_2$ in He at 350˚C~400˚C for two hours.

XPS was used to analyze the atomic surface concentration on each catalyst. The spectra were recorded on a Model X-ray photoelectron spectrometer using $AlK_\alpha$ (1486.7 eV) as a radiation source at 300 Watts. The powdered catalysts were mounted onto the sample holder and degassed overnight at room temperature at a pressure on the order $10^{-7}$ torr. Binding energies (BE) were measured for C1s, O1s, Ti 2p, V2p 3/2, S 2p, Na, Ca, W. Sample charging effects were eliminated by turning on the sputtering gun. Chemical shift was corrected according to the observed spectra with the C 1s binding energy (BE) value of 285 eV.

#### 5.1.5.2.3 Mass Spectrometer

To determine the NO conversion, the exhaust and feed from the above FTIR cell was sampled by Prisma™ QMS 100 quadrupole mass spectrometer from Balzers Pfeiffers using a Faraday cup and SEM (Secondary electronic measuring) detector. This instrument was equipped with a heated capillary inlet and valve, and was capable of measuring concentrations in the 1 ppm range. By analyzing the feed and effluent from the reactor with

the mass spectrometer, the NO conversion during the SCR reaction over the various vanadia catalysts can be determined.

### *5.1.6 Results and Discussion*

A series of experiments designed to clarify the kinetics and deactivation mechanisms of commercial SCR catalysts after exposure in coal and biomass effluent provide the basis of much of our work. This portion of the project used, commercial (vendor-supplied) SCR catalysts and BYU-manufactured, research catalysts. The commercial catalysts provide immediate relevance to practical application while the research catalyst provides less fettered ability to publish details of catalyst properties. The five commercial catalysts selected for use come from the most commercially significant catalyst manufacturers at the time this project began and provide a wide range of catalyst designs and compositions. The in-house catalyst allows detailed analysis and publication of results that may be more difficult with the commercial systems. This catalyst suite provides a comprehensive test and analysis platform from which to determine rates and mechanisms of catalyst deactivation.

A series of *in situ* FTIR-MS investigation conducted on lab-prepared fresh, sulfated, and poisoned vanadia catalysts provides fundamental data about the surface chemistry and intrinsic kinetics of vanadia catalyst during SCR of NO with $NH_3$.

#### 5.1.6.1 CCS

The CCS quantitatively determines deactivation mechanisms by measuring specific, intrinsic catalyst reactivity of custom (laboratory) and commercial catalysts under a variety of conditions. These catalysts are impregnated with a variety of contaminants, including Ca, Na, and K. In addition, the CCS characterizes samples of catalyst from slipstream field tests to determine similar data and changes in characteristics with exposure. Advanced surface and composition analyses determine composition, pore size distribution, surface area, and surface properties (acidity, extent of sulfation, etc.).

##### 5.1.6.1.1 Powder catalyst tests

First-order reaction kinetics (Eq.(5-8)) and first-order rate constants were computed by performing a material balance across the packed bed and integrating the resulting expression (Eq. (5-2)), as did Chen *et al.* In this way, our results are directly comparable to the literature results.

In our analysis, $r_{NO}$ is the rate of reaction of NO, $C_{NO}$ and $C_{NO,0}$ are local and *inlet* NO concentrations, respectively [moles/volume], $k$ is the rate constant [volume/mass of total catalyst sample/time], $F_{NO,0}$ is inlet feed rate of NO [moles/time], $X_{NO}$ is NO outlet conversion, and $W$ is mass of catalyst sample. Eq. 5-9 contains variables that are known or measurable and thus the observed first-order rate constant, $k_{obs}$, may be determined from experiment.

$$-r_{NO} = kC_{NO} \tag{5-8}$$

$$k_{obs} = \frac{F_{NO,0}}{C_{NO,0}W}\ln(1-X_{NO}) \tag{5-9}$$

It should be emphasized that Eq. 5-9 rests on several assumptions, including:

1. The gas flow through the bed is uniform with no significant radial or angular flow or concentration gradients.
2. The catalyst bed is isothermal.
3. Expansion effects due to reaction stoichiometry or pressure changes across the bed are negligible.
4. The rate can be modeled according to a first-order model, i.e, Eq. 5-8.

After a series of investigations of particle size effects on the kinetics regime, we feel comfortable running tests with powders in the 90-106 micron range since they do not appear to be significantly affected by mass transfer or pore diffusion limitations until the reactor temperature exceeds 375°C, at which point the effectiveness factor drops below 0.9 (see Figure 5.14).

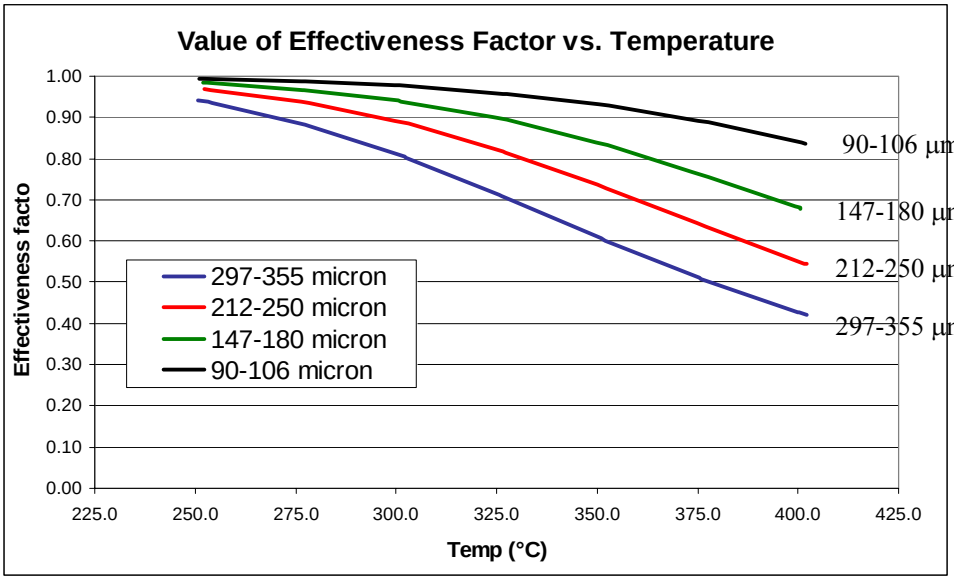


**Figure 5.14. Plot of effectiveness factor, $\eta$, versus temperature for various pellet sizes.**

Thus we are comfortable to make the last assumption, which is

5. Film mass transfer and catalyst pore diffusion effects are nonexistent (i.e. the gas composition at any axial position through the bed, including inside the pellets, is uniform).

Concentration gradients in the direction of flow through the bed are treated in the data analysis.

*Poisoning study*

A poisoning study similar to that reported by Chen, Buzanowski, *et al.* was conducted on the BYU SCR catalyst in the 90-106 micron particle range that had been poisoned at various levels with Ca and Na. In our investigation, 50 mg of catalyst was used. Prior to reaction, the catalyst was "steam treated" overnight at around 400 °C with 10% water, 2% $O_2$, and balance He at 150 sccm flow. The reaction conditions of the two investigations are compared in Table 5.9.

Data obtained from running the catalyst both wet and dry appear in Figure 5.15. This figure illustrates that addition of water vapor appears to inhibit the reaction (i.e., reduces the value

of the observed first-order rate constant), while it can also be seen that Na is a stronger poison than Ca, resulting in almost complete deactivation when the molar Na:V ratio is 1. Ca is not as strong of a poison at the same poison-to-vanadium ratio. This is consistent with the fact that Na forms a stronger base and thus has a greater effect on the surface Brønsted acidity.

**Table 5.9. Comparison of conditions in poisoning investigation by BYU to those of Chen, Buzanowski, *et al.***

| | **BYU** | **Chen, Buzanowski, *et al.*** |
|---|---|---|
| **Catalyst Composition** | 1% $V_2O_5$/0-9% $WO_3/TiO_2$ | 5% $V_2O_5/TiO_2$ |
| **Poisons** | Ca, Na | Ca, Na, K, Li, P, As, Pb, Rb, Cs |
| **Reaction Conditions** | 340 °C<br>NO = $NH_3$ = 900 ppm<br>2% $O_2$<br>10% $H_2O$ (when used)<br>balance He<br>flowrate = 380 sccm<br>(estimated ~1,000,000 $hr^{-1}$ based on solid catalyst volume (!) with 0.022 $cm^3$-50 mg-catalyst) | 300 °C<br>NO = $NH_3$ = 1000 ppm<br>2% $O_2$<br>no $H_2O$<br>balance $N_2$<br>space velocity = 15,000 $hr^{-1}$<br>(500 sccm with 2 $cm^3$ of pellets) |
| **Pellet/granule sizes** | 90-106 μm (170-140 mesh) | 500-812 μm (32-20 mesh) |
| **BET surface area** | ~32 $m^2/g$ | 30.6 $m^2/g$ |

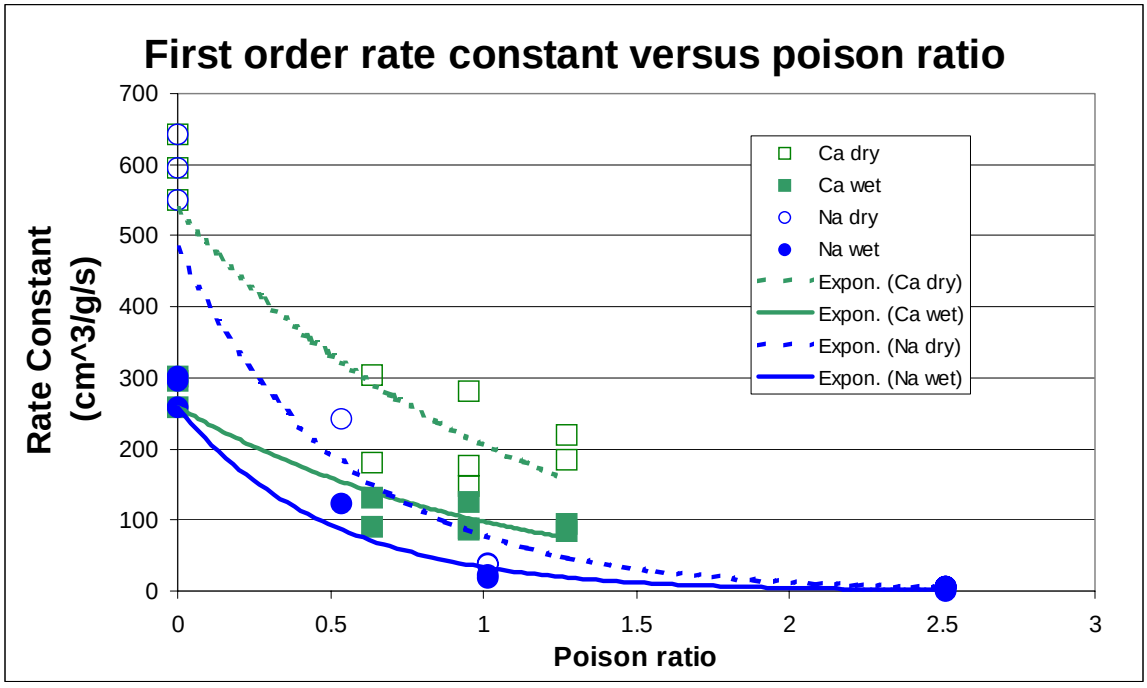


**Figure 5.15. Plot of observed rate constants at various poison levels for Na and Ca with and without water for catalysts containing no tungsten.**

Normalized catalytic *activity* as a function of poison level is shown for Ca (Figure 5.16) and for Na (Figure 5.17). Normalized activity is defined here as the observed rate constant at any given poison level divided by the observed rate constant for the fresh catalyst. Data obtained

with the same poisons by Chen, Buzanowski, *et al.* are also plotted in these figures for comparison.

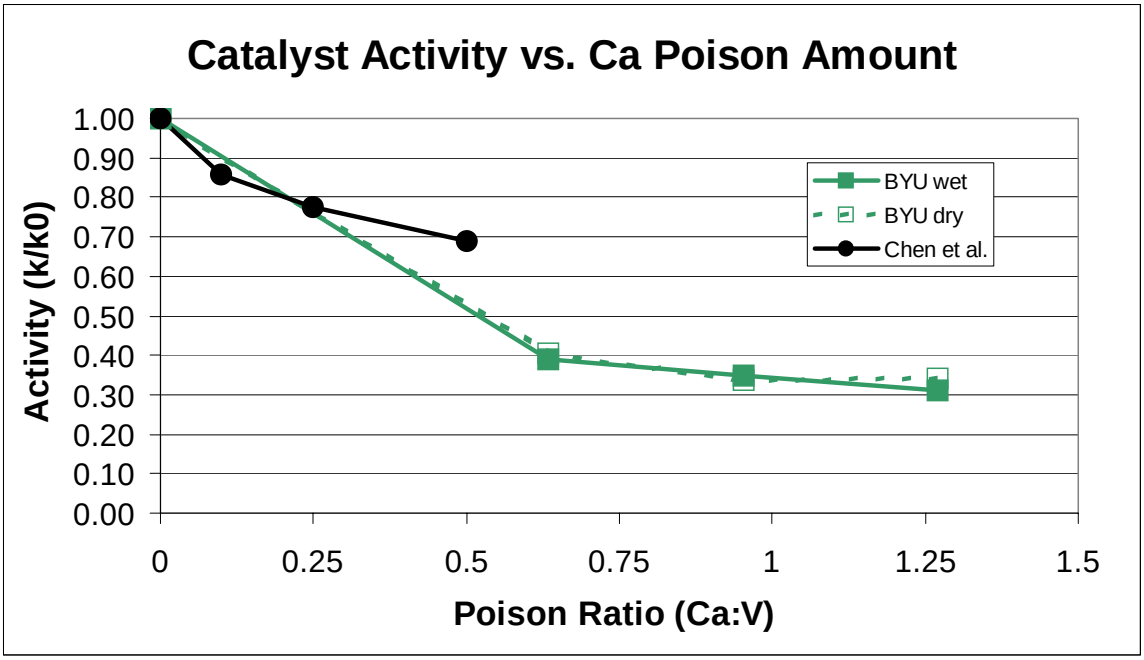


**Figure 5.16. Catalyst activity versus Ca:V ratio.**

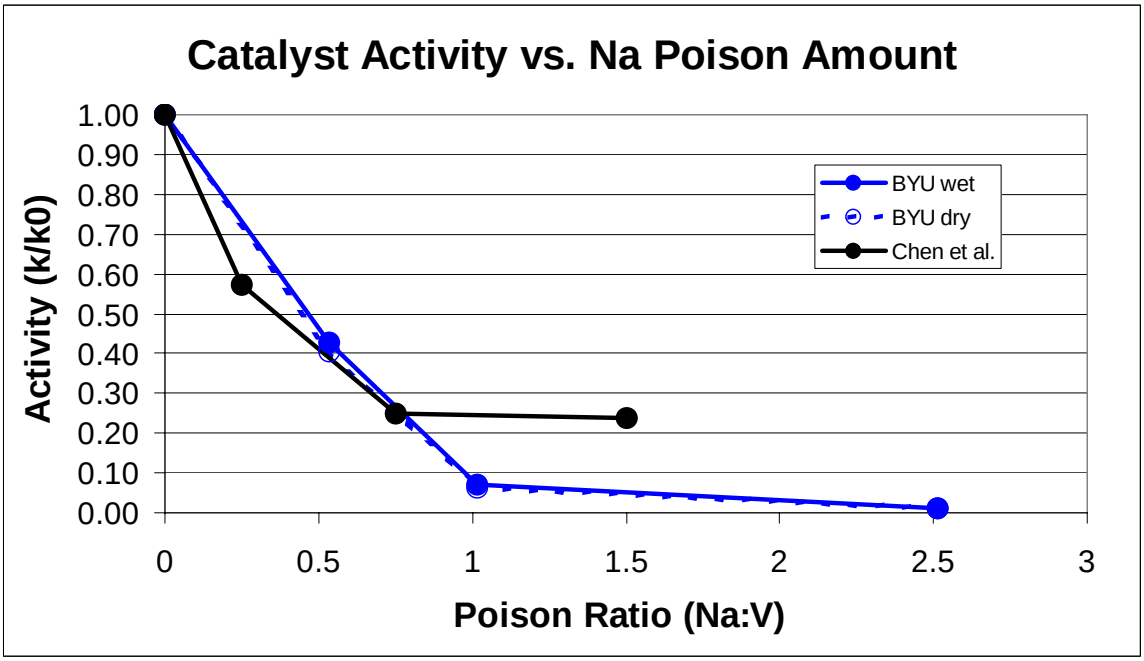


**Figure 5.17. Catalyst activity versus Ca:V ratio for samples containing no tungsten.**

Two observations are important at this point. First, although addition of water vapor does lower the observed rate constant, it does not affect normalized activity. Second, the same trends in activity loss with poison ratio are observed in the two investigations for both poisons, i.e., the activity levels off at a higher value for Ca-doped catalysts relative to Na-doped catalysts. The Na-doped catalysts of this investigation were essentially completely poisoned at Na:V = 1, in contrast to the Ca-poisoned samples, which appeared to level off at around 30% of original activity.

These data illustrate the strong potential poisoning impact of Na and Ca on catalysts when such contaminants intimately contact the catalyst surface – in this case are mixed directly into the catalyst preparation. This does not necessarily indicate that commercially exposed catalysts, in which less efficient contacting of the contaminants with the catalyst occurs, would suffer the same deactivation. Thus, a series NO reduction activity tests were conducted on commercial and home-made monolith and plate vanaida catalysts which had been exposed in a slipstream reactor.

#### 5.1.6.1.2 Monolith and Plate Catalyst Tests

As a separate activity within this research effort, a slipstream reactor was designed and built (in conjunction with Reaction Engineering International and the University of Utah, both in Salt Lake City, UT) in which BYU-prepared and commercial catalysts could be exposed for relatively long times at commercial utilities. The details of this reactor appear in the Section 5.2. This slipstream reactor provided samples from commercial environments for the present investigation.

Table 5.10 summarizes how many samples of each catalyst type provided data for this investigation. Catalyst suppliers required that the specific identities of the catalysts not be disclosed, but the sample IDs that begin with M indicate monolith catalysts and those that begin with P indicate plate catalysts. Figure 5.18 to Figure 5.21 show a comparison of NO conversion for the fresh catalysts versus the exposed catalysts. The 95% confidence intervals were found by fitting the data to a second order polynomial using Igor Pro® and calculating the activity based on these fits. For C6 and C2, the 2,063-hour exposed catalysts exhibited the same activity as the fresh catalyst and the 3,800-hour exposed catalysts exhibited less activity than the fresh catalyst. For C3 and C4, the exposed catalysts exhibited less activity than that of the fresh catalyst, while the 3,800-hour exposed catalysts exhibited less activity than the 2,063-hour exposed catalyst. In all cases illustrated in these figures, exposure was to low-rank coals. Additional exposure to coal-biomass blends are discussed later.

**Table 5.10. Samples Run for Each Catalyst.**

| Catalyst | Fresh | 2063 hr Exposure | 3800 hr Exposure |
|---|---|---|---|
| C6 | 3 | 3 | 2 |
| C2 | 3 | 3 | 2 |
| C3 | 3 | 3 | 6 |
| C4 | 3 | 3 | 3 |

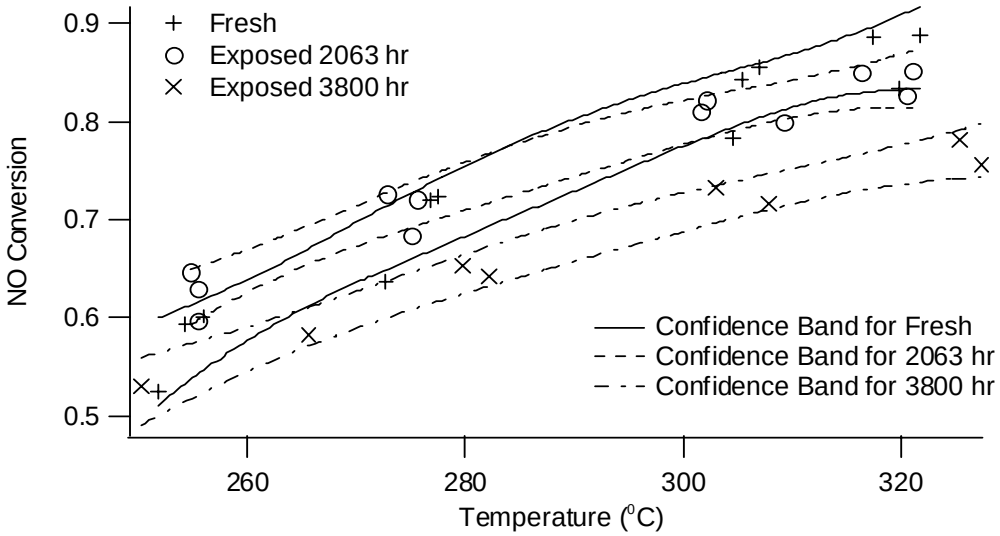


**Figure 5.18. C6 conversion results as a function of temperature and exposure time in a slipstream reactor with 95% confidence intervals.**

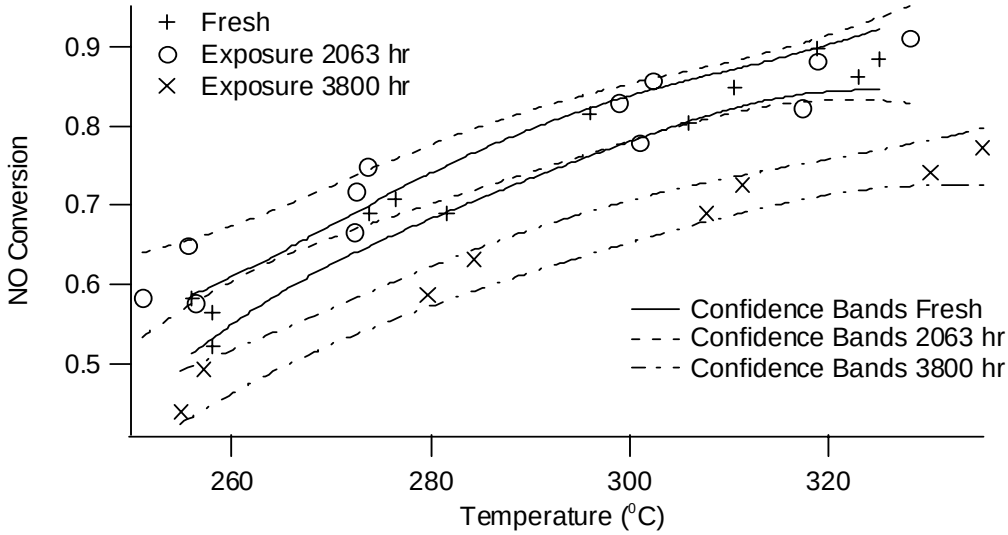


**Figure 5.19. C2 conversion results as a function of temperature and exposure time in a slipstream reactor with 95% confidence intervals.**

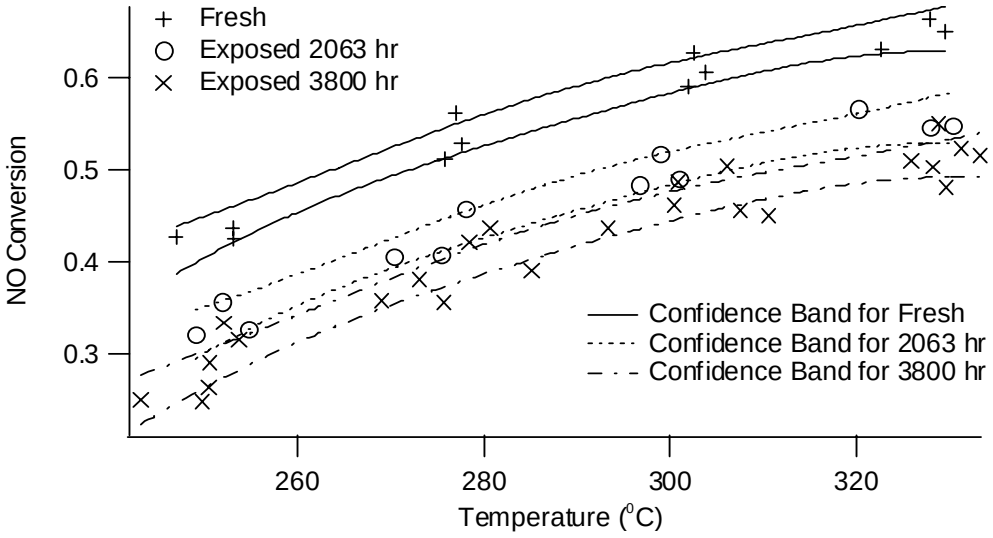


**Figure 5.20. C3 conversion results as a function of temperature and exposure time in a slipstream reactor with 95% confidence intervals.**

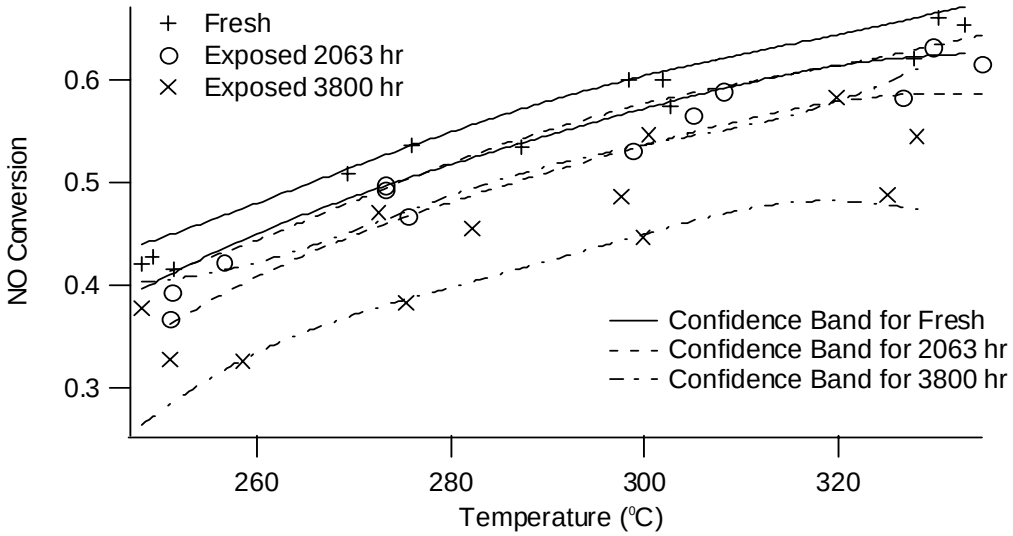


**Figure 5.21. C4 conversion results as a function of temperature and exposure time in a slipstream reactor with 95% confidence intervals.**

The 3,800-hour exposed C3 and C4 were taken from both the top and bottom sections in the slipstream reactor. The 3,800-hour exposed C3 samples taken from the top of the slipstream-reactor chamber were compared to those taken from the bottom of the chamber. Figure 5.22 indicates that samples taken from both positions exhibit similar activities.

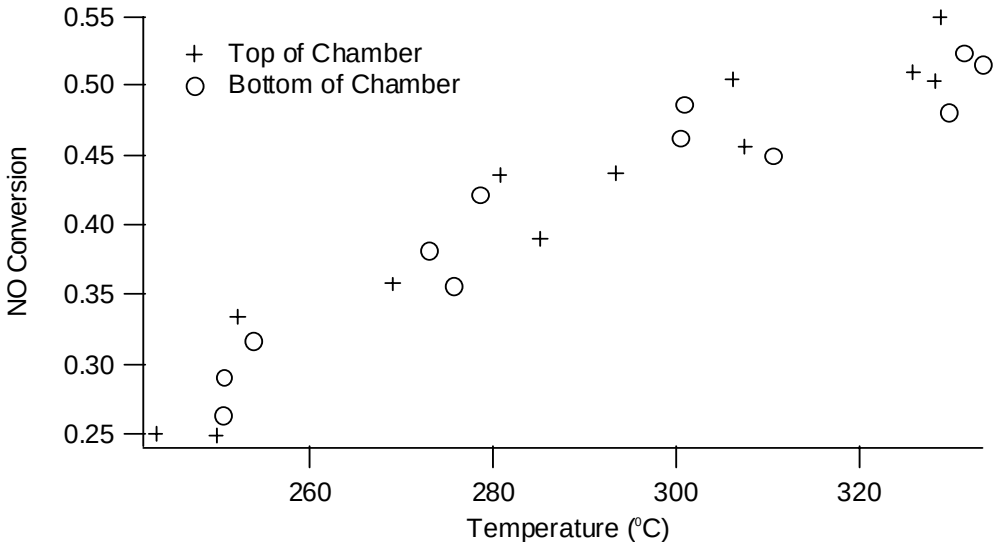


**Figure 5.22. Top of chamber versus bottom of chamber for C3, exposed for 3,800 hours.**

### 5.1.6.2 Reaction Rate Constant, Activation Energy, and Activity of C6 and C2 Catalysts

The Chen model (derivation in the Appendix) describes monolith catalyst deactivation in SCR**,** provides a quantitative means of tracking deactivation and a potential means of incorporating such deactivation in a combustion simulation code. The model comparisons between the activity of the exposed catalysts and the fresh C6 and C2 catalysts appear below. The essentially one-dimensional Chen model predicts NO conversion ($X_{NO}$) of an exposed catalyst:

$$X_{NO} = 1 - \exp\left( -\frac{\sigma_{cat} L}{u A_{cs}} \frac{1}{\frac{1}{k_m} - \frac{1}{(D_e k a)^{1/2}} \frac{\exp(-2\phi)+1}{\exp(-2\phi)-1}} \right) \tag{5-10}$$

where

$$\phi = \left( \frac{h^2 k a}{D_e} \right)^{1/2} \tag{5-11}$$

$\sigma_{cat}$ = perimeter length of a monolith cell
$L$ = monolith length
$u$ = linear gas velocity in cell
$A_{cs}$ = cross-sectional area of a cell
$k_m$ = mass-transfer coefficient
$D_e$ = effective diffusivity of NO
$k$ = first order reaction rate constant

$a$ = activity
$\Phi$ = Thiele modulus
$h$ = wall half-thickness

To compare the activities, the reaction rate constants ($\underline{K}$) were found over a range of temperatures for each of the fresh catalysts by setting activity ($a$) equal to one. The pseudo-first-order Arrhenius' reaction rate pre-exponential factor ($A$) and activation energy ($E_a$) for each sample resulted from a non-linear least-squares analyses of the measured conversions and temperatures. (Igor Pro® was used to fit the data):

$$k = A\exp\left(-\frac{E_a}{RT}\right) \tag{5-12}$$

$R$ = ideal gas constant
$T$ = temperature

The results appear in Table 5.11 and the fit is appears in Figure 5.23.

**Table 5.11. Pre-exponential factor (A) and activation energy (Ea) values for the fresh catalyst samples C6 and C2.**

| Catalyst | $A$ ($cm^3$/(g*s)) | $E_a$ (kJ/mol) |
|---|---|---|
| C6 | $1.06 * 10^{10}$ | 87.7 |
| C2 | $2.65 * 10^{10}$ | 97.4 |

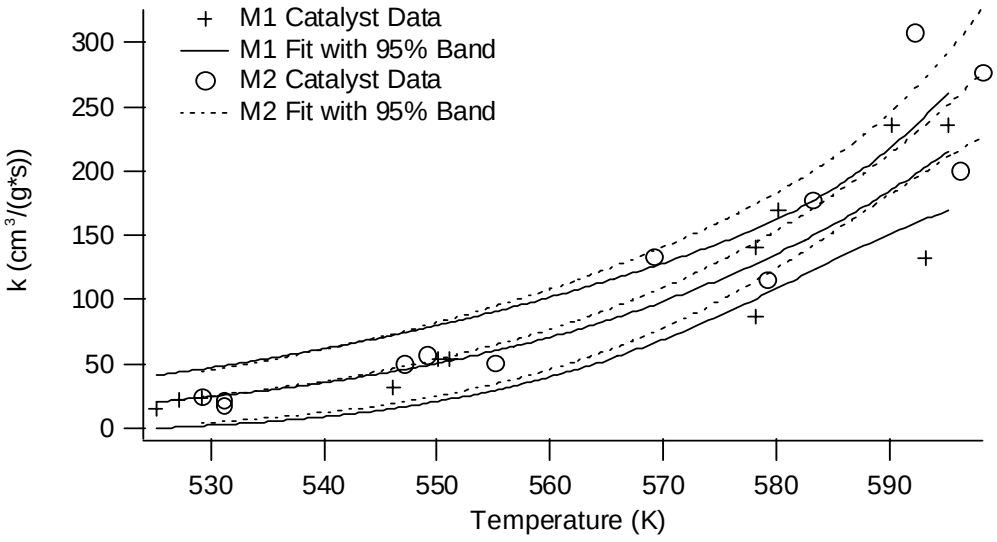


**Figure 5.23. Arrhenius law fit for C6 and C2.**

By holding the reaction rate coefficients constant, conversion data from the exposed catalysts determine values of the activity factor (*a*) in the Chen model. These values appear in Table 5.12. Figure 5.24 and Figure 5.25 compare the Chen model fits to the actual data.

**Table 5.12. Activity Factor Fits for Exposed Catalysts.**

| Catalyst | 2,063-hr Exposure | 3,800-hr Exposure |
|---|---|---|
| C6 | 1.029 | 0.533 |
| C2 | 1.152 | 0.413 |

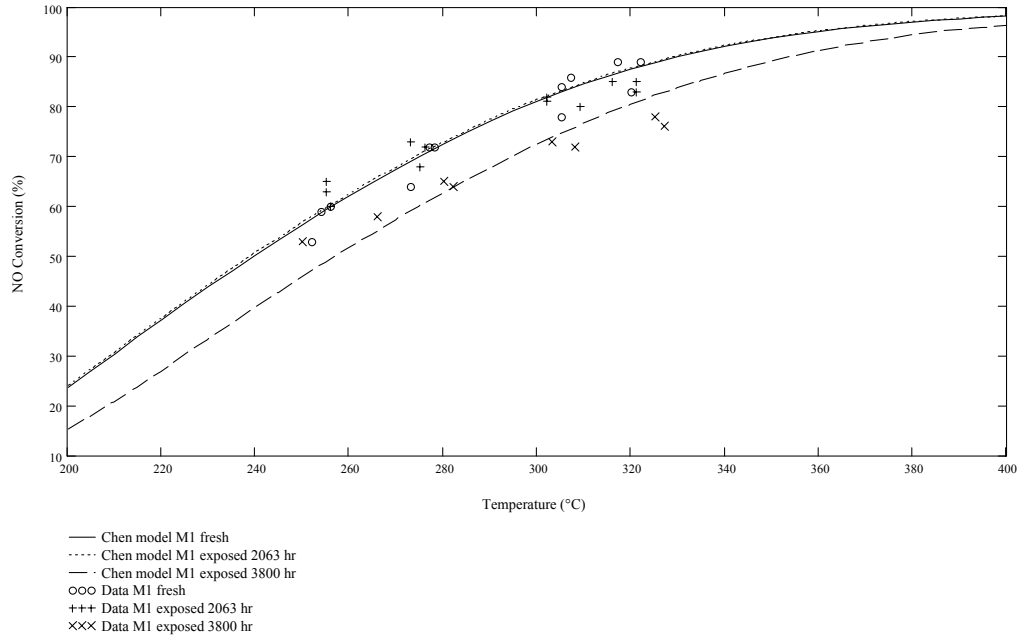


**Figure 5.24. C6 comparison of data to Chen model prediction.**

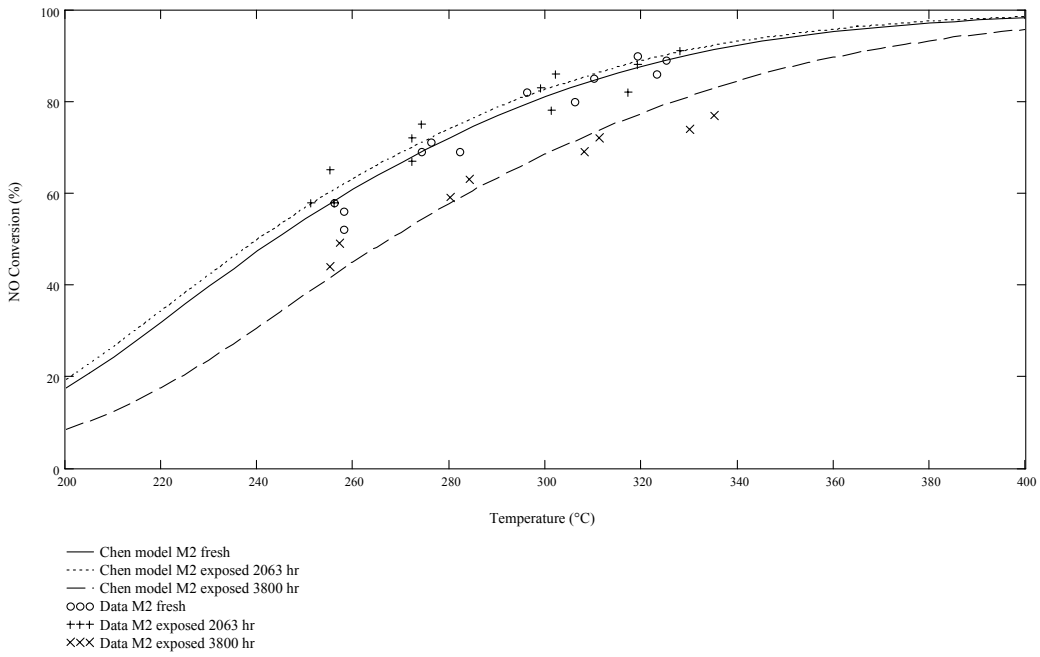


**Figure 5.25. C2 comparison of data to Chen model prediction.**

Values of the activity factor, *a*, from the Chen model, indicate that activity increases slightly after 2,063 hours of exposure, presumably due to catalyst sulfation. However, after 3,800 hours of exposure the activity decreases significantly.

XPS analyses on fresh and 2,063-hour exposed commercial monolith samples, as shown in Figure 5.26 and Figure 5.27, indicated that Na and Ca, plus sulfate had accumulated on the exposed samples. Our previous investigation has demonstrated that alkali metal Na and alkaline earth metal Ca poison the vanadia catalyst. The subsequent NO reduction activity tests on those exposed samples show that the 2,063-hour exposed C6 and C2 exhibited almost the same and even slightly higher NO reduction activity than the corresponding fresh catalysts C6 and C2 in the lower temperature region, the NO reduction activities of 2,063-hour exposed C3 and C4 catalysts are only slightly lower than the corresponding fresh samples, although with poisons deposited onto the catalyst samples. It seems that Na and Ca attached to the catalyst surface but they did not poison the 2,063-hour exposed catalyst. With the extended exposure, the 3,800 hour exposed samples including C6, C2, C3, and C4 exhibited obviously decreased NO reduction activity. The different physical character of 2,063- and 3,800-hour exposed samples (Figure 5.28) suggested that fine ash particles started gradually accumulating on the monolith walls on 2,063-hour exposed samples, and plugged about 70% of the monolith channels of the 3,800-hour exposed samples. These observations explain the pattern of NO activity we observed. At 2,063 exposed hours, surface fouling appears as no major problem, and no significant decrease of the NO reduction activity occurs. But after having been exposed for 3,800 hours, monolith surface fouling becomes detrimental, and the catalysts NO reduction activity greatly decreases. Therefore, the results from commercial exposed samples suggest that surface fouling instead of poisoning contributes significantly to the deactivation of monolith catalyst for coal-fired boilers applications. We postulate competing effects, with sulfation increasing activity and surface fouling decreasing activity and the net effect being an initial increase in activity after followed by a long decrease in activity.

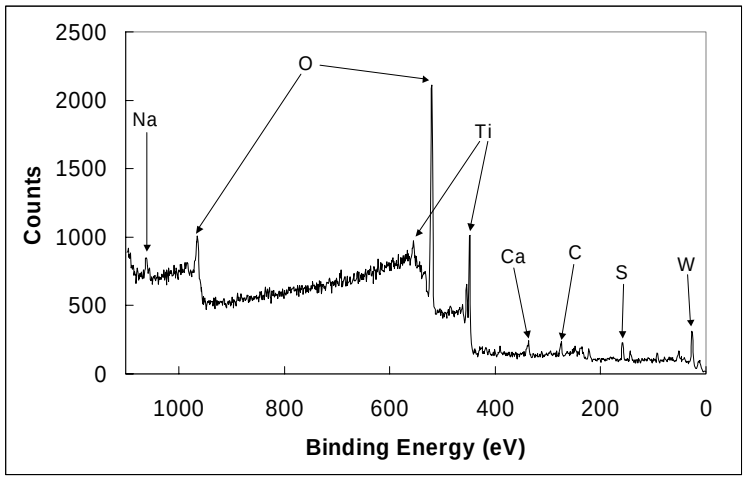


**Figure 5.26. XPS analysis of C6.**

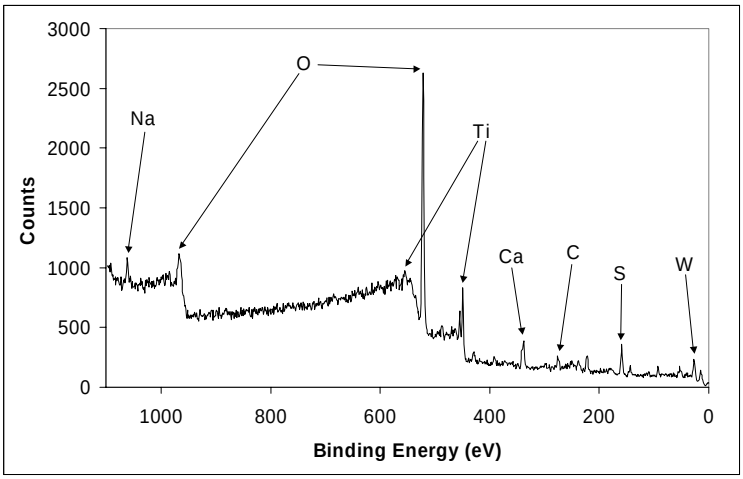


**Figure 5.27. XPS analysis of C2.**

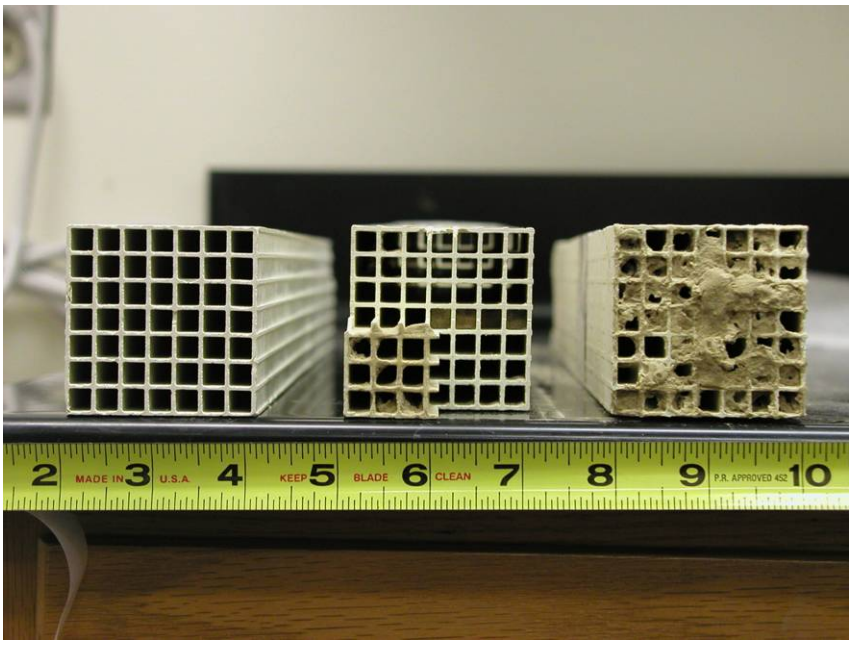


**Figure 5.28. Picture of fresh, 2,063-hour, and 3,800-hour exposed commercial monolith samples.**

The 2,063-hour exposed C6 and C2 exhibited slightly higher NO reduction activity than the corresponding fresh catalysts C6 and C2, one explanation is that sulfate species built up on the catalyst surface during the exposure, and brought higher activity to the catalyst. To verify this presumption, the effect of sulfation on titania and vanadia catalyst surface chemistry and NO reduction activity were conducted with an in situ FTIR-MS system. Besides, the effect of poisons including potassium, sodium, and calcium were also investigated. The results appear summarized in the following section ISSR.

#### 5.1.6.2 ISSR

The ISSR system involves *in situ* FTIR-MS analysis that provides surface-adsorbed species identification and intrinsic kinetic investigation. The effect of sulfation and poisoning of vanadia catalysts were specifically investigated. The motivations for sulfation investigation are:

Much of the existing literature focuses on SCR reactions in $SO_2$-free environments. A significant effort in the ISSR laboratory relates to analyzing SCR reactions under coal-relevant conditions ($SO_2$ laden flows).

1. Much of the existing literature focuses on SCR reactions in $SO_2$-free environments as are common in natural-gas-fired systems. A significant effort in the ISSR laboratory relates to analyzing SCR reactions under coal-relevant conditions ($SO_2$-laden flows).
2. Most ash-derived contaminants and oxide components of the catalyst are exposed to relatively high concentrations of $SO_2$ under conditions where coals high in sulfur content are burned (such is the case at many utility boilers in the United States). Sulfates thus formed or deposited on the catalyst surface may profoundly affect surface acidity and hence activity (since the active sites for SCR are thought to include acid functions).
3. Most investigations have been conducted either in the absence of $SO_2$ or under conditions and/or during short periods unfavorable for sulfate formation. Accordingly, it is questionable if these investigations are relevant to “realistic” industrial conditions involving long exposures to $SO_2$ in the presence of water.
4. There are conflicting views in the literature as to whether vanadium species on the catalyst surface sulfate.

This work section of the project focuses on the effect of sulfation and poisoning on the vanadia catalyst surface chemistry and NO reduction activity. The objective of the sulfation investigation is to identify the surface sites with which sulfate species interact and the effect of sulfate species on vanadia catalyst activity. Addition of poisons to the catalysts is designed to explore the poisoning mechanism of the vanadia catalyst exposed to similar commercial combustion situations. The test matrix appears in Table 5.12.

**Table 5.13. ISSR test matrix.**

| Samples | | | | Adsorption (FTIR) | Reactivity (MS) | Surface Characterization (BET, XPS, SEM, ToFSIMS) |
|---|---|---|---|---|---|---|
| | $V\%/TiO_2$ | Poisons | sulfation | | | |
| B | 0 | 0 | × | 2 | 2 | 2 |
| Y | 0 | 0 | | 2 | 2 | 2 |
| U | 1 | 0 | × | 2 | 2 | 2 |
| \| | 1 | 0 | | 2 | 2 | 2 |
| P | 5 | 0 | × | 2 | 2 | 2 |
| R | 5 | 0 | | 2 | 2 | 2 |
| E | 1 | K | × | 2 | 2 | 2 |
| P | 1 | K | | 2 | 2 | 2 |
| A | 1 | Na | × | 2 | 2 | 2 |
| R | 1 | Na | | 2 | 2 | 2 |
| E | 1 | Ca | × | 2 | 2 | 2 |
| D | 1 | Ca | | 2 | 2 | 2 |

×: work that has been accomplished

#### 5.1.6.2.1 Experimental quality confirmation

*FTIR quality confirmation*

To obtain accurate and detailed information from FTIR, the quality control tests involving comparing system performance with known standards were performed first. NO adsorption on Rh/ZSM5 provides data to compare with previous research results that were obtained with the same FTIR apparatus. The main peaks of NO adsorption on the Rh/ZSM5 catalyst appear at the same spectral position as those observed in the previous experiments, as illustrated in Figure 5.29 and Figure 5.30. The new data report results over a wavenumber range shifted somewhat toward the visible compared with the previous results. The two characteristic NO adsorption peaks at 1869 and 1783 $cm^{-1}$ are even clearer than those in the former results.

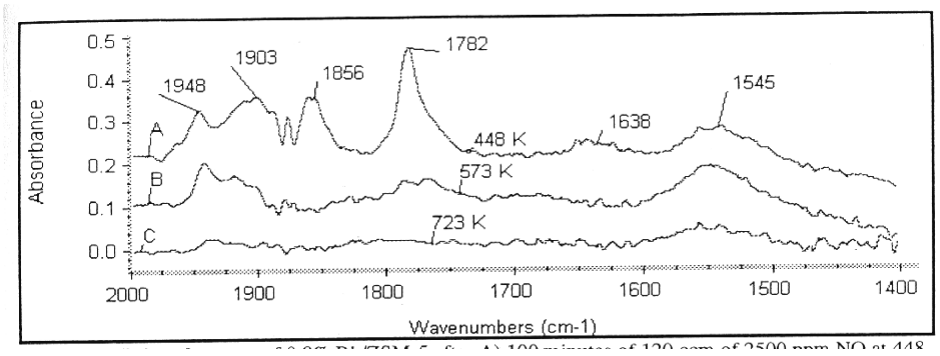


**Figure 5.29. NO adsorption from previous experiments.**


**Figure 5.30. NO adsorption with current FTIR system, total flow = 20 ccm, 1000ppm NO at 448K.**

*Kinetic investigation method determination*

Both conversion and kinetic activity data derived from mass-spectrometer-based analyses of reactor effluent streams provide quantitative measures of the impact of sulfation on activity. The kinetic data require knowledge of film and pore diffusion impacts in addition to conversion results. Means of estimating these impacts are discussed prior to the kinetic parameter determination below.\

*Pore diffusion limitation*

SCR tests on 5 and 2 % $V_2O_5/TiO_2$ catalysts at 350 ˚C resulted in NO conversions of about 80% and 72% respectively, which indicates that increasing vanadia content enhances NO reduction activity. However, at conversions as high as 80 and 72%, pore diffusion resistance could be dominant. For example, the calculated Thiele modulus ($M_T$) for 5% $V_2O_5/TiO_2$ is 1.06, substantially exceeding the 0.4 upper limit for $M_T$ customarily accepted for negligible pore diffusion resistance. In addition, the Weisz modulus ($M_W$) for 5% $V_2O_5/TiO_2$ is 1.13, exceeding the 0.13 upper limit for $M_W$ customarily accepted for negligible pore diffusion resistance.

$$M_T = L\sqrt{\frac{(n+1)}{2}\frac{k'''C^n_{As}}{D_{eff}C_{As}}} \tag{5-10}$$

$$M_w = \frac{L^2(-r'''_A)_{obs}}{D_{eff}C_{As}} \tag{5-11}$$

$L$ = Z/2 for flat plate, Z = thickness
$L$ = r/2 for cylinders, r = radius
$L$ = r/3 for spheres
n = reaction order
$D_{eff}$ = effective diffusivity
$C_{As}$ = reactant concentration on catalyst surface

Pore diffusion impacts the kinetic reaction rates in these cases. Operation in regimes without such impacts provides more accurate intrinsic kinetic data. Therefore, NO reduction was tested on 1% $V_2O_5/TiO_2$ at 18% conversion with temperatures of about 250 ˚C and a 30% conversion at temperatures of 300 ˚C. These conditions correspond Thiele modulus ($M_T$) of about 0.25 (250 ˚C) and 0.34 (300 ˚C), respectively. Both are smaller than 0.4. Therefore the

pore diffusion effects can be neglected at these lower temperatures with the 1% vanadia catalyst. Commercial catalyst preparations typically contain about 1% vanadia.

Film diffusion limitation

Both theoretical and experimental results show that film diffusion can be neglected during SCR tests on 1% $V_2O_5/TiO_2$ at temperatures up to 350˚C and under the conditions of these experiments.

Film diffusion resistance is determined according to

$$K_c = \frac{1-\phi}{\phi}\left(\frac{D_{AB290}}{d_p}\right)Sh' \qquad (5\text{-}12)$$

ø = void fraction of packed bed
$D_{AB}$ = gas-phase diffusivity, $m^2/s$
$d_p$ = particle diameter, m
$Sh'$ =Sherwood number

The calculated result indicates that the film resistance accounts for about 0.3% of the total resistance (combined resistance of film diffusion and kinetic resistance).

Experimentally, film diffusion investigations on SCR catalysts (1% $V_2O_5/TiO_2$) involved three different flow rates (93, 121, 187 ml/min). This range of space velocities in the catalyst provides significant variation in the boundary layer thickness along the catalyst surface and therefore should result in different conversions if film resistance plays a significant role in NO reduction. Similar NO conversions (17.6% at 93.3 ml/min, 18% at 121 ml/min, and 17.4% at 187ml/min at 250 ˚C) resulted from each experiment, consistent with the mathematical expectation of negligible impact of film resistance. Therefore, the following SCR reactions were investigated on 1% $V_2O_5/TiO_2$ catalysts with 700 ppm $NH_3$ and NO, 5% $O_2$, helium (balance) with a total flow rate of 187 ml/min and at a temperature range of 250-350 ˚C, where both film diffusion and pore diffusion resistance can be neglected. This investigation involved catalyst reacting in the intrinsic kinetic range.

*Kinetic parameter calculation*

Since NO reduction experiments did not involve film or pore diffusion, kinetic parameters depend directly on NO conversion based on following equation (assuming the surface reaction is first-order in NO concentration):

$$K = -\frac{Q_0}{W_{cat}}\ln(1-X) \qquad (5\text{-}13)$$

$K$ = reaction rate coefficient
$Q_0$ = total gas flow rate, ml/min
$W_{cat}$ = catalyst weight
$X$ = NO conversion
And also

$$K = A\exp\left(-\frac{E_a}{RT}\right) \quad (5\text{-}14)$$

$A$ = pre-exponential factor
$E_a$ = activation energy
$R$ = gas constant 8.314 J/mol·K
$T$ = temperature, K

A matrix of reaction rate coefficient ($K$) values and temperatures result from measuring NO reduction as a function of temperature. Non-linear least-squares fits of these data determine the parameters $A$ and $E_a$ and their confidence intervals.

#### 5.1.6.2.2. Sulfation effect

With confirmed good detection quality of the current FTIR system, sulfation investigations on titania support and vanadia catalysts were conducted, which involved 24-hour sulfation tests under both dry and wet conditions on $TiO_2$, 2% $V_2O_5/TiO_2$, and 5% $V_2O_5/TiO_2$. *In situ* IR spectra were collected during the sulfation of each sample. Surface chemical compositions of fresh, dry and wet sulfated $TiO_2$, 2% $V_2O_5/TiO_2$, and 5% $V_2O_5/TiO_2$ were obtained from XPS analyses. The FTIR spectra indicate that intensities of sulfate peaks on vanadia catalysts, an indication of surface sulfate content, decrease with increasing vanadia content on catalyst surfaces. The XPS surface elemental concentration analysis agrees with FTIR results. Furthermore, XPS analyses indicate that the vanadia oxidation state is 5+ and remains unchanged upon sulfate species addition. This indicates no vanadyl sulfate, the product of sulfated vanadia species with vanadia oxidation state of 4+, forms on the vanadia catalyst surface. Each of these investigations is discussed below.

In situ *FTIR investigation*

Many sulfation tests resulted in several best practices regarding sulfation analyses on these samples. For example, $CaF_2$ window should be used during sulfation since they resist sulfation, unlike KCl or NaCl windows which otherwise may have some advantages. For XPS analysis, the original pellet sample should be tested instead of ground powder catalyst from the original pellet as the former preserves the same surface state whereas the latter creates significant new surface, most of which will not be sulfated. After choosing repeatable and accurate procedures, final sulfation conditions were determined, as summarized in Table 5.14.

**Table 5.14. Sulfation conditions for $TiO_2$, 2 and 5% $V_2O_5/TiO_2$ under both wet and dry conditions.**

| Sample Name | Sample Details | Notes | Gas Stream Composition, % | | | | Flow (sccm) | Temp (°C) |
|---|---|---|---|---|---|---|---|---|
| | | | He | $O_2$ | $SO_2$ | $H_2O$ | | |
| VTOD | 5% $V_2O_5/TiO_2$ | Preoxidation | 88.2 | 11.8 | | 0 | 56.7 | 380 |
| | | 24 Hours Sulfation | 89.01 | 10.72 | 0.27 | 0 | 62.3 | 380 |
| VTOF | 2% $V_2O_5/TiO_2$ | Preoxidation | 88.2 | 11.8 | | 0 | 56.7 | 380 |
| | | 24 Hours Sulfation | 89.01 | 10.72 | 0.27 | 0 | 62.3 | 380 |
| TiO8 | $TiO_2$ | Preoxidation | 88.2 | 11.8 | | 0 | 56.7 | 380 |
| | | 24 Hours Sulfation | 89.01 | 10.72 | 0.27 | 0 | 62.3 | 380 |
| VTHF | 5% $V_2O_5/TiO_2$ | Preoxidation | 88.2 | 11.8 | | 0 | 56.7 | 380 |
| | | 24 Hours Sulfation | 87.33 | 10.51 | 0.267 | 1.88 | 63.54 | 380 |
| VTHG | 2% $V_2O_5/TiO_2$ | Preoxidation | 88.2 | 11.8 | | 0 | 56.7 | 380 |
| | | 24 Hours Sulfation | 87.33 | 10.51 | 0.267 | 1.88 | 63.54 | 380 |
| TiO9 | $TiO_2$ | Preoxidation | 88.2 | 11.8 | | 0 | 56.7 | 380 |
| | | 24 Hours Sulfation | 87.33 | 10.51 | 0.267 | 1.88 | 63.54 | 380 |

*Sulfate peak identification*

During sulfation, only one peak located at around 1370 $cm^{-1}$ appears in the IR spectrum for all the samples including 0, 2, and 5% $V_2O_5/TiO_2$. Figure 5.31 illustrates the IR confirmation of this only peak formed during the sulfation of 5% $V_2O_5/TiO_2$. Literature sources designate this peak as a S=O stretching mode of the surface sulfate (references), therefore, sulfate species formed on 5% vanadia catalyst during the sulfation. This sulfate species formation has been observed on $TiO_2$, 2 and 5% $V_2O_5/TiO_2$ under both dry and wet sulfation.

*Dry sulfation of 5 and 2% $V_2O_5/TiO_2$, and $TiO_2$*

Figures 5.32 through 5.34 summarize the *in situ* IR spectra collected during the sulfation of each sample.

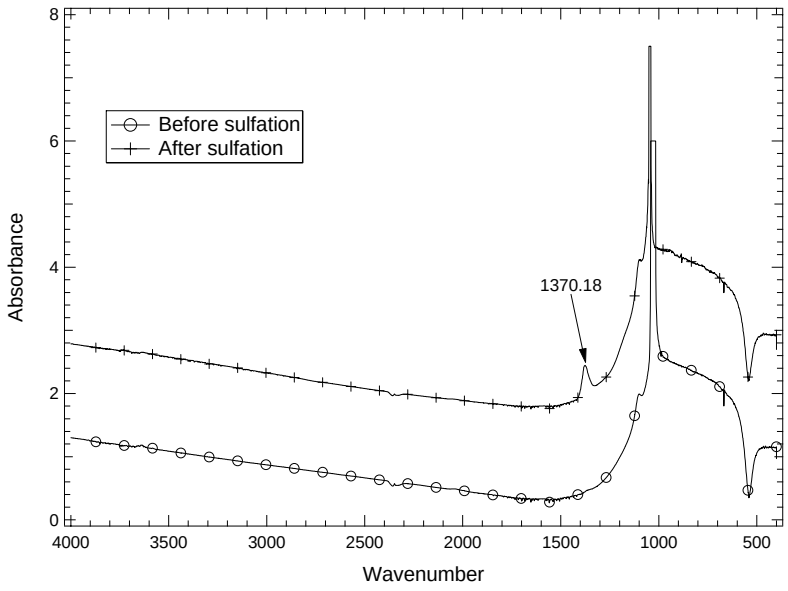


**Figure 5.31. IR spectra comparison of 5% $V_2O_5/TiO_2$ before and after sulfation.**

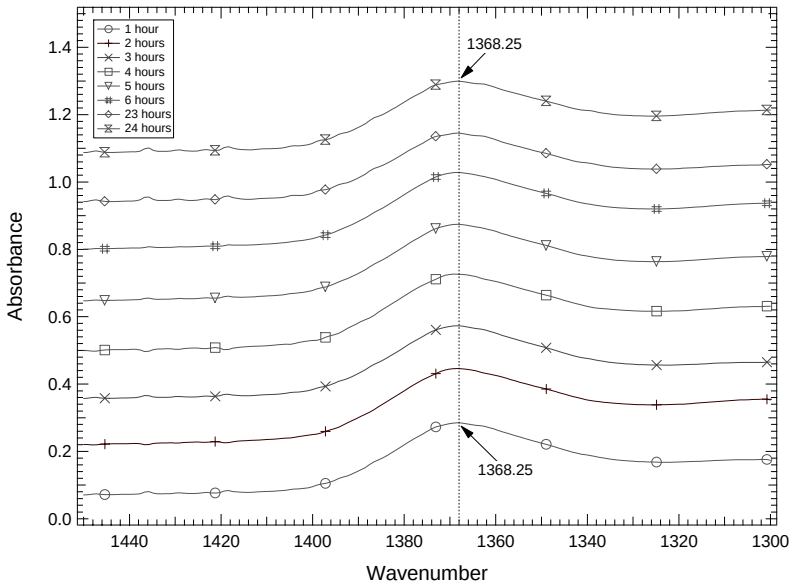


**Figure 5.32.** ***In situ*** **IR spectra of dry sulfation on 5% $V_2O_5/TiO_2$.**

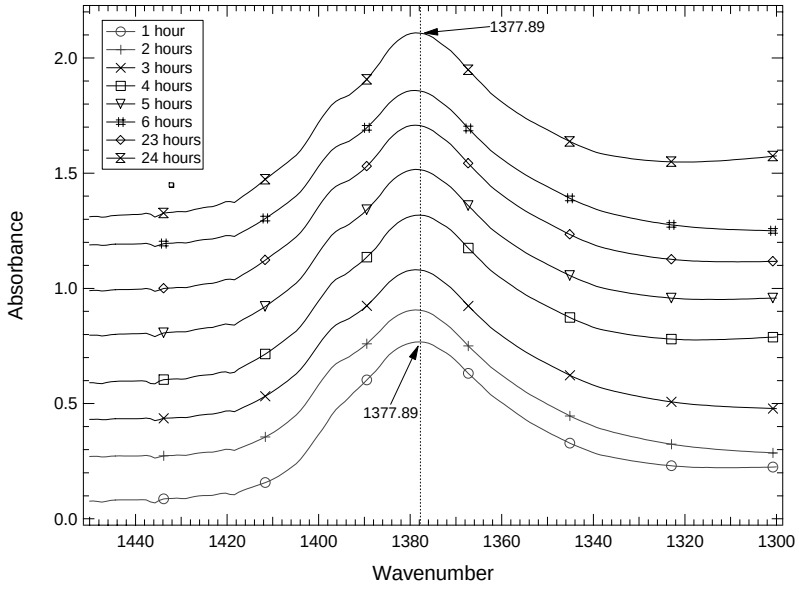


**Figure 5.33.** ***In situ*** **IR spectra of dry sulfation on 2% $V_2O_5/TiO_2$.**

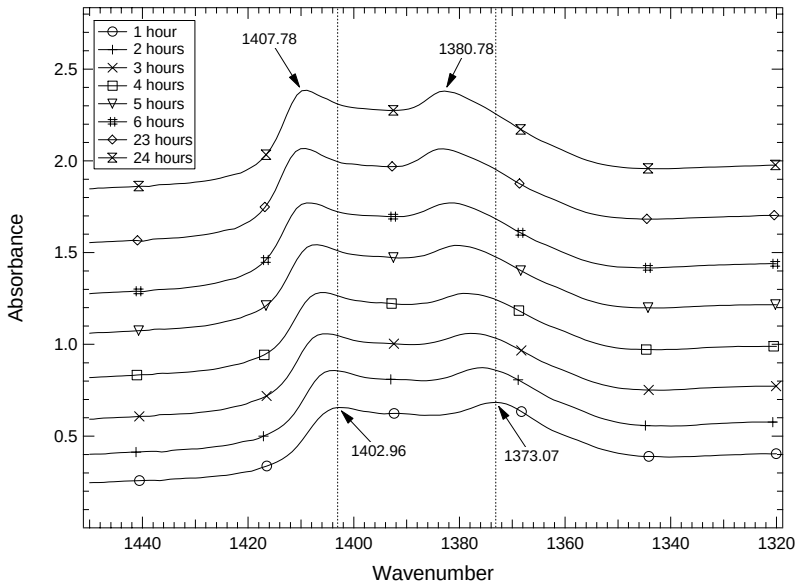


**Figure 5.34.** ***In situ*** **IR spectra of dry sulfation on $TiO_2$.**

*Wet sulfation of 5 and 2% $V_2O_5/TiO_2$, and $TiO_2$*

Figures 5.35 through 5.37 summarize the *in situ* IR spectra collected during the sulfation of each sample.

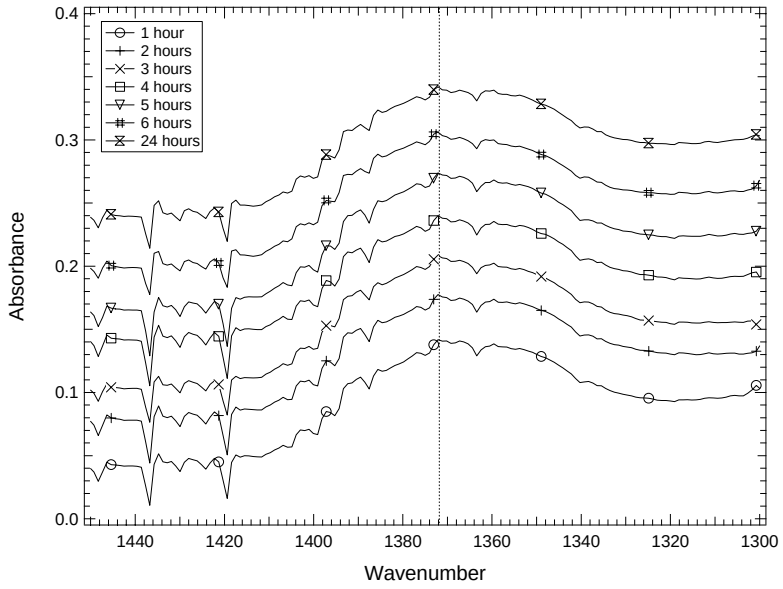


**Figure 5.35.** ***In situ*** **IR spectra of wet sulfation on 5% $V_2O_5/TiO_2$.**

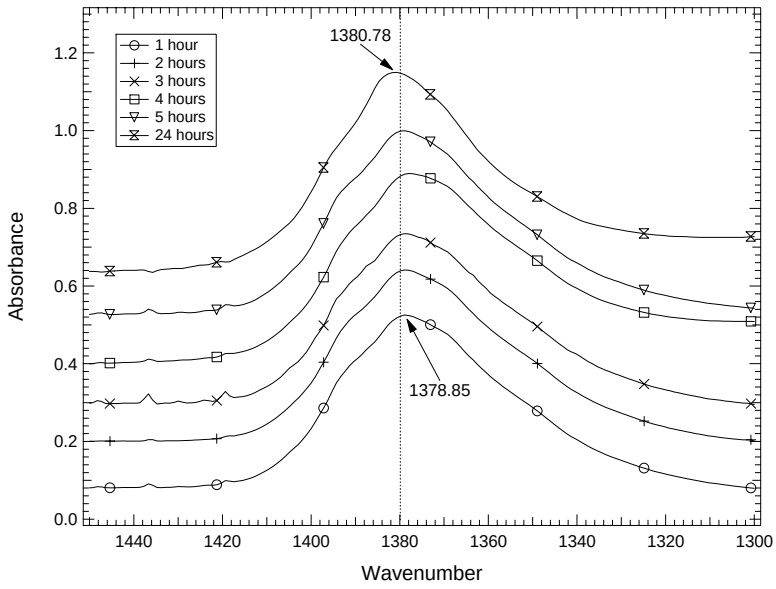


**Figure 5.36.** ***In situ*** **IR spectra of wet sulfation on 2% $V_2O_5/TiO_2$.**

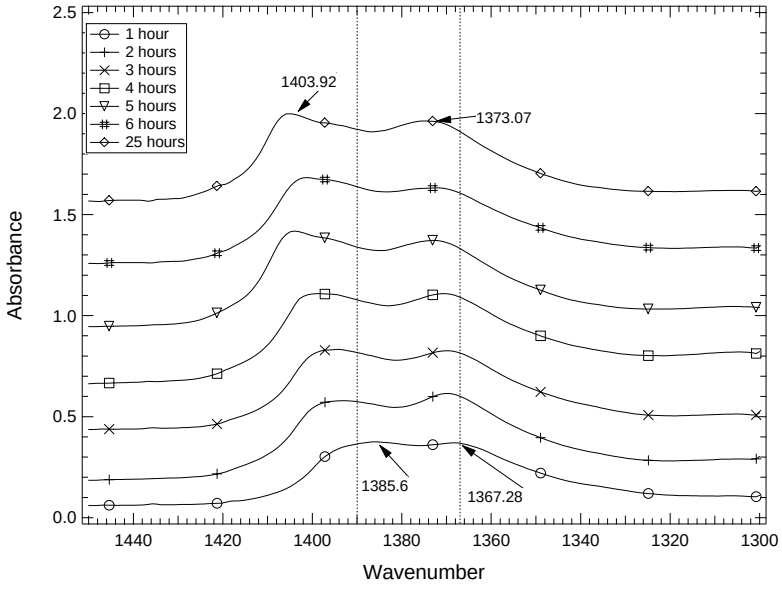


**Figure 5.37.** ***In situ*** **IR spectra of wet sulfation on $TiO_2$.**

*Sulfate peak intensity variation with vanadium content*

Comparing the entire sulfate peaks collected during dry and wet sulfation, the peak intensities increase with decreasing vanadia content. Figure 5.38 illustrates the comparison of sulfate peak areas after 24 hour sulfation, which provides the most quantitative results, that generally the sulfate peak area decreases with increasing vanadia content on the catalyst surface, except the last point, which represents the sulfate peak area of the wet sulfated 5% $V_2O_5/TiO_2$. This observation indicates that the presence of vanadia species does not favor the sulfation species formation on the catalyst surface. Therefore, the sulfate species may not form on the vanadia sites, but instead on the titania sites.

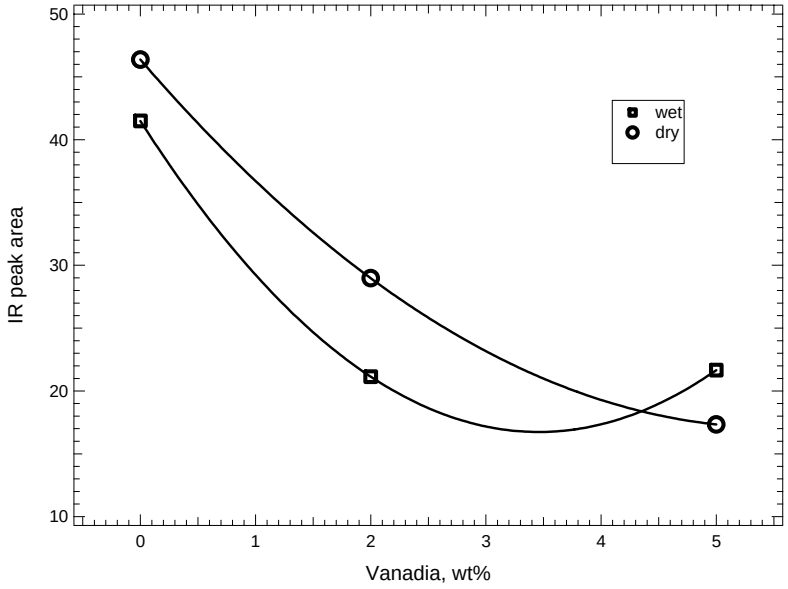


**Figure 5.38. Sulfate peak area comparison.**

*Water effect on sulfate IR peak*

On the other hand, the IR sulfate peak areas of wet sulfated samples are smaller than those of the dry sulfated samples for both $TiO_2$ and 2 % $V_2O_5/TiO_2$, it seems water decrease the sulfate peak intensity. Water removes the 1375 $cm^{-1}$ sulfate peak at 375 ˚C, and this peak appears after dehydration. Therefore, water definitely diminishes the IR activity of this sulfate peak.

The reason could be that water changes the sulfate structure, thus changing the vibration mode of hydrated sulfate, resulting in the decrease of sulfate IR peak area. R.T. Yang et al. (1998) and O. Saur et al. (1986) suggested that the structure of sulfate on the titania surface is $(M\text{-}O)_3S{=}O$ under dry conditions, and changes to bridge bidentate $(M_2SO_4)H$ under wet conditions based on their isotope exchange and IR results. This explains why the 1375 $cm^{-1}$ sulfate peak in IR spectra, which is designated to S=O vibration, are diminished to some degree after water introduction, as the S=O bond is changed to $S\text{-}O_2H$, as shown in Figure 5.39.

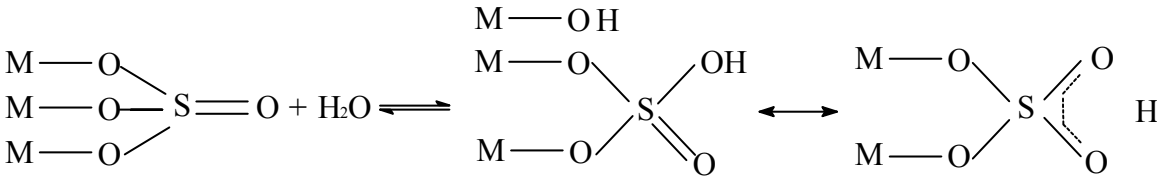


**Figure 5.39. Sulfate transformation between dry and wet conditions.**

*Doublet sulfate peak from $TiO_2$.*

Doublet sulfate IR peak signals appear on sulfated titania samples under both dry and wet sulfation conditions, and this sulfate peak increases gradually with time. A doublet peak is also reported in Yang et al.'s work, although their IR peak around 1380 $cm^{-1}$ is more intense than the one around 1401 $cm^{-1}$ (Chen and Yang, 1993). Our results, on the other hand, showed the IR peak around 1401 $cm^{-1}$ to be more intense. Moreover, the peak positions shifted to higher frequencies with increasing time during the sulfation test, indicating increasing sulfate acidity with time/surface coverage.

*XPS analysis comparison*

The XPS technique measures composition of near-surface layers (say how deep). Results of XPS analyses for all six samples after 24-hour exposure to dilute $SO_2$ are summarized in Table 5.15. The third column of the table identifies the element and its electronic orbital analyzed by XPS.

The sulfur binding energies of all the six samples appear around 168.5~169.5 eV. The change in the binding energies (BE) of sulfur in the XPS analysis is insignificant, with the small differences attributable to instrument responses during the measurement. Therefore, sulfur in all three samples should be in the same oxidation state. Moreover, the binding energy around 168.5~169.5 eV indicates that the sulfur species on the catalyst surface should be sulfate, which forms during the sulfation on both titanium dioxide and vanadia catalyst surface under either dry or wet conditions, no other sulfur compounds form. This conclusion agrees with the *in situ* FTIR results that also indicate only one sulfate species, which is more related to titanium dioxide than vanadia, was generated on the surface of samples during sulfation.

**Table 5.15. XPS results.**

| Sample | | Elements | B.E. | Atom % | Sample | | Element | B.E. | Atom % |
|---|---|---|---|---|---|---|---|---|---|
| 5VTO | 5% V | C1s | 285.00 | 24.2 | 5VTH | 5% V | C 1s | 285.00 | 5.3 |
| | Sulfation | O1s | 533.99 | 56 | | Sulfation | O 1s | 533.39 | 65.8 |
| | without | S2p | 168.46 | 1.5 | | with | S 2p | 168.55 | 2.8 |
| | water | Ti2p | 458.19 | 16.5 | | water | Ti 2p | 458.14 | 20.2 |
| | | V 2p3/2 | 516.72 | 3.3 | | | V 2p3/2 | 516.68 | 3.3 |
| 2VTO | 2% V | C 1s | 285.00 | 8.3 | 2VTH | 2% V | C 1s | 285.00 | 10.1 |
| | Sulfation | O 1s | 533.74 | 67.7 | | Sulfation | O 1s | 530.63 | 65.2 |
| | without | S 2p | 168.97 | 2.1 | | with | S 2p | 169.25 | 2.4 |
| | water | Ti 2p | 458.16 | 20.9 | | water | Ti 2p | 458.72 | 20.2 |
| | | V 2p3/2 | 516.36 | 1.9 | | | V 2p3/2 | 517.24 | 2.1 |
| $TiO_2$-O | Titanium dioxide | C 1s | 285.00 | 8.7 | $TiO_2$-H | Titanium dioxide | C 1s | 285.00 | 10.2 |
| | Sulfation | O 1s | 529.48 | 66.4 | | Sulfation | O 1s | 530.48 | 70.7 |
| | without | S 2p | 168.47 | 2.8 | | with | S 2p | 169.50 | 3.4 |
| | water | Ti 2p | 458.42 | 23.2 | | water | Ti 2p | 459.50 | 15.6 |

Sulfur content versus vanadia concentration on the catalyst surface from XPS analyses was plotted in Figure 5.40.

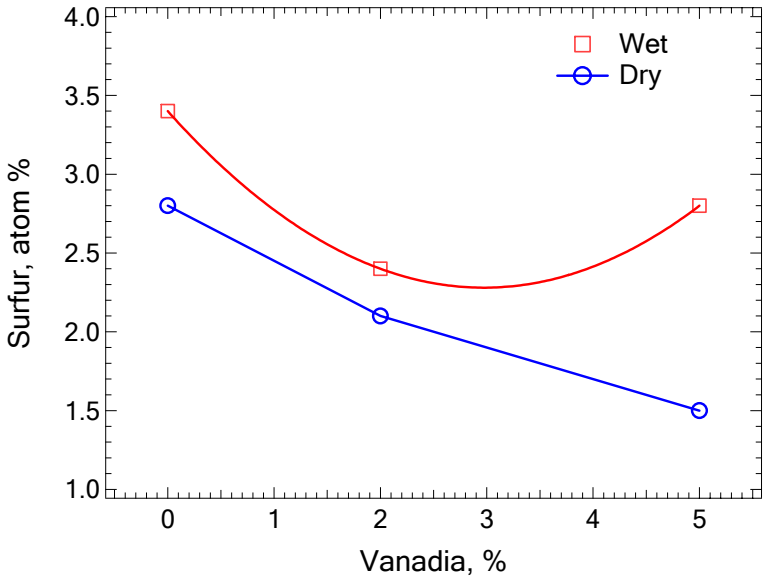


**Figure 5.40. Sulfur content on $TiO_2$ and $V_2O_5/TiO_2$ as determined by XPS.**

The XPS results show that the sulfur content decreases with increasing vanadia concentration on the catalyst surface. This result agrees with the observation from *in situ* FTIR analyses, where the peak featured at 1370-1375 $cm^{-1}$ in the FTIR spectra, decreased with increasing vanadia content on the catalyst surface. This peak is essentially not present on 5% vanadia catalyst during and after the sulfation moist test. Therefore, XPS results also indicate that vanadia species do not favor the sulfation.

Water apparently enhances accumulation of sulfur on both the titanium dioxide support and vanadia catalysts, especially above 2% percent vanadia content. For either dry or wet sulfation, the highest sulfur content was obtained on titanium dioxide. Vanadia catalyst sulfur content is smaller relative to that of sulfated titanium dioxide; but it is still a major constituent on the surface. Noticeably, in the absence of water vapor, sulfur content decreases linearly with increasing vanadia content on the catalyst surface, with a non-linear trend obtained during wet sulfation. The sulfur content decreases on 2% vanadia catalyst compared to that on titanium dioxide, but it increases a little on 5% vanadia catalyst surface while is still lower than that on titanium dioxide in case of wet sulfation.

Vanadium in an unsulfated SCR catalyst exists as vanadia, or vanidum pentoxide ($V_2O_5$) with vanadium in a +5 oxidation state. Thermochemical equilibrium predictions suggest that vandadium in the presence of gas-phase $SO_2$ forms vanadyl sulfate ($VOSO_4$) in which the oxidation state of vanadium is +4. Vandadium sulfate ($V(SO4)_2$), predicted to exist at higher temperatures in the presence of gas-phase $SO_2$ also includes vanadium in the +4 oxidation state. Therefore, all reasonably expected sulfation products of vanadium pentoxide reduce the vanadium oxidation state from +5 to +4.

X-ray photon spectroscopy (XPS) measures surface composition and oxidation state, the latter being measured in terms of binding energy. XPS results (Figure 5.41) from catalysts exposed to $SO_2$ under commercially relevant conditions indicate that both 2% and 5% vanadia catalysts, whether sulfated under dry or wet conditions, include vanadium in a +5

oxidation state, consistent with the spectroscopy-based conclusion that vanadia does not sulfate.

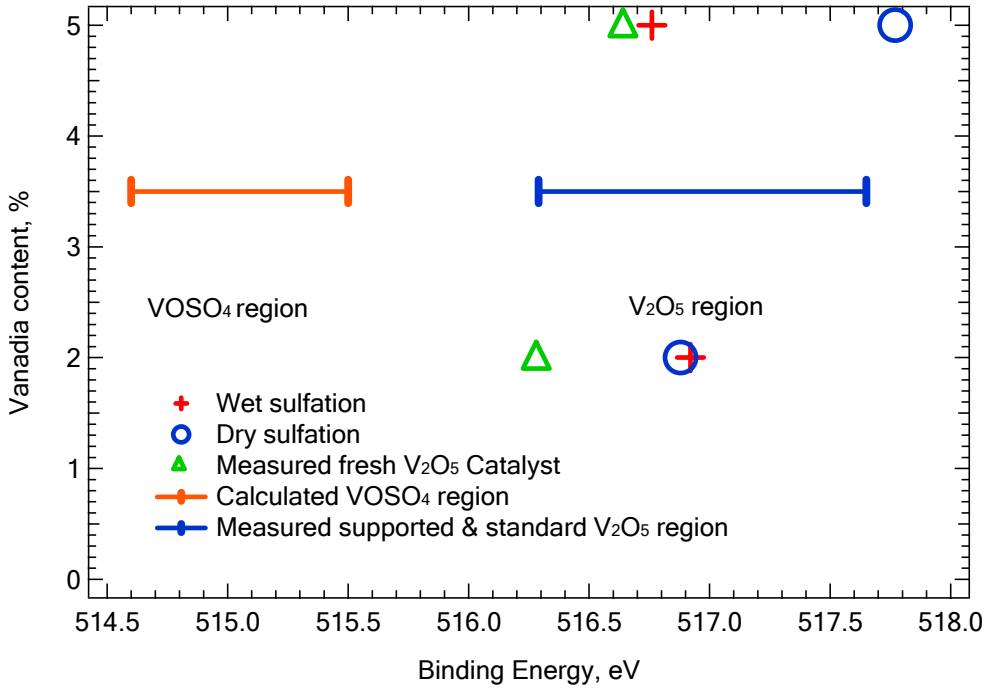


**Figure 5.41. XPS binding energies for wet and dry sulfated vanadia catalysts.**

The existence of the surface vanadium in a non-equilibrium state is not surprising for several reasons. These include; (1) the system is actively reacting and therefore clearly not in equilibrium, although it could possibly be in local equilibrium; (2) the thermochemical properties used to predict the equilibrium condition are based on bulk samples – small surface grains introduce forces on the compounds that can and commonly do shift equilibrium from the bulk condition; and (3) the prediction does not include non-ideal interactions or other features that could compromise its accuracy.

Subsequent $NH_3$ and NO adsorption tests were conducted to investigate the effects of sulfation on the catalysts acidity and surface chemistry.

*$NH_3$ adsorption*

1000 ppm ammonia adsorption was also compared on fresh and sulfated samples, as shown in Figures 5.42 through 5.45.

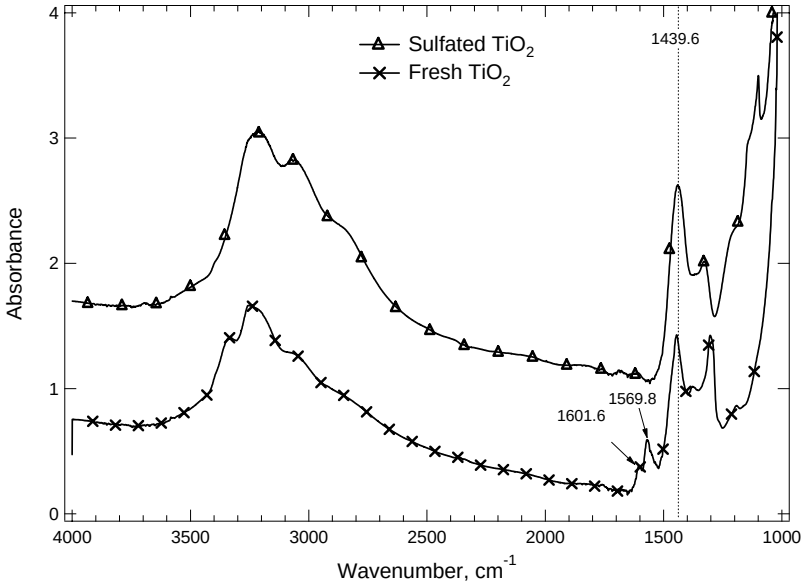


**Figure 5.42. 1000 ppm $NH_3$ adsorption on non-sulfated and 24-hour sulfated $TiO_2$ at 20 ˚C.**

On fresh titania, as shown in Figure 5.42, four major ammonia adsorption peaks appear. Peaks at 1601 and 1302.7 $cm^{-1}$ correspond to coordinately adsorbed ammonia on Lewis acid sites, the peak at 1440 $cm^{-1}$ is due to ammonia chemisorbed on Brønsted acid sites, and the peak at 1569.8 is from amide ($–NH_2$) species (references). On 24-hour sulfated titania, only chemisorbed ammonia on Brønsted acid sites at 1440 $cm^{-1}$ can be observed, and it is more intense than that from fresh titania. Therefore, sulfation reduces the number of Lewis acid sites and increases the number of Brønsted acid sites on the titania surface. It is possible that sulfate species transform Lewis acid sites into Brønsted acid sites on the titania surface.

Similar results were observed by comparing ammonia adsorption on fresh and sulfated 1, 2 and 5% $V_2O_5/TiO_2$, as shown in Figure 5.43, Figure 5.44 and Figure 5.45 correspondingly. Weakly coordinated adsorbed ammonia on Lewis acid site appears on fresh 1% $V_2O_5/TiO_2$, while only chemisorbed ammonia on Brønsted acid sites appears on the same catalyst sulfated for 24 hours. Moreover, on 2 and 5% catalyst, only chemisorbed ammonia on Brønsted acid sites was detectable, and this adsorption was intensified after sulfation on each sample. These results further confirm that sulfates reduce the number of Lewis acid sites and increase the number of Brønsted acid sites. However, the acidity of individual sites in not affected since ammonia adsorption peak wavenumber does not shift with sulfation.

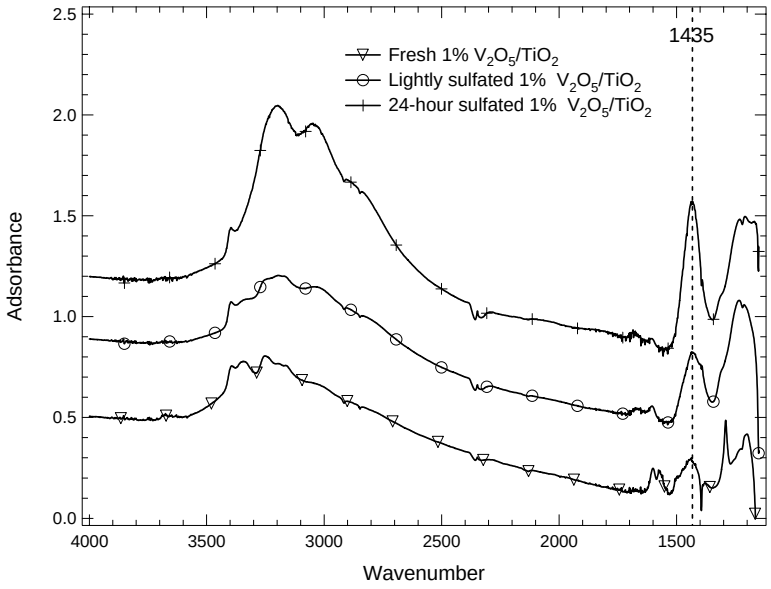


**Figure 5.43. 1000ppm $NH_3$ adsorption on fresh, lightly sulfated, and 24-hour sulfated 1% $V_2O_5/TiO_2$ at 20 ˚C.**

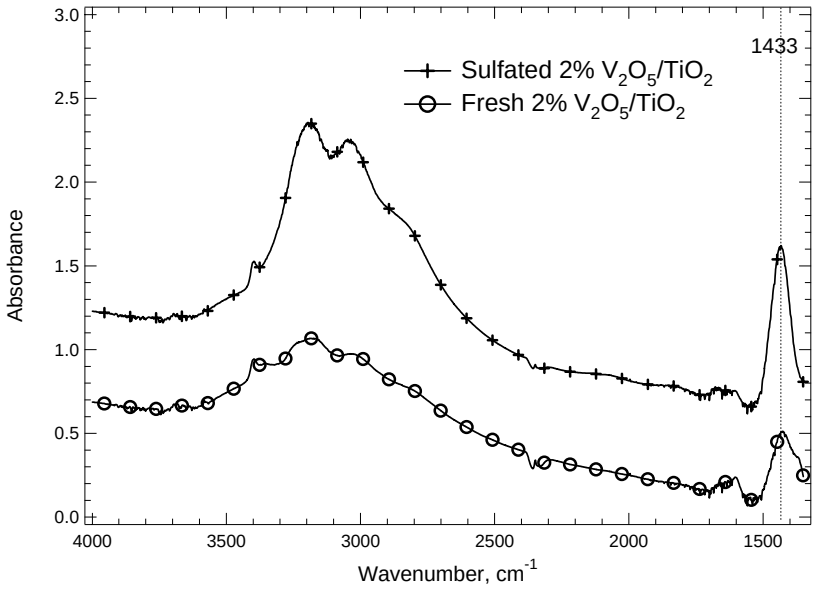


**Figure 5.44. 1000ppm $NH_3$ adsorption on fresh, lightly sulfated, and 24-hour sulfated 2% $V_2O_5/TiO_2$ at 20 ˚C.**

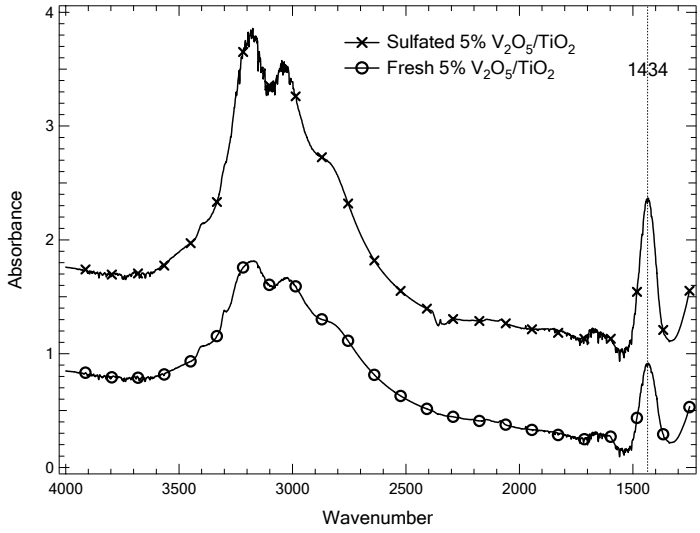


**Figure 5.45. 1000 ppm $NH_3$ adsorption on fresh, lightly sulfated, and 24-hour sulfated 5% $V_2O_5/TiO_2$ at 20 ˚C.**

Previous results indicate that vanadia does not sulfate. Those results, combined with these results, indicate that surface sulfation decreases Lewis acid site concentrations for all catalysts thus far studied, confirming that catalytic activity under commercial coal-based SCR conditions occurs primarily on Brønsted acid sites and would be susceptible to decrease by basic impurities such as alkali and alkaline earth oxides, chlorides, and alkali/alkaline earth sulfates.

*$NH_3$ adsorption as a function of temperature*

Figure 5.46 shows 1000 ppm ammonia (helium balance) adsorption on sulfated 1% $V_2O_5/TiO_2$ at different temperatures from 20-380 ˚C. The intensity of the ammonia adsorption peak (1428 cm $^{-1}$) decreases with increasing temperature, which indicates that ammonia gradually desorbs from the catalyst surface as the temperature increases at a ramp rate of 5 ˚C/min. After the temperature reached 300 ˚C, ammonia desorbs from the surface is nearly complete. At 380 ˚C, the sulfation peak (1372 cm$^{-1}$) reappears. The adsorbed ammonia modifies the sulfate sites such that they do not vibrate with their characteristic frequency.

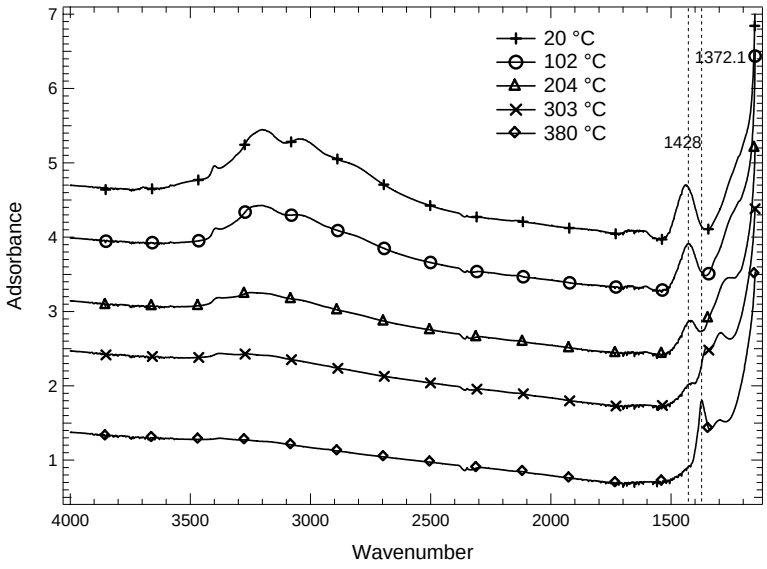


**Figure 5.46. 1000 ppm ammonia (helium balance) adsorption on sulfated 1% $V_2O_5/TiO_2$.**

*NO adsorption*

During the NO adsorption experiment, 1000 ppm NO in argon was introduced to the sample at room temperature (20 ˚C). NO adsorption is only observable in the presence of oxygen.

Figure 5.47 shows the NO adsorption on 1% $V_2O_5/TiO_2$ with various sulfation degrees. NO adsorption peaks on the fresh 1% $V_2O_5/TiO_2$ catalyst are intense, but decrease with increasing sulfation time. It seems sulfate species inhibit NO adsorption, possibly by competing for the same surface sites. Similar tendency was observed for NO adsorption on $TiO_2$ (Figure 5.48) with various sulfation degrees. As the sulfate species content increases, NO adsorption intensity decreases.

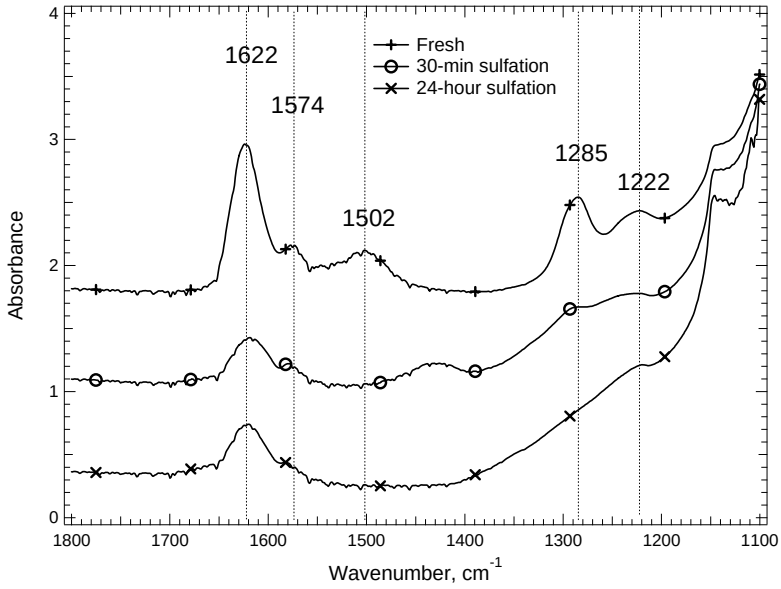


**Figure 5.47. NO adsorption comparison on 1% $V_2O_5/TiO_2$ with various sulfation degrees.**

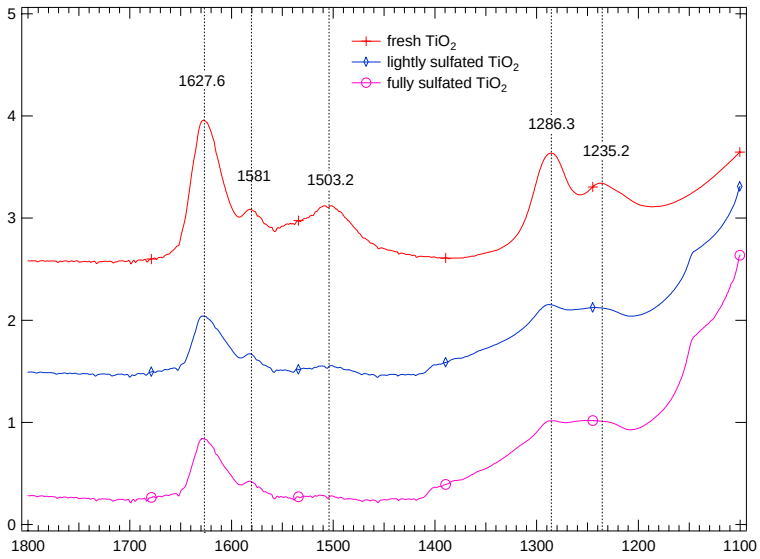


**Figure 5.48. NO adsorption comparison on $TiO_2$ with various sulfation degrees.**

*NO reduction activity comparison*

In Figure 5.49, the indicated symbols represent measured NO conversion data from fully (24-hour exposure) sulfated, lightly sulfated, and fresh 1% $V_2O_5/TiO_2$ SCR catalysts. The solid lines represent the curve fits based on the non-linear least squares algorithm for each conversion data set. The upper and lower dotted lines indicate the 95% confidence interval for activity ($K$) at a given temperature. The results indicate that differences observed among the samples are statistically significant. Typically, sulfation increases intrinsic activity by about 40% in these tests. Furthermore, although $K$ increases significantly upon catalyst sulfation, the activation energy $E_a$ remains statistically unchanged for sulfated and non-sulfated samples, with $E_a$ = 44921~52566 J/mol. The differences in the rate coefficients appear primarily in the pre-exponential factor, $A$. Results of curve fitting show that sulfated samples have larger pre-exponential factors ($A$ = 1716400 and 300888 $cm^3/g$ s) than fresh samples ($A$ = 182000 $cm^3/g$ s).

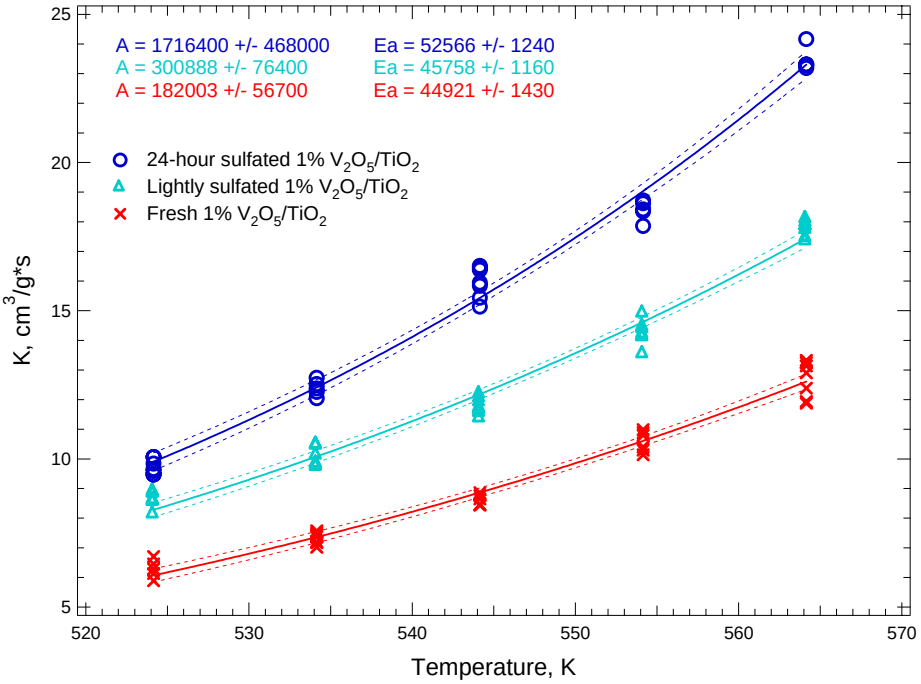


**Figure 5.49. Kinetic parameter (A, Ea) estimations with confidence intervals of fresh, lightly sulfated, and 24-hour sulfated 1% $V_2O_5/TiO_2$.**

The parameters of such global reaction rate expressions should not be over interpreted, but there is a consistent if not entirely fundamentally justified interpretation of these data. They agree with the *in situ* spectral results that indicate sulfation does not impact the vanadia grains on the catalyst. As indicated by the spectra, surface sulfation impacts the ammonia absorption on the surface by providing more Brønsted acid sites without changing the sites acidity, thus more opportunities for $NH_3$-NO interaction and interacting frequency was increased, which is related to $A$. At the same time, the acidity remains the same, and activation energy remains unchanged. Therefore the correlation between the increase of the number of active sites and pre-exponential factor A, and same Brønsted acid site acidity and activation energy before and after sulfation suggests that Brønsted acid site are the active sites for the NO reduction with $NH_3$.

These data also confirm the interpretation from the field tests, in which slight increases in activity were seen after modest catalyst exposure. These data indicate clear increases in

activity with increasing sulfation. Commercial catalysts deployed in coal-fired systems should sulfate rapidly (within twelve hours) whereas the deactivation mechanisms take much longer, resulting in an initial increase followed by a gradual decrease in catalyst activity.

#### 5.1.6.2.3 Vanadia content effect

*$NH_3$ adsorption comparison with various vanadia contents*

1000 ppm ammonia adsorbs on fresh titania, and 1 and 2 % $V_2O_5/TiO_2$ samples at room temperature. Figure 5.50 compares ammonia adsorption on the catalyst surface with vanadia content from 0 to 2%. Ammonia adsorbed on Lewis acid sites appears at 1602 and 1301 $cm^{-1}$, while $NH_3$ adsorbed on Brønsted acid sites appears at 1444 $cm^{-1}$. Adsorption on Lewis acid sites occurs most prominently for the fresh $TiO_2$ and to significantly lower extent on 1% $V_2O_5/TiO_2$ catalysts. There is no indication of adsorption on Lewis sites in the 2% sample. However, all three samples show substantial adsorption on Brønsted sites and the adsorption intensity increase upon addition of more vanadia species on the catalyst surface. Therefore, the results indicate that the addition of vanadia decreases the amount of Lewis acid sites, and increases the amount of Brønsted acid sites. Moreover, an adsorption peak at 1568.8 $cm^{-1}$, which is assigned to amide ($–NH_2$) species, was observed on titania, but not on 1% and 2% vanadia catalysts.

Literature sources report that the $TiO_2$ surface possesses only Brønsted acid sites, but no Lewis acid sites. Our observation, however, indicates the existences of both Brønsted and Lewis acid sites on the $TiO_2$ surface. (Donovan said) Wachs I.E. (will be quoted later) conducted an experiment and verified that what kind of acid site appears on the $TiO_2$ surface is determined by the material the preparation method. Therefore, it is not unusual that Brønsted acid site appears on the $TiO_2$ applied in our experiment.

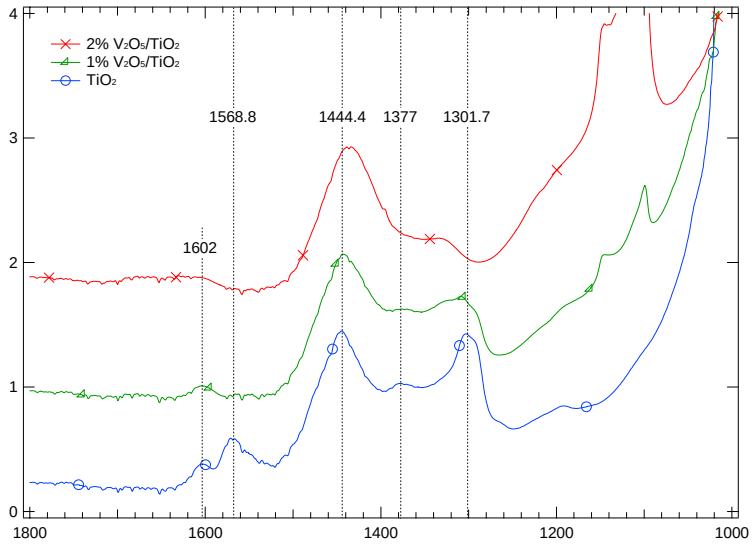


**Figure 5.50. 1000ppm $NH_3$ adsorption comparison on $TiO_2$, 1 and 2 % $V_2O_5/TiO_2$ at 20 ˚C.**

These results illustrate that commercial, non-sulfated catalysts (typically about 1% vanadia) exhibit primarily Brønsted acid activity with respect to ammonia adsorption.

*NO adsorption*

NO adsorption IR bands appear at room temperature on non-sulfated $V_2O_5/TiO_2$ catalysts with vanadia content ranging from 0-5 %, as illustrated in Figure 5.51. The NO adsorption bands appear at the same frequencies for all catalysts, suggesting that the same adsorbed NO species form on all samples. These bands correspond to surface nitrate species (Ramis and Busca, 1990).

Most researchers have observed NO adsorption on pure $TiO_2$ and on reduced vanadia catalysts, but not on fully oxidized vanadia catalysts (Topsøe et al., 1995; Ozkan et al., 1995; Yang et al., 1998). The $V_2O_5/TiO_2$ used in this experiment had been preoxidized at 400 ˚C for four hours before NO adsorption; therefore, the vanadia valence should be $5^+$. Thus, NO adsorption was observed on fresh vanadia catalysts.

The amount of adsorbed NO, which is proportional to the NO adsorption peak area, decreases with increasing vanadia content on the titania surface, as shown in Table 5.16. It seems that addition of vanadia species suppresses NO adsorption. The strongest NO adsorption happens on the fresh titania support surface, whereas the NO adsorbs weakly on the 5% vanadia catalyst. One possible explanation for this observation is that vanadia species occupy the same surface sites as NO, which could be surface $OH^-$ group on the titania support.

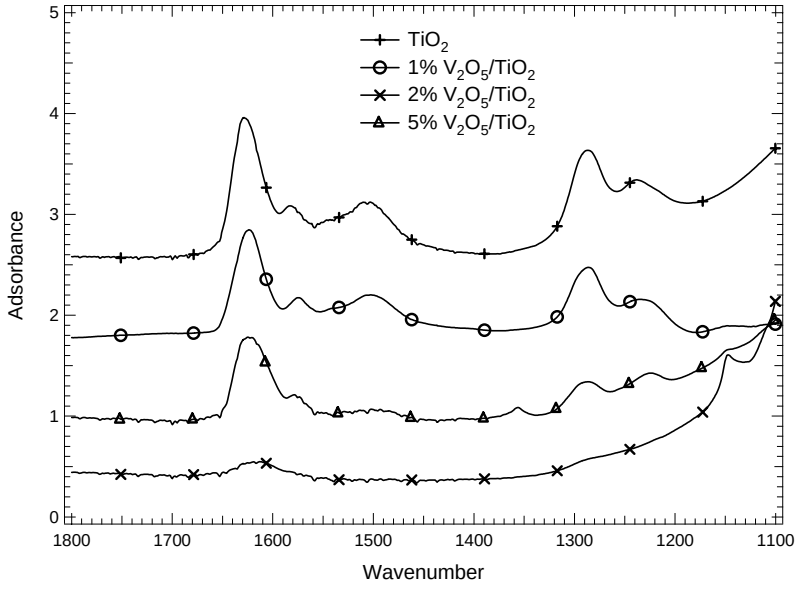


**Figure 5.51. NO adsorption comparison.**

**Table 5.16. Room temperature NO adsorption peak area comparison on fresh $TiO_2$ and vanadia catalysts.**

| | 1630-1570 $cm^{-1}$ | ~1500 $cm^{-1}$ | 1285-1220 $cm^{-1}$ |
|---|---|---|---|
| Pure $TiO_2$ | 45.41 | 15.19 | 48.14 |
| Fresh 1% $V_2O_5/TiO_2$ | 43.29 | 9.78 | 24.23 |
| Fresh 2% $V_2O_5/TiO_2$ | 43.64 | 2.46 | 17.3 |
| Fresh 5% $V_2O_5/TiO_2$ | 8.07 | | |

*NO adsorption at different temperatures*

Figure 5.52 illustrates the effect of temperature on NO adsorption of fresh 1% $V_2O_5/TiO_2$. During the test, the NO adsorption peaks at 1626.7, 1582.3, and 1286.3 $cm^{-1}$ gradually decreased when the temperature gradually increased from 25 to 380 ˚C. During the heating process, NO adsorption bands at 1623 and 1575 $cm^{-1}$ disappeared from the IR spectrum at 300 ˚C, while no band at 1285 $cm^{-1}$ could be observed after the temperature reached 200 ˚C. The NO adsorption on the vanadia catalyst is visible up to 300 ˚C further confirming the adsorption species formed on vanadia catalyst surface is nitrate.

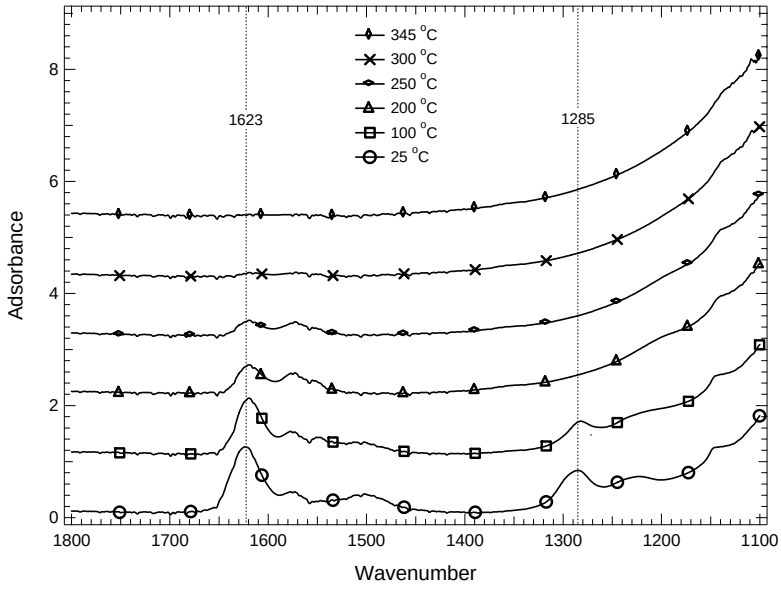


**Figure 5.52. NO adsorption on fresh 1% $V_2O_5/TiO_2$ at different temperatures.**

*NO reduction activity comparison with various vanadia content*

SCR tests on 5 and 2 % $V_2O_5/TiO_2$ catalysts at 350 ˚C resulted in NO conversions of about 80% and 72%, respectively, which indicates that increasing vanadia content enhances NO reduction activity.

The correlation between the Brønsted acid site intensity and vanadia species indicates that the addition of vanadia species onto the titania surface introduces more Brønsted acid site to the titania support. On the other hand, kinetics investigations show that NO reduction activity increases with increasing surface vanadia content. The above two observations indicate that Brønsted acid sites rather than Lewis acid sites are the active sites for the catalytic reduction of NO with $NH_3$.

#### 5.1.6.2.4 Tungsten (W) effect

*$NH_3$ adsorption*

In the Figure 5.53, the ammonia adsorption peak at 1172 $cm^{-1}$ represents ammonia adsorption on Lewis acid sites, and the adsorption peak at 1430 $cm^{-1}$ is from ammonia adsorption on the Brønsted acid sties. The existence of tungsten apparently decreases the ammonia adsorption on Lewis acid sites, probably because tungsten consumes the Lewis acid sites, but increases ammonia adsorption on Brønsted acid sites, probably because more Brønsted acid sites were introduced by addition of tungsten.

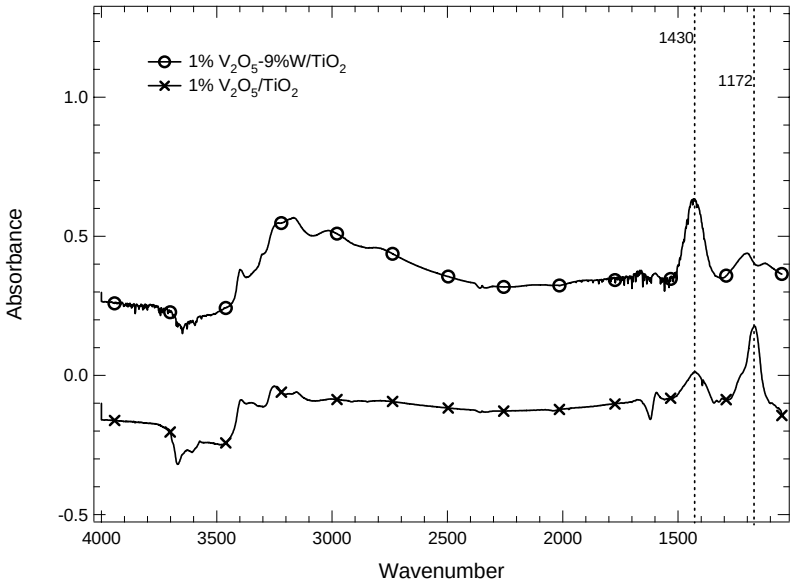


**Figure 5.53. 1000ppm $NH_3$ adsorption on 1% $V_2O_5/TiO_2$ and 1% $V_2O_5$ – 9%W/$TiO_2$ at 20 ˚C.**

*NO reduction activity comparison*

SCR of NO with $NH_3$ was also conducted on 1% $V_2O_5$/9%W/$TiO_2$. To remain in the intrinsic kinetics regime, the reaction temperature varied from 200 ˚C to 250 ˚C. The non-linear least squares fit results are compared in Figure 5.54. The 1% $V_2O_5$ – 9%W/$TiO_2$ catalyst exhibits about three times higher NO reduction activity than 1% $V_2O_5/TiO_2$, and possesses higher activity even than 24-hour sulfated 1% $V_2O_5/TiO_2$ catalyst by about 80%. Thus, tungsten appearance on the vanadia catalyst surface greatly increases the catalyst NO reduction ability. The enhancement, by comparing the analyzed results of $A$ and $Ea$, is due to a larger $A$, the pre-exponential factor, which is an indication of the number of active sites. The activation

energy, on the other hand, remains unchanged, indicating the reaction mechanism should remain the same. Therefore, the addition of tungsten to the vanadia catalyst increases the amount of active sites, with little impact on reaction mechanism. This is supported by *in situ* IR spectra that indicate that tungsten creates more Brønsted acid sites without changing the acidity. The correlation between kinetic investigation and IR results suggests that Brønsted acid sites are the active sites on the catalyst surface.

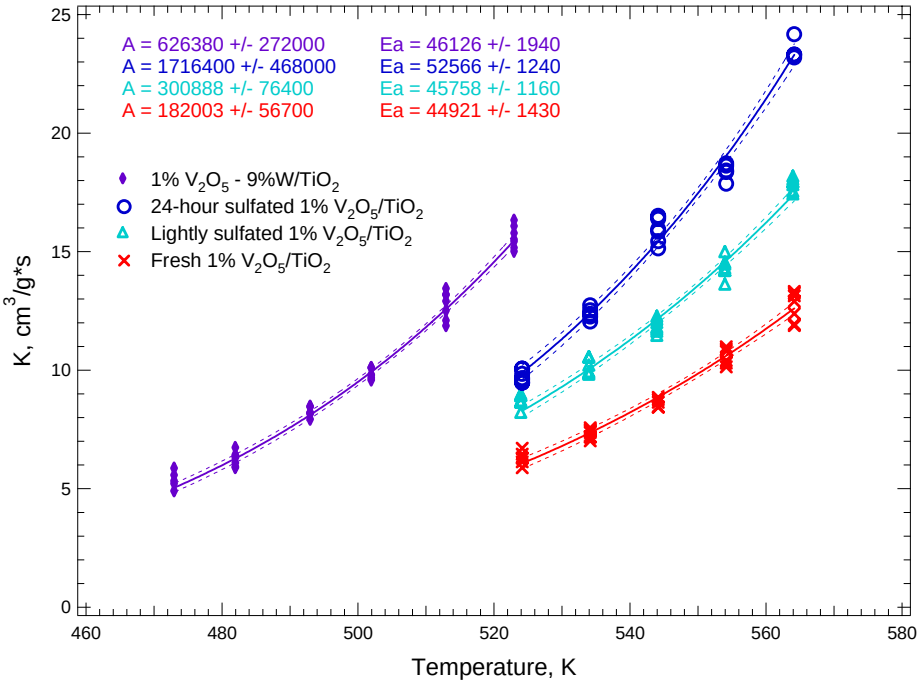


**Figure 5.54. Kinetic parameter (A, Ea) estimations with confidence intervals of fresh, lightly sulfated, and 24-hour sulfated 1% $V_2O_5/TiO_2$, and fresh 1% $V_2O_5$ – 9%W/$TiO_2$.**

### 5.1.6.2.5 Alkali- (K and Na) and alkaline-earth-metals (Ca) effect

Alkali and alkaline earth metals commonly appear in the flue gas from boilers that burn coal and biomass. They contribute potentially to the catalyst deactivation by poisoning the catalyst active sites. As discussed in conjunction with the field tests, they (K, Na, and Ca) accumulate on the catalyst surface. The ISSR, on the other hand, tries to determine the mechanism and the extent of poisoning by K, Na, and Ca.

*$NH_3$ adsorption*

In Figure 5.55 and Figure 5.56, the top line represents IR peak of ammonia adsorbed on fresh catalysts, and the bottom line is from $NH_3$ adsorption on 0.5 K doped catalysts. It is obvious that the addition of potassium to the vanadia catalyst decreases the intensities of ammonia adsorption on both the Brønsted and Lewis acid sites. Table 5.17 summarizes how the ammonia adsorption intensity, which is reflected by IR peak area, decreases by about 20% on the Brønsted acid sites and 40% on Lewis acid sites on 1% $V_2O_5/TiO_2$, and 56% on both Brønsted and Lewis acid sites on 1% $V_2O_5$ -9%W/$TiO_2$ upon potassium addition. Moreover, the 1424 $cm^{-1}$ IR peak, which represents ammonia adsorption on the Brønsted acid site, shifts down to a low wave number on the 1% $V_2O_5/TiO_2$ catalyst, but remains at the same position on the 1% $V_2O_5$ -9%W/$TiO_2$. This phenomenon indicates that K addition decreases the Brønsted acid site acidity on the 1% $V_2O_5/TiO_2$ catalyst surface, but has little effect on the

Brønsted acid site acidity on the 1% $V_2O_5$ -9%W/$TiO_2$, probably because tungsten helps to protect Brønsted acid sites on the vanadia catalyst. On the other hand, potassium has a negligible effect on the Lewis acid site acidity because the IR peak at 1170 $cm^{-1}$ remains esssentially unchanged before and after K addition.

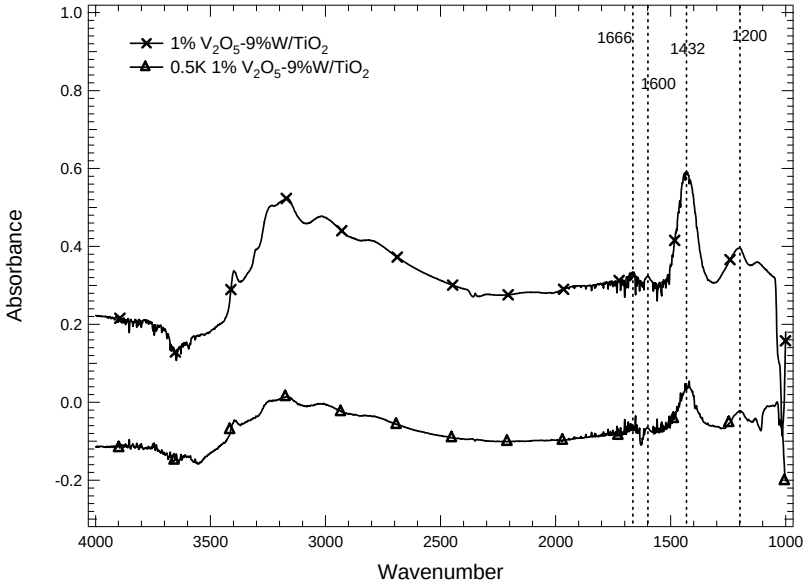


**Figure 5.55. 1000ppm $NH_3$ adsorption on fresh and k doped 1% $V_2O_5$ – 9%W/$TiO_2$.**

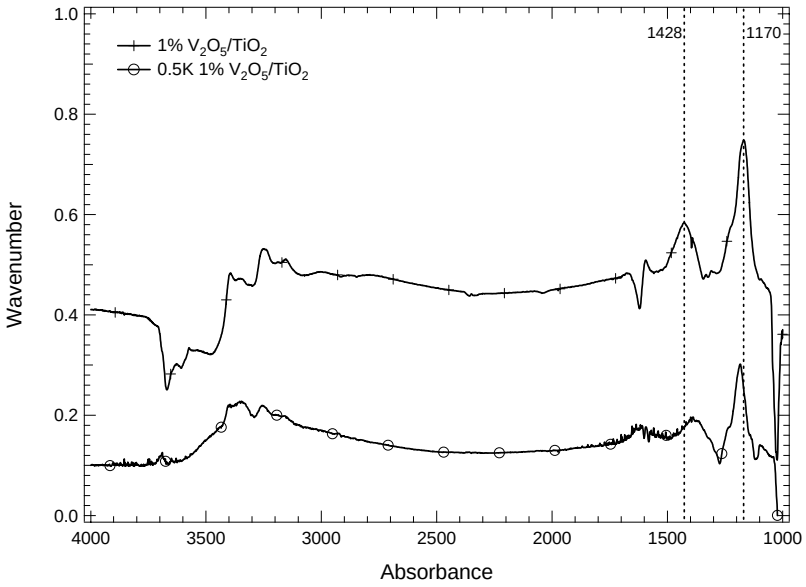


**Figure 5.56. 1000ppm $NH_3$ adsorption on fresh and K-doped 1% $V_2O_5$/$TiO_2$.**

**Table 5.17. $NH_3$ adsorption IR peak area comparison.**

| Catalysts | IR Peak Area | |
|---|---|---|
| | 1424 $cm^{-1}$ | 1170 $cm^{-1}$ |
| 1% $V_2O_5/TiO_2$ | 10.3 | 22 |
| 0.5 K doped 1% $V_2O_5/TiO_2$ | 8.6 | 13.3 |
| 1% $V_2O_5$ -9%$WO_3/TiO_2$ | 24.54 | 4.482 |
| 0.5 K doped 1% $V_2O_5$ -9%$WO_3/TiO_2$ | 10.8 | 1.964 |

1000 ppm $NH_3$ adsorption on various poison-doped 1% $V_2O_5$ -9%$WO_3/TiO_2$ was compared in Figure 5.57. The major IR peaks on both fresh or poison-doped samples are from ammonia adsorbed on Brønsted acid sites locate at 1427 $cm^{-1}$. This peak intensity decrease in the order of fresh > Ca doped > Na doped > K doped 1% $V_2O_5$ -9%$WO_3/TiO_2$. The basicity of Ca, Na, and K follows Ca < Na < K, therefore, the decrease of the peak intensity of ammonia adsorbed on Brønsted acid sites is proportional to the basicity strength of those metals. Moreover, potassium doped 1% $V_2O_5$ -9%$WO_3/TiO_2$ also shows the largest downward shifts of ammonia adsorption peaks on Brønsted acid sites. That is, stronger bases form stronger poisons.

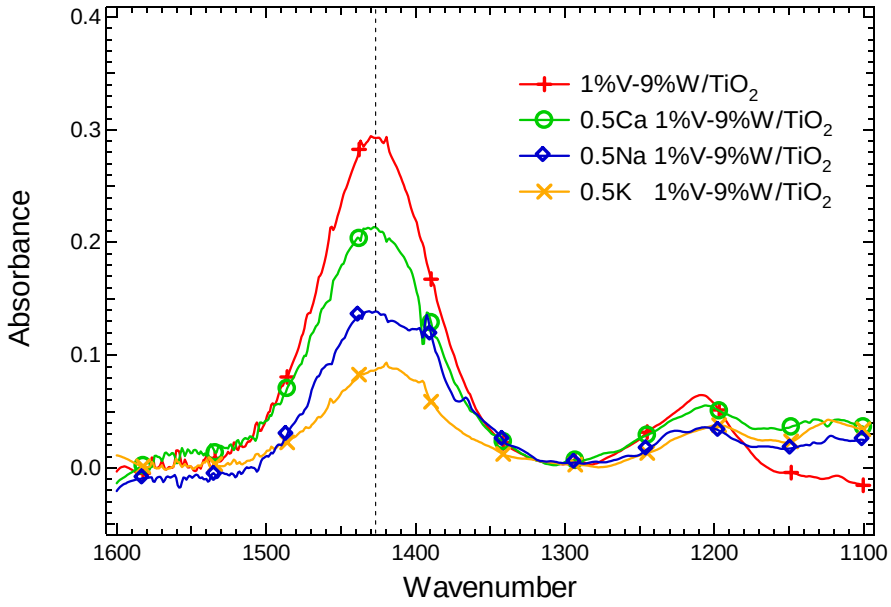


**Figure 5.57. 1000ppm NH3 adsorption on fresh and K-, Na-, and Ca-doped 1% $V_2O_5$ – 9%$W/TiO_2$ at 20 ˚C.**

*NO adsorption*

NO adsorption was also compared on fresh and potassium doped 1% vanadia catalyst. Clearly, the presence of potassium on the vanadia catalyst surface weakens the NO adsorption, as shown in Figure 5.58.

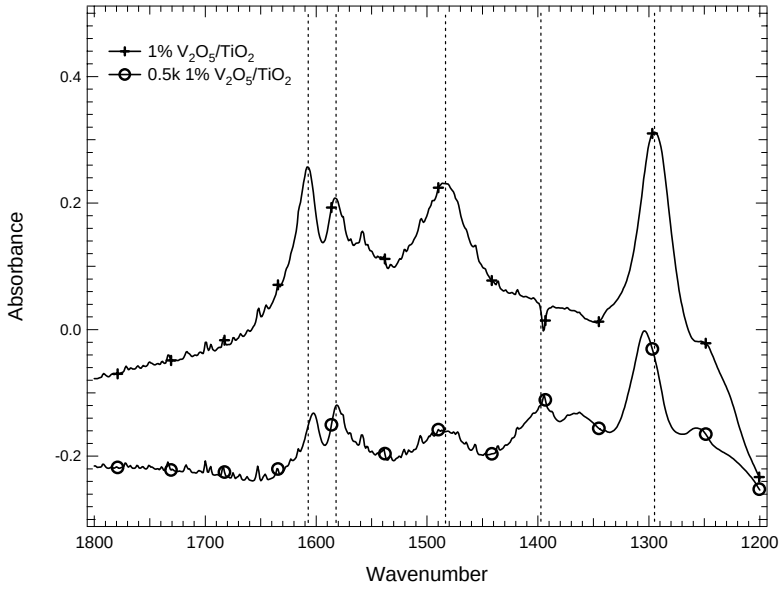


**Figure 5.58. NO adsorption on fresh and K-doped 1% vanadia catalyst.**

*NO reduction activity comparison*

SCR of NO with $NH_3$ reaction activity was compared with two pairs of catalysts, 1% $V_2O_5$ – 9%W/$TiO_2$ vs. 0.5 K and 0.5 Na doped 1% $V_2O_5$ – 9%W/$TiO_2$ (Figure 5.59), and 1% $V_2O_5$/$TiO_2$ vs. 0.5 K doped 1% $V_2O_5$/$TiO_2$ (Figure 5.60).

The addition of potassium greatly decreases the NO reduction activity of both 1% $V_2O_5$ – 9%W/$TiO_2$ and 1% $V_2O_5$/$TiO_2$ catalysts. This decrease becomes more predominant as temperature increases. Comparing pre-exponential factor ($A$) and activation energy ($E_a$) before and after potassium addition indicates that potassium introduction to the catalyst reduces values of both $A$ and $E_a$, which explains temperature dependence of the poisoning mechanism.

Smaller $A$ and $E_a$ values after potassium and sodium doping indicate that the number of active sites was reduced, probably due to potassium and sodium occupying or neutralizing some of the active sites, and the acidity (active sites are acid sites) was also decreased as indicated by smaller $E_a$, although potassium appears to be a stronger poison than sodium, which is reasonable since K is a stronger base than Na. On the other hand, the IR spectra of ammonia adsorption on fresh and poisoned vanadia catalyst illustrate that the addition of potassium and sodium decrease the ammonia adsorption intensities on Brønsted acid sites, with potassium possessing a more predominant effect on Brønsted acid site. Therefore, the kinetic investigation agrees with the IR spectra investigation that potassium and sodium decrease the amount and strength of active sites, which probably are the Brønsted acid sites, and the extent of decrease follows the order of the basicity of the metals.

At this point, all the kinetic investigations, including fresh, sulfated, and poisoned vanadia catalyst and IR spectral investigations, agree with each other and suggest that Brønsted acid sites are the active sites, sulfate species and tungsten enhance the catalyst activity by the generation of more active sites without changing the acidity, and potassium and sodium decrease the catalyst activity by decreasing the number and acidity of Brønsted acid sites.

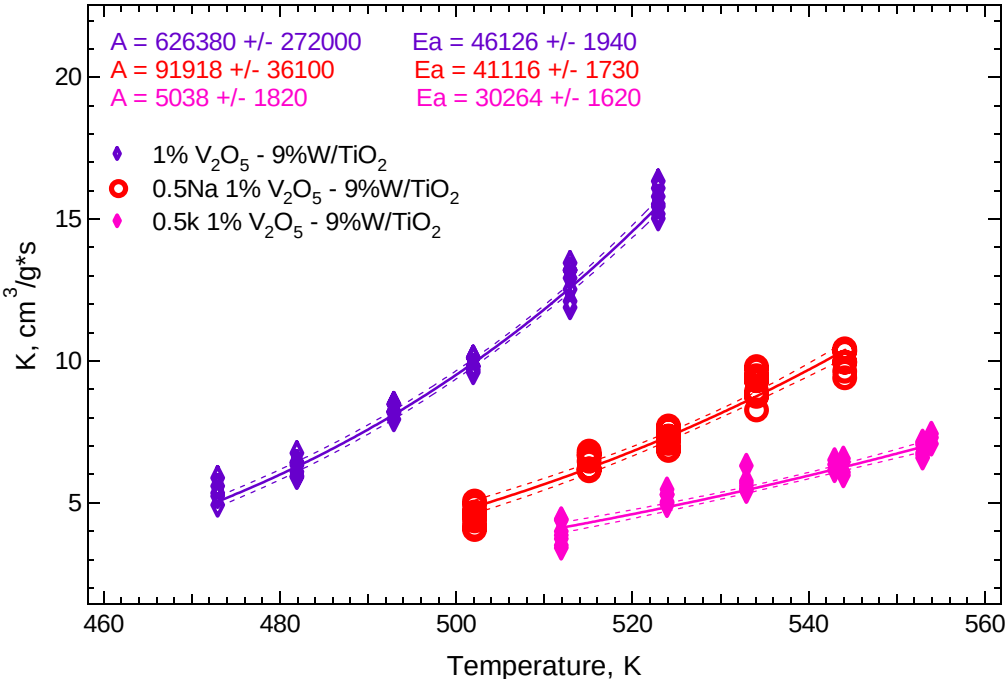


**Figure 5.59. Kinetic parameter (A, Ea) estimations with confidence intervals of fresh and 0.5 K-doped 1% $V_2O_5$ – 9%W/$TiO_2$.**

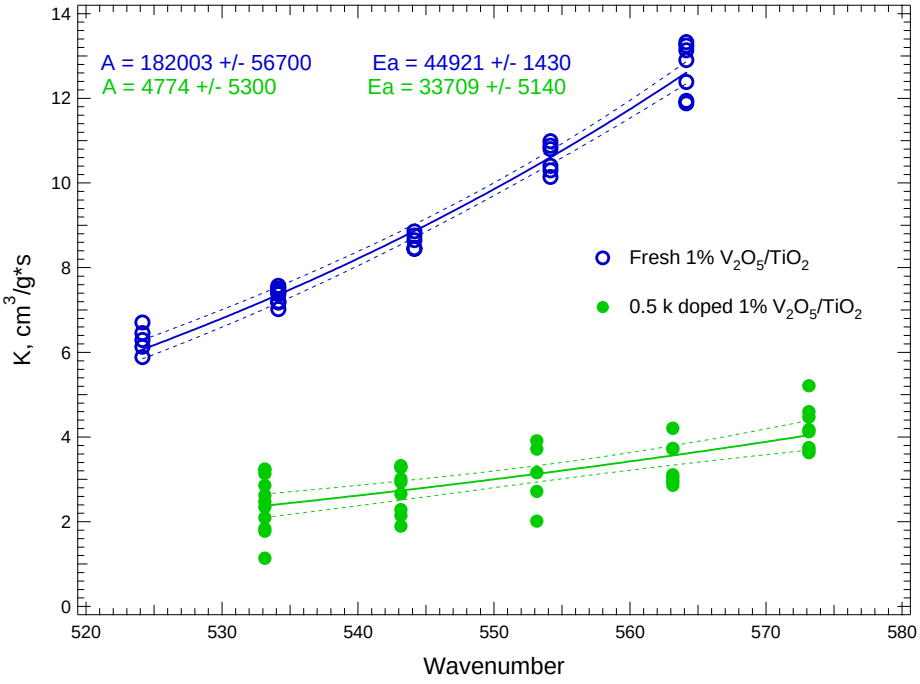


**Figure 5.60. Kinetic parameter (A, Ea) estimations with confidence intervals of fresh and 0.5 K-doped 1% $V_2O_5$ /$TiO_2$.**

#### 5.1.6.2.6 Mechanism interpretation

Figure 5.61 illustrates IR spectra collected on pure $TiO_2$, and 1 and 2% $V_2O_5/TiO_2$ catalyst wafers run in helium and $O_2$ at room temperature after pretreatment. During the pretreatment, all the wafers were heated in 5% $O_2$ and helium (balance) for four hours at 380 ˚C. Three major peaks on the spectra located at 3700-3600, 3550-3000, and ~1625 $cm^{-1}$ appear in the spectra, which correspond to a free or non-bonded $OH^-$ stretch group (3700-3600 $cm^{-1}$), an H-bonded $OH^-$ stretch group (3000-3500 $cm^{-1}$), and an $OH^-$ bend group (~1625 $cm^{-1}$) (Coates, 2000). Quantitative comparisons of these spectra are difficult in this form. Integration of the peaks determines areas that indicate surface OH group concentration and that provide more meaningful quantitative results, as tabulated in Table 5.18. The surface $OH^-$ concentration decreases upon introduction of vanadia to the titania surface over the range of vanadia concentrations studied (0-2%). This agrees with the suggestion by Topsøe that vanadia interacts with $OH^-$ groups present on the titania surface.

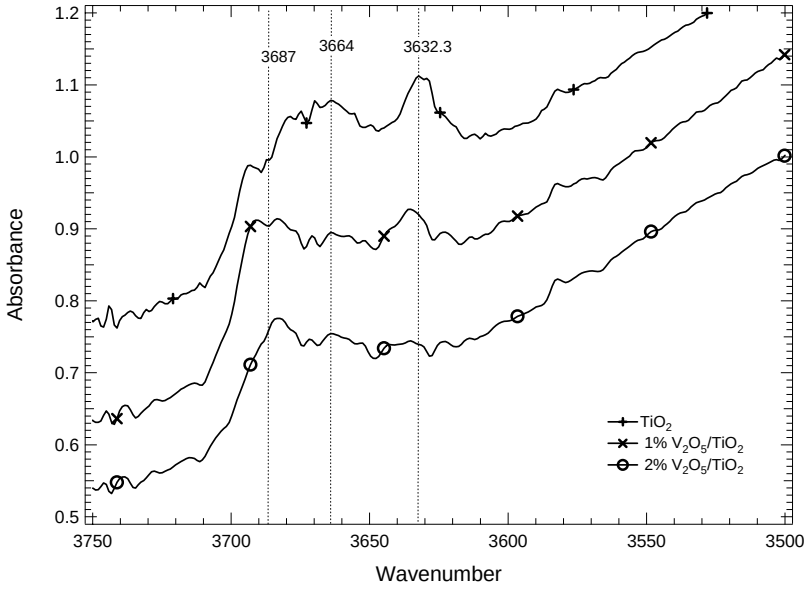


**Figure 5.61. Fresh catalyst comparison.**

**Table 5.18. Surface OH- group peak area comparison on fresh TiO2 and vanadia catalysts.**

| | 3720-3600 $cm^{-1}$ | 3550-3000 $cm^{-1}$ | ~1625 $cm^{-1}$ |
|---|---|---|---|
| | Free OH stretching | H bonded OH stretching | OH bending |
| Pure $TiO_2$ | 10.62 | 372.40 | 21.02 |
| Fresh 1% $V_2O_5/TiO_2$ | 8.73 | 314.06 | 20.68 |
| Fresh 2% $V_2O_5/TiO_2$ | 4.31 | 256.02 | 16.34 |

The effect of sulfation on $OH^-$ group concentration was also compared on titania surfaces, as shown in Figure 5.62. The OH adsorption peak almost disappears on both lightly and 24-hour sulfated $TiO_2$, which indicates the sulfate species may occupy the surface hydroxyl group on the titania surface.

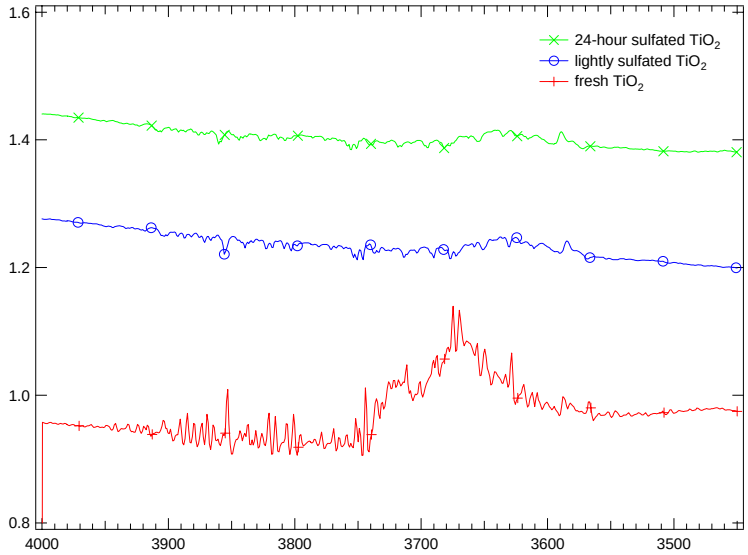


**Figure 5.62. The effect of sulfation on $OH^-$ group concentration on titania surfaces.**

Upon NO adsorption on $TiO_2$, and 1 and 2% $V_2O_5/TiO_2$ catalyst (Figure 5.63), the band intensities of the free surface $OH^-$ stretch groups (3720 – 3600 $cm^{-1}$) significantly decreased for all samples. The largest OH group loss appears on $TiO_2$, which also possesses the strongest NO adsorption. It seems the intensity of NO adsorption is proportional to the loss of OH group, which indicates that NO occupies surface OH groups on both titania and vanadia surfaces. Since titania possess the most abundant $OH^-$ group, it also exhibits the strongest NO adsorption.

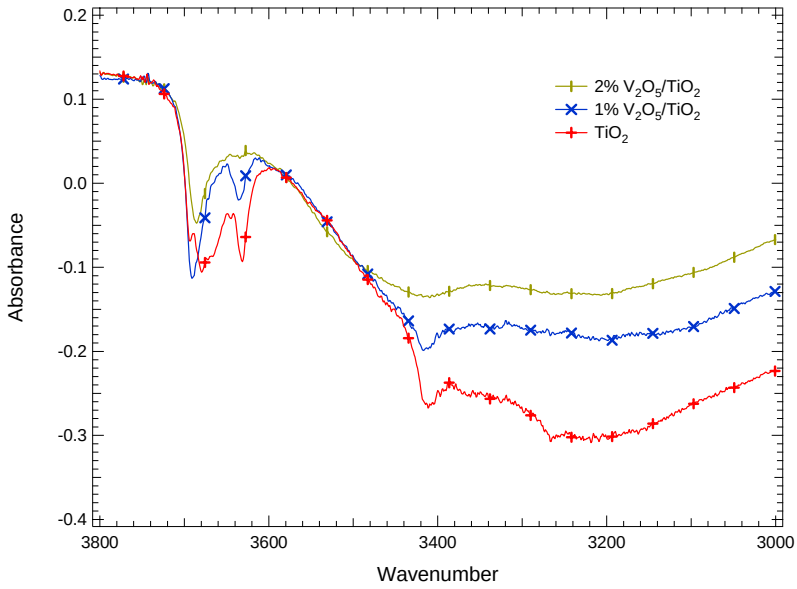


**Figure 5.63. NO adsorption comparison as a function of vanadia content.**

Therefore, both vanadia species and sulfate species occupy hydroxyl groups on the titania surface, and NO adsorbs on titania and vandia catalyst surfaces through interaction with surface $OH^-$ groups as well. Vanadia and sulfate species both inhibit NO adsorption, which does not suggest vandia suppresses the reaction since the mechanism is believe to be of Eily-Reidel type with NO as the non-absorbed gas. NO is one of the two reactant gases. Vanadia provides the active sites, and sulfate species apparently increase the activity. Therefore, all of the above three species, NO, V, and S impact the SCR reaction, and they do not favor each other but inhibit each other. One explanation for the observation is that instead of vanadia species being the active center, the edge between the vanadia and titania could be the active center.

#### 5.1.6.2.7 BET analysis

BET surface area analyses for pore size distribution were conducted on three homemade samples: densified $TiO_2$, 2% w/w $V_2O_5/TiO_2$, and 5% w/w $V_2O_5/TiO_2$. The results were shown in Table 5.19.

**Table 5.19. BET surface area and pore size distribution.**

| | Pure $TiO_2$ | 2% w/w $V_2O_5/TiO_2$ | 5% w/w $V_2O_5/TiO_2$ |
|---|---|---|---|
| BET surface area | 27.9 | 15.4 $m^2/g$ | 18.6 $m^2/g$ |
| Surface area of pores | 37.19 $m^2/g$ | 16.98 $m^2/g$ | 19.25 $m^2/g$ |
| Mean pore size | 39.30 nm | 32.41 nm | 26.61 nm |

The mean pore size changes reasonably, it decreases with increasing vanadia content on the catalyst surface. This is due to pores filled or blocked with vanadia particles. However, the surface area of 2% w/w $V_2O_5/TiO_2$ is less than that of 5% w/w $V_2O_5/TiO_2$. This is in the same trend with the surface area of pores, where 5% w/w $V_2O_5/TiO_2$ has a larger pore area than that of 2% w/w $V_2O_5/TiO_2$. From the pore size distribution it is observed that small pores still exist on 5% w/w $V_2O_5/TiO_2$, where for 2% w/w $V_2O_5/TiO_2$, there are almost no small pores exits on this catalyst, thus it has smaller surface area.

### *5.1.7 Summary*

Vanadia supported on titania material represents the predominant commercial SCR catalyst applied to reduce $NO_x$ with $NH_3$ from boilers burning coal-biomass and coals. Although of the SCR high efficiency, the relative fast deactivation of vanadia catalyst appears as the major problem encountered during the industrial applications, contributing to the cost increase and applying difficulties. Therefore, a series activity test and surface chemistry investigations have been designed and conducted on both commercial supplied fresh and exposed samples, and lab prepared samples, to investigate the reaction and deactivation mechanism of vanadia catalyst for coal-biomass and coal-firing boilers. The current results indicate that:

1. Fouling instead of poisoning is the major deactivation mechanism for vanadia catalyst applied for coal fired boilers
2. Sulfation of vanadia catalyst happens on titiania sites but not on vanadia sites
3. Sulfation enhances vanadia catalyst NO reduction activity by providing more active sites without changing the reaction activation energy
4. Tungsten greatly expedient vanadia catalyst NO reduction activity by about 250%. This large increase originates from the largely increased amount of active sites

5. Alkali metals potassium (K and Na) and alkaline earth metals (Ca) are poisons of the vanadia catalyst. The deactivation happens when poisons interact with active sites and decrease both the number and acidity of the active sites
6. Results of investigation the effects of sulfation, tungsten, and poisons suggests that from acid sites point of view, Brønsted acid sites are the active sites on vanadia catalyst; from structure point of view, the results of NO adsorption comparison on various amount of vanadia and sulfate samples suggest that the active sites locate at the edge between titania and vanadia sites

The above conclusions should help to elucidate the reaction and deactivation mechanism of vanadia catalyst during SCR application, furthermore, those results should help to generate better management of vanadia catalyst during the application, and create regeneration method of deactivation vanadia catalyst.

## *5.2 Evaluation of Commercial SCR Catalysts for Power Plant Conditions*

### *5.2.1 Slipstream Reactor Design*

#### 5.2.1.1 Background

The original goal of this subtask was to simulate a commercial SCR system by circulating vitiated gases and particles through a flow system containing samples of four commercial vanadium-based catalysts and to monitor deactivation. The experiment was to operate continuously for up to six months simulating flue gas from each of two different fuels (coal and a coal-biomass mixture). The change in $NO_x$ and $SO_2$ concentration before and after the catalyst and the ammonia slip were to be monitored at least once per hour.

Since this was proposed, however, a significant amount of new information came to light that impacted how this subtask should proceed. Conversations with EPRI, University of North Dakota EERC, Southern Company and catalyst manufacturers that have previously conducted slipstream testing of catalyst, as well as review of the more recent literature that was not available at the time of the original proposal, showed that a minimum of six weeks (1000 hours) was needed to see significant deactivation. Even longer time would be required to get the information on deactivation as a function of time that is needed for developing a kinetic mechanism. Thus the original idea of three months per coal mixture did not appear to be adequate.

Originally, the flow system testing was to have been carried out at the University of Utah's large coal combustion facility (L1500). However, if the length of testing were extended in order to see significant deactivation, the cost of carrying out the tests would be greatly increased because of additional costs for fuel and operating labor. Therefore, it was decided that slipstream testing for six-month periods be carried out at full-scale utility power plants in order to ensure that the cost was affordable and to obtain a better representation of the flue gas than originally planned.

As input for design of the slipstream reactor, we reviewed the more recent literature that was not available at the time of the original proposal and held conversations with EPRI, University of North Dakota EERC, Southern Company and catalyst manufacturers that have previously done slipstream testing of catalysts. This led to a clearer definition of the design of the reactor as well as the best approach to take for the testing. Some of the relevant background information will be summarized here, followed by suggestions for how best to conduct the testing.

There are three mechanisms for deactivation of SCR catalyst in coal-fired power plants that have been identified as:

1. Fouling (surface deposition)
2. Pore condensation (and/or pore blockage)
3. Poisoning

For a given situation one or more of these mechanisms may be occurring. We should not expect that a test on a single type of coal (e.g., PRB) would give us information on all of these mechanisms.

For PRB coals, there is a widely held belief that fouling by calcium sulfate deposits is the primary mechanism for catalyst deactivation (Siemens, 2000). In some cases, sodium and potassium may be important. This may be due to poisoning (and perhaps pore-filling) when ash particles containing alkali sulfate come in contact with water if the catalyst drops below the dew point of the gas. This might be poisoning from the alkali or pore condensation. Either way, water washing should regenerate the active sites. (This is in contrast to arsenic poisoning, which is irreversible.)

The fouling phenomenon in SCR catalysts exposed to PRB coals is thought to occur via the following steps:

1. Deposition of ash particles containing CaO

2, Reaction of CaO in the ash with $SO_3$ in the gas phase.

It has been noted that the deactivation and observed particle deposition occur in regions of higher turbulence at the inlet to the catalyst layer. The limiting step may be the deposition of submicron CaO particles on the catalyst surface. Free calcium in the ash, particularly in the finer (submicron) ash fractions will therefore be very important. The $SO_3$ and water contents of the gas are also important, both for production of calcium sulfate and in determining the acid dew point. The latter is more likely to be important for the sodium/potassium routes to deactivation.

Limited information is available from Europe on the effect of biomass co-firing on SCR catalyst deactivation. A Danish study was conducted on a 150 $MW_e$ pc-fired boiler firing up to 20% straw (on an energy basis) (Wieck-Hansen et al, 2000). Three different catalyst samples (70 cm in length) were exposed to both high-dust and low-dust conditions. Catalyst activity was measured as a function of time. Electron microscopy and element profiling were done on the exposed coupons to quantify the composition of deposits on the catalyst surface as a function of depth.

The activity of the catalyst was reduced by about 8% per thousand hours for the high dust exposure for all three commercial catalysts. The authors judged this to be much higher than on a purely coal-fired unit. There was a layer of ash on the catalyst surface that contained primarily sulfur, silicon and aluminum, with smaller amounts of calcium, phosphorous, and potassium. The deactivation under high dust conditions was therefore presumed to be due to deposition of ash on the catalyst surface. The authors speculated that a minor amount of the deactivation might have been due to poisoning of active sites by potassium.

Experience was also gained in Sweden from firing 100% wood in both a pc-fired boiler and a circulating fluidized bed (CFB) boiler (Odenbrand et al, 2000). Four commercial catalysts were evaluated. Deactivation of catalyst was faster in the CFB boiler as compared to the pc-boiler. Because of the amount of potassium found on the surface of the catalyst, the authors speculated that potassium played a role in deactivation and that only certain forms of potassium in the ash were important for deactivation.

With biomass, care must be taken to avoid being too general. The composition of biomass ash varies greatly with the type of plant material burned; there is much more variation in ash composition than found in different ranks of coal, for example. But, preliminary information suggests that masking seems to be the primary mechanism for

deactivation of catalysts exposed to high-dust flue gas in plants firing biomass. Potassium has been implicated as an important element in certain cases, but it is not yet clear whether this is from pore condensation or blockage or from poisoning.

This brief review of the literature suggested the following:

- Characterization of the ash particles, particularly submicron ash particles, will be needed to generalize the results of the PRB field test to other PRB coals.
- Although limited data exist on biomass co-firing from Europe, there has heretofore been no information on the behavior of catalysts under conditions representative of US utility practice.
- Characterization of ash from biomass co-firing will also be important, since there is a much smaller pool of information on this ash in the literature. Testing with and without co-firing will also be needed.
- A hopper sample may not accurately reflect the composition or amount of fine particles. Collection of an in-flight ash sample is the best way to accomplish this.
- Measurement of the CaO surface area on the ash would be enormously valuable; the measurement is made difficult by the tendency to form a surface layer of calcium sulfate on the ash in the flue gas.
- Characterization of the deposits on the catalyst surface will be important. Scanning Electron Microscopy Energy Dispersive X-Ray (SEM/EDX) analysis should be done; handling the sample so as not to damage the deposit will be important.
- Measurement of the temperature history of the catalyst during testing will be required.

Based on these considerations, the slipstream reactor must meet the following requirements:

- Withdraw flue gas from the duct (at a point between the economizer exit and the air preheater inlet) with a temperature of approximately 350$^{o}$C (660$^{o}$F);
- Provide a reasonably accurate representation of the fly ash at the inlet to the slipstream reactor, particularly of the submicron fly ash (which has been implicated in masking of catalyst exposed to PRB ash);
- Inject anhydrous ammonia at the inlet to the catalysts based on the inlet $NO_x$ concentration;
- Provide for measurement of NO, at the inlet to the reactor and at the outlet of each individual catalyst chamber;
- Maintain constant gas velocity across the catalyst (i.e., constant volumetric flow rate) for the duration of the test;
- Remove ash accumulation at the leading edge of the catalyst periodically to maintain the proper flow through the catalyst;
- Maintain the catalyst above the acid gas dew point to prevent condensation on the catalyst;
- Provide the ability to remove parts of the catalyst to be sent back to BYU for characterization;
- Return the flue gas back into the duct once it leaves the slipstream reactor.

A reactor was designed to accommodate these constraints and is discussed below.

### 5.2.1.2 Quantifying Activity

There are two approaches to quantifying catalyst deactivation from flow reactor tests:

1. Periodic measurement of inlet/outlet $NO_x$
2. Long-term, continuous measurement of inlet/outlet $NO_x$

In both methods, a section of the catalyst would be removed periodically and taken back to the lab where the activity would be measured under well-controlled conditions. Discussions with catalyst vendors suggested that it was critical to remove catalyst samples periodically from the flow reactor and test their activity under well-controlled laboratory conditions (such as the test system being built at BYU under Subtask 4.1).

In Method 1, which has been used by other groups such as University of North Dakota EERC, inlet and outlet $NO_x$ are only measured at the time that the catalyst is removed from the field reactor, typically every 4-8 weeks. At that time a portable continuous emission monitor system is used to measure inlet and outlet $NO_x$ for a short period of time (typically for several hours), thus giving a snapshot of the activity in the field.

In Method 2, the inlet and outlet $NO_x$ are measured using a dedicated, continuous emission monitors throughout the entire duration of the test. To our knowledge, this has never been done in the field. The advantages of Method 2 are that one obtains a curve of deactivation as a function of time, which can be used to infer kinetic mechanisms, as well as activity data under more relevant conditions. Method 1, by contrast, only gives points (and infrequent ones at that) on the deactivation curve. The conditions in the slipstream flow reactor (temperature, $NO_x$, water, etc.) will, in all likelihood, not be constant, and it will be hard to correct the observed activity for all those changes. Added to that concern is the difficulty of getting accurate and reliable inlet and outlet $NO_x$ measurements for several months.

We had planned originally for only on-line measurement of $NO_x$, $SO_2$ and ammonia in the flow reactor testing using existing equipment at the University of Utah. However, moving the flow reactor testing to a power plant slipstream increases the cost of making continuous measurements of gas composition. More rugged, field-ready equipment (particularly instrumentation capable of unattended operation for long periods of time) would have to be purchased or leased.

On-line continuous measurement of $NO_x$ at the inlet and outlet of the flow reactor (Method 2) would provide unprecedented information on catalyst activity as a function of time, which would provide a more detailed description of deactivation and would serve to enhance the laboratory measurements of activity.

### 5.2.1.3 Reactor Design

Four catalyst manufacturers were contacted and all provided catalyst specimens to the program. These represented both plate catalysts and honeycomb catalysts. The requirements given to the catalyst manufacturers were to provide samples with a cross-sectional area that would fit into the individual holders for catalyst (approximately 2 inches square) and provide enough length to give approximately 75% $NO_x$ removal in the slipstream reactor under clean conditions. Per the request of the catalyst manufacturers,

we did not identify the catalyst manufacturer when we discussed characterization or results in reports. Table 5.20 summarizes the catalyst properties.

**Table 5.20. Catalyst Properties.**

| Chamber: | C1 (BYU) | C2 | C3 | C4 | C5 | C6 |
|---|---|---|---|---|---|---|
| Catalyst type: | Monolith | Monolith | Plate | Plate | Monolith | Monolith |
| Chamber porosity: | 57.8% | 75.4% | 83.4% | 85.1% | 70.0% | 67.6% |
| Length of catalyst in chamber (inch): | 24.0 | 21.6 | 43.0 | 39.5 | 19.3 | 19.8 |
| Area per chamber ($ft^2$): | 0.028 | 0.028 | 0.128 | 0.144 | 0.031 | 0.030 |
| Number of sub-chambers: | 4 | 4 | 1 | 1 | 4 | 4 |
| Geometric surface area ($ft^2/ft^3$): | 148.83 | 153.7 | 106.1 | 106.1 | 149.3 | 138.0 |
| Volume of catalyst block ($ft^3$): | 0.200 | 0.200 | 0.458 | 0.475 | 0.202 | 0.198 |

The SCR reactor set-up consisted of the slipstream reactor referred to as the SCR unit, a data acquisition and control enclosure (CONTROL BOX), an air supply controls enclosure (AIR BOX), an enclosure for sample conditioning and switching between lines (SEQUENCER) and a cabinet for housing the $NO_x$ and $O_2$ continuous analyzers (CEMS). In addition the reactor was connected to an ammonia supply manifold and a suite of calibration gases. The complete system for the slipstream reactor consisted of the equipment listed in Table 5.21. The following is a brief description of these components.

Figure 5.64 shows a schematic drawing of the reactor. There were six identical chambers. The overall flow through the system was controlled by a single eductor just upstream of the system exhaust. A venturi flowmeter at the inlet to the system provided feedback to a controller that adjusted a valve on the air line to the eductor. The eductor had a large flow range and turndown ratio. To ensure that the flow rates through the catalyst chambers were equal, the pressure drops were set equal by adjusting the flow of compressed air through eductors downstream of the catalysts. Air flow to the eductors flowed through a set of six differential pressure control valves located in the AIR BOX.

Anhydrous ammonia could be injected into the flue gas stream, and blended with a static mixer, housed in a spool piece located above the catalyst chambers. The ammonia feed rate was maintained by a mass flow controller, and adjusted based on the measured amount of $NO_x$ entering the system. The molar ratio of $NH_3/NO_x$ was typically set at approximately 1.1 in order to ensure that $NO_x$ destruction is not limited by stoichiometry and to give margin for swings in $NO_x$ levels.

**Table 5.21. Components of SCR Slipstream Reactor.**

| Quantity | Item |
|---|---|
| 1 | SCR Reactor |
| 1 | CONTROL BOX |
| 1 | AIR BOX |
| 1 | CEMs |
| 1 | SEQUENCER |
| 4 | Ammonia cylinders |
| 3 | Calibration gas cylinders |
| 1 | Local PC (located in office space) |

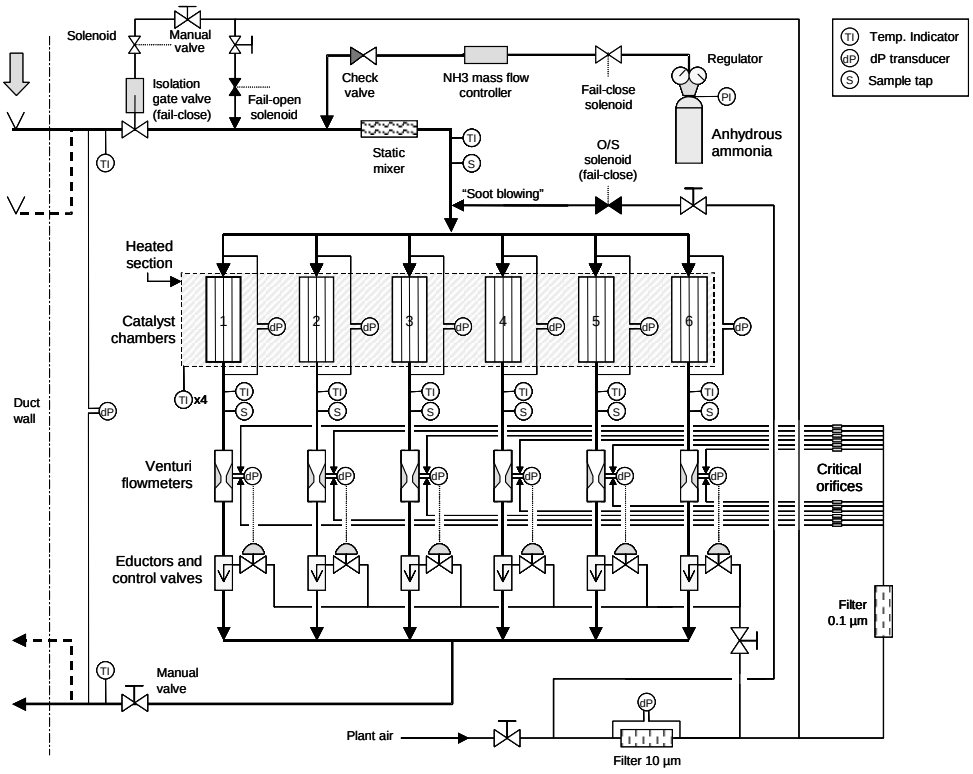


**Figure 5.64. Schematic of SCR slipstream reactor.**

The six catalysts, four monolith and two plate, were configured as shown in Figure 5.65.

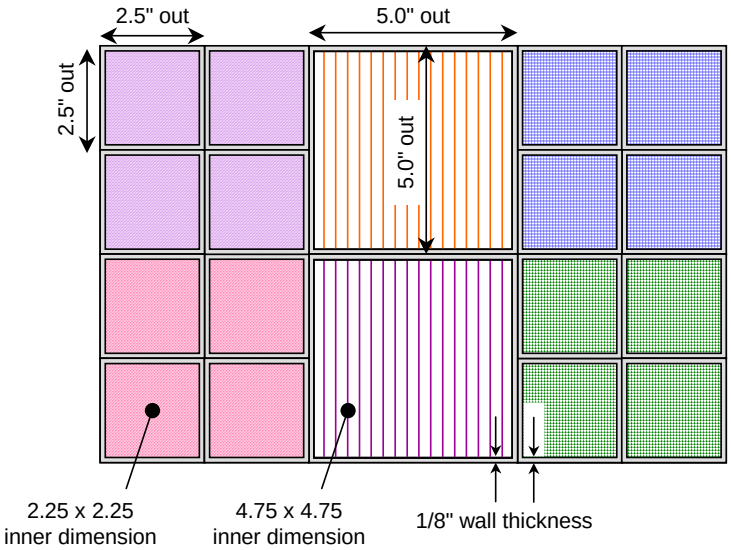


**Figure 5.65. Arrangement of catalysts (plan view).**

The four monolith catalysts were installed in four sections each. Each section had a cross section of 2.25 by 2.25 inches, and was housed in a 48-inch long aluminum square tube with outer dimensions of 2.5 by 2.5 inches and 1/8" wall thickness. The overall cross section of each monolith catalyst was 4.5 x 4.5 inches. The four tubes were bunched together as a square with outer dimensions 5.0 x 5.0 inches.

The plate catalysts were housed in square aluminum tubes with an inside dimension of 4.75 inches (5.0 inches outside, 1/8" wall thickness). Roughly 20 plates were placed in the tube, resting in slots along opposite walls. This configuration had the same outer dimensions as the groupings of monolith catalysts.

Samples of monolith catalyst were taken by removing one of the four chambers entirely. The opening that remained was blocked off at the inlet by a sloped cover to minimize ash deposition and flow disturbances. Plate catalyst samples were taken by removing every fourth plate, and replacing it with a non-reactive dummy plate.

The open cross section of the catalyst system decreases as samples are removed. To keep the flow velocity constant through the chambers, the overall flow through the system is decreased correspondingly as catalysts are removed, as described above in the section on the flow control system. The pressure drops across the six catalyst sections (divided by catalyst type) were adjusted with butterfly valves so that the flow velocity per catalyst chamber should be the same throughout the duration of the tests.

In order to minimize ash buildup in the system and maintain catalyst activity, large volumes of high-pressure air were periodically blown through the system. A line connected to the plant's compressed air system (~100 psig) ran to an automatic open/shut valve. This supplied air to a bank of "soot-blowing" nozzles placed above the catalyst chambers. When open, air was blown downwards into the catalyst chambers for about 10 seconds. The volumetric flow rate of this air was several times higher than that normally flowing through the system. Prior to activating the "soot-blowing" sequence, the sampling system was isolated.

The system had seven sampling ports, one before the catalyst chambers and one after each of the six catalyst sections. The ports themselves consisted of thin tubes that entered the channel and bent downwards, in line with gas flow. Each sampling port was fitted with a stainless steel frit for removal of particles laden in the sample. A sample drawn either from the SCR inlet or exit via a heated stainless steel line was sent to a sample-conditioning module housed in an enclosure called the SEQUENCER. The inlet sample had a 30-foot heated line (upstream of the sample conditioning unit), ¼" SS; the six outlet samples have 10-ft heated lines, ¼" SS. The sample lines were heated to about 250$^{o}$F. The sequencer housed a sampling pump, a thermoelectric cooler for removal of moisture, candle filter and a bank of solenoid valves for sample line selection. Through an automatic valve-switching sequence set in the software, one of these gases at a time was sent to the CEM via heated stainless steel line. In the sequencer, provisions were also made for blowback of the sample lines.

The CEMs consisted of a Horiba Model CLA-510 Chemiluminescent NO-NOx Analyzer and a Horiba Model MPA-510 Magnetopneumatic Paramagnetic $O_2$ Analyzer. In order to maximize accuracy, the pre-catalyst gas was analyzed before each post-catalyst measurement. Thus, analyses were performed in the order: pre, post 1, pre, post 2, pre,

post 3, etc. The data from the analyses were logged and could be remotely accessed via modem or network. The control system was created specifically for this program and is described in more detail below.

The reactor flue gas intake was attached to boiler at the economizer outlet where up to 250 scfm of gases could be withdrawn through a probe inserted in an existing port. The probe aws also fitted with a thermocouple for monitoring the temperature of the flue gas as it exited the economizer. After passing through the reactor, the gases were exhausted through an existing port at the air heater exit. The reactor itself was approximately 8 feet long, with a 25 x 30 inch footprint, and weighs approximately 1000 lbs. The reactor was insulated and securely fastened.

Anhydrous ammonia (stored in cylinders that hold approximately 150 lb each) was introduced into the slipstream reactor just downstream of the knife valve. Below the 4-inch inlet pipe, the SS pipe changed from round to rectangular to enter the catalyst housing. The housing was ~20" x 15" x 50"long. On the bottom of the catalyst housing wais a bank of venturi flowmeters and eductors to draw the exhaust gases through the apparatus. From here the shell returned to 6" ID low-carbon steel pipe that returned the gases to the system downstream of the air heater.

The testing plan called for the reactor to be operated continuously at remote power plant sites, under harsh environmental conditions for a period of six months, with very little if any on-site human interaction. These requirements called for an autonomous, rugged, reliable and remotely accessible control system that could be implemented under the budget constraints of the project. In order to meet these goals, REI chose National Instrument's LabVIEW RT running on a FieldPoint FP-2010 module with analog, digital and temperature modules providing I/O capabilities. RT handles numerous PID control loops, error and warning checking and data transfers to a host PC. The host PC, located in the office building at the plant, runs LabVIEW 6.1 and handles web-based user interaction and data logging.

The reactor operated as follows: When the pneumatic gate valve on the inlet of the reactor opened, flue gas from the power plant flue gas duct was allowed to enter the reactor. Upon entering, the nitrogen oxide concentration in the gas stream was measured using the gas analyzer. Using this information, a mass flow controller connected to ammonia storage tanks injected a stoichiometrically appropriate amount of reagent into the stream. From here, the gas entered six catalyst chambers, each with a different type of catalyst. The flow rate through each of the chambers was controlled using eductors (which create low pressure in the chambers) and associated pressure control valves, which drove the eductors. Feedback for this control came from six venturi flow meters connected to differential pressure transducers. This system allowed the flow rate through each of the chambers to be controlled independently as required for different catalyst types and conditions. Since the flow rates through the catalysts were not independent of one another, an iterative approach was used where PID was applied to each chamber several times in sequence. This sequence through the chambers was then repeated to convergence. After leaving the chambers, the gas was returned to the flue duct.

The temperature of the reactor was closely monitored and controlled using electric heaters and thermocouple measurements taken at various locations within the reactor.

Flue gas flowing through the reactor was sampled to measure oxygen, nitrogen oxide and carbon dioxide both before and after the catalysts. These data defined the effectiveness of the chemical reactions in the catalysts. A sootblowing system minimized ash buildup and maintained catalyst activity.

Figure 5.66 shows a diagram of the control system. It consisted of an on-site PC, a bank of NI Fieldpoint modules (including an FP-2010), differential pressure transducers, thermocouples, solenoid control valves, pressure control valves, a mass-flow controller and gas sampling equipment. The control software consisted of an RT application running on the FP-2010 and LabVIEW 6.1 on the host PC.

The heart of the control software was on the Fieldpoint RT module. This software controled all functions of the reactor including the state machine logic, temperature control (PID), ammonia control, chamber flow control (PID), data acquisition, communication and error handling. The RT software ran independently of the host PC and was not subject to the instabilities and indeterminism often associated with the Windows operating system.

A state machine provided the intelligence for the RT software. It provides a high degree of autonomous control, with the ability to recover from a range of error conditions and, if necessary, to shutdown the reactor and inform personnel of the problem. This error handling is important since we use ammonia, which is dangerous if released.

The Host PC Application_logs data broadcast from RT and provided both a local and remote user interface for the control software. Transfer of data from RT to the host occurred via a datasocket connection. These data blocks were sent at a user-specified interval and contained information regarding reactor state, RT software status etc. User interface controls on the RT virtual instruments made available to users (items such as PID parameters, state machine status etc) were set using VI server calls. Remote interaction with the host occurs using a web browser. This was trivial to implement using LabVIEW 6.1’s web publishing capabilities.

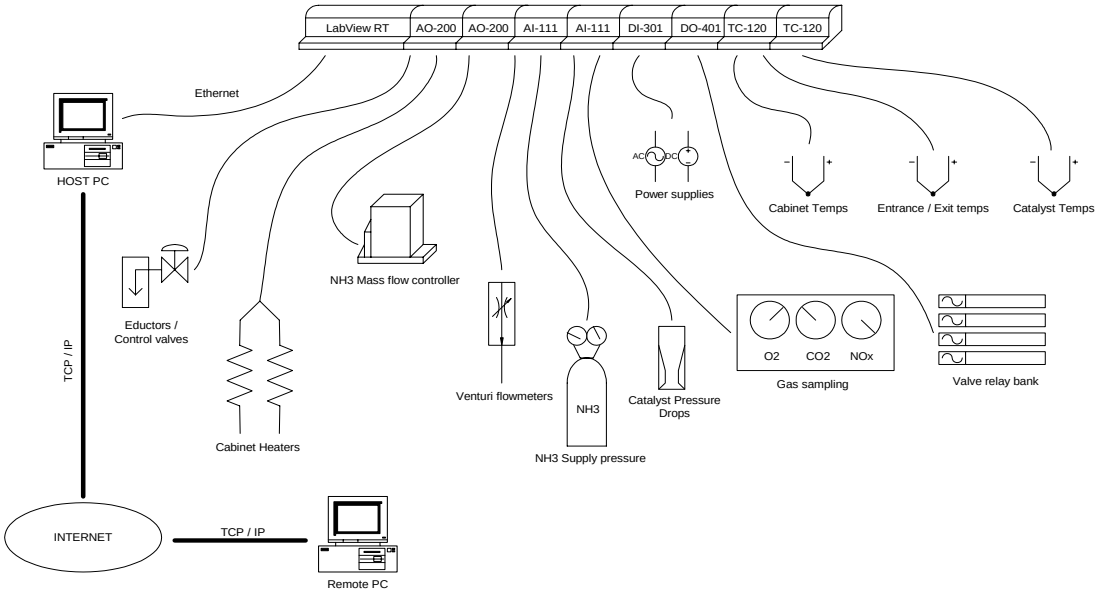


**Figure 5.66. Conceptual diagram of the control system.**

When an unrecoverable error was read from RT (such as a component failure), the host application set indicators and sent out email. Although the host provided information about the critical error to the user, RT actually handled the error.

Figures 5.67 and 5.68 show views from the host PC application VI. The Status view shows data coming from RT such as temperatures, pressures, errors and warnings and state machine status. Elements on this view are read-only. The Control view allowed the user to make changes to RT such as the state of the state machine, clear error, setpoints, and sootblowing and ammonia parameters. Views not shown in these figures are used for error and warning ranges, host configuration and manual operation, etc.

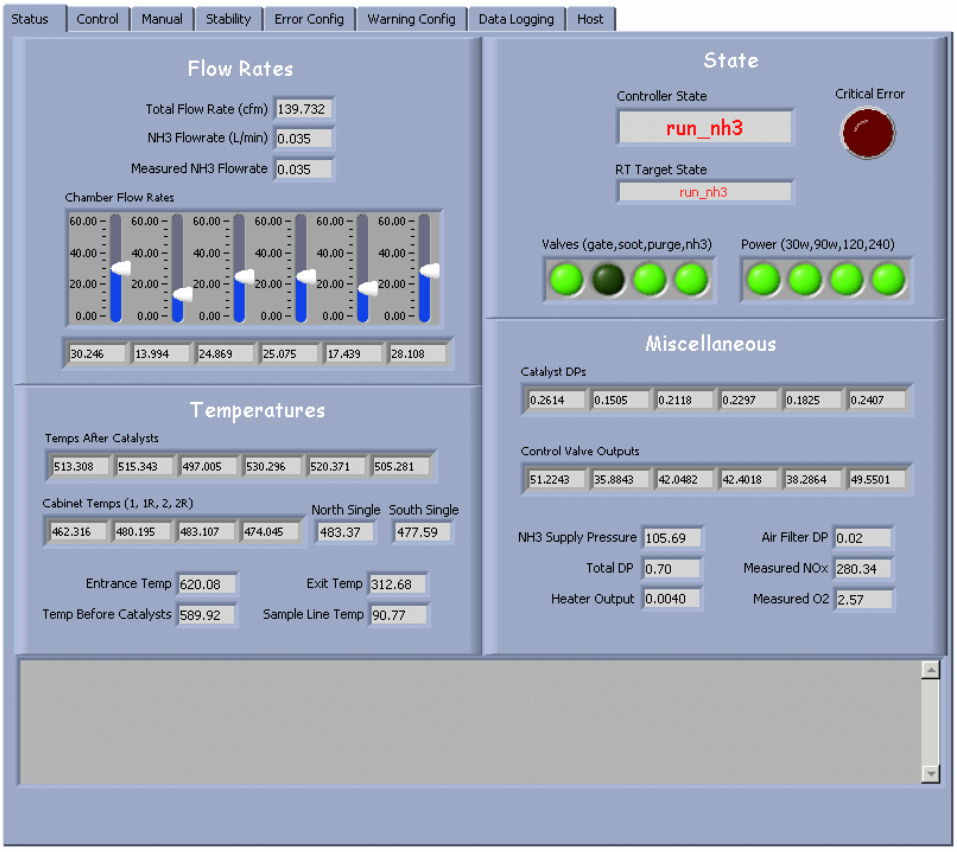


**Figure 5.67. Host PC LabVIEW application Status view.**

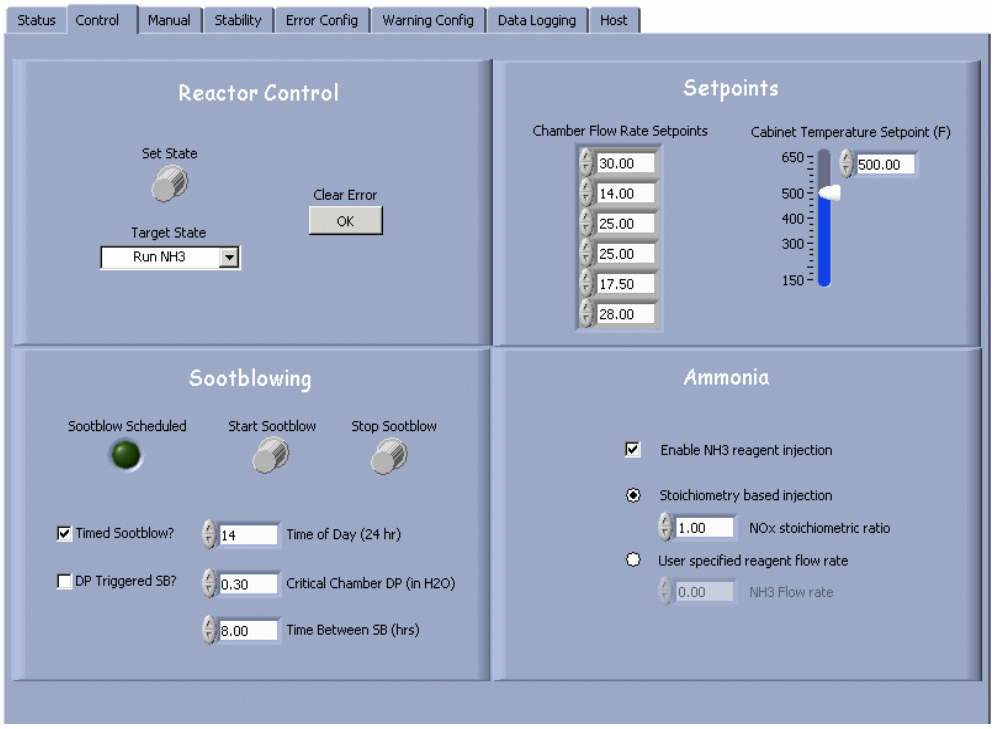


**Figure 5.68. Host PC LabVIEW application Control view**

#### 5.2.1.4 Shakedown Testing

The reactor was assembled by the University of Utah at their L1500 combustion facility. The L1500 is a 3m x 3m x 13m pilot scale furnace. Pilot plant and ancillary equipment include:

- 5 MMBtu/hr dual-swirl coal-fired burner.
- Air preheat system to heat secondary and tertiary combustion air to 800$^{o}$F.
- Solid feeding system for pulverized coal including: feeders, hoppers, and eductors.
- Opto 22 distributed control system.
- Continuous emissions monitoring equipment for real time measurement of $O_2$, $CO_2$, CO, $NO_x$, and THC emissions.
- 6500 CFM wet venturi scrubber for abatement of $SO_2$ and particulate emissions
- 400 ton cooling tower and shell and tube heat exchanger for indirect cooling of flue gases.

The reactor was installed at the end of the shell and tube heat exchanger using a 4-inch flexible steel pipe. Figure 5.69 shows the reactor, which was installed vertically. Gases flowed downward through the catalyst chambers as installed. Below the catalyst chambers were the venturi flow meters and eductors. There were also sampling ports located at the exit of each chamber. After the eductors, the gases were combined into a 6-inch exhaust pipe. The reactor exhaust was fed back into the main flue gas stream.

Figures 5.70 and 5.71 show the hardware for the control system, which resided in two electrical boxes. The main control functions resided on an embedded controller (seen in Figure 5.70) that communicated with a PC via an Ethernet connection. The host PC could not be accessed over the internet to download data or change control set points. Another box (Figure 5.71) contained pressure transducers and relays.

The goals of the shakedown testing were as follows:

1. Check for leaks (cold)
2. Check for leaks (hot and after thermal cycling)
3. Verify ability of control system to monitor all inputs
4. Verify operation of flow control loops
5. Develop start-up and shut down procedures
6. Verify all emergency shutdown procedures
7. Test data-logging system
8. Test mass flow controller operation
9. Test sootblowing system and pressure drop control loop

During most of this testing, natural gas was fired in the furnace. For a limited series of tests, coal and coal-sawdust blends were fired in the furnace.


**Figure 5.69. Multi-catalyst slipstream reactor with outer doors removed to show catalyst chambers.**

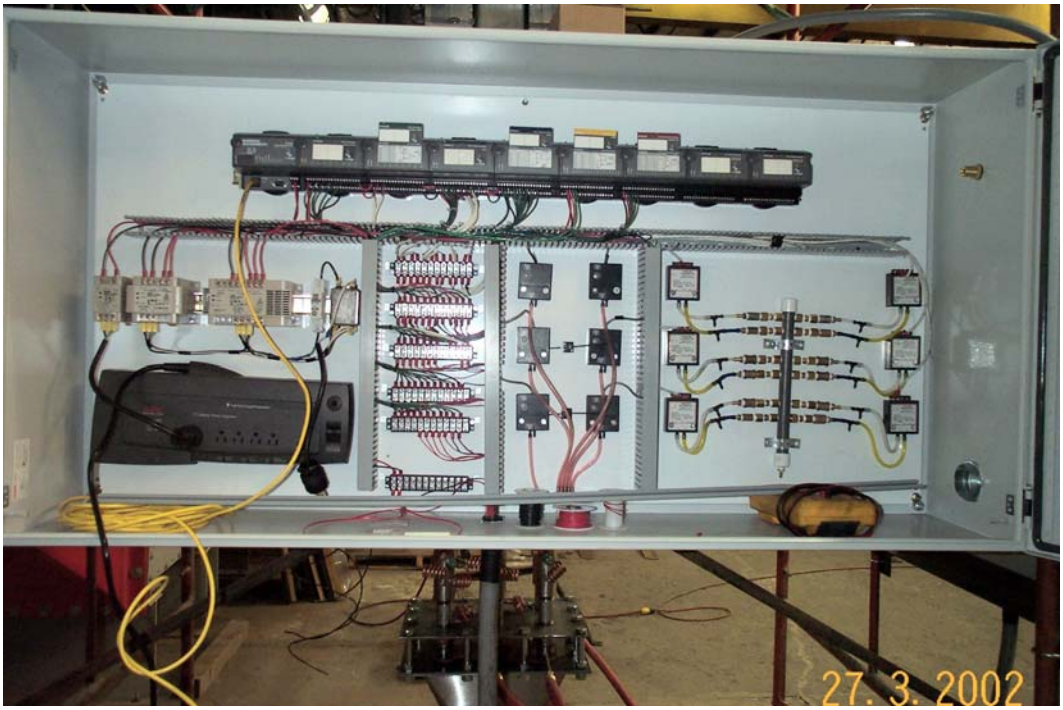


**Figure 5.70. Control box for the slipstream reactor, which contains the Fieldpoint bus with embedded controller (the black strip at the top) plus power conditioning and relays.**


**Figure 5.71. Electronics box for the slipstream reactor.**

### *5.2.2 PRB-Bituminous Co-firing Tests at Rockport*

#### 5.2.2.1 Site Description

The site of the first slipstream reactor test, AEP's Rockport plant, consisted of two 1300 $MW_e$ B&W opposed wall-fired boilers. These were supercritical boilers that burned a blend of about 13% bituminous coal and 87% subbituminous coal. The SCR slipstream reactor was installed in the flue gas duct downstream of the economizer and upstream of the air preheater on Unit 1. Figure 5.72 is a schematic of the slipstream SCR reactor as installed at Rockport. A sampling probe was inserted through an existing port in the duct wall. The probe extended approximately three feet into the duct and had a 2-ft long slot, oriented 90° from the direction of flow in the duct. An isolation valve was placed on the inlet line just outside the duct wall. This valve was coupled to the control system, and closed automatically if the flue gas became too cold in order to prevent condensation in the catalyst units. The reactor exhaust line was connected to the horizontal duct downstream of the air preheater. Anhydrous ammonia was injected into the flue gas stream near the entrance to the reactor, and blended with a static mixer.

#### 5.2.2.2 Installation at Rockport

Personnel from REI and the University of Utah worked with plant personnel to install the reactor on Rockport Unit 1, Air Heater #2. REI personnel completed connection of the reactor control system to a local host computer; this host computer was connected to the Internet through the plant's Local Area Network. REI verified that the SCR reactor could be accessed remotely from REI's offices in Salt Lake City; using remote access, operating data could be downloaded, settings could be changed and the control system program could be updated. An operating manual was prepared for the plant containing procedures and detailed information on the control system. Figures 5.73 through 5.75 show pictures of the reactor during and after installation.

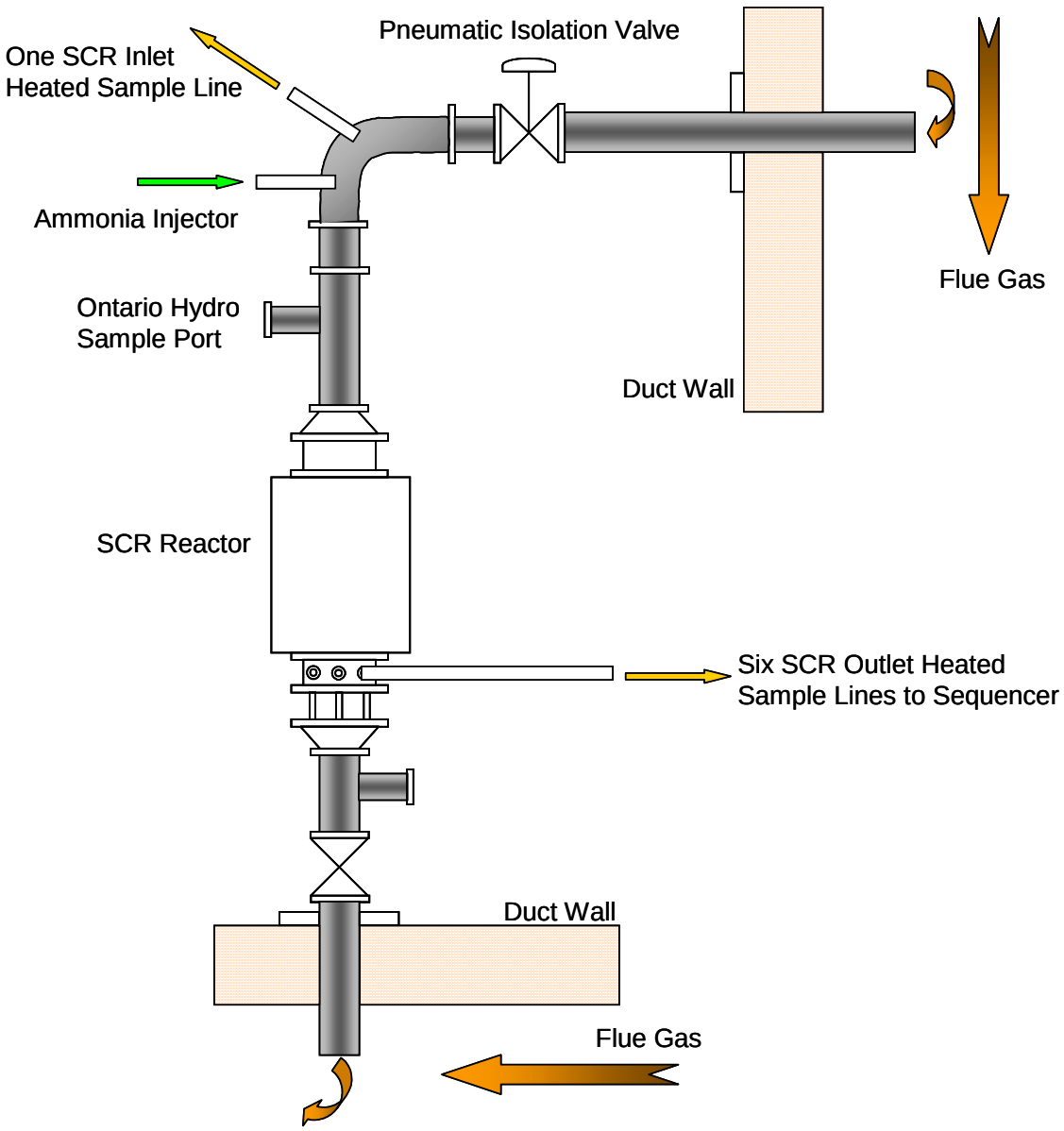


**Figure 5.72. SCR slipstream reactor.**

**Figure 5.73. Installation of the SCR flue gas intake pipe at Rockport.**

**Figure 5.74. SCR Unit installed between the economizer and the air heater at Rockport Plant.**

**Figure 5.75. CEMS and SEQUENCER cabinets installed at Rockport Plant.**

One of the important issues for the plant was safe handling of ammonia. Ammonia was delivered to the plant in 150-lb cylinders. This was liquid, anhydrous ammonia in the cylinders; once the pressure was released, it was converted to gaseous ammonia for delivery to the reactor. The ammonia manifold was set up to handle four cylinders, with two at a time connected to the system. At the estimated usage rate, therefore, the valves on the manifold would need to be switched every six weeks.

**Figure 5.76. Ammonia cylinders being prepared for hauling to the installation site.**

Figures 5.76 and 5.77 show the ammonia tanks being prepared for installation and their location in the Fan room after they have been connected to the ammonia manifold. By the end of March, 2003 initial tests with ammonia flow were .

**Figure 5.77. Four 150-lb ammonia cylinders connected to the ammonia supply manifold in the Unit 1 Fan room.**

### 5.2.2.3 Shakedown testing

In February, 2003 SCR reactor shakedown tests commenced. Some of the questions that needed to be answered during the shakedown tests were:

- Does the flue gas heat up the SCR sufficiently?
- Do the SCR heaters provide adequate heating?
- Can the SCR reactor maintain temperature at the set point value?
- Do we get the same $NO_x$ and $O_2$ readings at the inlet and the outlet of the SCR?
- How do the analyzer readings compare with plant CEMs?
- How does the flow control perform at low flow rates?
- Is the ammonia manifold leak-proof?
- Are all the ammonia safety precautions in place?

The tests started with heating up the SCR reactor using the electrical heaters mounted around it. In the first stage one of the heat-up procedure, the SCR was heated electrically to 500°F with the flue gas inlet gate valve closed. The temperature of the flue gas at the

economizer intake was 720°F. Upon opening the gate valve, the temperature of gases at the inlet of the SCR just before catalysts was 149° F. The unit was left running overnight. In spite of this, the temperature before catalysts did not improve. Initially it was thought that the flue gas temperature dropped due to heat losses to the 6-inch schedule 80 carbon steel standpipe leading into the SCR. It was then decided to troubleshoot for causes of the temperature drop using a variety of approaches. It was later discovered that the flue gas intake line to the SCR unit was blocked with ash in the duct wall region. This occurred after the plant was shut down for an outage, allowing ash to consolidate in the suction probe. Measures were taken to clear the blockage and flue gas flow into the SCR was established.

Other problems encountered during the shakedown tests included CEMS not receiving sample gases from the SEQUENCER, difficulties in controlling low flow rates through the SCR unit, blockage of the SCR chambers with ash at very low flow rates, leakage of the SCR unit at the top flange and plugging of sample line filters with ash.

Initial testing on the reactor focused on the ability to measure $NO_x$ and $O_2$ using the CEM system. During these tests, Unit 1 was operating near full load and load was stable. Figure 5.78 compares data reported from the plant PI database (three-minute averages) of oxygen at the economizer outlet as compare with the inlet sample from the reactor CEM. Multiple oxygen probes were located in the economizer outlet ducts; we have chosen two for this comparison. The reactor CEM measurement, which was reported on a dry basis, has been corrected to 10% water. The reactor CEM measured $O_2$ concentrations that corresponded well to the plant PI data.

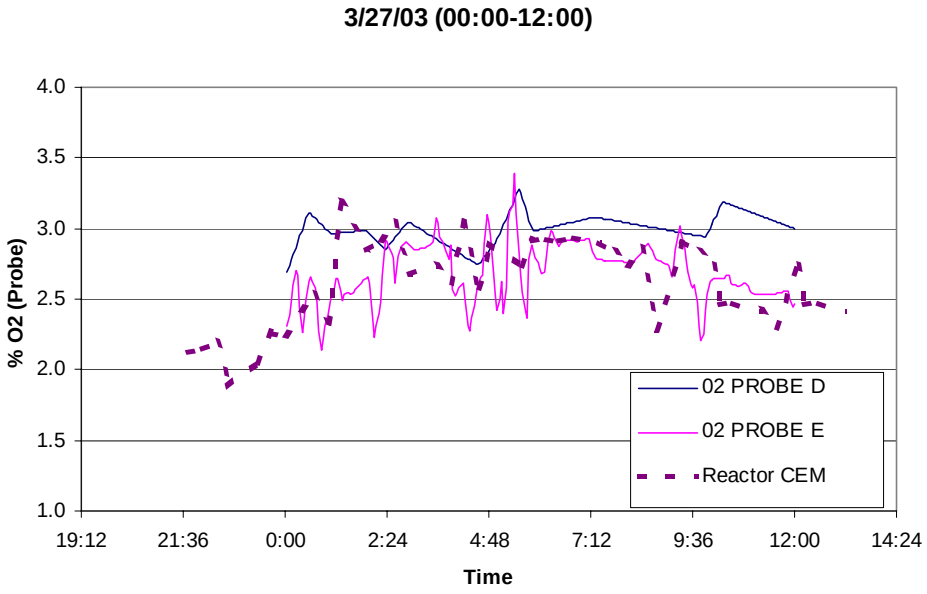


**Figure 5.78. Oxygen at economizer outlet, Unit 1: Plant measurements (Probes D and E) compared with inlet value measured by SCR reactor CEM.**

$NO_x$ was not measured routinely by the plant at the economizer outlet. Plant PI data contain $NO_x$ measured at the stack. The $NO_x$ in the stack was lower than the $NO_x$ measured by the reactor CEM by about 100 ppm (Figure 5.79). Previous testing at the plant of $NO_x$ levels at the economizer outlet duct under full load conditions showed higher levels of $NO_x$, similar to the CEM values; these are also shown on the figure. Perhaps there is some stratification in the $NO_x$ exiting the furnace. In any case, the reactor CEM produced $NO_x$ measurements that corresponded to measurements made at the economizer outlet duct, even though these did not match the stack $NO_x$ measurements.

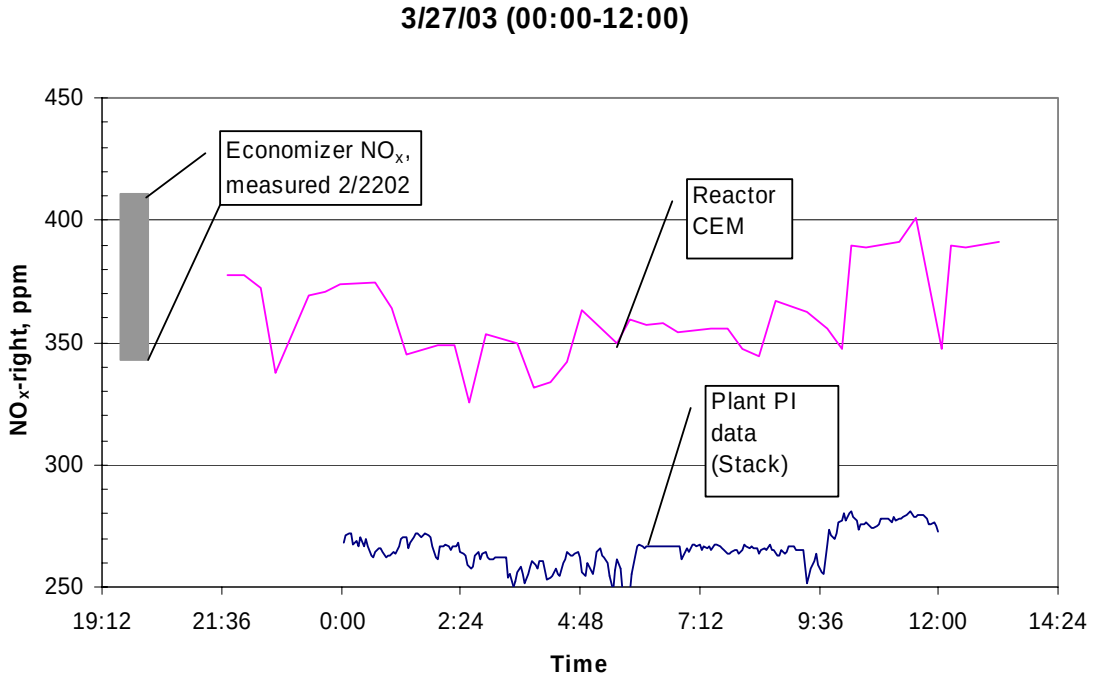


**Figure 5.79. $NO_x$, Unit 1: Plant measurements at the stack compared with inlet value measured by SCR reactor CEM.**

### 5.2.3.4 Problems encountered during operation

There were number of operational and equipment problems that needed to be solved during the test program. Chief among these were sample line plugging, catalyst plugging, heater malfunction and ammonia tank pressure build-up and venting.

#### 5.2.3.4.1 Sample Line Plugging

At the end of the first week of April, 2003 the CEMS stopped giving meaningful results. All sample lines were reading zero $NO_x$ and 21 % $O_2$. It appeared as if the CEMS was failing to receive gas samples from the SEQUENCER. Intense troubleshooting of the SEQUENCER sampling protocol ensued. With the help of plant personnel, the SEQUENCER sample line selector switches were examined for proper positioning. The

sampling pump was also checked to see if it was functioning properly. Further, with the help of Baldwin Environmental (the suppliers of the SEQUENCER) and the plant personnel, the sample line relays and switching sequence were thoroughly examined. All these did not seem to solve the problem. Eventually at the end of April Reaction Engineering International decided to send its own engineers to examine the SEQUENCER closely.

A systems engineer worked on troubleshooting the SEQUENCER for electrical faults. There were no faults found with the SEQUENCER electrical wiring. Individual troubleshooting of the pump and sample line selector solenoid valves showed that both the pump and the solenoid valves were in good working condition. Later, the systems engineer and the project engineer performed troubleshooting of flow in the sequencer, the sampling pump and the CEMS. The sampling system was configured in such a way that the SEQUENCER pump pulled gas samples from the SCR and discharged them to a filter located in the SEQUENCER unit. From the SEQUENCER filter, the sample gas was pulled by another vacuum pump located in the CEMS cabinet. When the sample line at the SEQUENCER filter was disconnected, a positive pressure in the sample line indicated that the SEQUENCER pump was working and discharged the gas sample to the filter, as it should. The sample line was then reconnected and later disconnected at the CEMS pump side at the filter. At this moment, it was noticed that there was suction in the sample line. However, upon further troubleshooting of the sample line upstream of the SEQUENCER pump it was found that when the sample line was broken at a Tee Swagelok fitting between the hot box and the sample coolers, there was no suction. It was later discovered that the sample line was clogged at the inlet to the first cooler (see Figure 5.80). The ash that clogged the sample line had cemented out and could not be removed even by blowing with 110 psi compressed air. The ash could only be removed with a screwdriver. Thus, flow to the CEMS was re-established and the expected $NO_x$ and $O_2$ readings restored.

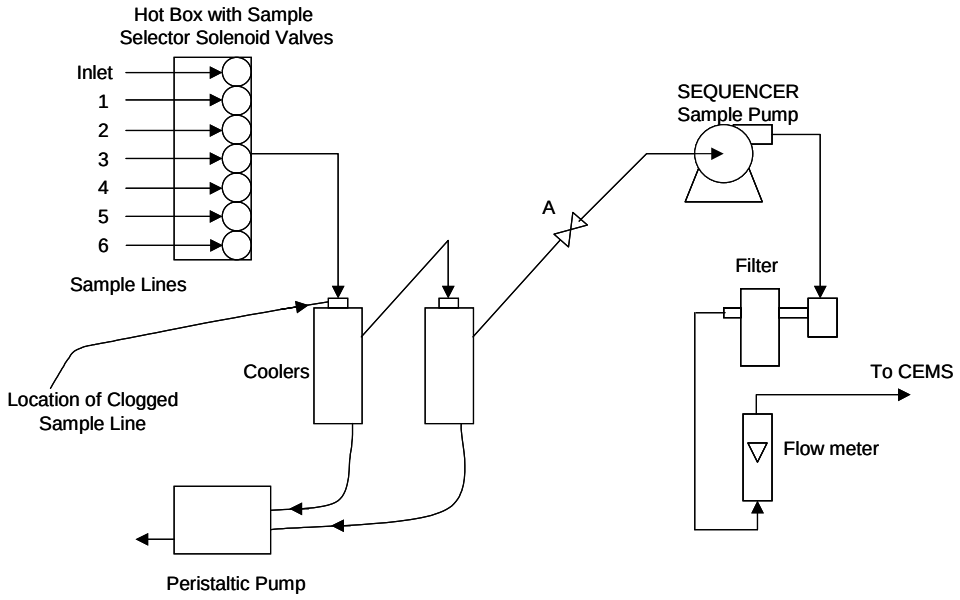


**Figure 5.80. Simplified sample flow loop in the SEQUENCER.**

During the first test series, the sample gases were routed through the sample conditioning and switching unit: seven lines come in from the reactor and one line went out either to the $NO_x/O_2$ analyzer or to the mercury CEM. The switching valves are in a heated box, heated to 175°F. There is blowback air for these valves. Problems were encountered with plugging of ash on the sintered metal filters; the sample lines had to be blown back before each sample.

There was concern after the first test series that the heated switching valve box was too cold and this might result in loss of oxidized mercury, which could explain the apparent loss of total mercury across the catalysts observed in the first test series. The temperature of the heated switching box was turned up, but this caused one of the components to fail. Even after the manufacturer repaired the switching box, ash plugging in the switching box remained a problem. Therefore, the sample lines were individually and manually connected to an inertial separation probe for most of the second test series. This is a heated stainless steel probe that has taps to withdraw small sample flows. Gas passing through the sample taps first passes through a sintered metal tube, providing another stage of filtering. Using the inertial separation probe reduced the ash pluggage, but increased the sample time because the sample lines had to be manually disconnected, blown out with air and then reconnected for each sample.

#### 5.2.3.4.2 Catalyst Plugging

The SCR shut itself down due to an unscheduled outage during the weekend of April 19-20, 2003. Upon restarting the reactor on Monday April 21, 2003 it was noticed that flue gas flow through all the catalyst chambers was lost except chamber number 3. The SCR had to be taken apart and the flow tubes exiting the SCR bottom cleaned. The tube in chamber 4 was completely clogged with ash that appeared to have "cemented out". A crowbar-like tool had to be used to chisel out the ash. All the catalyst chambers were

found to be clogged excerpt for a few open channels mostly in chamber number 3. Figure 5.81 shows pictures of the clogged catalyst chambers.

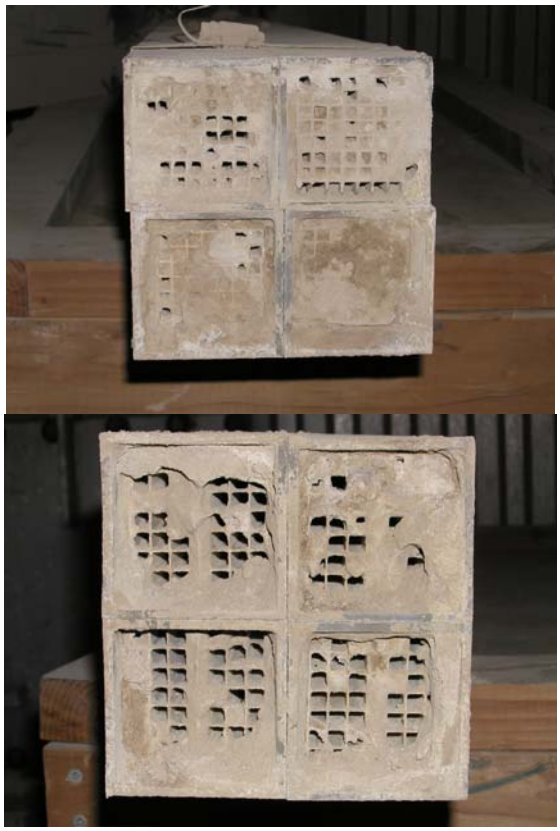

**Figure 5.81. Catalyst channel plugging by ash due to moisture condensation.**

There were two possible causes of catalyst plugging. One cause was a large quantity of ash accumulated upstream of the gate valve. When the gate valve was shut down for extended periods of time, ash accumulated in the flue gas intake pipe. Once the gate valve was opened for catalyst testing, a large quantity of ash flows into the catalyst chambers, inundating the flow channels since the eductors were unable to pull it all through the chambers. As a consequence, ash accumulates in the catalyst channels. This problem was found to be more serious with the monolith type catalysts than the plate type. The solution to this problem was to prevent accumulated ash from entering the SCR when the gate valve is first opened following a period of inactivity. To this end, a manual air blowback line was installed upstream of the gate valve. The reactor operating procedures were modified to start with a blowback of the flue gas intake line prior to opening the gate valve. This measure resulted in extended SCR operating time without the catalyst chambers plugging up with ash.

Another identified cause of catalyst plugging was condensation of water that occured during boiler outages. During the shutdown, the SCR heaters also stopped and the chamber temperatures dropped below the dew point of water, causing ash cementation. Since the PRB ash was prone to consolidating into a cemented solid in the presence of moisture, the SCR operating procedure was modified to keep the heaters on and maintain

a temperature of 300°F during outages. The lower section of the reactor, downstream of the catalyst chambers was insulated to prevent condensation of water in the eductor sections.

#### 5.2.3.4.3 Ammonia Venting

The ammonia cylinders were connected to a manifold which supplied ammonia to the SCR. The manifold has the ability to connect to four cylinders, where two are in use and two remain on standby. For safety, the manifold was provided with pressure relief valves which would vent out the ammonia in case the cylinder pressure rose above 250 psi. During this quarter, the ammonia safety relief valves were triggered and vented the tanks. The plant reported that this happened on days when the ambient air temperatures were excessively high. Figure 5.82 is a schematic of the ammonia manifold setup showing the location of the safety relief valves. We are currently working with the plant and the ammonia vendors to find ways of preventing the occurrence of ammonia venting.

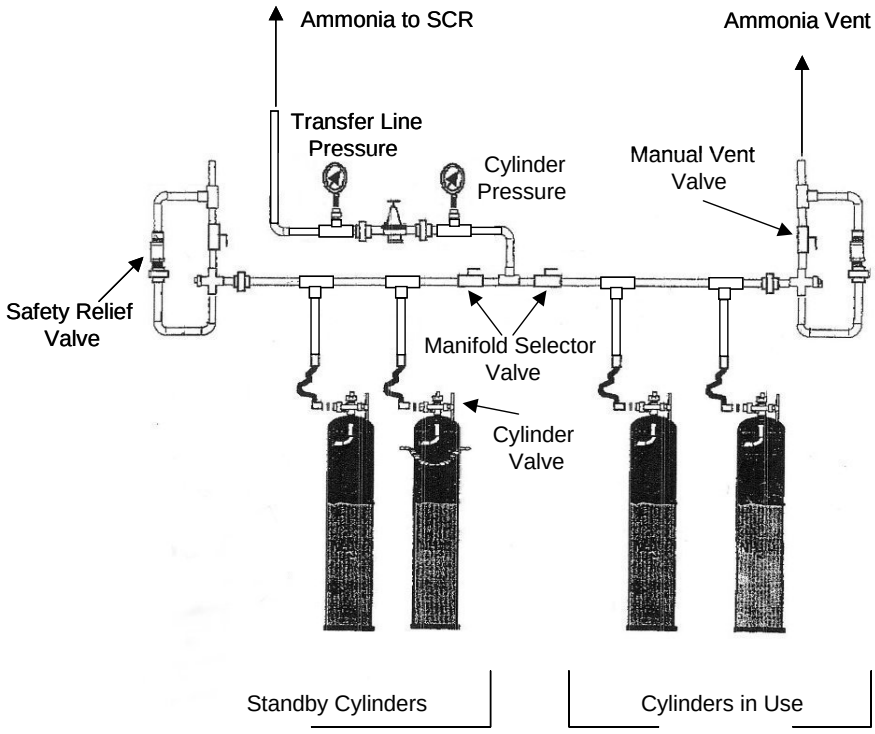


**Figure 5.82. Ammonia supply manifold for the slipstream reactor.**

#### 5.2.3.4.4 Other Operational Bottlenecks

A malfunctioning Fieldpoint module, heater power controller, and gate valve power supply unit were replaced during the field test. The gate valve solenoid power cables were also rewired. A longer flexible spool piece was installed at the top of the SCR to allow for expansion and improve the SCR seal. Two angle iron bars were also added to

assist with fastening the SCR top in order to improve reactor sealing. The eductors were clogged and had to be taken out and cleaned. The new operating procedures required the eductors to have a flow of air all the time in order to prevent clogging with ash. The electric heater connecting cables broke several times. New and more robust wires installed for the heaters.

### 5.2.2.5 Coal and Ash Data

Table 5.22 presents the coal data on an as-received basis from the first test series (March-April, 2003). The coal blend was nominally 87% PRB subbituminous and 13% eastern bituminous. The heating value of the coal was commensurate with the blend, as was the coal chlorine content. The ash composition of the coal was measured using the standard ASTM Ash Chemistry method. This composition is shown in Table 5.23 for one day, calculated on an $SO_3$-free basis. The ash compositions were also measured in the economizer ash and the ESP ash; these are shown for comparison with the coal ash in Table 5.23. As expected from the blend, the ash contained significant calcium (about 16 wt% as CaO) and more iron than might be found in a typical Powder River Basin subbituminous coal. The sodium content of coal was about 1.5 wt% $Na_2O$.

**Table 5.22. Coal analyses from first test series.**

| Date | 3/28/03 | 4/1/03 | 4/2/03 |
|---|---|---|---|
| **ULTIMATE ANALYSIS (As Received):** | | | |
| Carbon | 50.67 | 51.80 | 51.75 |
| Hydrogen | 3.51 | 3.64 | 3.46 |
| Oxygen | 10.89 | 11.04 | 11.18 |
| Nitrogen | 0.76 | 0.78 | 0.75 |
| Sulfur | 0.32 | 0.30 | 0.37 |
| Ash | 5.12 | 5.99 | 6.10 |
| Moisture | 28.74 | 26.45 | 26.39 |
| HHV, Btu/lb | 8,723 | 8,989 | 8,989 |
| Hg, µg/g, dry basis | 0.0881 | 0.118 | 0.0911 |
| Cl, µg /g, dry basis | 120 | 160 | 200 |
| $SO_2$, lb/MBtu | 0.74 | 0.67 | 0.82 |
| Hg, lb/TBtu | 7.20 | 9.66 | 7.46 |
| Hg, ug/$dnm^3$ (5%$O_2$) | 8.02 | 10.82 | 8.46 |

Ash samples were analyzed for loss on ignition (LOI), Hg and Cl, as shown in Table 5.24. The LOI content of these samples was generally low. Since the ash was a pale tan color, the carbon content of the ash was probably even lower than indicated by the LOI values. In any case, the ash had a very low amount of unburned carbon. The ESP ash had 15 to 20 times more mercury than the economizer ash sample; this suggests that there was some adsorption of mercury by the ash that took place between the economizer and the ESP (probably post-air preheater). However, the amount of mercury adsorbed on the ESP ash was less than 0.5% of the mercury in the coal. Thus, the fly ash from Rockport was very unreactive toward mercury.

The chlorine content of the ash was fairly constant from the economizer to the ESP sample, suggesting that any reaction of gaseous chlorine compounds with ash took place at temperatures above the economizer exit temperatures. Very little of the chlorine in the

coal ended up in the ash, from 1.2% to 1.7% of the total chlorine was in the ash. This means that most of the chlorine in the coal would be expected to be in the gas phase at the SCR inlet.

**Table 5.23. Ash composition: Major elements as wt% oxides, $SO_3$-free basis.**

| | Coal 3/28/03 | Economizer Ash 3/28/03 | ESP Ash 3/38/03 |
|---|---|---|---|
| $SiO_2$ | 46.7 | 47.9 | 47.5 |
| $Al_2O_3$ | 19.9 | 19.5 | 20.1 |
| $TiO_2$ | 1.4 | 1.3 | 1.3 |
| $Fe_2O_3$ | 6.4 | 6.3 | 5.8 |
| CaO | 16.3 | 16.3 | 16.6 |
| MgO | 4.9 | 4.9 | 4.6 |
| $K_2O$ | 1.1 | 0.9 | 1.0 |
| $Na_2O$ | 1.6 | 1.3 | 1.4 |
| $P_2O_5$ | 1.0 | 0.8 | 1.0 |
| SrO | 0.25 | 0.25 | 0.27 |
| BaO | 0.46 | 0.44 | 0.49 |
| MnO | 0.03 | 0.03 | 0.02 |

**Table 5.24. Composition of ash collected from ESP silos 3 and 4 (first test series).**

| **Ash sample** | **Date** | **LOI, wt%** | **Hg, µg/g** | **Cl, µg/g** | **% Hg in Ash** | **%Cl in Ash** |
|---|---|---|---|---|---|---|
| Economizer | 3/28/03 | 0.08% | 0.0053 | 28.6 | 0.03% | 1.71% |
| ESP, silos 3&4 | 3/28/03 | 0.31% | 0.0809 | 20.2 | 0.41% | 1.21% |
| ESP, silos 3&4 | 3/31/03 | 0.37% | 0.118 | 24.6 | -- | -- |
| ESP, silos 3&4 | 4/1/03 | 0.31% | 0.127 | 23.6 | 0.44% | 1.20% |
| ESP, silos 3&4 | 4/2/03 | 0.34% | 0.101 | 26.8 | 0.55% | 1.11% |

The composition of the flue gas can be estimated from the coal composition. Based on the ash composition, we assume that all of the chlorine in the coal is present as HCl. $NO_x$ was not measured during the first test period, but just prior to the test period, $NO_x$ was about 400 ppm at full load. Table 5.25 gives the estimated flue gas composition for the first test series.

**Table 5.25. Flue gas composition estimated from coal composition for first test series, except as noted.**

| | 3/28/03 | 4/1/03 | 4/2/03 |
|---|---|---|---|
| **Excess Air** | 35% | 35% | 35% |
| $O_2$ | 4.0% | 4.0% | 4.0% |
| $CO_2$ | 13.3% | 13.4% | 13.5% |
| $H_2O$ | 10.6% | 10.2% | 10.0% |
| $N_2$ | 72.0% | 72.3% | 72.4% |
| $SO_2$ [ppm] | 317 | 292 | 360 |
| HCl [ppm] | 7.5 | 10.1 | 12.8 |
| $NO_x$ [ppm]* | 400 | 400 | 400 |
| Hg, ug/dnm$^3$ (5%$O_2$) | 8.02 | 10.82 | 8.46 |

*Estimated from previous measurements

During the second test series, coal samples were obtained at the outlet of Mills 1 and 2, and Mills 6 and 7. The samples were composited and analyzed. The results are presented in Table 5.26. The coal blend was the same as in the first test series, nominally 87% PRB subbituminous and 13% eastern bituminous. The heating value of the coal was commensurate with the blend, as was the coal chlorine content.

The ash composition of the coal was not measured for the second test series. The heating value, sulfur and ash contents of the August coal samples were consistent with the March coal samples on a dry basis. However, the average moisture content of the August coal samples was low compared to the moisture content of the March samples: 16% versus 26%. The mercury content was also lower in the August samples on a dry basis.

It is likely that the hot air introduced into the pulverizer drove off some of the mercury and moisture from the coal into the combustion air. This could account for the apparent decrease in coal mercury (and moisture content) as compared to the first test series.

**Table 5.26. Coal analyses from second test series.**

| Date | 8/7/2003 | 8/8/2003 | 8/10/2003 | 8/11/2003 | 8/12/2003 | 8/13/2003 | 8/15/2003 | 8/16/2003 |
|---|---|---|---|---|---|---|---|---|
| **(As Received):** | | | | | | | | |
| Carbon | 60.79 | 60.75 | 61.31 | 60.77 | 61.57 | 61.62 | 61.70 | 61.36 |
| Hydrogen | 3.87 | 4.11 | 4.16 | 4.03 | 4.02 | 3.74 | 3.16 | 3.25 |
| Oxygen | 12.27 | 11.32 | 11.96 | 11.29 | 11.47 | 12.00 | 12.79 | 13.30 |
| Nitrogen | 0.86 | 0.93 | 0.90 | 0.91 | 0.92 | 0.90 | 0.85 | 0.88 |
| Sulfur | 0.35 | 0.38 | 0.38 | 0.37 | 0.40 | 0.40 | 0.40 | 0.39 |
| Ash | 5.71 | 6.17 | 6.14 | 6.02 | 6.07 | 6.05 | 6.56 | 6.23 |
| Moisture | 16.15 | 16.34 | 15.15 | 16.61 | 15.55 | 15.30 | 14.53 | 14.60 |
| HHV , Btu/lb | 10,337 | 10,120 | 10,395 | 10,314 | 10,346 | 10,418 | 10,404 | 10,471 |
| **(Dry Basis):** | | | | | | | | |
| Hg, ug/g | 0.062 | 0.045 | 0.049 | 0.050 | 0.046 | 0.048 | 0.055 | 0.049 |
| Cl, ug/g | 104.0 | 97.4 | 125.0 | 110.0 | 101.0 | 244.0 | 241.0 | 166.0 |
| $SO_2$, lb/MBtu | 0.68 | 0.74 | 0.73 | 0.71 | 0.77 | 0.76 | 0.77 | 0.75 |
| Hg, lb/TBtu | 5.04 | 3.74 | 3.99 | 4.01 | 3.78 | 3.91 | 4.51 | 4.01 |
| Hg, ug/dnm$^3$ (5%$O_2$) | 5.98 | 4.29 | 4.67 | 4.70 | 4.40 | 4.64 | 5.48 | 4.93 |

The composition of the flue gas can be estimated from the coal composition. Based on the ash composition, we assume that all of the chlorine in the coal is present as HCl. $NO_x$ averaged about 330 ppm (wet basis, 5% $O_2$) during the tests. Table 5.27 gives the estimated flue gas composition. Since it seems likely that moisture was lost in the pulverizer, the concentrations have been adjusted to a coal moisture content of 26.5%, which was the moisture content of the March coal samples.

**Table 5.27. Flue gas composition for second test series estimated from coal composition, except as noted; coal moisture content adjusted to 26.5%.**

| | 8/7/2003 | 8/8/2003 | 8/10/2003 | 8/11/2003 | 8/12/2003 | 8/13/2003 | 8/15/2003 | 8/16/2003 |
|---|---|---|---|---|---|---|---|---|
| $O_2$ | 5.0% | 5.0% | 5.0% | 5.0% | 5.0% | 5.0% | 5.0% | 5.0% |
| $CO_2$ | 12.8% | 12.6% | 12.6% | 12.6% | 12.7% | 12.9% | 13.3% | 13.2% |
| $H_2O$ | 9.1% | 9.3% | 9.3% | 9.2% | 9.2% | 8.9% | 8.5% | 8.6% |
| $N_2$ | 73.0% | 73.0% | 72.9% | 73.0% | 73.0% | 73.1% | 73.1% | 73.0% |
| $SO_2$ [ppm] | 278 | 293 | 295 | 286 | 307 | 312 | 324 | 318 |
| HCl [ppm] | 6.1 | 5.6 | 7.3 | 6.4 | 5.9 | 14.4 | 14.8 | 10.2 |
| $NO_x$ [ppm]* | 330 | 330 | 330 | 330 | 330 | 330 | 330 | 330 |
| Hg, ug/dnm$^3$ (5%$O_2$) | 5.94 | 4.26 | 4.64 | 4.67 | 4.37 | 4.60 | 5.44 | 4.89 |

*Estimated from previous measurements

### 5.2.2.3 $NO_x$ Performance

$NO_x$ data were obtained in late March and early April (approximately 750 hours of operating time on flue gas) and in late August (approximately 2200 hours of operating time on flue gas). These data will be analyzed to look at the effects of operating conditions and catalyst age on $NO_x$ reduction. Figure 5.83 shows the build-up of reactor operating time accrued monthly.

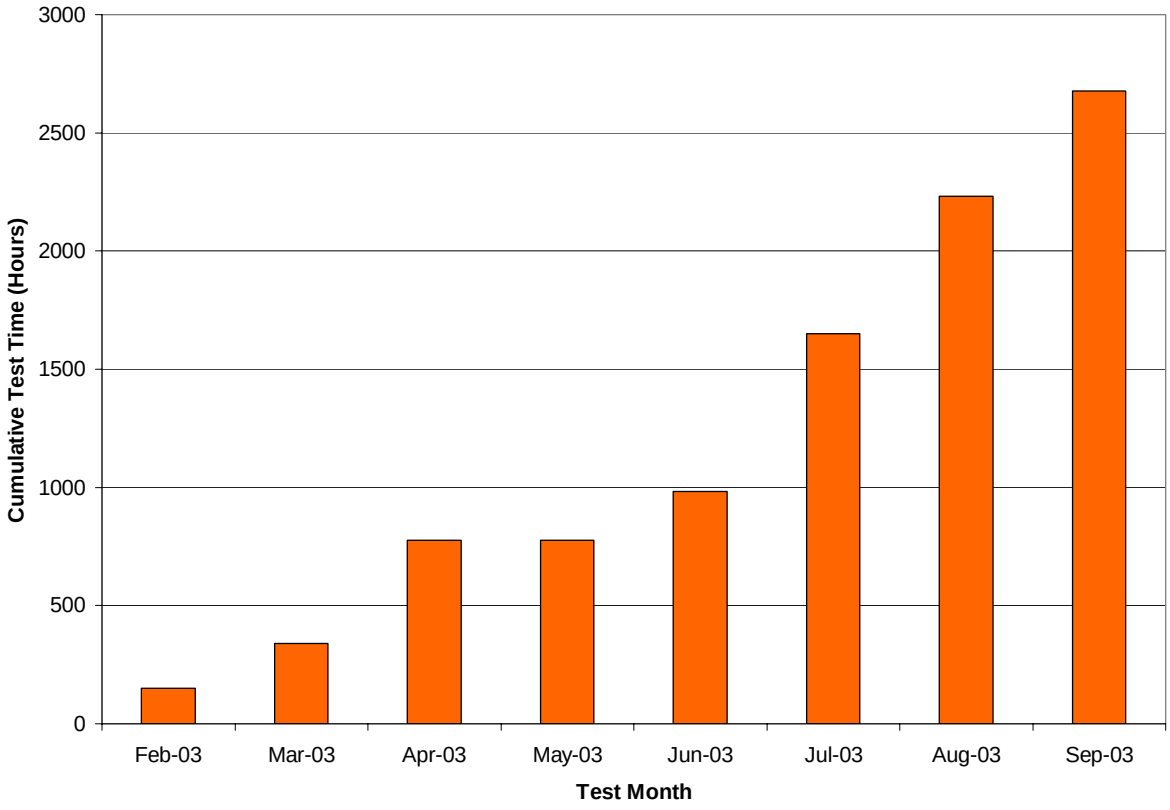


**Figure 5.83. Monthly cumulative catalyst exposure time to dusty flue gas at Rockport.**

The $NO_x$ concentration at the inlet was calculated at 5% $O_2$. The inlet concentration has been interpolated based on measurements of the inlet concentration made before and after the measurement of the $NO_x$ concentration at the outlet of each chamber. The ammonia concentration was calculated at 5% $O_2$, based on the total flow measured in the slipstream reactor and the set point of the ammonia mass flow controller. The $NH_3$/NO ratio was calculated from the ammonia concentration divided by the estimated inlet $NO_x$ concentration. The average catalyst chamber temperature is calculated from the average of the temperature before the catalyst and at the exit of the catalyst chamber. The space velocity was calculated at $0^oC$ ($32^oF$). Tables 5.28 through 5.33 contain the $NO_x$ data from the blank catalyst as well as catalysts C2 through C6. The $NO_x$ concentration at the inlet is calculated at 5% $O_2$.

**Table 5.28. $NO_x$ data for blank monolith.**

| Chamber | Date | Inlet $NO_x$ ppm (est) | $NO_x$ reduc. | T before cat, F | $NH_3$/NO | Avg T catal, F | SV, $hr^{-1}$ |
|---|---|---|---|---|---|---|---|
| one | 3/26/03 | 329 | 6.1% | 655 | 1.40 | 625 | 6,279 |
| one | 3/27/03 | 318 | 3.1% | 662 | 1.35 | 634 | 6,283 |
| one | 8/11/03 | 334.5 | 6.1% | 617 | 1.02 | 555 | 2,745 |
| one | 8/12/03 | 332.7 | -0.3% | 678 | 1.05 | 602 | 1,406 |
| one | 8/13/03 | 318.9 | 3.1% | 617 | 0.94 | 553 | 1,803 |
| one | 8/21/03 | 392.5 | -4.8% | 696 | 0.88 | 654 | 4,050 |
| one | 8/21/03 | 383.3 | 1.8% | 698 | 1.00 | 655 | 4,126 |
| one | 8/21/03 | 370.7 | 5.7% | 691 | 1.23 | 647 | 4,225 |
| one | 8/21/03 | 373.4 | 12.8% | 691 | 1.25 | 646 | 4,242 |

**Table 5.29. $NO_x$ data for catalyst C2 (monolith).**

| Chamber | Date | Inlet $NO_x$ ppm (est) | $NO_x$ reduc. | T before cat, F | $NH_3/NO$ | Avg T catal, F | SV, $hr^{-1}$ |
|---|---|---|---|---|---|---|---|
| two | 3/26/03 | 329.4 | 83.2% | 657 | 1.43 | 627 | 7064 |
| two | 3/27/03 | 323.8 | 83.8% | 662 | 1.43 | 628 | 7,087 |
| two | 3/27/03 | 335.9 | 85.4% | 662 | 1.32 | 629 | 7,080 |
| two | 3/27/03 | 311.8 | 85.7% | 655 | 1.32 | 623 | 7,073 |
| two | 3/27/03 | 308.5 | 83.5% | 660 | 1.40 | 630 | 7,119 |
| two | 3/27/03 | 328.6 | 85.1% | 658 | 1.29 | 628 | 7,076 |
| two | 3/27/03 | 239.6 | 78.4% | 668 | 1.62 | 649 | 7,099 |
| two | 3/27/03 | 317.0 | 83.6% | 667 | 1.26 | 648 | 7,093 |
| two | 4/5/03 | 301.4 | 83.8% | 685 | 1.27 | 648 | 8510 |
| two | 4/5/03 | 301.4 | 83.7% | 685 | 1.27 | 646 | 8501 |
| two | 8/11/03 | 334.5 | 71.4% | 617 | 1.02 | 554 | 5,687 |
| two | 8/12/03 | 331.7 | 76.7% | 644 | 1.20 | 570 | 3,568 |
| two | 8/13/03 | 318.9 | 62.2% | 611 | 0.93 | 553 | 4,841 |
| two | 8/15/03 | 331.4 | 70.7% | 612 | 1.23 | 543 | 5,125 |
| two | 8/21/03 | 383.6 | 74.8% | 694 | 0.94 | 658 | 8,682 |
| two | 8/21/03 | 391.2 | 75.4% | 698 | 0.94 | 661 | 8,654 |
| two | 8/21/03 | 382.7 | 75.4% | 698 | 1.14 | 661 | 8,641 |
| two | 8/21/03 | 378.1 | 74.5% | 692 | 1.16 | 656 | 8,696 |
| two | 8/21/03 | 371.1 | 73.5% | 691 | 1.29 | 654 | 8,756 |
| two | 8/21/03 | 373.4 | 73.6% | 691 | 1.27 | 654 | 8,751 |
| two | 8/22/03 | 361.6 | 72.2% | 674 | 0.94 | 636 | 8,656 |
| two | 8/22/03 | 350.5 | 70.9% | 678 | 0.92 | 641 | 8,800 |
| two | 8/22/03 | 337.5 | 69.2% | 676 | 0.89 | 640 | 8,859 |
| two | 8/22/03 | 344.9 | 70.1% | 683 | 0.92 | 645 | 8,967 |
| two | 8/22/03 | 365.7 | 72.0% | 690 | 0.97 | 653 | 8,963 |
| two | 8/22/03 | 364.2 | 71.5% | 690 | 0.96 | 654 | 8,973 |
| two | 8/22/03 | 345.5 | 70.6% | 689 | 1.00 | 653 | 8,940 |
| two | 8/22/03 | 362.3 | 72.5% | 690 | 0.98 | 654 | 8,837 |
| two | 8/22/03 | 351.9 | 71.2% | 688 | 0.96 | 652 | 8,878 |

**Table 5.30. $NO_x$ data for catalyst C3 (plate).**

| Chamber | Date | Inlet $NO_x$ ppm (est) | $NO_x$ reduc. | T before cat, F | $NH_3/NO$ | Avg T catal, F | SV, $hr^{-1}$ |
|---|---|---|---|---|---|---|---|
| three | 3/26/03 | 311.3 | 93.0% | 658 | 1.48 | 646 | 3113 |
| three | 3/27/03 | 324.0 | 92.8% | 661 | 1.41 | 648 | 3,092 |
| three | 3/27/03 | 329.9 | 91.4% | 665 | 1.21 | 652 | 3,105 |
| three | 3/27/03 | 309.4 | 91.2% | 653 | 1.34 | 641 | 3,103 |
| three | 3/27/03 | 319.1 | 90.7% | 659 | 1.34 | 649 | 3,092 |
| three | 3/27/03 | 327.4 | 92.0% | 656 | 1.29 | 646 | 3,127 |
| three | 3/27/03 | 319.2 | 92.0% | 661 | 1.52 | 651 | 3,101 |
| three | 3/27/03 | 318.7 | 89.3% | 667 | 1.27 | 662 | 3,085 |
| three | 3/27/03 | 316.7 | 88.4% | 668 | 1.27 | 663 | 3,103 |
| three | 4/5/03 | 301.4 | 97.2% | 685 | 1.27 | 666 | 3120 |
| three | 8/16/03 | 349.1 | 56.8% | 599 | 3.44 | 573 | 1,115 |
| three | 8/12/03 | 331.7 | 71.5% | 678 | 0.97 | 652 | 2,583 |
| three | 8/13/03 | 318.9 | 64.7% | 610 | 0.92 | 591 | 2,587 |
| three | 8/11/03 | 334.5 | 74.5% | 619 | 1.01 | 600 | 2,599 |
| three | 8/16/03 | 349.1 | 84.2% | 645 | 1.06 | 631 | 3,715 |
| three | 8/22/03 | 351.4 | 78.7% | 688 | 0.97 | 673 | 5,251 |
| three | 8/22/03 | 363.3 | 79.9% | 689 | 0.98 | 674 | 5,267 |
| three | 8/21/03 | 390.0 | 81.6% | 700 | 1.02 | 683 | 5,293 |
| three | 8/21/03 | 382.0 | 81.5% | 698 | 1.17 | 682 | 5,298 |
| three | 8/21/03 | 384.1 | 81.0% | 695 | 0.95 | 679 | 5,322 |
| three | 8/21/03 | 377.0 | 80.3% | 693 | 1.19 | 677 | 5,325 |
| three | 8/22/03 | 343.9 | 78.3% | 690 | 1.01 | 674 | 5,330 |
| three | 8/21/03 | 371.4 | 80.0% | 692 | 1.28 | 675 | 5,339 |
| three | 8/21/03 | 373.4 | 79.7% | 692 | 1.24 | 675 | 5,345 |
| three | 8/22/03 | 365.9 | 79.3% | 690 | 0.96 | 673 | 5,373 |
| three | 8/22/03 | 336.2 | 76.7% | 678 | 0.90 | 659 | 5,409 |
| three | 8/22/03 | 366.2 | 79.5% | 690 | 0.97 | 673 | 5,421 |
| three | 8/22/03 | 351.6 | 78.2% | 679 | 0.92 | 661 | 5,438 |
| three | 8/22/03 | 342.9 | 77.1% | 685 | 0.92 | 667 | 5,446 |
| three | 8/22/03 | 363.0 | 78.6% | 677 | 0.93 | 658 | 5,464 |
| three | 8/21/03 | 407.5 | 82.5% | 695 | 0.27 | 679 | 5,334 |

**Table 5.31. $NO_x$ data for catalyst C4 (plate).**

| Chamber | Date | Inlet $NO_x$ ppm (est) | $NO_x$ reduc. | T before cat, F | $NH_3/NO$ | Avg T catal, F | SV, $hr^{-1}$ |
|---|---|---|---|---|---|---|---|
| four | 3/26/03 | 312.0 | 92.1% | 663 | 1.31 | 650 | 2154 |
| four | 3/27/03 | 324.4 | 94.5% | 660 | 1.37 | 647 | 2,148 |
| four | 3/27/03 | 322.4 | 94.6% | 661 | 1.32 | 648 | 2,158 |
| four | 3/27/03 | 307.7 | 94.3% | 658 | 1.45 | 644 | 2,147 |
| four | 3/27/03 | 336.4 | 94.8% | 659 | 1.26 | 647 | 2,154 |
| four | 3/27/03 | 326.4 | 94.8% | 656 | 1.36 | 645 | 2,152 |
| four | 3/27/03 | 328.3 | 94.1% | 663 | 1.46 | 654 | 2,984 |
| four | 3/27/03 | 325.0 | 87.0% | 669 | 1.28 | 665 | 3,064 |
| four | 4/5/03 | 301.4 | 88.8% | 685 | 1.27 | 676 | 6007 |
| four | 4/5/03 | 301.4 | 61.3% | 489 | 1.26 | 456 | 6001 |
| four | 8/12/03 | 331.7 | 75.1% | 617 | 1.19 | 605 | 2,541 |
| four | 8/13/03 | 318.9 | 64.0% | 626 | 0.91 | 615 | 2,669 |
| four | 8/22/03 | 350.8 | 86.9% | 686 | 0.97 | 673 | 3,196 |
| four | 8/22/03 | 364.3 | 87.4% | 690 | 0.98 | 677 | 3,220 |
| four | 8/22/03 | 342.3 | 86.2% | 691 | 1.02 | 677 | 3,224 |
| four | 8/22/03 | 366.7 | 86.3% | 689 | 0.97 | 676 | 3,325 |
| four | 8/22/03 | 367.5 | 87.2% | 690 | 0.95 | 677 | 3,421 |
| four | 8/22/03 | 352.7 | 84.9% | 680 | 0.93 | 666 | 3,917 |
| four | 8/22/03 | 340.8 | 84.4% | 686 | 0.93 | 671 | 4,012 |
| four | 8/22/03 | 364.4 | 84.9% | 678 | 0.93 | 663 | 4,031 |
| four | 8/22/03 | 335.0 | 83.3% | 676 | 0.92 | 663 | 4,059 |
| four | 8/11/03 | 334.5 | 79.8% | 617 | 1.02 | 603 | 4,169 |
| four | 8/21/03 | 376.0 | 87.2% | 693 | 1.32 | 679 | 4,170 |
| four | 8/21/03 | 371.7 | 86.7% | 692 | 1.27 | 678 | 4,216 |
| four | 8/21/03 | 389.0 | 87.8% | 701 | 1.04 | 685 | 4,235 |
| four | 8/21/03 | 381.3 | 87.4% | 697 | 0.85 | 683 | 4,250 |
| four | 8/21/03 | 384.5 | 87.4% | 695 | 0.94 | 680 | 4,250 |
| four | 8/21/03 | 373.4 | 86.5% | 691 | 1.18 | 676 | 4,323 |
| four | 8/21/03 | 405.1 | 88.3% | 696 | 0.53 | 681 | 4,308 |

**Table 5.32. $NO_x$ data for catalyst C5 (monolith).**

| Chamber | Date | Inlet $NO_x$ ppm (est) | $NO_x$ reduc. | T before cat, F | $NH_3/NO$ | Avg T catal, F | SV, $hr^{-1}$ |
|---|---|---|---|---|---|---|---|
| five | 3/26/03 | 330.9 | 88.3% | 663 | 1.39 | 638 | 6988 |
| five | 3/27/03 | 320.0 | 90.4% | 663 | 1.32 | 637 | 6,997 |
| five | 3/27/03 | 321.6 | 88.9% | 660 | 1.25 | 635 | 7,026 |
| five | 3/27/03 | 303.5 | 89.2% | 659 | 1.44 | 633 | 7,068 |
| five | 3/27/03 | 334.6 | 89.1% | 658 | 1.29 | 635 | 7,016 |
| five | 3/27/03 | 326.9 | 88.5% | 656 | 1.40 | 633 | 6,977 |
| five | 3/27/03 | 333.1 | 98.4% | 663 | 1.36 | 641 | 7,021 |
| five | 3/27/03 | 328.7 | 79.7% | 663 | 1.23 | 649 | 6,993 |
| five | 3/27/03 | 313.8 | 85.7% | 668 | 1.31 | 656 | 7,047 |
| five | 4/5/03 | 301.4 | 83.2% | 684 | 1.27 | 646 | 10772 |
| five | 4/5/03 | 301.4 | 67.2% | 528 | 1.27 | 457 | 10924 |
| five | 8/12/03 | 331.7 | 72.4% | 607 | 1.19 | 543 | 3,635 |
| five | 8/13/03 | 318.9 | 66.1% | 608 | 0.92 | 547 | 4,564 |
| five | 8/16/03 | 349.1 | 68.0% | 645 | 1.18 | 604 | 6,973 |
| five | 8/21/03 | 385.0 | 90.7% | 695 | 0.94 | 665 | 9,742 |
| five | 8/21/03 | 402.9 | 90.7% | 697 | 0.79 | 667 | 9,742 |
| five | 8/21/03 | 387.9 | 90.6% | 698 | 1.06 | 669 | 9,743 |
| five | 8/21/03 | 380.6 | 90.7% | 696 | 1.01 | 667 | 9,741 |
| five | 8/21/03 | 375.3 | 90.6% | 694 | 1.23 | 663 | 9,740 |
| five | 8/21/03 | 371.9 | 90.3% | 692 | 1.28 | 662 | 9,741 |
| five | 8/21/03 | 373.4 | 90.9% | 691 | 1.15 | 660 | 9,743 |
| five | 8/22/03 | 365.9 | 89.6% | 677 | 0.94 | 646 | 9,740 |
| five | 8/22/03 | 353.9 | 89.3% | 680 | 0.93 | 649 | 9,738 |
| five | 8/22/03 | 333.7 | 88.3% | 677 | 0.91 | 646 | 9,743 |
| five | 8/22/03 | 338.7 | 88.5% | 686 | 0.94 | 654 | 9,741 |
| five | 8/22/03 | 367.2 | 89.6% | 689 | 0.96 | 658 | 9,744 |
| five | 8/22/03 | 369.2 | 89.5% | 689 | 0.95 | 658 | 9,742 |
| five | 8/22/03 | 340.7 | 89.3% | 691 | 1.02 | 660 | 9,743 |
| five | 8/22/03 | 365.2 | 90.3% | 691 | 0.98 | 660 | 9,739 |
| five | 8/22/03 | 350.3 | 89.4% | 685 | 0.98 | 656 | 9,740 |
| five | 8/16/03 | 349.1 | 58.7% | 608 | 3.75 | 544 | 2,593 |

**Table 5.33. $NO_x$ data for catalyst C6 (monolith).**

| Chamber | Date | Inlet $NO_x$ ppm (est) | $NO_x$ reduc. | T before cat, F | $NH_3$/NO | Avg T catal, F | SV, $hr^{-1}$ |
|---|---|---|---|---|---|---|---|
| six | 3/26/03 | 324.0 | 81.6% | 660 | 1.41 | 632 | 7198 |
| six | 3/27/03 | 313.1 | 79.9% | 663 | 1.31 | 633 | 7,174 |
| six | 3/27/03 | 320.2 | 81.3% | 663 | 1.34 | 632 | 7,191 |
| six | 3/27/03 | 309.7 | 79.2% | 658 | 1.40 | 629 | 7,208 |
| six | 3/27/03 | 325.9 | 79.3% | 655 | 1.35 | 628 | 7,213 |
| six | 3/27/03 | 334.3 | 81.5% | 667 | 1.45 | 641 | 7,170 |
| six | 4/5/03 | 301.4 | 70.4% | 684 | 1.27 | 649 | 10745 |
| six | 4/5/03 | 301.4 | 67.7% | 554 | 1.28 | 494 | 10737 |
| six | 8/12/03 | 331.7 | 64.4% | 603 | 1.22 | 555 | 2,219 |
| six | 8/13/03 | 318.9 | 58.2% | 613 | 0.93 | 566 | 2,314 |
| six | 8/21/03 | 387.9 | 86.2% | 695 | 0.94 | 673 | 9,619 |
| six | 8/21/03 | 400.9 | 86.2% | 696 | 0.79 | 674 | 9,632 |
| six | 8/21/03 | 386.9 | 85.8% | 697 | 1.04 | 675 | 9,606 |
| six | 8/21/03 | 379.9 | 85.9% | 694 | 1.19 | 673 | 9,611 |
| six | 8/21/03 | 374.7 | 86.2% | 693 | 1.30 | 671 | 9,615 |
| six | 8/21/03 | 372.1 | 86.0% | 693 | 1.27 | 671 | 9,631 |
| six | 8/22/03 | 367.3 | 88.2% | 676 | 0.92 | 655 | 9,614 |
| six | 8/22/03 | 355.0 | 87.1% | 679 | 0.92 | 657 | 9,631 |
| six | 8/22/03 | 332.5 | 83.9% | 679 | 0.92 | 657 | 9,660 |
| six | 8/22/03 | 336.5 | 85.7% | 687 | 0.98 | 665 | 9,618 |
| six | 8/22/03 | 367.7 | 87.6% | 689 | 0.97 | 668 | 9,623 |
| six | 8/22/03 | 370.9 | 88.3% | 687 | 0.94 | 667 | 9,639 |
| six | 8/22/03 | 339.1 | 87.0% | 691 | 1.03 | 670 | 9,630 |
| six | 8/22/03 | 366.2 | 88.9% | 691 | 0.98 | 670 | 9,640 |
| six | 8/22/03 | 349.7 | 88.3% | 685 | 0.98 | 664 | 9,603 |
| six | 8/22/03 | 357.7 | 80.6% | 685 | 0.98 | 662 | 9,626 |
| six | 8/22/03 | 364.5 | 79.1% | 691 | 0.98 | 669 | 9,634 |

The March/April data were taken at excess ammonia ($NH_3/NO$ ~ 1.2-1.6) in order to remove any effects of ammonia concentration. The average catalyst temperatures were in the range of 325 to 345°C (620 to 650°F). The main factor that affected the $NO_x$ reduction was the space velocity. Figure 5.84 shows the $NO_x$ reduction as a function of space velocity for all five catalysts for the first test series. The $NO_x$ reduction for catalysts C2, C3 and C4 appeared to follow a single curve with space velocity. Catalysts C5 and C6 had different levels of $NO_x$ reduction from the other three; the slopes were about the same, but the intercepts were different. In general, the catalysts all appeared capable of achieving about 90% $NO_x$ reduction at a space velocity of 3,000 $hr^{-1}$, which is typical of full-scale installations.

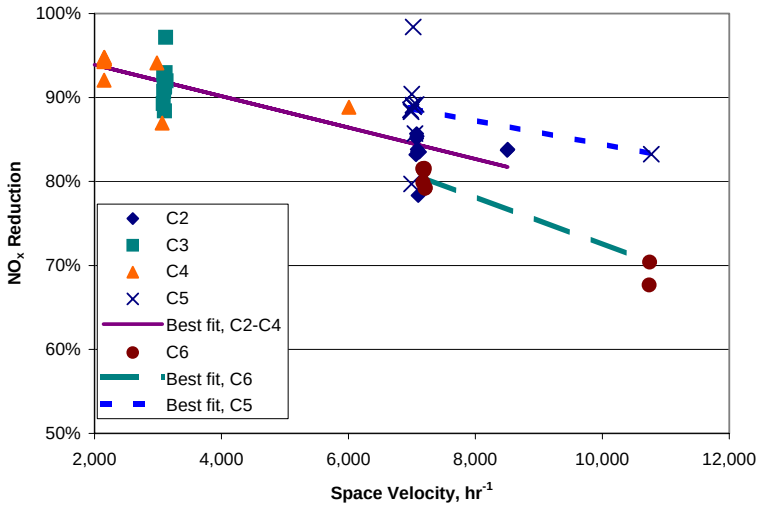


**iFigure 5.84. NO reduction as a function of space velocity for commercial catalysts from March/April for excess ammonia and catalyst temperatures in the range of 620-650°F.**

Figure 5.85 shows the NO reduction as a function of temperature, ammonia and space velocity for the second test series (August 2004). There were differences in the temperatures, space velocities and ratios of $NH_3/NO$ between the March/April data and the August data. In order to compare the $NO_x$ reduction, the effects of these parameters must first be characterized.

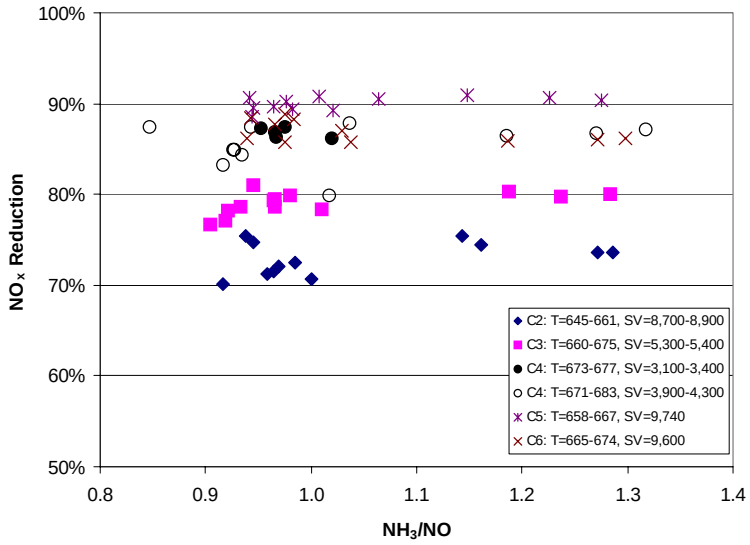


**Figure 5.85. $NO_x$ reduction as a function of $NH_3/NO$ ratio for commercial catalysts from August; temperatures (in degrees F) and space velocities (in $hr^{-1}$) as indicated on legend.**

The effect of temperature on $NO_x$ reduction can also be seen in the August data. Figure 5.86 shows the $NO_x$ reduction as a function of temperature at a fixed space velocity, all for $NH_3/NO > 0.95$. Since the March/April data

were obtained at different temperatures and space velocities than the August data, the August data were corrected for temperature by using the curvefits shown in Figure 5.86 and Table 5.34. Such curvefits should not be used for large temperature corrections; however, the upper end of the range of temperatures in March/April data is generally close (0 to 8 F) to the lower end of the August temperature range for catalysts C2 through C5. There is a 20°F gap in temperature ranges for C6; therefore extrapolation of the C6 data is suspect.

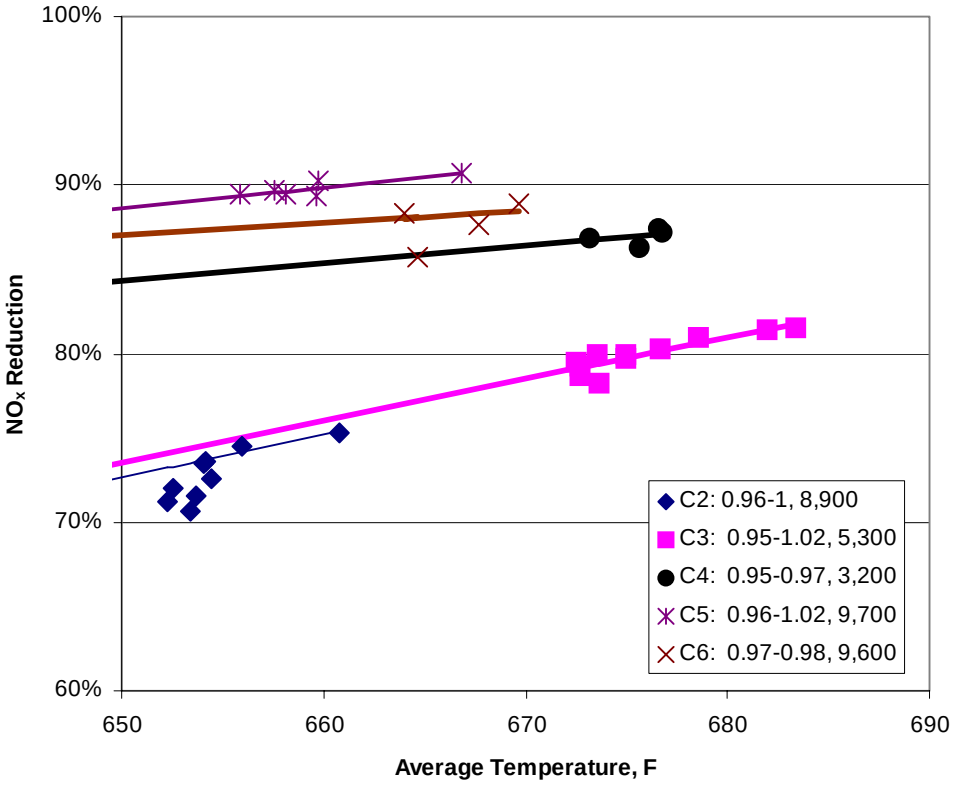


**Figure 5.86. $NO_x$ reduction as a function of temperature for commercial catalysts from August; $NH_3$/NO ratios and space velocities (in $hr^{-1}$) as indicated on legend.**

**Table 5.34. Relationship between $NO_x$ reduction and temperature from August test data.**

| Catalyst | C2 | C3 | C4 | C5 | C6 |
|---|---|---|---|---|---|
| Space velocity, $hr^{-1}$ | 8,900 | 5,300 | 3,200 | 9,700 | 9,600 |
| $NH_3/NO$ | 1.14-1.29 | 0.95-1.02 | 0.97-0.97 | 0.96-1.02 | 0.97-0.98 |
| Temperature range, $^oF$ | 653-661 | 674-683 | 676-685 | 660-669 | 670-675 |
| $r^2$ | 0.95 | 0.80 | 0.38 | 0.68 | 0.12 |
| Intercept | -97.2 | -87.1 | 16.7 | 9.2 | 39.4 |
| Slope | 0.261 | 0.247 | 0.104 | 0.122 | 0.073 |

Figure 5.87 compares the March/April $NO_x$ data with the August $NO_x$ data. The August data show the range of $NO_x$ reductions that correspond to the temperature range of the data of the March/April data. Catalysts C2, C3 and C4 appear to have lower $NO_x$ reduction in August as compared to March/April. Catalyst C5 has about the same $NO_x$ reduction. Catalyst C6 appears to have higher $NO_x$ reduction in August as compared to March/April; however, extrapolating the C6 $NO_x$ reduction to the range of temperatures of the March/April tests may produce larger errors than for the other catalysts, as discussed previously.

The deactivation of commercial SCR catalysts exposed to a flue gas is measured in two ways: (1) by direct measurement of the $NO_x$ composition of the flue gas before and after it flows through a catalyst in the slipstream reactor in the presence of ammonia; and (2) by laboratory evaluation of the catalysts after periodical removal from the slipstream reactor. Catalyst activity has been defined as the ratio:

$$Catalyst\ \ Activity = \left( \frac{NO_{X\,(in)} - NO_{X\,(out)}}{NO_{X\,(in)}} \right) \qquad (5\text{-}10)$$

In ideal conditions, the $NO_{X\,(out)}$ reading for the most effective catalyst would be zero and the catalyst activity would be 1. As the catalyst deactivates, the $NO_{X\,(out)}$ reading would gradually rise making the activity less than one. In the limiting condition where the catalyst is totally deactivated, $NO_{X\,(out)}$ would be the same as $NO_{X\,(in)}$ and the catalyst activity would be zero.

Figure 5.88 is a comparison of average catalyst activity from $NO_x$ measurements taken last quarter on April 4, 2003 and this quarter on August 24, 2003. The figure shows a general decline in catalyst activity over the test period.

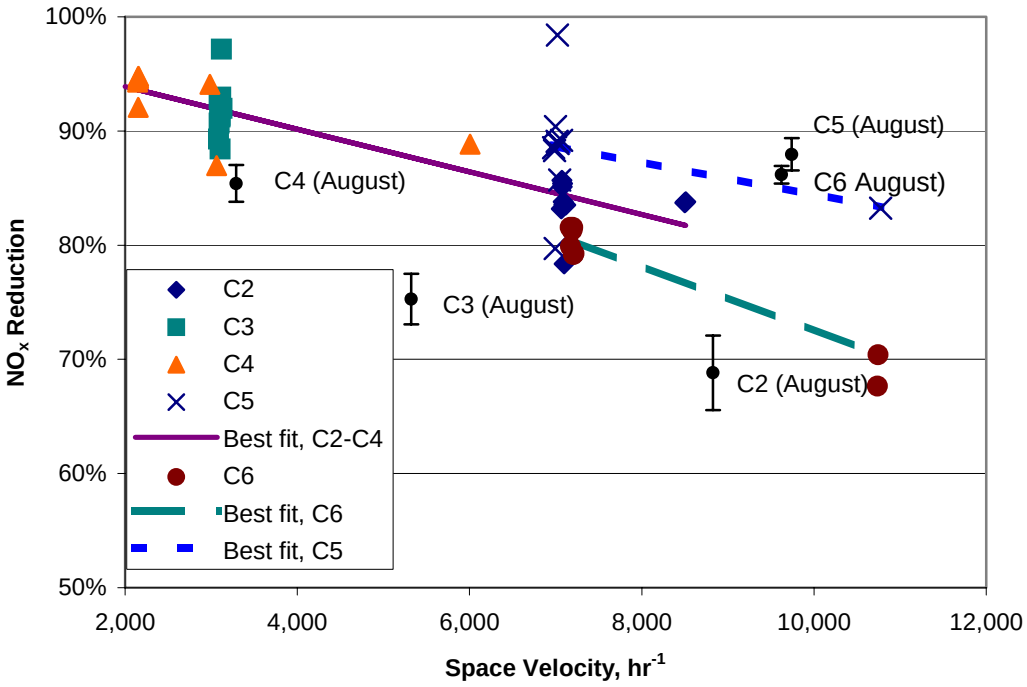


**Figure 5.87. $NO_x$ reduction as a function of space velocity for commercial catalysts from March/April for excess ammonia and catalyst temperatures in the range of 620-650°F compared with August data (extrapolated to the appropriate temperature range.**

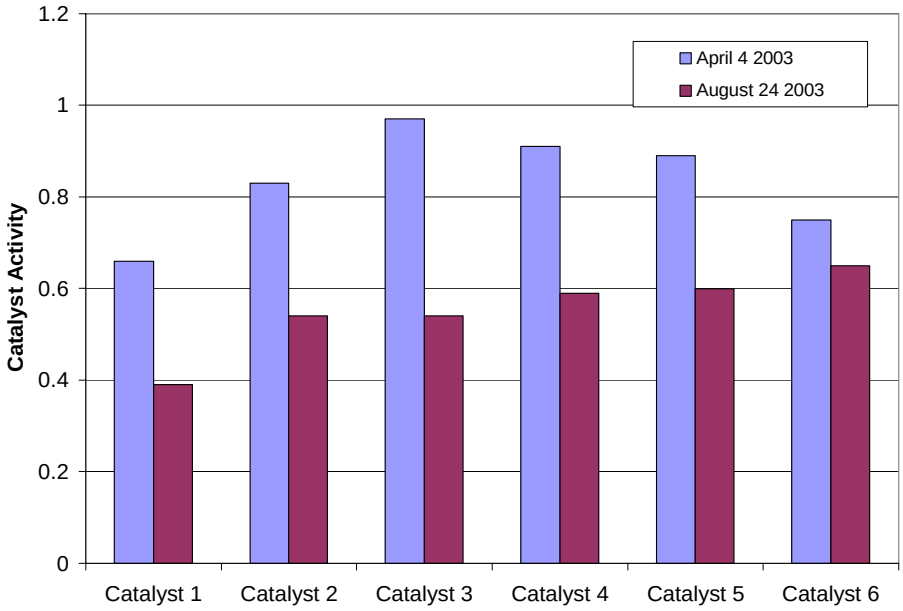


**Figure 5.88. Comparison of catalyst activities measured in April 4, 2003 and August 24, 2003.**

### *5.2.3 Biomass Co-firing Tests at Gadsden*

#### 5.2.3.1 Site Description

The Gadsen Plant (Figure 5.89) is located in Gadsden, Alabama, and has two 70 MW tangentially fired boilers. It had been burning switchgrass as part of a three-year DOE program, firing switchgrass seven to eight hours per day, five days a week, in Unit 2. The difficulty in running switchgrass for extended periods of time on Unit 2, prompted Southern Company and REI to consider firing sawdust on Unit 1 by co-milling sawdust at about 5% weight basis. The plant personnel believed that they could co-mill 5% sawdust twenty-four hours per day. This had the advantage of longer exposure times for the catalysts to biomass and a

**Figure 5.89. Plant Gadsden.**

fairly steady fuel source.

#### 5.2.3.2 Installation at Gadsden

Work with plant engineers identified a location for the reactor on Unit 1. Figure 5.90 shows a sketch of the piping required to bring flue gas (upstream of air heater) to the slipstream reactor and return the flue gas (downstream of the air heater).

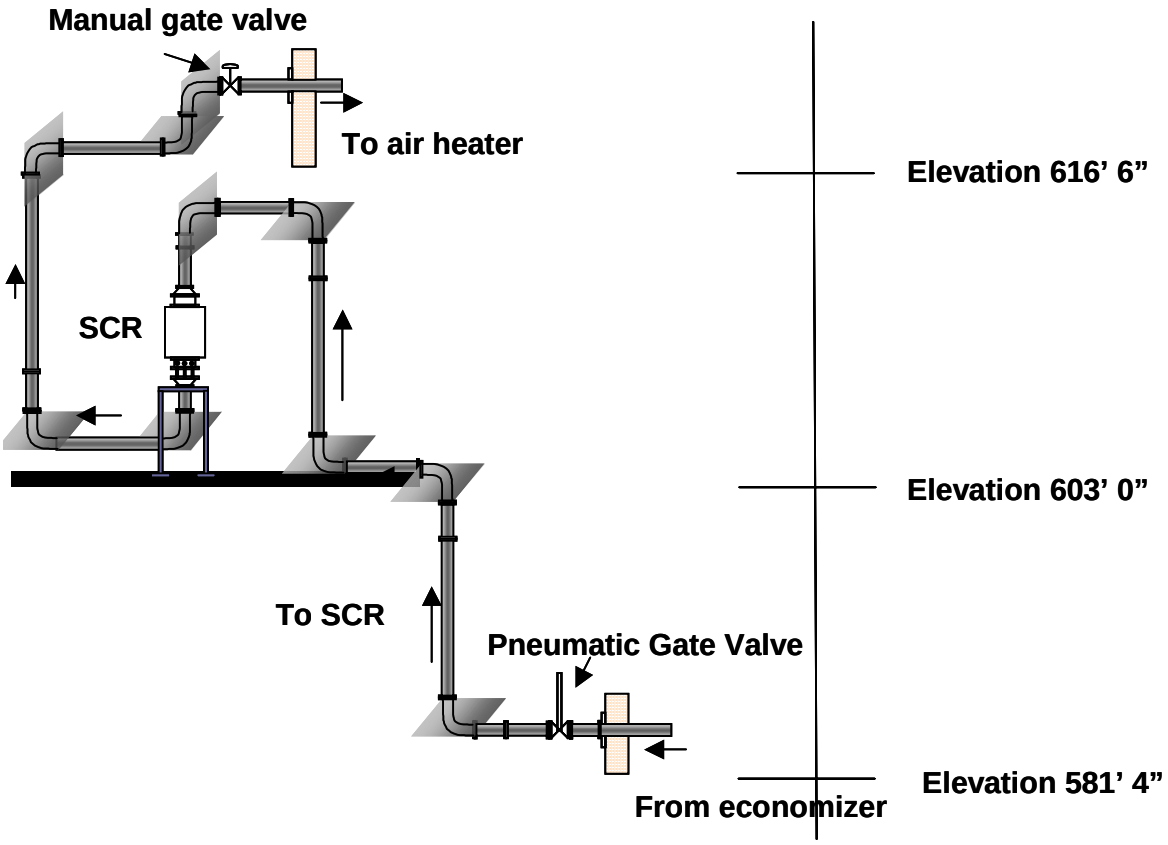


**Figure 5.90. SCR layout at Gadsden.**

The slipstream reactor was installed on Unit 1. Inlet and outlet ports were installed at Gadsden Unit 1 for the slipstream reactor during an outage. The inlet port is at the economizer exit (Figure 5.91) and the outlet port is downstream of the air preheater (Figure 5.92).

**Figure 5.91. Inlet port installed at economizer exit at Plant Gadsden.**

**Figure 5.92. Outlet port installed at air preheater exit at Plant Gadsden.**

During August and September of 2004, the reactor was assembled at Gadsden. Most of the components had been shipped to the plant from Rockport in the previous quarter. Certain components were fabricated in Salt Lake City and shipped to the plant, while other components were fabricated on-site. During this time, Unit 1 was not operating because the plant was idled during ozone season (which ended at the end of September).

The reactor was assembled (Figure 5.93). After assembly, electrical and plumbing connections were made. The heaters and flow system were tested, and then the reactor was insulated (Figure 5.94). As at Rockport, the Control Box and CEM sequencer cabinet were located next to the reactor (Figure 5.95).

An Ethernet cable was run from the Control Box to the control room and connected to the host PC. After several false starts, a modem connection was established over a dedicated phone line, allowing REI to download information (although at a low data transfer rate).

**Figure 5.93. Assembly of slipstream reactor.**

**Figure 5.94. Slipstream reactor after insulation.**

**Figure 5.95. Control Box and Sequencer.**

As can be seen from Figure 5.90, there is a considerable amount of piping needed to connect the slipstream reactor to the boiler. Piping was run from the inlet (Figure 5.96) to the reactor and then to the outlet (Figure 5.97). The inlet and outlet ports were located upstream and downstream of the air heater, respectively. The ammonia delivery manifold had to be refabricated because the black iron pipe used for the manifold had rusted. The manifold was refabricated out of stainless steel. The ammonia tanks could were installed in the fan room.

**Figure 5.96. Inlet port located upstream of air heater.**

**Figure 5.97. Outlet port located downstream of air heater.**

### 5.2.3.3 Fuel and Ash Data

Fuel samples (coal plus sawdust) were taken from the inlet to the pulverizer. The slipstream reactor experienced ash blockage at the end of 2004. The fuel sample contained approximately 5% sawdust by weight. A sample was taken at the pulverizer inlet. Table 5.35 gives the fuel composition. The flue gas composition can be estimated from the ultimate analysis, as shown in Table 5.36. The $SO_2$ content of the flue gas is moderately high.

**Table 5.35. Fuel ultimate and proximate analyses from Gadsden.**

| Analyte | As-rec'd | Dry Basis |
|---|---|---|
| Cl | ---- | 209 µg/g |
| *Proximate analysis* | | |
| Total Moisture | 4.88 wt. % | ---- |
| Moisture Air Dry | 3.87 wt. % | ---- |
| Moisture Oven Dry | 1.05 wt. % | ---- |
| Ash | 14.22 wt. % | 14.95 wt. % |
| Total Sulfur | 2.02 wt. % | 2.12 wt. % |
| Calorific Value | 11,884 BTU/lb | 12,493 BTU/lb |
| Volatile Matter | 28.83 wt. % | 30.31 wt. % |
| Fixed Carbon | 52.07 wt. % | 54.74 wt. % |
| *Ultimate Analysis* | | |
| Total Moisture | 4.88 wt. % | ---- |
| Ash | 14.22 wt. % | 14.95 wt. % |
| Total Sulfur | 2.02 wt. % | 2.12 wt. % |
| Carbon | 70.08 wt. % | 73.68 wt. % |
| Hydrogen | 5.24 wt. % | 4.93 wt. % |
| Nitrogen | 1.44 wt. % | 1.51 wt. % |
| Oxygen (by difference) | 2.67 wt% | 2.81 wt% |

A sample of the ESP hopper ash was taken at the same time as the fuel sample. Table 5.36 compares the mineral analysis of the fuel and the ESP hopper ash, normalized on a sulfur-free basis.

The ash is low in sodium and very low in calcium. However, the potassium content (2.65 wt%) is significant. The composition of the ESP ash corresponds well with the fuel ash composition. Sodium appears to be depleted in the ESP ash.

**Table 5.36. Flue gas composition estimated from ultimate analysis.**

| Species | |
|---|---|
| $O_2$ | 4.69% |
| $CO_2$ | 12.88% |
| $H_2O$ | 6.19% |
| $N_2$ | 75.99% |
| $SO_2$ [ppm] | 1,389 |
| HCl [ppm] | 13 |

**Table 5.37. Composition of mineral fraction in fuel and ESP hopper ash, normalized to a sulfur-free basis.**

| | Coal Ash | ESP Hopper Ash |
|---|---|---|
| Silicon Dioxide | 53.14 | 54.86 |
| Aluminum Oxide | 25.52 | 26.86 |
| Titanium Dioxide | 1.23 | 1.25 |
| Iron Oxide | 14.24 | 11.31 |
| Calcium Oxide | 1.01 | 0.91 |
| Magnesium Oxide | 0.98 | 0.97 |
| Potassium Oxide | 2.65 | 2.76 |
| Sodium Oxide | 0.42 | 0.29 |
| Phosphorus Pentoxide | 0.41 | 0.42 |
| Barium Oxide | 0.26 | 0.26 |
| Manganese Dioxide | 0.04 | 0.03 |
| Strontium Oxide | 0.08 | 0.09 |

During the months of November and December, 2004 and January, 2005, the average sawdust content of the fuel was 3.85 wt%. Figure 5.98 shows the daily average sawdust content of the fuel, as reported by the plant.

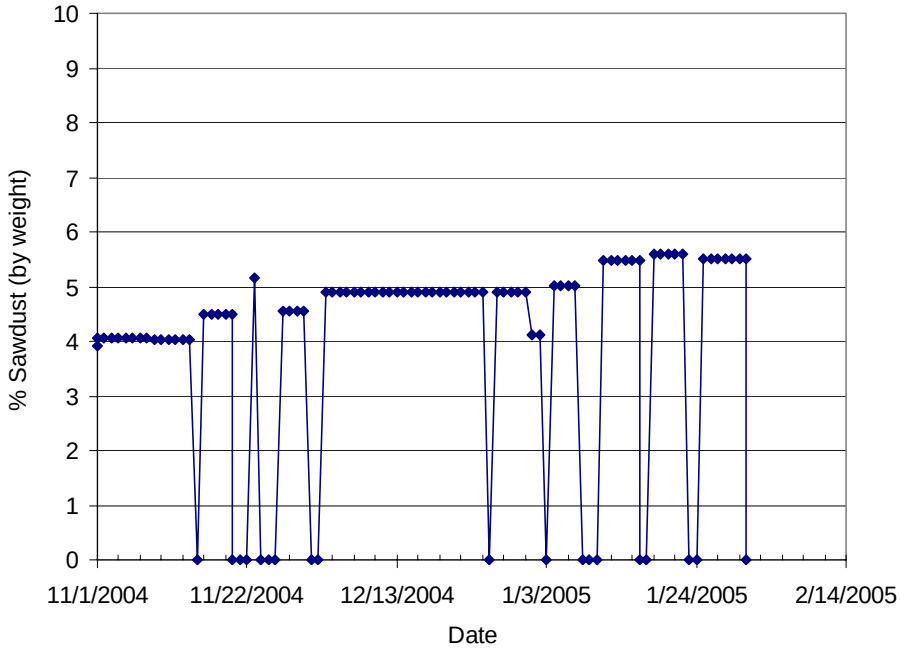


**Figure 5.98. Sawdust feed rate at Gadsden Unit 1, in wt% of total fuel flow.**

### 5.2.3.4 $NO_x$ Performance

The reactor started up the week of November 15, 2004. The total exposure to flue gas in the slipstream reactor at Gadsden was about 350 hours, as shown in Figure 5.99. Problems with plugging of the slipstream reactor and with the remote communications limited the operation of the slipstream reactor at Gadsden. Furthermore, the boiler was not operational during all of the six-month period due to dispatch requirements and outages.

On November 18 and 20, 2004, an initial survey of the $NO_x$ activity (reduction) of each catalyst was carried out. $NO_x$ activity was computed by measuring the inlet $NO_x$ and the outlet $NO_x$ from each chamber using the CEM. During most of the measurements, the inlet $NO_x$ was fairly stable. The $O_2$-content of the flue gas was 3 to 4% for the sample chambers. Certain inlet measurements showed very high $O_2$, which indicated a leak in the sampling system. Those measurements were not used for further analysis.

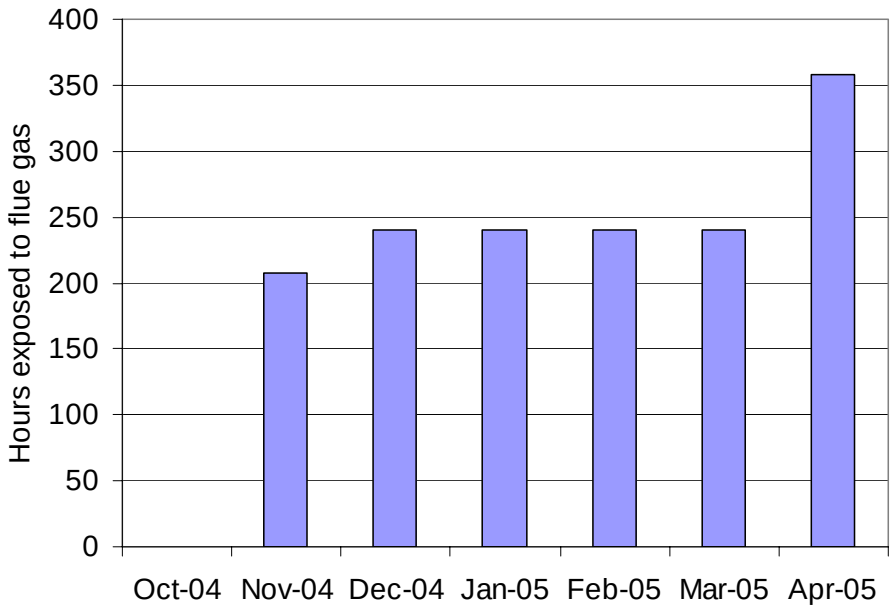


**Figure 5.99. Exposure time of catalysts to flue gas at Plant Gadsden.**

Tables 5.387 and 5.39 summarize the $NO_x$ data. Inlet $NO_x$ values are corrected to 3% $O_2$ (dry basis). The ammonia was computed on a wet basis and the $NH_3$/NO ratio is computed on this basis. Space velocity was computed at 32 $^oF$.

**Table 5.38. $NO_x$ Data and Activity from 11-18-04.**

| Sample | Time | Average inlet $NO_x$ (3% $O_2$, dry) | $NO_x$ reduction | Total flow, scfm | $NH_3$, ppm | $NH_3$/NO (act. Basis) | T-average, F | SV, $hr^{-1}$ |
|---|---|---|---|---|---|---|---|---|
| INLET | 18:28-18:47 | 445 | | 131 | 430 | 1.03 | 547 | |
| ONE | 18:49-18:52 | 451 | 21.85% | 130 | 431 | 1.02 | 548 | 3,735 |
| TWO | 18:54-18:56 | 451 | 65.70% | 126 | 444 | 1.05 | 546 | 8,499 |
| ONE | 18:58-19:01 | 451 | 72.13% | 125 | 449 | 1.06 | 547 | 3,714 |
| INLET | 19:05-19:07 | 457 | | 125 | 451 | 1.05 | 547 | |
| FOUR | 19:09-19:12 | 445 | 91.02% | 124 | 452 | 1.08 | 550 | 3,296 |
| FIVE | 19:13-19:17 | 445 | 89.25% | 125 | 449 | 1.07 | 537 | 5,699 |
| SIX | 19:18-19:21 | 445 | 82.08% | 127 | 443 | 1.06 | 536 | 4,505 |
| INLET | 19:25-19:28 | 433 | | 126 | 447 | 1.10 | 544 | |
| THREE | 19:30-19:33 | 433 | 96.82% | 126 | 445 | 1.09 | 562 | 2,187 |
| TWO | 19:34-19:37 | 433 | 65.40% | 126 | 445 | 1.09 | 543 | 8,502 |

**Table 5.39. $NO_x$ Data and Activity from 11-20-04.**

| Sample | Time | Average inlet $NO_x$ (3% $O_2$, dry) | $NO_x$ reduction | Total flow, scfm | $NH_3$, ppm | $NH_3$/NO (act. Basis) | T-average, F | SV, $hr^{-1}$ |
|---|---|---|---|---|---|---|---|---|
| INLET | 8:17-8:19 | 416 | | 100 | 413 | 1.06 | 548 | |
| ONE | 8:21-8:24 | 408 | 20.59% | 100 | 417 | 1.09 | 550 | 2,987 |
| TWO | 8:26-9:29 | 408 | 81.82% | 100 | 414 | 1.08 | 543 | 4,865 |
| THREE | 8:30-8:33 | 408 | 96.95% | 96 | 432 | 1.13 | 567 | 2,147 |
| INLET | 8:37-8:40 | 401 | | 94 | 441 | 1.17 | 549 | |
| FOUR | 8:41-8:44 | 404 | 96.54% | 94 | 442 | 1.17 | 550 | 2,339 |
| FIVE | 8:46-8:49 | 404 | 93.56% | 94 | 443 | 1.17 | 534 | 3,455 |
| SIX | 8:51-8:53 | 404 | 78.24% | 94 | 443 | 1.17 | 539 | 4,972 |
| INLET | 8:58-9:01 | 408 | | 94 | 443 | 1.15 | 548 | |
| THREE | 9:02-9:05 | 412 | 96.72% | 95 | 438 | 1.13 | 565 | 2,120 |
| TWO | 9:07-9:10 | 412 | 81.75% | 95 | 437 | 1.13 | 543 | 4,810 |
| ONE | 9:12-9:14 | 412 | 25.43% | 91 | 458 | 1.18 | 548 | 2,770 |
| INLET | 9:18-9:21 | 417 | | 90 | 462 | 1.18 | 546 | |
| FOUR | 9:23-9:25 | 417 | 97.50% | 88 | 474 | 1.21 | 547 | 2,137 |
| FIVE | 9:27-9:30 | 417 | 95.70% | 87 | 477 | 1.22 | 532 | 3,284 |
| SIX | 9:32-9:35 | 417 | 81.52% | 87 | 476 | 1.21 | 535 | 4,553 |
| ONE | 9:44-9:46 | 417 | 20.09% | 94 | 401 | 1.02 | 546 | 2,797 |
| TWO | 9:48-9:51 | 417 | 81.70% | 95 | 400 | 1.02 | 540 | 4,679 |
| THREE | 9:53-9:56 | 417 | 97.69% | 88 | 431 | 1.10 | 560 | 1,966 |
| FOUR | 10:04-10:07 | 417 | 97.47% | 86 | 448 | 1.14 | 543 | 2,092 |
| FIVE | 10:08-10:11 | 417 | 96.01% | 86 | 447 | 1.14 | 528 | 2,998 |
| SIX | 10:13-10:16 | 417 | 86.28% | 88 | 437 | 1.11 | 533 | 4,629 |
| ONE | 10:25-10:28 | 417 | 18.84% | 89 | 411 | 1.05 | 544 | 2,712 |
| TWO | 10:29-10:32 | 417 | 79.00% | 90 | 408 | 1.04 | 537 | 4,573 |

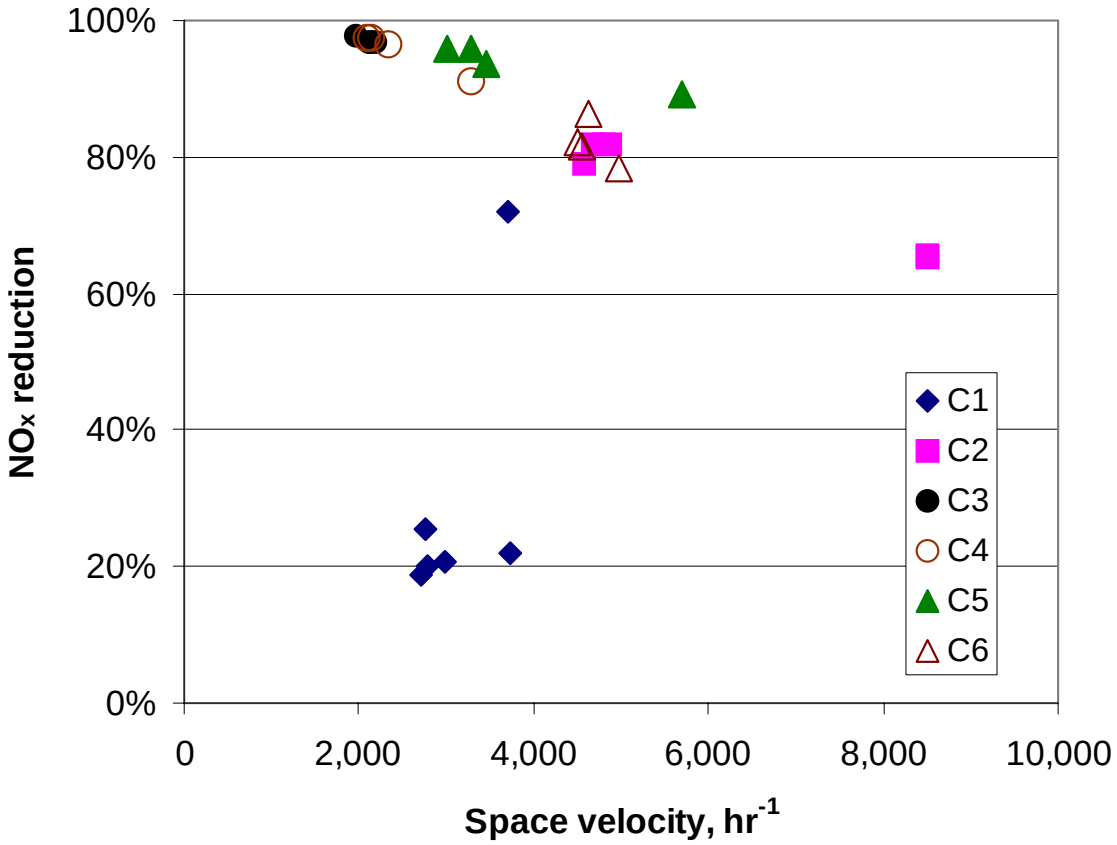


**Figure 5.100. $NO_x$ activity from 11/18/04 and 11/20/04 as a function of space velocity at a temperature of 550°F, $NH_3$/NO = 1.1.**

Figure 5.100 illustrates the $NO_x$ reduction as a function of space velocity. Catalysts C1, C2, C5 and C6 are honeycomb catalysts; catalysts C3 and C4 are plate catalysts. The temperature of the catalysts was low, circa 550 °F. The $NH_3$/NO ratio was about 1.1, which was high enough to ensure that the ammonia does not limit the reduction reaction. $NO_x$ reductions were high for all catalysts except the BYU catalyst (C1).

### *5.2.4 Summary of Slipstream Reactor Testing*

The site of the first slipstream reactor test, AEP's Rockport plant, consisted of two 1300 $MW_e$ B&W opposed wall-fired supercritical boilers. The SCR slipstream reactor was installed in the flue gas duct downstream of the economizer and upstream of the air preheater on Unit 1. A sampling probe was inserted through an existing port in the duct wall. The probe extended approximately three feet into the duct and had a 2-ft long slot, oriented 90° from the direction of flow in the duct. The reactor exhaust line was connected to the horizontal duct downstream of the air preheater. Anhydrous ammonia was injected into the flue gas stream near the entrance to the reactor, and blended with a static mixer. The coal blend was nominally 87% PRB subbituminous and 13% eastern bituminous. The heating value of the coal was commensurate with the blend, as was the coal chlorine content. The ash contained significant calcium (about 16 wt% as CaO) and

more iron than might be found in a typical Powder River Basin subbituminous coal. The sodium content of coal was about 1.5 wt% $Na_2O$. The LOI content of the ash samples was generally low. $NO_x$ data were obtained in late March and early April (approximately 750 hours of operating time on flue gas) and in late August (approximately 2200 hours of operating time on flue gas). Activity measured from field data showed a general decline in catalyst activity over the test period.

The site of the second slipstream reactor test, Alabama Power's Gadsden plant, consisted of two 70 $MW_e$ tangentially fired boilers. The SCR slipstream reactor was installed in the flue gas duct downstream of the economizer and upstream of the air preheater on Unit 1. The coal blend was approximately 95% Alabama bituminous coal and 5% sawdust (by weight). The $SO_2$ content of the flue gas was moderately high. The ash is low in sodium and very low in calcium. However, the potassium content (2.65 wt%) is significant. The composition of the ESP ash corresponds well with the fuel ash composition. Sodium appears to be depleted in the ESP ash. Due to difficulties with ash blockage in the slipstream reactor and outages at the plant, only 350 hours of flue gas data could be obtained with the slipstream reactor. At 350 hours, NO reduction was high (90-95%).

## *5.3 Effectiveness of Catalyst Regeneration*

Figure 5.101 illustrates typical conversion data for SCR catalyst systems. Our data suggest that the mechanisms leading to SCR inactivity are, in order of significance, channel plugging, surface fouling, pore plugging, and poisoning. In addition to these issues, surface sulfation increases activity. These data illustrate that the fresh catalyst activity initially increases (conversions increase) because of surface sulfation. In this particular sample, this increase is marginally significant, especially at the higher temperatures where conversion tends to be transport rather than kinetically limited.

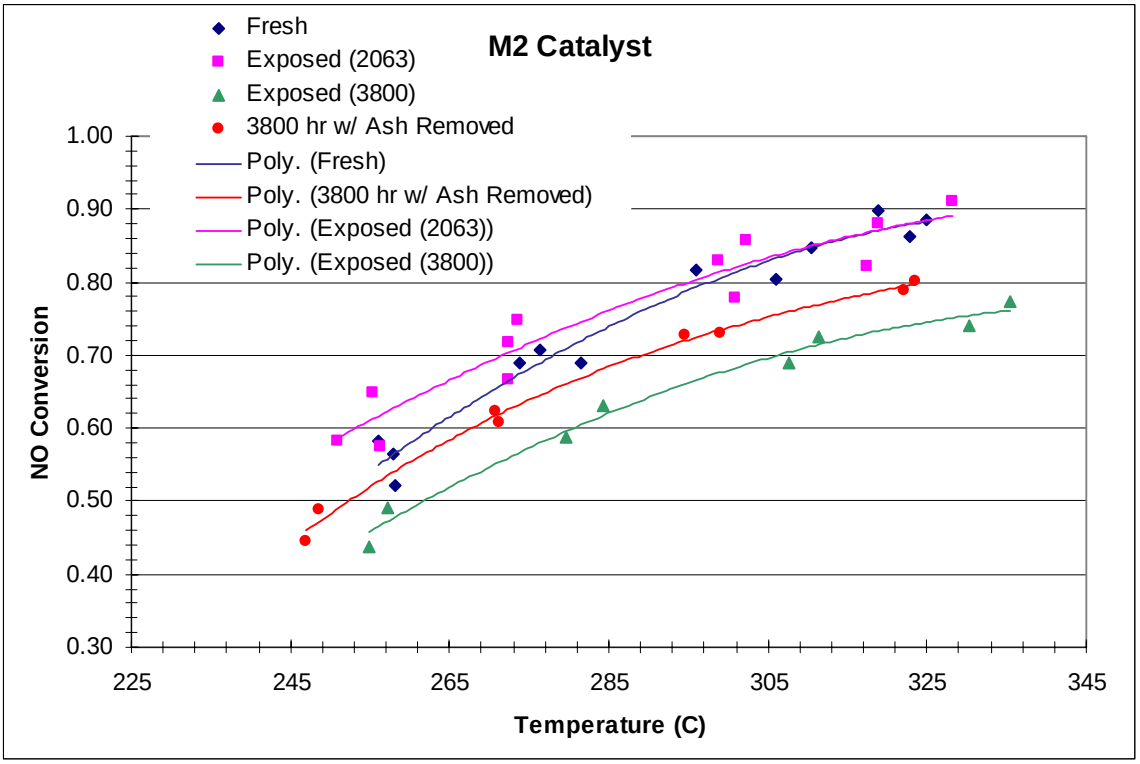


**Figure 5.101. NO conversion as a function of temperature and exposure time for catalyst C2 (M2), exposed to flue gas at Rockport.**

With increasing exposure, surface fouling and pore plugging become increasingly important. If the surface fouling layer is removed, the conversion/activity becomes intermediate between that of the fresh catalyst and that of the fully fouled material, in this case indicating surface fouling alone accounts for a about half of the activity change between 0 and 3800 hours. The other approximately half of the difference is associated with a combination of pore plugging and poisoning. The impacts of channel plugging are not apparent in these data but are apparent from the condition of the samples returned from the field in which several channels were nearly completely plugged which would reduce their apparent activity to near zero.

These data suggest activity can be effectively restored by physical cleaning of the catalyst, especially if physical cleaning includes both removal of the fouling layer as is indicated above and removal of pore plugging, the latter probably requiring a liquid treatment.

Most of the current efforts for catalyst regeneration are focused on taking out the exposed catalyst and regenerating it with certain procedures, for example, washing with water or with sulfuric acid solution, followed by sulfation. Section 5.2 demonstrated the importance of sulfation on catalyst activity. These regeneration techniques can recover about 80 % of the original activity; however, they require an outage to remove catalyst and to re-install it after regeneration. Modifications of the vanadia catalyst, for instance, in terms of the mechanical aspects (as opposed to the chemical aspects), to extend catalyst lifetime and at the same time to reduce the requirement for post-SCR regeneration could increase SCR catalyst performance.

## 5.4 Modeling SCR Catalyst Deactivation

### 5.4.1 $NO_x$ Conversion Model

The reduction of NO by ammonia across vanadia-titania catalysts can be expressed by the following overall reaction:

$$2NO + 2NH_3 + ½\ O_2 => 2N_2 + 3H_2O \quad (5\text{-}11)$$

Detailed mechanisms for reduction of NO across SCR catalysts have been developed (e.g., Dumesic et al., 1992; Dumesic et al., 1996). For power plant applications, a number of simplifying assumptions can be justified, leading to the use of first-order kinetics for NO reduction combined with diffusion in the porous catalyst walls (Buzanowski and Yang, 1990).

The mass balance of NO (here denoted as component *i*) in the axial direction *z* in a single catalyst channel can be written as

$$\frac{dy_{i,b}}{dz} + \frac{k_m P}{uA}\left(y_{i,b} - y_{i,s}\right) = 0 \quad (5\text{-}12)$$

where $u$ is the average gas velocity in the channel, $P$ is the perimeter of the channel, $k_m$ is the mass transfer coefficient in the channel and $A$ is the cross-sectional area of the channel. The mass transfer coefficient is used after Beeckman and Hegedus (1991) for developing laminar flow in rectangular ducts. For plate catalysts, the shape factor (asymptotic Sherwood number) is taken from Ramanathan et al. (2004).

Mass-transfer in the channel and within the porous walls must be taken into account. Previous work has shown that the NO reduction reaction is partially mass-transfer limited. For example, Dumesic et al. (1992) measured effectiveness factors for NO under industrial SCR conditions that ranged from 0.22 to 0.38. Beeckman (1991) measured effective diffusion coefficients for NO within the walls of commercial SCR catalysts.

The distribution of NO (component *i*) in the porous wall follows this equation, assuming first-order kinetics of NO reduction:

$$\frac{d^2 y_i^*}{dx^{*2}} = \Phi^2\ y_i^* \quad (5\text{-}13)$$

The dimensionless variables are

$$x^* = x/h \text{ and } y_i^* = y_i/y_{ib} \quad (5\text{-}14)$$

where $h$ is the half-width of the porous catalyst wall. The Thiele modulus is defined by the following

$$\Phi^2 = \frac{h^2 ka}{D_i^e} \quad (5\text{-}15)$$

$D_i^e$ is the effective diffusivity in the porous wall of component *i* and $a$ is the surface area per unit volume in the porous catalyst. $D_i^e$ for NO in SCR catalyst was taken as the value measured at 300 $^oC$ (Beeckman, 1991) and then assumed to be proportional to the bulk diffusivity of NO in order to scale the diffusivity to different temperatures.

Continuity at the surface of the catalyst provides one boundary condition:

$$x^* = 0, y_s^* = 1 + \frac{1}{Bi}\left(\frac{dy^*}{dx^*}\right)_{x^*=0} \tag{5-16}$$

where the Biot modulus is defined as $Bi = k_m h / D_i^e$. Symmetry at the center provides the other boundary condition:

$$x^* = 1, dy^*/dx^* = 0 \tag{5-17}$$

The solution to Eq. 5-13 yields the concentration distribution of NO and, because the NO reduction reaction is stoichiometric (Eq. 5-11), the concentration distribution of ammonia as well. Solving Eq. 5-13 also gives the concentration of NO at the wall surface, $y_{i,s}$, which can be used to solve Eq. 5-12 and obtain the following expression for the bulk concentration of NO as a function of length:

$$y_i(z) = y_{i,o} \exp\left[-\left(\frac{Pz}{uA}\right)\frac{1}{\frac{1}{k_m} - \frac{1}{\sqrt{D_i^e ka}}\left(\frac{e^{-2\Phi}+1}{e^{-2\Phi}-1}\right)}\right] \tag{5-18}$$

Several sets of data of $NO_x$ reduction for both plate and monolith catalysts were used to verify the applicability of the first-order model for SCRs in power plants.

Beeckman and Hegedus (1991) measured NO conversion in a laboratory experiment with simulated flue gas, using two commercial monolith catalysts, A and B. The catalyst had the same pitch and surface area, but catalyst A had twice as much vanadia as catalyst B. The authors measured the activation energies of the two catalysts, using powdered samples, as 19 kcal/mole and 14 kcal/mole, respectively.

$NO_x$ conversion in the monolith catalyst was measured as a function of temperature and space velocity for Catalyst A (Figure 5.102). $NO_x$ conversion was predicted using an activation energy of 19 kcal/mole and a single pre-exponential factor. The pre-exponential factor was selected to provide the most consistent fit to the data. The pre-exponential factor is proportional to the number of active sites in the catalyst and thus will vary with the vanadium content and with the poisoning of the catalyst as it ages. The model reproduced the data well at the two highest temperatures, but not at 281°C at a high space velocity (12,000 $hr^{-1}$). These conditions are outside the range of typical operating conditions for SCRs in coal-fired power plants. Figure 5.103 shows the $NO_x$ conversion as a function of temperature for catalysts A and B at $NH_3$/NO ratios of 1 and space velocities of 8,600 $hr^{-1}$ and 6,700 $hr^{-1}$, respectively. The model reproduced the measured conversions well.

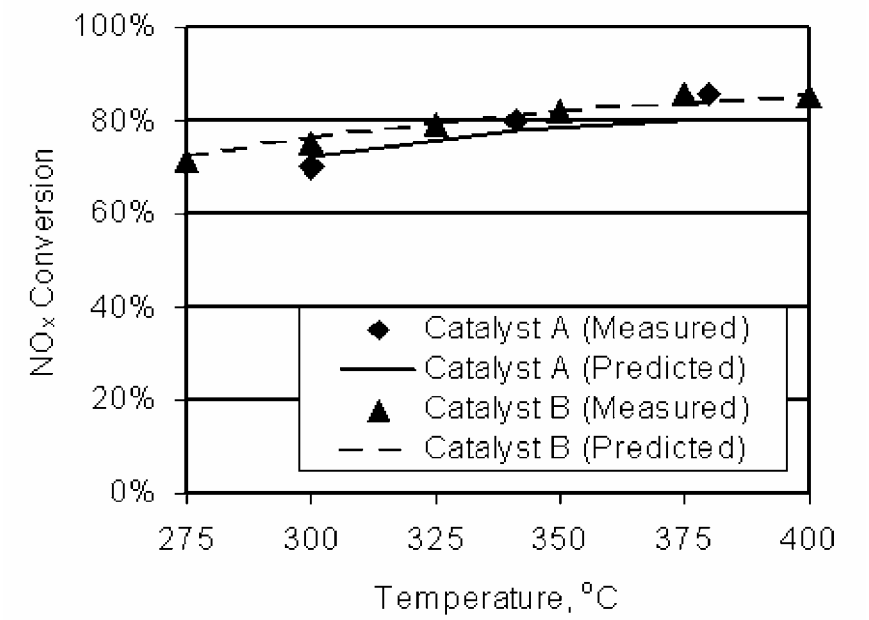


**Figure 5.102. Measured and predicted $NO_x$ conversion as a function of $NH_3$/NO ratio, temperature and space velocity for catalyst A. Data from Beeckman and Hegedus, 1991.**

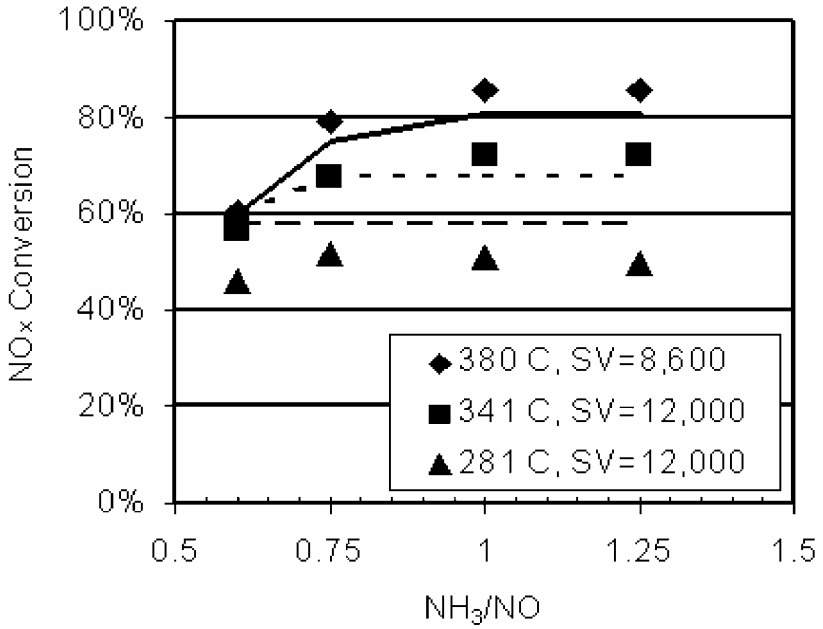


**Figure 5.103. Measured and predicted $NO_x$ conversion as a function of temperature at $NH_3/NO=1$. Space velocity of catalyst A is 8,600 $hr^{-1}$ and catalyst B, 6,700 $hr^{-1}$. Data from Beeckman and Hegedus, 1991.**

Data were taken on a slipstream reactor using a number of commercial SCR catalysts in parallel at a plant burning a blend of subbituminous and eastern bituminous coals as described above in Section 5.2. $NO_x$ reduction was measured across individual catalysts. Table 5.40 gives the parameters used in the model for these catalysts. Figure 5.104 shows a comparison of the measured and predicted $NO_x$ reductions from one measurement campaign in which the catalysts were new (about 300 hours of exposure to flue gas). An activation energy of 14 kcal/mole was used for all catalysts, with the pre-exponential factor adjusted for each catalyst. Several sets of data of $NO_x$ reduction for both plate and monolith catalysts were used to verify the applicability of the first-order model for SCRs in power plants.

**Table 5. 40. Parameters in NO conversion model for commercial catalysts.**

| | | C2 (M2) | C6 (M1) | C3 (P1) | C4 (P2) |
|---|---|---|---|---|---|
| Catalyst type | | monolith | monolith | plate | monolith |
| Catalyst pitch | (mm) | 8.2 | 7.4 | 5.7 | 8.2 |
| Wall thickness | (mm) | 1.3 | 1.3 | 0.9 | 1.3 |
| Length | (m) | 0.55 | 0.50 | 1.00 | 0.55 |
| Surface area | ($m^2/g$) | 60.0 | 64.5 | 60.0 | 60.0 |
| Space velocity | ($hr^{-1}$) | 5,050 | 2,200-3,900 | 1,930-2,440 | 2,400-4,000 |
| Temperature | ($^oC$) | 300-350 | 314-336 | 300-340 | 313-345 |
| Inlet NO | (ppm) | 310 | 310 | 310 | 310 |
| Pre-exponential factor | (cm/s) | 3.6E+04 | 7.0E+04 | 2.2E+01 | 8.5E+00 |
| Activation energy | (kJ/mol) | 58.6 | 58.6 | 58.6 | 58.6 |

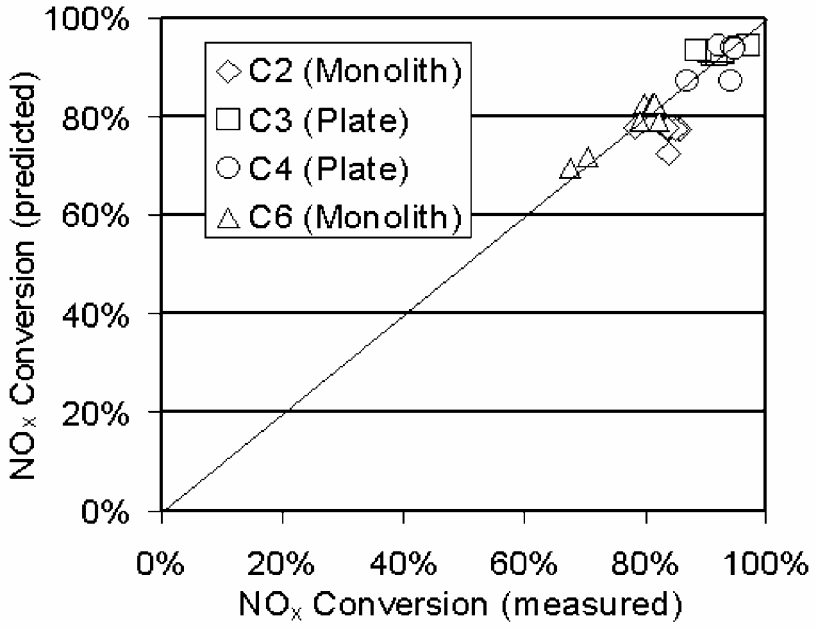


**Figure 5.104. Measured versus predicted NOx conversion across four different catalysts in slipstream reactor.**

### 5.4.2 Deactivation Model

#### 5.4.2.1 Diffusion through Ash

Diffusion coefficients, $D_{ash}$ ($m^2$/sec), through ash can be estimated by the correlation of Hampartsoumian et al. (1989).

$$D_{ash} = D_{AB} \cdot \theta_{ash}^{2.5} \qquad (5\text{-}19)$$

$\theta_{ash}$ is the porosity of the deposited ash and will be a user input with a default value of 0.17.

#### 5.4.2.2 Thickness of Ash Layer

The literature data are not available to develop a full correlation for ash layer thickness as a function of time in service and the channel length. For now, we will assume exponential decay of the layer thickness with increasing distance from the inlet of the channel under a given channel length (r) and a given thickness of layer at the inlet ($d_i$), as illustrated in Figure 5.105. The layer thickness at the inlet ($d_i$) is an input. And we will assume that the thickness of the deposited layer is zero at the outlet of the reactor channel.

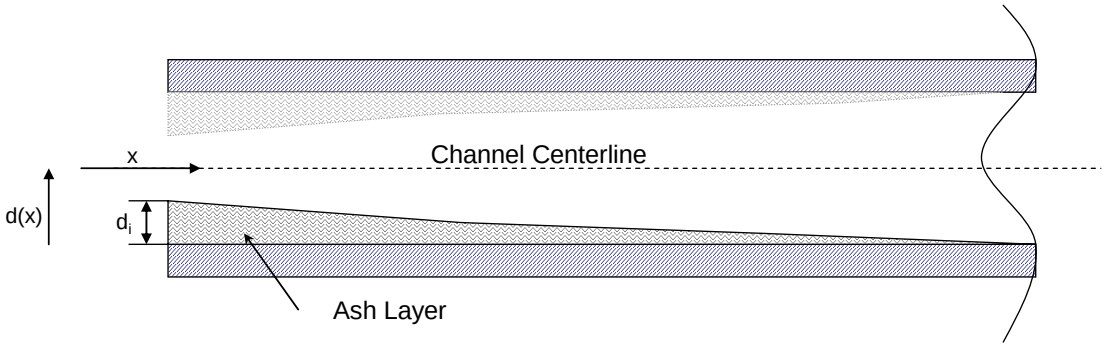


**Figure 5.105. Sketch of the build-up of ash layer on catalyst channel.**

Then, the correlation would be:

$$d(x) = \frac{\exp(-x/d_h) - \exp(-r/d_h)}{1 - \exp(-r/d_h)} \cdot d_i \qquad (5\text{-}20)$$

where d(x) is the thickness of the layer (from one side only), r the whole length of the channel, $d_h$ is the clean hydraulic diameter of the channel and $d_i$ the initial deposit layer thickness at the inlet. Ash deposition is assumed to occur in the same way at the other side.

We can use the following correlation based on time in service (in hr) assuming a logarithmic increase of the layer thickness:

$$d_i(t) = \ln\left(\frac{e^{p/4} - 1}{t_c} \cdot t + 1\right) \qquad (5\text{-}21)$$

where p is the width of the channel (m), t the time in service (hr), and $t_c$ is the service time that needs to accumulate a thickness of p/4. t, p, and $t_c$ are user inputs.

Then, the overall expression for d(x) would be:

$$d(x,t) = \frac{\exp(-x/d_h) - \exp(-r/d_h)}{1 - \exp(-r/d_h)} \cdot \ln\left(\frac{e^{p/4} - 1}{t_c} \cdot t + 1\right) \qquad (5\text{-}22)$$

The deactivation model was run with a space velocity of 8600 $hr^{-1}$ a temperature of 341°C and a $NH_3$/NO ratio of 1. It was assumed that an ash thickness of 1 mm at the leading edge of the catalyst formed over 2000 hrs of service. Figure 5.106 shows the $NO_x$ conversion as a function of time in service. The $NO_x$ conversion falls from a value of 80% to 73.4% at 4000 hrs.

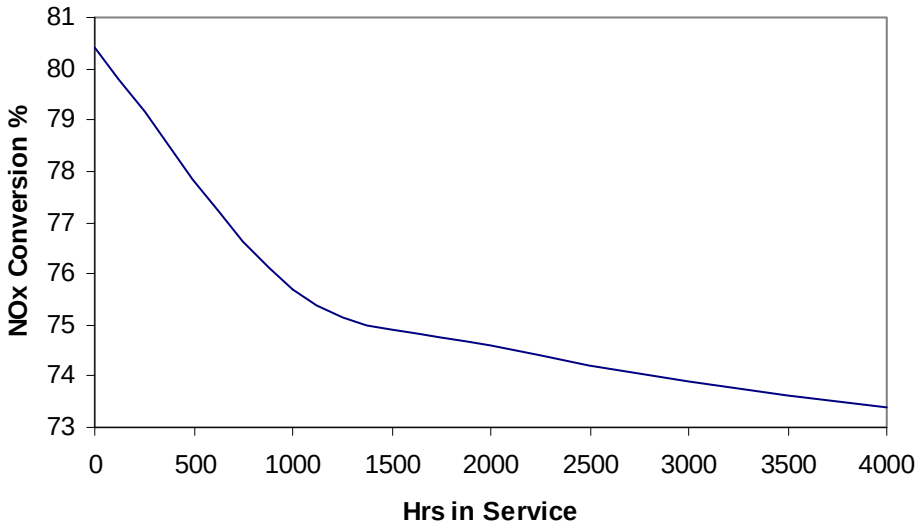


**Figure 5.106. Calculated $NO_x$ conversion as a function of hours in service with a space velocity of 8600 $hr^{-1}$ a temperature of 341 °C and a $NH_3$/NO ratio of 1.**

## *5.5 Summary*

Vanadia supported on titania material represents the predominant commercial SCR catalyst applied to reduce $NO_x$ with $NH_3$ from boilers burning coal-biomass and coals. Although of the SCR high efficiency, the relative fast deactivation of vanadia catalyst appears as the major problem encountered during the industrial applications, contributing to the cost increase and applying difficulties. Therefore, a series activity test and surface chemistry investigations have been designed and conducted on both commercial supplied fresh and exposed samples, and lab prepared samples, to investigate the reaction and deactivation mechanism of vanadia catalyst for coal-biomass and coal-firing boilers. The current results indicate that:

1. Fouling instead of poisoning is the major deactivation mechanism for vanadia catalyst applied for coal fired boilers
2. Sulfation of vanadia catalyst happens on titiania sites but not on vanadia sites
3. Sulfation enhances vanadia catalyst NO reduction activity by providing more active sites without changing the reaction activation energy
4. Tungsten greatly expedient vanadia catalyst NO reduction activity by about 250%. This large increase originates from the largely increased amount of active sites
5. Alkali metals potassium (K and Na) and alkaline earth metals (Ca) are poisons of the vanadia catalyst. The deactivation happens when poisons interact with active sites and decrease both the number and acidity of the active sites
6. Results of investigation the effects of sulfation, tungsten, and poisons suggests that from acid sites point of view, Brønsted acid sites are the active sites on vanadia catalyst; from structure point of view, the results of NO adsorption comparison on various amount of vanadia and sulfate samples suggest that the active sites locate at the edge between titania and vanadia sites

The above conclusions should help to elucidate the reaction and deactivation mechanism of vanadia catalyst during SCR application, furthermore, those results should help to generate better management of vanadia catalyst during the application, and create regeneration method of deactivation vanadia catalyst.

The deactivation of commercial SCR catalysts exposed to a flue gas was measured in two ways: (1) by direct measurement of the $NO_x$ composition of the flue gas before and after it flows through a catalyst in the slipstream reactor in the presence of ammonia; and (2) by laboratory evaluation of the catalysts after periodical removal from the slipstream reactor.

The average catalyst activity from $NO_x$ measurements taken at 750 hours of operation on flue gas was compared with average catalyst activity from $NO_x$ measurements taken at 3,800 hours of operation on flue gas. Activity measured from field data showed a general decline in catalyst activity over the test period.

Our data suggest that the mechanisms leading to SCR inactivity are, in order of significance, channel plugging, surface fouling, pore plugging, and poisoning. In addition to these issues, surface sulfation increases activity. These data illustrate that the fresh

catalyst activity initially increases (conversions increase) because of surface sulfation. In this particular sample, this increase is marginally significant, especially at the higher temperatures where conversion tends to be transport rather than kinetically limited.

With increasing exposure, surface fouling and pore plugging become increasingly important. If the surface fouling layer is removed, the conversion/activity becomes intermediate between that of the fresh catalyst and that of the fully fouled material, in this case indicating surface fouling alone accounts for a about half of the activity change between 0 and 3800 hours. The other approximately half of the difference is associated with a combination of pore plugging and poisoning.

Activity can be effectively restored by physical cleaning of the catalyst, especially if physical cleaning includes both removal of the fouling layer and removal of pore plugging, the latter probably requiring a liquid treatment. Most of the current efforts for catalyst regeneration are focused on taking out the exposed catalyst and regenerating it with certain procedures, for example, washing with water or with sulfuric acid solution, followed by sulfation. These regeneration techniques can recover about 80 % of the original activity; however, they require an outage to remove catalyst and to re-install it after regeneration. Modifications of the vanadia catalyst, for instance, in terms of the mechanical aspects (as opposed to the chemical aspects), to extend catalyst lifetime and at the same time to reduce the requirement for post-SCR regeneration could increase SCR catalyst performance.

A first-order kinetic model was developed to predict NO reduction across commercial catalysts. The model took into account surface catalysis as well as diffusion along the length of the channels, through the porous catalyst and through a porous deposit of ash on the catalyst surface.

## *5.6 References*

Amiridis, M. D., I. E. Wachs, G. Deo, J. M. Jehng and D. S. Kim "Reactivity of $V_2O_5$ catalysts for the selective catalytic reduction of NO by $NH_3$: Influence of vanadia loading, $H_2O$, and $SO_2$." *Journal of Catalysis* **1996**, *161(1)*, 247-253.

Beeckman, J.W. "Measurement of the Effective Diffusion Coefficient of Nitrogen Monoxide through Porous Monolith-Type Ceramic Catalysts." *Ind. Eng. Chem. Res.* **1991**, *30*, 428-430.

Beeckman, J.W., Hegedus, L.L. "Design of Monolith Catalysts for Power Plant $NO_x$ Emission Control." *Ind. Eng. Chem. Res.* **1991**, *29*, 969-978.

Busca, G., L. Lietti, G. Ramis and F. Berti "Chemical and mechanistic aspects of the selelctive catalytic reduction of $NO_x$ by ammonia over oxide catalysts: A Review." *Appl. Catal B: Environmental* **1998**, *1-2*, 1-36.

Buzanowski, M.A., Yang, R.T. "Simple Design of Monolith Reactor for Selective Catalytic Reduction of NO for Power Plant Emission Control." *Ind. Eng. Chem. Res.* **1990**, *29*, 2074-2078.

Centeno, M.A., Carrizosa, I., and Odriozola, J.A. "NO-$NH_3$ coadsorption on vanadia/titania catalysts: determination of the reduction degree of vanadium." *Appl. Catal. B-Environ*. **2001**, *4*, 307.

Chen, J.P. and Yang, R.T. Mechanism of Poisoning of the $V_2O_5/TiO_2$ Catalyst for the Reduction of NO by $NH_3$." *Journal of Catalysis* **1990**, *2*, 411.

Chen, J.P. and Yang, R.T. "Selective catalytic reduction of NO with $NH_3$ on $SO_4^{-2}/TiO_2$ superacid catalyst." *Journal of Catalysis* **1993**, 277.

Chen, Buzanowski, Yang, and Cichanowicz. (1990). "Deactivation of the Vanadia Catalyst in the Selective Catalystic Reduction Process." *Journal of the Air & Waste Management Association* **1990**, *40(10)*, 1403-1409.

Choo, S. T., Y. G. Lee, I. S. Nam, S. W. Ham and J. B. Lee. "Characteristics of $V_2O_5$ supported on sulfated $TiO_2$ for selective catalytic reduction of NO by $NH_3$." *Applied Catalysis A-General* **2000**, *200(1-2)*, 177-188.

Coates, J. "Interpretation of infrared spectra, a practical approach." In *Encyclopedia of Analytical Chemistry*, 2000, .p. 10815.

DOE, *Selective Catalytic Reduction (SCR) Technology for the Control of Nitrogen Oxide Emissions from Coal-Fired Boilers*. Clean Coal Technology, Topical report number 23, (2005).

Dumesic, J.A., Topsøe, N.-Y., Slabiak, T., Morsing, P., Clausen, B.S., Törnqvist, E., Topsøe. H. "Microkinetic Analysis of the Selective Catalytic Reduction (SCR) of Nitric Oxide over Vanadia/Titania-Based Catalysts." *New Frontiers in Catalysis* (Gucsi, L. et al., eds.), Elsevier Science Publishers, 1992.

Dumesic, J.A., Topsøe, N.-Y., Topsøe. H., Chen, Y., Slabiak, T. "Kinetics of Selective Catalytic Reduction of Nitric Oxide by Ammonia over Vanadia/Titania." *J. Catalysis* **1996**, *163*, 409-417.

Dunn, J. P., P. R. Koppula, H. G. Stenger and I. E. Wachs. “Oxidation of sulfur dioxide to sulfur trioxide over supported vanadia catalysts.” *Applied Catalysis B-Environmental* **1998a**, 103-117.

Dunn, J. P., J. M. Jehng, D. S. Kim, L. E. Briand, H. G. Stenger and I. E. Wachs. "Interactions between surface vanadate and surface sulfate species on metal oxide catalysts." *Journal of Physical Chemistry B* **1998b**, *102(32)*, 6212-6218.

EPA, *Clean Air Markets-Progress and Results*, 2000, http://www.epa.gov/airmarkets/progress/index.html.

Farrauto, R. J. and C. H. Bartholomew. *Fundamentals of Industrial Catalytic Processes*. London, Blackie Academic & Professional, 1997.

Forzatti, P. and L. Lietti. "Recent advances in De-NO(x)ing catalysis for stationary applications." *Heterogeneous Chemistry Reviews* **1996**, *3*, 33-51.

Forzatti, P. "Present status and perspective in de-NOx SCR analysis." *Appl. Catal A: General* **2001**, *222*, 221-236.

Franklin, H.N. “The effect of fuel properties and characteristics on selective catalytic reduction systems.” ASME International Joint Power Generation Conference, 1996.

Hadjiivanov, K. “Indentification of neutral and charged $N_xO_y$ surface species by IR spectroscopy.” *Catal. Rev.* **2000**, *1-2*, 71.

Hampartsoumian, J.E., Pourkashanian, M., Williams, A, *Journal of the Institute of*

*Energy* **1989**, March, 48.

Khodayari, R. and Odenbrand, C.U.I. “Deactivating effects of lead on the selective catalytic reduction of nitric oxide with ammonia over a $V_2O_5/WO_3/TiO_2$ catalyst for waste incineration applications.” *Industrial & Engineering Chemistry Research* **1998**, *4*, 1196.

Khodayari, R. and C. U. I. Odenbrand (2001). Regeneration of commercial SCR catalysts by washing and sulphation: Effect of sulphate groups on the activity. *Applied Catalysis B: Environmental* **2001**, *33*, 277-291.

Lani, B.W., et al. “A review of DOE/NETL's Advanced NOx control Technology R&D Program for Coal-Fired Power Plants.” DOE/NETL NOx R&D Program Review, 2005.

Lietti, L. and Forzatti, P. “Temperature-Programmed Desorption - Reaction of Ammonia over $V_2O_5/TiO_2$ De-NO(x)Ing Catalysts.” *Journal of Catalysis* **1994**, *1*, 241.

Lietti, L., G. Ramis, F. Berti, G. Toledo, D. Robba, G. Busca and P. Forzatti. "Chemical ; structural and mechanistic aspects on $NO_x$ SCR over commercial and model oxide catalysts." *Catalysis Today* **1998**, *42*, 101-116.

Lin, W.Y. and Biswas, P. “Metallic Particle Formation and Growth Dynamics During Incineration.” *Combustion Science and Technology* **1994**, *1-6*, 29.

Lisi, L., G. Lasorella, S. Malloggi and G. Russo. "Single and combined deactivating effect of alkali metals and HCl on commercial SCR catalysts." *Applied Catalysis B-Environmental* **2004**, *50(4)*, 251-258.

Odenbrand, I., Khodayari, R., Andersson, C., "SCR Catalysts in Biofuelled Power Stations," http://www.chemeng.lth.se/Ingemar.Odenbrand/scrpage2.shtml, December 15, 2000.

Orsenigo, C., L. Lietti, E. Tronconi, P. Forzatti and F. Bregani. "Dynamic investigation of the role of the surface sulfates in $NO_x$ reduction and $SO_2$ oxidation over $V_2O_5$-$WO_3/TiO_2$ catalysts." *Industrial & Engineering Chemistry Research* **1998**, *37*, 2350-2359.

Ozkan, U.S., Kumthekar, M.W., and Cai, Y.P.P. "Selective Catalytic Reduction of Nitric-Oxide over Vanadia/Titania Catalysts - Temperature-Programmed Desorption and Isotopically Labeled Oxygen-Exchange Studies." *Industrial & Engineering Chemistry Research* **1994**, *12*, 2924.

Ozkan, U.S., Cai, Y., and Kumthekar, M.W., Mechanistic studies of selective catalytic reduction of nitric oxide with ammonia over $V_2O_5/TiO_2$ (anatase) catalysts through transient isotopic labeling at steady state." *Journal of Physical Chemistry* **1995**, 2363.

Pritchard, S., DeFranesco, C., Kaneko, S., Kobayashi, N., Suyama, K. "Opitmizing SCR catalyst design and performance for coal-fired boilers." Presented at EPA/EPRI 1995 Joint Symposium on $NO_x$ Control, May 16-19, 1995.

Ramanathan, K. Balakotaiah, V., West, D.H. "Bifurcation Analysis of Catalytic Monoliths with Nonuniform Catalyst Loading." *Ind. Eng. Chem. Res.* **2004**, *43*, 288-303.

Ramis, G. and Busca, G. "Fourier Transform Infrared Study of the Adsorption and Coadsorption of Nitric oxide, Nitrogen Dioxide and Ammonia on $TiO_2$ anatase." *Appl. Catal.* **1990**, 243.

Ramis, G. and G. Busca. "Fourier Transform Infrared Study of the Adsorption and Coadsorption of Nitric oxide, Nitrogen Dioxide and Ammonia on TiO2 anatase." *Applied Catalysis* **1990**, *64*, 243-257.

Reddy, B.M., Ganesh, I., and Chowdhury, B. "Design of stable and reactive vanadium oxide catalyst supported on binary oxides." *Catal. Today* **1999**, 115.

O. Saur, M.B., A.B. Mohammed Saad, J.C. Lavalley, C. P. Tripp, B.A. Morrow. "The Structure and Stability of Sulfated Alumina and Titania." *Journal of Catalysis* **1986**, 104.

Siemens AG. "Powder River Basin (PRB) Coal and High Arsenic Concentrations: Catalyst Specific Issues and Operating Experience," presented at the Workshop on Selective Catalytic Reduction, April 18-21, 2000.

Srnak, T. Z., J. A. Dumesic, B. S. Clausen, E. Tornqvist and N. Y. Topsøe. "Temperature-Programmed Desorption Reaction and Insitu Spectroscopic Studies of Vanadia Titania for Catalytic Reduction of Nitric-Oxide." *Journal of Catalysis* **1992**, *135*, 246-262.

Stuart, B.J. and Kosson, D.S. "Characterization of Municipal Waste Combustion Air-Pollution Control Residues as a Function of Particle-Size." *Combustion Science and Technology* **1994**, *1-6*, 527.

Tokarz, M.J., S.; Persson, B. Eka Nobel AB, Surte, Swed. "Poisoning of de-NOx SCR catalyst by flue gases from a waste incineration plant." *Studies in Surface Science and Catalysis, Catal. Deact.* **1991**, 523.

Topsøe, N.Y. and T.Z. Srnak, J.A.D., B.S. Clausen, E. Tornqvist. "Temperature-Programmed Desorption/Reaction and in Situ Spectruscopic Studies of Vanadia/Titania for Catalytic Reduction of Nitric Oxide." *J. Catal.* **1992**, 246.

Topsøe, N.Y., Topsøe, H., and Dumesic, J.A. "Vanadia-Titania Catalysts for Selective Catalytic Reduction (SCR) of Nitric-Oxide by Ammonia .1. Combined Temperature-Programmed in-situ FTIR and Online Mass-Spectroscopy Studies." *Journal of Catalysis* **1995**, *1*, 226.

Topsøe, N.Y., Dumesic, J.A., and Topsøe, H. "Vanadia-Titania Catalysts for Selective Catalytic Reduction of Nitric-Oxide by Ammonia .2. Studies of Active-Sites and Formulation of Catalytic Cycles." *Journal of Catalysis* **1995**, 1, 241.

Topsøe, N.Y. "Characterization of the Nature of Surface Sites on Vanadia Titania Catalysts by FTIR." *Journal of Catalysis* **1991**, *2*, 499.

Wachs, I.E. and Weckhuysen, B.M. "Structure and reactivity of surface vanadium oxide species on oxide supports*." Appl. Catal. A-General* **1997**, *1-2*, 67.

Wachs, I. E., G. Deo, B. M. Weckhuysen, A. Andreini, M. A. Vuurman, M. deBoer and M. D. Amiridis (1996). "Selective catalytic reduction of NO with NH3 over supported vanadia catalysts." *Journal of Catalysis* **1996**, *161(1*), 211-221.

Wieck-Hansen, K., Overgaard, P., and Larsen, O.H., "Cofiring coal and straw in a 150 $MW_e$ power boiler experiences," Biomass and Bioenergy, **2000**, 19, 395-409.

Went, G. T., L. J. Leu, S. J. Lombardo and A. T. Bell. "Raman-Spectroscopy and Thermal-Desorption of $NH_3$ Adsorbed on $TiO_2$ (Anatase)-Supported $V_2O_5$." *J Phys Chem.* **1992a**, *96(5)*, 2235-2241.

Went, G. T., L. J. Leu, R. R. Rosin and A. T. Bell. "The Effects of Structure on the Catalytic Activity and Selectivity of $V_2O_5/TiO_2$ for the Reduction of NO by $NH_3$." *J Catal.* **1992b**, *134(2)*, 492-505.

Yang, R.T., Li, W.B., and Chen, N. "Reversible chemisorption of nitric oxide in the presence of oxygen on titania and titania modified with surface sulfate." *Appl. Catal. A-General* **1998**, *2*, 215.

Zheng, Y.J., Jensen, A.D., and Johnsson, J.E. "Laboratory investigation of selective catalytic reduction catalysts: Deactivation by potassium compounds and catalyst regeneration." *Industrial & Engineering Chemistry Research* **2004**, *4*, 941.

# 6. Ammonia Adsorption on Fly Ash

This chapter describes the results of an experimental project at Brown University on the fundamentals of ammonia / fly ash interactions with relevance to the operation of advanced $NO_x$ control technologies such as selective catalytic reduction. The project focused on the measurement of ammonia adsorption isotherms on commercial fly ash samples subjected to a variety of treatments and on the chemistry of dry and semi-dry ammonia removal processes. This project was carried out at Brown University under subcontract to Reaction Engineering International. The following report contains a detailed description of the samples, experimental procedures, and results. The results in this chapter are divided into two parts corresponding to the two tasks in the Brown project. The chapter is organized as follows:

- Introduction
- Fundamentals of Ammonia Adsorption on Fly Ash
- Ammonia Removal by Dry and Semi-Dry Processes
- Summary
- References cited in this chapter
-

## *6.1 Introduction*

Ammonia vapor comes into contact with fly ash during pulverized solid fuel combustion if the unit is configured for $NO_x$ control by selective catalytic reduction (SCR) or selective non-catalytic reduction (SNCR), or if it employs ammonia addition for electrostatic precipitator conditioning (Castle, 1980, Golden, 2001). Typically some portion of the vapor phase ammonia adsorbs or deposits on fly ash, where it has the potential to cause problems in ash utilization, handling, and disposal (Larrimore,2000). Of particular concern for disposal is the possibility for high ammonia contents in surface and groundwater near ash ponds (Golden, 2001) and at landfill sites in runoff, leachate and surrounding atmosphere (Golden, 2001, Lowe et al., 1989). Problems with ash utilization in concrete arise not from degradation of concrete properties (Golden, 2001, Novak and Rych, 1989), but rather from worker exposure to odor, especially during enclosed pours. Current OSHA standards specify the threshold limit value for 8-hr exposure to ammonia vapor as 50 ppm. Ammonia odors are commonly perceived as a sufficiently serious nuisance when the ammonia content of ash reaches 300 ppm — these or higher levels can effectively destroy the ash utilization market. Acceptable ammonia levels to fully avoid problems in utilization and disposal have been cited by different sources as less than 50, 60, or 100 ppm (Novak and Rych, 1989, Necker, 1989).

There are few publications in the archival scientific literature on ash / ammonia interactions, exceptions being the work of Janssen et al. (Janssen et al., 1986), which focused on catalysis of the $NO/NH_3$ reaction and most notably the work of Turner et al. (Turner et al., 1994), which focused on the mechanism of *adsorption* and its potential impact on the operation of flue gas treatment technologies. Recently, however, there has been a flurry of applied studies reported in the conference literature, patent literature, and in industry reports, motivated by current projections of widespread SCR unit installation in the U.S. in the coming years (Golden, 2001, Larrimore, 2000, Muzio et al., 1995, Hinton, 1999, Brendel et al., 2001, Levy et al., 2001, Rubel

et al., 2001, Ramme and Fisher, 2001, Bittner et al., 2001). These sources discuss many aspects of the ammonia / ash problem and present a number of new ideas for remediation processes. The factors governing the extent of ammonia contamination are not fully understood, but are believed to depend on the concentration of unreacted ammonia leaving the SCR unit (the "ammonia slip"), duct temperatures/time history, ash composition (Muzio et al., 1995), and $SO_3$ concentration in the flue gas (Larrimore, 2000, Turner, 1994, Muzio et al., 1995). Ammonia associated with fly ash can be in the form of ammonium sulfate or more commonly bisulfate particles (Golden, 2001, Rubel et al., 2001), or ammonia species adsorbed on carbon sites (Rubel et al., 2001), likely on carbon surface oxides, or mineral surfaces (Turner, 1994). Ammonia is well known to chemisorb on acidic surface sites (Sahu et al., 1998), and indeed is extensively used as a titrant to characterize the acidity of surfaces (Gedeon et al., 2001).

There is almost no information in the archival scientific literature on methods of ammonia *removal* from fly ash, despite great commercial interest in a variety of competing techniques (Golden, 2001, Larrimore, 2000), including thermal methods (Levy et al.,2001), combustion-based methods (Giampa, 2001), and water-based methods (Gasioroski and Hrach, 2000, Katsuya et al., 1996, Hwang, 1999).

The objectives of the present study are: (1) to measure complete isotherms of ammonia on carbon and fly ash surfaces for a more fundamental understanding of the adsorption process, and (2) to investigate the chemistry of room temperature methods for ammonia removal from fly ash using moisture and oxidizing agents, alone or in combination. These two objectives form the basis for the two tasks described below:

Task 5.1 Fundamentals of Ammonia Adsorption on Fly Ash

Task 5.2 Ammonia Removal by Dry and Semi-Dry Processes

In Task 5.2 on ammonia removal, special emphasis was placed on controlled addition of small amounts of moisture to avoid wet ash handling, so-called "semi-dry processing", which is the basis for several industrial patents (Gasioroski and Hrach, 2000, Katsuya et al., 1996), and on the use of ozone, which has recently been found to passivate unburned carbon surfaces in fly ash and thus improve air entrainment properties of problem ash streams (Gao et al., 2001).

## *6.2 Fundamentals of Ammonia Adsorption on Fly Ash*

### *6.2.1 Experimental Methods*

This task deals with fundamental adsorption isotherms for ammonia on carbon-containing fly ash samples. First the surface area and porosity of fly ash samples were thoroughly characterized using standard volumetric gas adsorption experiments. These experiments were performed using an Autosorb-1 system from Quantachrome Corp. The fly ash sample was placed into the appropriately sized sample holder and, prior to the analysis, was outgassed for several hours at constant temperature (573 K) in vacuum.

In the adsorption experiments involving $N_2$, the customary temperature of 77 K was maintained using a liquid nitrogen bath. In the adsorption experiments involving $CO_2$ and $NH_3$, a bath temperature of 273 K was maintained using ice and water. At a temperature of 273 K, the generally accepted (Bridgeman, 1927) saturation pressure for liquid $CO_2$ is 26144.1 torr (= 3484.8 kPa). There remains some controversy in the literature regarding the phase of the sorbed $CO_2$, especially as regards the density of the sorbed layer. This reflects itself in an enormous range of values being reported for its sorption cross-section (Garrido et al., 1987). Meanwhile, the very high value of saturation pressure, taken together with the operating limits of the available device (760 torr maximum pressure) suggests that $CO_2$ will only be useful for exploring microporosity. The experiments were, however, conducted below the critical temperature for $CO_2$, which is 304.14 K.

The saturation pressure for ammonia at 273.15 K is 429.62 kPa (=3223 torr) (Haar and Gallagher, 1978). Again, the critical temperature for ammonia is 405.5 K, so these experiments were conducted well below the critical point for this gas. The Brunauer, Emmet and Teller (BET) theory (Gregg and Sing, 1982) was used for calculating surface areas and Dubinin-Radushkevich (DR) theory (Gregg and Sing, 1982) has been used for determining the microporosity of the fly ash samples. It should be recalled that the earlier reported work established that the main source of micropores in fly ashes is unburned carbon.

As is standard in the literature, the convention used here involves calling any pores smaller than 20Å in width “micropores”, any pores between 20 and 500 Å “mesopores” and pores larger than 500 Å “macropores”. The term “supermicropores” has recently come into use to describe the micropores between about 8 and 20Å. This terminology has been adopted by some workers in recognition of what is thought to be an upper limit of micropores that can be filled in a “standard” micropore filling process, in which the enhancement of gas-solid interactions plays a significant role. The 8 Å size roughly reflects twice the molecular diameter of typically employed molecular probes such as nitrogen and carbon dioxide. It may also be crudely estimated that the “primary” micropore filling process takes place at relative pressures between $10^{-5}$ and $10^{-2}$ and secondary micropore filling in the supermicropores takes place between $10^{-2}$ and 0.3. In this range of pore filling, some adsorbate-adsorbate interactions are also likely to play a role (Sing, 1995). This means that mesopore filling is also possible.

### *6.2.2 Results and Discussion*

The comparative study of the adsorption behavior of different gases on fly ash was carried out using a representative fly ash sample. Fly ash sample 21 was selected from our sample bank for this purpose. This sample is typical of a class F type of ash, and has an LOI of 6.1%. The sample is typical of ashes produced by pulverized combustion of bituminous coals at the Brayton Point Power Station in Fall River, Massachusetts. This fly ash sample had been previously analyzed using the earlier reported flow microcalorimetric technique, and it was determined that the sample has a very small fraction (9%) of its surface in the form of polar functional groups. Its foam index behavior is consistent with this value, as this sample shows itself to be very active towards AEA adsorption.

This section begins with a thorough characterization of this ash sample using standard adsorbates (nitrogen, carbon dioxide) and methods, and then proceeds to the special case of ammonia adsorption. The nitrogen adsorption isotherm for this sample is shown in Figure 5.1. The isotherm is shown in a typical form. The ordinate is given as STP cc of gas adsorbed per gram of solid and the abscissa as relative pressure $P/P_0$, where $P_0$ is the saturation vapor pressure of the adsorptive at the temperature of the experiment (in this case, 760 torr for liquid nitrogen). This type of isotherm is characteristic of microporous samples. The fact that the isotherm is seen to rise very steeply at very low relative pressure is indicative of sample microporosity. A very good linear BET plot is obtained, and a nominal surface area for the whole fly ash is 3.7 $m^2/g$. Earlier we reported on similarly obtained nitrogen isotherms on this ash. From the earlier data obtained after complete carbon removal by combustion, it was possible to back-calculate the surface area contribution from the carbon alone. The value that was obtained, 49 $m^2/g$-carbon, is very typical of the values seen for a great number of carbons from class F ashes.

The DR plot for the isotherm results of Figure 6.1 is shown in Figure 6.2. This plot is seen to be very linear in the micropore region, and it appears that a good estimate of micropore volume is therefore available. It will, however, be seen below that this estimate represents only an upper bound on the microporosity. There is evidence of a well-known problem[33] associated with inability to distinguish mesopore and supermicropore contributions to this estimate. The DR plot provides a micropore volume estimate of $1.5 \cdot 10^{-3}$ cc/g, which is attributable almost entirely to the carbon in the ash.

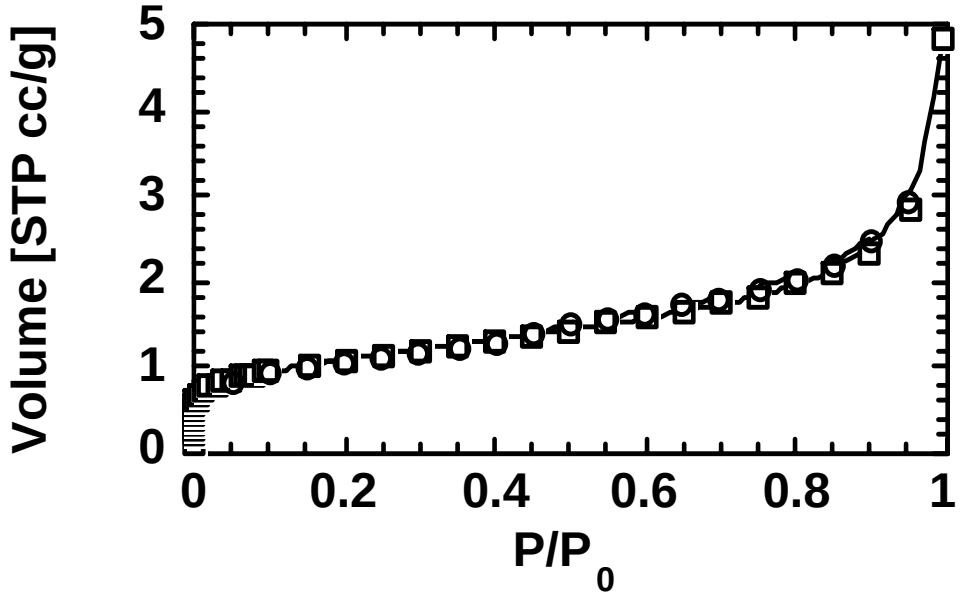


**Figure 6.1. Nitrogen isotherm (77 K) for "standard" fly ash 21 from the Brown University sample bank.**

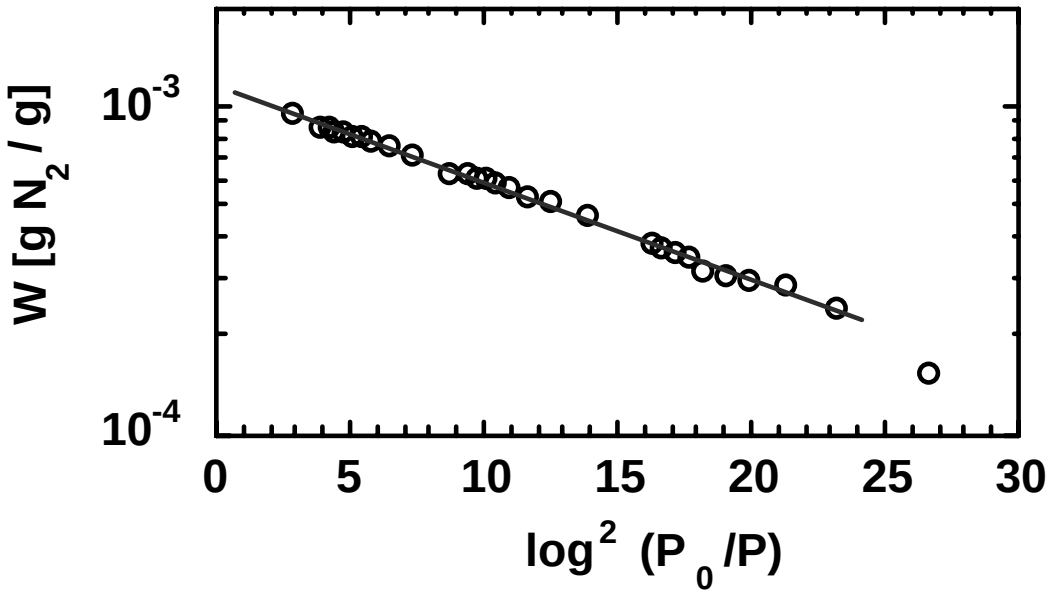


**Figure 6.2. Dubinin-Radushkevich plot for nitrogen on fly ash 21.**

An alternative method for estimating microporosity involves construction of the so-called alpha plot (Gregg and Sing, 1982, Rodriguez-Reinoso and Linares-Solano, 1989). In this procedure, it is assumed that an entire class of adsorbate-adsorbent interactions must follow the same general rules, dictated by the nature of the particular adsorbate-adsorbent interactions. All isotherms are normalized relative to a "standard" isotherm for the adsorbate-adsorbent pair (in this case, nitrogen on carbon). The result of the procedure is shown in Figure 6.3, again for the data of 5.ure 1. Quantachrome Corporation provided the nitrogen-carbon normalization isotherm. The alpha plot shows a form that is typical for microporous samples. A long linear region is seen at high alpha values, and there is a marked curvature of the data towards the origin at low alpha values. The latter behavior indicates a microporous sample, consistent with expectations. The extrapolation of the linear portion of the alpha plot to $\alpha$=0 provides an estimate of the micropore volume which in this case gives 2.2 •$10^{-4}$ cc/g.

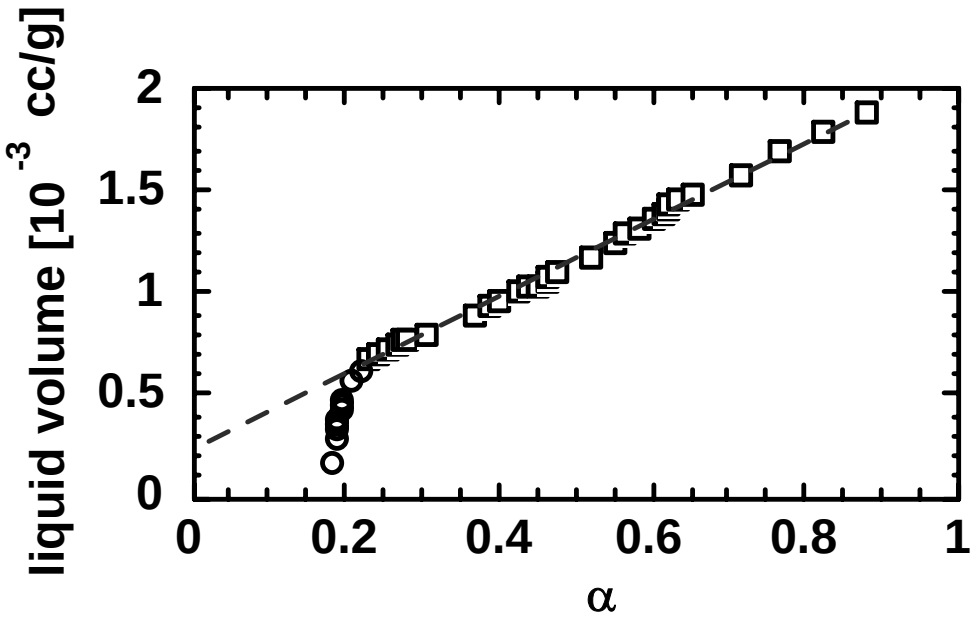


**Figure 6.3. Alpha plot for nitrogen on "standard" fly ash 21 from the Brown University sample bank.**

It can be seen that the alpha plot procedure yields a considerably lower estimate of porosity than does the DR method. Nitrogen DR analysis will sometimes miss wider microporosity (Rodriguez-Reinoso, 1997), but as noted above, it might also sometimes erroneously include mesoporosity. Given the discrepancy noted here, it appears that the inclusion of mesoporosity is plausible. Nevertheless, it must be remembered that both analyses are being applied to a highly heterogeneous material, including both ash and carbon components. There is a high degree of uncertainty in the estimates. The alpha plot procedure will be strongly influenced by external surface area of non-porous ash material, at high relative pressures. This will necessarily have an influence on the slope of the alpha plot, and this might well invalidate the extrapolation procedure.

In order to understand better the nature of the microporosity in this sample sample, $CO_2$ was also employed as an adsorptive. Figure 6.4 shows the adsorption isotherm obtained at 273 K. It should be noted that the results do not extend to very high relative pressures. This is because the saturation pressure of $CO_2$ at 273 K is 3484 kPa, and the instrument can probe no higher than 101 kPa. Nevertheless, this is an important range of relative pressures for examining microporosity.

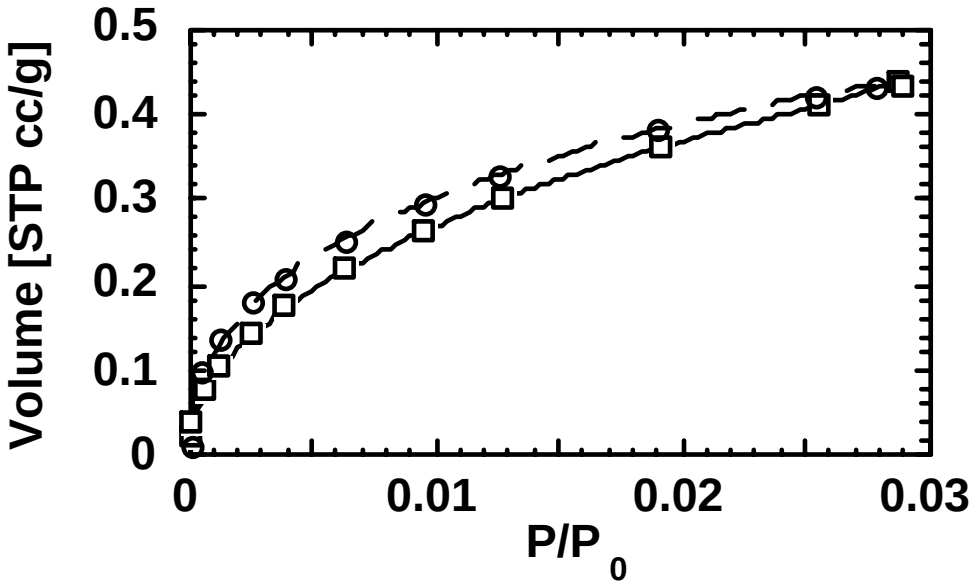


**Figure 6.4. Carbon dioxide isotherm (273 K) on "standard" fly ash 21 from the Brown University sample bank. Adsorption - solid line; desoprtion - dashed line.**

The narrow relative pressure range of Figure 6.4 should be noted. Were this figure plotted on the same scale as was Figure 6.1, the isotherm would be steeply compressed near the ordinate. The isotherm shows a modest degree of hysteresis even in the very low pressure range involved. It is not possible to reliably determine a BET surface area from the data at such low relative pressures. A Dubinin-Radushkevich plot of the same data is shown in Figure 6.5.

This DR plot displays a well-known deviation from linearity at high relative pressures (or low values of $\log^2 [P_0/P]$). Such deviations are not uncommon in carbons that have been activated (burned off) to a high degree (Rodriguez-Reinoso, F., Linares-Solano, 1989). By extrapolation of the linear portion of the plot to the ordinate, as illustrated, another estimate of microporosity is obtained. In the present case, a micropore volume of $6.2 \cdot 10^{-5}$ cc/g is obtained (assuming as typical a $CO_2$ density of 1.04 g/cc, consistent with $CO_2$ in between a solid and liquid phase). Using a density of 0.91 g/cc, which is more representative of liquid $CO_2$, the micropore volume would be only slightly higher, $7.0 \cdot 10^{-5}$ cc/g. In either case, it appears that the earlier estimate from the nitrogen DR plot might well have included supermicropores and/or mesopores, as that estimate was about an order of magnitude larger. The present value is much closer to the estimate of microporosity from the alpha plot for nitrogen.

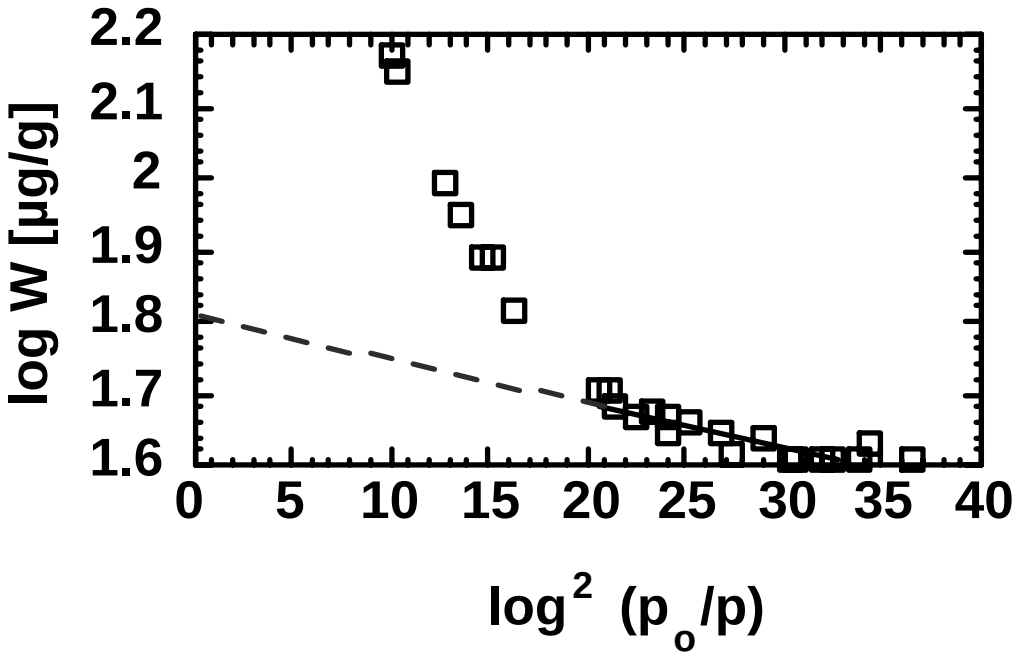


**Figure 6.5. Carbon dioxide DR plot (273 K) on "standard" fly ash 21 from the Brown University sample bank.**

The implication of the above results is that this class F fly ash contains a significant amount of microporosity, probably characterized by a wide distribution of sizes. The question of size distribution in the porosity will be addressed again below.

Ammonia is not a common choice as a standard adsorptive. It is a polar molecule, which means that it would be expected to have a significant polarity mismatch with normally non-polar carbon surfaces. It was therefore anticipated that the isotherms of ammonia on fly ash would show relatively low uptake. Three replicate experiments were performed with ammonia on fly ash sample 21. All gave quite reproducible results. A typical isotherm is shown in Figure 6.6.

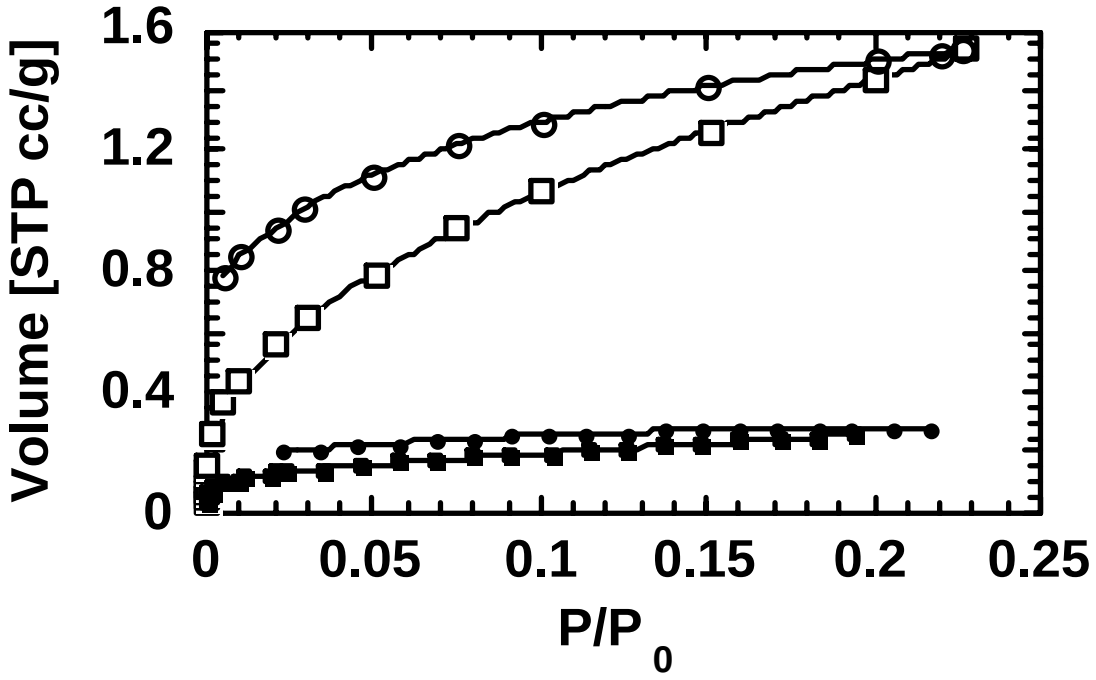


**Figure 6.6. Ammonia isotherms on "standard" fly ash 21 from the Brown University sample bank. Open points - whole fly ash, closed points - fly ash with carbon removed by oxidation. Squares - adsorption, circles, desorption.**

Note that again because the saturation pressure of ammonia at 273 K exceeds 760 torr, the experiments were only performed up to a relative pressure of approximately 0.25. The ammonia isotherms showed a significant degree of hysteresis, as is evident from Figure 6.6. In addition to the hysteresis, it was noted that desorption times became extremely long, during the low pressure desorption experiments. These results are suggestive of an irreversible sorption process. This would not be surprising, given that the earlier cited literature suggested this as a possible result of reactions with functional groups on the carbon.

The ammonia isotherms permitted calculation of a BET surface area, as there were enough points in the appropriate relative pressure range. The value obtained was approximately 5.4 $m^2/g$. This is a bit higher than the surface area calculated from the nitrogen results. There were, however, a significant number of assumptions that went into the calculation. First, the coverage area of the ammonia molecule had to be estimated from liquid ammonia densities; the value which was obtained was 14.0 $Å^2$. Also, despite the knowledge that the isotherm showed evidence of hysteresis probably due to irreversible reaction, it was assumed that the simple BET physisorption model applied to the adsorption results. Taking these factors into account, the surface area obtained here was in surprisingly good agreement with the nitrogen BET value. Use of the desorption branches of the isotherms gave an area of 4.7 $m^2/g$, in better agreement with the nitrogen values. It should also be recalled that heats of adsorption of ammonia on carbons have suggested that the behavior might be intermediate between that of solid and liquid (Spencer et al., 1958, Holmes and Beebe, 1957). Thus just as in the case of $CO_2$, it is not clear what the appropriate condensed phase density might be, and therefore, whether the 14.0 $Å^2$ estimate might be too high. Values of 12.9 $Å^2$ have been used by other (Turner, 1993,Young and Crowell, 1962,

Ashmore, 1963). Use of this value with the desorption branch of the isotherm gives an area of 4.3 $m^2/g$.

The information of most interest with respect to the ammonia slip issue is contained in the region of the isotherm most near the zero relative pressure axis. To show the behavior at low pressures more clearly, the isotherms can be plotted on a logarithmic scale. The results are shown in Figure 6.7. A very notable feature of Figure 6.7 is the sudden increase in adsorption volume near a relative pressure of $10^{-4}$. This feature was reproducible in all of the experiments with the as-received fly ash 21 sample. A similar feature is not visible, at either the same relative pressure or at the same absolute pressure, in the results from nitrogen and carbon dioxide. A comparison of the isotherms for all three of these adsorptives is shown in Figure 6.8.

In the very low relative pressure range associated with filling the smallest micropores, ammonia, carbon dioxide and nitrogen all show somewhat comparable behavior and adsorption amounts. There are, of course, significant differences as well. The ammonia shows the already described abrupt change in slope of the isotherm. The absolute amounts of adsorption differ by a factor of three or more, for the three gases. Ammonia shows behavior intermediate between that for carbon dioxide and that for nitrogen.

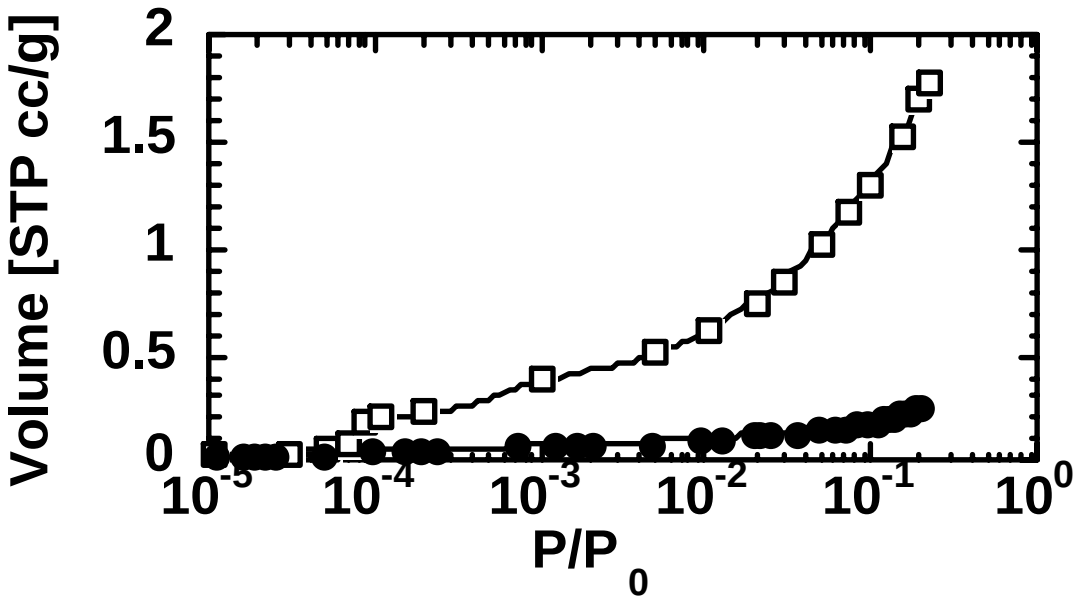


**Figure 6.7. Ammonia adsorption isotherms of Fig. 6.6 on logarithmic pressure scale.**

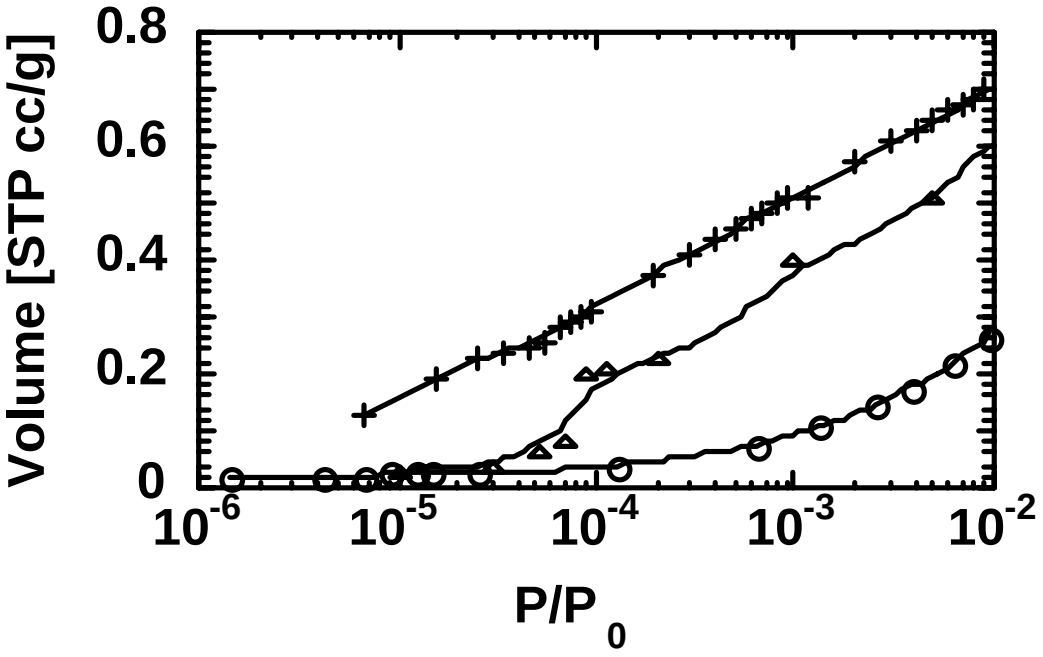


**Figure 6.8. Comparison of nitrogen (crosses), ammonia (triangles), and carbon dioxide (circles) isotherms.**

The adsorption behavior of ammonia on this fly ash sample is dominated by the adsorption on carbon. This is consistent with an earlier similar conclusion regarding the relative roles of carbon and mineral components in nitrogen adsorption. The relative contributions of the two components may be judged from Figure 6.6, which shows a comparison of the whole ash isotherm (already discussed) with the isotherm for the ash with the carbon completely removed. It is clear that most of the adsorption takes place on the carbon. Bearing in mind that the carbon represents about 6 % by mass of the whole ash, the importance of the carbon in the adsorption process is put into very clear perspective.

The ammonia-BET surface area of the carbon-free ash is 0.7 $m^2/g$, which is in excellent agreement with the values earlier obtained from nitrogen isotherms. The fact that there is good agreement between nitrogen and ammonia BET values for the carbon-free ash is not necessarily inconsistent with the less good agreement between these values for the carbon-containing ash. This is because most of the surface area in the mineral portion of the ash is external surface area. For illustration, a spherical particle of 10 μm diameter and 1 g/cc density would have an external surface area of 0.6 $m^2/g$, in reasonable order of magnitude agreement with the above estimate.

Figure 6.7 shows the ammonia isotherm for the carbon-free ash, plotted on the logarithmic relative pressure scale. Here the comparison emphasizes the low relative pressure results. The contribution of the mineral portion is again seen to be very small in comparison with the contributions of the carbon, particularly after the sudden jump at a relative pressure of about $10^{-4}$. Figure 6.9 replots this data with the Y-axis converted to ppm,w on the ash and includes data for ozonated samples. Ozonation of the carbon surfaces is seen to enhance the 'jump" feature, while the rest of the isotherm is not significantly altered, suggestion that this feature is related to surface oxides on carbon. There have been a significant number of studies concerned with the

adsorption of ammonia on carbons (e.g. Boehm et al., 1964 and Hofman et al. 1950). These studies have also shown that oxide groups on the surface of a carbon enhance the adsorption of ammonia. It is often hypothesized that the acidic functional groups associated with the surface oxides act as Brønstead acids towards ammonia, which is a strong base (Zawadski, 1989). These acid functionalities donate a proton to the ammonia in an acid-base interaction, yielding an ammonium ion, $NH_4^+$. There is also evidence of formation of groups which cannot be hydrolyzed in acid solution. The suggestion has been made that the ammonia reacts with surface acid groups, probably yielding amides, or possibly even imides. As the temperature of the complexes is raised, the irreversibly formed amide groups can decompose, eventually giving rise to cyano groups on the carbon surface. Hence, the adsorption process involving reaction of ammonia with acid groups to form amides may be observed to be irreversible, even at high temperatures.

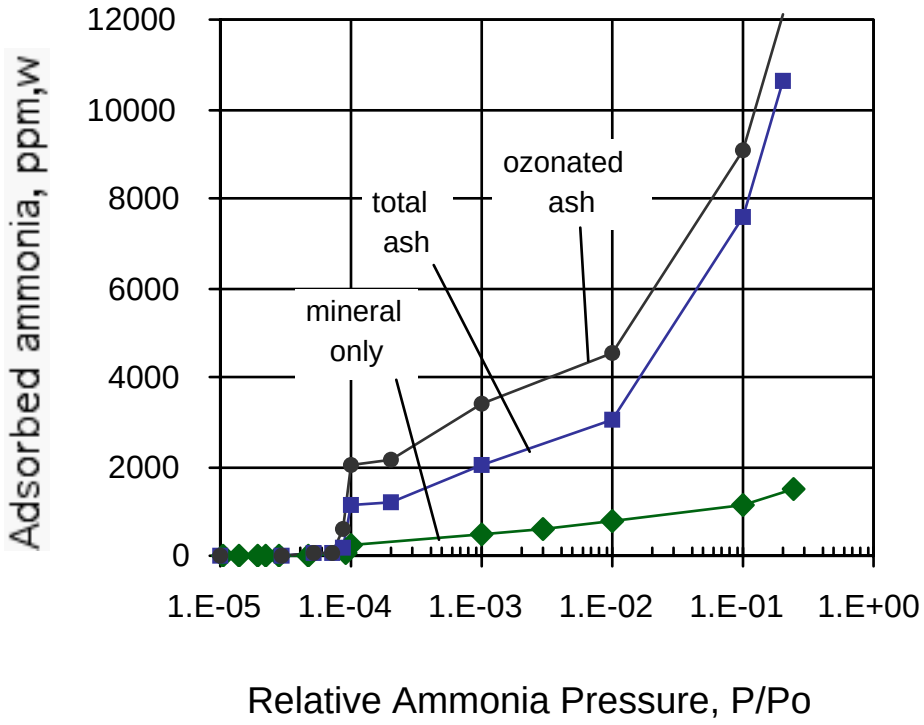


**Figure 6.9. Full ammonia adsorption isotherms on A21 fly ash (6.2% LOI from Brayton Point) at 273 K before and after carbon removal by air oxidation plooted as ppm,w on ash. Also shown is the ammonia isotherm on fly ash subjected to ozonation.**

The information of most interest with respect to the ammonia slip issue is contained in the region of the isotherm most near the zero relative pressure axis (1-20 ppm). To show the behavior at low pressures more clearly, the isotherms can be expanded on the X-axis and the partial pressure units converted to an equivalent ppm by volume in a 1 atm gas (e.g. flue gas). The results are shown in Figure 6.10. A low-concentration asymptotic value in Figure 6.10 appears to be about 20 ppm and independent of the carbon content. This is comparable to the theoretical amount of ammonia corresponding to one monolayer on the geometric external surface of the mineral grains. In fact analysis of this isotherm yields an ammonia-BET surface area of 0.7 $m^2/g$, which is in excellent agreement with the values earlier obtained from nitrogen isotherms for the carbon-

free ash. It appears that this monolayer coverage of the mineral grains occurs at very low vapor concentrations, while at higher ammonia concentrations carbon begins to dominant the adsorption process.

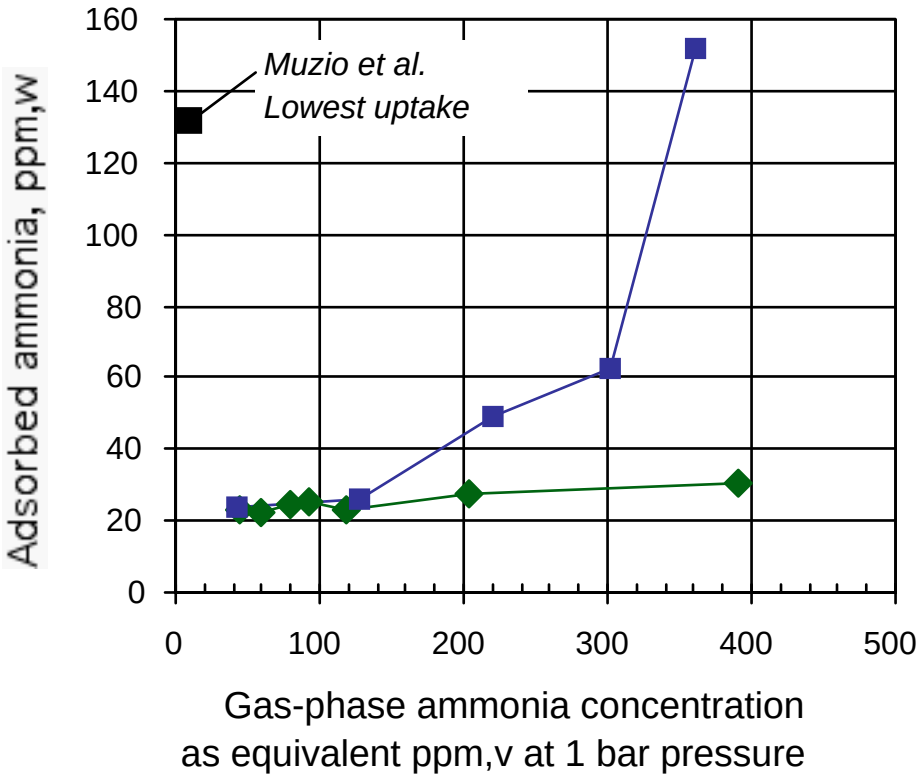


**Figure 6.10. Ammonia isotherms with the low partial pressure region expanded and the X-axis units converted to those commonly used to express ammonia slip concentrations.**

Of particular interest in Fig. 6.10 is the comparison between the present results and the experiments of Muzio et al. (1995) in simulated flue gas. Muzio et al. measure 132-347 ppm,w of ammonia adsorbed on a range of ash samples exposed to 10 ppm ammonia slip at 150 ºC — the lowest of these data points is shown on Fig. 6.10 for comparison. The low uptake in the present experiments cannot be explained by the low temperature (273 K vs. 423 K in Muzio et al.), as we have observed decreases in uptake with increasing temperature above 273 at constant partial pressure.

The reason for the discrepancy between the values observed in the field and the present isotherm is not fully understood. It might be that the present sample does not have as high an ammonia capacity as some other samples, due to its low surface polarity. On the other hand, the influence of processing conditions also cannot be overlooked. It is possible that SCR and SNCR processes somehow create greater ammonia capacity in ashes. This might involve a change in the carbon surface oxide population, or a creation of a sorbed water

layer on the carbon. A third possibility may be inferred from the literature on carbon blacks. There has been reported a very slight increase in ammonia adsorption capacity with temperature in carbon blacks (Holmes and Beebe, 1957, Bomchil et al., 1979). This is contrary to the temperature trends observed in the earlier work on ashes, however, and is therefore less likely as an explanation.

The micropore capacity of the ash towards ammonia may be examined with the aid of a DR plot. This plot is shown as Figure 6.11. Extrapolation of the fit to the somewhat scattered low pressure data gives a micropore volume estimate of $1.5 \cdot 10^{-3}$ cc/g. This value is in very good agreement with the micropore estimate provided by nitrogen, using the DR analysis. Again, there may be some contribution of small mesopores to this value. The fact that both the ammonia and nitrogen provided values that were an order of magnitude higher than those given by carbon dioxide is not necessarily troubling. It is well known that carbon dioxide can only fill the smallest micropores (Garrido et al., 1987; Rodriguez-Reinoso and Linares-Solano, 1989).

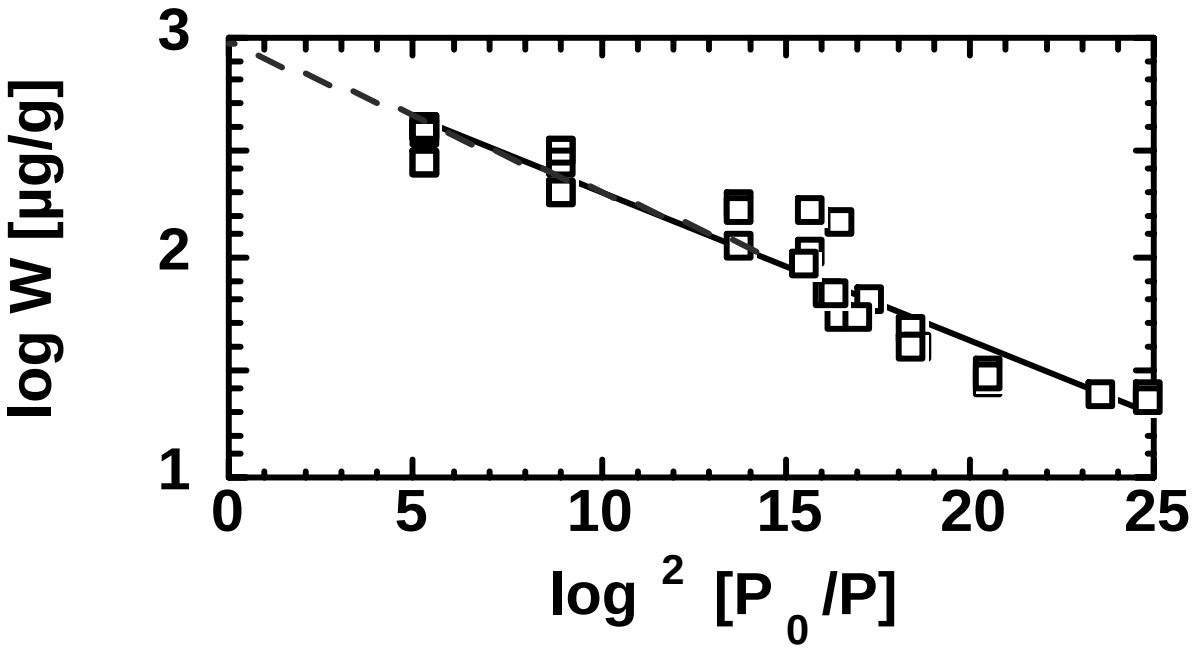


**Figure 6.11. D-R plot for ammonia on fly ash 21.**

The implication of the above suite of results is that ammonia, like nitrogen, can be adsorbed into micropores in comparable amounts at very low relative pressures. The present results are entirely consistent with the observation by Turner[8] that ammonia on outgassed ("pretreated") fly ash is held to an extent which is comparable to that revealed by ordinary surface area probing techniques. Our samples were outgassed at 300°C, so they should be comparable to his "pretreated" samples. Moreover, Turner's experiments were performed in dry flowing gas, so the adsorption conditions were also quite comparable to ours. This dry ammonia adsorption process explained about two-thirds of the capacity of the as-received ash for ammonia in Turner's work. The remaining capacity was hypothesized by Turner to be due to moisture and oxides on the ash

surfaces, which are lost on heating. We believe that our work has made it clear that it is the carbon in the ash that is mainly responsible for this dry adsorption capacity.

The present results appear to be inconsistent with the results obtained by Muzio et al. (1995). They obtained adsorption capacities that were considerably higher than what would be predicted from our experiments. One possible reason is that not all of the fly ash samples are comparable. The Huntley sample of Muzio et al. had a higher LOI (10.81%) and a higher surface area (8.1 $m^2/g$) than the sample used in this work It is the surface area that is really the more important factor. Assuming for their sample a typical mineral surface area of 0.7 $m^2/g$, the carbon surface area of the sample would be 7.5 $m^2/g$-ash (about 69 $m^2/g$-carbon). This makes the available surface for adsorption of ammonia in the Huntley sample 2.5 times higher than the surface area of carbon on our sample (which is 0.061• 49 = 3.0 $m^2/g$). Similar calculations for their other samples yield 0.5 $m^2/g$ for the Russel ash, 15 $m^2/g$ for the Salem Harbor ash and 12 $m^2/g$ for the Arapahoe ash. The available adsorption surface cannot, however, be used to explain the observed differences. The Russel ash exhibited an ammonia capacity of 132 ppm, the Salem Harbor 344 ppm, the Arapahoe nearly 347 ppm and the Huntley sample 190 ppm, all for 300°F (149 °C), 10 ppm concentrations and 60 minutes equilibration. Again, at such low relative pressures, our work would suggest a capacity that would be no more than 20 ppm.

The experiments of Muzio et al. differed from ours in one important respect. Their experiments were conducted with the ammonia in humidified and acid gas ($SO_2$) containing air. The absorption of ammonia by water or acid sites could have played some role in yielding the high capacities that they observed. In the absence of the acid component in the gas, the ash itself would have very little moisture content at the temperature of their experiments. Data are available on solutions of ammonia and $SO_2$ in water (Emmert and Pigford, 1963). The partial pressures of ammonia and $SO_2$ above such solutions are given by:

$$p_{NH_3}(\text{torr}) = F_2(T)\,\frac{C\,(C-S)}{(2\,S - C)} \qquad (6\text{-}1)$$

and

$$p_{SO_2}(\text{torr}) = F_1(T)\,\frac{(2\,S - C)^2}{C - S} \qquad (6\text{-}2)$$

where

$$\log_{10} F_1(T) = 5.865 - [2368 / T\,(K)]$$
$$\log_{10} F_2(T) = 13.680 - [4987 / T(K)]$$

The parameter C represents the concentration of $NH_3$, in mols/100 mols of water, and the parameter S the concentration of $SO_2$ in mols/100 mols of water. The actual correlations were developed for the temperature range from 308 K < T < 363 K, and ammonia concentrations in the range 5.8 < C < 22.4 mols/100 mols water. Clearly these correlations are intended for conditions somewhat out of the current range of interest, but it is instructive to examine the implications of an extrapolation.

A short temperature extrapolation is possible to the lower end of the temperature range examined by Muzio et al. (T = 120 °C = 393 K). At this condition, $F_1 = 0.691$ and $F_2 = 9.78$. It may be shown that:

$$P_{NH3}P_{SO2} = F_1F_2\,(2\,y+C)\,C \qquad (6\text{-}3)$$

and that

$$P_{NH3} = F_2\,C\,y/(-2y + C) \qquad (6\text{-}4)$$

where y = (C – S). It can also be shown that the solutions to this pair of equations will normally yield values of y <<C, for the conditions of present interest. In this case,

$$P_{NH3} \approx F_2\,y \qquad (6\text{-}5)$$

and

$$P_{NH3}P_{SO2} \approx F_1F_2\,C^2 \qquad (6\text{-}6)$$

For $P_{NH3}$ = 20 ppm = 20 • $10^{-6}$ • 760 = 1.52 • $10^{-2}$ torr and $P_{SO2}$ = 1500 ppm = 1500 • $10^{-6}$ • 760 = 1.14 torr, y = 1.55 • $10^{-3}$, C = 0.051 and S = 0.049. These values are excellent approximations to the actual exact solutions. To the extent that the extrapolations involved reflect the real situation in an ash particle, it is possible to estimate the moisture content on the particle surface. If *f* represents the fraction by mass ammonia on the particle, then this quantity must be given by:

$$f = C \bullet m \bullet (100\ \text{mol.water} / 1800\ \text{g-water}) \bullet 17\ \text{g}\ NH_3/\text{mol}\ NH_3 \qquad (6\text{-}7)$$

where m is the g-moisture/g-ash. Assuming a typical *f* value of 200 ppm, the moisture content in this case would be 0.4%, assuming that all of the ammonia is held in the water phase.

The above calculation illustrates only that a small water film, assuming that it exists and that it can be modeled using bulk phase behavior, can explain a significant enhancement of ammonia capacity. At 120°C, the vapor pressure of water above an $SO_2$ solution with S = 0.49 would be around1480 torr, in the absence of the ammonia (Emmert and Pigford, 1963). This is sufficiently high that it is not clear that a water film is even possible under the conditions used by Muzio et al. Still, it appears that the most plausible explanation for the considerably higher ammonia capacity observed in that study compared with ours is that there is some interaction of ammonia with $SO_2$ in the condensed phase. Again assuming the present model reflects to some degree the real situation, it is also clear that if the partial pressure of $SO_2$ is somewhat lower than that used by Muzio et al. the ammonia capacity is also greatly diminished. Assuming, for example, that $P_{SO2}$ = 100 ppm = $10^{-4}$ • 760 = 7.6 • $10^{-2}$ torr, keeping all other values constant, then C decreases to 0.013, implying roughly a factor of four decrease in the ammonia capacity at the same moisture content. At such levels, the dry adsorption capacity becomes significant in comparison.

The above discussion points out the importance of studies on co-operative adsorption in these systems.

## *6.3 Ammonia Removal by Dry and Semi-Dry Processes*

### *6.3.1 Experimental Methods*

#### 6.3.1.1 Samples

Four commercial ash samples were selected for this study from among the 80 ash samples in the Brown University ash sample bank (Kulaots, 2001). Properties of the selected samples are shown in Tables 6.1 and 6.2. FA1 and FA2 are ammoniated ash samples, one with high and one with low pH, from two power stations in the New England region operating SNCR units and burning bituminous coals. FA3 and FA4 are typical non-ammoniated ashes from eastern and western U.S. coals respectively, and are used in experiments in which ammonia is loaded on the ash under a variety of laboratory conditions. Note that both the carbon content and the ammonia content of FA1 are unusually high. At 1060 ppm this ash has more than ten times the amount of ammonia that is commonly cited as the desired amount to avoid ash utilization problems (Larrimore, 2000). The basic nature of FA1 is unusual for a class F ash whose alkaline and alkaline earth components sum to only 10.0 wt-% on a carbon-free basis (see Table 6.2). It can be shown by simple equilibrium calculations for the reaction $NH_3 + H_2O \rightarrow NH_4^+ + OH^-$ that this basicity is in part due to its very high ammonia content.*

**Table 6.1. Fly ash sample properties.**

| Designation[a] | Class | LOI[b] | as-received ammonia ppm,w | pH |
|---|---|---|---|---|
| FA1 (A22) | F | 33.6% | 1060 | 11.2 |
| FA2 (A74) | F | 10.0% | 240 | 7.9 |
| FA3 (A21) | F | 6.1% | ~ 0 | 7.1 |
| FA4 (A73) | C | 0.5% | ~ 0 | 11.4 |

[a] in parentheses are given the codes in the Brown University sample bank, allowing cross-reference to other documents.

[b] "Loss on ignition," an approximate measure of unburned carbon content (see text).

* Consider 1 gm of ash in 30 ml of water, as used in our pH measurement procedure. If the 1060 ppm of ammonia is completely desorbed from the surfaces into solution in the aqueous phase, a pH of 10.3 would be

**Table 6.2. Inorganic elemental composition of commercial ammoniated ash samples.**

| *Element* | FA1, bulk[a] wt-% | FA1, XPS[a] wt-%[b] | FA2, bulk[a] wt-% |
|---|---|---|---|
| Aluminum as $Al_2O_3$ | 19.6 | 20.6 | 28.8 |
| Calcium as CaO | 4.0 | 12.6 | 1.3 |
| Iron as $Fe_2O_3$ | 7.2 | 4.3 | 4.7 |
| Magnesium as MgO | 3.2 | 1.5 | 0.97 |
| Manganese, as MnO | 0.06 | -- | 0.02 |
| Phosphorus as $P_2O_5$ | 0.05 | -- | 0.2 |
| Potassium as $K_2O$ | 2.1 | -- | 2.4 |
| Silicon as $SiO_2$ | 60.0 | 44.6 | 58.4 |
| Sodium as $Na_2O$ | 0.56 | 0.84 | 0.91 |
| Sulfur as $SO_3$ | 2.3 | 14.1 | 0.44 |
| Titanium as $TiO_2$ | 0.92 | 1.0 | 1.8 |

[a] carbon-free, oxide basis

[b] near-surface composition, converted from atom-%

### 6.3.1.2 Experimental Procedures

Loss-on-ignition values were determined by weighing samples before and after air oxidation at 750 $^oC$. Inorganic elemental compositions were determined for the ammonia-containing field ashes at Huffman Analytical Labs (Golden, CO) and near-surface elemental compositions were determined by XPS at Evans East Laboratory (East Windsor, NJ). The XPS results are similar to the bulk analysis, which the exception of calcium and sulfur, which show signs of significant surface enrichment. XPS also detected nitrogen, and the high resolution N1s XPS spectrum suggests multiple peak behavior. This spectrum may contain information on nitrogen/ammonia forms, but low signal-to-noise ratio made the peak assignments and quantification uncertain.

† Consider 1 gm of ash in 30 ml of water, as used in our pH measurement procedure. If the 1060 ppm of ammonia is completely desorbed from the surfaces into solution in the aqueous phase, a pH of 10.3 would be observed before significant volatilization occurred if the remainder of the ash constituents (mineral phases and carbon surfaces) were neutral. Thus part of the basicity of the ash can be attributed to the ammonia itself.

The ammonia content of a test fly ash sample was determined by mixing two grams of ash with 3 ml of 2 v/v-% $H_2SO_4$ and 37 ml distilled water. The suspension was dispersed in an ultrasonic bath for 5 minutes, and the solid ash was separated from the solution by a 10-minute centrifugation. The supernatant solution was then filtered and 30 ml used to measure ammonium ion concentration by specific ammonium electrode and Corning pH/ion analyzer model 455 as well as by Corning's Ammonia Combination Electrode, which measures dissolved ammonia and pH. Potassium ion is known to interfere with the accurate measurement of ammonium, but the potassium levels in Table 6.2 are too low for the interference to be significant for these samples and the separate determinations of total ammonia based on ammonium ion detection and dissolved ammonia detection were in good agreement.

The acid/base character of test fly ash samples were measured by mixing 1 gm of ash with 30 ml distilled water and dispersing the particles in an ultrasonic bath for 5 minutes. After centrifugation and filtration as above, the pH of the solution is measured by a Corning pH/ion analyzer 455. For some ash samples, pH values continue to change slowly for up to 30-45 minutes, presumably due to slow dissolution of basic mineral species. The pH values presented here are those existing after 5 minutes of ultrasonic dispersion and should not be interpreted necessarily as equilibrium values. The thermal desorption results were obtained with an Autosorb vapor adsorption apparatus used in outgassing mode to desorb $NH_3$ from 3-5 gm ash samples as a function of temperature and time under vacuum.

For experiments in static humid air, ash samples were enclosed in a laboratory dessicator that also contained calibrated aqueous solutions designed to provide gas environments of known $H_20$ and/or ammonia partial pressure. In the first type of experiment, 5 gms of an ammonia-containing fly ash was placed in a 50 x 9 mm dish and loaded into a 150 mm dessicator. A separate 90 x 50 mm dish was prepared with 40 ml of standard salt solutions designed to provide fixed relative humidity according to the procedure of Wexler and Seinfeld (1991). Using 20 gm salt in 40 ml of water at 25 C the relative humidity (RH) values are 75% (NaCl), 84% (KCl), 92% ($KNO_3$). Both the ammonia content and the moisture content of the ash samples were measured before and after exposure.

The second type of experiment is identical to the first, except that calibrated solutions of ammonium salts were used instead of KCl, NaCl, or $KNO_3$. Dilute ammonium hydroxide solutions were prepared at various concentrations and the ammonia vapor concentration measured in the dessicator for calibration (Fujisaki, 2000]. These experiments create vapor environments with both $H_2O$ and $NH_3$ and, although designed to load $NH_3$ onto ash, in fact are capable of producing a net adsorption or net desorption of ammonia on/from ash, depending on ash type and conditions.

For experiments in flowing humid air, a fixed/fluidized bed reactor was used to contact ash with a continuous stream of air at a fixed relative humidity. Ten grams of ash were placed in a 25 mm diameter glass tube fitted with a porous glass distributor disc at the bottom with 0.15-0.18 mm pores and subjected to continuous mechanical vibration. The air flow to the reactor bottom was set at either 0.3 lit/min or 0.8 lit/min and was pre-humidified in a series of two water-filled tubes, while the humidity was measured at the reactor inlet using a digital hygrometer with an accuracy

of 2% RH. Ash moisture and ammonia contents were measured before and after treatment by ion electrodes as described above.

Experiments with flowing fog were similar to those in humid air, but an ultrasonic nebulizer was used to introduce ultrafine water droplets to the humidified air upstream of the contact vessel, and some mechanical stirring was carried out manually or with a magnetic stir bar. Here 10 gm of ash are placed in a 40 mm diameter reactor fitted with the same porous distributor (0.15-0.18 mm pore size) and exposed to a fog-containing upward airflow of 0.7 lit/min. After water addition the sample was removed and the ammonia content measured. Half of the sample (5 gm) was returned to the glass reactor and dried in flowing air without water mist at a flow rate of 0.3 lit/min. The time between the end of the fog treatment and the beginning of the drying stage was always 1 minute. All experiments were at ambient temperature.

Additional experiments were conducted for acidic ashes in which basic additives, NaOH or $Ca(OH)_2$, were introduced into the liquid feed for fog generation, or in the case of $Ca(OH)_2$ were added as dry powder to the ash prior to treatment. In another variant on the basic experiment, ozone-containing air or oxygen was used in place of pure air as the drying gas or fog carrier gas, and/or a 30 wt-% $H_2O_2$ was employed as the liquid feed for fog generation in place of water. Joint treatment with ozone and $H_2O_2$ is the "peroxone" route to aqueous ammonia oxidation (Kuo et al., 1997]. Experiments were also carried out in which dry ozone-containing air or oxygen is passed through the fixed bed of ash without moisture addition.

### *6.3.2 Ammonia Removal by Dry and Semi-Dry Processes*

Figures 6.12-5.15, 6.17-6.22 and Table 6.3 summarize the experimental results on the ammonia removal task. Figure 6.12 on thermal treatement shows that 200 $^oC$ is insufficient to remove significant ammonia, but that a majority of the ammonia in these ash samples can be removed by thermal treatment alone at 300 $^oC$. Figure 6.12 shows that the required desorption times are long at 300 $^oC$, either due to desorption/decomposition kinetics or to slow diffusion through the deep sample beds. This simple thermal desorption experiment does not provide sufficient information to positively identify the ammonia form or forms, but significant evolution does occur at temperatures characteristic of ammonium bisulfate compositions (decomposition onset 214 C in inert[13]).

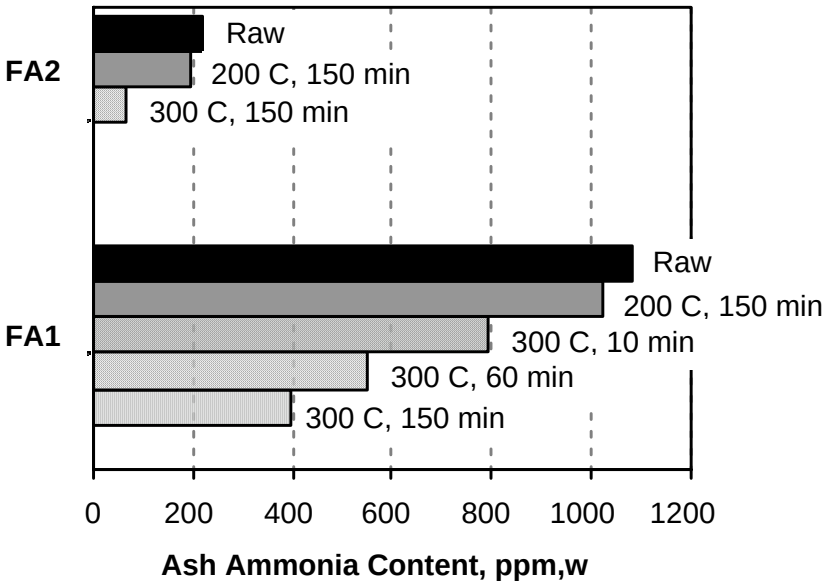


**Figure 6.12. Vacuum thermal desorption behavior of two ammonia-containing ash samples from the field.**

Figures 6.13-6.19, 6.21, 6.22 and Table 6.3 summarize a large set of ammonia-removal experiments using controlled amounts of moisture at ambient temperature. Figure 6.13 presents results from the earliest set of experiments, those using static humid air in closed dessicators. The plot shows that ammonia can be completely removed from the high-pH ash, FA1, simply by placing it near a dish with an aqueous salt solution - i.e. under conditions where no liquid water is added directly to the ash sample. Exposure to static humid air is observed to increase ash moisture content from about 0.8% initially to values ranging form 1.3-1.9%. It is believed that slight condensation in and around the individual ash/carbon particles causes the ammonia species to desorb, enter solution, and be converted to the highly volatile $NH_3$ form according to:

$$NH_3\,(aq) + H_2O\,(liq) \Longleftrightarrow NH_4^+\,(aq) + OH^-\,(aq) \qquad (6\text{-}8a)$$

$$NH_3\,(aq) \Longleftrightarrow NH_3\,(vap) \qquad (6\text{-}8b)$$

$$H_2O\,(liq) \Longleftrightarrow H^+\,(aq) + OH^-\,(aq) \qquad (6\text{-}8c)$$

$NH_3$ is highly volatile so equilibrium 1b favors partitioning to the vapor phase, while equilibrium 1a is highly dependent on solution pH. At 20 $^oC$ $pK_b = 4.767$, which upon rearrangement gives

$$\log\{[NH_4^+]/[NH_3]\} = 9.23 - pH \qquad (6\text{-}9)$$

so this combined reaction system leads to $NH_3$ as the predominate species thus extensive ammonia volatilization whenever pH values are greater than about 10 in the condensed film. Water vapor is always below saturation in the Fig. 6.13 experiments, so partial condensation occurs by adsorption on surfaces and capillary condensation in pores and fine intraparticle spaces. It is notable that ammonia removal can occur with the addition of so little liquid water (1.3-1.9 wt-%) that ash handling characteristics are not greatly affected.

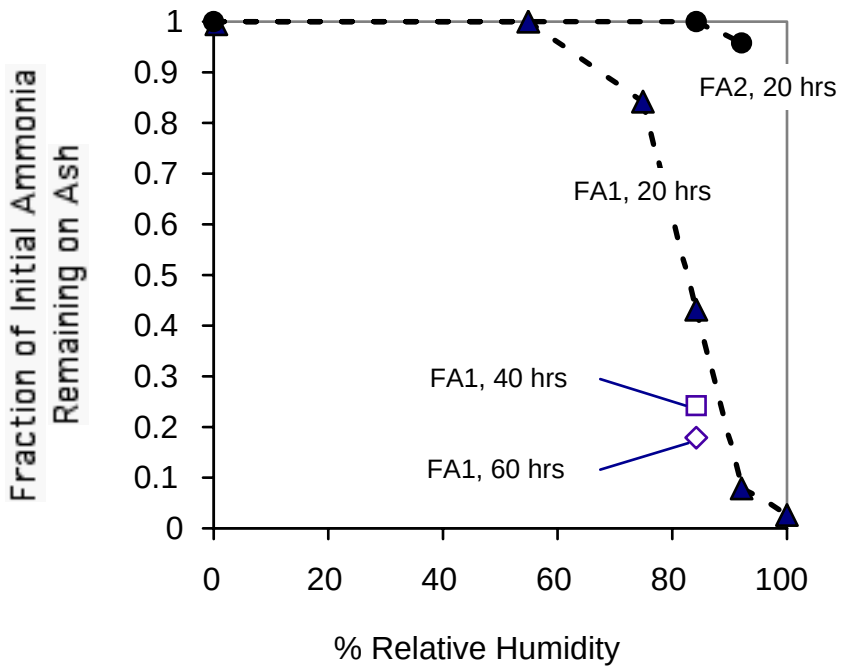


**Figure 6.13. Results of experiments on ammonia removal in static humid air. Initial ash moisture contents were 0.82 wt-% for FA1, and 0.80 wt-% for FA2. Moisture contents of selected treated ash samples shown on this figure were as follows: 1.3% for FA2 at RH84 (20 hrs); 1.6% for FA2 at RH94 (20 hrs); 1.6% for FA1 at RH84 (20-60 hrs); and 1.9% for FA1 at RH92 (20 hrs).**

Figure 6.13 also shows that the process is not effective for the low-pH ash, FA2. The critical role of solution pH is further illustrated in Fig. 6.14, which presents results for two acidic and two basic ashes placed in proximity to aqueous ammonia solutions. The standard solutions were designed to create vapor environments with known partial pressures of ammonia. Although the original goal of these experiments was to load ammonia onto ash, it was found that this exposure can either increase or decrease ash ammonia content depending on ash type. Both acidic ashes (FA2,3) adsorbed ammonia from the solutions, as expected (see Fig. 6.14), but the basic ash, FA1, experienced a large ammonia loss. Further, adding a basic additive to the acidic ash, FA3, eliminated the uptake completely. Additional experiments on other ash samples show the same trends with pH (Fujisaki, 2000]. We conclude that in the presence of near-saturated humid air, we can remove but not add ammonia to basic ashes, and conversely we can add but not remove ammonia from acidic ashes.

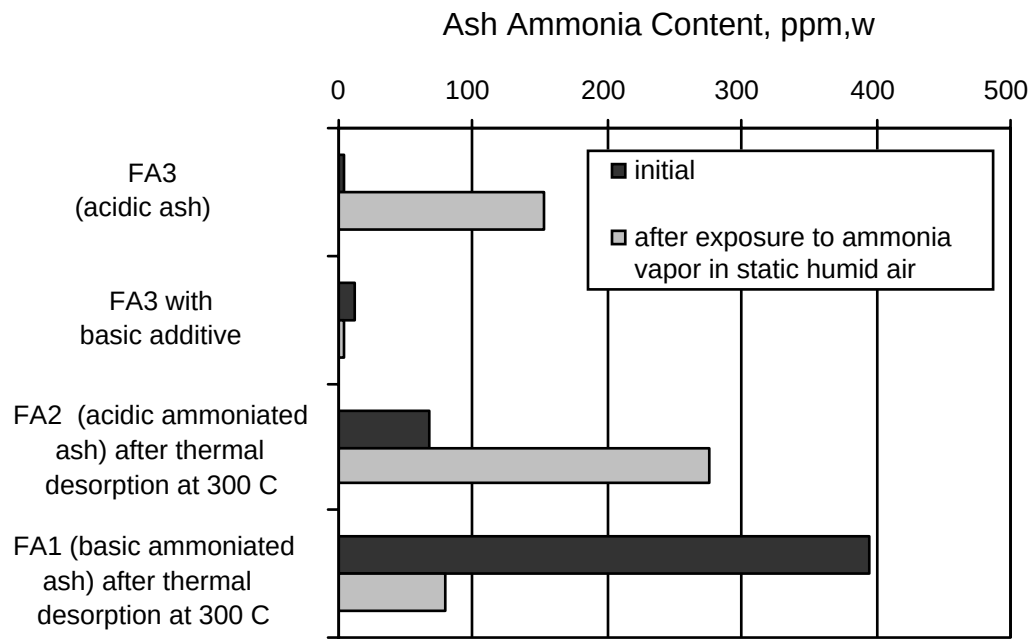


**Figure 6.14. Effect of pH on the removal or addition of ammonia in static mixtures of humid air and ammonia vapor (700 ppm) established with a calibrated ammonium hydroxide solution. The basic additive was CaO as a dry powder added to the ash. Similar results were obtained when CaO was added in solution, or using $Ca(OH)_2$ either as a dry powder or in solution.**

These results combined show that the ammonia release is governed by solution chemistry as embodied by Eq. 6-8, despite the very low moisture levels. It appears that above 1-2% moisture, a water film forms in and around individual particles and is sufficiently continuous to dissolve the adsorbed or deposited ammonia and to mediate its release in a way that is at least qualitatively similar to bulk solution behavior. This is not an obvious result considering the dry physical appearance of the ash and the lack of macroscopic evidence of a continuous water phase. The effectiveness of small amounts of water is claimed in several process patents (Gasiorowski and Hrach, 2000, Katsuya et al., 1996), where the authors quote the advantages of rapid ammonia release and quasi-dry ash handling. We demonstrate here that even exposure to static humid air can bring about these effects. Indeed, using small amounts of water minimizes the inventory of ammonia in solution and thus favors its partitioning to the vapor phase. As pointed out by Gasiorowski et al. (2000]) smaller amounts of moisture also produce higher pH values (provided the ash is intrinsically basic or made basic by solid additives), since any water in excess of that required to activate the aqueous solution chemistry serves only as a diluant, bringing the solution closer to pH neutrality and inhibiting ammonia release.

More effective than static humid air is a contacting scheme employing a continuous stream of humidified air passed through a fixed bed of ash in upflow configuration. Figure 6.15 illustrates that this contacting method is effective at removing ammonia from the basic ash at moisture levels of less than 3 wt-%. The rate of removal increases with increasing moisture content, but the total contact times are still long. The long times are believed to be the result of (1) the slow rate of water addition due to the limited carrying capacity for water vapor in room temperature

air (0.023 mole fraction), (2) the low driving force for water addition to the solid phase, which at these subsaturated conditions is driven by adsorption and capillary condensation, and (3) slow diffusion of dissolved species within the microscopic water film.

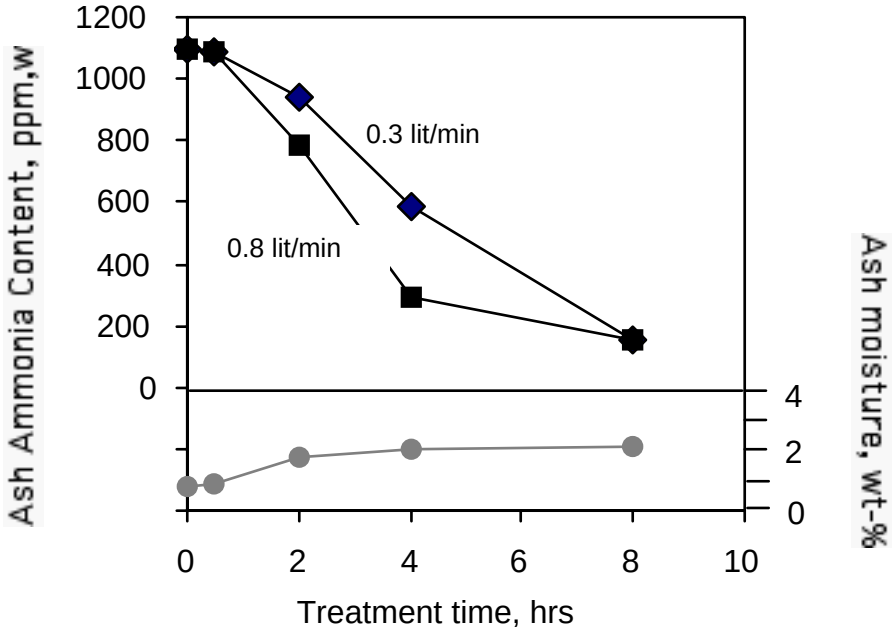


**Figure 6.15. Results of ammonia removal experiments in flowing humid air (RH 93%) passed upward through 10 gm fixed beds of ash at one of two different flowrates. Sample: basic fly ash, FA1.**

The structure and properties of the water film can be appreciated by several simple calculations. Figure 6.16 shows the geometric relationship between moisture content and water film thickness for a ideal ensemble of monodisperse, non-contacting spheres of density 2.2 gm/cm$^3$, similar to the density of mineral phases in fly ash. The small amounts of water employed here give rise to a nominal film thickness well below 1 μm. For the humid air experiments, we further expect the water film to be highly non-uniform, consisting of very thin mono- or multi-layer adsorbed films on external particle surfaces or large pore surfaces in carbon, coexisting with bulk moisture in fine pores and fine neck regions lying at points of particle contact. The Kelvin equation describes this sub-saturation condensation, and for the simple case of spherical geometry yields a maximum size of filled pores (or filled particle interstitial regions) of 1.5 nm at 50% RH, 5 nm at 80% RH, and 21 nm at 95% RH under these conditions. We therefore expect bulk water only in nanometric (meso) pores and nanometric interstitial regions. We expect much of the ash surface to be covered only by a multi-layer adsorbed film, making the water phase only semi-continuous and leading to slow diffusion of dissolved species. On the other hand, desorption may be aided by the fact that ammonium salts and adsorbed ammonia species may serve as attractive sites for preferential water adsorption or condensation.

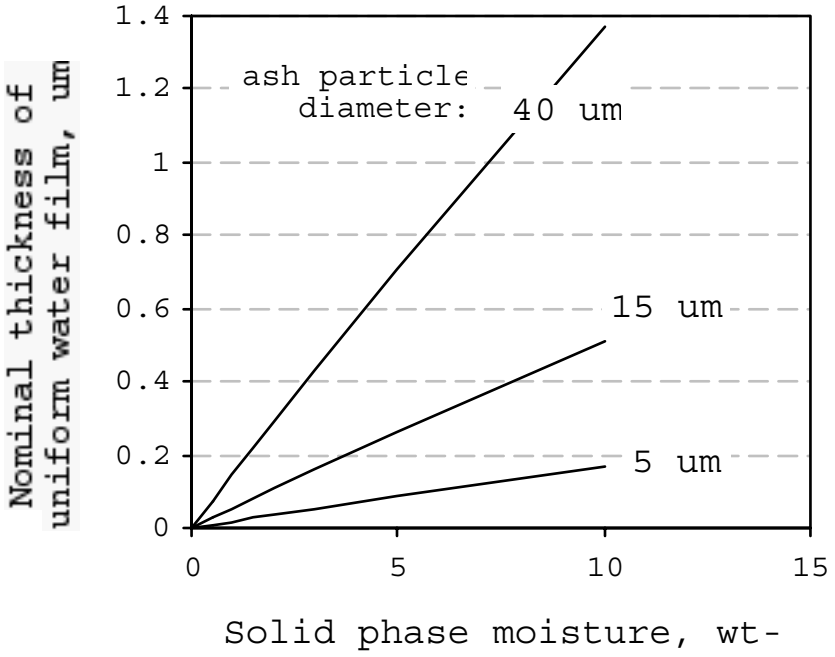


**Figure 6.16. Thickness of uniform water film on collection of ideal, nonporous, monodisperse spherical particles of typical mineral density, 2.2 g/cm$^{-3}$. This calculation demonstrates that the water film produced by most humid air and flowing fog experiments (moisture contents 1-5%) have sub-micron mean dimensions.**

*Flowing fog*

In an attempt to reduce required contact times, experiments were performed in which 2-3 wt-% water is introduced quickly to the ash using an ultrasonic nebulizer to create a fine fog in the flowing humid air stream. The ultrafine water droplets remain in a quasi-stable aerosol as they pass through the porous distributor disk and enter the agitated ash bed. Figure 6.17 shows the effect of the fog on ammonia removal under a variety of conditions. These experiments take place in two parts: a fog addition stage lasting 1.5-8 minutes followed by a 30 minute drying stage in air. The labeled data points give the ash moisture content at the end of the fog stage and prior to the onset of drying. As moisture levels rise above 2 wt-%, ammonia liberation becomes very rapid.

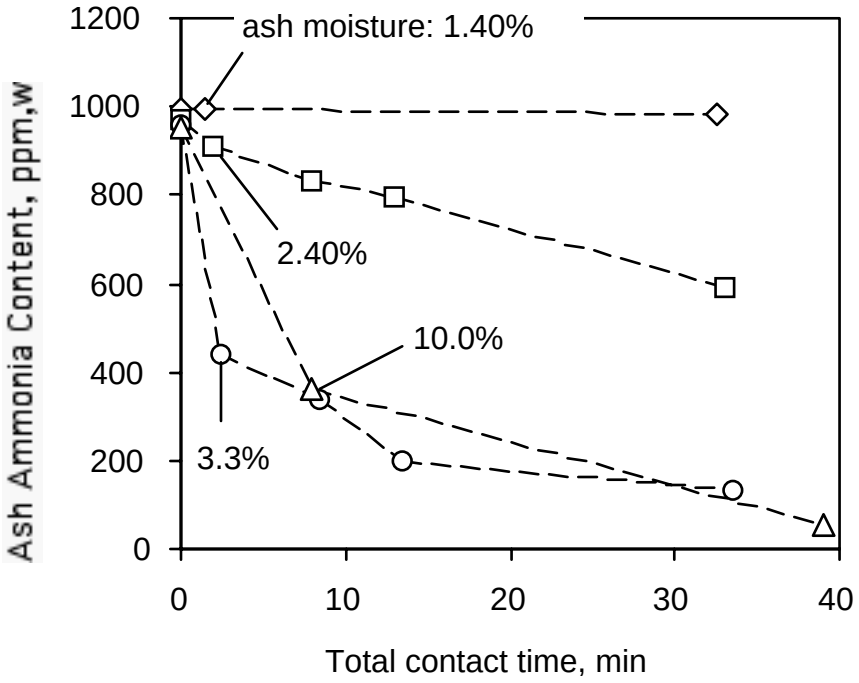


**Figure 6.17. Results of four time-resolved experiments on ammonia removal with flowing fog. The first data point corresponds to the end of fog addition and the beginning of the air drying stage. Sample: basic ash, FA1. The extent of moisture addition is varied by varying the total fog generation time from 2-8 minutes. Moisture-in-ash measurements are shown on graph at the end of the fog addition prior to the start of air drying.**

Adding 3.3 wt-% water in 2.5 minutes drives off half of the adsorbed ammonia with no drying time. Figure 6.18 shows the time resolved measurements of both ammonia and ash moisture in another flowing fog experiment. At moisture levels above 3 wt-%, ammonia removal is rapid, but the rate falls off quickly when moisture levels drop to about 2% during the subsequent drying stage. During the transfer of samples for measurement a strong ammonia odor was noticed when moisture contents were 3% or greater. These combined results show promise for practical processes involving rapid uniform addition of small amounts of moisture followed by limited air drying to achieve high levels of ammonia removal.

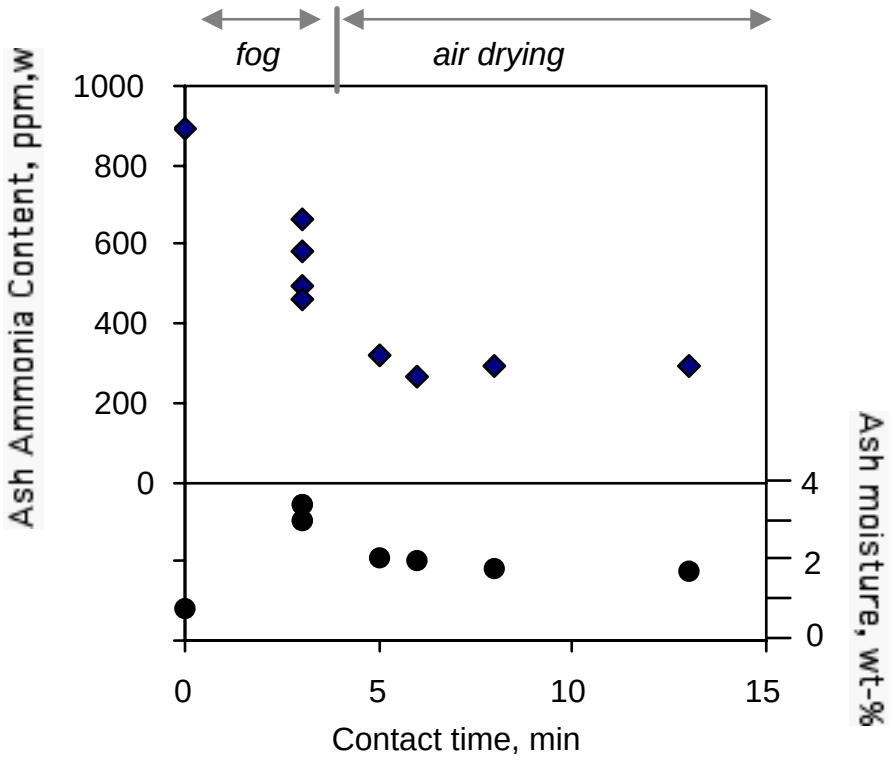


**Figure 6.18. Ammonia removal by flowing fog. Plot shows time resolved values of both ash moisture and ammonia content during fog addition and air drying. Multiple points at 3 minutes represent duplicate experiments.**

Flowing fog treatment produces rapid ammonia release, but was observed in separate experiments to be ineffective for acidic ashes, which represent a technologically important fly ash class. Several industrial patents (Gasiorowski and Hrach, 2000,Katsuya et al., 1996] and the results of Fig. 5.13 in static humid air suggest that acidic ashes can be successfully treated after introduction of inexpensive basic additives. Figure 6.19 and Table 6.3 confirm this behavior for the flowing fog treatment using NaOH solutions for fog generation (Table 6.3) or $Ca(OH)_2$ added as a dry powder to the ash.

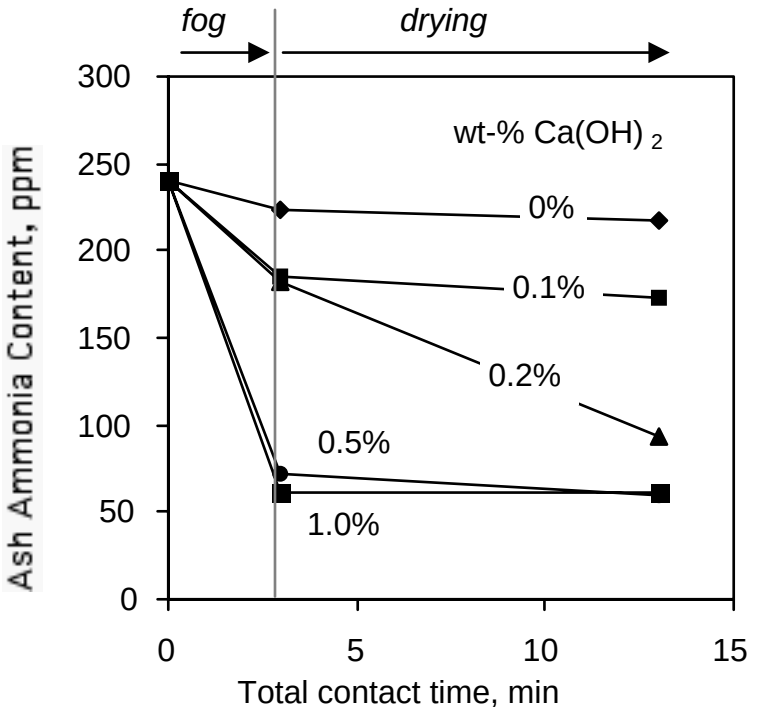


**Figure 6.19. Effect of dry $Ca(OH)_2$ as basic additive on ammonia removal from acidic ash (FA2) with flowing fog. Moisture levels in the ash were similar in the 5 experiments, ranging from 3.3% to 3.9% directly after fog addition, and ranging from 2.1% to 2.7% after drying.**

**Table 6.3. Results of ammonia removal with high-pH fog† from acidic Ash, FA2 (initial ammonia content 240 ppm).**

| Processing conditions | Ash properties after fog stage | | Ash properties after drying stage | |
|---|---|---|---|---|
| | *moisture (wt-%)* | *ammonia (ppm,w)* | *moisture (wt-%)* | *ammonia (ppm,w)* |
| 3 min fog / 10 min dry | 1.0 | 240 | 0.1 | 229 |
| 6 min fog / 10 min dry | 2.6 | 94 | 1.5 | 62 |
| 10 min fog / 10 min dry | 5.2 | 62 | 3.9 | 56 |

† 4 M NaOH solution

*Experiments with ozone*

Figure 6.20 shows the effect of ozonation on ammonia under dry conditions as a function of ozone concentration and temperature. Ozone reduces ash ammonia content under all conditions, but the truly significant reductions are observed at elevated concentration (2 vol-%) and temperature (150 $^{o}$C). The primary measurement in these experiments is residual ammonia on

ash, and thus the data do not directly distinguish between removal and destruction, although direct oxidative attack leading to destruction of on ammonia species is the most likely mechanism. The experiment in oxygen alone proves that gas stripping is not responsible for the loss of ammonia.

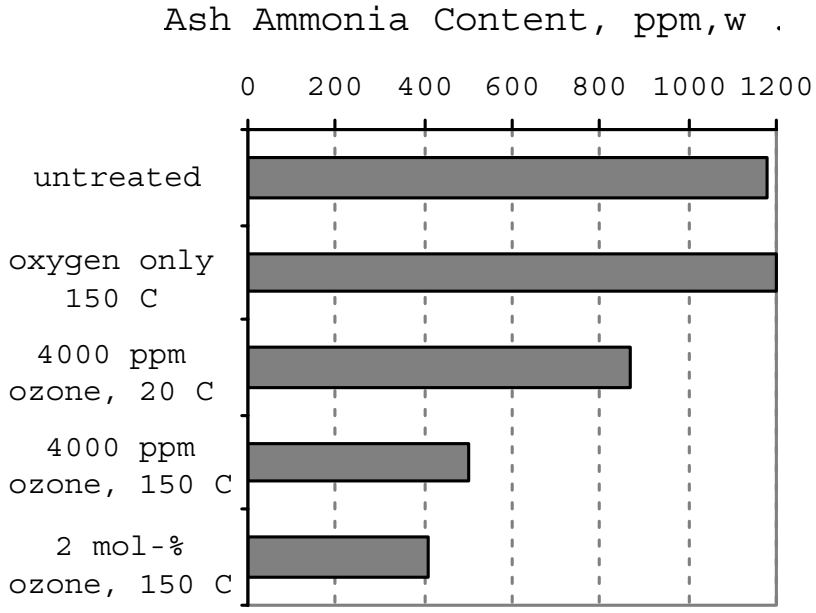


**Figure 6.20. Reduction in fly ash ammonia content by dry ozone treatment. Sample: 8 gm bed of basic fly ash, FA1. Flowrate: 2 lit/min ozone-containing oxygen; contact time: 30 minutes in each case, except the 2% case at 20°C for which the contact time was 60 min.**

The cumulative amount of ozone fed to the reactor in these Fig. 6.20 experiments ranged from 51 to 251 gm-ozone/kg ash and are factors of 4 to 21 higher than the minimum theoretical stoichiometric requirement for complete $NH_3$ oxidation to nitrate and water. This high ozone usage is likely due to kinetic limitations of the ozone / ammonia reaction, which has been previously studied in aqueous solution where it exhibits reaction times on the order of minutes or greater (Kuo et al. 1997, Singer and Zilli, 1975], and to competition from the ozone/carbon chemisorption reaction, which is fast (Gao et al., 2001]. The ozone/carbon chemisorption reaction is known to improve the air entrainment behavior of these high carbon ashes by reducing hydrophobic surface area (Gao et al., 2001], but here the reaction rapidly consumes ozone that would otherwise be available for ammonia destruction. The extent of ammonia removal/destruction by ozone increases with increasing temperature to 150 °C, further suggesting kinetic limitations for this reaction.

Several experiments were conducted to explore whether ozone has a beneficial effect during the drying stage of wet ammonia removal processes, which could eliminate the need for off-gas treatment. Figure 6.21 shows experiments in which 3 vol-% ozone was substituted for the drying air in the flowing fog experiment. This plot shows that the ammonia removal is sensitive to the moisture content directly after fog addition (as observed previously), and that ozone has no

substantial enhancing effect on ammonia release. It is likely that the release of ammonia from the liquid phase is too fast under these conditions to allow significant aqueous-phase reaction with ozone, which exhibits finite kinetics (Kuo et al. 1997, Singer and Zilli, 1975).

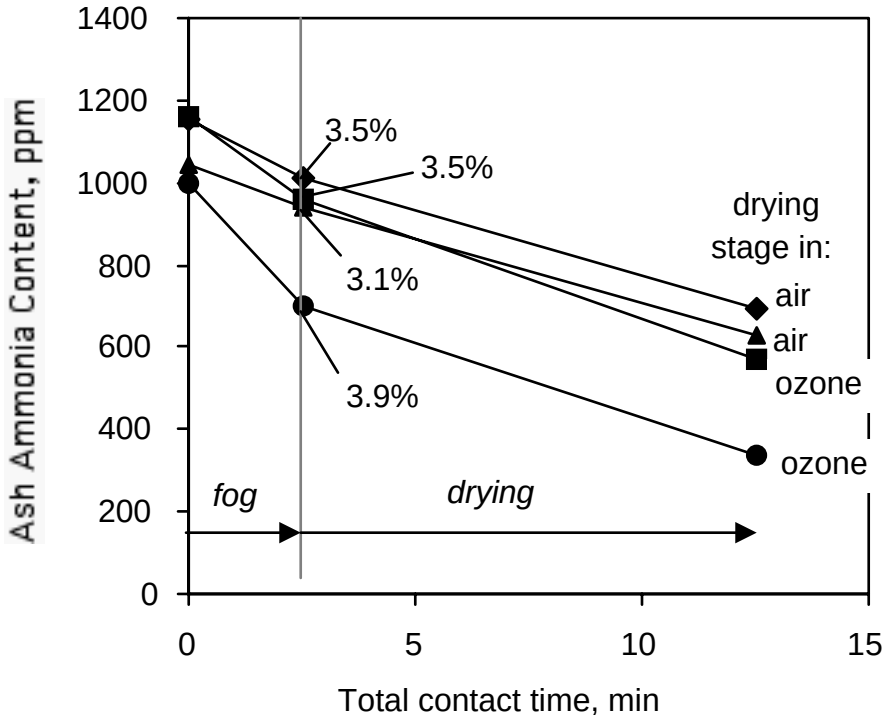


**Figure 6.21. Effect of ozone addition during the drying stage of ammonia removal. Sample: basic fly ash, FA1. The ozone containing stream was 3 vol-% ozone in air.**

In acidic ashes by contrast the ammonia species remain in solution where they may be available for aqueous oxidative attack. Figure 6.22 shows the effect of $H_2O_2$ and ozone as joint (peroxone) oxidizing agents during the semi-dry treatment of the acidic ash FA2 with flowing fog. Only modest reductions in ammonia are observed over a 60-minute treatment interval. Ammonia ozonation is heavily favored at equilibrium, so this result implies slow kinetics, again with likely competition from the ozone/carbon reaction. Peroxone oxidation is known to attack dissolved ammonia preferentially to ammonium ion, and the kinetics are thus sharply pH dependent (Kuo et al., 1997]. Under these conditions the peroxone kinetics are too slow to achieve substantial ammonia reductions, likely due to low concentrations of dissolved ammonia at the prevailing low pH. Perversely, at high pH ammonia is rapidly evolved as vapor, so effective peroxone destruction of ammonia would require careful control of pH at *intermediate* levels, if indeed it is possible at all in this system.

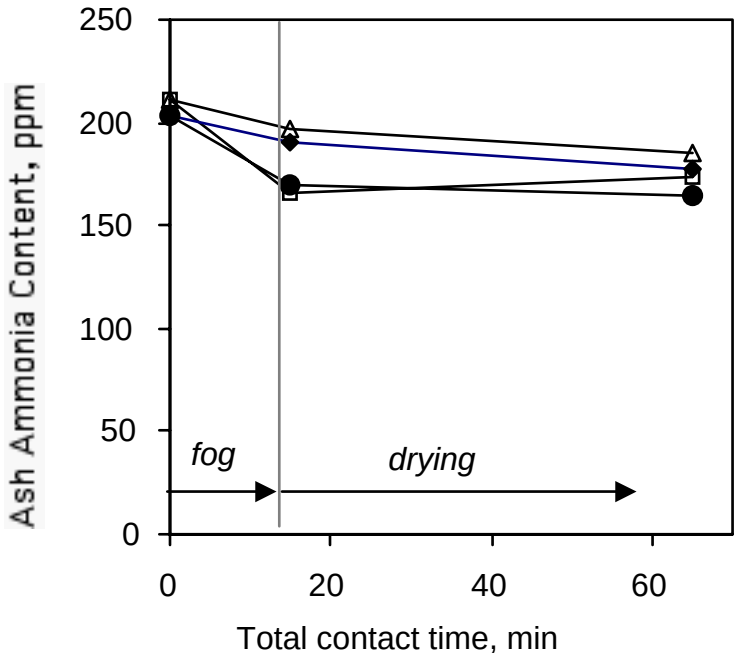


**Figure 6.22. Effect of $H_2O_2$ / $O_3$ fog on ammonia removal / destruction from acidic ash (FA2). Fog contained 30 wt-% $H_2O_2$ and was transported using 0.7 lit/min of 3% ozone in oxygen. The drying stage used 0.3 lit/min of 5% ozone in dry oxygen. Moisture levels in the ash were similar in the 2 experiments, ranging from 12.7% to 13.7% directly after fog addition, and from 6.1% to 7.2% after drying. Similar results were seen for 3 min fog addition, in which the initial ash moisture contents were 2.8-3%.**

## *6.4 Summary*

This work presents the first fundamental ammonia isotherms on carbon-containing fly ash samples obtained after a custom retrofit of a commercial vapor adsorption apparatus for compatibility with ammonia. Ammonia adsorption near room temperature is shown to be dominated by adsorption on carbon with only of order 20 ppm on the mineral component. The adsorption on carbon is a combination of physisorption and chemisorption on acidic surface sites. Introduction of additional oxygen functional groups on carbon increases ammonia adsorption by increasing the number of these acidic sites. The absolute amounts of ammonia adsorbed on fly ash in this study are much less than those of concern in the utility sector and much less than those found by Muzio in a study using simulated flue gas. Secondary components of the flue gas, either water, $SO_2$, or $SO_3$ are likely responsible for most of the ammonia observed associated with ash in utility practice, with a lesser component attributed to true adsorption on carbon surfaces.

This work also demonstrates that ammonia species can be removed from fly ash at or near room temperature by a variety of dry and semi-dry techniques. The work confirms industrial reports that aqueous solution chemistry takes place upon the introduction of even very small amounts of water, while the ash remains in a semi-dry state for handling. Rapid ammonia removal occurs from a microscopic water film on surfaces, in fine pores, and in ash particle interstitial regions whenever the film pH is high — achieved either by dissolution of the natural basic components of the ash or by the separate introduction of soluble basic additives. Flowing humid air and flowing water aerosol (fog) are promising methods for the uniform addition of small amounts of water to fly ash for semi-dry ammonia removal. Ozone is capable of destroying ammonia on ash in the dry state, but is less effective under semi-dry conditions due to kinetic limitations on the aqueous phase reaction at the lower pH values needed to keep ammonia in solution.

## *6.5 References*

Ashmore, P.G. *Catalysis and Inhibition of Chemical Reactions*, Butterworths, London, 1963.

Bittner, J.; Gasiorowski, S.; Hrach, F. *14th International Symposium on Management and Use of Coal Combustion Products*, **2001,** San Antonio, Electric Power Research Institute, Palo Alto, CA.

Brendel G.; Rathbone, R.; Frey, R. *14th International Symposium on Management and Use of Coal Combustion Products*, **2001** San Antonio, Electric Power Research Institute, Palo Alto, CA.

Bomchil, G, Harris, N., Leslie, M., Tabony, J., White, J.W., Gamlen, P.H., Thomas, R.K. and Treweren, T.D., *J. Chem. Soc. Faraday I, 75*, 1535 (1979).

Bridgeman, O.C., *J. Am Chem . Soc., 49*, 1174 (1927).

Castle, G.S.P. *IEEE Trans. Ind. App.* **1980**, *1A-16* 297-302.

Emmert, R.E. and Pigford, R.L. in *Perry's Chemical Engineer's Handbook, 4th Edition*, chapter 14, McGraw-Hill, 1963. This article cites Johnstone *I&EC, 27*, 587 (1935) and *30*, 101 (1938) as the source of the data.

Fujisaki, G., Sc.B. Honors Thesis, 2000; Division of Engineering, Brown University, Providence, RI.

Gao, Y.; Külaots, I.; Chen, X.; Aggarwal, R.; Mehta, A.; Suuberg, E. M.; Hurt, R. H. *Fuel* **2001**, *80* 765-768.

Garrido, J., Linares-Solano, A., Martin-Martinez, J.M., Molina-Sabio, M., Rodriguez-Reinoso, F., and Torregrosa, R., *Langmuir, 3,* 76 (1987).

Gasiorowski; S. A.; Hrach, F. J. Jr.; Frank J. U.S. Patent US1999000256128, issued June 20, 2000.

Gedeon, A.; Lassoued, A.; Bonardet, J.L.; Fraissard, J.; *Microporous and Mesoporous Materials,* **2001**, *44*, 801-806.

Giampa,V.M.; *14th International Symposium on Management and Use of Coal Combustion Products*, **2001**, San Antonio, Electric Power Research Institute, Palo Alto, CA.

Gregg, S.J. and Sing, K.S.W., *Adsorption, Surface Area and Porosity*, Academic Press, 1982.

Haar, L. and Gallagher, J.S., *J. Phys. Chem. Ref. Data*, *7*, 635 (1978).

Hinton, S.; "Investigation of Ammonia Adsorption on Fly Ash and Potential Impacts of Ammoniated Ash," EPRI Report, Palo Alto, CA 1999: TR-113777.

Holmes, J.M. and . Beebe, R.A., *Can. J. Chem., 35*, 1542 (1957).

Hwang, J.-Y.; "Method for Removal of Ammonia from Fly Ash," International Patent WO9948563A1, issued Sept. 30, 1999.

Janssen, F.; Van der Kerkof, F.; Lefers, J.; Lodder, P.; Luierweert, L. *Anal. Chim. Acta* **1986**, *190* 245-254.

Katsuya, M., Taisuke, S., Yukio K., Tamotsu, N., Japanese Patent JP8187484A "Deammonification Treatment of Coal Ash and Apparatus Therefore," issued July 23, 1996.

Kulaots, I. Ph.D. Dissertation, Division of Engineering, Brown University, 2001.

Golden, D.; *14th International Symposium on Management and Use of Coal Combustion Products*, **2001**, San Antonio, Electric Power Research Institute, Palo Alto, CA.

Kuo, C.; Yuan, F.; Hill D. *Ind. Eng. Chem. Res.* **1997**, *36* 4106-4113.

Larrimore, L. *EPRI Conference on the Effects of Coal Quality on Power Plant Management*, The Electric Power Research Institute, May 2000.

Levy, E., Huang, d., Herrea, C., *14th International Symposium on Management and Use of Coal Combustion Products*, **2001** San Antonio, Electric Power Research Institute, Palo Alto, CA.

Lowe, P. A.; Ellison, W. A.; Makansi, J. *Power* **1989**, 130 53-56.

Muzio, L. J.; Kim, E. N.; McVickar, M.; Quartucy, G. C.; McElroy, M.; Winegar, P. *Joint EPRI/EPA Symposium on Stationary Combustion NOx Control*, **1995**, Kansas City.

Novak, M.; Rych, H. G. *1989 Symposium on Stationary Combustion Nitrogen Oxide Control*, Electric Power Research Institute, Volume 2 pp. 7A-1 to 7A-26.

Necker, P.; *1989 Symposium on Stationary Combustion Nitrogen Oxide Control*, Electric Power Research Institute, Volume 2 pp. 6A-19 to 6A-38.

Ramme, B.; Fisher, B. *14th International Symposium on Management and Use of Coal Combustion Products*, **2001**, San Antonio, Electric Power Research Institute, Palo Alto, CA.

Rodriguez-Reinoso, F., Linares-Solano, A., *Chem. and Phys. Carbon, 21,* p1, Dekker, New York (1989).

Rubel, A.; Rathbone, R.; Stencel, J. *14th International Symposium on Management and Use of Coal Combustion Products*, **2001**, San Antonio, Electric Power Research Institute, Palo Alto, CA.

Sahu N.; Arora, M. K.; Upadhyay, S. N.; Sinha, A. S. K. *Ind. Eng. Chem. Res.* **1998**, *37* 4682-4688.

Sing, K.S.W. in *Porosity in Carbons*, J. W. Patrick, Ed., p. 49 Halstead Press, New York, 1995.

Singer, P. C.; Zilli, W. B. *Water Research* **1975**, *9* 127-134.

Spencer, W.B., Amberg, C.H. and Beebe, R.A., *J. Phys. Chem. 62*, 719 (1958).

Turner, J. R. "*Studies in Reaction Engineering of Nitrogen Oxides Abatement*" Doctoral thesis, Washington University, St. Louis, December 1993.

Turner, J. R.; Chone, S.; Dudukovic, M. P.; *Chemical Engineering Science*, **1994**, *49 24A* 4315-4325.

Wexler, A. S.; Seinfeld, J. H. *Atmospheric Environment*, **1991**, *25A* 2731.

Young, D.M. and Crowell, A.D. *Physical Adsorption of Gases*, Butterworths, London, 1962.

# 7. Conclusions

## *7.1 In-Furnace $NO_x$ Control*

Rich Reagent Injection (RRI) is a $NO_x$ reduction strategy that is based on injecting urea or anhydrous ammonia into fuel rich regions in the lower furnace. The ability of the RRI process to significantly reduce $NO_x$ emissions from a staged cyclone-fired furnace operating with overfire air was successfully demonstrated in two field tests of this technology.

- NOx reductions of 30% with less than 1-ppm ammonia slip were obtained with RRI under full load conditions (120 MWe, nameplate = 130 MW) in a three-barrel cyclone-fired furnace. RRI in combination with SNCR was found to yield up to 55% $NO_x$ reduction under full load conditions, to reduce $NO_x$ emissions from this unit to as low as 0.23 lb/MMBtu, with less than 5 ppm ammonia slip. Tests indicated that $NO_x$ reduction due to RRI and SNCR was nearly additive, i.e. SNCR performance did not appear to be negatively impacted by RRI.

- $NO_x$ reductions of approximately 30% with less than 1 ppm ammonia slip were obtained with RRI under full load conditions in a ten cyclone, 500 MW furnace. RRI was found to reduce $NO_x$ emissions from this unit to 0.27 lb/MMBtu from baseline levels (with OFA) of 0.38 lb/MMBtu using reagent flow rates corresponding to an NSR of approximately 3. It is expected that these emissions could be obtained with reduced reagent flow rates through optimization of individual injector flow rates. Modeling of this unit also suggests that NOx reductions could be improved through modification of FGR operation as well as through reduction of lower furnace stoichiometry. In particular, the modeling results indicate the combination of deeper staged conditions with RRI and SNCR would reduce $NO_x$ emissions to less than 0.15 lb/MBtu. Long term testing to evaluate deep cyclone barrel staging performed at this boiler (not part of this program) showed that staging to an average cyclone barrel SR of approximately 0.85-0.90 reduced full load $NO_x$ emissions (with OFA) to approximately 0.30 lb/MBtu. No significant detrimental boiler impacts of operation were observed under these staging conditions. No measurable change to unburned carbon in the fly ash or noticeable changes to slag tapping behavior were encountered. These observations are consistent with the CFD model predictions.

The field testing confirmed the CFD model predictions and demonstrated the importance of accurate CFD modeling to a successful RRI design. Based on the results of the testing of both the 130 MW and 500 MW units, the modeling predictions of $NO_x$ reduction, ammonia slip, and reagent usage were consistent with the field observations. The CFD modeling results have proven to be very reliable, and are considered essential to proper location and configuration of the injectors.

PC-fired boilers make up approximately 80% of the generating capacity associated with coal fired utility boilers. The potential payoff is quite large if RRI can be successfully demonstrated in a PC-fired boiler. To assess the performance of RRI in a PC-fired boiler a reduced mechanism $NO_x$ model was developed to account for the products of devolatilization and char oxidation and to handle $NO_x$ precursor species, such as HCN. The new reduced chemistry model compares

well with the detailed chemistry under both fuel lean and fuel rich conditions. Several PC units were modeled to evaluate the potential of RRI to reduce $NO_x$ in PC-fired boilers. Our work on RRI in cyclone furnaces demonstrated that RRI performance is very sensitive to the time, temperature and stoichiometry in the local gas field through which the reagent droplets travel. Hence, it is expected that different classes of boilers may require different approaches on how and where to inject the reagent. In general, RRI has the potential to significantly reduce $NO_x$ reduction in PC-fired furnaces. Considerable attention, however, has to be given to evaluating reagent injection and distribution in the furnace model prior to testing. If the reagent is not effectively targeted in the fuel rich region, no $NO_x$ reduction or significant $NO_x$ production can take place. The main conclusion is that RRI performance in PC units under staged conditions is very site specific.

The CFD modeling and field results from this program have demonstrated the potential benefits of RRI for an in-furnace NOx control. However, additional research is warranted. In particular, longer term studies are needed to evaluate RRI's performance under substoichiometric conditions over the wide range of normal operating conditions that occur in practice, including changes to load, level of air staging, cyclone barrel biasing, soot blowing cycles, etc. The life span of injectors and maintainability of injector materials under extreme lower furnace conditions also need to be evaluated.

## *7.2 Minimization of Impacts*

### *7.2.1 Waterwall Corrosion*

The goal of this task was to field test a novel multi-pronged approach for managing waterwall corrosion in coal-fired utility boilers. The overall objective of the test program was to evaluate a prototype multi-sensor, real-time, electrochemically-based instrumentation and on-line system for monitoring and managing corrosion in coal-fired utility boilers. The specific objectives included:

- Application of Computational Fluid Dynamic (CFD) software with state-of-the-art corrosion submodels to predict locations and approximate rates of corrosion within a boiler for a meaningful range of operating conditions.

- Development, testing and application of a multi-sensor technology utilizing electrochemical techniques for quantitative, real-time monitoring of waterwall corrosion in a coal-fired boiler.

- Application of an advanced precision metrology technique and inexpensive coupon-based technology to verify predicted and measured corrosion rates.

- Development of a methodology for combining predicted and measured data into corrosion management guidelines for a coal-fired boiler**.**

The importance of assessing wastage in real-time is that minor changes in boiler operation have the very real possibility to greatly reduce corrosion attack and thus improve boiler availability

and reduce maintenance costs and expensive waterwall replacements or weld overlay. This has become an increasingly important issue with the installation of low-$NO_x$ burner/OFA systems throughout the power industry. This task has demonstrated that corrosion can be measured accurately in real-time and, hence, waterwall wastage can be assessed immediately following changes in boiler operation. This capability can provide plant personnel the opportunity to optimize operations on a continuous basis in order to minimize tube wastage.

Recommendations for improving the corrosion instrumentation system described in this project include:

- Provide more rigorous and site-tailored installation specifications, including requirements for clean instrument air and reliable instrumentation power supplies for such equipment.

- Further refine the sensor design to improve temperature response and, where appropriate, avoid slag deposits, especially in boilers that are known to be susceptible to slagging in regions where sensors may be installed (though it should be noted that the service condition of the sensor should reflect accurately that of adjacent tubes and hence if a slag layer is generally present, the sensor should be similarly located beneath a slag layer in order that tube corrosion conditions are modeled appropriately).

- Develop an improved training scheme for on-site personnel with the objective of improving system supervision and collection of boiler operating data (i.e., data not supplied by the plant PI system such as fuel type, burners out of service, changes in air port settings, etc.).

- Obtain additional corrosion data and plant operating data to confirm correlation trends observed in this program.

As a means of further developing and testing the technology, REI is participating in three commercial projects during 2005-2006 where the corrosion instrumentation will be used to support short-term boiler tests. These projects will provide further knowledge of the system performance, the development of improved design and installation procedures, additional experience with multiple-sensor systems, and supplementary data for the correlation if CFD predictions with measured corrosion rates, boiler operating conditions, and combustion chemistry.

### *7.2.2 Soot Formation*

Low-$NO_x$ firing systems and combustion modifications, such as Over Fire Air (OFA), have been implemented by many US utilities to meet existing and impending restrictions on NOx emissions. In boilers with OFA system, part of the combustion air is introduced into the furnace above the firing zone, which is taken from the burner secondary air. By delaying mixing between fuel and air, lower furnace becomes sub-stoichiometric conditions that inhibit NOx production. However, a reducing environment within the boiler can result in significant concentrations of sub-micron soot particles. The potential impacts of soot include increases in fine particulate emissions and opacity, boiler heat imbalances due to enhanced lower furnace radiation, potential decrease in the effectiveness of air staging for NOx control, and ash salability. In addition, soot particles can deposit on the surface of heat transfer

device within a convective pass resulting in performance degradation. In this study we have implemented into REI's two phase combustion CFD code, *GLACIER*, an advanced soot model that utilizes Fletcher's chemical percolation devolatilization (CPD) model for tar and soot formation during pyrolysis and a semi-empirical model for soot oxidation and gasification. Computer simulations have been performed for the University of Utah 1.5Mw pilot-scale test facility and a full-scale coal fired utility boiler to evaluate the impact of burner and OFA operation on soot formation and destruction. Verification of the soot model was performed by comparing simulation results with soot measurements taken within the University of Utah 1.5Mw pilot-scale test furnace using a real-time monitoring Photoacoustic (PA) system.

Comparisons of the predicted and measured soot values for the pilot- scale test furnace and the results of our full scale boiler simulations highlight the potential impacts of burner operating conditions on soot and $NO_x$ generation within a coal fired utility boiler:

- An advanced soot model (tailored for coal combustion) implemented in *GLACIER* showed good agreement with the measurements in a pilot-scale application.

- The impact of burner stoichiometry and OFA location can be significant on soot formation/destruction as well as $NO_x$ emissions. Reducing condition formed by burner staging at the lower furnace will increase the formation of soot while limiting $NO_x$ generation.

- The results of full-scale application show limited mixing in the system can cause inefficient destruction of soot in the upper furnace even at high temperatures (> 1500 K) resulting in potential soot emission in flue gas.

- The level of detail provided by the simulations can be a valuable aid in understanding the mechanisms by which combustion modifications affect soot formation/destruction and $NO_x$ emissions.

## *7.3 SCR Catalyst Testing*

Vanadia supported on titania material represents the predominant commercial SCR catalyst used to reduce $NO_x$ from boilers burning coal or co-firing coal and biomass. The relatively rapid deactivation of the vanadia catalyst is a major problem encountered in practice, contributing to the operational costs for a SCR and to the difficulty of transferring successful SCR designs to new applications. Hence, a series of catalyst activity tests and surface chemistry investigations were designed and conducted on fresh commercial catalyst samples, commercial catalyst samples that had been exposed to boiler flue gas and laboratory prepared catalyst samples. The purpose of the tests was to investigate the reaction and deactivation mechanism of vanadia catalyst under coal and coal-biomass co-firing conditions. The results of the study suggest the following:

1. fouling, instead of poisoning, is the major deactivation mechanism for vanadia catalyst used in coal fired boiler applications;

2. sulfation of vanadia catalyst occurs on titiania sites, but not on vanadia sites;

3. sulfation enhances vanadia catalyst NO reduction activity by providing more active sites without changing the reaction activation energy;

4. Tungsten increases vanadia catalyst NO reduction activity by about 250%, due to the greatly increased number of active sites;

5. Alkali metals (K and Na) and alkaline earth metals (Ca) are poisons to vanadia catalyst. The deactivation occurs when poisons interact with active sites and decrease both the number and acidity of the active sites; and

6. results of the investigation into the effects of sulfation, tungsten, and poisons suggests:

    a) from an acid sites point of view, Brønsted acid sites are the active sites on vanadia catalyst;

    b) from a structure point of view, the results from NO adsorption comparisons on vanadia and sulfate samples suggests that the active sites are located at the edge, between the titania and vanadia sites;

The results from these tests will help to elucidate the reaction and deactivation mechanism of vanadia catalyst during SCR applications. In addition, the results will assist in developing better management of vanadia catalyst during use in SCRs, and lead to better methods to regenerate deactivated vanadia catalyst.

The deactivation of commercial SCR catalysts exposed to a flue gas was measured in two ways: (1) by direct measurement of the $NO_x$ composition of the flue gas before and after it flows through a catalyst in the slipstream reactor in the presence of ammonia; and (2) by laboratory evaluation of the catalysts after periodical removal from the slipstream reactor.

The average catalyst activity from $NO_x$ measurements taken at 750 hours of operation on flue gas was compared with average catalyst activity from $NO_x$ measurements taken at 3,800 hours of operation on flue gas. Activity measured from field data showed a general decline in catalyst activity over the test period.

Our data suggest that the mechanisms leading to SCR inactivity are, in order of significance,

1. channel plugging,
2. surface fouling,
3. pore plugging, and
4. poisoning.

In addition to these issues, surface sulfation increases activity. These data illustrate that the fresh catalyst activity initially increases (conversions increase) because of surface sulfation. In this particular sample, this increase is marginally significant, especially at the higher temperatures where conversion tends to be transport rather than kinetically limited.

With increased exposure, surface fouling and pore plugging become increasingly important. If the surface fouling layer is removed, the conversion/activity becomes intermediate between that of the fresh catalyst and that of the fully fouled material, in this case indicating surface fouling alone accounts for a about half of the activity change between 0 and 3800 hours. The other approximately half of the difference is associated with a combination of pore plugging and poisoning.

Activity can be effectively restored by physical cleaning of the catalyst, especially if physical cleaning includes both removal of the fouling layer and removal of pore plugging, the latter probably requiring a liquid treatment. Most of the current efforts for catalyst regeneration are focused on taking out the exposed catalyst and regenerating it with certain procedures, for example, washing with water or with sulfuric acid solution, followed by sulfation. These regeneration techniques can recover about 80 % of the original activity; however, they require an outage to remove catalyst and to re-install it after regeneration. Modifications of the vanadia catalyst, for instance, in terms of the mechanical aspects (as opposed to the chemical aspects), to extend catalyst lifetime and at the same time to reduce the requirement for post-SCR regeneration could increase SCR catalyst performance.

A first-order kinetic model was developed to predict NO reduction across commercial catalysts. The model took into account surface catalysis as well as diffusion along the length of the channels, through the porous catalyst and through a porous deposit of ash on the catalyst surface.

## *7.4 Ammonia Adsorption on Fly Ash*

In this task, the first fundamental ammonia isotherms on carbon-containing fly ash samples were obtained after a custom retrofit of a commercial vapor adsorption apparatus for compatibility with ammonia. Ammonia adsorption near room temperature was shown to be dominated by adsorption on carbon with only of order 20 ppm on the mineral component. The adsorption on carbon is a combination of physisorption and chemisorption on acidic surface sites. Introduction of additional oxygen functional groups on carbon increases ammonia adsorption by increasing the number of these acidic sites. The absolute amounts of ammonia adsorbed on fly ash in this study are much less than those of concern in the utility sector and much less than those found by Muzio in a study using simulated flue gas. Secondary components of the flue gas, either water, $SO_2$, or $SO_3$ are likely responsible for most of the ammonia observed associated with ash in utility practice, with a lesser component attributed to true adsorption on carbon surfaces.

The work in this task also demonstrated that ammonia species can be removed from fly ash at or near room temperature by a variety of dry and semi-dry techniques. The work confirms industrial reports that aqueous solution chemistry takes place upon the introduction of even very small amounts of water, while the ash remains in a semi-dry state for handling. Rapid ammonia removal occurs from a microscopic water film on surfaces, in fine pores, and in ash particle interstitial regions whenever the film pH is high — achieved either by dissolution of the natural basic components of the ash or by the separate introduction of soluble basic additives. Flowing humid air and flowing water aerosol (fog) are promising methods for the

uniform addition of small amounts of water to fly ash for semi-dry ammonia removal. Ozone is capable of destroying ammonia on ash in the dry state, but is less effective under semi-dry conditions due to kinetic limitations on the aqueous phase reaction at the lower pH values needed to keep ammonia in solution.

# Appendix A

### *Derivation of the Chen model*[1]

Figure A.1 schematically illustrates a two-dimensional reactor in which a reactant from the bulk flow is transported to a porous wall containing catalyst. The dimension in the direction of flow is $z$ and the dimension perpendicular to the low is $x$. The origin is taken from the reactor entrance at the center of the porous catalyst. If we assume Fickian diffusion, that the catalyst is isothermal and homogeneous and that the surface reaction is first order in reactant, that the flux in the flow direction is negligible compared to the flux in the direction perpendicular to the flow, and that bulk diffusion does not influence the conversion rate, then the flux at any point in the catalyst can be equated to the rate of reaction in the catalyst as follows, where the dependence of the mole fraction of reactant on both coordinate directions is emphasized.

$$cD_e \frac{d^2y}{dx^2} = h^2 k a c y(x,z) \qquad \text{(A-1)}$$

where $c$ represents gas concentration, $D_e$ represents the diffusivity of the reactant in the porous media, and $a$ represents a time-dependent and dimensionless activity factor, defined as the ratio of the chemical activity in the catalyst at arbitrary time divided by its initial value. The value of $a$ generally decreases from unity with chemical deactivation but could exceed unity because of catalyst activity increases caused, for example, by catalyst sulfation. Extensions of this model to accommodate surface fouling, bulk diffusion, and similar impacts will be discussed in the final report.

1 Chen, J.P. and Yang, R.T., Mechanism of Poisoning of the $V_2O_5/TiO_2$ Catalyst for the Reduction of NO by $NH_3$. *Journal of Catalysis* **1990**, 2, 411.

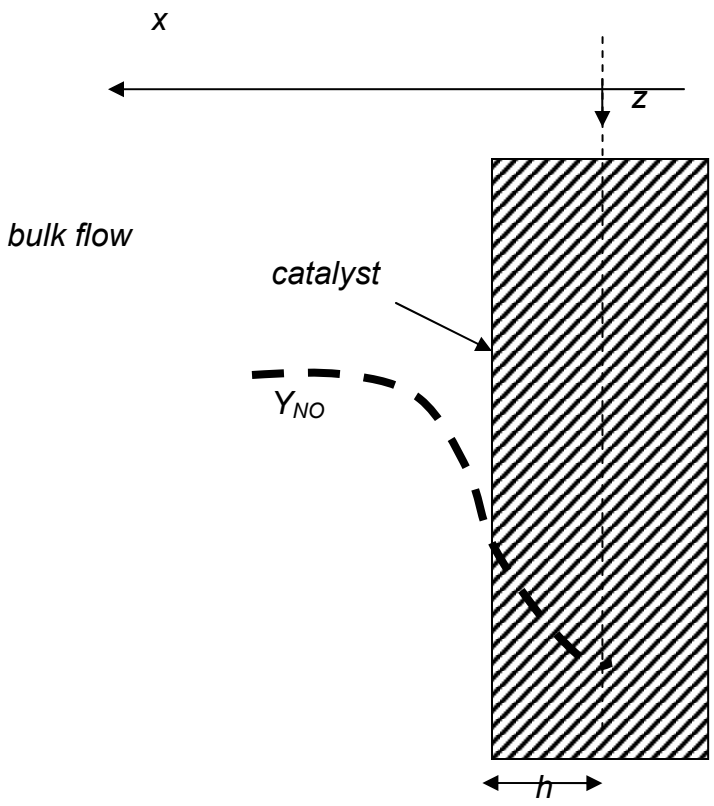


**Figure A.1. Schematic diagram of a two-dimensional reactor.**

This equation can be written in dimensionless form as follows:

$$\frac{d^2y'}{dx'^2} = \frac{h^2kay'}{D_e} \qquad \text{(A-2)}$$

where

$$x' = \frac{x}{h}$$

and

$$y' = \frac{y_{NO}}{y_{NO}^{\infty}}$$

are based on the half-thickness of the wall ($h$) and the bulk mole fraction in the cell ($y^{\infty}_{NO}$). The boundary conditions are:

$$y'\Big|_{x'=0} = 1 + Bi^{-1}\frac{dy'}{dx'} \qquad \text{(A-3)}$$

$$\left.\frac{dy'}{dx'}\right|_{x'=1} = 0$$

The solution gives the concentration profile within the wall:

$$y' = \frac{e^{\phi(x'-2)} + e^{-\phi x'}}{1 - e^{-2\phi} - \frac{\phi}{Bi}\left(e^{-2\phi} - 1\right)} \tag{A-4}$$

where

$$\phi^2 = \frac{h^2 ka}{D_e}$$

and

$$Bi = \frac{k_m h}{D_e}$$

This equation describes the relative impacts of film mass transfer, pore diffusion and surface reaction on conversion.

Considering the reactor, the mass balance along the axial direction of the reactor, $z$, is:

$$\frac{dy_{NO}^{\infty}}{dz} + \frac{k_m \sigma}{uA}\left(y_{NO}^{\infty} - y_{NO}^{s}\right) = 0 \tag{A-5}$$

where $u$ is the linear gas velocity in the cell which is assumed to be constant, $\sigma$ is the perimeter length of a cell in the monolith and $A$ is the cross-sectional area of a cell. The boundary condition is:

$$y_{NO}^{\infty}\Big|_{z=0} = y_{NO}^{\infty,0} \tag{A-6}$$

and the bulk and surface NO concentrations are related by:

$$y_{NO}^{\infty} = y_{NO}^{s}\left(1 - \frac{\phi}{Bi}\frac{e^{-2\phi} - 1}{e^{-2\phi} + 1}\right) \tag{A-7}$$

The overall conversion, $X$, of NO in the reactor at axial position $L$ is given by:

$$X = \frac{y_{NO}^{\infty,0} - y_{NO}^{NO,L}}{y_{NO}^{\infty,0}} \tag{A-8}$$

Combining these results, the NO conversion is given by:

$$X = 1 - \exp\left[-\frac{\sigma L}{uA\left(\frac{1}{k_m} - \frac{1}{\sqrt{D_e ka}}\frac{e^{-2\phi} + 1}{e^{-2\phi} - 1}\right)}\right] \tag{A-9}$$